Advances in drought analytical tools for better understanding of current and future climate change

Edited by
Ahmed Kenawy, Sergio M. Vicente-Serrano, Conor Murphy
and Luis Gimeno

Published in
Frontiers in Earth Science
Frontiers in Environmental Science

About Frontiers

Frontiers is more than just an open access publisher of scholarly articles: it is a pioneering approach to the world of academia, radically improving the way scholarly research is managed. The grand vision of Frontiers is a world where all people have an equal opportunity to seek, share and generate knowledge. Frontiers provides immediate and permanent online open access to all its publications, but this alone is not enough to realize our grand goals.

Frontiers journal series

The Frontiers journal series is a multi-tier and interdisciplinary set of open-access, online journals, promising a paradigm shift from the current review, selection and dissemination processes in academic publishing. All Frontiers journals are driven by researchers for researchers; therefore, they constitute a service to the scholarly community. At the same time, the *Frontiers journal series* operates on a revolutionary invention, the tiered publishing system, initially addressing specific communities of scholars, and gradually climbing up to broader public understanding, thus serving the interests of the lay society, too.

Dedication to quality

Each Frontiers article is a landmark of the highest quality, thanks to genuinely collaborative interactions between authors and review editors, who include some of the world's best academicians. Research must be certified by peers before entering a stream of knowledge that may eventually reach the public - and shape society; therefore, Frontiers only applies the most rigorous and unbiased reviews. Frontiers revolutionizes research publishing by freely delivering the most outstanding research, evaluated with no bias from both the academic and social point of view. By applying the most advanced information technologies, Frontiers is catapulting scholarly publishing into a new generation.

What are Frontiers Research Topics?

Frontiers Research Topics are very popular trademarks of the *Frontiers journals series*: they are collections of at least ten articles, all centered on a particular subject. With their unique mix of varied contributions from Original Research to Review Articles, Frontiers Research Topics unify the most influential researchers, the latest key findings and historical advances in a hot research area.

Find out more on how to host your own Frontiers Research Topic or contribute to one as an author by contacting the Frontiers editorial office: frontiersin.org/about/contact

Advances in drought analytical tools for better understanding of current and future climate change

Topic editors

Ahmed Kenawy — Mansoura University, Egypt

Sergio M. Vicente-Serrano — Spanish National Research Council (CSIC), Spain

Conor Murphy — Maynooth University, Ireland

Luis Gimeno — University of Vigo, Spain

The authors declare that the research was conducted in the absence of any commercial or financial relationships that could be construed as a potential conflict of interest

Table of contents

Editorial: Advances in drought analytical tools for better understanding of current and future climate change

Ahmed M. El Kenawy[1]*, Sergio M. Vicente-Serrano[2],
Conor Murphy[3] and Luis Gimeno[4]

[1]Department of Geography, Mansoura University, Mansoura, Egypt, [2]Instituto Pirenaico de Ecología (IPE-CSIC), Zaragoza, Spain, [3]Irish Climate Analysis and Research Units, Department of Geography, Maynooth University, County Kildare, Ireland, [4]Environmental Physics Laboratory (EPhysLab), Centro de Investigación Mariña, Universidade de Vigo, Campus da Auga, Ourense, Spain

Editorial on the Research Topic
Advances in drought analytical tools for better understanding of current and future climate change

When considering the effects on the economy, society, and environment, drought ranks near the top of the hydroclimatic hazards. Many social, economic, and ecological systems are negatively impacted by droughts, including water quality and supply, crop yield, biodiversity, aquatic, and riparian habitat quality, urban and industrial water supply, and hydropower generation. Accelerating urbanization and a warming planet only compound these impacts. As such, there is a growing need to enhance current knowledge of drought and develop more precise and timely forecasts of this phenomenon. Recently, more precise drought monitoring and analysis at various spatial and temporal scales have been made possible by high-resolution meteorological and satellite data and high-performance computing resources.

This Research Topic focuses on recent developments in understanding drought processes from local to global scales, and how these advances can improve current plans and strategies for reducing drought risks. Recent examples observed in different environments are introduced in this Research Topic, particularly in North America, Asia, and Africa, demonstrating the need for societal-level resilience initiatives to enhance drought preparedness and to accommodate the negative impacts of drought on natural systems and socioeconomic sectors. It is emphasized that strengthening resilience to drought risks is not an easy task; it calls for the confluence of many different drivers and processes. Also, different types of drought (e.g., meteorological, agricultural, hydrological, and socioeconomic), varying metrics, different assumptions, and interactions between natural and anthropogenic factors add to the complexity of drought resilience. It is noted that while drought is a global phenomenon, exacerbated by human-caused climate change due to increases in evapotranspiration and temperature, it is crucial to quantify drought risks on detailed spatial scales.

In ten articles with contributions from 45 authors, this Research Topic features novel and cutting-edge methods for describing, attributing, and forecasting drought events in

the context of both current and future climate conditions, together with related challenges and opportunities. In their global assessment of drought variability, Fuentes et al. employed a variety of drought, vegetation, and runoff indices to quantify the duration, severity, and intensity of drought across a wide range of Köppen climate types. They found that drought has a more immediate effect on water runoff and streamflow than on plant life. However, the duration and intensity of this response vary across large regions and over time. Their research reveals that droughts are getting worse and expanding across southern South America, Australia, and south-western Africa, having remarkable negative effects on vegetation and hydrology. The article by Yu et al. analyzed data from 47 weather stations on the Yunnan-Guizhou Plateau (YGP), China, to determine the spatio-temporal distribution and zonal patterns of drought across the region using the Standardized Precipitation Evapotranspiration Index (SPEI), the Mann-Kendall test, and principal component analysis (PCA). Drought characteristics (e.g., duration, severity, intensity, and frequency) exhibited strong zonal patterns, as indicated by a positive multivariate linear correlation with longitude, latitude, and elevation. Jansen et al. examined the effects of climate change on streamflow and urban water demand in North America and developed an empirical model to estimate municipal water shortage risks and quantify supply and demand forecast risks. Five global climate models were used to simulate 2080–2099 streamflow under two climate scenarios (RCP4. 5 and RCP8.5). The models were validated by comparing their simulations with municipal water consumption data from 47 North American cities. Finally, they identified water-scarce areas. In another paper, Huang et al. developed a Standardized Groundwater Index (SGI) to assess groundwater drought in Xuchang (China) from 1980 to 2018. In this study, Morlet's continuous complex wavelet transform was used to analyze groundwater drought cycles over multiple timescales and across different geographic areas. In the paper of Zheng et al., the role of climatic variables (e.g., precipitation, air temperature, and evaporative demand) in drought occurrence in the Luanhe River Basin (LRB), China, was quantified using deep learning techniques. The interplay between evaporative demand, solar radiation, and wind velocity was largely responsible for drought evolution. Moving to Iran, Band et al. assessed the severity and duration of the drought and investigated changes in the drought into the future in Semnan city. They examined the impact of differentiation operations on improving the static and modeling accuracy of the Standardized Precipitation Index (SPI) time series. The findings point to hybrid differentiation as providing the most reliable indication of stability. Also, Li et al. used the SPI, trend tests, Run Theory, Moran's I, and General G to evaluate meteorological drought in arid and semiarid regions of Northwest China from 1960 to 2018. Global Moran's I (GMI) suggests that drought is more

dispersed in winter and more damaging in summer and autumn. Afroz et al. conducted a systematic review to determine the relative importance of compound or concurrent extremes (CEs) hotspots, events, parameters (frequency and severity), large-scale drivers, and impacts (e.g., on yield loss and fire risk). This study summarized three CE analysis frameworks for drought- and heatwave-associated CEs: CE parameters (event-event), driver association (event-driver), and impacts (event-impact). They demonstrate that southern Africa, Australia, South America, and Southeast Asia are the most frequently reported hotspots of these CEs in global studies. Using the global outputs from the Lagrangian FLEXPART model, Stojanovic et al. conducted a case study over Ethiopia, pinpointing the primary sources of annual climatological moisture for 12 river basins. They identified major oceanic moisture sources (e.g., the Mediterranean Sea, Red Sea, and Indian Ocean), in addition to major terrestrial moisture sources (such as the Arabian Peninsula). The northeastern, southwestern, and western basins get the majority of their moisture from the African continent, while the southeastern basins get their water primarily from the Indian Ocean.

Overall, this Research Topic highlights advanced techniques used or developed to improve drought quantification under current and future climate conditions, outlining the main challenges and opportunities through case studies from different regions worldwide. Finally, we thank all authors and reviewers for their contributions to this Research Topic.

Author contributions

All authors listed have made a substantial, direct, and intellectual contribution to the work and approved it for publication.

Conflict of interest

The authors declare that the research was conducted in the absence of any commercial or financial relationships that could be construed as a potential conflict of interest.

Publisher's note

All claims expressed in this article are solely those of the authors and do not necessarily represent those of their affiliated organizations, or those of the publisher, the editors and the reviewers. Any product that may be evaluated in this article, or claim that may be made by its manufacturer, is not guaranteed or endorsed by the publisher.

Assessment of Future Risks of Seasonal Municipal Water Shortages Across North America

Joseph Janssen[1,2]*, Valentina Radić[1,2] and Ali Ameli[1,2]

[1]Department of Earth, Ocean and Atmospheric Sciences, University of British Columbia, Vancouver, BC, Canada,
[2]Institute of Applied Mathematics, University of British Columbia, Vancouver, BC, Canada

While anthropogenic climate change poses a risk to freshwater resources across the globe through increases in evapotranspiration and temperature, it is essential to quantify the risks at local scales in response to projected trends in both freshwater supply and demand. In this study, we use empirical modeling to estimate the risks of municipal water shortages across North America by assessing the effects of climate change on streamflow and urban water demand. In addition, we aim to quantify uncertainties in both supply and demand predictions. Using streamflow data from both the US and Canada, we first cluster 4,290 streamflow gauges based on hydrograph similarity and geographical location. We develop a set of multiple linear regression (MLR) models, as a simplified analog to a distributed hydrological model, with minimum input data requirements. These MLR models are calibrated to simulate streamflow for the 1993–2012 period using the ERA5 climate reanalysis data. The models are then used to predict streamflow for the 2080–2099 period in response to two climate scenarios (RCP4.5 and RCP8.5) from five global climate models. Another set of MLR models are constructed to project seasonal changes in municipal water consumption for the clustered domains. The models are calibrated against collected data on urban water use from 47 cities across the study region. For both streamflow and water use, we quantified uncertainties in our predictions using stochastic weather generators and Monte Carlo methods. Our study shows the strong predictive power of the MLR models for simulating both streamflow regimes (Kling-Gupta efficiency >0.5) and urban water use (correlation coefficient ≈0.7) in most regions. Under the RCP4.5 (RCP8.5) emissions scenario, the West Coast, the Southwest, and the Deep South (South-Central US and the Deep South) have the highest risk of municipal water shortages. Across the whole domain, the risk is the highest in the summer season when demand is high. We find that the uncertainty in projected changes to the water demand is substantially lower than the uncertainty in the projected changes to the supply. Regions with the highest risk of water shortages should begin to investigate mitigation and adaptation strategies.

Keywords: multivariate regression, North America, water supply, water demand, risk of municipal water shortage, streamflow

INTRODUCTION

Based on current climate projections, global mean temperature is likely to increase by at least 2°C, relative to the 1850s, by the end of the century (Forster et al., 2020). This warming will lead to unprecedented consequences for life on this planet including increased wildfire risk (Goss et al., 2020), decreased snowpack (Ashfaq et al., 2013), and decreased freshwater biodiversity (Reid et al., 2019). While every location on Earth is expected to experience increases in near-surface air temperature, ranging from a 1°C increase over oceans to over 5°C in higher latitude areas, the projected changes in precipitation are less certain and less spatially uniform (Hoegh-Guldberg et al., 2018). The projections of hydrologic drought and floods are consequently uncertain, while at the same time, highly costly in terms of their impact on property damage, food shortage, loss of jobs, and loss of lives (Howitt et al., 2015; Achakulwisut et al., 2018; Tellman et al., 2020). More accurate predictions of these extreme events can lead to better mitigation and adaptation procedures, such as green infrastructure, placing restrictions on water consumption, moving water in above-ground reservoirs to below-ground aquifers, or investing in technologies that could improve water use efficiency (Tanaka et al., 2006; Mei et al., 2018; Yang and Liu, 2020).

As anthropogenic climate change progresses and populations across North America continue to grow, freshwater resources on the continent may experience more strain. The United States (US) and Canada use the most water per capita (>1,000 cubic meters per person per year) compared to other G8 countries (100–900 cubic meters per person per year) (Ritchie and Roser, 2017). Despite the use of less than 20% of their available water resources every year, freshwater resources and potential vulnerability to water shortages are non-uniformly distributed throughout the continent (Rosegrant and Cai, 2002). Such shortages will act as a vulnerability multiplier leading to socioeconomic and physical health deterioration in groups such as migrants, poor families in urban areas, and farmers (Sugg et al., 2020). The Canadian Prairies are known to have been vulnerable to historical hydrologic droughts, although few assessments of drought risk across Canada have been made to date (MacDonald et al., 2008; Bonsal et al., 2011). In the US, the regions most severely hit by recent droughts include the Central US (Basara et al., 2019), California (Howitt et al., 2015), as well as the relatively wet areas in the US South (Chen et al., 2012). Further droughts in these areas as well as more widespread droughts throughout North America may come as a result of declining summer precipitation in the latter half of the 21st century, warming Pacific and North Atlantic Oceans, and escalating climate variability (Rosegrant and Cai, 2002; MacDonald et al., 2008; Schwalm et al., 2012). Droughts, however, are not the only climate pattern of concern. Snow is crucial in the western United States for sustaining water demand, thus decreasing snowpack as a result of increasing temperatures threatens water sustainability, though uncertainties remain large (Mankin et al., 2015).

Risk of freshwater shortage is measured in a variety of ways (Rosegrant and Cai, 2002; Foti et al., 2012; Dickson and Dzombak, 2019). For example, Foti et al. (2012) defined shortage risk as the difference between water supply and demand, or more specifically, as a probability for crossing the critical threshold when water demand exceeds supply. Different types of process-based or mechanistic models (e.g., Chien and Knouft, 2013; Mahat et al., 2017) and statistical or purely data-driven models (e.g., Barbarossa et al., 2017; Mendoza et al., 2017; Brunner et al., 2020) have been used to project changes in water supply and water demand globally and in North America. Mechanistic models are efficient tools for prediction of water supply and demand in regions where a wide range of data on climatic, landscape, and socioeconomic and demographic attributes are available. Despite great progress being made on developing advanced mechanistic models (Chen et al., 2017), the application of these models in ungauged watersheds, which cover more than 90% of lands globally and across North America, is unpractical due to poor data availability required for building such models (Blöschl et al., 2013). Statistical models, on the other hand, have become known as simple and fast tools for providing general insights on the estimation and forecast of water supply and demand with minimum data requirements. For example, simple regression techniques have been used to relate physical and climate characteristics to hydrological signatures such as flow duration curves and low flow statistics (Jehn et al., 2020). While statistical models are limited in their interpretation of causality among variables and rely on assumptions that cannot be adequately tested, these simple models are widely used to provide a general picture of ungauged watersheds' responses to climate change (Besaw et al., 2010; Razavi and Coulibaly, 2013; Saadi et al., 2019), and informing water resources planning and management. Further, regression models can capture implicit relationships between runoff and explanatory variables for which there is no theoretical explanation due to the co-evolution of climate, geology, and topography (Blöschl et al., 2013).

Most assessments of water supply and demand management focused on local areas across North America and only study either supply or demand with regression or physically based models (Balling and Gober, 2007; Breyer and Chang, 2014; Shamir et al., 2015; Byun et al., 2019). Foti et al. (2012), however, provided a comprehensive risk assessment of water shortages for the contiguous US using regression and physically based models. They projected annual water supply and consumption in response to changes in temperature and precipitation from three Global Climate Models (GCMs). Areas such as Central California, Utah, Arizona, and Central US were found to be most vulnerable to water shortages. A more recent assessment of future changes in streamflow regimes across the US found that the changes are expected to be most pronounced for currently melt-dominated regimes in the Rocky Mountains (Brunner et al., 2020). While five GCMs were used in the study, very little agreement was found among the GCM projections, pointing to a relatively large uncertainty caused by the choice of GCMs. In terms of changes to water consumption across the US, negligible changes were found when the projections were based solely on population growth, income growth, and changes in water-use efficiency, i.e., without accounting for climate change (Rosegrant and Cai, 2002; Foti et al., 2012). With climate change remaining a factor, however,

water consumption was projected to substantially increase, mainly due to expected increases in agricultural and landscape irrigation in response to rising potential evapotranspiration (Foti et al., 2012; Brown et al., 2013).

As the population and suburb-centered development continue to grow in North America, many municipalities in arid and semi-arid regions are acquiring water rights from agriculture in anticipation of an uptick in municipal water demand (MacDonald, 2010; Sabo et al., 2010; Maas et al., 2017). The percent of water demand used for domestic purposes is set to increase, thus the transfer of water resources from agricultural to municipal use represents an additional stressor for rural sustainability and food security (Rosegrant and Cai, 2002). Thus, changes in municipal water use in response to climatic and non-climatic factors are expected to have implications for regional water consumption as a whole. In the US, residential water use accounts for ~60% of municipal water use (Dieter et al., 2018), with 22–65% of the residential water use coming from outdoor water use (DeOreo et al., 2016), which is shown to be highly sensitive to changes in weather and climate (Gober et al., 2016). This high sensitivity of outdoor water use to climatic drivers has triggered the use of regression models to predict the water consumption based on a combination of weather predictors, such as air temperature, wind speed, precipitation, and evapotranspiration (Wong et al., 2010; Adamowski et al., 2012; Bakker et al., 2014; Chang et al., 2014). The models have revealed a high spatial heterogeneity in the sensitivity of municipal water consumption to changes in these predictors (Opalinski et al., 2020). Maximum daily temperature was found to be the predictor with the most explanatory power across the region, with stronger predictive power in dry regions (Opalinski et al., 2020). In the same study, dry regions were found to have greater seasonality in municipal water use perhaps due to increased seasonal climate variability, with the peak use in summer when there is an increased need for irrigation of the exciting green urban landscapes.

Knowledge on the risks of municipal water shortages is essential to inform science-based strategies and decision-making tools for water security (Byun et al., 2019; Dilling et al., 2019; Özerol et al., 2020). Current research has focused on forecasting the magnitude and seasonality of water supply (e.g., Chien and Knouft, 2013; Demaria et al., 2016; Mahat et al., 2017; Byun et al., 2019; Brunner et al., 2020) as well as magnitude of water demand (e.g., Ruth et al., 2007; DeOreo et al., 2016; Maas et al., 2017; Opalinski et al., 2020; Rasifaghihi et al., 2020). However, the magnitude and seasonality of water shortages, as a combined effect of water supply and water demand, are still relatively poorly characterized and forecasted in most parts of the globe including North America. Additionally, the forecast of water shortages, similar to other types of forecasts in environmental science, is prone to a wide range of uncertainties, which are generally challenging and difficult to quantify. Such uncertainties are mainly stemmed from uncertainties in time-varying climatic attributes (Katz, 2002), uncertainties associated with more static physical attributes of watersheds such as geology, land cover, and soil (Nilsson

et al., 2007; Addor et al., 2017), and uncertainties corresponding to future population growth and water use (Yang et al., 2016; Hart and Halden, 2019; Keilman, 2020). Furthermore, the more complex the modelling framework is, often relying on heavily calibrated mechanistic models of water supply and demand, the more difficult it is to track and quantify its sources of uncertainties (e.g., Foti et al., 2012). On the other hand, simple statistical models with low degrees of freedom present more readily available tools for quantifying these uncertainties. Characterizing and quantifying the risks of future seasonal water shortages, and their associated uncertainties, with the use of simple statistical models were the main motivations of this study.

This study has two main goals: 1) to investigate the use of simple statistical models, based on widely available climatic data, in simulating present and future (end of the 21st century) water shortages under a changing climate across North America (US and Canada); and 2) to assess uncertainties in the projections of water shortages originating from the uncertainties in climate scenarios from the ensemble of GCMs. To address goal 1), multivariate regression models for both supply and demand are developed and calibrated with daily time series of streamflow from river stations and daily time series of municipal water consumption from cities across the region. The models are forced by state-of-the-art climate reanalysis data representing the present climate and weather attributes (e.g., temperature, precipitation, windspeed, evapotranspiration, and rainfall/snowfall characteristics), while the future climate is represented by two emission scenarios from the ensemble of five GCMs. To address goal 2), we use stochastic weather generators as it is one of the recommended methods for estimating uncertainties in climate change projections (Katz, 2002) and in hydrological forecasting (e.g., Caron et al., 2008; Breinl, 2016). By combining the projections of water supply and demand, we aim to provide a spatial pattern of seasonal municipal water shortage risks, together with estimated credibility in these risks across the whole region.

DATA

Streamflow Data

Observations of daily streamflow for Canada are collected from the National Water Data Archive (Water Survey of Canada, 2019), while observations for the US are collected from the United States Geological Survey (USGS) surface-water data for the nation website (US Geological Survey, 2019). Only daily time series that have no missing data from Jan 1, 1993 to Dec 31, 2012 are considered in the analysis, which left 4,290 gauges in total, with 584 gauges in Canada and 3,706 in the US.

Climate Data
Present Climate
Surface weather data for the historical record is extracted from the ERA5 climate reanalysis (0.25 × 0.25, hourly) dataset (Copernicus Climate Change Service Climate Data Store, 2017), for the period

TABLE 1 | Characteristics of the five GCMs used in this study for future forecasts.

Model name	Modeling center	Country of origin	Spatial resolution (Lat × Lon)
GFDL-CM3	Geophysical Fluid Dynamics Laboratory	United States	2° × 2.5°
HadGEM2-ES	Met Office Hadley Centre	United Kingdom	1.25° × 1.875°
INM-CM4	Institute for Numerical Mathematics	Russia	1.5° × 2°
IPSL-CM5A-MR	Institut Pierre-Simon Laplace	France	1.2676° × 2.5°
CSIRO-Mk3.6.0	Commonwealth Scientific and Industrial Research Organization	Australia	1.8653° × 1.875°

1993–2012. Hourly time series of total precipitation, wind speed, air temperature, dewpoint temperature, and incoming solar radiation are extracted. Dewpoint temperature and air temperature are used to estimate relative humidity with the August-Roche-Magnus approximation (Lawrence, 2005). Cubic inverse distance weighting interpolation is performed to obtain a single time series of each weather variable at each streamflow station. Interpolated precipitation totals that are below 1 mm are set to 0 mm following (Islam and Cartwright, 2020) and (Tian et al., 2009). Evapotranspiration is calculated from the Penman-Monteith equations, as outlined by (Walter et al., 2000) using maximum and minimum air temperature, maximum and minimum relative humidity, wind speed, and incoming solar radiation at the surface. Hourly time series of total precipitation, wind speed, and air temperature at the surface are also extracted at the grid square closest to each city with water consumption data.

Future Climate

Future climate scenarios are obtained from five GCMs from Coupled Model Intercomparison Project phase five [CMIP5, **Table 1**, (Taylor et al., 2012)], henceforward abbreviated as: GFDL-CM3, HadGEM2-ES, INM-CM4, IPSL-CM5A-MR, and CSIRO-Mk3.6.0. The data is downloaded from the Lawrence Livermore National Laboratory's World Climate Research Programme database powered by the Earth System Grid Federation (Taylor et al., 2012; Cinquini et al., 2014). The five models are selected as they have the required variables in the desired time period and their current or earlier versions have been shown to have better performance relative to other CMIP5 models in simulating the past climate over North America (Radić and Clarke, 2011). The following variables are extracted as daily time series for each GCM: maximum and minimum air temperature, maximum and minimum relative humidity, wind speed, incoming solar radiation at surface, and total precipitation. For the projection period (2080–2099), we retrieved GCM data for two selected emission scenarios, referred to as Representative Concentration Pathways (RCPs; Moss et al., 2010): RCP4.5 and RCP8.5. The different scenarios indicate different amounts of radiative forcing by 2100, where RCP4.5 (RCP8.5) indicates 4.5 W/m^2 (8.5 W/m^2). The RCP4.5 emissions scenario is considered a medium stabilization emissions scenario and RCP8.5 is considered a high emissions scenario (Van Vuuren et al., 2011). To obtain the continuous GCM data for 1993–2012 for bias correcting, we use GCM historical runs from 1993 to 2005 and their RCP4.5 and RCP8.5 runs from 2006 to 2012. Evapotranspiration is calculated using GCM data from the Penman-Monteith equations as done with the reanalysis data.

For evapotranspiration, the bias between the present-climate GCM and ERA5 is corrected according to the quantile mismatches within the simulated cumulative distribution function (CDF) using the empirical quantile matching algorithm (Xu, 2015). This method has been shown to outperform other bias correction algorithms when the distribution of a climate variable is unknown or not gamma (Teutschbein and Seibert, 2012; Chen et al., 2013). For precipitation, the bias is corrected using the gamma quantile mismatch between ERA5 and each GCM, with a precipitation threshold of 1 mm, following the method in Xu (2015). Several studies have shown that the gamma quantile matching is one of the better methods for precipitation bias correction (Chen et al., 2013; Lafon et al., 2013).

Water Use and Population Data

To our knowledge, there is no database of daily municipal water use for cities across North America. To collect daily and monthly time series, we directly contacted municipalities. Each time series is at least 3 years in length from the period 1990–2018. We initially collected the data from 55 cities. The datasets from the cities that have strict water consumption laws, large population increases during summer months, or are not continuous or near continuous (missing data with valid observations for previous and subsequent entries) were removed. The gaps in the data are filled with estimates based on linear interpolation, resulting in a set of daily time series of continuous municipal water use for 38 cities and monthly time series of continuous municipal water use for nine cities for a total of 47 cities (**Figure 1B**). Though the data has high day-to-day variability which may cause the gap filling to be inaccurate, the gap filling causes little change in the results due to its rareness and the data smoothing applied later. Monthly datasets are converted to daily datasets by using the monthly value for each day within the month.

For each city, we also downloaded its population estimates from the US (United States Census Bureau, 2019) or Canadian (Statistics Canada, 2019a) Census datasets for 1990–2018. Since the datasets provide yearly population estimates, we used a piecewise linear interpolation to derive daily population estimates. County location data is derived from Hauer (2019) and Ramey (2014) for US counties, and Statistics Canada (2019) for Canadian census divisions (Canadian county equivalent). A total of 3,425 counties or county equivalents were used, with 293 coming from Canada and 3,132 from the US.

FIGURE 1 | Map of localities with **(A)** streamflow data (4,290 gauges), and **(B)** water consumption data (47 cities). In **(A)** each station dot is colored according to the cluster it belongs to (see *Clustering* section). In **(B)** blue and red indicate daily and monthly data, respectively. Some of the city officials asked to keep their cities anonymous, so this map is meant to keep the city names anonymous while showing the spatial extent of the data.

METHODS

Our overall methodology can be summarized in the following steps: first, we partition the study region into clusters based on similarity in the observed seasonal streamflow and proximity. Second, multiple linear regression (MLR) models, with climate predictors from the ERA5 reanalysis dataset, are calibrated at each river station in order to simulate its seasonal streamflow throughout the 1993–2012 period. Each MLR model is then used to predict the seasonal streamflow regime for 2080–2099 at each station. To do so, the models are forced by stochastically generated downscaled climate scenarios from an ensemble of five GCMs. Third, the same climate data (ERA5) is used to calibrate a set of MLR models to simulate the seasonality in municipal water consumption over the present climate for each of the 47 cities. The locally optimized regression coefficients from the 47 cities are then statistically upscaled to represent the coefficients for each county in the US and Canada. Future changes in seasonal municipal water consumption are then simulated for each county based on the stochastically generated GCM projections. Finally, we aggregate the changes in water supply and demand and assess the risk of water shortages for each region and each season. Seasons are separated into winter (December, January, and February—DJF), spring (March, April, and May—MAM), summer (June, July, and August - JJA), and Fall (September, October, and November—SON).

Clustering

While it is common to partition a large region into smaller domains in order to summarize the results of regional

hydrological modelling, there is no consensus on how to define these subregions through clustering (Sawicz et al., 2011). The US Water Resources Council, for example, clustered regions and subregions based on topography, which is the method that has been adopted in assessments of water shortages across the US (e.g., Foti et al., 2012; Mahat et al., 2017). Another common clustering method in hydrological studies is based on climate classification (e.g., Opalinski et al., 2020), or on a combined set of climate and streamflow indices (e.g., Sawicz et al., 2011).

As the objective of our paper is to predict seasonality of water shortage and its uncertainty, we chose to partition the study region into clusters on the basis of similarity in streamflow seasonality or regime curves [similar to Brunner et al. (2020)]. For each stream gauge, we derive the average observed streamflow regime over the 20-year current period for each station. The regime curve consists of 366 days in order to account for the measurements during leap years. For non-leap years, the average value from Feb 28 and March 1 is used to fill in for Feb 29. The regime curve of each station is standardized by subtracting it by its mean and dividing it by its standard deviation such that the clustering can focus on regime curve shape similarity rather than on absolute values. We use hierarchical clustering with Ward's algorithm (Ward, 1963), and we determine the optimal number of clusters by trial-and-error in a manner similar to (Knoben et al., 2018). The resulting clusters are then visually inspected on the map in order to further manually partition the clusters whose gauges lie in multiple distinct geographical areas. For example, streamflow regimes in the Pacific and South Atlantic regions were

FIGURE 2 | Workflow of methods for making predictions for each streamflow station and each window. Boxes indicate data matrices of streamflow (Q), precipitation (P), evapotranspiration (E), or snow days (N). Each row of data represents a single year, and each column indicates a different day.
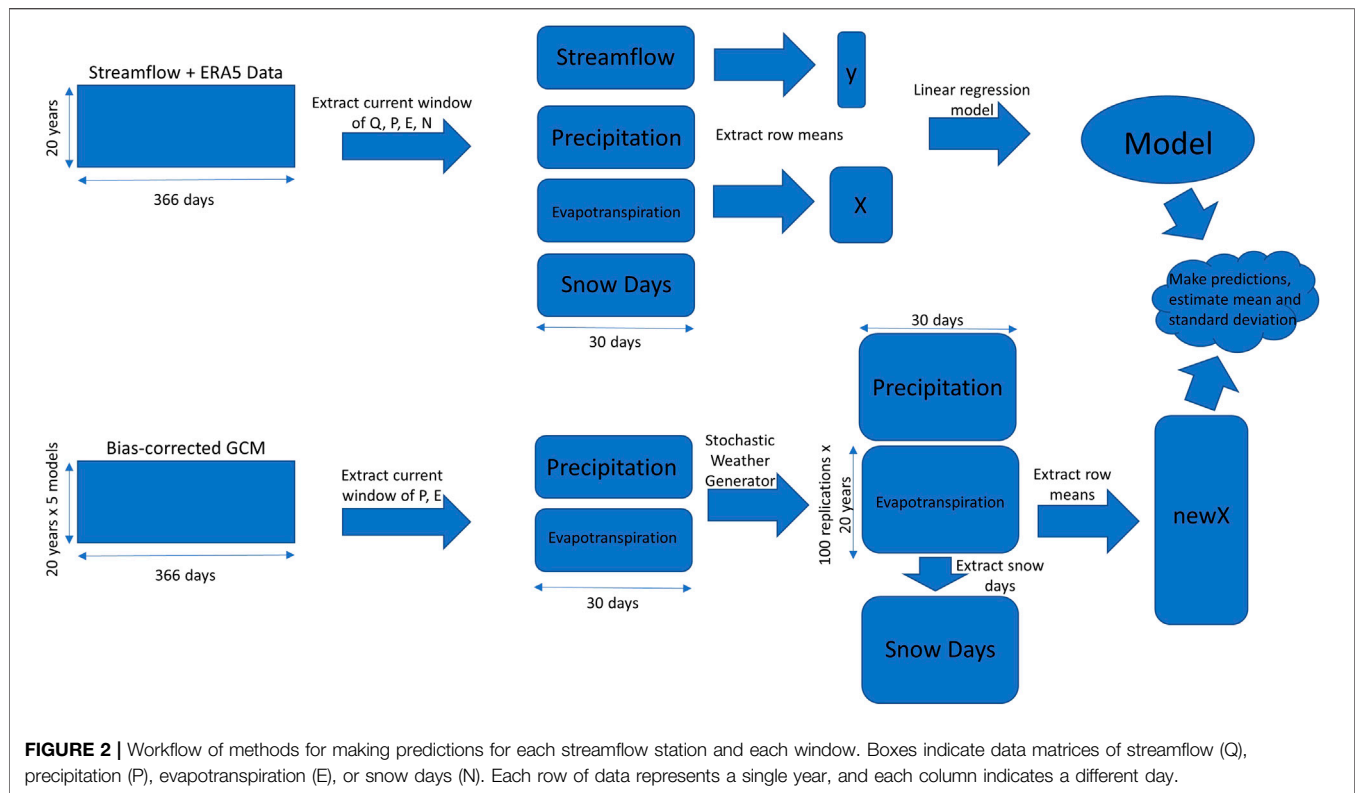
initially clustered together due to their similar streamflow regimes but were subsequently separated due to their distinct geographical locations. Stations that belong to a streamflow-regime cluster, but are located far outside the cluster's perimeter, are removed as "outliers". Similar to Ivancic and Shaw (2017), we hypothesize that these spatially isolated outliers are present due to significant human impact on the streamflow. Following the steps above, we partitioned the study region into 14 clusters or sub-regions (**Figure 1A**). The 4,290 original gauges are reduced to 3,852 due to the removal of outliers.

Streamflow Model
The MLR models are developed to predict the inter-annual variability of streamflow for each gauge using local weather. The MLR models are applied to the averaged streamflow and averaged climate variables (ERA5) using a 30-day moving window. In this way, the model is calibrated across the 20-year present period in order to simulate an average value for the same 30-day window (e.g., Jan 1 to Jan 30, Jan 2 to Jan 31, etc . . .) in each year and for each station. For each region, we validate the model using a validation set of the last 3 years. To obtain the streamflow projections at each station, the model is forced with stochastically generated downscaled climate variables from the ensemble of five GCMs. A well-known limiting assumption of most stationary models is that the model developed over the present climate is assumed valid under future climate conditions (e.g., Ekström et al., 2015). This assumption can be considered acceptable for multiple regression models as long as the variability in present variables (e.g., temperature, precipitation, streamflow)

is within the range of their variability in the future period. While the constant variance of the response would be difficult to verify due to the possible non-stationarity and the uncertainty of hydrological conditions over such timescales, we may assume each observation is independent as the observations are separated by a full year such that longer processes including snowmelt and groundwater flow will not affect adjacent years. Below, we provide details on the data smoothing procedure, calibration and validation of the model, and the simulations of future streamflow regimes (**Figure 2**).

Data Smoothing
For each station, we apply the MLR models using a selection of weather variables from ERA5 as predictors and streamflow data as the response. Prior to the model application, we apply smoothing to both predictor and response data in the following way: 30-day moving average is applied to the whole daily time series (1993–2012), where the first window spans from 1 Jan to 30 Jan, and the last window spans from 31 Dec to 29 Jan of the following year.

Calibration and Validation
The MLR models are applied for each of the 366 windows separately, so that the regression is calculated across the 20 (19) points, where each point represents the average value within the current window for the given year. The first model is applied to the first window (1 Jan) across all the years (1993–2012), the second model is applied to the second window (2 Jan) across all the years, etc. In this way, we derive

366 MLR models in total, each one with its own regression coefficients. The following variables are used as predictors: average daily precipitation (*P* units in mm), average daily evapotranspiration (*ET*, units in mm) and total number of days with snowfall (*N*), where *P* and *ET* are derived as the mean over the 30-day moving window, while *N* is calculated as the sum of days with snowfall >1 mm over the same window. We assume that when evapotranspiration is ≤0, temperature is below or equal to 0°C; consequently, a wet day when evapotranspiration is 0 indicates a snow day. For each window, the modelled streamflow ($Q_{i,j}$) (m^3/s) is derived from the MLR model with optimized regression coefficients (least squares method) as:

$$Q_{i,j} = a_{0,i,j} + a_{1,i,j}P_{i,j} + a_{2,i,j}ET_{i,j} + a_{3,i,j}N_{i,j} + \varepsilon_{i,j} \qquad (1)$$

where $a_{0,i,j}$–$a_{3,i,j}$ are the regression coefficients for station i and window j.

Considering that the MLR models are built on a small sample of 20 points (20 years of data), we use the first 17 years (1993–2009) of data as a training set and 3 years (2010–2012) of data as a test set to test the predictive skill of our methods. We calibrate the model over this reduced sample and predict the streamflow regime curve for the 3 years of left-out data. Similar to Brunner et al. (2020), we then assess the model performance with the Kling-Gupta Efficiency (KGE) between the observed and modelled 3-year streamflow regime curves (Gupta et al., 2009). As the procedure is repeated for each of the streamflow stations, we summarize the model predictive skill by the first quantile, median, and third quantile of the KGEs within each region. Kling has stated that a threshold of 0.5 (0.75) can be used to differentiate poor versus intermediate (good) simulation results using the slightly modified KGE metric, thus we utilize these thresholds to interpret our results (Kling et al., 2012; Thiemig et al., 2013). KGE may be sensitive to outliers and non-normally distributed streamflow (Pool et al., 2018), however, the widespread use of the KGE metric as well as its clear interpretation makes it a strong performance metric.

Postprocessing of Global Climate Model Data

To facilitate the assessment of uncertainties stemming from the GCMs, we input the downscaled precipitation and evapotranspiration time series into a stochastic weather generator so that 2,000 time series of each variable are generated (100 for each of the 20 years). Streamflow for 2080–2099 is then simulated by the MLR models using each of the 2,000 generated time series. For each window, the final simulation is calculated through Monte-Carlo simulations by randomly sampling 1,000 observations from the 100 predicted values from each year to get a large, bootstrapped sample of possible 20-year long time series; then, the values are averaged across the 20 years. In this way, we project 1,000 values of the average seasonal streamflow regime for 2080–2099 for each station and window. Final results are then compressed by representing each day with a mean and standard deviation.

The stochastic weather generator used in this study is developed similarly to the framework illustrated by Wilks and Wilby (1999). The output is generated separately for the two RCP

scenarios and for each of the 20 years in 2080–2099. The key steps are summarized as follows: First, for each 30-day window, we have a 5-GCM x 30-day block of data for both evapotranspiration and precipitation. For evapotranspiration, we assume a normal distribution conditioned on the day being wet or dry and derive its mean and standard deviation from the data points for each day type. Second, a transition matrix is calculated from the precipitation data by calculating the four transition probabilities (wet-wet, wet-dry, dry-wet, dry-dry). Then, a two-state Markov chain is created, where $p < 1$ mm is considered a dry day, and a wet day is assumed otherwise. One hundred 30-day time series of precipitation are generated using the Markov chain to determine wet-dry day occurrences, while the magnitude on wet days is determined by randomly sampling from the precipitation observations greater than 1 mm. The simulation of precipitation magnitude is robust, as no distribution needs to be estimated, so precipitation can be generated non-parametrically. The robust generation of evapotranspiration can be done parametrically because a large set of well-behaved daily data is available for parameter estimation (Semenov et al., 1998; Ababaei, 2014). Finally, evapotranspiration (ET) is derived by randomly generating data from either of the two normal distributions derived earlier dependent on if the Markov chain generated a wet or a dry day. This process generates 100 30-day time series of precipitation and evapotranspiration for each year in 2080–2099 for each 30-day window.

Water Use Model

Daily urban water consumption can be separated into three components that include: long-term (decadal) base water use, calendrical (weekly) water use, and seasonal water use (Wong et al., 2010). The seasonal variability in outdoor water use, which explains a relatively large fraction of variability in municipal water use (DeOreo et al., 2016), can be successfully simulated as a function of weather and climate attributes (Gober et al., 2016; Opalinski et al., 2020). Thus, our working assumption is that the seasonal component of municipal water use, represented by daily time series, needs to be decomposed into its long-term, seasonal, and short-term signal. After the signal decomposition, the model is developed for the seasonal signal only.

While the models are calibrated for selected cities, the objective is to model water use in each county. To do so, the model coefficients are upscaled from city-specific values to values representing each county. Finally, the model is forced by stochastically generated climate scenarios from the five GCMs for both the present and future periods. Below we provide details on the signal decomposition, model calibration, coefficient upscaling, and model projections.

Signal Decomposition

To focus on the seasonal signal in the municipal water use for each city, we remove the calendrical and long-term signals from the city's original time series. Though it may slightly contribute to the violation of observation independence, it is unlikely to distort our results, and removing the calendrical signal is necessary, thus we smooth our time series with a 15-day moving median. This will remove the effects of persistence, holidays, measurement

FIGURE 3 | Map of regression coefficient values from 47 MLR models for municipal water consumption: **(A)** coefficient that multiplies maximum temperature (b_1), **(B)** coefficient that multiplies wind speed (b_2), **(C)** coefficient that multiplies the binary variable for rain (b_3), and **(D)** coefficient that multiplies the binary variable for snow (b_4). The model is calibrated over the available observational record (at least 3 years within 1990–2018) for each city, yielding 47 sets of city-specific regression coefficients.

errors, and the day-of-the-week. Long-term variability is mainly driven by population and water efficiency (Wong et al., 2010). To remove the population effects, the smoothed water-use time series are divided by the daily population time series, yielding a daily time series of water efficiency.

Each city's water efficiency time series is normalized to be between 0 and 1. A common feature of these time series is their long-term decline that best resembles an exponential decay signal (**Supplementary Figure S1**). It has been shown that municipal water use per capita in the US has tended to decrease due to government actions that forced manufactures to make water-efficiency improvements for the bathroom and household appliances (Donnelly and Cooley, 2015). These changes were mainly established in the 1990s, so they can be expected to have diminishing returns as time goes on (Donnelly and Cooley, 2015). Empirically, we chose to represent this long-term decline in water use with an exponential decay function that is fitted to the normalized annual water-use time series of each city (**Supplementary Figure S1c**). Finally, the fitted function, interpolated from annual to daily values, is subtracted from the normalized water efficiency time series (**Supplementary Figure S1**). The residual daily time series for each city represents the characteristic seasonal municipal water use per capita.

Calibration, Validation, and Upscaling

Each city's remaining time series of daily water consumption per capita represents the response variable in an MLR model, while a set of weather variables from ERA5 data are used as predictors. Prior to training the MLR model, each response variable is standardized (subtracted by its mean and divided by its standard deviation) in order to facilitate the inter-comparison of regression coefficients across cities. After testing different combinations of predictors, we settled with the following list: maximum daily temperature (*T*, units in °C), daily mean wind speed (*U*, units in m/s), a binary variable for rain (R, wet/dry day for rain) and a binary variable for snow (W, wet/dry day for snow). Rain and snow days are differentiated using a maximum temperature threshold of 5°C, which is reasonable considering thresholds for mean temperatures are often between −5°C and 5°C (Rajagopal and Harpold, 2016). Standardized per-capita water consumption (*C*) is modeled with:

$$C_k = b_{0,k} + b_{1,k}T_k + b_{2,k}U_k + b_{3,k}R_k + b_{4,k}W_k \qquad (2)$$

where $b_{0,k}$-$b_{4,k}$ are the regression coefficients for city k, and $R(W)$ is the binary variable for rainfall (snowfall) which equals 1 if rainfall (snowfall) exceeds 1 mm and 0 otherwise. The model is calibrated for each city, yielding 47 sets of city-specific regression coefficients (**Figure 3**).

Finally, the model coefficients need to be upscaled from their city-specific values to values representing each county. A study with a similar modelling approach to ours found that climatic regression coefficients are correlated in space, with nearby cities yielding more similar regression coefficients than the cities further apart (Opalinski et al., 2020). Thus, we assume that by spatially interpolating the regression coefficients from 47 cities unevenly distributed over the map to the grid of counties, we can obtain a first-order approximation for regression coefficients at each county. We choose to apply smoothed optimal inverse distance weighting with weights set as $1/(1 + d)^p$, where d is the distance from the county's geographical centre (latitude, longitude) to the city's location, and p is the parameter that needs to be optimized.

We optimized p by maximizing the correlation between interpolated and observed C_{mod} using the following procedure: one out of 47 cities is left out from the sample of known regression coefficients, and its regression coefficients are instead derived from the interpolation method with each possible p. This procedure is iterated until all 47 cities are removed once from the original sample. The final value of p is the one that yields the largest mean correlation between interpolated and observed C across all the cities. The optimization yielded $p = 2.1$ (**Supplementary Figure S2**).

Post-processing of Climate Data

Time series of normalized water consumption per capita (C) for each county for both the present (1993–2012) and future (2080–2099) periods are simulated by the MLR model forced by stochastically generated climate data. Similar to the supply model, data from the five GCMs and two RCP scenarios are used as inputs to the stochastic weather generator. Present climate data is patched from the GCM historical runs from 1993 to 2005 and their RCP4.5 runs from 2006 to 2012. Because changes in the water use per county are assessed as a difference between modelled future and modelled present water use, from the same ensemble of GCMs, no bias-correcting is applied.

The predictors in the model (Equation 2) are stochastically generated in the following way: precipitation wet/dry days are derived from a two-state Markov chain where the transition probabilities are estimated from a 31-day moving window of GCM precipitation time series. For temperature, using the same 31-day moving window, we assume a normal distribution and derive its means and standard deviations conditioned on the presence of precipitation. For wind speed, a Weibull distribution is chosen following previous studies (e.g., Seguro and Lambert, 2000; Alizadeh et al., 2019), and we also assume that the wind speed is conditioned on the day being wet or dry. As a result of this assumption, two sets of two-parameter Weibull distributions are estimated using maximum likelihood estimation. The differentiation between snowfall and rainfall is determined by a maximum temperature threshold of 5°C as was done in the calibration phase.

One hundred time series of each weather variable is generated for each year (100 × 20 sets of 365-day time series). Each of the 2,000 generated sets of weather time series are then used to predict a 365-day time series of C. To obtain the uncertainty

estimate for C for each day, we randomly select 1,000 outcomes from each of the 100 time series of each year. Like with the water-supply model, we take the average C across the 20 years, so a total of 1,000 20-year average time series of normalized water consumption per capita for each county are simulated. The final results are presented as the mean ± a standard deviation of C for each day in the present period, and the mean ± a standard deviation of C for each day in the future period for both RCP4.5 and RCP8.5.

Risk Scores

Defining vulnerability or risk of water shortages is difficult to do so precisely while also being implementable (Foti et al., 2012). Due to this limitation, each previous assessment of water shortage risk has developed their own risk assessment score (Hurd et al., 1999; Foti et al., 2012; Roy et al., 2012; Dickson and Dzombak, 2019). For example, Foti et al. (2012) defined vulnerability as the probability that demand will be less than supply in a region, while Dickson and Dzombak (2019) defines an overall risk index from five components of risk including 1) annual proportion of use of local water supply, 2) summer proportion of use of local water supply, 3) projected increase in demand, 4) summer proportion of use of local water demand, and 5) proportion of groundwater withdrawal to total withdrawal.

Building on previously proposed risk scores, we introduce a metric as a proxy for the risk imposed by climate change on water resources for each subregion in the study domain. The metric, defined as the risk score (RS), combines the projected changes in water supply for each station with the projected changes in water demand for each county, and congregates them by sub-region in the following way:

$$RS = D + CD + S + SC, \qquad (3)$$

where D is the probability of a water demand increase from 1993-2012 to 2080–2099, CD is the normalized demand, S is the probability of a supply decrease from 1993-2012 to 2080–2099, and SC is one minus the normalized supply. Each river station is already assigned a sub-region (**Figure 1**), while each county is assigned to the sub-region to which the closest river station belongs. The probability D is calculated by forming a new normal random variable, X, for each RCP scenario with the mean determined by the projected demand in 2080–2099 subtracted by the estimated demand in 1993–2012 and variance set as the sum of the variances of projected demand and estimated current demand. S is calculated in the same way as D, but using the projected streamflow in 2080–2099 and the streamflow regime curve from 1993–2012 to form a random variable Y. In summary, for day i, region j, county k and streamflow station l:

$$D_{i,j} = mean_k\left(P\left(X_{i,j,k} \geq 0\right)\right) \qquad (4)$$

$$S_{i,j} = mean_l\left(P\left(Y_{i,j,l} \leq 0\right)\right) \qquad (5)$$

D and S become a 365-day x 14-region matrix with values between 0 and 1. To compute CD and SC, the demand and supply regime curves for 1993–2012 are scaled to be between 0 and 1 by

FIGURE 4 | Clusters with their average normalized streamflow regime curve. The clusters are: 1) West Coast, 2) Southwest, 3) Deep South, 4) Mid-Atlantic, 5) South-Central US, 6) Florida, 7) Hawaii, 8) Rockies, 9) Alaska, 10) Midwest, 11) Northeast, 12) West, 13) Central US, 14) Eastern Canada. The colors of the regime curve indicate the regime categories where red, black, and blue indicate rain dominated, rain-on-snow dominated, and snowmelt dominated regimes respectively. Vertical dashed curves in the graphs are placed at the transition of seasons (winter, spring, summer, fall).

subtracting by their minimums and dividing by the difference of their maximums and minimums. For each subregion, final CD is calculated as the mean CD across all stations belonging to the region, while final SC is calculated as the mean SC across all counties belonging to the region. Thus, each final CD and SC is a 365-day x 14-region matrix with values between 0 and 1. RS is thus a 365-day x 14-region matrix with values between 0 and 4, where 0 implies no risk and 4 implies maximum risk of water shortages.

RESULTS

Regional Clusters

The clustering of streamflow data across the region yielded 14 clusters or subregions (**Figure 4**). Below we describe the main characteristics of the average streamflow regime and some general climatic attributes for each cluster:

1) The first cluster, which we name "the West Coast", is characterized by high winter streamflow and minimum

flows in late August. The cluster includes Vancouver Island, western half of Washington, Oregon, and California. The climate in these areas is characterized by high frequency of precipitation events in winter that are predominately rainfall rather than snowfall. Thus, relative to other clusters, the streamflow is mainly driven by rainfall.

2) The "Southwest" cluster is comprised of the desert areas of California and Arizona. Although very little precipitation is available in these areas, precipitation may occur periodically in winter months. These rainfall events are usually of high intensity, potentially causing infiltration-excess overland flow. Thus, these catchments are rainfall dominated and have relatively quick responses to precipitation input.

3) The "Deep South" cluster includes Louisiana, Mississippi, Alabama, Georgia, Tennessee, and South Carolina. These states are known to have warm and humid summers with some precipitation. Winter and spring have the highest precipitation. The landscape is covered by forests which implies overland flow is less likely compared to the Southwest cluster. With such active storage, the streams'

response to precipitation may be slower despite being a rain-dominated region with a peak in the late winter months and low flows in late-summer.

4) The "Mid-Atlantic" cluster includes North Carolina, Kentucky, Virginia, West Virginia, Ohio, Pennsylvania, Maryland, Delaware, New Jersey, southern New York, Connecticut, and Southern Ontario. Mostly covered in forest, this region is known for its hot summers and very cold winters, where winter temperatures are often at or below freezing. Precipitation is often high, with precipitation being fairly evenly distributed throughout the year. This region may be hydrologically dominated by rain-on-snow events in winter, with all snow melting by early spring. The streamflow regime curve in this region has a peak in early spring and a low in mid-summer.

5) The "South-Central US" consists of Northeast Texas, Southeastern Oklahoma, Arkansas, and northern Louisiana. These areas are covered by grass, shrubs, with some forested areas further east. Precipitation is usually highest in the spring in these areas, with little to no snowfall, leading to highest streamflow in the spring with a seasonal drought in mid-summer.

6) The "Florida" cluster is largely covered by wetlands in the southern half and forest in the north. Since Florida is subtropical and tropical in some areas, precipitation occurs throughout the year. Summers are slightly wetter and more humid than are winters. The regime curve in this region has little variance, with highs in the late summer and lows in early summer.

7) The "Hawaii" cluster is in the tropics with precipitation and warm, humid weather throughout the year. The streamflow regime curve in this region has extremely low variability, with no clear high or low.

8) The "Rockies" cluster consists of Northern Wyoming, Idaho, Montana, Eastern Washington, and parts of British Columbia and the Yukon. This region is extremely cold in winters, often with extensive snow cover. The streamflow stations are in snow-dominated catchments, so the hydrographs are characterized by low streamflow in winter when no snowmelt is present, followed by peak streamflow in late spring to early summer as snowmelt intensifies.

9) The "Alaska" cluster, similarly to the Rockies, is a snow-dominated region; however, in Alaska, the colder climate and extensive snow cover, as well as glacierized terrain, allows for the snowmelt and/or glacier runoff to last throughout the summer; thus, giving hydrographs with a wide peak throughout the summer.

10) The "Midwest" cluster contains Illinois, Wisconsin, Iowa, Minnesota, North and South Dakota, as well as Southern Alberta and Saskatchewan. This region's land use mainly consists of agricultural areas and grasslands. This region is fairly dry; nevertheless, snow cover persists throughout much of the winter, with melt occurring in the spring leading to the peak in streamflow.

11) The "Northeast" cluster consists of New York, Vermont, New Hampshire, Maine, Southern Quebec, New Brunswick, Nova Scotia, Prince Edward Island, and Southern

TABLE 2 | The first quantile, median, and third quantile of KGE values for predicted water supply regime curves for each region.

Region number	Region name	Q1	Median	Q3
1	West Coast	0.62	0.82	0.89
2	Southwest	0.11	0.61	0.74
3	Deep South	0.57	0.73	0.80
4	Mid-Atlantic	0.62	0.73	0.81
5	South-Central US	0.55	0.65	0.77
6	Florida	0.09	0.37	0.61
7	Hawaii	0.54	0.59	0.68
8	Rockies	0.60	0.73	0.85
9	Alaska	0.82	0.89	0.93
10	Midwest	0.37	0.59	0.71
11	Northeast	0.55	0.70	0.81
12	West	0.51	0.71	0.83
13	Central US	0.18	0.46	0.60
14	Eastern Canada	0.12	0.52	0.75

Newfoundland. This region is covered by forest and has very cold winters; hence, snow builds in the winter and then snowmelt generates peak streamflow in April.

12) The "West" cluster includes parts of British Columbia, Alberta, Idaho, Montana, Utah, Nevada, California, and Arizona. The hydrographs in this region peak in spring as a result of snowmelt.

13) The "Central US" cluster consists of Southern Minnesota, Iowa, Nebraska, Missouri, Kansas, and Oklahoma. The hydrographs in this region peak in spring.

14) The "Eastern Canada" cluster includes northern Newfoundland, Quebec, Ontario, and Manitoba. The hydrographs in this region peak in spring. Winters are cold and snow cover is prevalent, so runoff is driven by spring snowmelt.

According to these characteristics we can group the 14 subregions into three general regime categories: rainfall dominated streamflow regime (West Coast, Southwest, Deep South, South-Central US, Florida, and Hawaii), rain-on-snow dominated regime (Mid-Atlantic, Midwest, and Central US), and snow dominated regions (Rockies, Alaska, Northeast, West, and Eastern Canada).

Simulations of Water Supply
Model Performance
The KGE is estimated for all streamflow stations within each region for the 3-year test set (**Table 2**). The West Coast (0.82) and Alaska (0.89) have high median KGEs. Predictions for the Southwest (0.61), Deep South (0.73), Mid-Atlantic (0.73), Rockies (0.73), South-Central US (0.65), Hawaii (0.59), Northeast (0.70), West (0.71), Midwest (0.59), and Eastern Canada (0.52) are also fairly reliable. On the other hand, our simulations perform poorly in Central US (0.46) and Florida (0.37).

Projections of Streamflow
An example of modelled future (2080–2099) versus present (1993–2012) streamflow regime curves are shown in **Figure 5** for a streamflow station in California. The streamflow at this station is expected to substantially increase in late winter and
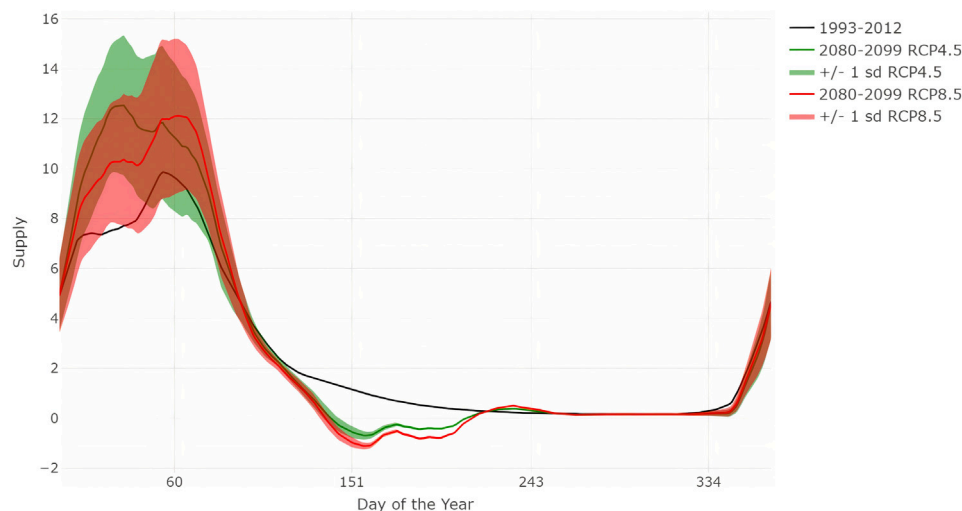
FIGURE 5 | Modelled seasonal streamflow (measured in m³/sec) regime curves for 1993–2012 (black), and 2080–2099 according to RCP4.5 (green) and RCP8.5 (red) scenarios for a station in California (34.35, −119.31). The shading indicates the uncertainty (±one standard deviation).

early spring, while the streamflow will remain almost unchanged throughout the rest of the year. The uncertainty interval for both RCP scenarios is large, especially for the time window with the largest projected increase in streamflow. We estimate the water-supply components of the risk score for this station (Equation 3): on a seasonal scale, the largest CS is in the fall (median CS = 1.00) and the smallest is in the winter (CS = 0.26), while the likely decrease in streamflow is projected for the summer (S = 1.00 for RCP4.5; S = 1.00 for RCP8.5), and the least likely decrease is projected for the winter (S = 0.27 for RCP4.5; S = 0.27 for RCP8.5).
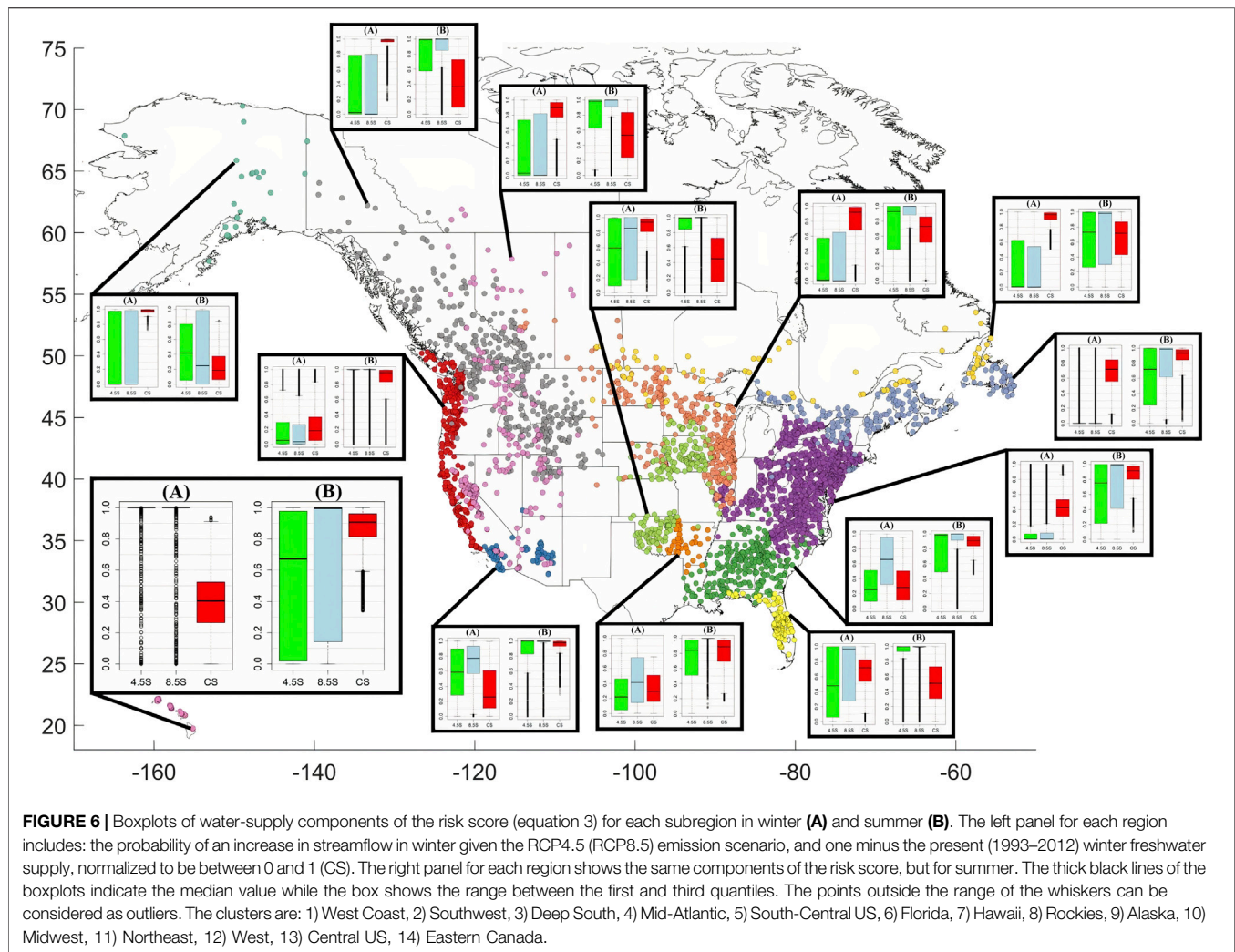
Next, we summarize the results of regional streamflow projections for each season, with more focus on subregions where the model has higher predictive capabilities (larger KGE) relative to other subregions: Results for winter streamflow (DJF; **Figure 6**) reveal that the likelihood of a downward change in streamflow is linked to latitude. Specifically, for low-latitude regions (Hawaii, Southwest, Florida, Central US), streamflow is projected to decrease for one or both RCP scenarios. For these regions, the average S is 0.56 (0.68) for RCP4.5 (RCP8.5) scenario, while the average CS is 0.70. Out of these regions, only Central US and Florida have KGE <0.5 implying a low confidence in the projections. The probability of a decrease in Hawaii is certain with the interquartile range (IQR) of 0 for both RCP4.5 and RCP8.5 scenarios. The IQRs for Southwest, Florida, and Central US are much larger, ranging from 0.35 for Southwest's RCP8.5 scenario to 0.95 for Florida's RCP4.5 scenario. Streamflow is projected to increase in Alaska, the Rockies, the Midwest, the West Coast, and the Northeast. According the KGE values, however, we have higher confidence in the projections for the West Coast (KGE = 0.82), Alaska (KGE = 0.89) and less certain for Rockies (KGE = 0.73), Midwest (KGE = 0.59), and Northeast (KGE = 0.70).

In simulating the streamflow in spring (MAM), under the RCP4.5 scenario, Hawaii and the West Coast will experience decreases in streamflow (their average S is 0.76 and there IQRs are 0 and 0.48), whereas the Deep South, East Coast, Southern Central US, Central US, Northeast, and the Midwest will experience increases (their average S is 0.13 and their IQRs are 0.19, 0.11, 0.25, 0.17, 0.38, and 0.10 respectively). Like the RCP4.5 scenario, RCP8.5 will lead to decreases in streamflow in Hawaii, West Coast, Florida, and the Southwest (their average S is 0.75 and their IQRs are 0, 0.59, 0.12, and 0.38 respectively). These results are particularly of note for Hawaii, the Southwest, and Florida as these regions experience low present water supply in the spring relative to other seasons (their average CS is 0.64).

Projections of summer (JJA) streamflow reveal that water resources will experience strain across most of North America (**Figure 6**). According to the RCP4.5 scenario, the West Coast, the Southwest, South Central US, Florida, the Deep South, Central US, and the Midwest will all likely experience decreased water supply (their average S is 0.80). Following the RCP8.5 scenario, in addition to the regions affected by the RCP4.5 scenario, Hawaii, the East Coast, the Northeast, and Eastern Canada will see decreases in summer streamflow (their average S is 0.81). The IQRs of decrease probabilities are small for the West Coast (0 for RCP4.5, 0 for RCP8.5), Southwest (0.18, 0), Florida (0.08, 0), and Central US (0.18, 0).

For the projections of autumn (SON) streamflow, regardless of the RCP scenario followed, eastern regions are most likely going to be affected by decreases in their streamflow, including the Deep South, the East Coast, Southern Central US, Florida, Midwest, Northeast, and Central US (their average S is 0.73 and 0.69 for RCP4.5 and RCP8.5, respectively). The IQRs of decrease probabilities are small for the Southern Central US (0.05 for RCP4.5, 0 for RCP8.5) and the Deep South (0.20, 0.10).

FIGURE 6 | Boxplots of water-supply components of the risk score (equation 3) for each subregion in winter **(A)** and summer **(B)**. The left panel for each region includes: the probability of an increase in streamflow in winter given the RCP4.5 (RCP8.5) emission scenario, and one minus the present (1993–2012) winter freshwater supply, normalized to be between 0 and 1 (CS). The right panel for each region shows the same components of the risk score, but for summer. The thick black lines of the boxplots indicate the median value while the box shows the range between the first and third quantiles. The points outside the range of the whiskers can be considered as outliers. The clusters are: 1) West Coast, 2) Southwest, 3) Deep South, 4) Mid-Atlantic, 5) South-Central US, 6) Florida, 7) Hawaii, 8) Rockies, 9) Alaska, 10) Midwest, 11) Northeast, 12) West, 13) Central US, 14) Eastern Canada.

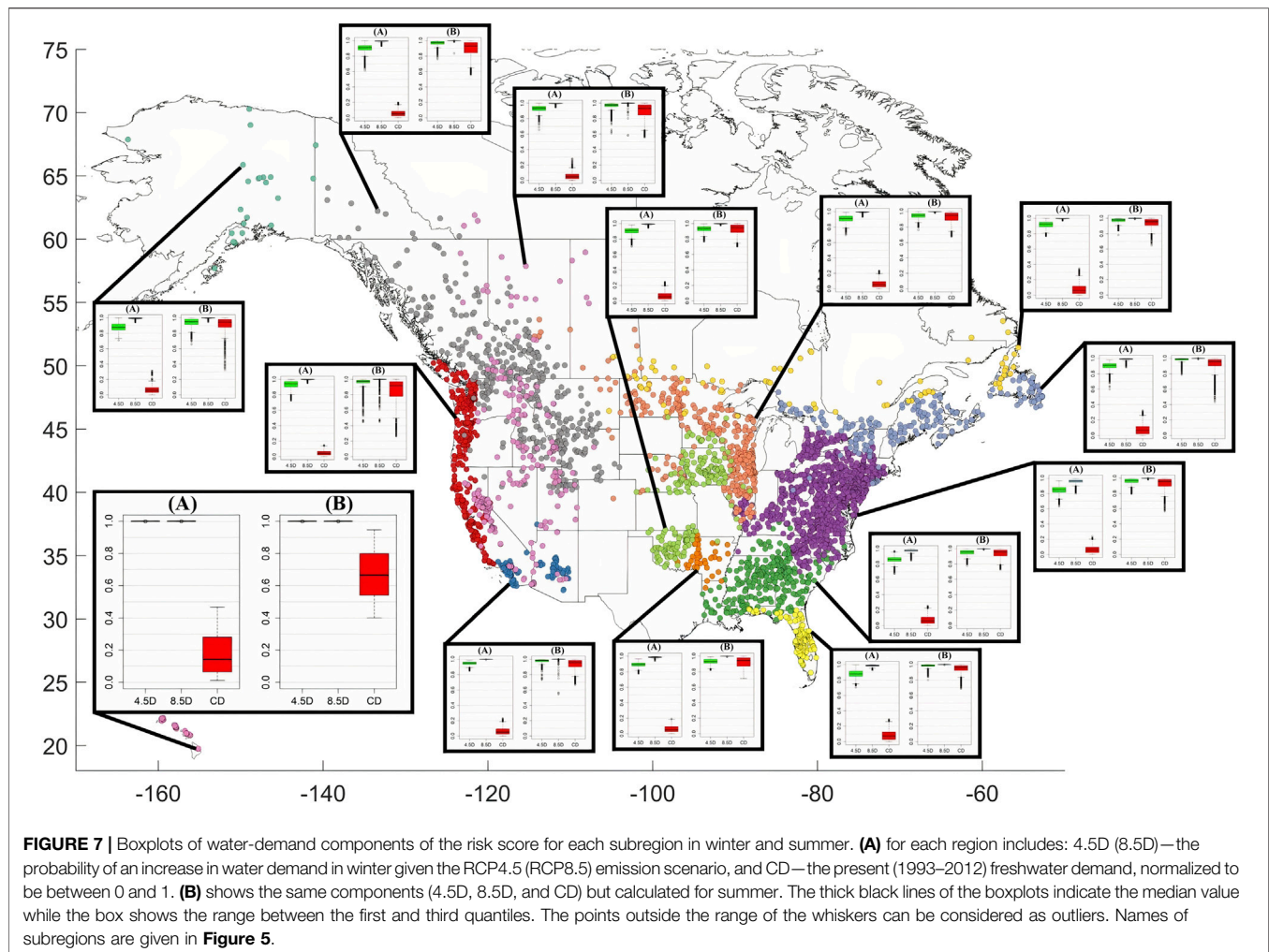## Simulations of Water Demand
Model Performance
Supplementary Figure S2 shows the mean correlation (0.69) between predicted and observed daily water efficiency with optimal inverse distance weighting calculated using leave-one-out cross validation. All locations have at least 1,000 observations of daily water use efficiency, so this correlation is significant (average p-value < 0.01), and the predictions are representative of the observations.

Projections of Municipal Water Use
An example of modelled future versus present water consumption per capita is shown in **Supplementary Figure S3** for a county in Alabama. As illustrated in the figure, there is a pronounced seasonal cycle in the water consumption, with the highest consumption during the summer months. The changes in water demand are projected to occur in all seasons, with the largest increases in summer, and the lowest in winter. These results are reflected in the water-use components of the risk score (Equation 3): the largest CD is in summer (CD = 0.95) and the smallest CD is winter (CD = 0.08).

The likelihood that this county will experience an increase in demand is also the largest in summer (D = 0.97 for RCP4.5; D = 1.00 for RCP8.5), and the smallest in winter (D = 0.86 for RCP4.5; D = 0.98 for RCP8.5).

Projections for each subregion and each season reveal that the changes in water consumption are relatively uniform across seasons, with the main difference being between winter and summer water consumption (**Figure 7**). For all regions, the current water demand is the largest in summer and lowest in winter (their average CD is winter is 0.07, and their average CD in summer is 0.92). In all regions, RCP4.5 will substantially increase the annual water demand (average D = 0.93 for RCP4.5), while more increase is expected for RCP8.5 (average D = 0.99 for RCP8.5). Most of this increase is expected in the summer season (average summer D = 0.95 for RCP4.5; D = 1.00 for RCP8.5). The top three subregions with the highest projected increase in demand in summer given the RCP4.5 and RCP8.5 scenarios are Hawaii and Florida, and their average summer D is 0.99 and 1.00, respectively. The top three subregions with the highest projected increase in demand for RCP4.5 (RCP8.5) in winter are: Hawaii, Southwest, and West Coast (Hawaii, Southwest, and

FIGURE 7 | Boxplots of water-demand components of the risk score for each subregion in winter and summer. **(A)** for each region includes: 4.5D (8.5D)—the probability of an increase in water demand in winter given the RCP4.5 (RCP8.5) emission scenario, and CD—the present (1993–2012) freshwater demand, normalized to be between 0 and 1. **(B)** shows the same components (4.5D, 8.5D, and CD) but calculated for summer. The thick black lines of the boxplots indicate the median value while the box shows the range between the first and third quantiles. The points outside the range of the whiskers can be considered as outliers. Names of subregions are given in **Figure 5**.

Eastern Canada), and their average winter D = 0.96 (1.00). During all seasons and in all regions, increases in municipal water demand are expected, regardless of the RCP scenario followed, however the increases are more certain under RCP8.5 compared to RCP4.5. The interquartile range of all regions and seasons given the RCP4.5 scenario ranges from 0 to 0.1, whereas the IQRs given RCP8.5 remain at 0.

Risk Assessment

Risk scores (RS) for each region and RCP scenario are quantified for each season. Because of consistently higher demand in summer (**Figure 7**), total risk is consistently highest in the summer, so only summer risk scores are shown (**Figure 8**). According to the RCP4.5 scenario, the region with the highest risk of freshwater shortage in the summer (highest median RS) is the Southwest (region 2), followed by the West Coast (region 1) and the Deep South (region 3). The West Coast and Southwest both have low uncertainty (IQRs of 0.30 and 0.10), but the Deep South has high uncertainty (IQR = 0.55) stemming from high uncertainty of streamflow projections in this region. According to the RCP8.5 scenario, the regions with the highest risk are:

Southern Central United States (region 5), the Deep South (region 3), and Northeast (region 11). The IQRs of these risk scores are low for Southern Central US (0.40) and the Deep South (0.37).

DISCUSSION

Summary of Results

GCMs generally agree that the entirety of North America will experience temperature increases throughout this century, while precipitation will change over time as a function of latitude, where southern areas will see decreases in precipitation, and northern areas will experience increases (Roy et al., 2012; Forster et al., 2020). This will likely lead to decreases in the fraction of precipitation falling as snow, increases in evapotranspiration, and changes in available water. But how this change in climate will alter the supply and demand of freshwater is poorly understood. Here we aimed at building a better understanding of these uncertainties while obtaining a general overview of where and when the risk of supply deficits is greatest.
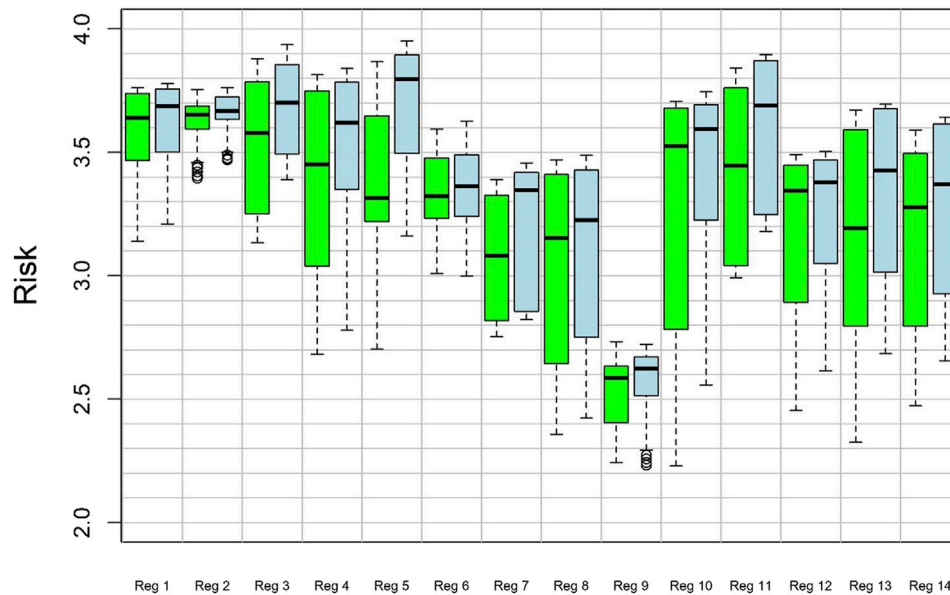
FIGURE 8 | Box plot of risk scores (RS) derived for the summer for each of the 14 subregions. Green box plot is for the RCP4.5 emissions scenario, and blue is for the RCP8.5 emissions scenario. The list of regions is as follows: 1) West Coast, 2) Southwest, 3) Deep South, 4) Mid-Atlantic, 5) South-Central US, 6) Florida, 7) Hawaii, 8) Rockies, 9) Alaska, 10) Midwest, 11) Northeast, 12) West, 13) Central US, and 14) Eastern Canada. The thick black lines of the boxplots indicate the median value while the box shows the range between the first and third quantiles. The points outside the range of the whiskers can be considered as outliers.

We focused our paper on two objectives: First, we aimed to determine the viability of using simple regression models to capture the variability in streamflow and water consumption using globally available climate reanalysis data while assessing the risk of water shortage in multiple regions across North America. The viability of simple regression models for the use of modeling streamflow varied by region, as measured by the validation phase KGE. Florida and Central US had the lowest median KGEs. The other regions had highly acceptable KGEs, especially when the regime curves do not change much from year to year, as is the case in Alaska. Further, the correlation between simulated and observed water use was high. This result means that urban water use in a city can robustly be estimated from population data and climate data in conjunction with water use data from surrounding cities. We found that demand is consistently highest in the summer, thus making water shortage risks consistently highest in the summer. In summer, the highest risk scores are in the Southwest (Southern Central US), West Coast (Deep South), and Deep South (Northeast) given the RCP4.5 (RCP8.5) scenario.

As a second objective, we sought to quantify the uncertainties in predicting streamflow and water consumption and therefore water shortage stemming from GCM climate projections. We found that almost all of the risk score uncertainty is derived from the uncertainty of streamflow projections from GCM data, while there is little-to-no uncertainty in demand projections from GCM data. This occurs because the supply is driven by precipitation while demand is driven by maximum temperature, and GCM projections of temperature have a narrower spread of projections from the weather generator compared to precipitation.

Comparison With Previous Works

Similar to previous studies that used regression models for predicting streamflow (e.g., Barbarossa et al., 2017; Mendoza et al., 2017), we found the MLR models to be reliable in most of our 14 subregions. However, in some regions (e.g., Florida and Central US), the model performance was relatively poor. The poor performance in these regions is not limited to simple regression models. Brunner et al. (2020), using physically based models, also found that Central US was the most difficult region to reliably simulate water supply.

For the US, our projections of streamflow generally agree with the previous findings that the annual streamflow will substantially decrease in South and Western US (Hurd et al., 1999; Foti et al., 2012; Chien and Knouft, 2013; Mahat et al., 2017). Throughout the region, summer streamflow was shown to be more susceptible to decreases (Maurer and Duffy, 2005; Chien and Knouft, 2013) than streamflow in other seasons. In particular, under the RCP4.5 scenario, we projected that Florida may experience significant streamflow decreases in the summer, corroborating previous findings in (Mahat et al., 2017). Furthermore, under the RCP8.5 scenario, our results also agree with Mahat et al. (2017) that the Southwest, Southern Central US, and Florida will experience substantial drops in streamflow. These projections are relatively consistent across the climate projections stochastically generated from the five GCMs.

Our projections of water use agree with those is Foti et al. (2012), showing that climate-driven water use will increase across the United States, as well as Canada, and uncertainties around these projections will decrease as temperatures rise further. Since maximum temperature is the dominant driver of water consumption (Opalinski et al., 2020), and all CMIP5 models

agree that temperatures are projected to rise across the entire United States (Mahat et al., 2017), this is in-line with expectations. The MLR modeling of municipal water demand showed that most of our city-specific regression coefficients are highly spatially dependent as previously found in (Opalinski et al., 2020). The regression coefficient that shows the contribution of the number of snowy days to water demand is negatively correlated with latitude, implying that the impacts of snowy days on water demand is greater in lower latitude areas. For example, at low latitudes, the snowfall-day coefficient is between 0.6 and 1.4, while in Canada, the coefficient drops to 0.2. The regression coefficient that shows the contribution of the maximum temperature is also spatially varying, with the highest values in western and southern areas (0.08–0.19), and the lowest in northern and eastern areas (0.03–0.08). In the West Coast, southwest US, and Florida regions, the coefficient multiplying the wind speed is normally positive (0–0.15), while in other places, the coefficient of wind is normally negative (−0.15–0), implying that warm winds could raise water demand, while colder winds could decrease demand. However, the coefficient in Texas is negative, so this hypothesis should be tested further. Rain-day coefficients seem to not be spatially dependent. We compared our spatially distributed coefficient values with those derived in Opalinski et al. (2020) and found general agreement for the coefficient multiplying the maximum temperature. In Opalinski et al. (2020), however, the link with the latitude is not as clear as in our case which is likely because we extended the assessment to Canadian cities while their study only provides the results for the contiguous US. Regarding precipitation, Opalinski et al. (2020) found that the increase in precipitation in cold regions was associated with an increase in water consumption. One interpretation for this finding is that the increased snowfall is linked to increased water use, which is also consistent with our results.

To our knowledge, there have been relatively few up-to-date assessments of water resource vulnerabilities and shortage risks due to climate change across the entire US or North America. Dickson and Dzombak (2019) as well as Foti et al. (2012) used physically based models to project streamflow, while Roy et al. (2012) calculated available precipitation (precipitation minus evaporation) instead of streamflow. Previously, urban water-demand projections have been made based on changes in population and electricity production (Roy et al., 2012; Dickson and Dzombak, 2019), or climate regression techniques combined with the effects of income, population, and efficiency (Foti et al., 2012). Our study is the first that focused on both the US and Canada, and the first to combine the use of regression models for both supply and demand projections.

Our results generally agree with those in the previous studies for the regions where the previous projections of risks have been assessed. For example, the probability of water shortage was calculated across the U.S. by Foti et al. (2012) and probabilities were highest in the same areas as our study indicated, namely the southwestern United States and the coast of California, though they showed a high risk for the central US as well. Roy et al. (2012) found that the southwest and central US as well as Florida will have the

highest risk index in 2050. The latest assessment of risk showed that central California, and parts of Nevada have the highest risk of water shortage (Dickson and Dzombak, 2019). Regardless of the methods, data, or scenario chosen, all of these studies agree that California and the US Southwest have the most troubling futures, relative to other parts of North America, when it comes to the effects of climate change on water resources.

Limitations

Though we used an expansive collection of streamflow data, continuous, long-term hydrologic data is often limited to large rivers and our conclusions may not accurately extrapolate to smaller basins (Kovach et al., 2019). In a similar fashion, the water use data is mostly limited to medium-sized cities and the captured relationships between water use and weather may not extrapolate to extremely large cities or small towns. Although some hydrological extremes are included in the 20-year period of analysis used in this paper (e.g., the 2000–2004 drought in western North America), the length of time used may be seen as too modest as the full extent of climate extremes in all areas may not be present and therefore learnable in our data (Schwalm et al., 2012). Rather than developing the best possible prediction model, we aimed at exploring how well a relatively simple model (MLR) can explain interannual and seasonal variability in water consumption and streamflow. Likewise, our water shortage vulnerability framework is relatively narrow in scope. For a more complete risk assessment, one would have to consider biological and ecological sensitivity as well as adaptive capacity (Kovach et al., 2019). Though we utilized stochastic weather generators to increase the number of cases in our ensemble of future scenarios, we only included five GCMs as a baseline, so the results could be sensitive to our choice in GCMs.

Due to the number of models included for projecting streamflow, the assumptions of linear behavior and constant variance over the long period of study could not be verified. The least success in terms of MLR performance among the streamflow models is found for Central US and Florida. One of the key reasons for the poor performance is the fact that runoff could be controlled by non-linear threshold-like belowground hydrologic processes (Jones et al., 2019). In some catchments, precipitation can fall and either quickly flood the surface when the soil is saturated or recharge the groundwater system. Thus, water from similar sized precipitation events may be transferred toward the stream immediately or a few months to several decades later. The "memory" in the hydrological system, which acts on multiple time scales, is not possible to be captured by the linear regression model used in our paper. In deforested, arid, urbanized, or agricultural areas with little snowfall and little interactions between precipitation and belowground attributes, streamflow response to precipitation is relatively fast. In these regions, as well as in regions with similar year-to-year regimes, our ensemble of regression models is deemed acceptable to forecast future water shortage and its uncertainty.

With regards to our projections of water use, unlike previous studies, we did not consider water use from sectors such as agriculture or thermoelectric power which admittedly take up

a large portion of water (Foti et al., 2012; Roy et al., 2012; Dickson and Dzombak, 2019). Climate successfully explained a large portion of the variability in our urban water use data, and climate change will likely explain much of the future changes in use, however, non-climatic changes can also be substantial factors. For instance, age of the population, household size, and other sociodemographic attributes can explain some water use behavior (March and Saurí, 2010). While the effects of population, income, and technological efficiency growth have been shown to negate overall, individual regions or cities may experience outsized effects of one or another (Rosegrant and Cai, 2002). City or building specific attributes related to water use such as building type, tree fraction, building age, impervious surface percentage, and population density can also change over time and should be seriously considered (Stoker and Rothfeder, 2014; Chang et al., 2017). General attitudes towards conservation and lawn upkeep are yet other examples of features that may change in tandem with water use (Hong and Chang, 2014). Further, we assumed that spatially interpolating our estimated regression coefficients from cities with data to the grid of counties gives a good enough first-order approximation of the effects of climate on water use in each county. Though the validation provides some confidence that interpolating the regression coefficients yielded optimal results for the purpose of our study, some subregions had little-to-no data (e.g., Hawaii and the Deep South), and therefore uncertainty in their results remains unaccounted for.

CONCLUSION

Here we presented a new method for quantifying future risks of municipal water shortages across North America in response to climate change. We applied a set of multiple regression models to project the changes in streamflow regimes (water-supply) and urban water use regimes (water-demand) in response to climate scenarios stochastically generated from an ensemble of five GCMs, for the RCP4.5 and RCP8.5 emission scenarios. The models were calibrated over the present period (1993–2012) and then used for projections over the 2080–2099 period. The results were analyzed for each of 14 identified clusters or subregions across the original domain (the US and Canada).

Results show that risk scores are considerably higher in the summer compared to the rest of the year, since urban water demand is high regardless of the location chosen. The resulting risk scores for water shortages by the end of the 21st century under the RCP4.5 emissions scenario, indicate a high risk for the West Coast, the Deep South, and the Southwestern US. Under the RCP8.5 scenario, the regions with the highest risk are Southern Central US, the Deep South, and Northeast, while the regions with the lowest risk are Alaska, Rockies, and Hawaii. The high risk scores are due to high and increasing demand concurrently happening with low and decreasing supply. Almost all uncertainty in the risk scores is rooted in the uncertainty of streamflow projections

from GCM data, while there is little-to-no uncertainty in water-demand projections from GCM data. Overall, the predictive power of our streamflow model is shown to be sufficient in most subregions, while for Florida and Central US, the model yielded low predictive power. Our study reveals that simple statistical models can produce projections of water shortages that agree with those derived from more complex methods used in previous studies. Nevertheless, more work is needed to identify and implement mitigation strategies to prevent water resource shortages. In particular, the regions that we identified as those with high risk scores, should be examined in more detail so that their water resources can be analyzed at the community level. Future research should also aim to employ more complex methods, especially in those regions shown with our simple method to have high risk and relatively large uncertainty in predicted water shortages. To capture the long-term 'memory' and non-linear threshold-like behavior of hydrologic systems, due to snowmelt characteristics or differing geological water partitioning systems, more complex and computationally expensive methods are needed, such as Long-Short-Term Memory models (e.g., Shen, 2018), as well as diverse climatic and physical data.

DATA AVAILABILITY STATEMENT

Publicly available datasets were analyzed in this study. This data can be found here: CMIP5 data is available *via* https://esgf-node. llnl.gov/search/cmip5/. ERA5 data is available *via* https://cds. climate.copernicus.eu/cdsapp#!/dataset/reanalysis-era5-single-levels?tab=overview. Streamflow data for US and Canada can be obtained from USGS (https://waterdata.usgs.gov/nwis/sw) and the HYDAT database (https://www.canada.ca/en/environment-climate-change/services/water-overview/quantity/monitoring/survey/data-products-services/national-archive-hydat.html). The water use data for each city has been provided by individual municipalities and is not currently publicly available, however, some of the data can be shared if the corresponding author is contacted directly.

AUTHOR CONTRIBUTIONS

JJ carried out data collection and data analysis. JJ and VR drafted the manuscript. JJ, VR, and AA designed the methods and edited the manuscript.

FUNDING

ACKNOWLEDGMENTS

REFERENCES

Ababaei, B. (2014). Are Weather Generators Robust Tools to Study Daily Reference Evapotranspiration and Irrigation Requirement? *Water Resour. Manage.* 28 (4), 915–932. doi:10.1007/s11269-014-0524-3

Achakulwisut, P., Mickley, L. J., and Anenberg, S. C. (2018). Drought-sensitivity of fine dust in the US Southwest: Implications for air quality and public health under future climate change. *Environ. Res. Lett.* 13 (5), 054025. doi:10.1088/1748-9326/aabf20

Adamowski, J., Fung Chan, H., Prasher, S. O., Ozga-Zielinski, B., and Sliusarieva, A. (2012). Comparison of multiple linear and nonlinear regression, autoregressive integrated moving average, artificial neural network, and wavelet artificial neural network methods for urban water demand forecasting in Montreal, Canada. *Water Resour. Res.* 48 (1), 1528. doi:10.1029/2010wr009945

Addor, N., Newman, A. J., Mizukami, N., and Clark, M. P. (2017). The CAMELS data set: catchment attributes and meteorology for large-sample studies. *Hydrol. Earth Syst. Sci.* 21 (10), 5293–5313. doi:10.5194/hess-21-5293-2017

Alizadeh, M. J., Kavianpour, M. R., Kamranzad, B., and Etemad-Shahidi, A. (2019). A weibull distribution based technique for downscaling of climatic wind field. *Asia-pacific J. Atmos. Sci.* 55 (4), 685–700. doi:10.1007/s13143-019-00106-z

Ashfaq, M., Ghosh, S., Kao, S.-C., Bowling, L. C., Mote, P., Touma, D., et al. (2013). Near-term acceleration of hydroclimatic change in the western U.S. *J. Geophys. Res. Atmos.* 118 (19), 676–693. doi:10.1002/jgrd.50816

Bakker, M., Van Duist, H., Van Schagen, K., Vreeburg, J., and Rietveld, L. (2014). Improving the performance of water demand forecasting models by using weather input. *Proced. Eng.* 70, 93–102. doi:10.1016/j.proeng.2014.02.012

Balling, R. C., and Gober, P. (2007). Climate variability and residential water use in the city of Phoenix, Arizona. *J. Appl. Meteorology Climatology* 46 (7), 1130–1137. doi:10.1175/jam2518.1

Barbarossa, V., Huijbregts, M. A. J., Hendriks, A. J., Beusen, A. H. W., Clavreul, J., King, H., et al. (2017). Developing and testing a global-scale regression model to quantify mean annual streamflow. *J. Hydrol.* 544, 479–487. doi:10.1016/j.jhydrol.2016.11.053

Basara, J. B., Christian, J. I., Wakefield, R. A., Otkin, J. A., Hunt, E. H., and Brown, D. P. (2019). The evolution, propagation, and spread of flash drought in the Central United States during 2012. *Environ. Res. Lett.* 14 (8), 084025. doi:10.1088/1748-9326/ab2cc0

Besaw, L. E., Rizzo, D. M., Bierman, P. R., and Hackett, W. R. (2010). Advances in ungauged streamflow prediction using artificial neural networks. *J. Hydrol.* 386 (1-4), 27–37. doi:10.1016/j.jhydrol.2010.02.037

Blöschl, G., Bloschl, G., Sivapalan, M., Wagener, T., Savenije, H., and Viglione, A. (2013). *Runoff Prediction in ungauged basins: synthesis across Processes, Places and scales*. Cambridge: Cambridge University Press.

Bonsal, B. R., Wheaton, E. E., Chipanshi, A. C., Lin, C., Sauchyn, D. J., and Wen, L. (2011). Drought research in Canada: A review. *Atmosphere-Ocean* 49 (4), 303–319. doi:10.1080/07055900.2011.555103

Breinl, K. (2016). Driving a lumped hydrological model with precipitation output from weather generators of different complexity. *Hydrological Sci. J.* 61 (8), 1395–1414. doi:10.1080/02626667.2015.1036755

Breyer, B., and Chang, H. (2014). Urban water consumption and weather variation in the Portland, Oregon metropolitan area. *Urban Clim.* 9, 1–18. doi:10.1016/j.uclim.2014.05.001

Brown, T. C., Foti, R., and Ramirez, J. A. (2013). Projected freshwater withdrawals in the United States under a changing climate. *Water Resour. Res.* 49 (3), 1259–1276. doi:10.1002/wrcr.20076

Brunner, M. I., Melsen, L. A., Newman, A. J., Wood, A. W., and Clark, M. P. (2020). Future streamflow regime changes in the United States: assessment using

SUPPLEMENTARY MATERIAL

functional classification. *Hydrol. Earth Syst. Sci.* 24 (8), 3951–3966. doi:10.5194/hess-24-3951-2020

Byun, K., Chiu, C.-M., and Hamlet, A. F. (2019). Effects of 21st century climate change on seasonal flow regimes and hydrologic extremes over the Midwest and Great Lakes region of the US. *Sci. Total Environ.* 650, 1261–1277. doi:10.1016/j.scitotenv.2018.09.063

Caron, A., Leconte, R., and Brissette, F. (2008). An improved stochastic weather generator for hydrological impact studies. *Can. Water Resour. J.* 33 (3), 233–256. doi:10.4296/cwrj3303233

Chang, H., Bonnette, M. R., Stoker, P., Crow-Miller, B., and Wentz, E. (2017). Determinants of single family residential water use across scales in four western US cities. *Sci. Total Environ.* 596-597, 451–464. doi:10.1016/j.scitotenv.2017.03.164

Chang, H., Praskievicz, S., and Parandvash, H. (2014). Sensitivity of urban water consumption to weather and climate variability at multiple temporal scales: The case of Portland, Oregon. *Int. J. Geospatial Environ. Res.* 1 (1), 7.

Chen, G., Tian, H., Zhang, C., Liu, M., Ren, W., Zhu, W., et al. (2012). Drought in the Southern United States over the 20th century: variability and its impacts on terrestrial ecosystem productivity and carbon storage. *Climatic change* 114 (2), 379–397. doi:10.1007/s10584-012-0410-z

Chen, J., Brissette, F. P., Chaumont, D., and Braun, M. (2013). Finding appropriate bias correction methods in downscaling precipitation for hydrologic impact studies over North America. *Water Resour. Res.* 49 (7), 4187–4205. doi:10.1002/wrcr.20331

Chen, Y., Li, J., Wang, H., Qin, J., and Dong, L. (2017). Large-watershed flood forecasting with high-resolution distributed hydrological model. *Hydrol. Earth Syst. Sci.* 21 (2), 735–749. doi:10.5194/hess-21-735-2017

Chien, H., and Knouft, J. (2013). Modeling future streamflow variability in the Mobile River watershed in the southeastern United States using SWAT coupled with climate change projections. *AGU Fall Meet. Abstr.* GC23A–0901.

Cinquini, L., Crichton, D., Mattmann, C., Harney, J., Shipman, G., Wang, F., et al. (2014). The Earth System Grid Federation: An open infrastructure for access to distributed geospatial data. *Future Generation Comp. Syst.* 36, 400–417. doi:10.1016/j.future.2013.07.002

Copernicus Climate Change Service Climate Data Store (2017). *ERA5: Fifth generation of ECMWF atmospheric reanalyses of the global climate*. United States: CDS.

Demaria, E. M. C., Palmer, R. N., and Roundy, J. K. (2016). Regional climate change projections of streamflow characteristics in the Northeast and Midwest U.S. *J. Hydrol. Reg. Stud.* 5, 309–323. doi:10.1016/j.ejrh.2015.11.007

DeOreo, W. B., Mayer, P. W., Dziegielewski, B., and Kiefer, J. (2016). *Residential end uses of water*. United States: Water Research Foundation.

Dickson, K. E., and Dzombak, D. A. (2019). Water Supply Risk in the United States 2015-2050 Considering Projected Changes in Population and Thermoelectric Power Demand. *Environ. Sci. Technol.* 53 (24), 14113–14122. doi:10.1021/acs.est.9b02435

Dieter, C. A., Maupin, M. A., Caldwell, R. R., Harris, M. A., Ivahnenko, T. I., Lovelace, J. K., et al. (2018). Estimated use of water in the United States in 2015: U.S. Geological Survey Circular 1441. Supersedes USGS Open-File Report 2017–1131, 65. doi:10.3133/cir1441

Dilling, L., Daly, M. E., Kenney, D. A., Klein, R., Miller, K., Ray, A. J., et al. (2019). Drought in urban water systems: Learning lessons for climate adaptive capacity. *Clim. Risk Manag.* 23, 32–42. doi:10.1016/j.crm.2018.11.001

Donnelly, K., and Cooley, H. (2015). *Water Use Trends*. Oakland, California: Pacific Institute.

Ekström, M., Grose, M. R., and Whetton, P. H. (2015). An appraisal of downscaling methods used in climate change research. *Wires Clim. Change* 6 (3), 301–319. doi:10.1002/wcc.339

Forster, P. M., Maycock, A. C., McKenna, C. M., and Smith, C. J. (2020). Latest Climate Models Confirm Need for Urgent Mitigation. *Nat. Clim. Chang.* 10 (1), 7–10. doi:10.1038/s41558-019-0660-0

Foti, R., Ramirez, J. A., and Brown, T. C. (2012). *Vulnerability of US water supply to shortage: a technical document supporting the Forest Service 2010 RPA Assessment. Gen. Tech. Rep. RMRS-GTR-295*, 147. Fort Collins, CO: US Department of Agriculture, Forest Service, Rocky Mountain Research Station, 295.

Gober, P., Quay, R., and Larson, K. L. (2016). Outdoor Water Use as an Adaptation Problem: Insights from North American Cities. *Water Resour. Manage.* 30 (3), 899–912. doi:10.1007/s11269-015-1205-6

Goss, M., Swain, D. L., Abatzoglou, J. T., Sarhadi, A., Kolden, C. A., Williams, A. P., et al. (2020). Climate Change is Increasing the Likelihood of Extreme Autumn Wildfire Conditions Across California. *Environ. Res. Lett.* 15 (9), 094016. doi:10.1088/1748-9326/ab83a7

Gupta, H. V., Kling, H., Yilmaz, K. K., and Martinez, G. F. (2009). Decomposition of the mean squared error and NSE performance criteria: Implications for improving hydrological modelling. *J. Hydrol.* 377 (1-2), 80–91. doi:10.1016/j.jhydrol.2009.08.003

Hart, O. E., and Halden, R. U. (2019). On the need to integrate uncertainty into U.S. water resource planning. *Sci. Total Environ.* 691, 1262–1270. doi:10.1016/j.scitotenv.2019.07.164

Hauer, M. E. (2019). Population projections for U.S. counties by age, sex, and race controlled to shared socioeconomic pathway. *Sci. Data* 6 (1), 190005–190015. doi:10.1038/sdata.2019.5

Hoegh-Guldberg, O., Jacob, D., Bindi, M., Brown, S., Camilloni, I., Diedhiou, A., et al. (2018). *Impacts of 1.5 C global warming on natural and human systems.* Global warming of 1.5 C. An IPCC Special Report. Geneva: IPCC Secretariat.

Hong, C.-y., and Chang, H. (2014). Uncovering the influence of household sociodemographic and behavioral characteristics on summer water consumption in the Portland Metropolitan Area. *Int. J. Geospatial Environ. Res.* 1 (2), 2.

Howitt, R., MacEwan, D., Medellín-Azuara, J., Lund, J., and Sumner, D. (2015). "Economic analysis of the 2015 drought for California agriculture. UC Davis Center for Watershed Sciences," in *ERA, Economics* (California: UC Agricultural Issues Center CA).

Hurd, B., Leary, N., Jones, R., and Smith, J. (1999). Relative Regional Vulnerability of Water Resources to Climate Change. *J. Am. Water Resour. Assoc* 35 (6), 1399–1409. doi:10.1111/j.1752-1688.1999.tb04224.x

Islam, M. A., and Cartwright, N. (2020). Evaluation of climate reanalysis and space-borne precipitation products over Bangladesh. *Hydrological Sci. J.* 65 (7), 1112–1128. doi:10.1080/02626667.2020.1730845

Ivancic, T. J., and Shaw, S. B. (2017). Identifying spatial clustering in change points of streamflow across the contiguous U.S. between 1945 and 2009. *Geophys. Res. Lett.* 44 (5), 2445–2453. doi:10.1002/2016gl072444

Jehn, F. U., Bestian, K., Breuer, L., Kraft, P., and Houska, T. (2020). Using hydrological and climatic catchment clusters to explore drivers of catchment behavior. *Hydrol. Earth Syst. Sci.* 24 (3), 1081–1100. doi:10.5194/hess-24-1081-2020

Jones, C. N., Ameli, A., Neff, B. P., Evenson, G. R., McLaughlin, D. L., Golden, H. E., et al. (2019). Modeling Connectivity of Non-floodplain Wetlands: Insights, Approaches, and Recommendations. *J. Am. Water Resour. Assoc.* 55 (3), 559–577. doi:10.1111/1752-1688.12735

Katz, R. (2002). Techniques for estimating uncertainty in climate change scenarios and impact studies. *Clim. Res.* 20 (2), 167–185. doi:10.3354/cr020167

Keilman, N. (2020). Uncertainty in population forecasts for the twenty-first century. *Ann. Rev. Res. Econ.* 12, 449–470.

Kling, H., Fuchs, M., and Paulin, M. (2012). Runoff conditions in the upper Danube basin under an ensemble of climate change scenarios. *J. Hydrol.* 424-425, 264–277. doi:10.1016/j.jhydrol.2012.01.011

Knoben, W. J. M., Woods, R. A., and Freer, J. E. (2018). A Quantitative Hydrological Climate Classification Evaluated with Independent Streamflow Data. *Water Resour. Res.* 54 (7), 5088–5109. doi:10.1029/2018wr022913

Kovach, R. P., Dunham, J. B., Al-Chokhachy, R., Snyder, C. D., Letcher, B. H., Young, J. A., et al. (2019). An integrated framework for ecological drought across riverscapes of North America. *BioScience* 69 (6), 418–431. doi:10.1093/biosci/biz040

Lafon, T., Dadson, S., Buys, G., and Prudhomme, C. (2013). Bias correction of daily precipitation simulated by a regional climate model: a comparison of methods. *Int. J. Climatol.* 33 (6), 1367–1381. doi:10.1002/joc.3518

Lawrence, M. G. (2005). The relationship between relative humidity and the dewpoint temperature in moist air: A simple conversion and applications. *Bull. Amer. Meteorol. Soc.* 86 (2), 225–234. doi:10.1175/bams-86-2-225

Maas, A., Dozier, A., Manning, D. T., and Goemans, C. (2017). Water storage in a changing environment: The impact of allocation institutions on value. *Water Resour. Res.* 53 (1), 672–687. doi:10.1002/2016wr019239

MacDonald, G. M., Stahle, D. W., Diaz, J. V., Beer, N., Busby, S. J., Cerano-Paredes, J., et al. (2008). Climate Warming and 21st-Century Drought in Southwestern North America. *Eos Trans. AGU* 89 (9), 82. doi:10.1029/2008eo090003

MacDonald, G. M. (2010). Water, climate change, and sustainability in the southwest. *Proc. Natl. Acad. Sci.* 107 (50), 21256–21262. doi:10.1073/pnas.0909651107

Mahat, V., Ramírez, J. A., and Brown, T. C. (2017). Twenty-first-century climate in CMIP5 simulations: implications for snow and water yield across the contiguous United States. *J. Hydrometeorology* 18 (8), 2079–2099. doi:10.1175/jhm-d-16-0098.1

Mankin, J. S., Viviroli, D., Singh, D., Hoekstra, A. Y., and Diffenbaugh, N. S. (2015). The potential for snow to supply human water demand in the present and future. *Environ. Res. Lett.* 10 (11), 114016. doi:10.1088/1748-9326/10/11/114016

March, H., and Saurí, D. (2010). The suburbanization of water scarcity in the Barcelona metropolitan region: Sociodemographic and urban changes influencing domestic water consumption. *The Prof. Geographer* 62 (1), 32–45. doi:10.1080/00330120903375860

Maurer, E. P., and Duffy, P. B. (2005). Uncertainty in projections of streamflow changes due to climate change in California. *Geophys. Res. Lett.* 32 (3), L03704. doi:10.1029/2004gl021462

Mei, C., Liu, J., Wang, H., Yang, Z., Ding, X., and Shao, W. (2018). Integrated assessments of green infrastructure for flood mitigation to support robust decision-making for sponge city construction in an urbanized watershed. *Sci. Total Environ.* 639, 1394–1407. doi:10.1016/j.scitotenv.2018.05.199

Mendoza, P. A., Wood, A. W., Clark, E., Rothwell, E., Clark, M. P., Nijssen, B., et al. (2017). An intercomparison of approaches for improving operational seasonal streamflow forecasts. *Hydrol. Earth Syst. Sci.* 21 (7), 3915–3935. doi:10.5194/hess-21-3915-2017

Moss, R. H., Edmonds, J. A., Hibbard, K. A., Manning, M. R., Rose, S. K., Van Vuuren, D. P., et al. (2010). The next generation of scenarios for climate change research and assessment. *Nature* 463 (7282), 747–756. doi:10.1038/nature08823

Nilsson, B., Højberg, A. L., Refsgaard, J. C., and Troldborg, L. (2007). Uncertainty in geological and hydrogeological data. *Hydrol. Earth Syst. Sci.* 11 (5), 1551–1561. doi:10.5194/hess-11-1551-2007

Opalinski, N. F., Bhaskar, A. S., and Manning, D. T. (2020). Spatial and Seasonal Response of Municipal Water Use to Weather across the Contiguous U.S. *J. Am. Water Resour. Assoc.* 56 (1), 68–81. doi:10.1111/1752-1688.12801

Özerol, G., Dolman, N., Bormann, H., Bressers, H., Lulofs, K., and Böge, M. (2020). Urban water management and climate change adaptation: A self-assessment study by seven midsize cities in the North Sea Region. *Sust. Cities Soc.* 55, 102066. doi:10.1016/j.scs.2020.102066

Pool, S., Vis, M., and Seibert, J. (2018). Evaluating model performance: towards a non-parametric variant of the Kling-Gupta efficiency. *Hydrological Sci. J.* 63 (13-14), 1941–1953. doi:10.1080/02626667.2018.1552002

Radić, V., and Clarke, G. K. (2011). Evaluation of IPCC models' performance in simulating late-twentieth-century climatologies and weather patterns over North America. *J. Clim.* 24 (20), 5257–5274.

Rajagopal, S., and Harpold, A. A. (2016). Testing and improving temperature thresholds for snow and rain prediction in the Western United States. *J. Am. Water Resour. Assoc.* 52 (5), 1142–1154. doi:10.1111/1752-1688.12443

Ramey, J. A. (2014). *noncensus: U.S. Census Regional and Demographic Data.* 1 ed. Vienna: CRAN.

Rasifaghihi, N., Li, S. S., and Haghighat, F. (2020). Forecast of urban water consumption under the impact of climate change. *Sust. Cities Soc.* 52, 101848. doi:10.1016/j.scs.2019.101848

Razavi, T., and Coulibaly, P. (2013). Streamflow prediction in ungauged basins: review of regionalization methods. *J. Hydrol. Eng.* 18 (8), 958–975. doi:10.1061/(asce)he.1943-5584.0000690

Reid, A. J., Carlson, A. K., Creed, I. F., Eliason, E. J., Gell, P. A., Johnson, P. T. J., et al. (2019). Emerging threats and persistent conservation challenges for freshwater biodiversity. *Biol. Rev.* 94 (3), 849–873. doi:10.1111/brv.12480

Ritchie, H., and Roser, M. (2017). *Water use and stress*. Oxford: Our World in Data.

Rosegrant, M. W., and Cai, X. (2002). Global Water Demand and Supply Projections. *Water Int.* 27 (2), 170–182. doi:10.1080/02508060208686990

Roy, S. B., Chen, L., Girvetz, E. H., Maurer, E. P., Mills, W. B., and Grieb, T. M. (2012). Projecting Water Withdrawal and Supply for Future Decades in the U.S. under Climate Change Scenarios. *Environ. Sci. Technol.* 46 (5), 2545–2556. doi:10.1021/es2030774

Ruth, M., Bernier, C., Jollands, N., and Golubiewski, N. (2007). Adaptation of urban water supply infrastructure to impacts from climate and socioeconomic changes: the case of Hamilton, New Zealand. *Water Resour. Manage.* 21 (6), 1031–1045. doi:10.1007/s11269-006-9071-x

Saadi, M., Oudin, L., and Ribstein, P. (2019). Random forest ability in regionalizing hourly hydrological model parameters. *Water* 11 (8), 1540. doi:10.3390/w11081540

Sabo, J. L., Sinha, T., Bowling, L. C., Schoups, G. H. W., Wallender, W. W., Campana, M. E., et al. (2010). Reclaiming freshwater sustainability in the Cadillac Desert. *Proc. Natl. Acad. Sci.* 107 (50), 21263–21269. doi:10.1073/pnas.1009734108

Sawicz, K., Wagener, T., Sivapalan, M., Troch, P. A., and Carrillo, G. (2011). Catchment classification: empirical analysis of hydrologic similarity based on catchment function in the eastern USA. *Hydrol. Earth Syst. Sci.* 15 (9), 2895–2911. doi:10.5194/hess-15-2895-2011

Schwalm, C. R., Williams, C. A., Schaefer, K., Baldocchi, D., Black, T. A., Goldstein, A. H., et al. (2012). Reduction in carbon uptake during turn of the century drought in western North America. *Nat. Geosci* 5 (8), 551–556. doi:10.1038/ngeo1529

Seguro, J. V., and Lambert, T. W. (2000). Modern estimation of the parameters of the Weibull wind speed distribution for wind energy analysis. *J. wind Eng. Ind. aerodynamics* 85 (1), 75–84. doi:10.1016/s0167-6105(99)00122-1

Semenov, M., Brooks, R., Barrow, E., and Richardson, C. (1998). Comparison of the WGEN and LARS-WG stochastic weather generators for diverse climates. *Clim. Res.* 10 (2), 95–107. doi:10.3354/cr010095

Shamir, E., Megdal, S. B., Carrillo, C., Castro, C. L., Chang, H.-I., Chief, K., et al. (2015). Climate change and water resources management in the Upper Santa Cruz River, Arizona. *J. Hydrol.* 521, 18–33. doi:10.1016/j.jhydrol.2014.11.062

Shen, C. (2018). A transdisciplinary review of deep learning research and its relevance for water resources scientists. *Water Resour. Res.* 54 (11), 8558–8593. doi:10.1029/2018wr022643

Statistics Canada (2019a). *Population estimates, July 1, by census subdivision, 2016 boundaries*. Available at: https://www150.statcan.gc.ca/t1/tbl1/en/tv.action?pid=1710014201.

Statistics Canada (2019b). *Census division 2016*. Available at: https://open.canada.ca/data/en/dataset/883964ca-be79-4d0d-ba9e-68babe59624e.

Stoker, P., and Rothfeder, R. (2014). Drivers of urban water use. *Sust. Cities Soc.* 12, 1–8. doi:10.1016/j.scs.2014.03.002

Sugg, M., Runkle, J., Leeper, R., Bagli, H., Golden, A., Handwerger, L. H., et al. (2020). A scoping review of drought impacts on health and society in North America. *Climatic Change*, 1–19. doi:10.1007/s10584-020-02848-6

Tanaka, S. K., Zhu, T., Lund, J. R., Howitt, R. E., Jenkins, M. W., Pulido, M. A., et al. (2006). Climate warming and water management adaptation for California. *Climatic Change* 76 (3), 361–387. doi:10.1007/s10584-006-9079-5

Taylor, K. E., Stouffer, R. J., and Meehl, G. A. (2012). An overview of CMIP5 and the experiment design. *Bull. Am. Meteorol. Soc.* 93 (4), 485–498. doi:10.1175/bams-d-11-00094.1

Tellman, B., Schank, C., Schwarz, B., Howe, P. D., and de Sherbinin, A. (2020). Using Disaster Outcomes to Validate Components of Social Vulnerability to Floods: Flood Deaths and Property Damage across the USA. *Sustainability* 12 (15), 6006. doi:10.3390/su12156006

Teutschbein, C., and Seibert, J. (2012). Bias correction of regional climate model simulations for hydrological climate-change impact studies: Review and evaluation of different methods. *J. Hydrol.* 456-457, 12–29. doi:10.1016/j.jhydrol.2012.05.052

Thiemig, V., Rojas, R., Zambrano-Bigiarini, M., and De Roo, A. (2013). Hydrological evaluation of satellite-based rainfall estimates over the Volta and Baro-Akobo Basin. *J. Hydrol.* 499, 324–338. doi:10.1016/j.jhydrol.2013.07.012

Tian, Y., Peters-Lidard, C. D., Eylander, J. B., Joyce, R. J., Huffman, G. J., Adler, R. F., et al. (2009). Component analysis of errors in satellite-based precipitation estimates. *J. Geophys. Res. Atmospheres* 114 (D24), D24101. doi:10.1029/2009jd011949

United States Census Bureau (2019). *City and Town Population Totals*. Available at: https://www.census.gov/data/tables/time-series/demo/popest/2010s-total-cities-and-towns.html.

US Geological Survey (2019). *USGS surface water data for the nation*. Available at: https://waterdata.usgs.gov/nwis/sw.

Van Vuuren, D. P., Edmonds, J., Kainuma, M., Riahi, K., Thomson, A., Hibbard, K., et al. (2011). The representative concentration pathways: an overview. *Climatic change* 109 (1), 5–31. doi:10.1007/s10584-011-0148-z

Walter, I. A., Allen, R. G., Elliott, R., Jensen, M., Itenfisu, D., Mecham, B., et al. (2000). ASCE's standardized reference evapotranspiration equation. *Watershed Manag. operations Manag. 2000*, 1–11.

Ward, J. H., Jr (1963). Hierarchical grouping to optimize an objective function. *J. Am. Stat. Assoc.* 58 (301), 236–244. doi:10.1080/01621459.1963.10500845

Water Survey of Canada (2019). *National Water Data Archive: HYDAT*. Available: https://www.canada.ca/en/environment-climate-change/services/wateroverview/quantity/monitoring/survey/data-products-services/nationalarchive-hydat.html#shr-pg0.

Wilks, D. S., and Wilby, R. L. (1999). The weather generation game: a review of stochastic weather models. *Prog. Phys. Geogr.* 23 (3), 329–357. doi:10.1191/030913399666525256

Wong, J. S., Zhang, Q., and Chen, Y. D. (2010). Statistical modeling of daily urban water consumption in Hong Kong: Trend, changing patterns, and forecast. *Water Resour. Res.* 46 (3), W03506. doi:10.1029/2009wr008147

Xu, Y. (2015). *Hyfo: hydrology and climate forecasting R Package for data analysis and visualization*. Available at: https://cran.r-project.org/web/packages/hyfo/index.html.

Yang, T.-H., and Liu, W.-C. (2020). A General overview of the risk-reduction strategies for floods and droughts. *Sustainability* 12 (7), 2687. doi:10.3390/su12072687

Yang, T., Shi, P., Yu, Z., Li, Z., Wang, X., and Zhou, X. (2016). Probabilistic modeling and uncertainty estimation of urban water consumption under an incompletely informational circumstance. *Stoch Environ. Res. Risk Assess.* 30 (2), 725–736. doi:10.1007/s00477-015-1081-x

frontiers
in Earth Science

Groundwater Drought and Cycles in Xuchang City, China

Jia Huang, Lianhai Cao*, Furong Yu, Xiaobo Liu and Lei Wang

North China University of Water Resources and Electric Power, Zhengzhou, China

The urban groundwater system is complex and affected by the interaction of natural and human factors. Groundwater scarcity can no longer reflect this complex situation, and the concept of groundwater drought can better interpret this situation. The groundwater drought cycle is the time interval in which groundwater droughts occur repeatedly and twice in a row. The study of the groundwater drought cycle can more comprehensively grasp the development characteristics of the groundwater drought, which is of great importance for the development, utilization, and protection of groundwater. This study used monthly observation data from seven groundwater wells in Xuchang, China, in the period 1980–2018. We applied the Kolmogorov–Smirnov test to select the best fitting distribution function and constructed a Standardized Groundwater Index (SGI). We analyzed groundwater drought at different time scales and used Morlet's continuous complex wavelet transform to analyze the groundwater drought cycles. The following results were obtained: 1) the maximum intensity of groundwater drought in the seven observation wells ranged from 104.40 to 187.10. Well-3# has the most severe groundwater drought; 2) the drought years of well-5# were concentrated in 1984–1987 and 2003–2012 and those in the other wells in 1994–1999 and 2014–2018; and 3) the groundwater drought cycles in the seven observation wells were 97–120 months, and the average period is about 110 months. The cycle length had the following order: well-7# > well-4# > well-5# > well-2# > well-1# > well-3# > well-6. Therefore, Morlet wavelet transform analysis can be used to study the groundwater drought cycles and can be more intuitive in understanding the development of regional groundwater droughts. In addition, through the study of the Xuchang groundwater drought and its cycle, the groundwater drought in Xuchang city has been revealed, which can help local relevant departments to provide technical support and a scientific basis for the development, utilization, and protection of groundwater in the region.

Keywords: Xuchang city, groundwater drought, Standardized Groundwater Index, wavelet analysis, drought period

INTRODUCTION

Drought is an extreme and complex natural disaster that can cause great economic losses and has the characteristics of long duration, wide impact, and high frequency. It seriously threatens the safety and stability of human society and is called a "spreading disaster" (Mishra and Singh, 2010; Wilhite, 2000). Climate change has a huge impact on hydrological processes (Intergovernmental Panel on Climate Change (IPCC), 2013; Wilhite, 2000; Oo et al., 2020), and its impact on groundwater resources cannot be ignored (Zhou et al., 2010; Kavitha and Chandran, 2015; Dua et al., 2020).

FIGURE 1 | Schematic diagram of groundwater drought pressure, state, and response.
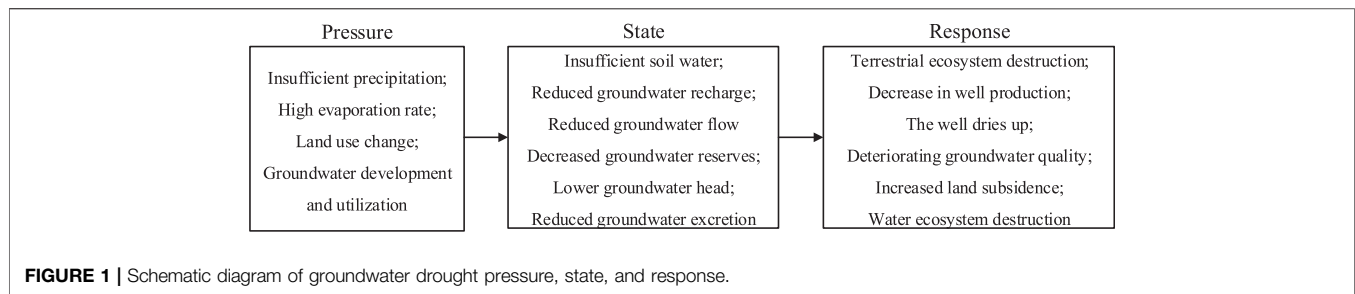
Groundwater drought, as a concept that links groundwater resources with drought, is gradually separating from hydrological drought and agricultural drought and has become a separate research area in recent years, gaining the attention of scholars from around the world. It is defined as a phenomenon in which the groundwater level is lower than the normal or the flow rate decreases in the spring (Van Loon and Anne, 2015; Marchant and Bloomfield, 2018). Like other common droughts, it is a natural disaster caused by the dual impact of social development and climate change, impeding the development and stability of society (Taylor et al., 2012; Medellín-Azuara et al., 2015). Natural factors causing such droughts include temperature and precipitation. Rising temperatures lead to an increase in evapotranspiration, and insufficient precipitation leads to a decrease in surface runoff and soil moisture, thus affecting groundwater replenishment. In addition, a large amount of groundwater is used for intensive farmland irrigation, and a small amount of groundwater is used in households and production. Overexploitation of groundwater makes it difficult for groundwater to return to normal levels, leading to groundwater drought. The pressure, state, and response of the groundwater drought are shown in **Figure 1**.

Under the combined influence of natural factors and human activities, groundwater drought may exhibit complex characteristics. In addition, due to the lack of direct observational data on groundwater resources, it is difficult to quantitatively assess groundwater drought. However, since groundwater drought has attracted the attention of scholars in the fields of meteorology, hydrology, and geology, it has become an important research topic. The Groundwater Resource Index (GRI), as a reliable tool in a multi-analysis approach for monitoring and forecasting drought conditions, was developed by Mendicino et al. (2008). Macdonald et al. (2009) studied the principles of groundwater drought using hydrogeological maps, while Li and Rodell (2015) used the Groundwater Drought Index (GWI) to assess groundwater drought in the central and northeastern United States. After the launch of the Gravity Recovery and Climate Experiment (GRACE) satellite, scholars will be able to use remote sensing methods to assess changes in groundwater reserves and use the results in response to drought (Scanlon BR. et al., 2012; Scanlon B. R. et al., 2012). Until 2017, Thomas et al. (2017) explicitly included and evaluated the Groundwater Drought Index based on GRACE observations to understand and identify groundwater drought and applied it in the Central Valley of California, thus pioneering the direct application of the GRACE satellite to assess groundwater drought. Seo and Lee (2019) combined GRACE satellite data and other remote sensing methods to build an artificial neural network model to monitor the groundwater drought in South Korea, thus providing a new idea for the use of satellite methods to monitor groundwater drought. Wang et al. (2020) used the GRACE Groundwater Drought Index (GGDI) as an indicator to assess groundwater drought and comprehensively identified the temporal evolution, spatial distribution, and trend characteristics of the drought in the North China Plain from 2003 to 2015. Afterwards, they used cross-wavelet transform technology to clarify the difference between GGDI and teleconnection factors. The relationship between relevant factors has achieved good results and gained new insights for the application of GRACE gravity satellites to monitor groundwater drought. The Standardized Water-Level Index (SWI) was originally developed by Bhuiyan (2004) to evaluate the hydrological drought with the help of the groundwater level recharge deficit and was later applied to the study of groundwater drought. Rahim et al. (2015) used SWI to estimate the groundwater recharge deficit in the pre-monsoon and post-monsoon seasons and then performed a spatial interpolation to determine the degree of groundwater drought in the study area. Nagarajan et al. (2015) used SWI as a Ground Observation Index combined with satellite information to evaluate the drought vulnerability of the Peddavagu watershed in the sub-basin of the Krishna River system on the Indian peninsula.

The Standardized Precipitation Index (SPI) is one of the most widely used evaluation indicators in the field of drought. Monitoring meteorological droughts can serve as a guide for planning and implementing groundwater management policies (CTGCD, 2011; Texas Water Code, 2016). Therefore, it is also used in the assessment of groundwater drought (Fiorillo and Guadagno, 2010; Fiorillo and Guadagno, 2012). Bhuiyan et al. (2006) combined SWI with SPI, Normalized Difference Vegetation Index (NDVI), Vegetation Condition Index (VCI), Temperature Condition Index (TCI), and Vegetation Health Index (VHI) to monitor drought dynamics in the Alawari region (India). On the basis of SPI, Bloomfield Marchant (2013) and Bloomfield et al. (2015) used monthly groundwater level data to construct the Standardized Groundwater-Level Index (SGI), which is specifically used to evaluate groundwater drought, and analyzed the correlation between SGI and SPI on multiple time scales. As a result, the use of SGI to assess groundwater drought has grown. Pathak et al. (2016)

performed a cluster analysis of the long-term monthly groundwater level in the Gataprabha River Basin in India. This study classified observation wells which performed the Mann-Kendall test in order to analyze annual and seasonal groundwater level trends and used SGI to evaluate the area groundwater drought. Motlagh et al. (2016) used stochastic models to predict the groundwater level and then used SGI to predict and warn the local groundwater drought. Liu et al. (2016) used monthly groundwater level data from 40 observation wells in Jiangsu Province, China, from 1989 to 2012, and used SGI to conduct a spatio-temporal analysis of groundwater drought in the province. However, the calculation method of SGI proposed by Bloomfield Marchant (2013); Bloomfield et al. (2015) considered both parametric and non-parametric cases. The monthly series of groundwater level were fitted with the gamma function, without considering whether the gamma function could be fitted with the monthly series data of groundwater level in other regions, which would have a certain impact on the final groundwater drought assessment. Based on this, Lorenzo-Lacruz et al. (2017) modified the SGI according to the Standardized Runoff Index (SSI) (Vicente-Serrano et al., 2012) and established an index according to different probability distributions of monthly series of groundwater level, which can ensure adaptability of calculated SGI to different climate and water conditions and can more accurately reflect the conditions of groundwater drought.

Drought monitoring and identification of characteristics are an important part of dealing with drought risks (Harisuseno, 2020; Kavianpour et al., 2020). Based on a quantitative assessment of groundwater drought conditions, some scholars have begun to identify the characteristics of groundwater drought. Groundwater drought has characteristics similar to traditional drought, which is a multivariate phenomenon. There is a certain correlation and dependence between several characteristic variables (e.g., drought duration, drought intensity, and drought influence range), so traditional analysis with one variable (e.g., drought frequency) may not be conducive to comprehensively study groundwater drought events, leading to insufficient and inaccurate drought risk assessment (Pathak and Dodamani, 2021). The Copula function has been widely used in drought field research (Zhou et al., 2012; Xu et al., 2015; Wu et al., 2018). It can fit into the distribution functions of multiple drought-characteristic variables and can effectively describe the correlation between variables. Although groundwater drought research started late, studies have shown that the Copula function can also be used in research and analysis of groundwater drought. For example, while Saghafian and Sanginabadi (2020) proposed a framework for statistical analysis of disturbed hydrological system, they carried out multivariate groundwater drought analysis based on the Copula function in an overexploited aquifer and used a goodness-of-fit test to compare Copula and the empirical groundwater drought frequency, which proved that the Copula model had sufficient accuracy in multivariate drought analysis. Pathak and Dodamani (2021) studied the response of groundwater drought to meteorological drought and the local aquifer characteristics using monthly groundwater level data in the tropical river basin of India and the Copula function to conduct a bivariate (drought intensity and drought duration) frequency analysis of groundwater drought.

However, research on the characteristics of groundwater drought is mainly concentrated in the return period (frequency analysis), and there is little research on the groundwater drought cycle. The return period is the frequency of events in a certain period, which is random and uncertain, and the drought return period is mainly used to evaluate the severity of drought events. A cycle is a cyclic law that exists in the development process of things, which is deterministic, and the drought cycle is the time interval between two adjacent droughts. Therefore, conducting research on the groundwater drought cycle can provide a more comprehensive understanding of groundwater drought characteristics, understand the law of regional groundwater development, and strengthen the groundwater drought early warning mechanism. Continuous wavelet transform is a common method in wavelet analysis. It can more effectively identify the non-monotonic trend of hydrological sequences (Sang et al., 2018) and is widely used in the field of hydrology. For example, Pathak et al. (2016) used wavelet transform methods to analyze seasonal temperatures, precipitation, and runoff trends in the Midwest of the United States. Djordje et al. (2021) used wavelet transform spectrum analysis (WTS) and other methods to study the long-term characteristics of the Danube water level and the flow and changes in natural cycles. Palizdan (2017) applied a continuous wavelet transform to analyze the long-term precipitation trend in the Langat River Basin (Malaysia), while Li and Zhu (2021) further improved the wavelet transform method to identify the runoff cycle of the Heihe River (China).

In this paper, we used the continuous wavelet transform method to identify the period of groundwater drought and to grasp the principles of groundwater drought in Xuchang city. The objectives of this study are 1) to determine changes in groundwater drought in different observation wells in Xuchang city from 1980 to 2018 and 2) to evaluate the change cycle of groundwater drought in Xuchang city.

DATA AND METHODS

Study Area

Xuchang city (34°16′–34°58′N, 112°42′–114°14′E) is located in the central part of Henan Province (China) and covers an area of 4,996 km². It is located in the transition zone between Funiu Mountain and the Eastern Henan Plain. Plains dominate with 72.8%, while hills and mountains account for 16.8 and 10.4%, respectively. The region has a temperate continental monsoon climate with an average annual temperature from 14.3 to 14.6°C and an average annual precipitation from 671 to 736 mm. According to the lithological characteristics of aquifers and the nature of groundwater storage in Xuchang area, regional groundwater can be divided into four types: loose rock pore water, clastic rock fissure water, carbonate rock fissure karst water, and magmatic rock fissure water. Pore water is distributed in vast plains and hilly areas, whereas fissure water and karst water are distributed in the bedrocks of the mountains.
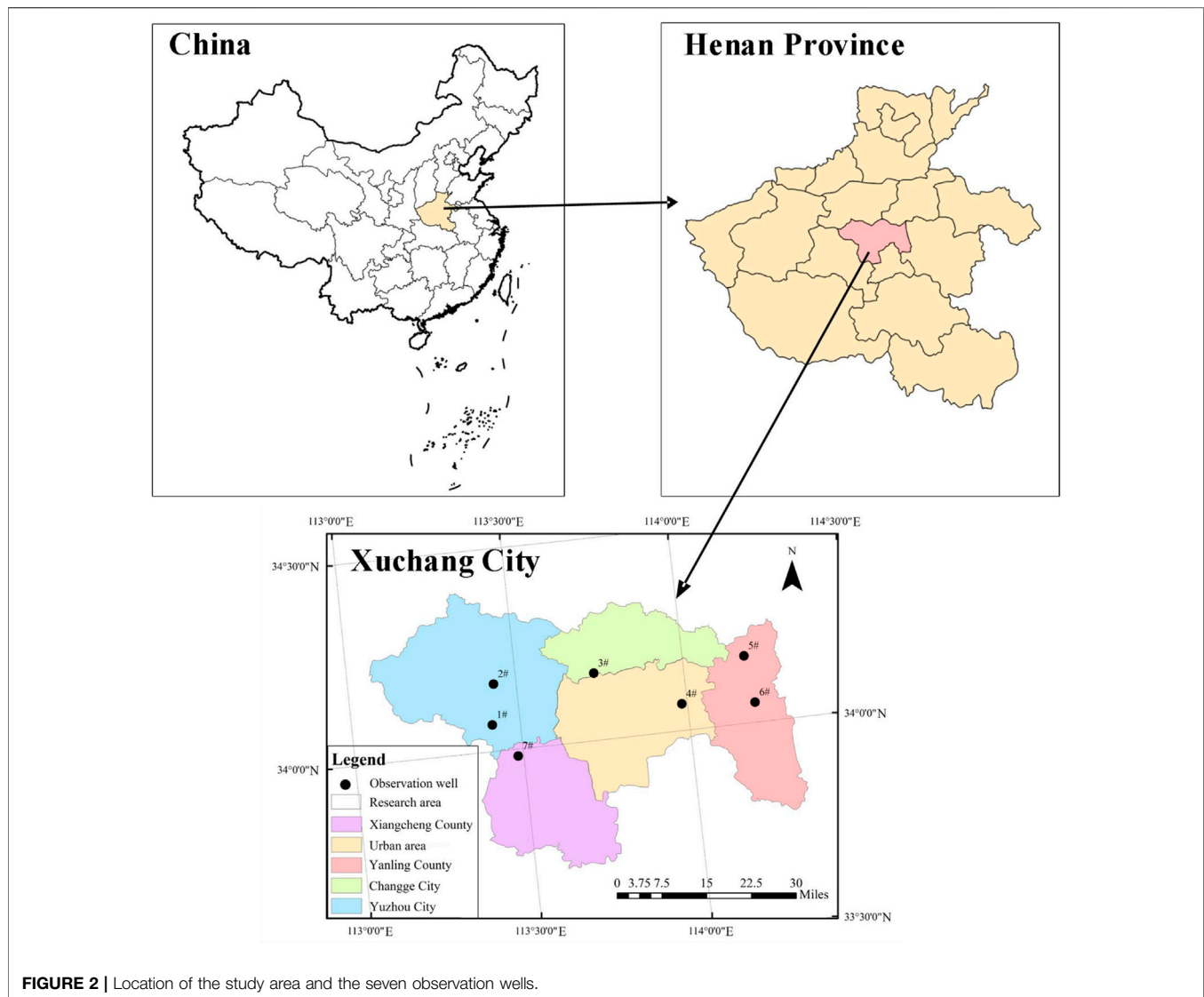
FIGURE 2 | Location of the study area and the seven observation wells.

The shallow loose rock-type pore is the most important water-bearing rock group in the region and the analyzed groundwater belongs to this group.

Data

Monthly groundwater level data were obtained from the local Hydrographic Bureau. We used the monthly data from seven observation wells with relatively complete datasets from 1980 to 2018. For some missing data, cubic spline function interpolation was used to supplement the data (Peng-zhu et al., 2015). The locations of the seven observation wells are shown in **Figure 2**.

Methods

Standardized Groundwater Index

The SGI is an indicator that measures the degree of groundwater drought based on changes in groundwater level. It is currently a more reliable tool for assessing groundwater drought. Bloomfield et al. (2015) revised the Standardized Precipitation Index (SPI)

and proposed the SGI for groundwater drought analysis. In their study, the SGI uses gamma distribution in SPI for fitting. However, the monthly distribution of groundwater may not be consistent with the gamma distribution (Liu et al., 2016), and therefore the method proposed by Lorenzo-Lacruz et al., 2017 can be used to calculate SGI for different fitting distribution functions in this study. The SGI calculation formula (Lorenzo-Lacruz et al., 2017) is as follows:

$$SGI = S\left(W - \frac{C_0 + C_1 W + C_2 W^2}{1 + d_1 W + d_2 W^2 + d_3 W^3}\right), \qquad (1)$$

$$W = \sqrt{-2\ln P}, \qquad (2)$$

where $F(x)$ is the cumulative distribution probability for determining the fitted distribution function, P is the groundwater level distribution probability related to function $F(x)$, x is the monthly groundwater level sample, and S is the positive and negative coefficient of probability density. If

$F(x) \geq 0.5$, $P = 1\text{-}F(x)$, $S = 1$; if not, $P = F(x)$, $S = -1$. C_0, C_1, C_2 and d_1, d_2, d_3 are the calculation parameters of the gamma distribution function converted into cumulative frequency in order to simplify the approximate solution formula. The constants are $C_0 = 2.515517$, $C_1 = 0.802853$, $C_2 = 0.010328$, $d_1 = 1.432788$, $d_2 = 0.189269$, and $d_3 = 0.001308$.

Based on this, the key to calculating the SGI is to find the most suitable fitting distribution function. Here, we used gamma distribution, beta distribution, log-normal distribution (logN), Weibull distribution (Web), normal distribution, and the generalized extreme value (GEV) distribution to fit the data of the seven observation wells. These distribution functions are not only more common but also have strong adaptability, satisfying the cumulative frequency calculation of monthly data series on groundwater levels in different situations (Guttman, 1998).

Prior to calculating the SGI, we normalized the original data column (x) and introduced the processed data column (x') in subsequent calculations. To facilitate subsequent distribution function fitting, we replaced 0 and 1 in the new data column with 0.001 and 0.999, respectively. The normalization formula (Chen et al., 2019) is as follows:

$$x' = \frac{\max(x) - x}{\max(x) - \min(x)}. \qquad (3)$$

After obtaining a normalized data column, we began to fit the distribution function. This step was performed with the help of the MATLAB 2018b software platform.

After that, the Kolmogorov–Smirnov (KS) test was performed on the fitting distribution results of the data of each observation well, and the fitting distribution function with the lowest statistic D was selected as the best fitting distribution function of the observation well, introduced into **Eq. 1**. The KS test equation (Xi-zhi and Wang, 1996) is as follows:

$$D = \max\left(\max_i\left|COF(x_i) - \frac{r-1}{n}, \frac{r}{n} - CDF(xi)\right|\right), \qquad (4)$$

where r is the rank of the observation i in ascending order.

Wavelet Analysis

Wavelet analysis, known as the "mathematical microscope," is particularly suitable for processing non-stationary signals because it can detect the characteristics of time-frequency detailed information and can reveal the main distribution of oscillation periods hidden in time series, which is useful for the future of the system. The development trend has been qualitatively estimated and is widely used in the research fields related to atmosphere, hydrology, and geography, among others (Aussen et al., 1997; Smith et al., 1998; Nason and Sapatinas, 2002).

When using wavelet to analyze practical problems, we have to choose the suitable basis for the wavelet function. Morlet is a harmonic smoothed by the Gaussian function and a complex wavelet that is widely used in the field of hydrology (Kulkarni, 2000). Therefore, we chose Morlet's continuous complex wavelet transform to analyze the characteristics of groundwater time series on multiple time scales. For a given wavelet function, continuous wavelet transform of the hydrological time series $f(t) \in L^2(R)$(Wang et al., 2005) is expressed as follows:

$$W_f(a,b) = |a|^{-\frac{1}{2}} \int_{-\infty}^{\infty} f(t)\overline{\psi}\left(\frac{t-b}{a}\right)dt, \qquad (5)$$

where a is the scaling scale $(a \neq 0)$, which reflects the characteristics of the frequency domain; b is the translation parameter, which reflects the characteristics of the time domain; $\overline{\psi}\left(\frac{t-b}{a}\right)$ is the complex conjugate function of $\psi(t)$; and $\psi(t)$ is the basis wavelet function. Here, $W_f(a,b)$ is the wavelet transform coefficient, which is the inner product of the continuous wavelet and the signal on the scale a and displacement b, indicating the degree of similarity between the signal and the wavelet represented by the point. When the value of a is small, a higher time domain resolution can be obtained; the opposite occurs for small value of a.

Because it is difficult to express a continuous sequence with digital symbols in actual application, a continuous time sequence is often discretized. This is also the case for hydrological time series. Total, average, or extreme values of the process state are often used as time series values, such as precipitation, water level, and runoff (Wu, 2014).

The discrete form of wavelet transform (Hou and Wang, 2011) is expressed as follows:

$$W_f(a,b) = |a|^{-\frac{1}{2}}\Delta t \sum_{k=1}^{N} f(k\Delta t)\overline{\psi}\left(\frac{k\Delta t - b}{a}\right), \qquad (6)$$

where $W_f(a,b)$ is a function that varies depending on the parameters a and b. Since the Morlet wavelet is a complex number, the transformed coefficients are also complex numbers. We took the real part of the wavelet coefficients, namely,b as the abscissa and a as the ordinate, in order to generate a two-dimensional contour map of $W_f(a,b)$, i.e., the contour plot of the real part of the wavelet coefficients.

When the scale a is the same, the process of changing the wavelet transform coefficients over time reflects the characteristics of the change of the hydrological time series on this scale: when the wavelet transform coefficient is greater than 0, it is in the multi period; when the wavelet transform coefficient is less than 0, it is in the minor period. Similarly, when the wavelet transform coefficient is 0, it is in the transition stage from minor to multi period or from multi to minor period (Hou and Wang, 2011).

By integrating the square value of the wavelet coefficient in the time translation domain (b), the wavelet variance Var (Cahill, 2002; Kang et al., 2009) can be obtained:

$$Var(a) = \int_{-\infty}^{\infty} |W_f(a,b)|^2 db. \qquad (7)$$

The discrete form is expressed as follows:

$$Var(a) = \frac{1}{N} \sum_{t=1}^{N} |W_f(a,x_t)|^2, \qquad (8)$$

where $Var(a)$ is the wavelet variance; N is the length of the groundwater level data column; and $W_f(a,x_t)$ is the square of the

TABLE 1 | Results of the Kolmogorov–Smirnov test for seven wells.

Observation well	D					
	Log-normal	**Gamma**	**Beta**	**GEV**	**Weibull**	**Normal**
1#	0.1261	0.0891	0.0567	0.0396	0.0609	0.0464
2#	0.1354	0.1275	0.0748	0.0721	0.1130	0.0992
3#	0.1258	0.0851	0.1188	0.1321	0.0879	0.1292
4#	0.1495	0.1380	0.0736	0.1046	0.1150	0.1033
5#	0.2697	0.1973	0.1301	0.1215	0.1875	0.1362
6#	0.0954	0.0892	0.0492	0.0696	0.0620	0.0744
7#	0.1878	0.1531	0.0826	0.0583	0.0859	0.1362
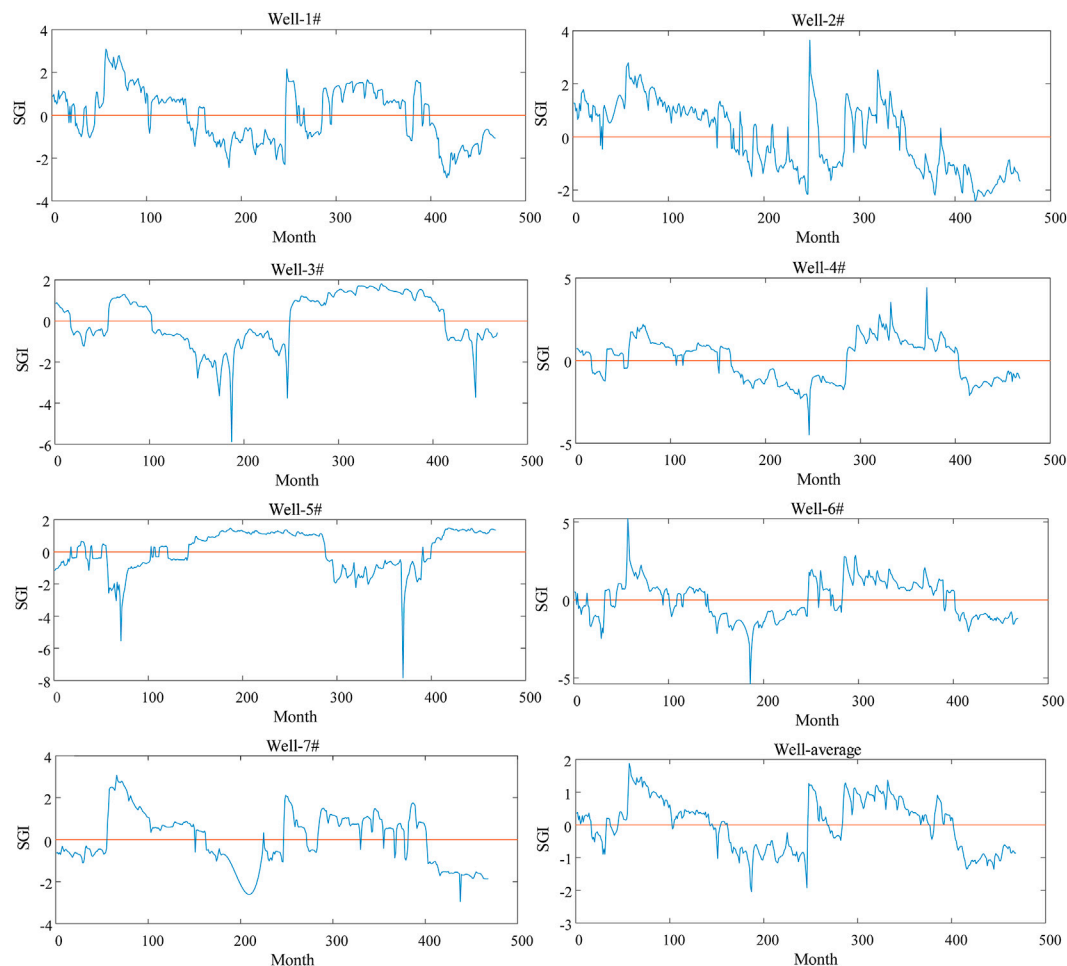
FIGURE 3 | SGI time series values.

wavelet coefficients on the scale a and time x_t, and it is the square of the coefficient modulus for complex coefficients.

The distribution diagram of the Var change during the period a is called the "wavelet variance distribution diagram" and can intuitively reflect the energy distribution of the signal fluctuation with the period a, determining the relative intensity of the different oscillation periods and the main oscillation period.
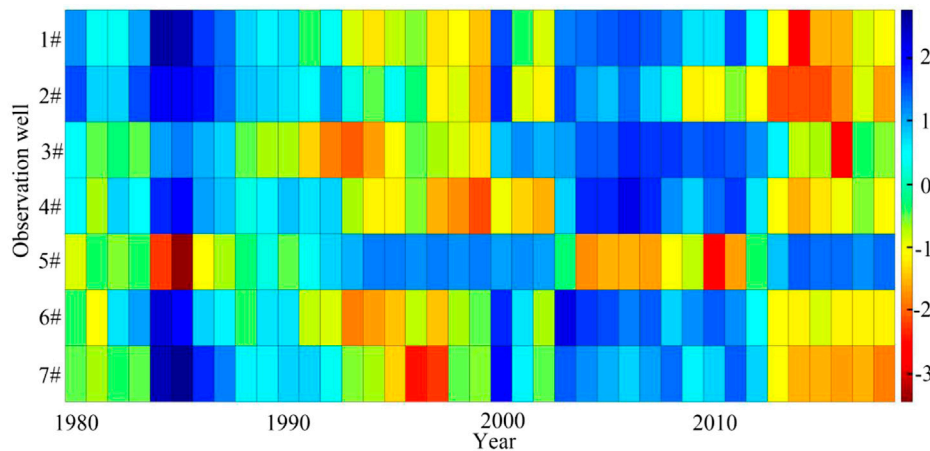
RESULTS

Selection of the Best Fit Function

As mentioned above, the key to SGI calculation is to select the fitting function. We used six more common functions to fit the data series from the seven observation wells and performed the KS test (**Eq. 4**) on the fitting results; finally, we

TABLE 2 | Drought characteristics based on SGI values for seven observation wells.

Observation well	No. of drought events				Total duration (months)	Maximum severity	Maximum duration (months)
	t = 2 months	2 months < t ≤ 12 months	t > 12 months	Total			
1#	2	6	3	11	223	104.90	85
2#	1	3	4	8	222	168.69	120
3#	0	0	3	3	242	187.10	146
4#	1	1	3	5	210	164.00	122
5#	1	4	4	9	225	133.25	103
6#	2	5	3	10	229	134.97	105
7#	1	2	4	7	223	104.40	67
Average	2	3	4	9	210	74.17	85

FIGURE 4 | Interannual variation of groundwater drought for all seven wells.

chose the function with the lowest test statistic D as the best fit function for the SGI calculation (Cui et al., 2020).

Table 1 shows that the best fitting distribution function for the well-1#, well-2#, well-5#, and well-7# is the GEV function, that for the well-3# is the gamma function, and that for the well-4# and well-6# is the beta function.

SGI Sequence Characteristics

We used **Eq. 1** to calculate 3,276 Standardized Groundwater Index values of monthly series of groundwater level from 1980 to 2018 for all observation wells. When SGI <0, drought occurs; when SGI = 0, the well is in a critical state; and when SGI >0, the conditions are normal. Here, we defined continuous drought (i.e., drought duration $t \geq 2$ months) as a drought event. The results show (**Figure 3**) that drought and non-drought occurred alternately in all observation wells, albeit at different intervals. Except for well-5#, the alternating drought and non-drought trends for the remaining six wells were similar, whereas those for well-5# showed the opposite pattern. In addition, the overall trend of the average SGI sequence curve was most similar to that of well-4#.

The number of drought events in the seven observation wells was from 3 to 11, the total drought duration was from 210 to

242 months, the maximum drought intensity was from 104.40 to 187.10, and the longest duration of drought events was from 67 to 146 months. Well-3# had the least drought events, which was three times. However, due to the drought duration, drought intensity, and drought severity characteristics, well-3# faced the most severe drought. Short-term drought often occurs in well-1# and well-6#. The drought intensity in well-7# is the weakest and the duration of the maximum drought event is the shortest. The total duration of drought is the shortest in well-4#. Detailed characteristics of the SGI sequence of the seven observation wells are shown in **Table 2**.

Interannual Variation of Groundwater Drought

Because groundwater drought is a cumulative condition, we used the SGI in December each year to represent the groundwater drought in that year. **Figure 4** shows the interannual variations of groundwater drought in the seven observation wells of nearly 39a (1980–2018) in Xuchang city (color represents SGI value). Groundwater drought in well-1#, well-2#, and well-4# occurred in 17 years. The strongest droughts occurred in 2014, 2015, and 1999. The coverage period of well-3# groundwater
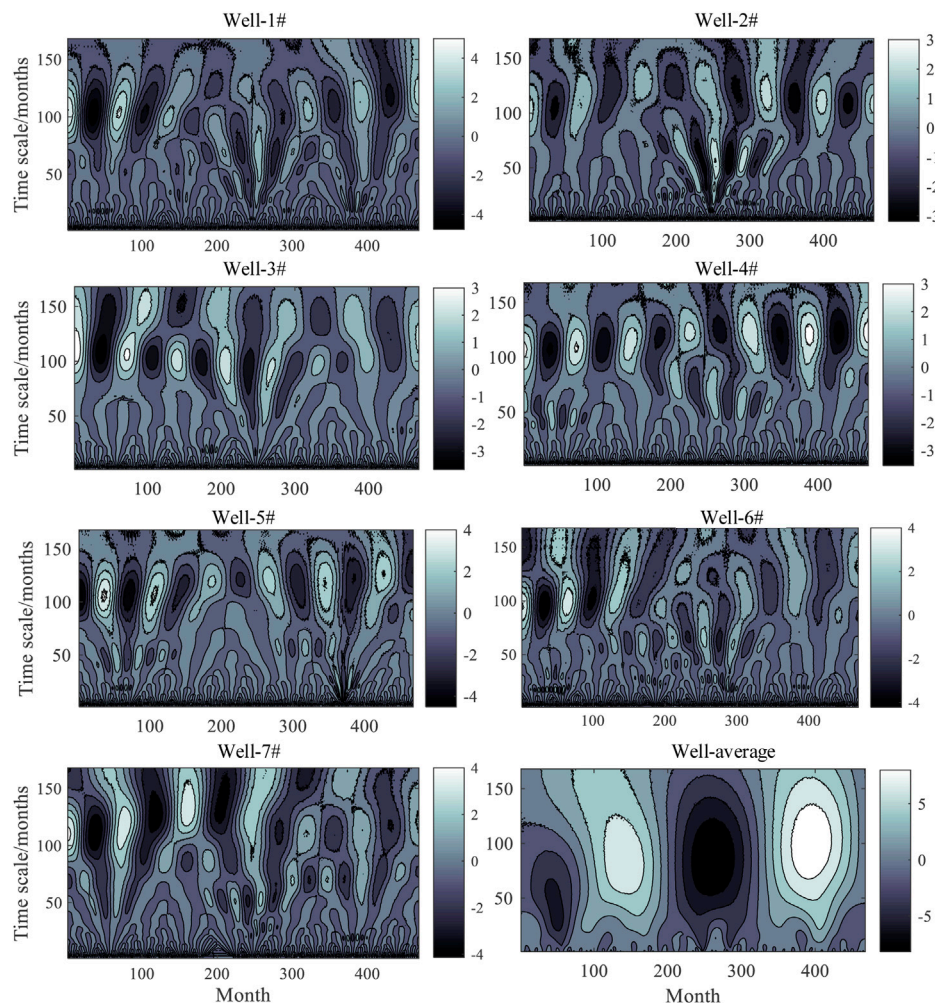
FIGURE 5 | Contour plot of the real part of the wavelet coefficients.

drought was 20 years, and the strongest drought occurred in 2016. Well-5# groundwater had the longest drought coverage period of 21 years, and the strongest drought occurred in 1985. The drought coverage period of well-6# was 19 years, and the strongest drought occurred in 1993. The well-7# groundwater drought coverage period was 18 years, and the strongest drought occurred in 1996.

Interestingly, the drought years of well-5# were basically spaced apart from those other six. When excluding well-5#, there were no groundwater droughts in the periods 1984–1987 and 2003–2008. In 1994, 1996–1999, and 2014–2018, droughts were observed in other six wells, while no groundwater drought was observed for well-5# during this period.

Characteristics of Groundwater Drought Cycle

In this paper, the 39a regional groundwater SGI sequence was used for wavelet transformation. In this step, we used the MATLAB wavelet toolbox to complete the wavelet transformation graph. We took the real part of the wavelet coefficients, the number of months as the abscissa (e.g., the abscissa 100 in **Figure 5** represents the 100th month) and the time scale as the ordinate, and drew the contour plot of the real part of the wavelet coefficients (**Figure 5**). To more intuitively understand the periodic changes of groundwater drought, the depth of color in **Figure 5** represents the size of the real part of the wavelet coefficient. The darker the color, the smaller the SGI value and the stronger the groundwater drought; the lighter the color, the greater the SGI value and the less severe the groundwater drought. Wavelet coefficients change characteristics can be used to characterize SGI time series change characteristics: when the real part of the wavelet coefficient is greater than 0, i.e., the SGI is greater than 0, there is no groundwater drought; when the real part of the wavelet coefficient is less than 0, i.e., the SGI is less than 0, there is groundwater drought. When the real part of the wavelet coefficient is 0, that is, SGI is equal to 0, it represents a turning point in the groundwater transition from drought to non-arid conditions or from non-arid conditions to drought.
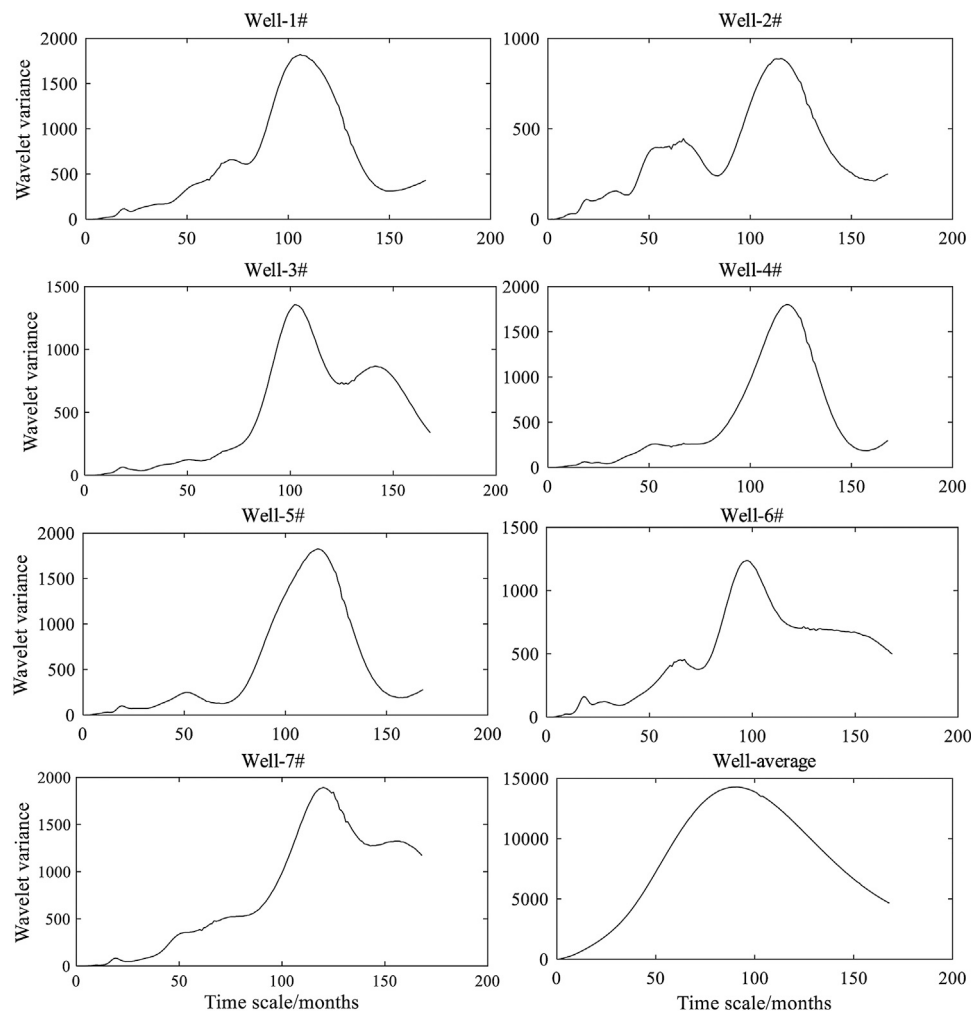
FIGURE 6 | Wavelet variance map.

The wavelet variance chart can reflect the distribution of the SGI time series fluctuation amplitude with the scale *a* and can be used to identify the intensity of disturbances and periodic changes at various scales, thereby determining the main period in the evolution of groundwater drought. We calculated the wavelet variance of the SGI time series of all observation wells according to **Eq. 8** and drew a wavelet variance graph (**Figure 6**) with the time scale *a* as the abscissa and the wavelet variance as the ordinate.

According to the results of the wavelet variance calculation, drawing a real part processing line diagram of the wavelet coefficients in the first and second main periods (**Figure 7**) can help understand the impact of the two main periods on groundwater drought throughout the study period. Usually, in the same period, the larger the amplitude of the wavelet coefficient real part processing line, the greater the influence in this period, that is, the period is dominated by the variation of the main period.

According to the results of the wavelet analysis, the characteristics of the groundwater drought oscillation period in seven observation wells can be obtained (**Table 3**). It can be seen from the table that there are 2–4 types of time scale laws in all observation wells, and different types of time scale laws correspond to different main periods. This paper analyzes only the first and second main periods that can best represent the characteristics of the groundwater drought oscillation cycle in each well. The first major period of groundwater drought in the seven observation wells was concentrated between 97 and 120 months, i.e., between 8 and 10 years. Apart from the fact that the second main period of well-3# and well-7# is longer than the first main period, the second main period of other wells basically fluctuates up and down half of the first main period. As can be seen from **Figure 6**, small cycles are included in the large cycles. As for the situation of well-3# and well-7#, it is very likely that the length of data is not enough, which leads to a larger main period not being found, but according to the size of the first and second main periods of other observation wells, we speculate that the actual first main period of the two wells is twice as long as the existing first main period. However, due to
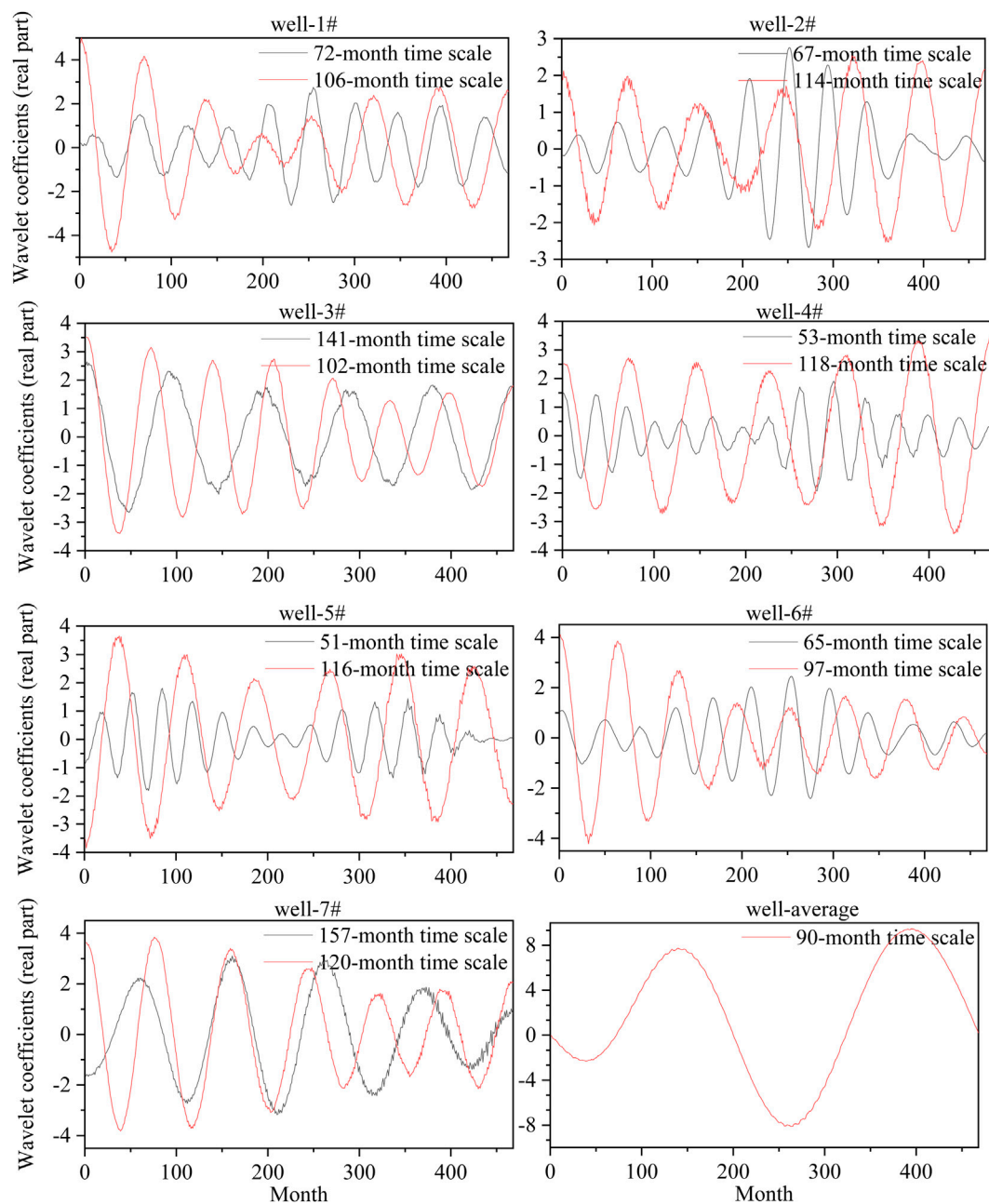
FIGURE 7 | Real part of the wavelet coefficient of groundwater drought time scale in the first two main periods.

TABLE 3 | Period characteristics of groundwater drought oscillation.

Observation well	Number of types of time scale laws	First main period (months)	Second main period (months)
1#	3	106	72
2#	4	114	67
3#	2	102	141
4#	2	118	53
5#	3	116	51
6#	3	97	65
7#	4	120	157
Average	1	90	—

the influence of the data, we can only roughly conclude that the first major periods of the two wells are 102 and 120 months, respectively. There is one type of time scale rule of the average SGI time series and it corresponds to a single main period (90 months), which is 20 months away from the average first main period (110 months) of each well.

DISCUSSION

Climate change and human activities are the main factors causing changes in groundwater levels (Dua et al., 2020; Kavitha and Chandran, 2015; Zhou et al., 2010), and in this study, the Groundwater Drought Index SGI is based on groundwater level data. So, the response of well-5# to changes in the environment differs from those of the other observation wells, most likely due to factors. Due the lack of data, we could not investigate this basic mechanism in more depth. However, it is now clear that conventional droughts can spread faster to groundwater droughts in areas that respond faster to factors.

Drought periods in the seven observation wells differed up to 23 months. Since all these observation wells contain shallow loose rock pore water, there is no difference in the lithology of the aquifer. Therefore, we believe that this difference may be due to regional climate change and human activities. In this sense, the definition of the impact on groundwater drought requires further analysis.

The second main periods of well-3# and well-7# were both longer than the first main period, and in **Figure 5**, the contours on the second main cycle time scale of these two wells are not closed. However, the unclosed contour loop had a closed trend. It is necessary to confirm whether the cycle of groundwater drought change of the two wells will have a higher periodicity in a certain period of time in the future.

Morlet wavelet transform analysis showed that the groundwater drought period in Xuchang city is 110 months, which is about 9 years. Previous studies have shown that drought periods are closely related to solar activity, and a small period of solar activity is 10 years (Li et al., 2015, Li et al., 2019), which is basically consistent with the results of this study (the subtle difference may be caused by human activities). Therefore, Morlet's continuous complex wavelet transform can be used to study the groundwater drought cycles. Our results provide a scientific basis for improved groundwater management.

CONCLUSION

Drought events occurred in all seven observation wells, of which the number of occurrences was the lowest in well-3#, but the drought was the worst. Well-1# has the highest number of drought events, but is dominated by short-lived droughts. Well-4# has the shortest total drought duration, and well-7# has the lowest drought intensity and the shortest duration of the longest drought event. The maximum

drought intensity in the seven observation wells is between 104.40 and 187.10.

The drought years of all observation wells were 17–21 years, and the drought years of well-5# were basically spaced apart from other six. The drought years of well-5# are concentrated in periods 1984–1987 and 2003–2012, while the drought years of other observation wells were concentrated in periods 1994–1999 and 2014–2018.

The contour map of the real part of the wavelet coefficients of each well showed a clear quasi-lateral, positive and negative interlaced closed center, distributed from low frequency to high frequency, which indicates an obvious period of oscillation for groundwater drought in Xuchang city. Wavelet transform analysis shows that the groundwater drought period of the seven observation wells was concentrated between 97 and 120 months, i.e., between 8 and 10 years. The groundwater drought period in well-7# was the longest with 120 months, and that of well-6# was the shortest with 97 months. Moreover, each observation well had a second main cycle of different sizes, indicating that the main periods of groundwater drought oscillations are different in different time periods. In addition, we infer that the time scale difference between the first and second main period is basically half of the first main period, and the change law of the small-time scale is included in the large time scale.

Wavelet analysis of the average SGI time series of the seven observation wells shows that the groundwater drought period (90 months) differed considerably from the average period of each well (approximately 110 months), indicating that the average SGI time series of the seven wells is not available. The results of the wavelet analysis can be used to determine the overall groundwater drought cycle in the region.

DATA AVAILABILITY STATEMENT

The data analyzed in this study are subject to the following licenses/restrictions: obtain the approval of the local hydrological department; requests to access these datasets should be directed to http://slj.xuchang.gov.cn/.

AUTHOR CONTRIBUTIONS

JH, LHC, and FRY contributed to conception and design of the study. LW organized the database. XBL performed the statistical analysis. JH wrote the first draft of the manuscript. JH, LHC, and FRY wrote sections of the manuscript. All authors contributed to manuscript revision, read, and approved the submitted version.

FUNDING

REFERENCES

Aussen, A., Campell, J., and Murtagh, F. (1997). Wavelet Based Feature Extraction and Decomposition, Strategies for Financial Forecasting [J]. *J. Comput. Intelligence Finance.* 6 (2), 5–12.

Bhuiyan, C. (2004). "Various Drought Indices for Monitoring Drought Condition in Aravalli Terrain of India," in XXth ISPRS Congress, Istanbul, Turkey, July 12–23, 2004.

Bhuiyan, C., Singh, R. P., and Kogan, F. N. (2006). Monitoring Drought Dynamics in the Aravalli Region (India) Using Different Indices Based on Ground and Remote Sensing Data. *Int. J. Appl. Earth Observation Geoinformation* 8 (4), 289–302. doi:10.1016/j.jag.2006.03.002

Bloomfield, J. P., and Marchant, B. P. (2013). Analysis of Groundwater Drought Building on the Standardised Precipitation index Approach. *Hydrol. Earth Syst. Sci.* 17 (12), 4769–4787. doi:10.5194/hess-17-4769-2013

Bloomfield, J. P., Marchant, B. P., Bricker, S. H., and Morgan, R. B. (2015). Regional Analysis of Groundwater Droughts Using Hydrograph Classification. *Hydrol. Earth Syst. Sci.* 19 (10), 4327–4344. doi:10.5194/hess-19-4327-2015

Cahill, A. T. (2002). Determination of Changes in Streamflow Variance by Means of a Wavelet-Based Test. *Water Resour. Res.* 38 (6), 1. doi:10.1029/2000wr000192

Chen, H., Zhang, Y., Qi, H., and Li, D. (2019). Detection of Ethanol Content in Ethanol Diesel Based on PLS and Multispectral Method. *Optik* 195, 162861. doi:10.1016/j.ijleo.2019.05.067

CTGCD (2011). *Central Texas Groundwater Conservation District -Drought Management Plan.* Burnet, TX: Central Texas Groundwater Conservation District, 4.

Cui, Y., Yongfu, W., Xu, X. M., and Liu, J. P. (2020). Groundwater Level Dynamics and its Response to Variations of Precipitation Based on Standardized Groundwater Index[J]. *Sci. Tech. Eng.* 20 (16), 6336–6342. doi:10.3969/j.issn.1671-1815.2020.16.004

Djordje, S., Ilija, B. B., Vladimir, D., and Suzana, B. (2021). Changes in Long-Term Properties and Natural Cycles of the Danube River Level and Flow Induced by Damming[J]. *Physica A: Stat. Mech. its Appl.* 566, 125607. doi:10.1016/s0378-4371(21)00007-8

Dua, K. S. Y., Imteaz, M. A., Sudiayem, I., Klaas, E. M. E., and Klaas, E. C. M. (2020). Assessing Climate Changes Impacts on Tropical Karst Catchment: Implications on Groundwater Resource Sustainability and Management Strategies[J]. *J. Hydrol.* 582, 124426. doi:10.1016/j.jhydrol.2019.124426

Fiorillo, F., and Guadagno, F. M. (2010). Karst Spring Discharges Analysis in Relation to Drought Periods, Using the SPI. *Water Resour. Manage.* 24 (9), 1867–1884. doi:10.1007/s11269-009-9528-9

Fiorillo, F., and Guadagno, F. M. (2012). Long Karst spring Discharge Time Series and Droughts Occurrence in Southern Italy. *Environ. Earth Sci.* 65 (8), 2273–2283. doi:10.1007/s12665-011-1495-9

Guttman, N. B. (1998). Comparing the Palmer Drought Index and the Standardized Precipitation Index. *J. Am. Water Resour. Assoc.* 34 (1), 113–121. doi:10.1111/j.1752-1688.1998.tb05964.x

Harisuseno, D. (2020). Meteorological Drought and its Relationship with Southern Oscillation Index (SOI). *Civ Eng. J.* 6 (10), 1864–1875. doi:10.28991/cej-2020-03091588

Hou, B., and Wang, M. (2011). Runoff Trend Analysis and Distribu- Ted Hourly Model Application Study of the Upper Reaches of Yangtze River[J]. *J. Chongqing Jiaotong University (Nat. Sci- ence)* 30 (2), 291–294. doi:10.3969/j.issn.1674-0696.2011.02.26

Intergovernmental Panel on Climate Change (IPCC) (2013). "Near-Term Climate Change: Projections and Predictability," in *Climate Change 2013 - the Physical Science Basis* (England: Cambridge University Press), 953–1028.

Kang, L., Yang, Z., and Jiang, T. (2009). The Periodical Analysis of the Danjiangkou Reservoir Inflow Based on the Morlet Wavelet[J]. *Comp. Eng. & Sci.* 31 (11), 149–152. doi:10.3969/j.issn.1007-130X.2009.11.040

Kavianpour, M., Seyedabadi, M., Moazami, S., and Aminoroayaie Yamini, O. (2020). Copula Based Spatial Analysis of Drought Return Period in Southwest of Iran. *Period. Polytech. Civil Eng* 64 (4), 1051–1063. doi:10.3311/PPci.16301

Kavitha, V., and Chandran, K. (2015). Intensive Farming and Sustainability of Groundwater Resource in Tamil Nadu[J]. *Agric. Econ. Res. Rev.* 28, 290.

Kulkarni, J. R. (2000). Wavelet Analysis of the Association between the Southern Oscillation and the Indian Summer Monsoon. *Int. J. Climatol.* 20 (1), 89–104. doi:10.1002/(sici)1097-0088(200001)20:1<89::aid-joc458>3.0.co;2-w

Li, B., and Rodell, M. (2015). Evaluation of a Model-Based Groundwater Drought Indicator in the Conterminous U.S. *J. Hydrol.* 526, 78–88. doi:10.1016/j.jhydrol.2014.09.027

Li, H. Y., Xue, L. J., and Wang, X. J. (2015). Relationship between Solar Activity and Flood/drought Disasters of the Second Songhua River Basin[J]. *J. Water Clim. Change.* 6 (3), 578. doi:10.2166/wcc.2014.053

Li, W., Li, H., Guo, X., Yang, W., and Ma, S. Z. (2019). Analysis and Trend Prediction of sunspot Activity Cycle[J]. *Water Resour. Hydropower Eng.* 50 (5), 53–62. doi:10.13928/j.cnki.wrahe.2019.05.007

Li, Y., and Zhu, X. (2021). Periodic Identification of Runoff in Hei River Based on Predictive Extension Method of Eliminating the Boundary Effect of the Wavelet Transform. *J. Hydrol. Eng.* 26 (5), 05021008. doi:10.1061/(asce)he.1943-5584.0002083

Liu, B., Zhou, X., Li, W., Lu, C., and Shu, L. (2016). Spatiotemporal Characteristics of Groundwater Drought and its Response to Meteorological Drought in Jiangsu Province, China. *Water* 8 (11), 480. doi:10.3390/w8110480

Lorenzo-Lacruz, J., Garcia, C., and Morán-Tejeda, E. (2017). Groundwater Level Responses to Precipitation Variability in Mediterranean Insular Aquifers. *J. Hydrol.* 552, 516–531. doi:10.1016/j.jhydrol.2017.07.011

Macdonald, A. M., Calow, R. C., Macdonald, D. M. J., Darling, W. G., and Dochartaigh, B. É. Ó. (2009). What Impact Will Climate Change Have on Rural Groundwater Supplies in Africa?. *Hydrological Sci. J.* 54 (4), 690–703. doi:10.1623/hysj.54.4.690

Marchant, B. P., and Bloomfield, J. P. (2018). Spatio-temporal Modelling of the Status of Groundwater Droughts. *J. Hydrol.* 564, 397–413. doi:10.1016/j.jhydrol.2018.07.009

Medellín-Azuara, J., MacEwan, D., Howitt, R. E., Koruakos, G., Dogrul, E. C., Brush, C. F., et al. (2015). Hydro-economic Analysis of Groundwater Pumping for Irrigated Agriculture in California's Central Valley, USA. *Hydrogeol J.* 23 (6), 1205–1216. doi:10.1007/s10040-015-1283-9

Mendicino, G., Senatore, A., and Versace, P. (2008). A Groundwater Resource index (GRI) for Drought Monitoring and Forecasting in a Mediterranean Climate[J]. *J. Hydrol.* 357 (3), 282–302. doi:10.1016/j.jhydrol.2008.05.005

Mishra, A. K., and Singh, V. P. (2010). A Review of Drought Concepts[J]. *J. Hydrol.* 391 (1–2), 202–216. doi:10.1016/j.jhydrol.2010.07.012

Motlagh, M. S., Ghasemieh, H., Talebi, A., and Abdollahi, K. (2016). Identification and Analysis of Drought Propagation of Groundwater during Past and Future Periods[J]. *Water Resour. Manag.* 31, 1–17. doi:10.1007/s11269-016-1513-5

Nagarajan, R., and Ganapuram, S. (2015). Micro-Level Drought Vulnerability Assessment Using Standardised Precipitation Index, Standardised Water-Level Index, Remote Sensing and GIS[C]//Asian Conference on Remote Sensing.

Nason, G. P., and Sapatinas, T. (2002). Wavelet Packet of Transfer Function Modeling of Nonstationary Time Series[J]. *Stat. Comput.* 12 (1), 45–56. doi:10.1023/a:1013168221710

Oo, H. T., Zin, W. W., and Kyi, C. C. T. (2020). Analysis of Streamflow Response to Changing Climate Conditions Using SWAT Model. *Civil Eng. J.* 2 (6), 194–209. doi:10.28991/cej-2020-03091464

Palizdan, N., Falamarzi, Y., Huang, Y. F., Lee, T. S., and Lee., T. S. (2017). Precipitation Trend Analysis Using Discrete Wavelet Transform at the Langat River Basin, Selangor, Malaysia. *Stoch Environ. Res. Risk Assess.* 31 (4), 853–877. doi:10.1007/s00477-016-1261-3

Pathak, A. A., and Dodamani, B. M. (2021). Connection between Meteorological and Groundwater Drought with Copula-Based Bivariate Frequency Analysis. *J. Hydrol. Eng.* 26 (7), 05021015. doi:10.1061/(asce)he.1943-5584.0002089

Pathak, P., Kalra, A., Ahmad, S., and Bernardez, M. (2016). Wavelet-aided Analysis to Estimate Seasonal Variability and Dominant Periodicities in Temperature, Precipitation, and Streamflow in the Midwestern United States[J]. *Water Resour. Manag.* 30 (13), 4649–4665.

Peng-zhu, Li., Feng-jun, L. I., Xing, L. I., and Zhou, Y. T. (2015). A Numerical Method for the Solutions to Nonlinear Dynamic Systems Based on Cubic Spline Interpolation Functions[J]. *Appl. Math. Mech.* 36 (8), 887–896. doi:10.3879/j.issn.1000-0887.2015.08.010

Rahim, A., Khan, D. K., Akif, A., and Jamal, R. (2015). The Geo Statistical Approach to Assess the Groundwater Drought by Using Standardized

Water Level Index(SWI) and Atandardised Precipitation index(SPI)in the Peshawar Regime of Pakistan. *J. Sci.Int.(Lahore)* 27 (5), 4111–4117.

Saghafian, B., and Sanginabadi, H. (2020). Multivariate Groundwater Drought Analysis Using Copulas. *Hydrol. Res.* 51 (4), 666–685. doi:10.2166/nh.2020.131

Sang, Y.-F., Sun, F., Singh, V. P., Xie, P., and Sun, J. (2018). A Discrete Wavelet Spectrum Approach for Identifying Non-monotonic Trends in Hydroclimate Data. *Hydrol. Earth Syst. Sci.* 22 (1), 757–766. doi:10.5194/hess-22-757-2018

Scanlon, B. R., Longuevergne, L., and Long, D. (2012a). Ground Referencing GRACE Satellite Estimates of Groundwater Storage Changes in the California Central Valley, USA. *Water Resour. Res.* 48, W04520. doi:10.1029/2011wr011312

Scanlon, B. R., Faunt, C. C., Longuevergne, L., Reedy, R. C., Alley, W. M., McGuire, V. L., et al. (2012b). Groundwater Depletion and Sustainability of Irrigation in the US High Plains and Central Valley. *Proc. Natl. Acad. Sci.* 109 (24), 9320–9325. doi:10.1073/pnas.1200311109

Seo, J. Y., and Lee, S. (2019). Spatio-Temporal Groundwater Drought Monitoring Using Multi-Satellite Data Based on an Artificial Neural Network. *Water* 11 (9), 1953. doi:10.3390/w11091953

Smith, L. C., Turcotte, D. L., and Isacks, B. L. (1998). Stream Flow Characterization and Feature Detection Using a Discrete Wavelet Transform. *Hydrol. Process.* 12, 233–249. doi:10.1002/(sici)1099-1085(199802)12:2<233:aid-hyp573>3.0.co;2-3

Taylor, R. G., Scanlon, B., Döll, P., Rodell, M., van Beek, R., Wada, Y., et al. (2012). Ground Water and Climate Change. *Nat. Clim Change.* 3, 322–329. doi:10.1038/nclimate1744

Texas Water Code (2016). *Water Code-Texas Constitution and Statutes.* Austin, TX: State of Texas, 2203. Available at: https://statutes.capitol.texas.gov/Docs/SDocs/WATERCODE.pdf.

Thomas, B. F., Famiglietti, J. S., Landerer, F. W., Wiese, D. N., Molotch, N. P., and Argus, D. F. (2017). GRACE Groundwater Drought Index: Evaluation of California Central Valley Groundwater Drought. *Remote Sens. Environ.* 198, 384–392. doi:10.1016/j.rse.2017.06.026

Van Loon, A. F., and Anne, F. (2015). Hydrological Drought Explained[J]. *WIREs Water* 2, 359–392. Wiley Interdiplinary. doi:10.1002/wat2.1085

Vicente-Serrano, S. M., López-Moreno, J. I., Beguería, S., Lorenzo-Lacruz, J., Azorin-Molina, C., and Morán-Tejeda, E. (2012). Accurate Computation of a Streamflow Drought Index. *J. Hydrol. Eng.* 17 (2), 318–332. doi:10.1061/(asce)he.1943-5584.0000433

Wang, F., Wang, Z., Yang, H., Di, D., Zhao, Y., and Liang, Q. (2020). Utilizing GRACE-based Groundwater Drought index for Drought Characterization and Teleconnection Factors Analysis in the North China Plain. *J. Hydrol.* 585, 124849. doi:10.1016/j.jhydrol.2020.124849

Wang, W. S., Ding, J., and Yue-qing, Li. (2005). *Hydrology Wavedet Analysis[M].* China: Chemical Industry Press.

Wilhite, D. A. (2000). Drought as a Natural Hazard: Concepts and Definitions[J]. *Drought A Global Assess.* 1 (1), 3–18. doi:10.1017/cbo9780511811845.006

Wu, J., Liu, Z., Yao, H., Chen, X., Chen, X., Zheng, Y., et al. (2018). Impacts of Reservoir Operations on Multi-Scale Correlations between Hydrological Drought and Meteorological Drought. *J. Hydrol.* 563, 726–736. doi:10.1016/j.jhydrol.2018.06.053

Wu, J. (2014). *The Diagnosis and Analysis of Hydrological Sequence Inconsistency in the Source Region of Yangtze River[D].* Nanjing: Hohai University.

Xi-zhi, W., and Wang, Z. J. (1996). *Nonparametric Statistical methods[M].* China: Higher Education Press.

Xu, K., Yang, D., Xu, X., and Lei, H. (2015). Copula Based Drought Frequency Analysis Considering the Spatio-Temporal Variability in Southwest China. *J. Hydrol.* 527, 630–640. doi:10.1016/j.jhydrol.2015.05.030

Zhou, Y., Yuan, X., Zhou, P., and Jin, J. (2012). Study on Frequency Analysis of Regional Drought Based on Ground Water Depth[J]. *J. Hydraulic Eng.* 39 (9), 10751083.

Zhou, Y., Zwahlen, F., Wang, Y., and Li, Y. (2010). Impact of Climate Change on Irrigation Requirements in Terms of Groundwater Resources. *Hydrogeol J.* 18 (7), 1571–1582. doi:10.1007/s10040-010-0627-8

Zonal Patterns of Meteorological Drought on the Yunnan-Guizhou Plateau, China

Hang Yu[1,2], Long Wang[2]* and Maoling Yang[3]

[1]*College of Hydrology and Water Resources, Hohai University, Nanjing, China, [2]College of Water Conservancy, Yunnan Agricultural University, Kunming, China, [3]Survey Design Institute of Water Conservancy and Hydropower in Zhaotong, Kunming, China*

Drought is a natural phenomenon caused by a shortage of water resources and has a great impact on agriculture, the economy, and the environment. To study the Spatio-temporal distribution and explore the zonal patterns of drought, this paper took the Yunnan-Guizhou Plateau (YGP) as the research region, selected the air temperature, relative humidity, sunshine duration, wind speed, and precipitation data from 47 meteorological stations on the YGP. First, the standardized precipitation evapotranspiration index (SPEI) was calculated, and then the Spatio-temporal distribution of YGP drought was analyzed with the SPEI, Mann–Kendall test, and principal component analysis (PCA). Finally, the correlations between the average SPEI, drought characteristics extracted from the SPEI, and longitude/elevation/latitude were analyzed with the linear regression method, and then the zonal patterns of the YGP drought were obtained. The results revealed that the annual and seasonal SPEI values mainly decreased. Because the first component of the SPEI (the largest eigenvalue makes it the most important component) in annual and winter had a poor relationship with longitude/elevation, its correlation was weak, while the average SPEI values in other seasons were significantly correlated with longitude/elevation ($\alpha = 0.001$), and the absolute value of the correlation coefficient was between 0.6879–0.9453. Except for PC1 in annual and winter, PC1 and PC2 were significantly correlated with longitude/elevation ($\alpha = 0.001$), and the absolute value of the correlation coefficient was between 0.5087–0.9501. The duration, severity, intensity, frequency of drought were significantly correlated with longitude/elevation ($\alpha = 0.001$) in most situations. The average SPEI values and drought characteristics showed a good multivariate linear correlation with longitude, latitude, and elevation, indicating that drought exhibited strong zonal patterns. This study will provide new ideas for drought research and technical support for regional industrial layouts, planting structure adjustments, and drought and disaster reduction.

Keywords: Yunnan-Guizhou Plateau, longitude, elevation, zonal patterns, drought

INTRODUCTION

Recent studies have demonstrated that global climate change has altered precipitation and temperature in different regions (Almazroui et al., 2016; Vinnarasi and Dhanya, 2016; Sung et al., 2017; Salman et al., 2017; Sa'adi et al., 2017; Pour et al., 2018; Tao et al., 2018) and affected the entire hydrological system (Zahabiyoun et al., 2013), thereby increasing the

frequency and intensity of drought events (Sung and Chung, 2014; Ahmed et al., 2015; Zhang et al., 2017; Mohsenipour et al., 2018). Furthermore, drought substantially impacts agriculture, the economy, and the ecological environment (Wilhite, 2005; Xiao et al., 2016; Fang et al., 2018; Fang et al., 2019; Huang et al., 2019).

As a result, an increasing number of researchers have studied droughts around the world. Under RCP8.5, global drought will continue to increase (Prudhomme et al., 2014; Chanda and Maity, 2017). In particular, a substantial increase is predicted in most parts of Africa, South America, and Asia (Chanda and Maity, 2017). Moreover, the return period of drought characteristics in North America and Asia will decrease the most by the middle of the century, while South America and Australia will experience the largest decline by the end of the century (Wu et al., 2021). On a smaller scale, many scholars used the Mann–Kendall test, principal component analysis (PCA), and other methods to analyze the spatial-temporal distribution of drought indicators [the Palmer drought severity index (PDSI), the standardized precipitation index (SPI), the standardized precipitation evapotranspiration index (SPEI), etc.] and/or drought characteristics (duration, severity, intensity, frequency, etc.) of South Korea (Azam et al., 2018), Syria (Mathbout et al., 2018), Northeast China (Fu et al., 2018), Southwest China (Wang et al., 2018), the Loess Plateau (Liu et al., 2016), Inner Mongolia (Huang et al., 2015), Turkey (Danandeh Mehr and Vaheddoost, 2020), Northeast Algeria (Merabti et al., 2018), Oklahoma (Tian and Quiring, 2019), Hungary (Alsafadi et al., 2020), Oman (El Kenawy et al., 2020), and South-central Asia (Adnan et al., 2016). The research results for the Yunnan-Guizhou Plateau (YGP) and its adjacent areas showed that the annual ($SPEI_{12}$) and seasonal ($SPEI_3$) droughts in Southwest China decreased from 1968 to 2018; the drought in the southern region was severe, and the drought frequency increased (Tang et al., 2021). In addition, the frequency, duration, and severity of drought in Southwest China have increased significantly in the past 40 years (Wang M. et al., 2021). According to the revised reconnaissance drought index (RDI) and Mann–Kendall methods, the RDI of the YGP declined annually and in summer, autumn, and winter, indicating that the severity of drought was increasing, but the opposite pattern was observed in spring. However, these trends were not significant, and there was no mutation on the YGP from 1960 to 2013 (Cheng Q. et al., 2020). From 1960 to 2017, the drought in spring and autumn in Guizhou increased, and the drought in summer and winter decreased (Wang Y. et al., 2021). From 1961 to 2015, the annual, summer, and autumn SPI of Yunnan significantly decreased, and there was an obvious drought trend in the Lancang River and Nanpan River Basins (Li Y. et al., 2019). The above research results show that many researchers have analyzed the temporal and spatial distribution of drought on a global scale or in a small region, but there are few studies specifically on the YGP. Therefore, the analysis of the temporal and spatial distribution of drought on the YGP will further enrich the research results in this area.

Drought is a natural phenomenon caused by a shortage of water resources. Therefore, drought is closely related to meteorological elements such as precipitation (precipitation is considered in many

drought indicators). However, meteorological elements such as precipitation have strong zonal patterns. For example, the precipitation in Sichuan (Zeng et al., 2016) and Hengduan Mountain (Yu et al., 2018) is influenced by elevation and latitude. In addition, there is a similar relationship for potential evapotranspiration (PET). For example, with the decline in elevation, the PET in the Xitugou Basin (Cheng W. J. et al., 2020) and Qilian Mountain (Yang et al., 2019) of China gradually increased. The above research results showed that the magnitude of meteorological elements related to drought (precipitation, PET, etc.) are related to their location. Does drought exhibit similar patterns? On a global scale, there are humid, semihumid, semiarid, and arid areas all over the world. On a regional scale, Mohammadi et al. (2020) found that extreme drought events occurred in the eastern Andes; Nuri Balov and Altunkaynak (2020) found that the drought characteristics of the West Black Sea and the Euphrates River basin in Turkey have a certain correlation with elevation. These studies have fully analyzed the spatial variation characteristics of drought and preliminarily explored the relationship between drought and elevation, but the research on the role of longitude and latitude is insufficient [since meteorological elements such as precipitation are related to longitude and latitude (Yu et al., 2018), it is necessary to study the relationship between drought and longitude and latitude]; in addition, there are few studies on the zonal patterns of drought. Therefore, to investigate the zonal patterns of drought, this paper uses the YGP as the study area based on the temporal and spatial distribution of drought, focuses on the relationship between drought and its characteristics and elevation/longitude/latitude, and analyzes the spatial patterns of drought. This research is different from previous research, providing a more in-depth study on the temporal and spatial distribution characteristics of drought. Specifically, this study incorporates the temporal and spatial distribution characteristics of drought to clarify its relationship with elevation/longitude/latitude. This study will provide new ideas for drought research and technical support for regional industrial layouts, planting structure adjustments, and drought and disaster reduction.

STUDY AREA

The YGP is located between 22.52–31.21°N and 100.03–111.33°E in Southwest China, including the eastern part of Yunnan Province, the entire Guizhou Province, the northwestern part of Guangxi, and the provincial borders of Sichuan, Hubei, Hunan, and Chongqing. The YGP is adjacent to the Qinghai–Tibet Plateau and Hengduan Mountains. The rich and diverse natural environment of the YGP results in high biodiversity (rich species of plants and animals) and high cultural diversity (a large number of ethnic minorities). The YGP has a subtropical monsoon climate as a whole, with simultaneous rain and heat and distinct dry and wet seasons. The southern region has a tropical monsoon climate due to its low elevation and latitude, which is strongly affected by the South Asian monsoon. At the same time, because it is located on the low-latitude plateau, there is no severe cold in winter and no intense heat in summer. In addition, affected by topography, the YGP climate also has obvious
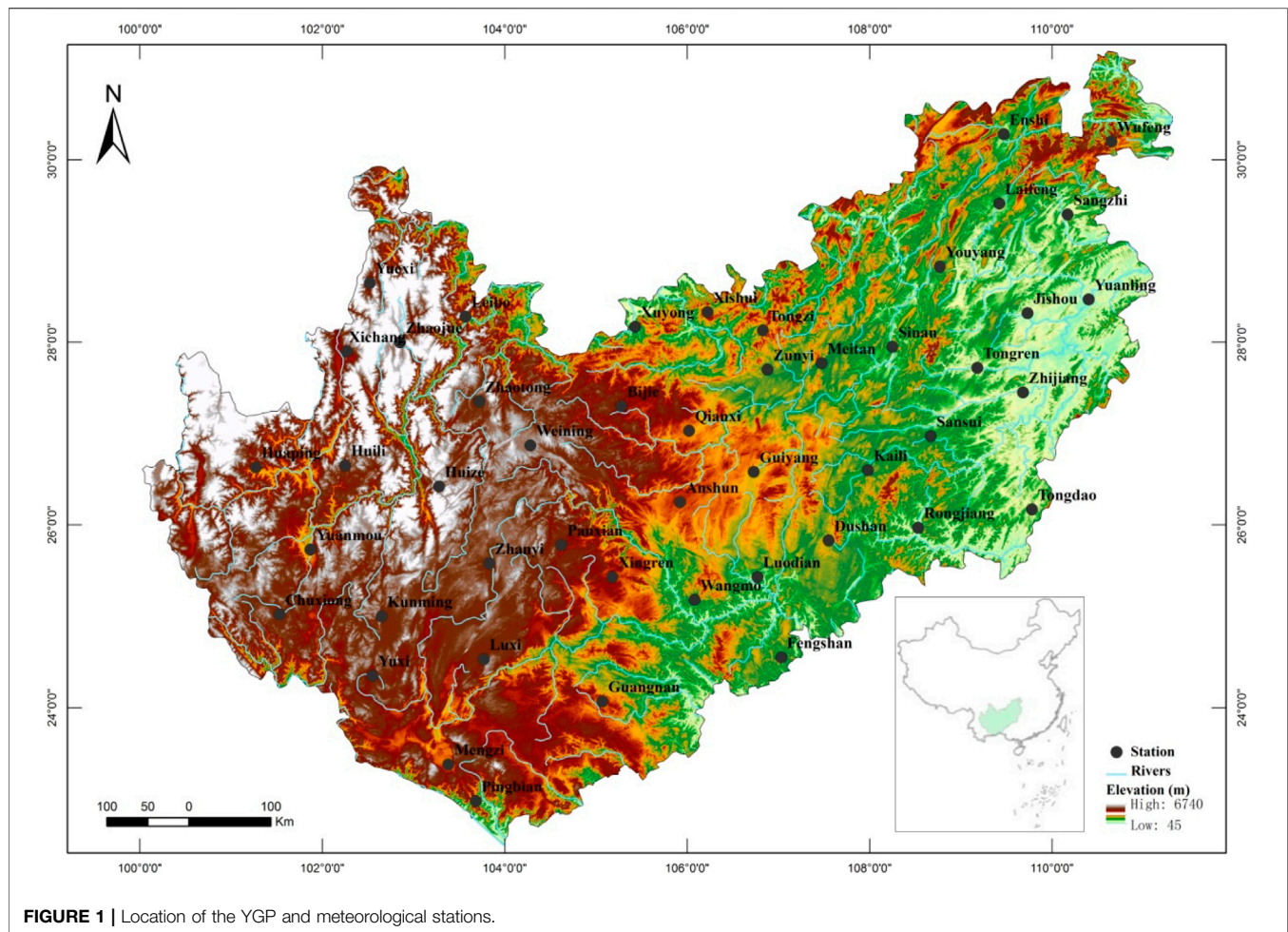
FIGURE 1 | Location of the YGP and meteorological stations.

vertical zonal characteristics and local climate characteristics. The YGP is at the intersection of south–north- and northeast–southwest-trending mountain ranges in China. The elevation is between 45 and 6,740 m and is higher in the northwest and lower in the southeast; that is, the elevation gradually decreases with increasing longitude. The YGP is the fourth largest plateau in China.

DATA DESCRIPTION

There are many meteorological stations in the study area, but the starting years of the data of each meteorological station are different. Moreover, some meteorological stations lack measurements for a certain period of time, so it is necessary to cut off the meteorological data in the study area uniformly to ensure that the starting and ending years of the data of each meteorological station are consistent and the data within the study time range are complete. Therefore, to investigate the zonal characteristics of drought, the monthly air temperature, relative humidity, sunshine duration, wind speed, and precipitation of 47 meteorological stations with relatively long observation times and relatively complete observation records (shown in **Figure 1**) were

TABLE 1 | Drought classes.

Level	Drought category	SPEI threshold
0	Non-drought	$0 \leq SPEI$
1	Mild drought	$-0.99 < SPEI < 0$
2	Moderate drought	$-1.42 < SPEI < -1.00$
3	Severe drought	$-1.82 < SPEI < -1.43$
4	Extreme drought	$SPEI \leq -1.83$

selected for the present study. The data records, sourced from the China Meteorological Data Network (http://data.cma.cn/), covered the period from January 1971 to December 2013. In addition, prior to the release of meteorological data, the China Meteorological Data Service Center carried out strict quality control, and the data had good homogeneity.

METHODS

To study the zonal pattern of drought, this study selected the meteorological data of the YGP and used the SPEI as the drought

FIGURE 2 | Diagram of duration and severity of drought.
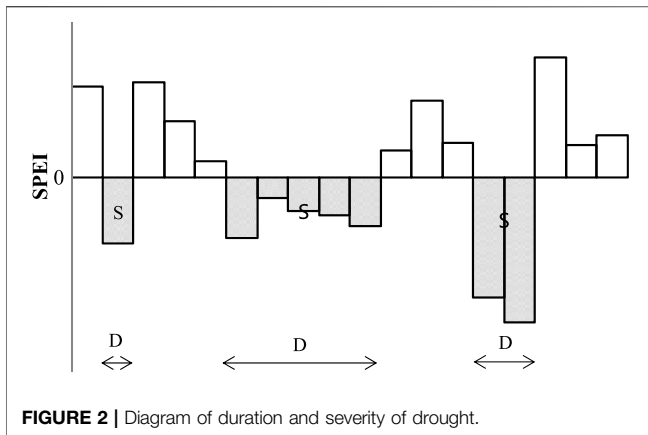
index on time scales of 1, 3, 6, and 12 months. Then, the quantitative method of Tang et al. (2021) was used to analyze the temporal and spatial distribution of the SPEI and the dependence of the characteristics of drought on the variation in longitude, latitude, and elevation on an annual scale (represented by the SPEI on a 12-months time scale ending in December in each year), during spring (from March to May, represented by the SPEI on a 3-months time scale ending in May in each year), summer (from June to August, represented by the SPEI on a 3-months time scale ending in August in each year), autumn (from September to November, represented by the SPEI on a 3-months time scale ending in November in each year), winter (from December to February of the following year, represented by the SPEI on a 3-months time scale ending in February in each year), the rainy season (from May to October, represented by the SPEI on a 6-months time scale ending in October in each year), and the dry season (from November to February of the following year, represented by the SPEI on a 6-months time scale ending in April).

SPEI

To analyze drought events, a drought index should first be selected. However, due to the different subjects and purposes, researchers have proposed numerous drought indices. As listed in the technical report of the World Meteorological Organization (WMO, 1975; 2016), there are as many as 58 drought indices from different countries (Wang et al., 2019). Among the many indices, the PDSI (Palmer, 1965), SPI (McKee et al., 1993), and SPEI (Vicente-Serrano et al., 2010a) are widely used. Among these, the PDSI and SPI have some defects and assumptions (Guttman, 1998; Vicente-Serrano et al., 2010a). The SPEI combines the advantages of the multi-timescale SPI and the sensitivity of the PDSI. In addition, the index considers not only the water shortage caused by precipitation reduction but also the water shortage caused by high evapotranspiration (Yang et al., 2020). Therefore, the SPEI is an effective drought index and is widely used in the context of global and regional climate change (Beguería et al., 2014; Jin et al., 2019; Danandeh Mehr et al., 2020; Danandeh Mehr and Vaheddoost, 2020). Therefore, the SPEI is selected as the drought index in the present study.

The SPEI is obtained by normalizing the cumulative probability of the difference between precipitation (P) and PET series. First, the Penman–Monteith (PM) method was used to calculate the monthly PET of the stations on the YGP; the difference between the monthly P and PET of each station was calculated, and the cumulative series of the difference on different time scales (at 1, 3, 6, and 12 months) were obtained. Different probability density functions were used to fit the series of different time scales to obtain a distribution function. Finally, the distribution functions at different stations on different time scales were standardized to obtain the SPEI values on different time scales. Detailed steps for calculating the SPEI (Vicente-Serrano et al., 2010a; Vicente-Serrano et al., 2010b; Vicente-Serrano et al., 2011a; Vicente-Serrano et al., 2011b) are shown as follows:

In this paper, the PM method (Allen et al., 1998), recommended by the Food and Agriculture Organization of the United Nations, is used to calculate the PET. Although the calculation of this method is more complex and requires considerable data, the calculation result is more accurate.

$$
PET = \left(0.408\Delta \left(R_n - G \right) + \gamma \frac{900}{T + 273} u_2 \left(e_s - e_a \right) \right) / (\Delta + \gamma \left(1 + 0.34 u_2 \right))
$$ (1)

where PET is the potential evapotranspiration (mm day^{-1}), R_n is the net radiation at the vegetation surface (MJ m^{-2} day^{-1}), G is the soil heat flux density (MJ m^{-2} day^{-1}), Δ is the slope vapor pressure curve (kPa°C^{-1}), γ is the psychrometric constant (kPa°C^{-1}), T is the mean daily air temperature at 2 m height (°C), u_2 is the wind speed at 2 m height (m s^{-1}), e_s is the saturation vapor pressure (kPa), and e_a is the actual vapor pressure (kPa).

The differences $D_{m,n}$ of the mth year and nth month are

$$
D_{m,n} = P_{m,n} - PET_{m,n}
$$ (2)

where m and n denote year and month, respectively.

The cumulant $X_{m,n}^k$ of different time scales (k denotes the temporal scale; k= 1, 3, 6, 12) can be calculated according to **Eq. 2**.

$$
\begin{cases} D_i = D_{m,n} \\ i = (m - m_0) \times 12 + n \end{cases}
$$ (3)

$$
X_i^k = \sum_{i-k+1}^{i} D_i
$$ (4)

$$
\begin{cases} X_{m,n}^k = X_i^k \\ m = m_0 + \text{int}\left[(i - 1)/12 \right] \\ n = \text{mod}\left[(i - 1), 12 \right] + 1 \end{cases}
$$ (5)

where i is the order number, m_0 is the initial year, and int and mod represent the integer and modulus of $(i - 1)/12$, respectively.

Because the $X_{m,n}^k$ of each station is different, this paper uses dozens of probability density functions to fit the cumulant $X_{m,n}^k$ of different time scales. Then, according to the Kolmogorov–Smirnov test, this paper selects the cumulative distribution function $F(x)$ and calculates the cumulative probability $P(X \leq x)$. Finally, the SPEI is calculated as standardized values of cumulative probability P:
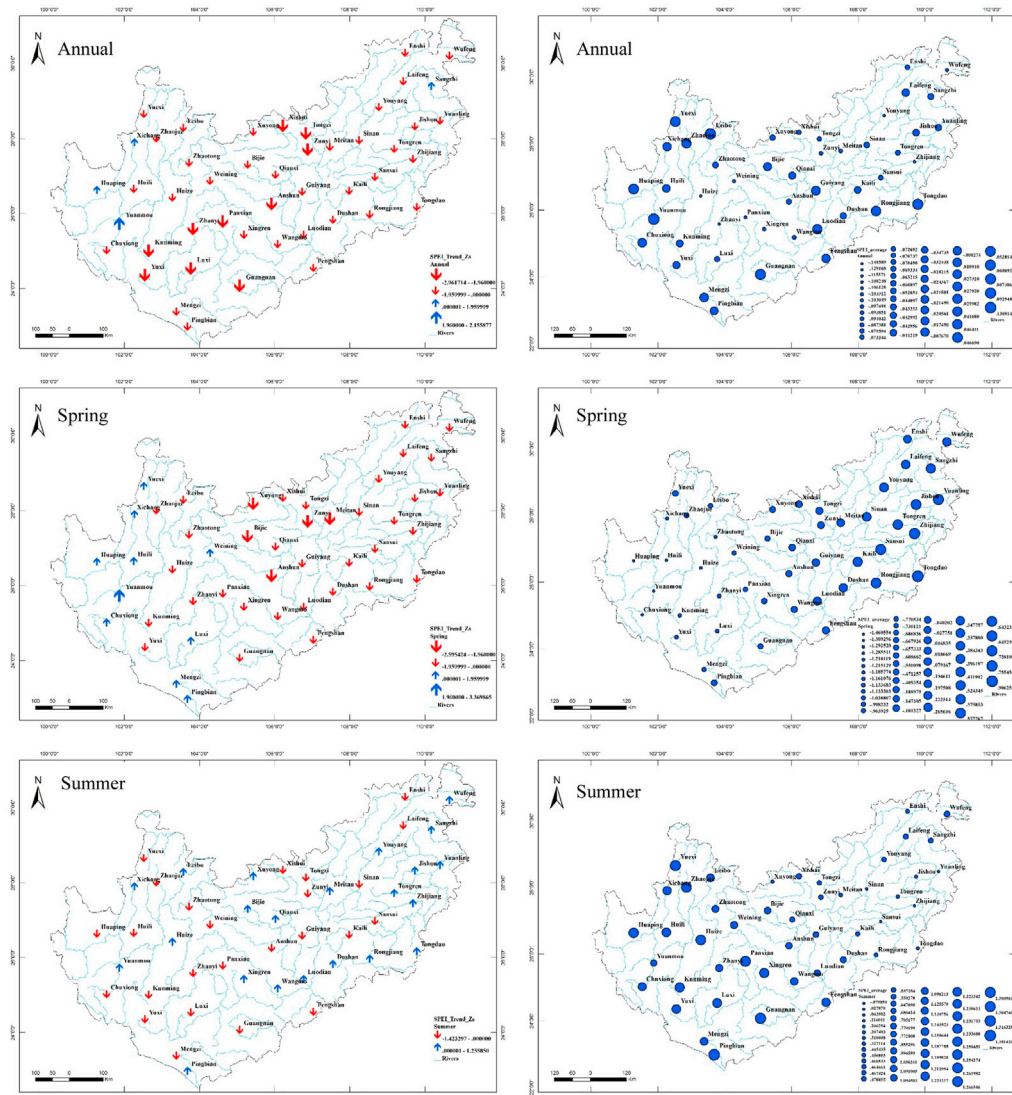
FIGURE 3 | Variation trend of the SPEI and distribution of the multiyear average SPEI on the YGP. The left side represents the variation trend of the SPEI; the right side represents the multiyear average SPEI. The downward arrow indicates a decrease, and the larger arrow indicates a significant decrease at confidence level α = 0.05. The upward arrow indicates an increase, and the larger arrow indicates a significant increase at confidence level α = 0.05.

$$SPEI = \Phi^{-1}(P) \tag{6}$$

where Φ is the standard normal distribution.

This paper uses the grading standard of the SPEI proposed by Danandeh Mehr et al. (2020). In addition, Danandeh Mehr et al. (2020) found that there is little difference between the SPI and SPEI corresponding to cumulative probabilities of 0.15–0.85; moreover, the residual with cumulative probability equal to 0.5 is almost equal to 0. In addition, many researchers have identified SPEI values less than 0 as indicative of drought (Banimahd and Khalili, 2013; Tan et al., 2015; Li X. et al., 2019). Therefore, this paper also takes SPEI equal to 0 as the critical value for dividing drought and wet conditions. The grading standard is shown in **Table 1**.

Mann–Kendall Test

The Mann–Kendall test (Mann, 1945; Kendall, 1975) is a nonparametric statistical test, also known as a distribution-free test. Its advantage is that it does not require samples to follow a specific distribution, nor is it subject to interference from a small number of outliers. Therefore, it is widely used in the trend detection of hydrometeorological factors (Huang et al., 2013; Wang et al., 2013; Sayemuzzaman and Jha, 2014). The calculation steps are as follows (Yu et al., 2018).

The Mann–Kendall test statistic S is calculated as

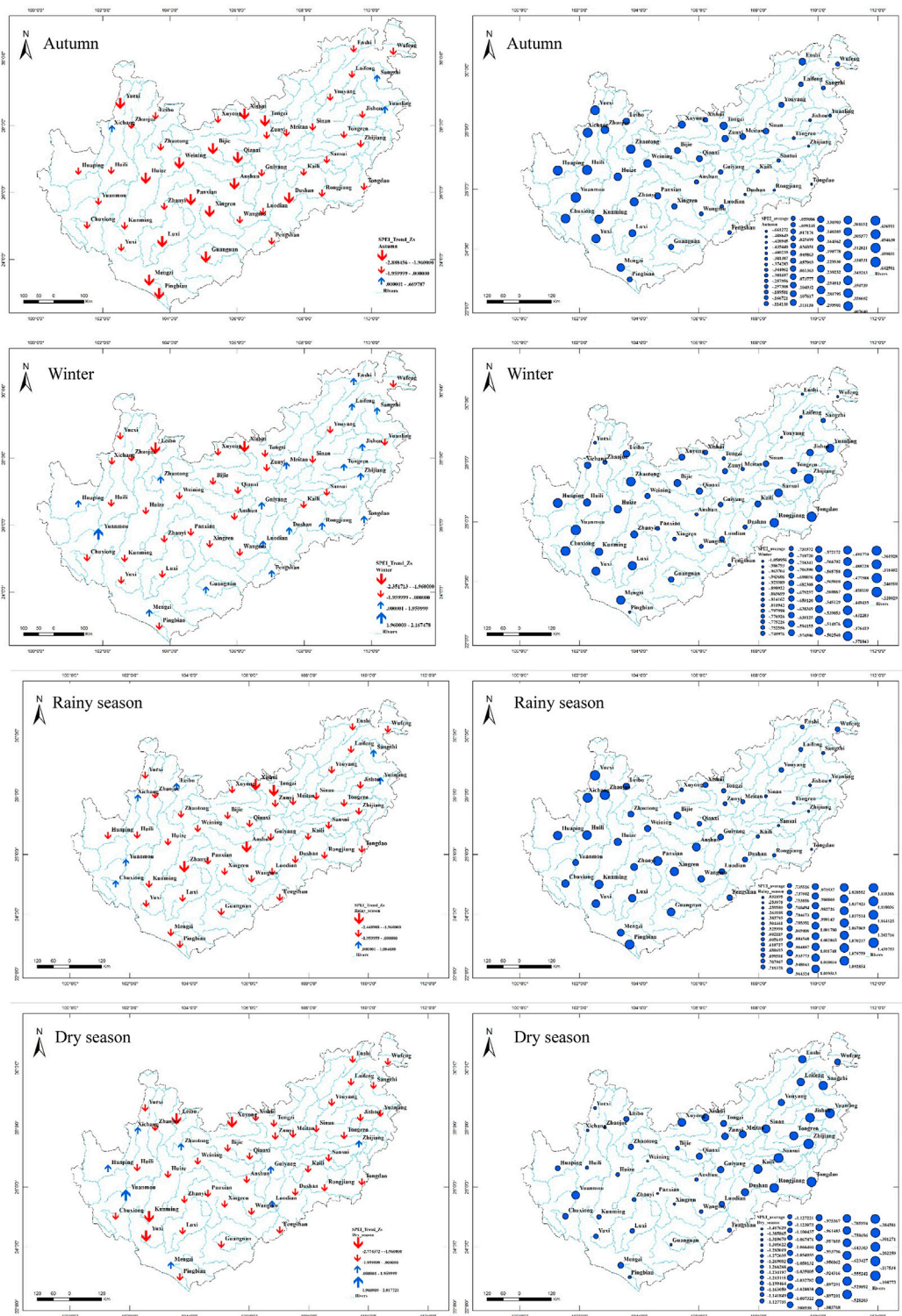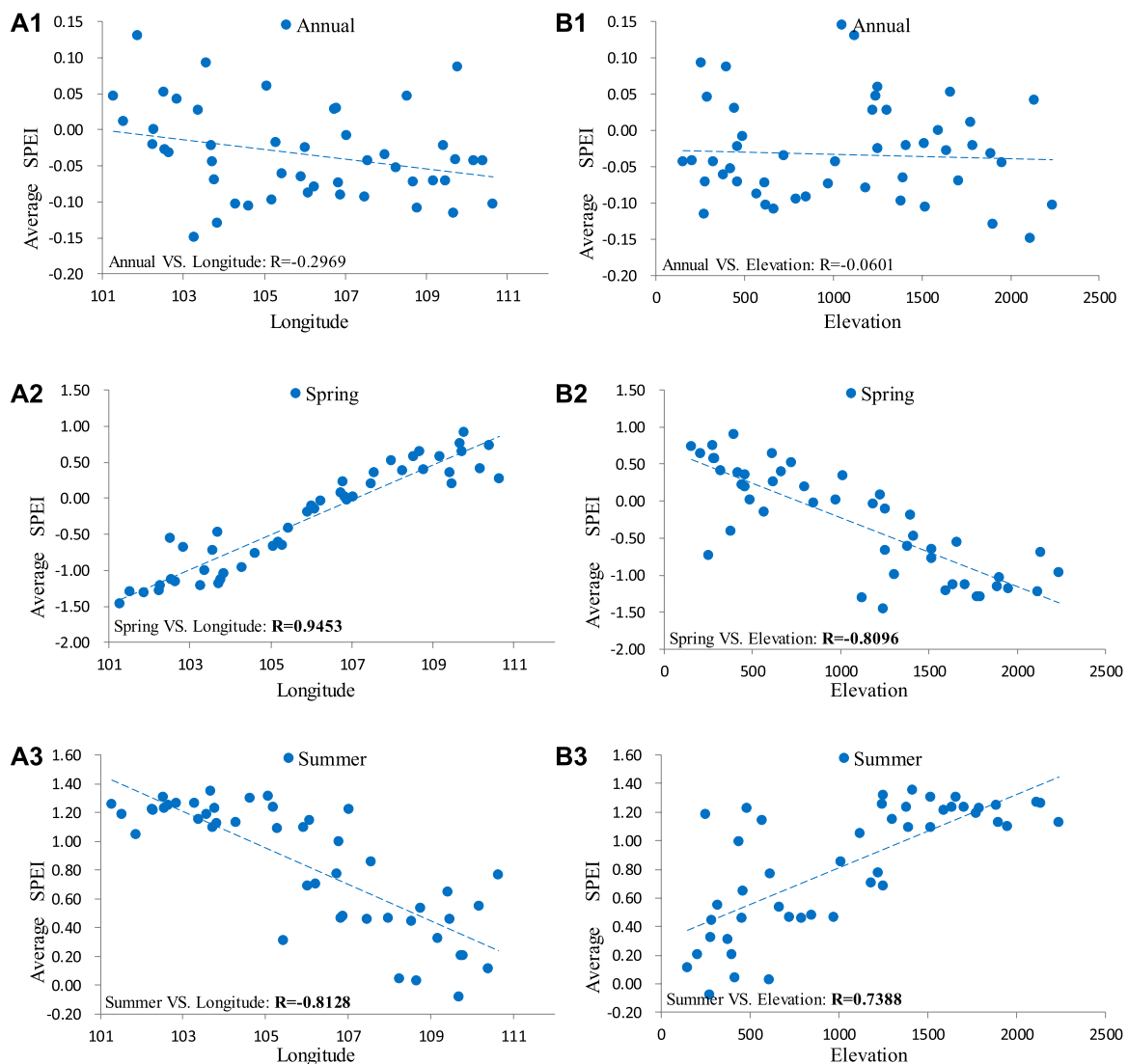$$S = \sum_{i=1}^{n-1} \sum_{j=i+1}^{n} \operatorname{sgn}(x_j - x_i) \tag{7}$$

FIGURE 3b |

FIGURE 4 | Correlations between the annual and seasonal averages of the SPEI and longitude and elevation. **(A1–A7)** represents the correlation between the average SPEI of annual, spring, summer, autumn, winter, rainy season, dry season and longitude; **(B1–B7)** represents the correlation between the average SPEI of annual, spring, summer, autumn, winter, rainy season, dry season and elevation. R represents the correlation coefficient, and the bold fonts indicate that the confidence level is $\alpha = 0.001$.

where n is the length of the data and x_i and x_j are the data values in time series i and j $(j > i)$, respectively. In addition, $sgn(x_j - x_i)$ is the sign function of $(x_j - x_i)$.

$$sgn\left(x_j - x_i\right) = \begin{cases} +1, & if\left(x_j - x_i\right) > 0 \\ 0, & if\left(x_j - x_i\right) = 0 \\ -1, & if\left(x_j - x_i\right) < 0 \end{cases} \quad (8)$$

The variance is computed as

$$V(S) = \left(n(n-1)(2n+5) - \sum_{k=1}^{m} t_k(t_k-1)(2t_k+5)\right)/18 \quad (9)$$

where m is the number of tied groups and t_k denotes the number of ties of extent k. A tied group is a set of sample data having the

same value. In cases where the sample size $n > 10$, the standard normal test statistic Z_S is computed using **Eq. 10**:

$$Z_S = \begin{cases} \dfrac{S-1}{\sqrt{V(S)}}, & if\ S > 0 \\ 0, & if\ S = 0 \\ \dfrac{S+1}{\sqrt{V(S)}}, & if\ S < 0 \end{cases} \quad (10)$$

The time series increases when the statistical variable Z_S is greater than 0 and decreases when Z_S is less than 0. There is a significant trend at the given confidence level $\alpha = 0.05$ when the absolute value of Z_S is greater than $Z_{\alpha/2}$.
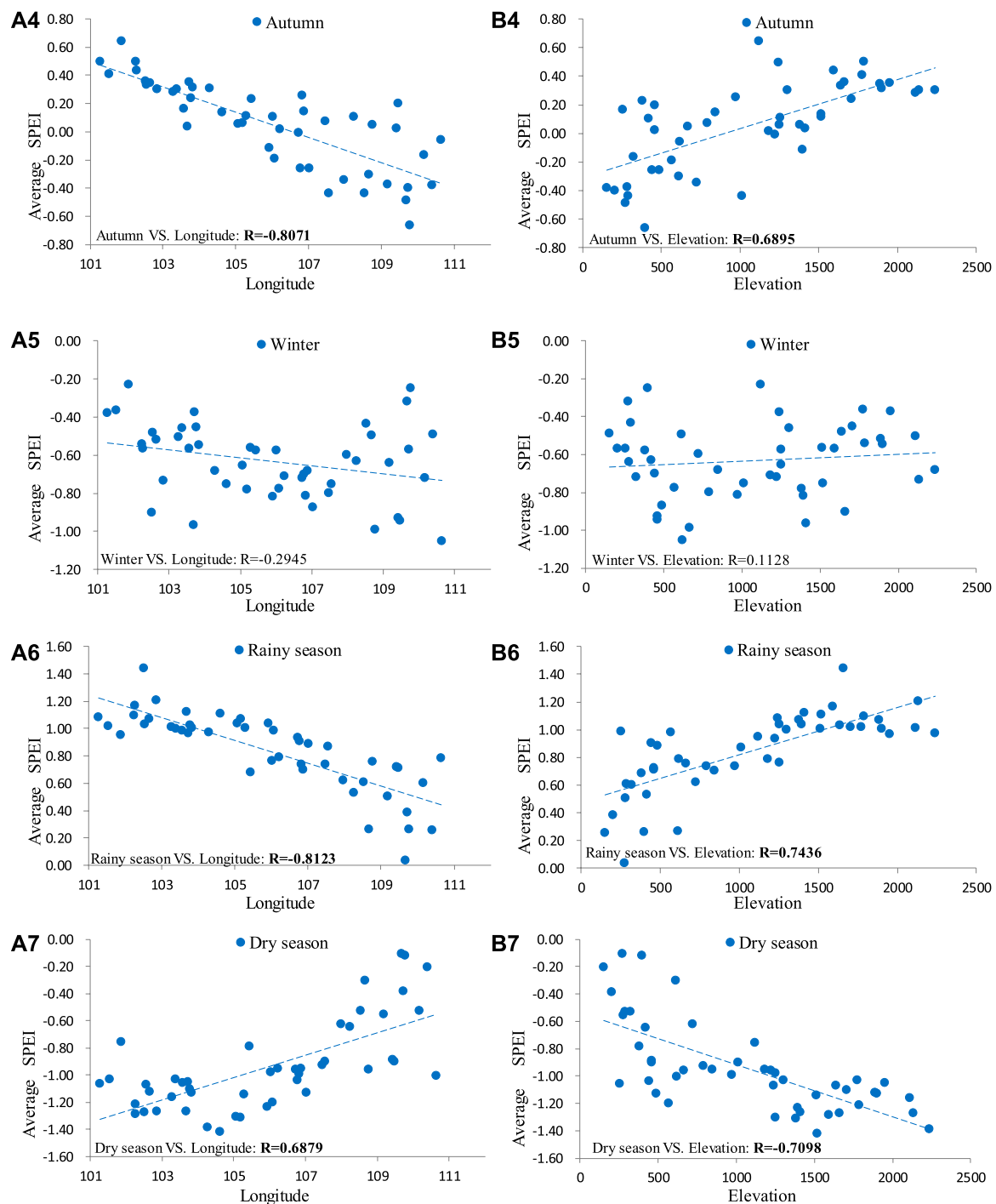
FIGURE 4b |

PCA

PCA is a widely used spatiotemporal analysis method. It can use a few linearly uncorrelated principal components to explain most of the total variance in the original data according to the calculation results of the covariance matrix and corresponding eigenvalues and eigenvectors (Raziei et al., 2009) without causing extreme loss of

information (Zhao et al., 2012; Polong et al., 2019). Therefore, according to drought indices such as the SPI or SPEI, a large number of scholars have used PCA to study the temporal and spatial variations in drought (Gocic and Trajkovic, 2014; Guo et al., 2018; Aryal and Zhu, 2021). As a result, PCA is also used to analyze the temporal and spatial variation characteristics of drought in this
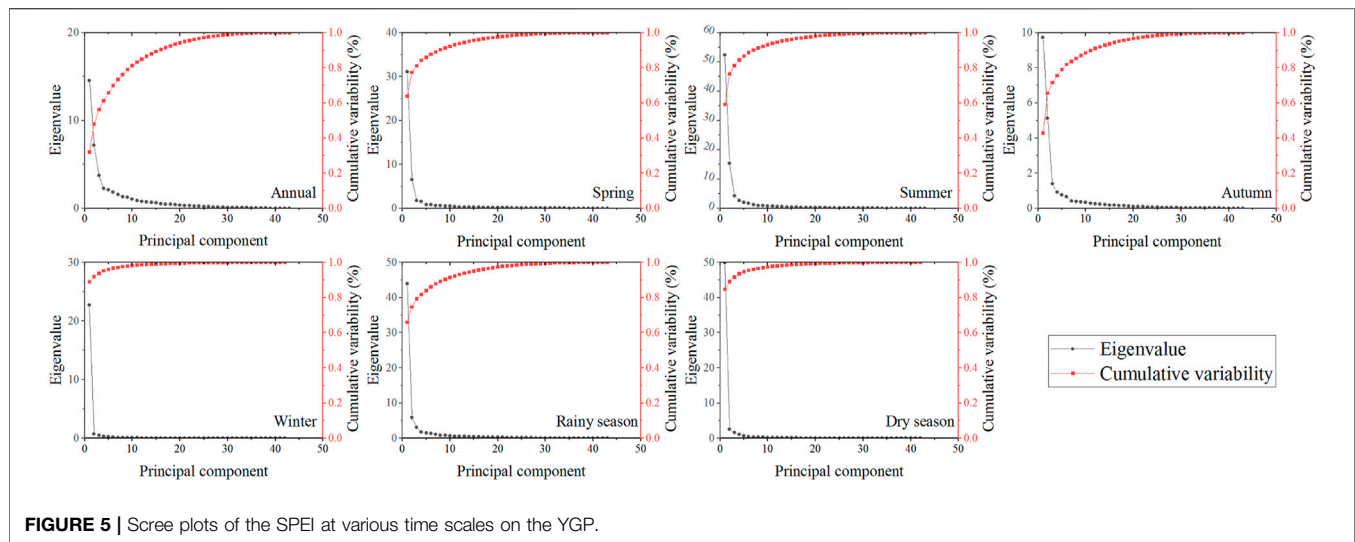
FIGURE 5 | Scree plots of the SPEI at various time scales on the YGP.

paper. The SPEI of the YGP is expressed as $s_{i,1}, s_{i,2}, \cdots s_{i,k}$, where k represents the number of stations and i represents the length of time. Therefore, the linear combination of principal components is expressed as follows (Polong et al., 2019):

$$\begin{cases} Y_{i,1} = a_{1,1}S_{i,1} + a_{1,2}S_{i,2} + \cdots a_{1,k}S_{i,k} \\ Y_{i,2} = a_{2,1}S_{i,1} + a_{2,2}S_{i,2} + \cdots a_{2,k}S_{i,k} \\ \vdots \\ Y_{i,k} = a_{k,1}S_{i,1} + a_{k,2}S_{i,2} + \cdots a_{k,k}S_{i,k} \end{cases} \quad (11)$$

where Y is a new orthogonal and linear uncorrelated variable that explains most of the total variance. The coefficient of linear combination is called the "load," which represents the correlation between the original data and the corresponding principal component time series. The number of principal components is determined according to eigenvalues and cumulative variability. For example, the cumulative variability adopted by Razei et al. (2009), Gunda et al. (2016), Gocic and Trajkovic (2014), Portela et al. (2015), Santos et al. (2010) was 54.96, 67/69, 68–69, 80.1, and 67–77%, respectively. Since different researchers adopt different standards, 70% is used in the present study as the standard to select the principal component. To visualize the spatial pattern of drought, the inverse distance weighting method is used to interpolate the principal components in ArcMap 10.0.

Characteristics of Drought

Drought can typically be characterized by four characteristics: duration, severity, intensity, and frequency (Mishra and Singh, 2010; Kimosop, 2019). The calculation methods are as follows:

Zero was used as the criterion to determine whether drought occurred in this study (as shown in **Table 1**); i.e., when the SPEI was less than 0, this value indicated the occurrence of drought. Drought duration represents the sum of the duration of each drought event (unit: month), and D in **Figure 2** is the duration of each drought event.

Drought severity is the sum of the SPEI of each drought event (the filled-in area in **Figure 2**). The smaller the drought severity is, the more severe the drought.

$$S = \sum_D SPEI \quad (12)$$

where D represents the drought duration and S represents the drought severity.

Drought intensity is the ratio of drought severity to the duration of each drought event.

$$I = \frac{S}{D} \quad (13)$$

where I represents the drought intensity.

Drought frequency is the ratio of the number of drought occurrences to the total number.

$$F = \frac{n}{N} \quad (14)$$

where F represents the drought frequency, n represents the number of drought occurrences (i.e., the number of SPEIs that are smaller than 0), and N represents the total number.

Multiple Linear Regression

In this paper, multiple linear regression is used to analyze the relationship between the average SPEI and drought characteristics and longitude, latitude, and elevation. This method is simple and easy to use. The mathematical equation is as follows (Chatzithomas et al., 2015):

$$Y = a + b_1X_1 + b_2X_2 + b_3X_3 \quad (15)$$

where Y is the dependent variable. X_1, X_2, and X_3 are the independent variables, which are latitude, longitude, and elevation, respectively. b_1, b_2, and b_3 are the coefficients of the variables, while a is the intercept. The closer the absolute value of R is to 1, the better the fitting of the multiple linear regression equation. From a statistical point of view, the smaller the significance p value is, the more reliable the correlation between the variables in the sample and the variables in the population and the better the fitting of the multiple linear regression equation.
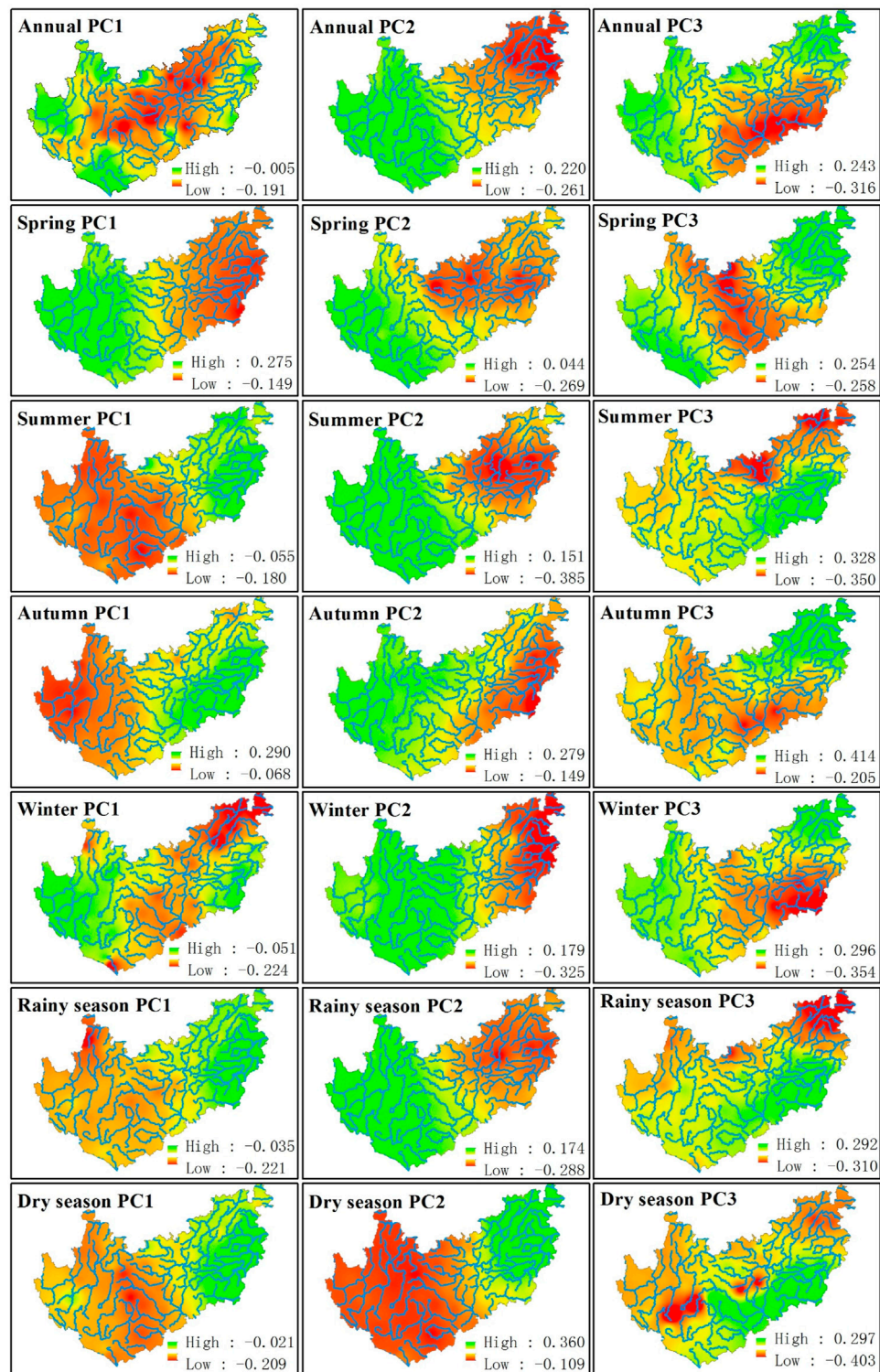
FIGURE 6 | Distribution of the first three principal components of the SPEI annually and in different seasons.
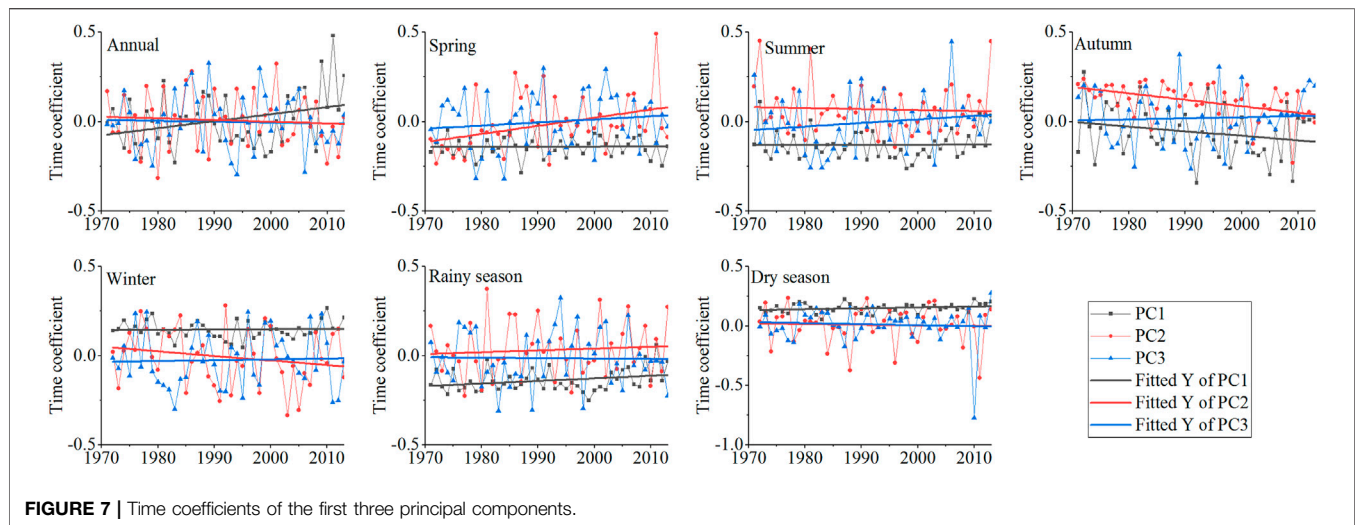
FIGURE 7 | Time coefficients of the first three principal components.

TABLE 2 | Linear correlation coefficients R between the first three principal components of the YGP and longitude and elevation.

	PC1		PC2		PC3	
	VS.					
	Elevation	Longitude	Elevation	Longitude	Elevation	Longitude
Annual	-0.1371	-0.2170	0.7550**	-0.8927**	0.2274	-0.2865
Spring	0.8187**	-0.9501**	0.5087**	-0.666**	-0.1323	0.1656
Summer	-0.7168**	0.7453**	0.7002**	-0.8077**	-0.1092	0.0606
Autumn	-0.6967**	0.8018**	0.7317**	-0.8244**	-0.3216	0.4629
Winter	0.1630	-0.3556	0.7291**	-0.8319**	0.2731	-0.2405
Rainy season	-0.7453**	0.7780**	0.7483**	-0.9027**	-0.0309	0.0307
Dry season	-0.7066**	0.6773**	-0.7133**	0.8566**	-0.2873	0.2025

RESULTS

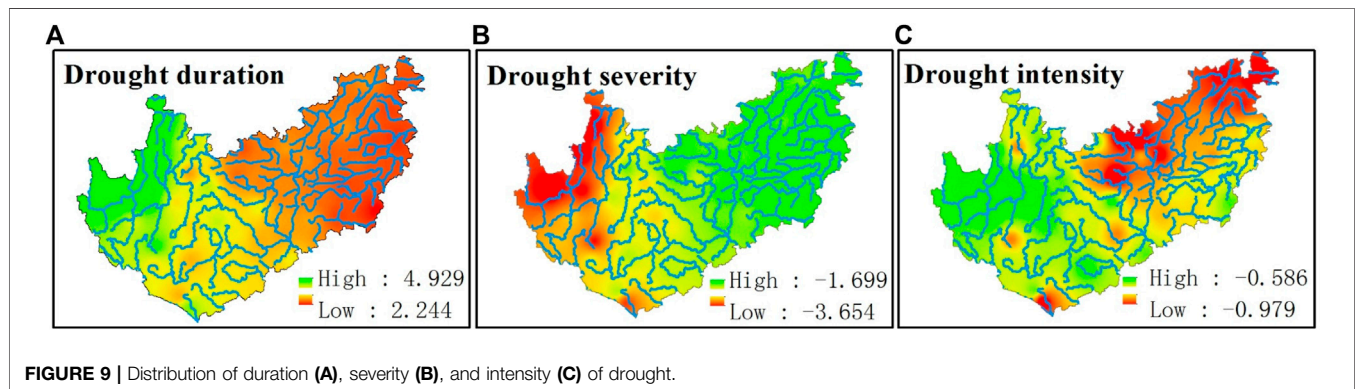Based on the SPEI calculation results, this paper first analyzes the temporal and spatial distribution of the SPEI and then investigates the zonal patterns of drought on the YGP, i.e., the variation pattern of drought according to longitude, latitude, and elevation.

Spatiotemporal Variation in the SPEI and its Relationship With Longitude and Elevation

In this paper, the SPEI was calculated based on the above-described method for 3-months (representing the drought index in spring, summer, autumn, and winter), 6-months (representing the drought index during the rainy and dry seasons), and 12-months (representing the annual drought index) time scales. The characteristics of spatiotemporal variation were then analyzed (as shown in **Figure 3**).

Figure 3 shows that the annual and seasonal SPEI values mainly decreased throughout the YGP area, although this trend was not significant at most stations. In addition, the spatial distributions of multiyear averages of annual and seasonal SPEI values were complex. In particular, the annual average SPEI values in the northwestern and southern sections of the YGP were relatively large, whereas those in the remaining areas were relatively small, and the SPEI values of most stations were smaller than 0, indicating the occurrence of drought; the average SPEI in spring was greater in the eastern section of the YGP and smaller in the western section, and the SPEI values of most stations were less than 0, indicating the occurrence of drought in most areas of the study region during spring. The SPEI values in summer were greater in the western section of the YGP and smaller in the eastern section of the YGP. Except for one station, the SPEI values of all other

FIGURE 8 | The spatial distribution of the first two components of SPEI in annual and each season. The first component of the SPEI was obtained by multiplying PC1 by the corresponding time coefficient and then taking the average. The second component of the SPEI was calculated by the same method.

FIGURE 9 | Distribution of duration (A), severity (B), and intensity (C) of drought.

stations during summer were greater than 0, indicating that drought did not occur in most of the study area during summer. The average SPEI in autumn was greater in the northwestern section of the YGP and smaller in other sections of the YGP, and the SPEI values of most stations were greater than 0, indicating that drought did not occur in most areas of the YGP in autumn. The average SPEI in winter

was relatively small in the central part of the YGP and relatively large in other parts of the YGP, and the SPEI values of all stations were less than 0, indicating the occurrence of drought in winter. The average SPEI during the rainy season was greater in the western part of the YGP and smaller in the eastern part of the YGP, and the SPEI values of all stations were greater than 0, indicating that there was no

	The first component of SPEI		The second component of SPEI	
	VS.			
	Elevation	Longitude	Elevation	Longitude
Annual	-0.1371	-0.2170	0.755**	-0.8927**
Spring	-0.8187**	0.9501**	-0.5087**	0.6660**
Summer	0.7168**	-0.7453**	0.7002**	-0.8077**
Autumn	0.6967**	-0.8018**	0.7317**	-0.8244**
Winter	0.1630	-0.3556	-0.7291**	0.8319**
Rainy season	0.7453**	-0.778**	0.7483**	-0.9027**
Dry season	-0.7066**	0.6773**	-0.7133**	0.8566**
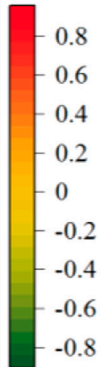
drought in the entire study area during the rainy season. The average SPEI during the dry season was relatively high in the eastern section of the YGP and smaller at most stations in the western section of the YGP, and the SPEI values of all the stations were less than 0, indicating the occurrence of drought on the YGP during the dry season.

In summary, the annual and seasonal SPEI values decreased to different degrees in most areas, indicating that drought might be aggravated. In addition, from the perspective of the multiyear average SPEI, mild drought occurred for the 12-months time scale in most areas throughout the year, and primarily mild drought conditions occurred for the 3-months time scale in part of the YGP during spring and autumn. No drought occurred in most regions during summer or the rainy season. However, drought on 3-months and 6-months timescales occurred throughout the YGP region during winter and the dry season, and drought conditions were mild in winter and moderate during the dry season.

Further analysis of **Figure 3** reveals that the annual and seasonal averages of the SPEI vary with the range. Therefore, this paper analyzed the correlation between the annual and seasonal averages of the SPEI and the longitude and elevation (as shown in **Figure 4**).
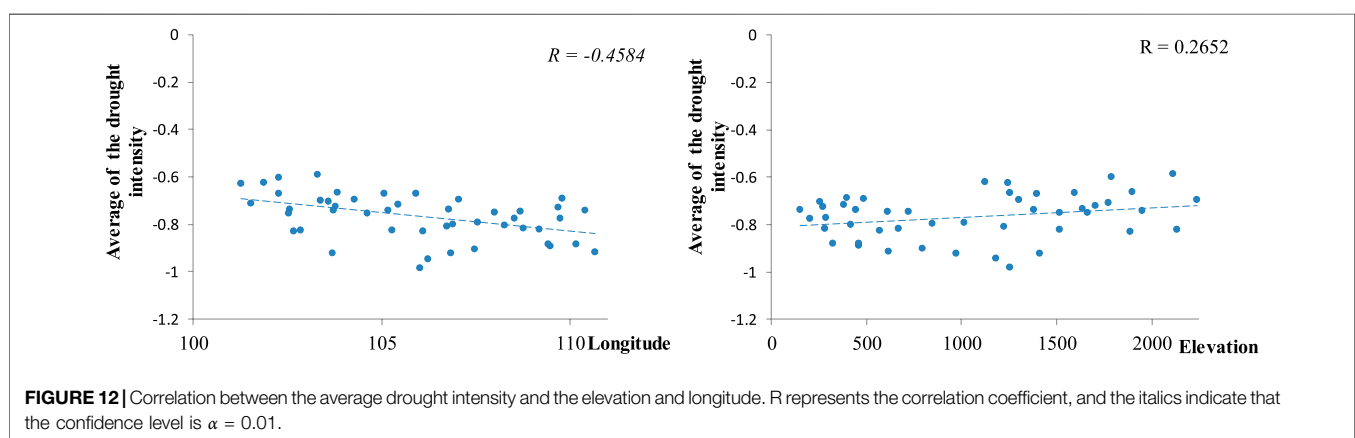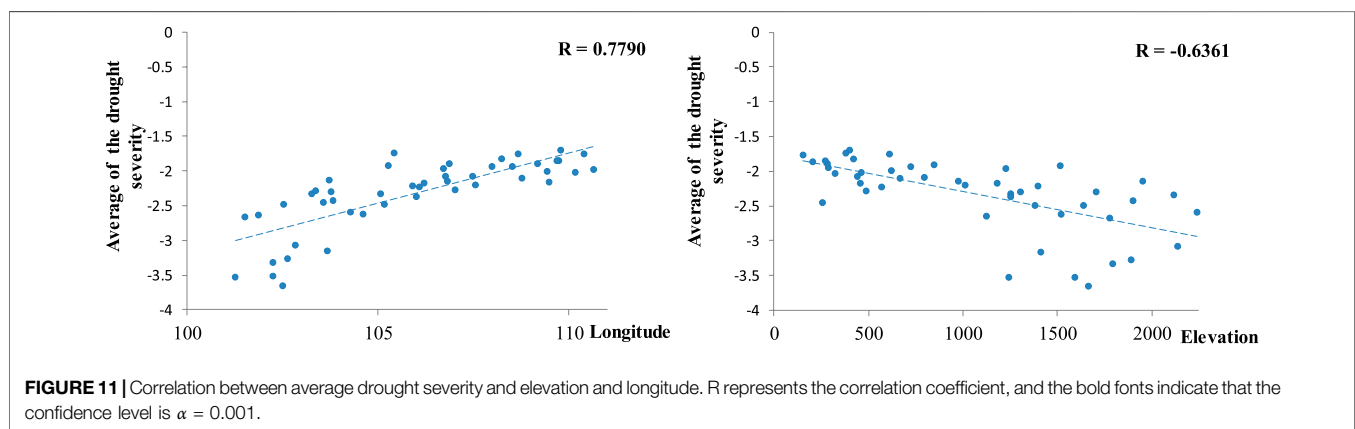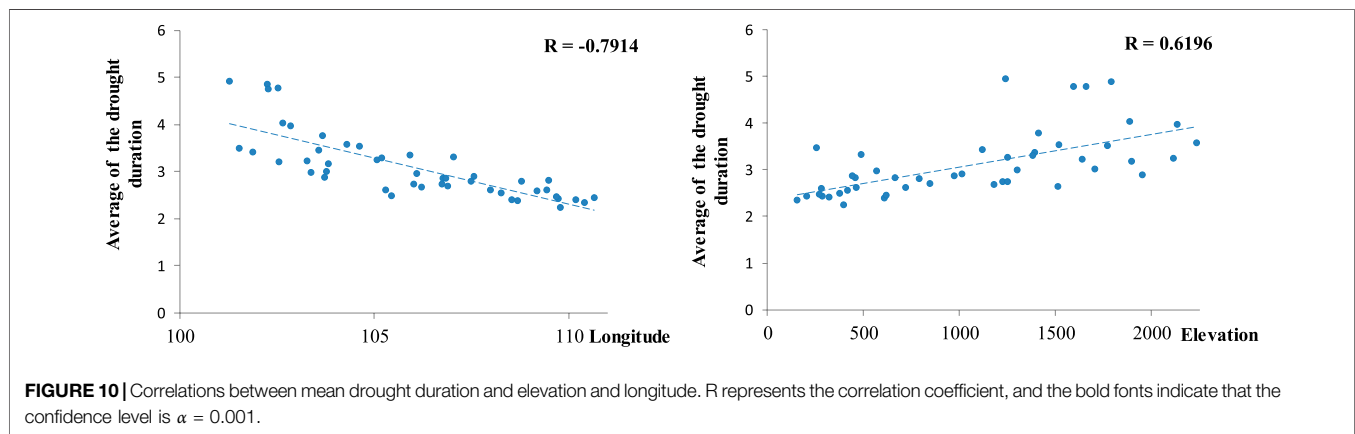
Figure 4 shows that, except for the annual average SPEI, the correlation between the average SPEI of other seasons and longitude is contrary to that of elevation. In particular, the average SPEI in spring and during the dry season had a significant positive correlation with longitude and a significant negative correlation with elevation. The average SPEI in summer, autumn, and during the rainy season had a significant negative correlation with longitude and a significant positive correlation with elevation. In general, except for the annual average SPEI and the average SPEI in winter, the average SPEI in spring, summer, autumn, and during the drought and rainy seasons was significantly correlated with elevation and longitude. In addition, the

correlation between the average SPEI and longitude was higher than that between the average SPEI and elevation (except during the dry season).

Spatial and Temporal Variability of Droughts Derived From PCA

According to the PCA method, the annual eigenvalues and cumulative variability of the SPEI of the YGP and each timescale were first calculated (as shown in **Figure 5**). The results show that except for annual variability, the contribution rate of the cumulative variability of the first three principal components in other seasons exceeded 70%. Therefore, the first three principal components can reflect the spatial changes in YGP drought. **Figures 6**, **7** show the principal components and time coefficients of drought annually and in each season, respectively.

The contribution rate of the cumulative variability of the first principal component was between 32 and 89%, which was much greater than that of other principal components. Therefore, it was considered that the spatial distribution of PC1 was the main distribution type of YGP drought. Except for PC1 at a few stations being greater than 0 in spring and autumn, PC1 at other time scales was less than 0, indicating that the drought and precipitation changes annually and in each season were consistent, showing wet and rainy conditions or drought and little rain throughout the year. In addition, the high value centers of PC1 were mainly distributed in the east and west of the YGP, reflecting that these areas were sensitive centers of drought and precipitation changes, with frequent interannual dry and wet alternations and large change ranges (the left side of **Figure 6**). Except for the time coefficient of PC1 in autumn, which weakly decreased, the time coefficient of PC1 on other time scales increased (**Figure 7**). The spatial distribution and time coefficient of PC1 showed that the drought of the YGP was becoming increasingly serious. The contribution rate of the cumulative variability of the second principal component was

FIGURE 10 | Correlations between mean drought duration and elevation and longitude. R represents the correlation coefficient, and the bold fonts indicate that the confidence level is $\alpha = 0.001$.

FIGURE 11 | Correlation between average drought severity and elevation and longitude. R represents the correlation coefficient, and the bold fonts indicate that the confidence level is $\alpha = 0.001$.

FIGURE 12 | Correlation between the average drought intensity and the elevation and longitude. R represents the correlation coefficient, and the italics indicate that the confidence level is $\alpha = 0.01$.

between 3 and 22%, which was also a typical spatial distribution type of YGP drought. Except for the dry season, the positive values of other time scales were mainly located in the west of YGP, and the negative values were mainly located in the east of YGP, indicating that the drought and precipitation changes in the east and west of YGP were opposite, and the east and west were the sensitive centers of drought and precipitation changes (the middle of **Figure 6**). The time coefficient of PC2 in the spring and rainy seasons increased, and the time coefficient of PC2 at other time scales decreased (**Figure 7**), indicating that the drought and precipitation changes on the YGP increased. The contribution rate of the cumulative variability of the third principal component was between 2 and 9%, accounting for a small proportion. The spatial distribution of PC3 on the YGP was complex, in which the
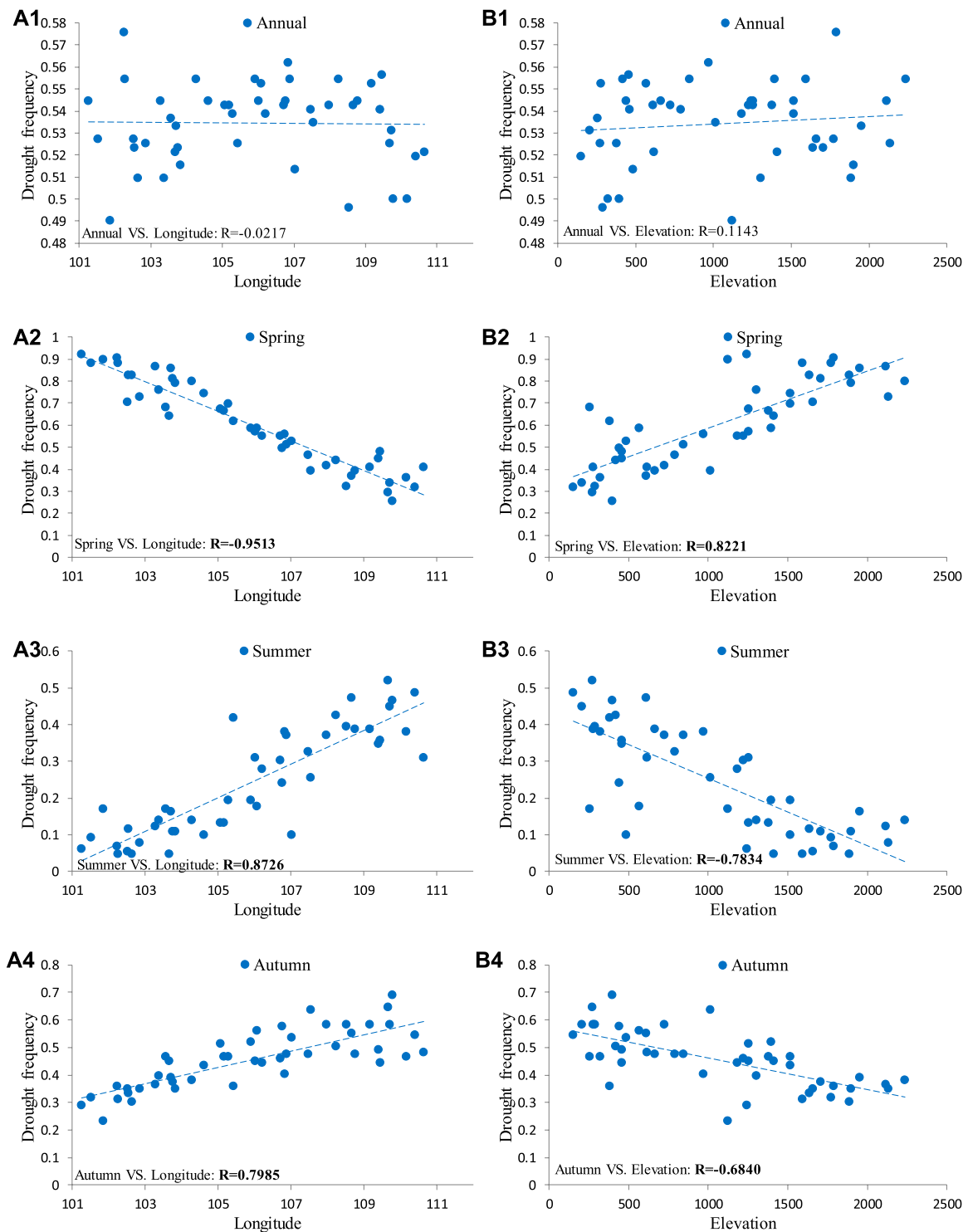
FIGURE 13 | Correlations between annual and seasonal drought frequency and longitude and elevation. **(A1–A7)** represents the correlation between drought frequency of annual, spring, summer, autumn, winter, rainy season, dry season and longitude; **(B1–B7)** represents the correlation between drought frequency of annual, spring, summer, autumn, winter, rainy season, dry season and elevation. R represents the correlation coefficient, and the bold fonts indicate that the confidence level is $\alpha = 0.001$.
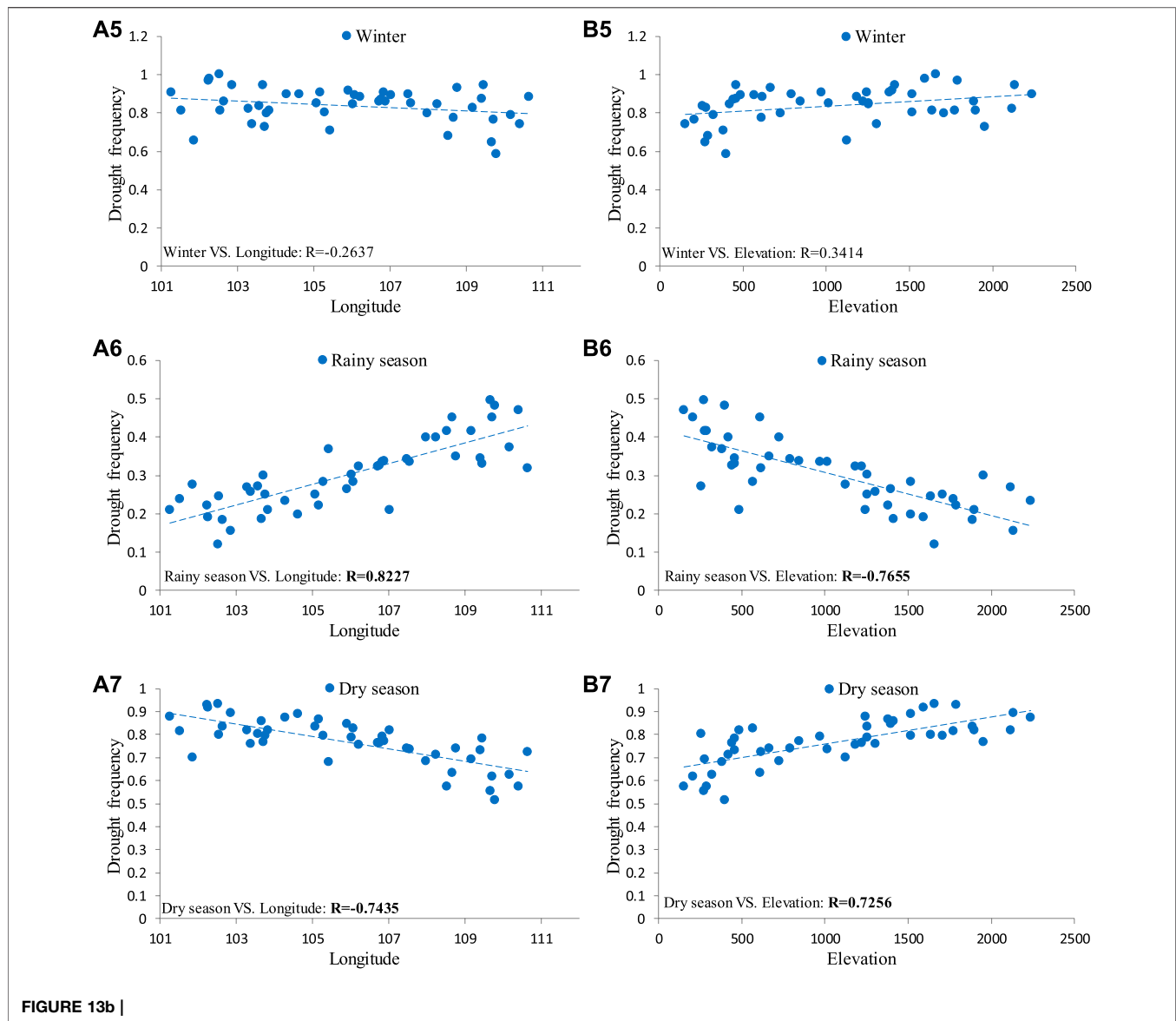
FIGURE 13b |

patterns annually and in autumn and winter were similar, and the negative values were mainly located in the southeast of the YGP. The negative value in spring was mainly located in the middle of the YGP. The negative values in summer and the rainy season were mainly located in the northeast of the YGP. The negative values in the dry season were mainly located in the west of the YGP (the right side of **Figure 6**). The distribution of PC3 on the YGP showed that the drought and wet changes were the opposite in different regions. The time coefficient of PC3 annually and in the rainy and dry seasons decreased, while that in other seasons increased (**Figure 7**).
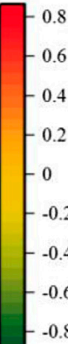
Figure 6 shows that the spatial distributions of the first two principal components were different in the eastern and western YGP. Therefore, this paper also analyzed their relationship with longitude and elevation (as shown in **Table 2**). **Table 2** shows that except for the annual and winter seasons, PC1 in other seasons

had a significant correlation with longitude and elevation at the significance level of $\alpha = 0.001$. There was a significant correlation between PC2 and longitude and elevation at the significance level $\alpha = 0.001$. For PC3, the correlation was weak. Overall, the spatial distribution of the first two principal components of the YGP drought had a good correlation with longitude and elevation. It is worth noting that these relationships do not reflect the correlation type (positive or negative correlation) of YGP drought with longitude and elevation. This is because the principal component only reflects the spatial distribution pattern of drought. It is necessary to reflect the relationship between drought and longitude and elevation, which needs to be multiplied by the time coefficient (as shown in **Figure 8** and **Table 3**).

The above analysis showed that the first two principal components had a good correlation with longitude and

TABLE 4 | Linear correlation coefficient R between the frequency of each drought grade and the longitude and elevation.

	Frequency of mild drought		Frequency of moderate drought		Frequency of severe drought		Frequency of extreme drought	
				VS.				
	Elevation	Longitude	Elevation	Longitude	Elevation	Longitude	Elevation	Longitude
Annual	-0.1940	0.3436	0.1347	-0.3265	0.6005**	-0.7382**	-0.2892	0.4682**
Spring	-0.1146	0.2886	0.6533**	-0.8814**	0.7403**	-0.8842**	0.7928**	-0.8358**
Summer	-0.6762**	0.7589**	-0.6150**	0.6474**	-0.6808**	0.7227**	-0.7531**	0.8621**
Autumn	-0.1412	0.2395	-0.7262**	0.782**	-0.7396**	0.8434**	-0.6775**	0.778**
Winter	0.2602	-0.2562	0.1044	0.0298	0.3702	-0.2999	0.2197	-0.1446
Rainy season	-0.4978**	0.5907**	-0.5996**	0.5952**	-0.6427**	0.6588**	-0.7825**	0.8415**
Dry season	0.0511	0.0397	0.5442**	-0.6981**	0.7733**	-0.8833**	0.7856**	-0.7413**
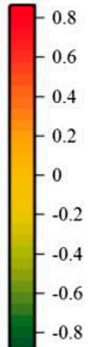
elevation. Therefore, the first two components of the SPEI were inversely calculated according to PC1 and PC2 and the corresponding time coefficients (as shown in **Figure 8**). **Figure 8** shows that except for annually and in winter, the first component of the SPEI in other seasons was related to longitude and elevation. The second component of the SPEI was related to longitude and elevation on each time scale (as shown in **Table 3**). Because the eigenvalue of PC1 was the largest, the first component of the SPEI played a major role. Hence, although the second component of the annual and winter SPEI had a good relationship with longitude and elevation, the overall relationship was poor (as shown in **Figure 4**).

The Relationship Between the Characteristics of Drought and Longitude/Elevation

In this paper, the SPEI was first calculated on a 1-month time scale according to the SPEI method. Then, based on the calculated SPEI on the 1-month time scale, the calculation method for drought characteristics was used to calculate the four drought characteristics—duration, severity, intensity (as shown in **Figure 9**), and frequency. Finally, the zonal patterns of the four characteristics of drought, i.e., the correlations between drought and longitude and elevation, were analyzed.

According to the statistical analysis of drought duration, the drought duration series were different at different stations. Therefore, this study used the average drought duration for analysis (as shown in **Figures 9**, **10**). **Figures 9**, **10** show that the average drought duration at each station is significantly correlated with longitude and elevation (confidence level α = 0.001), and the correlation between average drought duration and longitude was higher than that between average drought duration and elevation. The above analysis shows that with increasing longitude or decreasing elevation, the average drought duration decreases.

Drought severity indicates the severity of each drought event. According to the above method, the severity of each drought event is calculated (the drought severity is the corresponding series of drought durations), and then the correlations between the average drought severity and the longitude and elevation of each station are analyzed (as shown in **Figures 9**, **11**). **Figures 9**, **11** show that the average drought severity on the YGP was significantly correlated with longitude and elevation at a confidence level of α = 0.001, the average drought severity had a positive correlation with longitude and a negative correlation with elevation, and the correlation between average drought severity and longitude was higher than that between average drought severity and elevation. The above analysis reveals that with increasing longitude or decreasing elevation, the average drought severity increases.

Based on the calculated drought severity and drought duration, this study first calculated the drought intensity for each drought event and then analyzed the correlation between the average drought intensity and the longitude and elevation (as shown in **Figures 9**, **12**). **Figures 9**, **12** show that the mean drought intensity had a significant negative correlation with longitude at a confidence level of α = 0.01 but had no significant correlation with elevation. In other words, with increasing longitude, the average drought intensity decreased.

Drought frequency reflects the drought situation in the YGP area. In this study, we obtained the annual and seasonal drought frequencies according to the calculation method of drought frequency and analyzed the correlation between these frequencies and longitude and elevation (as shown in **Figure 13**). **Figure 13** shows that there is a significant correlation between drought frequency and longitude and elevation at a confidence level of α = 0.001 (except for the annual drought frequency and the drought frequency in winter). Moreover, drought frequency in spring and during the dry season was negatively correlated with longitude and positively correlated with elevation; the drought frequency in summer and autumn and during the rainy season was positively correlated with longitude and negatively correlated with elevation; and the correlation between drought frequency and longitude was higher than that between drought frequency and elevation. The above analysis shows that as longitude increased or
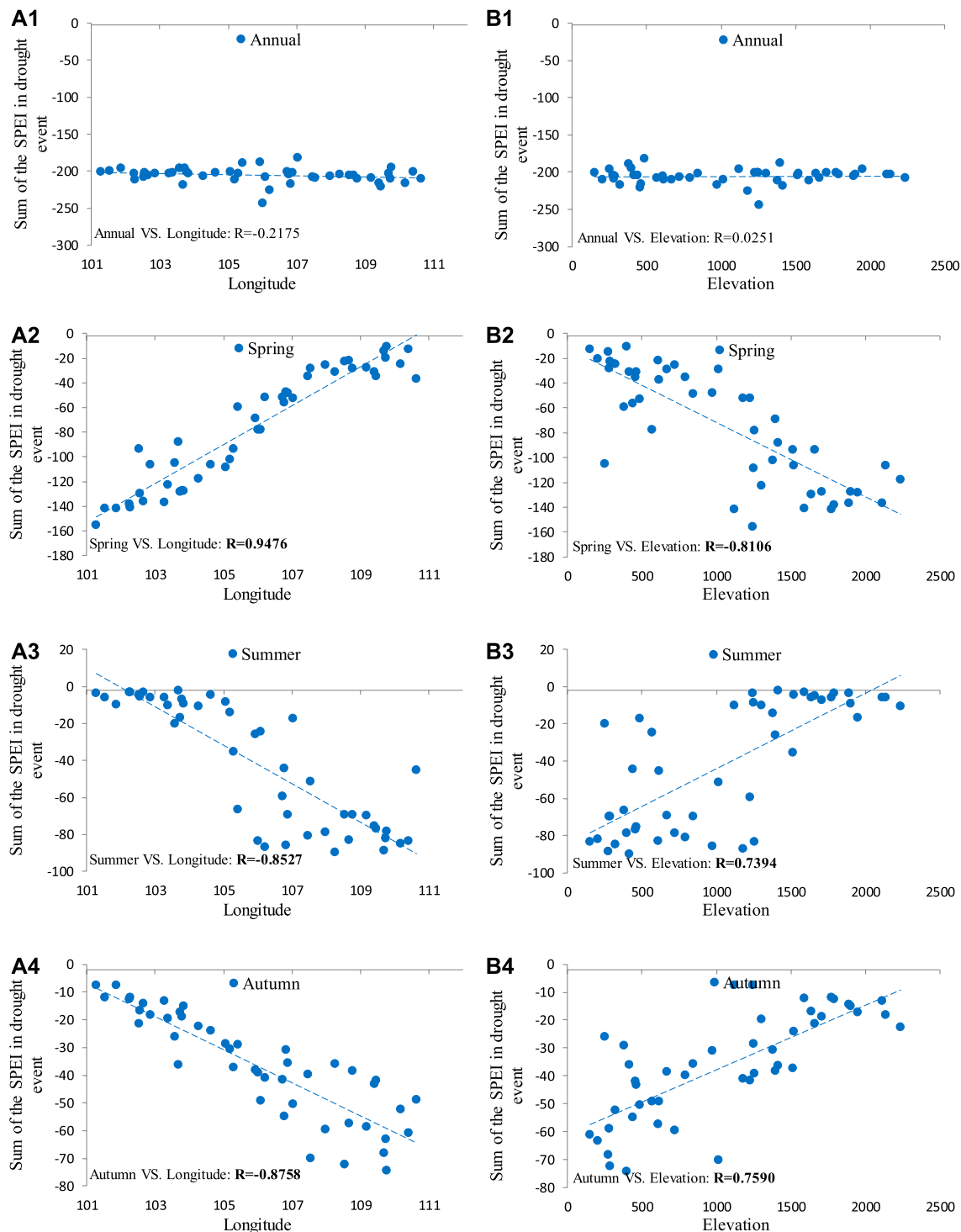
FIGURE 14 | Correlations between annual and seasonal SPEI sums of drought events and longitude and elevation. **(A1–A7)** represents the correlation between drought events of annual, spring, summer, autumn, winter, rainy season, dry season and longitude; **(B1–B7)** represents the correlation between drought events of annual, spring, summer, autumn, winter, rainy season, dry season and elevation. R represents the correlation coefficient, and the bold fonts indicate that the confidence level is $\alpha = 0.001$.

FIGURE 14b |
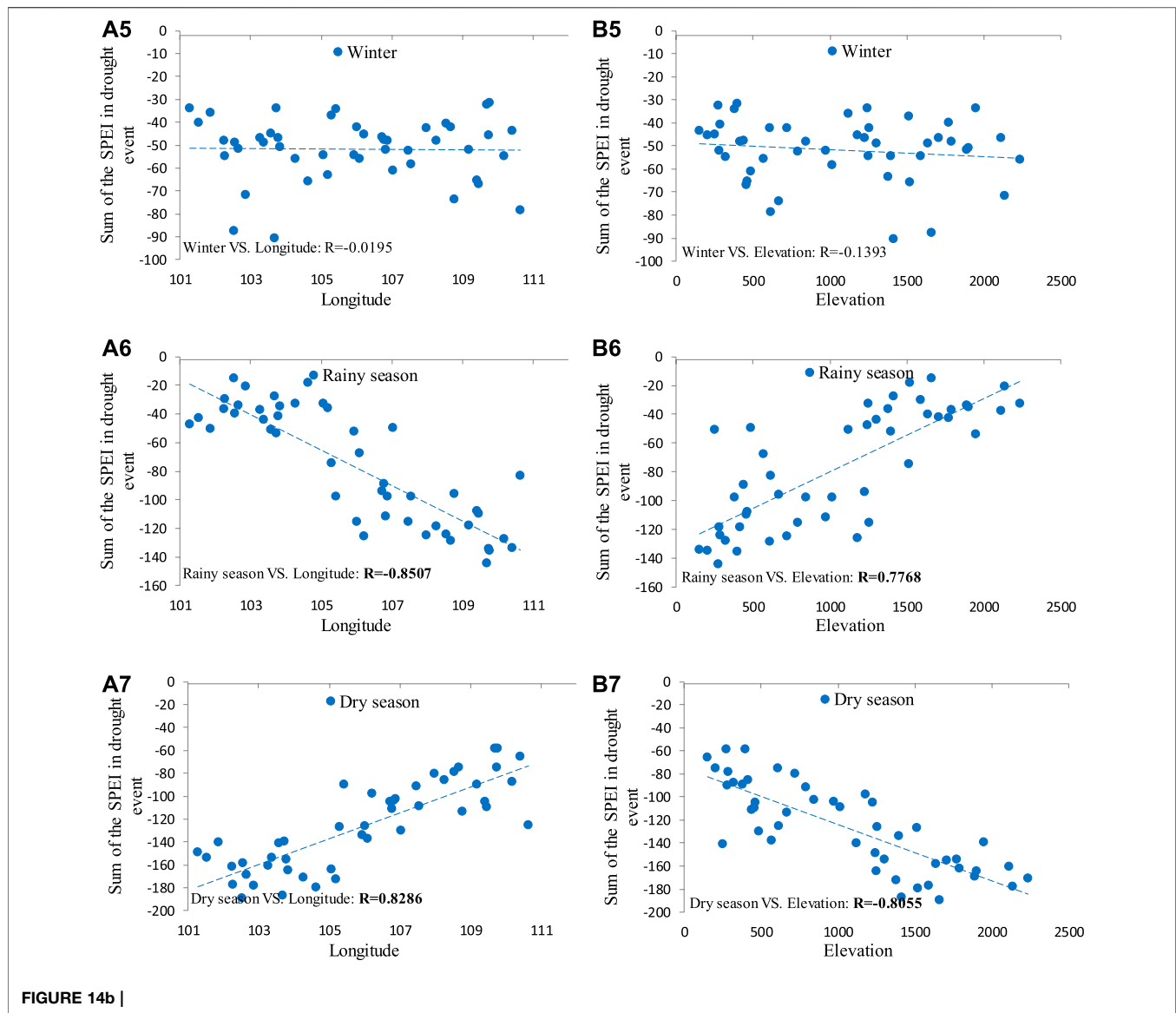
elevation decreased, the drought events increased (increased drought frequency) in summer and autumn and during the rainy season with more precipitation, and the drought events decreased (reduced drought frequency) in spring and during the dry season with less precipitation. In other words, except for the annual drought frequency and drought frequency in winter, the drought frequencies varied with changes in longitude and elevation.

In addition to analyzing the frequency of drought events, this paper also analyzed the correlation between the frequency of each drought grade (including mild, moderate, severe, and extreme drought, as shown in **Table 1**) and the longitude and elevation (as shown in **Table 4**). **Table 4** shows that the annual and seasonal frequencies of most drought grades were significantly correlated with longitude and elevation (confidence level $\alpha = 0.001$); i.e., the frequency of each drought grade varied with changes in longitude and elevation.
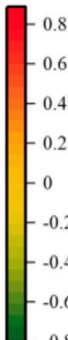
The sum of the SPEI values of the drought events during the study period also indicates the drought conditions in various regions. Therefore, this paper also analyzed the correlation between the annual and seasonal SPEI sum of the drought events and the longitude and elevation (as shown in **Figure 14**). **Figure 14** shows that, except for the annual SPEI sum and the SPEI sum in winter, the correlation between the SPEI sum and longitude was opposite to that between the SPEI sum and elevation (confidence level $\alpha = 0.001$), and the correlation between the SPEI sum and longitude was higher than that between the SPEI sum and elevation. In other words, with changes in longitude and elevation, the annual and seasonal SPEI sums also changed.

In addition, this study analyzed the correlation between the SPEI sum of each drought grade and the longitude and elevation (as shown in **Table 5**). **Table 5** shows that the SPEI sums of most drought grades exhibited significant correlations with longitude

TABLE 5 | Linear correlation coefficient R of the SPEI and the longitude and elevation of different drought classes.

	Sum of the SPEI in mild drought		Sum of the SPEI in moderate drought		Sum of the SPEI in severe drought		Sum of the SPEI in extreme drought	
	VS.							
	Elevation	Longitude	Elevation	Longitude	Elevation	Longitude	Elevation	Longitude
Annual	0.2151	−0.3913	−0.1709	0.3683	−0.6041**	0.7376**	0.3850	−0.5700**
Spring	−0.4309	0.4220	−0.6547**	0.8818**	−0.7442**	0.8852**	−0.7651**	0.8100**
Summer	0.7125**	−0.7722**	0.6171**	−0.6403	0.6819**	−0.726**	0.6701**	−0.8025**
Autumn	0.3987	−0.5380**	0.7271**	−0.7852**	0.7348**	−0.837**	0.6545**	−0.7678**
Winter	−0.0147	−0.1144	−0.1342	−0.0034	−0.3748	0.3019	−0.2160	0.1432
Rainy season	0.6029**	−0.6396**	0.5977**	−0.5939**	0.6406**	−0.6551**	0.6905**	−0.7889**
Dry season	−0.0447	−0.1027	−0.5685**	0.7286**	−0.7794**	0.8844**	−0.7501**	0.7133**

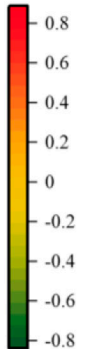and elevation (confidence level $\alpha = 0.001$); i.e., with changes in longitude and elevation, the SPEI sums of different drought grades changed in different regions.

Zonal Patterns of Drought

The above results mainly assess the relationships between the average SPEI and drought characteristics and longitude and elevation. To analyze the zonal patterns of drought, this paper studies not only the relationship with longitude and elevation but also the relationship with latitude. However, the relationship between the average SPEI and drought characteristics and latitude is poor, so this paper uses multiple linear regression methods (as shown in **Table 6**). **Table 6** shows that, except for the average SPEI in winter, drought intensity, drought frequency, and the sums of the annual and winter SPEI values, the other indicators have a strong correlation with longitude, latitude, and elevation. In other words, the YGP's drought characteristics exhibited strong zonal patterns.

DISCUSSION

The annual and seasonal SPEI values of the YGP primarily declined, indicating that drought in the YGP area became

TABLE 6 | Multiple linear regression analysis of average SPEI and drought characteristics with longitude and latitude and elevation.

						Coefficients		
		Multiple R	F	*p*-value	Intercept	Variable latitude	Variable longitude	Variable elevation
Average SPEI	Annual	0.5701	6.90	6.77E−04	2.27E+00	−2.40E−03	−2.03E−02	−8.07E−05
	Spring	0.9522	139.40	3.56E−22	−2.24E+01	−2.72E−02	2.17E−01	−1.84E−04
	Summer	0.8392	34.12	1.91E−11	1.04E+01	−4.01E−02	−8.18E−02	1.82E−04
	Autumn	0.8937	56.88	5.14E−15	8.79E+00	7.71E−02	−1.03E−01	5.90E−05
	Winter	0.3997	2.73	5.58E−02	3.43E+00	−2.44E−02	−3.12E−02	−1.00E−04
	Rainy season	0.8305	31.86	5.29E−11	7.31E+00	1.03E−02	−6.49E−02	1.23E−04
	Dry season	0.7398	17.33	1.59E−07	−5.02E+00	−7.57E−03	4.28E−02	−2.36E−04
Average of the drought duration		0.8128	27.90	3.56E−10	2.51E+01	8.55E−02	−2.29E−01	−3.03E−05
Average of the drought severity		0.7979	25.11	1.52E−09	−1.71E+01	−5.79E−02	1.54E−01	−3.64E−05
Average of the drought intensity		0.5156	5.19	3.78E−03	1.60E+00	−1.10E−02	−1.92E−02	−3.90E−05
Drought frequency	Annual	0.3251	1.69	1.83E−01	4.23E−01	3.50E−03	9.16E−05	7.40E−06
	Spring	0.9614	174.84	4.16E−24	6.65E+00	1.07E−02	−6.04E−02	5.72E−05
	Summer	0.8925	56.10	6.51E−15	−3.37E+00	1.08E−02	3.20E−02	−5.93E−05
	Autumn	0.8789	48.68	7.03E−14	−2.43E+00	−2.48E−02	3.37E−02	−2.06E−05
	Winter	0.4518	3.68	1.92E−02	8.59E−01	1.80E−02	−5.27E−03	5.04E−05
	Rainy season	0.8443	35.59	1.01E−11	−1.68E+00	−2.12E−03	1.97E−02	−4.45E−05
	Dry season	0.7886	23.57	3.54E−09	2.51E+00	9.19E−03	−1.93E−02	5.83E−05
Sum of the SPEI in drought event	Annual	0.3960	2.67	5.97E−02	−9.40E+00	−1.51E+00	−1.41E+00	−6.18E−03
	Spring	0.9527	140.97	2.86E−22	−1.50E+03	−2.36E−02	1.36E+01	−1.19E−02
	Summer	0.8762	47.39	1.09E−13	8.46E+02	−3.91E+00	−7.49E+00	9.81E−03
	Autumn	0.9176	76.33	2.93E−17	5.14E+02	3.19E+00	−6.06E+00	5.03E−03
	Winter	0.2715	1.14	3.43E−01	1.31E+02	−8.64E−01	−1.42E+00	−8.99E−03
	Rainy season	0.8710	45.04	2.51E−13	8.62E+02	−2.17E+00	−8.50E+00	1.83E−02
	Dry season	0.8643	42.32	6.80E−13	−8.31E+02	6.40E−01	6.73E+00	−2.44E−02

increasingly severe. In addition, overall, the spatial distributions of the annual average SPEI and the average SPEI in winter were relatively complex. The average SPEI values in spring and during the dry season were greater in the eastern part of the YGP and smaller in the western part of the YGP, whereas those in summer and autumn and during the rainy season were smaller in the eastern part of the YGP and greater in the western part of the YGP. Furthermore, the annual average SPEI and the average SPEI in spring were less than 0 at most stations, indicating that drought occurred in most areas of the YGP, whereas the average SPEI values in summer and autumn were the opposite; the average SPEI values of all stations were less than 0 in winter and during the dry season, indicating that drought occurred in the entire YGP area, whereas no drought occurred during the rainy season. This outcome occurred because southwestern China has a subtropical and temperate monsoon climate with an extremely uneven seasonal distribution of precipitation. Precipitation during the rainy and dry seasons accounted for 80–90% and 10–20% of the annual precipitation, respectively (Zhao, 1997). This outcome indicates that variation in precipitation is the primary cause of drought on the YGP (Xu et al., 2015). Xu et al. (2015) found that the SPI and SPEI values of the YGP significantly decreased. In addition, the drying trend is also evident in southwestern China (Liu et al., 2015). The above results are consistent with the results of this study and help elucidate the causes of drought on the YGP.

Except for the annual average SPEI and the average SPEI in winter, the average SPEI was significantly correlated with longitude and elevation at a confidence level of α = 0.001. Moreover, the average SPEI values were positively correlated with longitude and negatively correlated with elevation in spring and during the dry season, whereas the average SPEI values were negatively correlated with longitude and positively correlated with elevation in summer and autumn and during the rainy season. From the perspective of PCA, the first two principal components were significantly correlated with longitude and elevation at the confidence level of α = 0.001. In addition, the first two components of the SPEI also showed a good relationship with longitude and elevation. Although the second component of the SPEI had a significant correlation with longitude and elevation at the confidence level of α = 0.001 on all time scales, the relationship between the SPEI and longitude and elevation was poor annually and in spring because the first component was dominant. From the perspective of drought characteristics, average drought duration and average drought severity had a significant correlation with longitude and elevation (confidence level α = 0.001). Average drought duration was negatively correlated with longitude and positively correlated with elevation, average drought severity was positively correlated with longitude and negatively correlated with elevation, and drought intensity was negatively correlated with longitude at a confidence level of α = 0.01 and was nonsignificantly correlated with elevation. Because drought severity and drought duration were relatively small in high-longitude or low-elevation areas and were relatively large in low-longitude or high-elevation areas, the weak correlation

between the ratio of these two factors and longitude and elevation was reasonable. Except for the annual drought frequency and drought frequency in winter, drought frequency was significantly correlated with longitude and elevation at a confidence level of α = 0.001. Moreover, drought frequency was negatively correlated with longitude and positively correlated with elevation in spring and during the dry season, whereas drought frequency was positively correlated with longitude and negatively correlated with elevation in summer and autumn and during the rainy season. The annual and seasonal frequencies of most drought grades were significantly correlated with longitude and elevation at a confidence level of α = 0.001. Zhang et al. (2013) showed that the elevation in southwestern China has some impact on the frequency of extreme drought during the monsoon period; except for the annual SPEI sum of drought and the SPEI sum in winter, the SPEI sums of drought were significantly correlated with longitude and elevation, and the SPEI sums were positively correlated with longitude and negatively correlated with elevation in spring and during the dry season, whereas the SPEI sums were negatively correlated with longitude and positively correlated with elevation in summer and autumn and during the rainy season. The above analysis indicates that both the multiyear average SPEI and the characteristics of drought are strongly correlated with longitude and elevation, and in most cases, their correlation with longitude was higher than that with elevation. In addition, from multiple linear regression analysis, the average SPEI and drought characteristics have a good relationship with longitude, latitude, and elevation in most cases, indicating that drought on the YGP has zonal patterns. The zonal patterns of the YGP drought may be caused by changes in precipitation in the region. Previous studies have shown that annual precipitation in southwestern China, the Qinghai–Tibet Plateau, and the Hengduan Mountains was related to latitude and elevation (Lu et al., 2007; Tao et al., 2016; Yu et al., 2018). Therefore, drought and its characteristic values on the YGP have a good correlation with longitude, latitude, and elevation; that is, drought shows zonal patterns.

CONCLUSION

Based on meteorological data, the temporal and spatial distribution of drought on the YGP and the relationships between drought characteristics and longitude, latitude, and elevation were calculated and analyzed by SPEI, the Mann–Kendall test, PCA, linear regression, and multiple linear regression. The results show that the SPEI of the YGP is decreasing, and the drought is becoming increasingly severe. In addition, the spatial changes in SPEI in each season are different, but SPEI values in seasons are consistent spatially except annually and in winter; thus, YGP drought and its characteristics have a good correlation with elevation and longitude, indicating that YGP drought may be affected by elevation and longitude. The multiple linear regression results verify this conclusion, that is, YGP drought in most seasons is affected by elevation and longitude. In addition, it is also affected by latitude, showing strong zonal patterns. Taking the YGP as the research area and the SPEI as the drought index, based

on the analysis of the temporal and spatial distribution of YGP drought, this paper focuses on the relationship between drought and its characteristics and longitude and elevation and reveals the zonal patterns of YGP drought. The results may have certain limitations (regionality), but this article shows that drought has zonal patterns, which may be similar in other parts of the world. Therefore, the research results of this paper can provide new ideas for drought analysis in other regions and provide a scientific basis for industrial layout, planting structure adjustment, and drought relief.

DATA AVAILABILITY STATEMENT

The original contributions presented in the study are included in the article/supplementary materials, further inquiries can be directed to the corresponding authors.

AUTHOR CONTRIBUTIONS

HY calculated, analyzed and wrote this article. LW provided research ideas. MY prepared the data.

REFERENCES

Adnan, S., Ullah, K., and Shouting, G. (2016). Investigations into Precipitation and Drought Climatologies in South Central Asia with Special Focus on Pakistan over the Period 1951-2010. *J. CLIMATE* 29, 6019–6035. doi:10.1175/jcli-d-15-0735.1

Ahmed, K., Shahid, S., Harun, S. b., and Wang, X.-j. (2015). Characterization of Seasonal Droughts in Balochistan Province, Pakistan. *Stoch. Environ. Res. Risk Assess.* 30, 747–762. doi:10.1007/s00477-015-1117-2

Allen, R. G., Pereira, L. S., Raes, D., and Smith, M. (1998). "Crop Evapotranspiration. Guidelines for Computing Crop Water Requirements,". FAO Irrigation and Drainage Paper 56 (Rome: FAO).

Almazroui, M., Saeed, F., Islam, M. N., and Alkhalaf, A. K. (2016). Assessing the Robustness and Uncertainties of Projected Changes in Temperature and Precipitation in AR4 Global Climate Models over the Arabian Peninsula. *Atmos. Res.* 182, 163–175. doi:10.1016/j.atmosres.2016.07.025

Alsafadi, K., Mohammed, S. A., Ayugi, B., Sharaf, M., and Harsányi, E. (2020). Spatial-Temporal Evolution of Drought Characteristics over Hungary between 1961 and 2010. *Pure Appl. Geophys.* 177, 3961–3978. doi:10.1007/s00024-020-02449-5

Aryal, Y., and Zhu, J. (2021). Spatial and Temporal Variability of Drought Patterns over the Continental United States from Observations and Regional Climate Models. *J. Meteorol. Res.* 35, 295–312. doi:10.1007/s13351-021-0045-y

Azam, M., Maeng, S., Kim, H., Lee, S., and Lee, J. (2018). Spatial and Temporal Trend Analysis of Precipitation and Drought in South Korea. *Water* 10, 765. doi:10.3390/w10060765

Banimahd, S. A., and Khalili, D. (2013). Factors Influencing Markov Chains Predictability Characteristics, Utilizing SPI, RDI, EDI and SPEI Drought Indices in Different Climatic Zones. *Water Resour. Manage.* 27, 3911–3928. doi:10.1007/s11269-013-0387-z

Beguería, S., Vicente-Serrano, S. M., Reig, F., and Latorre, B. (2014). Standardized Precipitation Evapotranspiration index (SPEI) Revisited: Parameter Fitting, Evapotranspiration Models, Tools, Datasets and Drought Monitoring. *Int. J. Climatol.* 34, 3001–3023. doi:10.1002/joc.3887

Chanda, K., and Maity, R. (2017). Assessment of Trend in Global Drought Propensity in the Twenty-First Century Using Drought Management Index. *Water Resour. Manage.* 31, 1209–1225. doi:10.1007/s11269-017-1571-3

Chatzithomas, C., Alexandris, S., and Karavitis, C. (2015). Multivariate Linear Relation for Precipitation: a New Simple Empirical Formula. *Stud. Geophys. Geod* 59 (2), 325–344. doi:10.1007/s11200-013-1162-6

Cheng, Q., Gao, L., Zhong, F., Zuo, X., and Ma, M. (2020a). Spatiotemporal Variations of Drought in the Yunnan-Guizhou Plateau, Southwest China, during 1960-2013 and Their Association with Large-Scale Circulations and

Historical Records. *Ecol. Indicators* 112, 106041. doi:10.1016/j.ecolind.2019.106041

Cheng, W. J., Xi, H. Y., Si, J. H., and Li, A. L. (2020b). Study of Evapotranspiration Estimation and Drought Characteristics of Watershed in Low Coteau Area of Hexi Inland River. *Arid Zone Res.* 37 (5), 1105–1115. (in Chinese).

Danandeh Mehr, A., Sorman, A. U., Kahya, E., and Hesami Afshar, M. (2020). Climate Change Impacts on Meteorological Drought Using SPI and SPEI: Case Study of Ankara, Turkey. *Hydrological Sci. J.* 65, 254–268. doi:10.1080/02626667.2019.1691218

Danandeh Mehr, A., and Vaheddoost, B. (2020). Identification of the Trends Associated with the SPI and SPEI Indices across Ankara, Turkey. *THEOR. APPL. CLIMATOL* 139, 1531–1542. doi:10.1007/s00704-019-03071-9

El Kenawy, A. M., Al Buloshi, A., Al-Awadhi, T., Al Nasiri, N., Navarro-Serrano, F., Alhatrushi, S., et al. (2020). Evidence for Intensification of Meteorological Droughts in Oman over the Past Four Decades. *Atmos. Res.* 246, 105126. doi:10.1016/j.atmosres.2020.105126

Fang, W., Huang, S., Huang, Q., Huang, G., Meng, E., and Luan, J. (2018). Reference Evapotranspiration Forecasting Based on Local Meteorological and Global Climate Information Screened by Partial Mutual Information. *J. Hydrol.* 561, 764–779. doi:10.1016/j.jhydrol.2018.04.038

Fang, W., Huang, S., Ren, K., Huang, Q., Huang, G., Cheng, G., et al. (2019). Examining the Applicability of Different Sampling Techniques in the Development of Decomposition-Based Streamflow Forecasting Models. *J. Hydrol.* 568, 534–550. doi:10.1016/j.jhydrol.2018.11.020

Fu, Q., Zhou, Z., Li, T., Liu, D., Hou, R., Cui, S., et al. (2018). Spatiotemporal Characteristics of Droughts and Floods in Northeastern China and Their Impacts on Agriculture. *Stoch Environ. Res. Risk Assess.* 32, 2913–2931. doi:10.1007/s00477-018-1543-z

Gocic, M., and Trajkovic, S. (2014). Spatiotemporal Characteristics of Drought in Serbia. *J. Hydrol.* 510, 110–123. doi:10.1016/j.jhydrol.2013.12.030

Gunda, T., Hornberger, G. M., and Gilligan, J. M. (2016). Spatiotemporal Patterns of Agricultural Drought in Sri Lanka: 1881-2010. *Int. J. Climatol.* 36, 563–575. doi:10.1002/joc.4365

Guo, H., Bao, A., Liu, T., Jiapaer, G., Ndayisaba, F., Jiang, L., et al. (2018). Spatial and Temporal Characteristics of Droughts in Central Asia during 1966-2015. *Sci. Total Environ.* 624, 1523–1538. doi:10.1016/j.scitotenv.2017.12.120

Guttman, N. B. (1998). Comparing the Palmer Drought Index and the Standardized Precipitation Index. *J. Am. Water Resour. Assoc* 34, 113–121. doi:10.1111/j.1752-1688.1998.tb05964.x

Huang, J., Xue, Y., Sun, S., and Zhang, J. (2015). Spatial and Temporal Variability of Drought during 1960-2012 in Inner Mongolia, north China. *Quat. Int.* 355, 134–144. doi:10.1016/j.quaint.2014.10.036

Huang, J., Zhang, J., Zhang, Z., and Xu, C.-Y. (2013). Spatial and Temporal Variations in Rainfall Erosivity during 1960-2005 in the Yangtze River basin. *Stoch Environ. Res. Risk Assess.* 27, 337–351. doi:10.1007/s00477-012-0607-8

Huang, S., Wang, L., Wang, H., Huang, Q., Leng, G., Fang, W., et al. (2019). Spatio-temporal Characteristics of Drought Structure across China Using an Integrated Drought index. *Agric. Water Manag.* 218, 182–192. doi:10.1016/j.agwat.2019.03.053

Jin, L., Zhang, J., Wang, R., Zhang, M., Bao, Y., Guo, E., et al. (2019). Analysis for Spatio-Temporal Variation Characteristics of Droughts in Different Climatic Regions of the Mongolian Plateau Based on SPEI. *Sustainability* 11, 5767. doi:10.3390/su11205767

Kendall, M. G. (1975). *Rank Correlation Measures*. London: Charles Griffin.

Kimosop, P. (2019). Characterization of Drought in the Kerio Valley Basin, Kenya Using the Standardized Precipitation Evapotranspiration Index: 1960–2016. *Singapore J. Trop. Geogr.* 40 (2), 239–256. doi:10.1111/sjtg.12270

Li, X., Sha, J., and Wang, Z.-L. (2019b). Comparison of Drought Indices in the Analysis of Spatial and Temporal Changes of Climatic Drought Events in a basin. *Environ. Sci. Pollut. Res.* 26, 10695–10707. doi:10.1007/s11356-019-04529-z

Li, Y., Wang, Z., Zhang, Y., Li, X., and Huang, W. (2019a). Drought Variability at Various Timescales over Yunnan Province, China: 1961-2015. *THEOR. APPL. CLIMATOL* 138, 743–757. doi:10.1007/s00704-019-02859-z

Liu, X., Wang, S., Zhou, Y., Wang, F., Li, W., and Liu, W. (2015). Regionalization and Spatiotemporal Variation of Drought in China Based on Standardized Precipitation Evapotranspiration Index (1961-2013). *Adv. Meteorology* 2015, 1–18. doi:10.1155/2015/950262

Liu, Z., Wang, Y., Shao, M., Jia, X., and Li, X. (2016). Spatiotemporal Analysis of Multiscalar Drought Characteristics across the Loess Plateau of China. *J. Hydrol.* 534, 281–299. doi:10.1016/j.jhydrol.2016.01.003

Lu, C. X., Wang, L., Xie, G. D., and Leng, Y. F. (2007). Altitude Effect of Precipitation and Spatial Distribution of Qinghai-Tibetan Plateau. *J. Mountain Sci.* 25 (6), 655–663. (in Chinese).

Mann, H. B. (1945). Nonparametric Tests against Trend. *Econometrica* 13, 245–259. doi:10.2307/1907187

Mathbout, S., Lopez-Bustins, J. A., Martin-Vide, J., Bech, J., and Rodrigo, F. S. (2018). Spatial and Temporal Analysis of Drought Variability at Several Time Scales in Syria during 1961-2012. *Atmos. Res.* 200, 153–168. doi:10.1016/j.atmosres.2017.09.016

McKee, T. B., Doesken, N. J., and Kleist, J. (1993). "The Relationship of Drought Frequency and Duration to Time Scales," in Preprints, Eighth Conf. on Applied Climatology, Anaheim, CA, 17-22 January 1993 (Amer.Meteor. Soc.), 179–184.

Merabti, A., Martins, D. S., Meddi, M., and Pereira, L. S. (2018). Spatial and Time Variability of Drought Based on SPI and RDI with Various Time Scales. *Water Resour. Manage.* 32, 1087–1100. doi:10.1007/s11269-017-1856-6

Mishra, A. K., and Singh, V. P. (2010). A Review of Drought Concepts. *J. Hydrol.* 391, 202–216. doi:10.1016/j.jhydrol.2010.07.012

Mohammadi, B., Vaheddoost, B., and Danandeh Mehr, A. (2020). A Spatiotemporal Teleconnection Study between Peruvian Precipitation and Oceanic Oscillations. *Quat. Int.* 565, 1–11. doi:10.1016/j.quaint.2020.09.042

Mohsenipour, M., Shahid, S., Chung, E.-S., and Wang, X.-j. (2018). Changing Pattern of Droughts during Cropping Seasons of Bangladesh. *Water Resour. Manage.* 32, 1555–1568. doi:10.1007/s11269-017-1890-4

Nuri Balov, M., and Altunkaynak, A. (2020). Spatio-temporal Evaluation of Various Global Circulation Models in Terms of Projection of Different Meteorological Drought Indices. *ENVIRON. EARTH SCI.* 79. doi:10.1007/s12665-020-8881-0

Palmer, W. C. (1965). "Meteorological Droughts,". Weather Bureau Research Paper 45 (Washington DC: U.S. Department of Commerce), 58.

Polong, F., Chen, H., Sun, S., and Ongoma, V. (2019). Temporal and Spatial Evolution of the Standard Precipitation Evapotranspiration index (SPEI) in the Tana River Basin, Kenya. *THEOR. APPL. CLIMATOL* 138, 777–792. doi:10.1007/s00704-019-02858-0

Portela, M. M., Zelenáková, M., Santos, J. F., Purcz, P., Silva, A. T., and Hlavatá, H. (2015). Drought Analysis in Slovakia: Regionalization, Frequency Analysis and Precipitation Thresholds. *WIT Trans. Ecol. Environ.* 197, 237–248. doi:10.2495/RM150211

Pour, S. H., Shahid, S., Chung, E.-S., and Wang, X.-J. (2018). Model Output Statistics Downscaling Using Support Vector Machine for the Projection of Spatial and Temporal Changes in Rainfall of Bangladesh. *Atmos. Res.* 213, 149–162. doi:10.1016/j.atmosres.2018.06.006

Prudhomme, C., Giuntoli, I., Robinson, E. L., Clark, D. B., Arnell, N. W., Dankers, R., et al. (2014). Hydrological Droughts in the 21st century, Hotspots and Uncertainties from a Global Multimodel Ensemble experiment. *Proc. Natl. Acad. Sci. USA* 111, 3262–3267. doi:10.1073/pnas.1222473110

Razei, T., Saghafian, B., Paulo, A. A., Pereira, L. S., and Bordi, I. (2009). Spatial Patterns and Temporal Variability of Drought in Western Iran. *Water Resour. Manage.* 23, 439–455. doi:10.1007/s11269-008-9282-4

Sa'adi, Z., Shahid, S., Chung, E. S., and Ismail, T. (2017). Projection of Spatial and Temporal Changes of Rainfall in Sarawak of Borneo Island Using Statistical Downscaling of CMIP5 Models. *Atmos. Res.* 197, 446–460.

Santos, J. F., Pulido-Calvo, I., and Portela, M. M. (2010). Spatial and Temporal Variability of Droughts in Portugal. *Water Resour. Res.* 46, W03503. doi:10.1029/2009wr008071

Sayemuzzaman, M., and Jha, M. K. (2014). Seasonal and Annual Precipitation Time Series Trend Analysis in North Carolina, United States. *Atmos. Res.* 137, 183–194. doi:10.1016/j.atmosres.2013.10.012

Sung, J. H., and Chung, E.-S. (2014). Development of Streamflow Drought Severity-Duration-Frequency Curves Using the Threshold Level Method. *Hydrol. Earth Syst. Sci.* 18, 3341–3351. doi:10.5194/hess-18-3341-2014

Sung, J. H., Chung, E. S., Lee, B., and Kim, Y. (2017). Meteorological hazard Risk Assessment Based on the Detection of Trends and Abrupt Changes in the Precipitation Characteristics of the Korean Peninsula. *Theor. Appl. Climatol.* 127 (1), 305–326. doi:10.1007/s00704-015-1581-0

Tan, C., Yang, J., and Li, M. (2015). Temporal-spatial Variation of Drought Indicated by SPI and SPEI in Ningxia Hui Autonomous Region, China. *Atmosphere* 6, 1399–1421. doi:10.3390/atmos6101399

Tang, H., Wen, T., Shi, P., Qu, S., Zhao, L., and Li, Q. (2021). Analysis of Characteristics of Hydrological and Meteorological Drought Evolution in Southwest China. *Water* 13, 1846. doi:10.3390/w13131846

Tao, H., Diop, L., Bodian, A., Djaman, K., Ndiaye, P. M., and Yaseen, Z. M. (2018). Reference Evapotranspiration Prediction Using Hybridized Fuzzy Model with Firefly Algorithm: Regional Case Study in Burkina Faso. *Agric. Water Manag.* 208, 140–151. doi:10.1016/j.agwat.2018.06.018

Tao, J., Dong, J. X., Liu, G. L., Zhang, G. L., Zhu, J. T., Song, W. J., et al. (2016). Characteristics of Temperature and Precipitation Change along Increasing Elevation in Different Agriculture Regions of Southwest China. *Chin. J. Agrometeorology* 37 (4), 379–389. (in Chinese).

Tian, L., and Quiring, S. M. (2019). Spatial and Temporal Patterns of Drought in Oklahoma (1901-2014). *INT. J. CLIMATOL* 39, 3365–3378. doi:10.1002/joc.6026

Vicente-Serrano, S. M., Beguería, S., and López-Moreno, J. I. (2010a). A Multiscalar Drought Index Sensitive to Global Warming: The Standardized Precipitation Evapotranspiration Index. *J. Clim.* 23, 1696–1718. doi:10.1175/2009jcli2909.1

Vicente-Serrano, S. M., Beguería, S., López-Moreno, J. I., Angulo, M., and El Kenawy, A. (2010b). A New Global 0.5° Gridded Dataset (1901-2006) of a Multiscalar Drought Index: Comparison with Current Drought Index Datasets Based on the Palmer Drought Severity Index. *J. Hydrometeorol.* 11, 1033–1043. doi:10.1175/2010jhm1224.1

Vicente-Serrano, S. M., Beguería, S., and López-Moreno, J. I. (2011a). Comment on "Characteristics and Trends in Various Forms of the Palmer Drought Severity Index (PDSI) during 1900-2008" by Aiguo Dai. *J. Geophys. Res.* 116, D19112. doi:10.1029/2011JD016410

Vicente-Serrano, S. M., López-Moreno, J. I., Gimeno, L., Nieto, R., Morán-Tejeda, E., Lorenzo-Lacruz, J., et al. (2011b). A Multiscalar Global Evaluation of the Impact of ENSO on Droughts. *J. Geophys. Res.* 116, D20109. doi:10.1029/2011JD016039

Vinnarasi, R., and Dhanya, C. T. (2016). Changing Characteristics of Extreme Wet and Dry Spells of Indian Monsoon Rainfall. *J. Geophys. Res. Atmos.* 121, 2146–2160. doi:10.1002/2015jd024310

Wang, M., Ding, Z., Wu, C., Song, L., Ma, M., Yu, P., et al. (2021a). Divergent Responses of Ecosystem Water-Use Efficiency to Extreme Seasonal Droughts in Southwest China. *Sci. Total Environ.* 760, 143427. doi:10.1016/j.scitotenv.2020.143427

Wang, W., Xing, W., Yang, T., Shao, Q., Peng, S., Yu, Z., et al. (2013). Characterizing the Changing Behaviours of Precipitation Concentration in the Yangtze River Basin, China. *Hydrol. Process.* 27, 3375–3393. doi:10.1002/hyp.9430

Wang, Y., Liu, G., and Guo, E. (2019). Spatial Distribution and Temporal Variation of Drought in Inner Mongolia during 1901-2014 Using Standardized Precipitation Evapotranspiration Index. *Sci. Total Environ.* 654, 850–862. doi:10.1016/j.scitotenv.2018.10.425

Wang, Y., Wang, Z., Zhang, Z., Shen, D., and Zhang, L. (2021b). The Best-Fitting Distribution of Water Balance and the Spatiotemporal Characteristics of

Drought in Guizhou Province, China. *THEOR. APPL. CLIMATOL* 143, 1097–1112. doi:10.1007/s00704-020-03469-w

Wang, Z., Li, J., Lai, C., Huang, Z., Zhong, R., Zeng, Z., et al. (2018). Increasing Drought Has Been Observed by SPEI_pm in Southwest China during 1962-2012. *THEOR. APPL. CLIMATOL* 133, 23–38. doi:10.1007/s00704-017-2152-3

Wilhite, D. A. (2005). *Drought and Water Crises: Science, Technology, and Management Issues*. Boca Raton, FL: CRC Press.

WMO (1975). *Drought and Agriculture. WMO Technical Note No 138*. Geneva Switzerland: WMO-No 392, 127.

World Meteorological Organization (WMO) and Global Water Partnership (GWP) (2016). "Handbook of Drought Indicators and Indices," in *Integrated Drought Management Programme (IDMP), Integrated Drought Management Tools and Guidelines Series 2*. Editors M. Svoboda and B. A. Fuchs Geneva.

Wu, C., J.-F. Yeh, P., Chen, Y. Y., Lv, W., Hu, B. X., Huang, G., et al. (2021). Copula-based Risk Evaluation of Global Meteorological Drought in the 21st century Based on CMIP5 Multi-Model Ensemble Projections. *J. Hydrol.* 598, 126265. doi:10.1016/j.jhydrol.2021.126265

Xiao, M., Zhang, Q., Singh, V. P., and Liu, L. (2016). Transitional Properties of Droughts and Related Impacts of Climate Indices in the Pearl River basin, China. *J. Hydrol.* 534, 397–406. doi:10.1016/j.jhydrol.2016.01.012

Xu, K., Yang, D., Yang, H., Li, Z., Qin, Y., and Shen, Y. (2015). Spatio-temporal Variation of Drought in China during 1961-2012: A Climatic Perspective. *J. Hydrol.* 526, 253–264. doi:10.1016/j.jhydrol.2014.09.047

Yang, Y., Chen, R., Song, Y., Han, C., Liu, J., and Liu, Z. (2019). Sensitivity of Potential Evapotranspiration to Meteorological Factors and Their Elevational Gradients in the Qilian Mountains, Northwestern China. *J. Hydrol.* 568, 147–159. doi:10.1016/j.jhydrol.2018.10.069

Yang, Y., Gan, T. Y., and Tan, X. (2020). Spatiotemporal Changes of Drought Characteristics and Their Dynamic Drivers in Canada. *Atmos. Res.* 232, 104695. doi:10.1016/j.atmosres.2019.104695

Yu, H., Wang, L., Yang, R., Yang, M., and Gao, R. (2018). Temporal and Spatial Variation of Precipitation in the Hengduan Mountains Region in China and its Relationship with Elevation and Latitude. *Atmos. Res.* 213, 1–16. doi:10.1016/j.atmosres.2018.05.025

Zahabiyoun, B., Goodarzi, M. R., Bavani, A. R. M., and Azamathulla, H. M. (2013). Assessment of Climate Change Impact on the Gharesou River Basin Using SWAT Hydrological Model. *Clean. Soil Air Water* 41 (6), 601–609. doi:10.1002/clen.201100652

Zeng, W., Yu, Z., Wu, S., and Qin, J. (2016). Changes in Annual, Seasonal and Monthly Precipitation Events and Their Link with Elevation in Sichuan Province, China. *Int. J. Climatol.* 36, 2303–2322. doi:10.1002/joc.4496

Zhang, L., Jiao, W., Zhang, H., Huang, C., Huang, Q., and Tong, Q. (2017). Studying Drought Phenomena in the Continental United States in 2011 and 2012 Using Various Drought Indices. *Remote Sensing Environ.* 190, 96–106. doi:10.1016/j.rse.2016.12.010

Zhang, M., He, J., Wang, B., Wang, S., Li, S., Liu, W., et al. (2013). Extreme Drought Changes in Southwest China from 1960 to 2009. *J. Geogr. Sci.* 23, 3–16. doi:10.1007/s11442-013-0989-7

Zhao, G., Mu, X., Hörmann, G., Fohrer, N., Xiong, M., Su, B., et al. (2012). Spatial Patterns and Temporal Variability of Dryness/wetness in the Yangtze River Basin, China. *Quat. Int.* 282, 5–13. doi:10.1016/j.quaint.2011.10.020

Zhao, Ji. (1997). *Chinese Physical Geography*. 3rd ed. Beijing: Higher Education Press. (in Chinese).

Evaluation of Time Series Models in Simulating Different Monthly Scales of Drought Index for Improving Their Forecast Accuracy

Shahab S. Band[1], Hojat Karami[2]*, Yong-Wook Jeong[3]*, Mohsen Moslemzadeh[2], Saeed Farzin[2], Kwok-Wing Chau[4], Sayed M. Bateni[5] and Amir Mosavi[6,7,8,9]*

[1]Future Technology Research Center, College of Future, National Yunlin University of Science and Technology, Yunlin, Taiwan, [2]Department of Civil Engineering, Semnan University, Semnan, Iran, [3]Department of Architecture, Sejong University, Seoul, South Korea, [4]Department of Civil and Environmental Engineering, Hong Kong Polytechnic University, Hong Kong, China, [5]Department of Civil and Environmental Engineering and Water Resources Research Center, University of Hawaii at Manoa, Honolulu, HI, United States, [6]Faculty of Civil Engineering, Technische Universität Dresden, Dresden, Germany, [7]John von Neumann Faculty of Informatics, Obuda University, Budapest, Hungary, [8]Institute of Information Society, University of Public Service, Budapest, Hungary, [9]Institute of Information Engineering, Automation and Mathematics, Slovak University of Technology in Bratislava, Bratislava, Slovakia

Drought is regarded as one of the most intangible and creeping natural disasters, which occurs in almost all climates, and its characteristics vary from region to region. The present study aims to investigate the effect of differentiation operations on improving the static and modeling accuracy of the drought index time series and after selecting the best selected model, evaluate drought severity and duration, as well as predict future drought behavior, in Semnan city. During this process, the effect of time series on modeling different monthly scales of drought index was analyzed, as well as the effect of differencing approach on stationarity improvement and prediction accuracy of the models. First, the stationarity of time series data related to a one-month drought index is investigated. By using seasonal, non-seasonal, and hybrid differencing, new time series are created to examine the improvement of the stationarity of these series through analyzing the ACF diagram and generalized Dickey–Fuller test. Based on the results, hybrid differencing indicates the best degree of stability. Then, the type and number of states required to evaluate the models are determined, and finally, the best prediction model is selected by applying assessment criteria. In the following, the same stages are analyzed for the drought index time series data derived from 6-month rainfall data. The results reveal that the SARIMA $(2,0,2)$ $(1,1,1)_6$ model with calibration assessment criteria of MAE = 0.510, RMSE = 0.752, and R = 0.218 is the best model for one-month data from seasonal differencing series. In addition to identifying and introducing the best time series model related to the six-month drought index data (SARIMA $(3,0,5)$ $(1,1,1)_6$ seasonal model with assessment criteria of MAE = 0.430, RMSE = 0.588, and R = 0.812), the results highlight the increased prediction accuracy of the six-month time series model by 4 times the correlation coefficient in the calibration section and 8 times that in the validation section, respectively, relative to the one-month state. After modeling and comparing the results of the drought index between the selected model and the reality of the event, the severity and duration of the drought were also examined, and the results indicated a high agreement. Finally by applying

the best six-month drought index model, a predicted series of the SPI drought index for the next 24 months is created.

Keywords: differencing, time series, drought index, forecasting, standard precipitation

INTRODUCTION

Drought, as a natural disaster, causes terrible damage to natural ecosystems and human life and is considered as a climatic anomaly. Furthermore, drought is one of the most destructive climatic phenomena, which can occur in almost all climatic regimes. Among various definitions of drought, a more recognized and logical definition is that drought can be caused by a period of severe scarcity of water resources with respect to normal conditions corresponding to the place and time or a period of abnormal dry conditions that last long enough to create an imbalance in the hydrological condition. Regarding the involvement of factors such as rainfall, snow, runoff, evapotranspiration, and other indicators of water resources in the occurrence of drought, different indicators have been defined to monitor drought, each of which measures only one or several parameters involved in the occurrence of drought (Karamouz and Araghinejad, 2010). These indicators are generally expressed as a single number together with the raw data for designers and planners to make decision. Drought indicators show drought information in the region by summarizing drought information periodically (Hejazizadeh and Javizadeh, 2010). Some indicators of drought include the Percent of Normal Precipitation Index (PNPI), China-Z Standard Index (CZI), Deciles Index (DI), Rainfall Anomaly Index (RAI), and the Standard Precipitation Index (SPI). In recent years, a large body of research has been conducted on the relationship between the forecast of droughts in Iran and other parts of the world, aiming to obtain sufficient information about this natural disaster and develop effective and efficient steps to correctly manage and address this phenomenon (Karimi et al., 2019; Sobhani et al., 2019; Malik et al., 2020; Mehr et al., 2020; Sadeghian et al., 2020; Xu et al., 2020). In this regard, modeling and forecasting drought index time series are of great importance. By using rainfall data, Niknam et al. (2013) studied 19 climatic indices and previous values of the SPI and employed a fuzzy neural model to predict autumn drought in Zahedan city with different time delays. The results indicated that each input variable had certain ability to predict autumn drought at different time delays. Bahrami et al. (2019) studied the seasonal Standardized Precipitation Index (SPI) drought index and time series models to predict seasonal drought using climate data of 38 Iranian synoptic stations. Cryer and Chan (2008) intend to discover a suitable ARIMA model using dust storm data from northern China from March 1954 to April 2002. Poornima and Pushpalatha, (2019) used long short-term memory in recurrent neural network to predict the drought indices which handle the real-time nonlinear data well and good that can help authorities better prepare and mitigate natural disasters.

Negaresh and Aramesh (2012) predicted drought of Khash city by applying climatic elements of rainfall, relative humidity, temperature, and climatic indicators affecting drought in the region, as well as considering neural and regression network models for three periods, namely, 1 month, 3 months, and 1 year. Overall, 3-month drought prediction with the neural network (after diffusion) model showed the best performance. The results also showed that climatic indicators failed to have any effect on improving the performance of models in monthly forecast of drought. By analyzing rainfall statistics of Liqvan station and applying methods such as artificial neural network, adaptive neuro-fuzzy inference system (ANFIS) modeling without clustering (C-mean), and clustering-based ANFIS, Komasi et al. (2013) predicted drought in the Liqvan Chay catchment and introduced the clustering-based ANFIS model as the best model. Barua et al. (2012) simulated drought in the Yarra catchment in Victoria, Australia, by using the nonlinear aggregated drought index (NADI), statistical models (ARIMA), and artificial neural network (RMSNN/DMSNN). The results revealed that neural network models performed better than ARIMA models. By using rainfall statistics of Ajabshir station (southeast of East Azerbaijan), Shirmohammadi et al. (2013) utilized ANN and ANFIS models and applied wavelet transform in developing hybrid models of wavelet–ANN and wavelet–ANFIS, aiming to evaluate these models in predicting drought. The results showed that the use of wavelet transform in input data processing improved the performance of models and the wavelet–ANFIS model had the best performance compared to other models. Jalili et al. (2013) computed SPI time series by addressing monthly rainfall and temperature statistics in 701 selected stations in Iran. Then, they predicted drought using three drought indices, namely, the normalized difference vegetation index (NDVI), vegetation condition index (VCI), and temperature condition index (TCI) with neural network models (multilayer perceptron (MLP), radial-basis function (RBF), and support vector machine (SVM)). The output of these models was the SPI. Evaluating these models indicated a better performance of the MLP model with TCI input. By utilizing rainfall data of 39 synoptic stations located in the northwest of the country, Montaseri et al. (2016) determined the time series of drought and wet seasons based on the Standardized Precipitation Index (SPI) and rainfall anomaly index (RAI). Then, they examined the trend of changes in drought and wet periods using a non-parametric Mann–Kendall trend test and eliminating the significant effect of all autocorrelation coefficients with different delays. The results showed that both SPI and RAI drought indices could be used solely to determine the trend of changes in drought and wet periods, due to the high correlation between the two drought indices in assessing and determining the variation trend of drought and wet seasons. Sadeghian et al. (2018) presented appropriate models to predict drought in Semnan city, Iran, using time series, ANFIS, and artificial neural networks (MLP and RBF). The results showed that, among these models, the ANFIS model showed appropriate performance at each stage of training and testing. Vaziri et al. (2018) used the 40-year daily discharge data of the Tajan River in Iran to determine the best

hydrological drought assessment index. They selected the best statistical distribution of both drought duration and severity variables according to goodness of fitting tests and five functions fitted to the data. The results showed that the Galambus function was selected as the best copula function. Malik and Kumar (2020) used heuristic approaches including the co-active neuro-fuzzy inference system (CANFIS), multiple linear regression (MLR), and multilayer perceptron neural network (MLPNN) for prediction of meteorological drought based on the Effective Drought Index (EDI) in Uttarakhand State, India. The results of their study showed that the CANFIS and MLPNN models outperformed the MLR models at study stations. Malik et al. (2021a) hybridized the SVR (support vector regression) model with two different optimization algorithms, namely, Particle Swarm Optimization (PSO) and Harris Hawks Optimization (HHO), for prediction of the Effective Drought Index (EDI) at different locations of India. The results indicate that the SVR–HHO model outperformed the SVR–PSO model in predicting the EDI. Malik et al. (2021b) studied the capability of support vector regression (SVR) integrated with two meta-heuristic algorithms, i.e., Grey Wolf Optimizer (GWO) and Spotted Hyena Optimizer (SHO), in predicting the EDI (Effective Drought Index). For this objective, the two hybrid SVR–GWO and SVR–SHO models were constructed and the EDI was computed in the study regions by using monthly rainfall data. A comparison of results demonstrates that the hybrid SVR–GWO model outperformed the SVR–SHO model for all study stations.

In previous research, mainly the comparison of intelligent methods in forecasting the drought index has been carried out. However, in this study, the improvement of the time series of the SPI drought index under the influence of differentiation operations is studied. Also, in some previous research studies, various indicators were used for drought index prediction due to the nature of some intelligent methods, while in this research, drought has been studied only by using the precipitation parameter in the SPI drought index. As mentioned, drought prediction with different intelligent methods has been the interest of many researchers, among which the use of time series has been very useful due to its capabilities. Time series forecasting first analyses time series data using statistics and in the next step, performs modeling to predict and inform strategic decisions. The main aim of this research is to improve the forecasting accuracy of SPI monthly series taking advantage of the differencing property for the improvement of stationarity and prediction results. For this purpose, seasonal, non-seasonal, and one-time combined differencing are conducted on one- and six-month SPI data related to Semnan city in a 48-year (1973–2020) period. Finally, by comparing the forecast accuracy of different models, the best model is selected to forecast drought in the next 24 months.

MATERIALS AND METHODS

Data and Study Area

Semnan city, the capital of Semnan Province and Semnan County, is one of the cities of Iran, which is located in the south of the Alborz mountain range and the north of the Kavir plain on Tehran-to-Khorasan road. This city is located at 216 km from Tehran between Damghan and Garmsar cities at $53°\ 23'$ east longitude and $35°\ 34'$ north latitude, with an average altitude of 1,130 m above sea level. The climate of this city is hot in summer and cold in winter. The rainfall of this city is mostly in the cold seasons of the year, and its average annual rainfall is 140 mm. The average annual temperature is 17.01°C, while the maximum, absolute temperature is 43.5°C and the absolute minimum is −8.4°C. The synoptic meteorological station of Semnan city was established in 1965. This station is located at $53°\ 23'$ east longitude and $35°\ 34'$ north latitude, with an altitude of 1,130.8 m above sea level. The climatic identities and statistical yearbooks of the province are used to derive statistical information of the station. **Figure 1** illustrates the location of the meteorological station in Semnan city. Given the geographical location and the completeness of the measured information, data related to precipitation in Semnan city were used, which are taken from rainfall statistics from 1973 to 2020 and recorded in the synoptic meteorological station of Semnan city. Statistical data of annual rainfall are given in **Table 1**.

Standardized Precipitation Index

To study meteorological drought, various indicators have been developed. One of the most famous indicators is the Standardized Precipitation Index (SPI), which was introduced in 1993 by McKee et al. from the Colorado Climate Center, regarding different effects of rainfall shortage on groundwater, reserves, and surface water resources, soil moisture, and canal flow. This index is obtained based on the difference of precipitation (P) from the average for a specific time scale ($\bar{P}$) and then dividing it by the standard deviation (Sd) (SPI $= \frac{P-\bar{P}}{Sd}$). Indeed, precipitation is the only effective factor in calculating the Standardized Precipitation Index.

In calculating this index, first the appropriate statistical distribution should be fitted to long-term precipitation data and then the cumulative distribution function should be converted to the normal distribution using equal probabilities. Experience has shown that the precipitation probability distribution often follows the gamma probability distribution. The density function of the gamma distribution probability is as follows:

$$f(x) = \frac{1}{\beta^{\alpha}\Gamma(\alpha)} x^{\alpha-1} e^{-\frac{x}{\beta}}, \tag{1}$$

where $\alpha > 0$ is the shape parameter, $\beta > 0$ is the scale parameter, $x > 0$ is the amount of precipitation, and $\Gamma(\alpha)$ is the gamma function as follows:

$$\Gamma(\alpha) = \int_{0}^{\infty} y^{\alpha-1} e^{-y} dy. \tag{2}$$
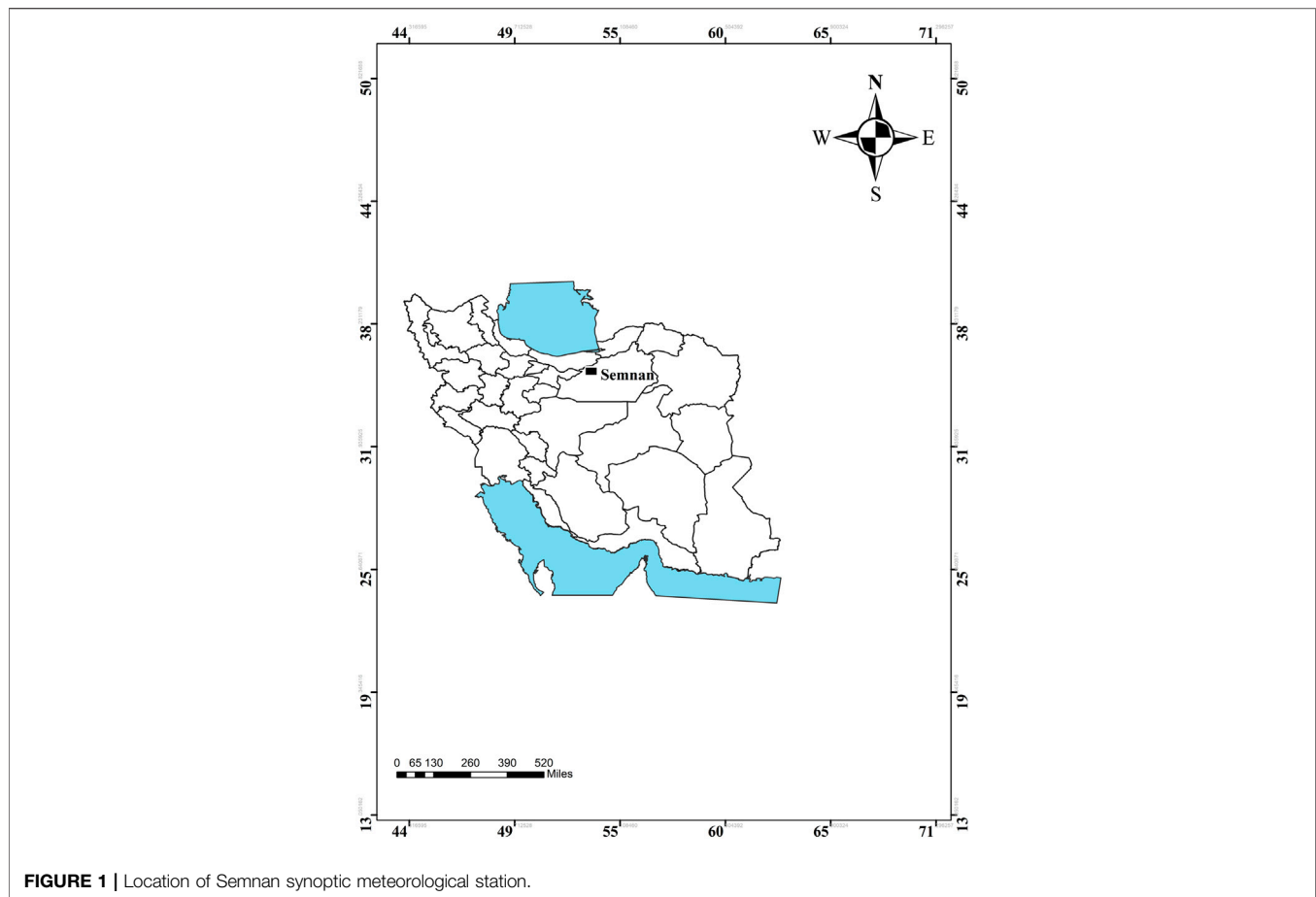
To fit the distribution parameters, α and β are estimated from the sample data:

$$\alpha = \frac{1}{4A}\left[1 + \sqrt{1 + \frac{4A}{3}}\right], \tag{3}$$

$$\beta = \frac{\bar{x}}{\alpha}, \tag{4}$$

where $\bar{x}$ is the mean precipitation and A is given by

FIGURE 1 | Location of Semnan synoptic meteorological station.

TABLE 1 | Statistical data of annual rainfall time series (1973–2020).

Skewness	Std. dev. (mm)	Minimum (mm)	Maximum (mm)	Mean (mm)
−0.01	42.94	60	222.5	138.77

$$A = \ln\left(\bar{x}\right) - \frac{\sum \ln(x)}{N}. \tag{5}$$

For a given month and time scale, the cumulative probability $G(x)$ of an observed amount of precipitation is given by

$$G(x) = \int_0^\infty f(x)dx = \frac{1}{\beta^\alpha \Gamma(\alpha)} \int_0^\infty x^{\alpha-1} e^{-\frac{x}{\beta}} dx. \tag{6}$$

Since the gamma function is not defined for $x = 0$ and the rainfall data always contain a large number of observations with zero rainfall, the cumulative probability of rainfall is calculated as follows:

$$H(x) = q + (1-q)G(x), \tag{7}$$

where q is the probability of zero rainfall in the data series, which is obtained by dividing the number of zero data by the total number of data. By calculating the cumulative probability of rainfall and using **Equations 8–11**, a normal distribution (Z) with a mean of zero and a standard deviation of one will be obtained.

$$Z = SPI = -\left[t - \frac{C_0 + C_1 t + C_2 t}{1 + d_1 t + d_2 t^2 + d_3 t^3}\right] 0 < H(x) \le 0.5, \tag{8}$$

$$Z = SPI = +\left[t - \frac{C_0 + C_1 t + C_2 t}{1 + d_1 t + d_2 t^2 + d_3 t^3}\right] 0.5 < H(x) < 1, \tag{9}$$

$$t = \sqrt{\ln\left(\frac{1}{H(x)^2}\right)}, 0 < H(x) \le 0.5, \tag{10}$$

$$t = \sqrt{\ln\left(\frac{1}{(1 - H(x))^2}\right)}, 0.5 < H(x) \le 1, \tag{11}$$

where C_0, C_1, C_2, d_1, d_2, and d_3 have constant coefficients of $C_0 = 2.5165$, $C_1 = 0.8029$, $C_2 = 0.0103$, $d_1 = 1.4328$, $d_2 = 0.1893$, and $d_3 = 0.0013$, respectively. Thus, the normalized SPI is converted to a normal Z, which reflects the amount of deviations above or below the mean. This index can be computed in short-term (1, 3, 6, and 9 months) and long-term (12, 24, 48, and 72 months) time scales. Drought index with different time scales has been used in various articles and research studies (Hosseini-Moghari and Araghinejad,

TABLE 2 | Classification of Standardized Precipitation Index assessment.

Drought situation	SPI
Extremely severe drought	< -2
Severe drought	−1.99–1.5
Moderate drought	−1.49–-1.0
Weak drought	−0.99–1.0
Normal	0
Weak wet year	0–0.99
Moderate wet year	1.0–1.49
Intense wet year	1.5–1.99
Extremely intense wet year	2 >

2015; Tan et al., 2015; Lee et al., 2017; Spinoni et al., 2017; Brito et al., 2018; Pramudya and Onishi, 2018; Diani et al., 2019; Mahmoudi et al., 2019). After having extracted rainfall data in different monthly or annual scales, a data homogeneity test is carried out and a time series is formed in the mentioned scales. Then, the cumulative probability of cumulative precipitation values is computed at each time scale using the gamma distribution. These values are converted to a normal standard random variable with a zero mean and a variance of one, which is the SPI value. **Table 2** presents different classes of drought in this index.

To determine the onset, end, and severity of drought from the SPI drought index according to the classifications presented in **Table 2**, SPI less than −1 indicates the beginning of a drought, which continues as long as this index is less than −1. On the other hand, SPI greater than 1 represents the beginning of a wet year period. The advantages of SPI include ease of computation, multipurposity to monitor drought conditions from meteorological and hydrological points of view, normal distribution, flexibility to different time scales, independence from soil moisture, and the possibility of use in all months of a year (Hejazizadeh and Javizadeh, 2010). This index has been used in several studies (Sobral et al., 2018; Tirivarombo et al., 2018; Marini et al., 2019; Wang et al., 2019; Zhang et al., 2019; Azimi and Moghaddam, 2020; Bhunia et al., 2020; Bong and Richard, 2020; Li et al., 2020; Won et al., 2020). The present study seeks to first compute the monthly drought index by using the abovementioned method for 576 steps, among which 460 initial data, which are equivalent to 80% of the data, are used for calibration and 116 final data are used to validate the time series model. **Figure 2** shows the time series diagram of the SPI drought index (one month) in Semnan.

Generally, it is possible to use a moving average for determining the drought index and selecting wet and drought periods such that the correct selection of the time base allows specifying wet and drought periods better. Hence, in addition to raw statistics of SPI

data, this study evaluates SPI statistics computed from 6-month rainfall data to predict the time series of the drought index. **Figure 3** provides the 6-month SPI time series discussed in this research. The six-month time scale for long-term forecasting of the drought is selected based on the fact that rainfall occurs in Semnan in cold seasons similar to most parts of the country, thus addressing the ombrothermic diagram of Semnan synoptic station (**Figure 4**).

Time Series Stationarity

If the mean, variance, and covariance are constant in a time series over certain periods (**Equations 12–15**), the time series is static. On the other hand, the time series will be strictly static if the joint distribution of $x(t_1)$ to $x(t_n)$ is similar to the joint distribution of $x(t_1 + h)$ to $x(t_n + h)$ for time points of t_1 to t_k at any time delay h [8]. In other words, the basic concept of stationarity is that the probabilistic rules governing the process do not change over time and, therefore, the process remains in statistical equilibrium (Johnson et al., 1977).

$$E\left(|x(t)|^2\right) < \infty, t \in Z \tag{12}$$

$$E(x(t)) = m_1, t \in Z \tag{13}$$

$$Var(x(t)) = m_2, t \in Z \tag{14}$$

$$\gamma_s(r, s) = \gamma_s(r + t, s + t), \{r, s, t\} \in Z \tag{15}$$

where x(t) represents time series, E and Var indicate the mathematical expectation and variance functions, γ_s shows the time series autocovariance function, and m_1 and m_2 are constant numbers.

The existence of a trend in data is one of the main causes of stationarity. Most climatic and hydrological parameters are seasonal, and the seasonal fluctuations complicate the trend. For this purpose, the seasonal Mann–Kendall test (**Equations 16–20**) was used to determine the trend in the data.

$$S' = \sum_{j=1}^{P} S_j \tag{16}$$

where P demonstrates the total number of seasons and Kendall statistics is related to season j $(j = 1, 2, \ldots, p)$ and computed according to

$$S_j = \sum_{i=1}^{n_j} \sum_{k=i+1}^{n_j - 1} sgn(x(i) - x(k)) \tag{17}$$

In the absence of sequential correlations in data, the variance is obtained from **Eq. 18**. If there is a sequential correlation in the time series data, the variance can be computed from **Eq. 19**:
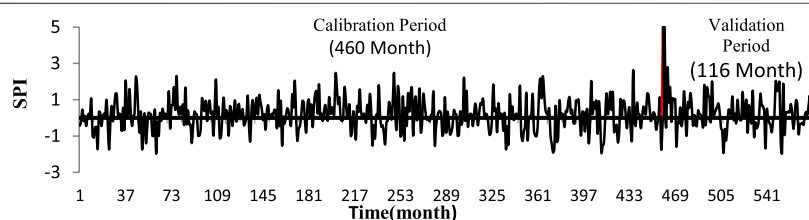
FIGURE 2 | Time series of one-month SPI drought index in Semnan.
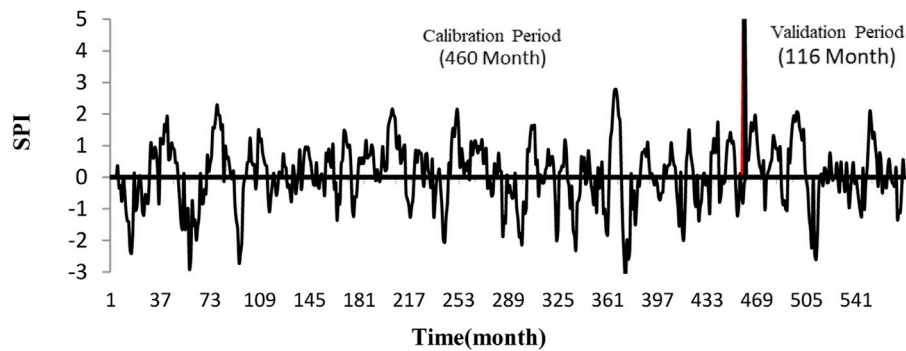
FIGURE 3 | Semnan 6-month drought index time series.
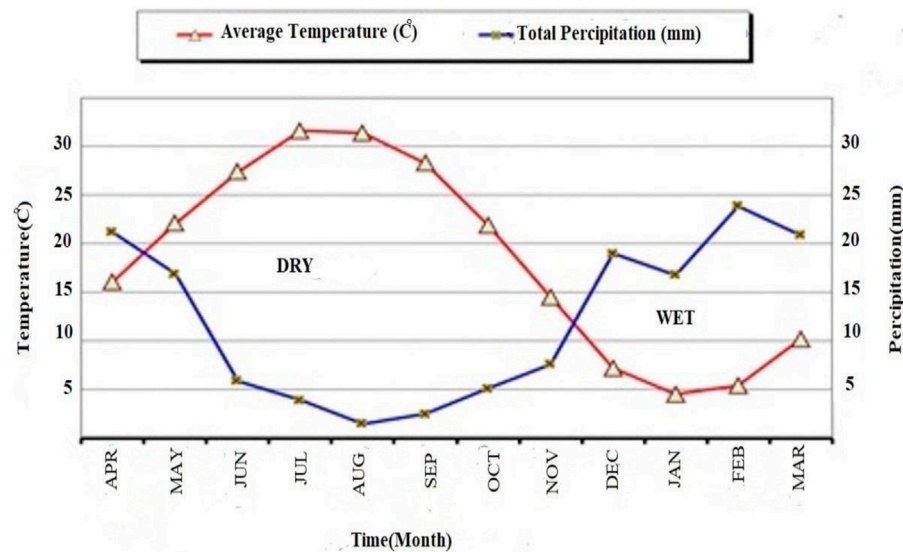
FIGURE 4 | Ombrothermic curve of Semnan synoptic station (during the statistical period).

$$\sigma_{S'}^2 = \sum_{j=1}^{P} Var(S_j) \tag{18}$$

$$\sigma_{S'}^2 = \sum_{j=1}^{P} Var(S_j) + \sum_{g=1}^{P-1} \sum_{h=g+1}^{P} \sigma_{gh} \tag{19}$$

where σ_{gh} shows the covariance between Kendall statistics in seasons g and h. With the assumption of data independence, it can be assumed that $cov(S_g, S_h) = 0$. Finally, a statistic named Z' is obtained from the following relationships:

$$Z' = \begin{cases} \dfrac{S' - 1}{\sigma_{S'}} \\ 0, S' = 0 \\ \dfrac{S' + 1}{\sigma_{S'}} \end{cases} \tag{20}$$

If the probability value Z computed according to **Eq. 20** is less than 5%, it indicates the existence of a trend in the time series.

Since the time series stationarity is a fundamental assumption in modeling and predicting the stationarity, it is possible to use the differencing approach to make series static as much as possible. In this research, an augmented Dickey–Fuller (ADF) test is used to determine how much the mentioned series become static after non-seasonal, seasonal, and combined differencing. This test (**Equations 21–24**) acts based on the presence or absence of a single root to specify the stationarity of the time series by examining the absence of a single root.

$$\Delta x(t) = \alpha + \beta_1 t + \beta_2 t^2 + \gamma x(t-1) \pm + \phi_1 \Delta x(t-1) + \dots$$
$$+ \phi_{p-1} \Delta x(t-p+1) + \varepsilon(t) \tag{21}$$

$$\tau = \frac{\hat{\gamma}}{\sigma_{\hat{\gamma}}} \tag{22}$$

$$H_0: \gamma = 0 \tag{23}$$

$$H_1: \gamma < 0 \tag{24}$$

where Δ represents the first-order differential operator and α, β_1, and β_2 indicate a constant value and coefficients of the linear and

quadratic trends, respectively. Furthermore, φ_i is the i-order autocorrelation coefficient, p is the maximum self-correlation, τ is the augmented Dickey–Fuller test statistic, γ is the estimated coefficient or root, $\sigma_{\hat{y}}$ is the estimated standard error, H_0 is the null hypothesis indicating the existence of a single root, and H_0 is the alternative hypothesis that implies the lack of existence of a single root.

After computing the parameter τ, if this statistic is less than the critical value in the Dickey–Fuller distribution, the null hypothesis is rejected, meaning that there is no single root and the series is static. Each of the values α, β_1, and β_2 can be considered as zero, according to which different states such as without constant and trend state, only constant, constant and linear trend, and the quadratic trend will be tested.

Since the augmented Dickey–Fuller test fails to consider the effect of the periodic component on instationarity of the series, it is necessary to use other tests for seasonal series. In this way, drawing a correlogram and examining it intuitively is one of the methods to retest the stationarity. This diagram shows the values of autocorrelation function (ACF) for different time steps. If the time series is static, this diagram will damp to zero exponentially or oscillating [9]. In this diagram, the value of data autocorrelation coefficient (ρ) will be plotted for different steps. The value of autocorrelation coefficient for step h is obtained from

$$\rho(h) = \frac{\sum_{t=h}^{n}\left(x(t) - \bar{x}\right)\left(x(t-h) - \bar{x}\right)}{\sum_{t=h}^{n}\left(x(t) - \bar{x}\right)^2} \quad h = 1, 2, ,, ..., n/4. \quad (25)$$

Time Series Models

Given the existence of different time series models based on Box–Jenkins theories, this research utilizes ARIMA models and their general form, multiplicative seasonal ARIMA, to predict the drought index. The multiplicative seasonal ARIMA model is presented with the following relationships (Salas et al., 1980):

$$\text{SARIMA}(p, d, q)(P, D, Q): \Phi(B^\omega)\varphi(B)(1 - B^\omega)^D(1 - B)^d x(t)$$
$$= \Theta(B^\omega)\theta(B)\varepsilon(t)$$
$$(26)$$

$$\Phi(B^\omega) = \left(1 - \Phi_1 B^\omega - \Phi_2 B^{2\omega} - ... - \Phi_P B^{P\omega}\right) \quad (27)$$

$$\phi(B) = \left(1 - \phi_1 B - \phi_2 B^2 - ... - \phi_P B^P\right) \quad (28)$$

$$\Theta(B^\omega) = \left(1 - \Theta_1 B^\omega - \Theta_2 B^{2\omega} - ... - \Theta_Q B^{Q\omega}\right) \quad (29)$$

$$\theta(B) = \left(1 - \theta_1 B - \theta_2 B^2 - ... - \theta_q B^q\right) \quad (30)$$

where $x(t)$: drought index time series, $\varepsilon(t)$: residual series, p: non-seasonal autocorrelation parameter order, q: non-seasonal moving average parameter order, P: seasonal autocorrelation parameter order, Q: seasonal moving average parameter order, ω: period, φ: non-seasonal autocorrelation parameter, θ: seasonal moving average parameter, Φ: seasonal autocorrelation parameter, Θ: seasonal moving average parameter, B: differential operator, $(1 - B^\omega)^D$: D-th seasonal differencing by step ω, and $(1 - B)^d$: d-th non-seasonal differencing operation.

The maximum order of parameters of the mentioned models in the relations (26) to (30) (p, q, P, Q) can be identified from the ACF diagram. If the orders required for parameters of each model are $p = \{0, 1, ..., l\}$, $q = \{0, 1, ..., m\}$, $P = \{0, 1, ..., n\}$, and $Q = \{0, 1, ..., o\}$, then the number of required models (NOM) is obtained according to the probability rule and based on

$$\text{NOM}_{\text{SARIMA}} = (l + 1)(m + 1)(n + 1)(o + 1) \quad (31)$$

Models Assessment Criteria

To achieve the most accurate model, valid assessment criteria are fitted on the desired time series. In this study, criteria of correlation coefficient (R), root mean square error (RMSE), and mean absolute error (MAE) are used to evaluate and analyze the model results. These criteria are shown as follows:

$$R = \frac{\sum_{i=1}^{n}\left(x_i^o - \bar{x}^o\right)\left(x_i^p - \bar{x}^p\right)}{\sqrt{\sum_{i=1}^{n}\left(x_i^o - \bar{x}^o\right)^2 \sum_{i=1}^{n}\left(x_i^p - \bar{x}^p\right)^2}} \quad (32)$$

$$\text{RMSE} = \sqrt{\frac{1}{n}\sum_{i=1}^{n}\left(x_i^p - x_i^0\right)^2} \quad (33)$$

$$\text{MAE} = \frac{1}{n}\sum_{i=1}^{n}\left|\left(x_i^0 - x_i^p\right)\right| \quad (34)$$

where x_i^o represents the observational values, x_i^p indicates the predicted values, $\bar{x}^o$ shows the mean observational values, and $\bar{x}^p$ is the mean predicted values. Based on the results, it can be said that the closer the RMSE and MAE values are to zero, the better the performance of the model will be. The value of the correlation coefficient, which varies between -1 and 1, is close to zero in a superior case.

After reviewing assessment criteria and selecting the best model, the suitability of residues from the results is examined and if approved, the model is selected. Finally, using the selected model, the drought index parameter can be predicted in future.

Evaluating the Independence of Residuals

If a time series model is correctly specified, then the residues obtained from the model fitting should approximately have the characteristics of independent normal random variables with a zero mean and a constant variance. In this study, the rest of the selected fitted model is examined and analyzed to ensure its accuracy. To this aim, the diagrams of the normal probability of residuals, residuals versus fitted values, residuals over time, residual histograms, and residual autocorrelation and partial autocorrelation functions are plotted and interpreted. If the selected model is identified correctly, it has signs among the abovementioned diagrams. If the residuals are along a straight line in the normal probability diagram, it indicates the normality of residuals. If the residuals are around the zero horizontal plane with a trendless rectangular scattering in the residual over time diagram, have no structure in the residuals versus fits and residual versus order plots, and have no special trend in ACF and PACF diagrams and do not exceed its permissible limits, it is possible to accept the constantness of variance and randomness and independency of the residuals, respectively.

TABLE 3 | Results of evaluating time series with the seasonal Mann–Kendall test.

Index type	Number of observations	Minimum	Mean	Maximum	Standard deviation	τ	S′	p value
One-month SPI	576	−2.450	0.161	3.0	0.866	0.017	464	0.547
Six-month SPI	571	−3.310	0.069	2.780	1.0	0.008	207	0.787

TABLE 4 | Results of the augmented Dickey–Fuller test for drought index time series.

Test type	Critical limit	d = 0, D = 0	d = 1, D = 0	d = 0, D = 1	d = 1, D = 1
Results of the augmented Dickey–Fuller test for one-month SPI series	−0.913	Stationary −8.967	Stationary −12.957	Stationary −10.003	Stationary −14.780
Results of the augmented Dickey–Fuller test for six-month SPI series	−0.893	Stationary −7.509	Stationary −11.604	Stationary −9.049	Stationary −14.780
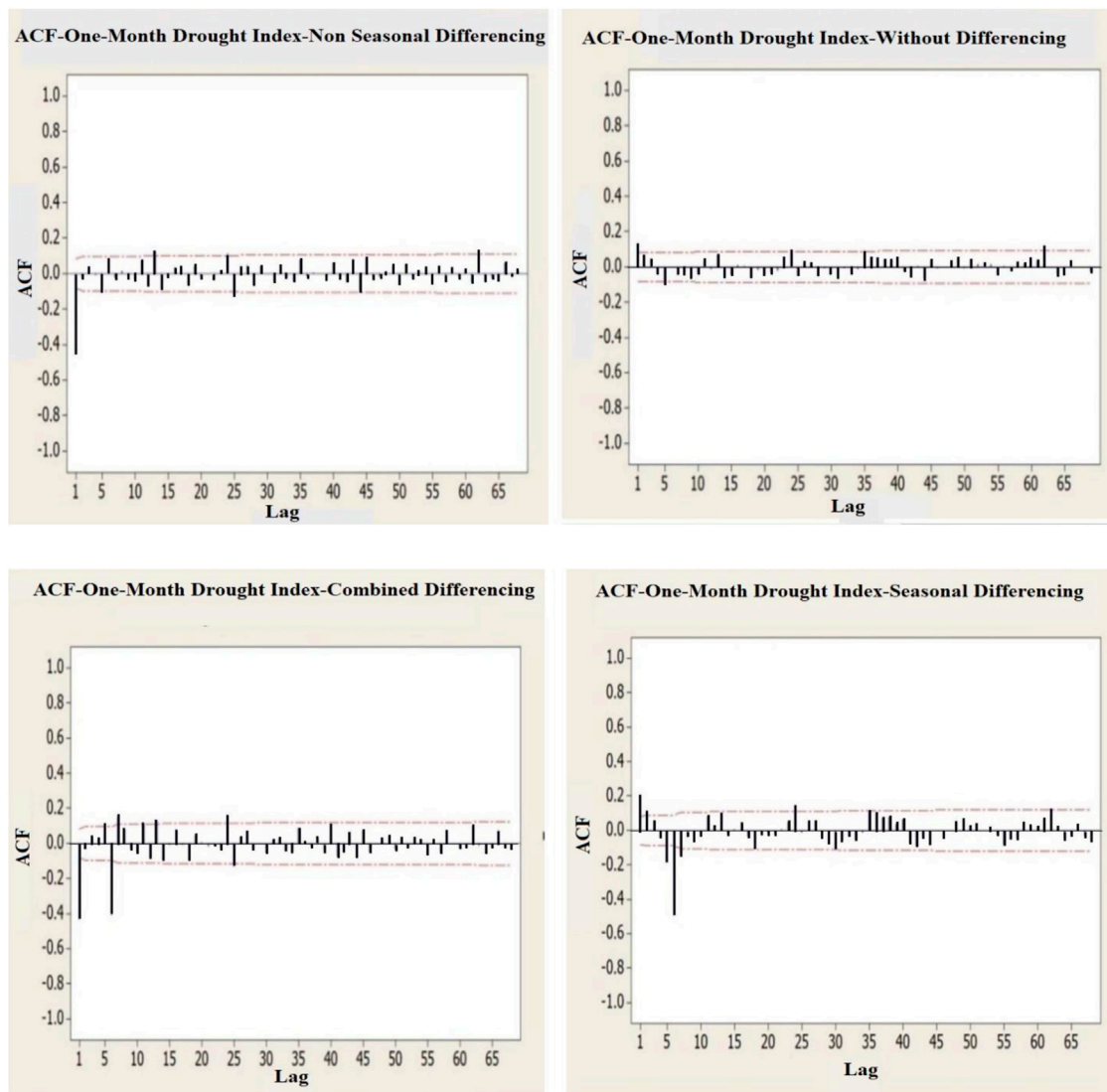
FIGURE 5 | Autocorrelation diagrams of different states of one-month drought index time series.
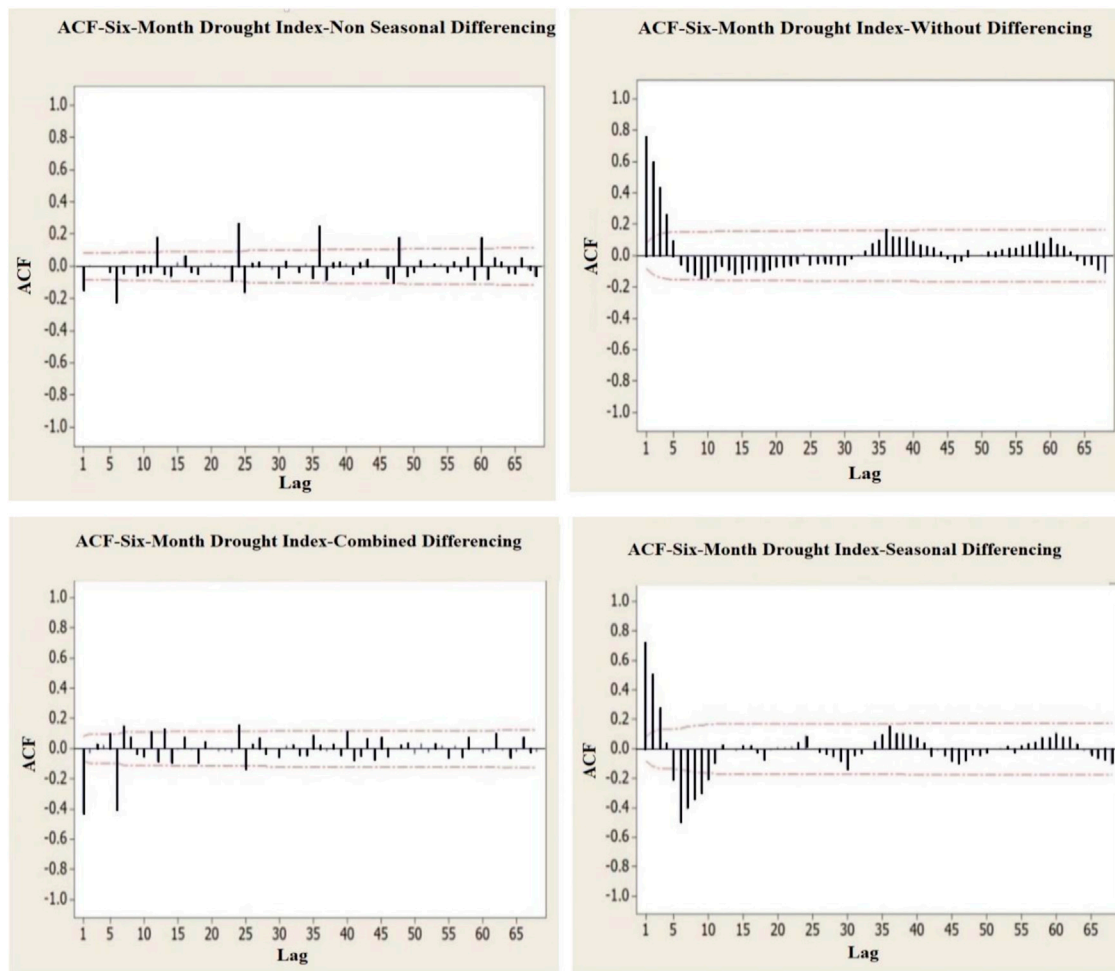
FIGURE 6 | Autocorrelation diagrams of different states of six-month drought index time series.

TABLE 5 | Orders of parameter and number of models required for the six-month drought index.

Series type	p	q	P	Q	Number of models
Without differencing	4	4	0	0	25
Non-seasonal differencing	1	1	1	1	16
Seasonal differencing	5	5	1	1	144
Combined differencing	1	1	1	1	16

In addition to graph methods, the Portmanteau test is used to examine the suitability of the model. This test uses residual autocorrelation to test the null hypothesis (H_0), i.e., the lack of any correlation between model residues, using test statistics Q. If the value of statistic Q is greater than the corresponding value of the chi-square probability table (χ^2), the hypothesis (H_0), which is sometimes called the model adequacy hypothesis, is rejected. It should be noted that the probabilistic values corresponding to this test (p value) are evaluated for the

confidence level of 95% by assuming the independence of residuals.

RESULTS AND DISCUSSION

This research seeks to study and compute two time series, one related to SPI monthly drought index data and the other related to six-month data of the SPI parameter, along with different differencing time series.

The drought index has different time divisions, and for some reason, one-month and six-month drought indexes are mostly used in resources. The one-month SPI is a short-term drought index and can be a better indicator of monthly percipitation for a given region compared to other time steps. The 6-month SPI shows medium-term percipitation trends and can be used to represent percipitation in different seasons much more effectively. The resulting information may also be related to abnormal flows and water reservoir levels. Before modeling the drought index time series, time series stationarity is examined

Series type	p	q	P	Q	Number of models
Without differencing	1	1	0	0	4
Non-seasonal differencing	3	3	0	0	16
Seasonal differencing	2	2	1	1	36
Combined differencing	3	3	1	1	64

using the seasonal Kendall test whose results are shown in **Table 3**. According to coefficients obtained for each of the series, the seasonal Mann–Kendall test reveals that both time

series are static. Furthermore, different types of non-seasonal (d = 1), seasonal (D = 1), and combined (d = 1, D = 1) differencing are performed on both time series, resulting in forming new time series. The role of different differencing operations in the time series stationarity is determined by using the augmented Dickey–Fuller (ADF) test. Results of the augmented Dickey–Fuller test for drought index time series are provided in **Table 4**. According to the results, it is observed how differencing operation leads to better stationarity of time series. Consequently, combined differencing shows the highest degree of stationarity compared to other cases.

However, the Dickey–Fuller test sometimes presents a poor performance in determining the stationarity of seasonal series. Furthermore, no information is available on the exact seasonality
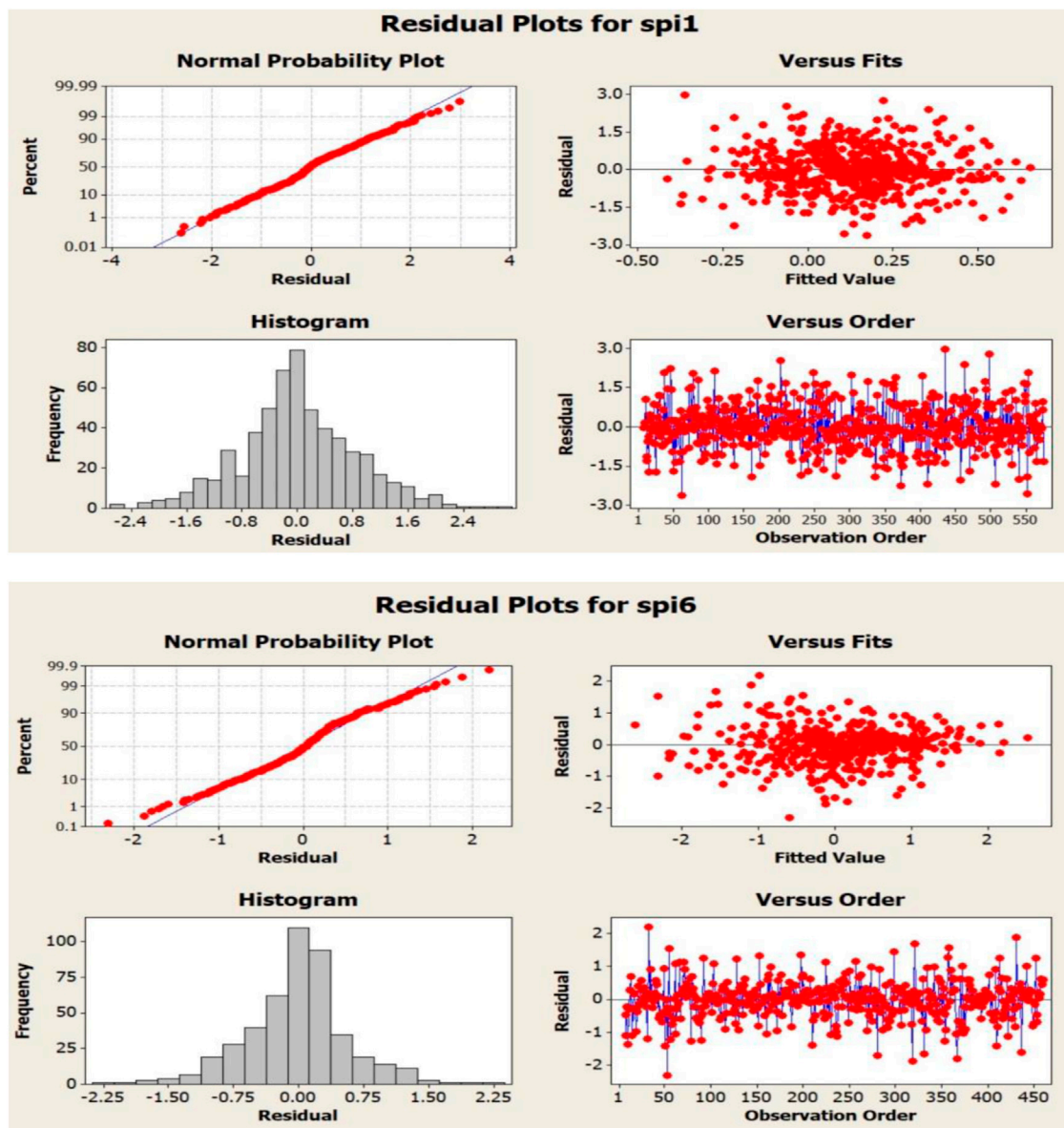
FIGURE 7 | Analysis diagrams of the residual of the selected model for one- and six-month drought index time series.

TABLE 7 | Results of evaluating the best models in differencing states for the six-month drought index.

Model	Calibration			Validation			Series type
	R	MAE	RMSE	R	MAE	RMSE	
ARMA (404)	0.79	0.48	0.62	0.30	0.70	0.92	Without differencing
ARIMA (110) (100)$_6$	0.77	0.49	0.66	0.24	1.13	1.36	Non-seasonal differencing
SARIMA (503) (111)$_6$	0.81	0.43	0.59	0.34	0.69	0.91	Seasonal differencing
SARIMA (111) (111)$_6$	0.80	0.44	0.60	0.28	0.75	0.95	Combined differencing

TABLE 8 | Results of evaluating the best models in differencing states for the one-month drought index.

Model	Calibration			Validation			Series type
	RMSE	MAE	R	RMSE	MAE	R	
ARMA (101)	0.76	0.52	0.17	0.84	0.61	0.05	Without differencing
ARIMA (111)	0.75	0.52	0.17	0.82	0.59	0.01	Non-seasonal differencing
SARIMA (202) (111)$_6$	0.75	0.51	0.22	0.82	0.59	0.04	Seasonal differencing
SARIMA (112) (111)$_6$	0.76	0.52	0.21	0.82	0.59	0.01	Combined differencing

TABLE 9 | Results of the Portmanteau test for the selected one- and six-month drought index models.

Model	Lag	12	24
SARIMA (202) (111)$_6$	Chi-square	8.3	25.2
SARIMA (202) (111)$_6$	p value	0.219	0.114
SARIMA (503) (111)$_6$	Chi-square	5	22.8
SARIMA (503) (111)$_6$	p value	0.081	0.064

of differenced data for the series studied in this research. Further validation is performed by drawing autocorrelation diagrams and the stationarity of different types of series without differencing and with non-seasonal, seasonal, and combined differencing is investigated with results as shown in **Figures 5**, **6**. As observed, none of the series is undamped and oscillating and has no periodicity, and consequently, all series approach zero after a few steps and are within the 95% confidence level, confirming the stationarity of the series.

By using correlogram diagrams (ACF and PACF diagrams), it is possible to determine the maximum number of parameters required for time series models, in addition to stationarity. This number, which is obtained based on steps with large values from this diagram, along with the number of models required to achieve the most accurate model is presented in **Tables 5**, **6**.

Another issue that can be deduced from **Figures 6**, **7** and **Tables 5**, **6** is the type of model suitable for modeling and forecasting. Therefore, by placing different orders of P, Q, p, and q, time series are modeled by different states and then predicted and evaluated in the validation period.

Tables 7, **8** report the most accurate models, along with the results of their assessment criteria, for both the calibration and validation periods for one- and six-month drought index time series. Accordingly, the seasonal SARIMA (202) (111)$_6$ model is introduced as the selected model of one-month drought index, while the seasonal SARIMA (503) (111)$_6$ model is chosen as the

selected model for the six-month drought index. Furthermore, the results reveal that the ratio of increasing the accuracy of forecasting the six-month drought index is highly significant compared to the one-month drought index. It is also worth mentioning that the comparison of drought index time series modeling in the study area with other artificial intelligence methods, such as the neural network or adaptive neuro-fuzzy inference system, has already been performed to show the superiority of the selected time series models in this field (Sadeghian et al., 2020).

Evaluating Model Adequacy

To ensure the accuracy of the selected model, residuals of the fitted model are analyzed. For this purpose, the Portmanteau test is conducted for each selected model, and then, various diagrams related to residuals are examined. **Table 9** provides the results of the Portmanteau test.

As observed, the p value for delays is greater than 0.05 even up to step 24, enabling us to accept the assumption that all autocorrelations are zero. Additionally, the graphs obtained from residuals of the models mentioned in **Figures 7**, **8** indicate the suitability and adequacy of the models. **Figure 7** shows the analysis diagrams of the residual of the selected model for one- and six-month drought index time series (SP1-1 and SPI-6). **Figure 8** shows the ACF and PACF diagrams of residual of the selected model for one- and six-month drought index time series.

Forecasting

After reviewing the different models and reaching the best selected model, the six-month model with the SARIMA format (3,0,5) (1,1,1) and the resulting values of the model along with the drought index values that occurred in reality were plotted. As shown in **Figure 9**, the results of
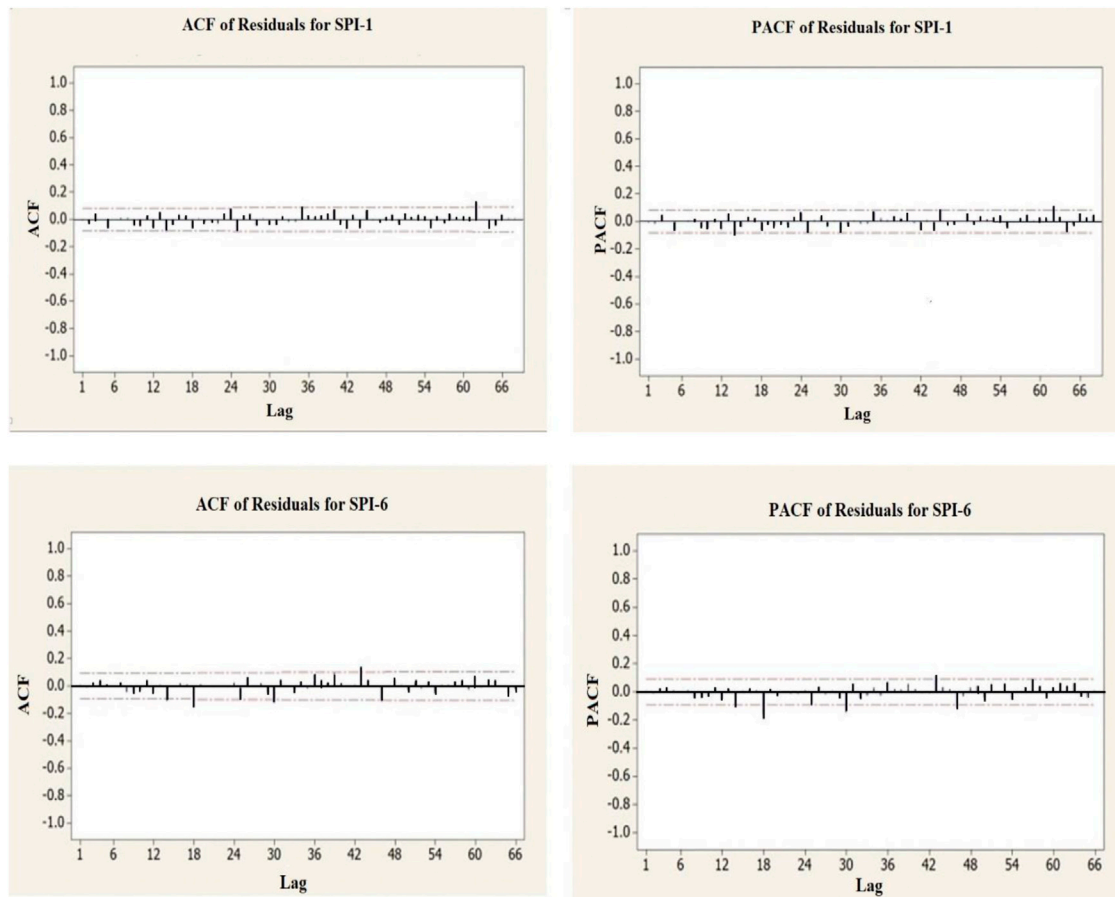
FIGURE 8 | ACF and PACF diagrams of residual of the selected model for one- and six-month drought index time series.

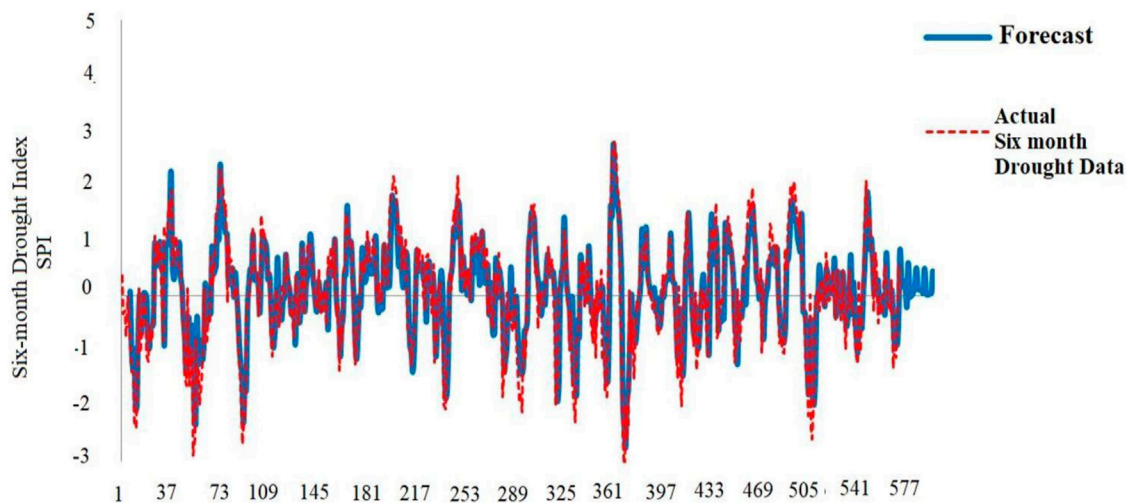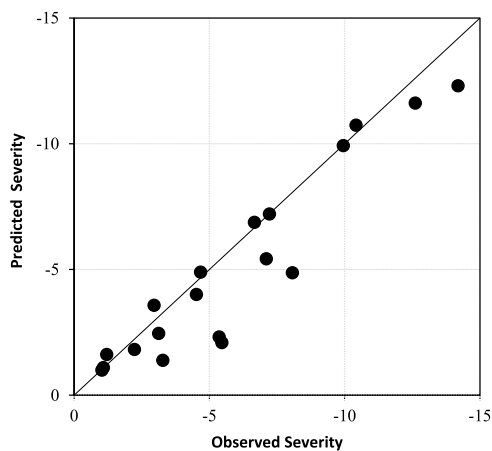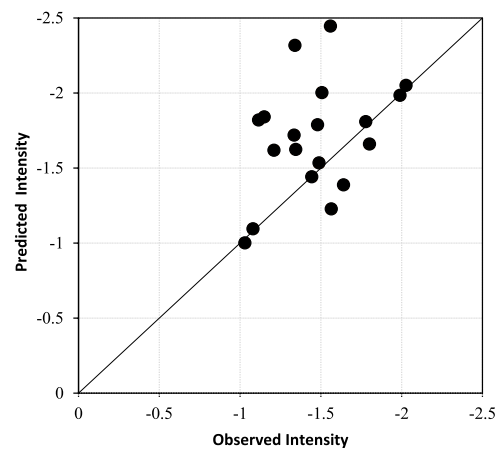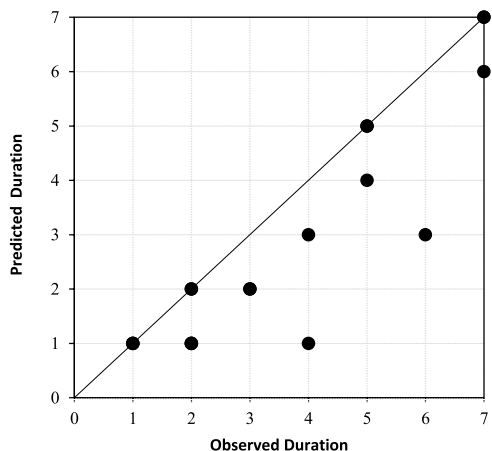**FIGURE 9 |** Diagram of the selected model for forecasting drought index data.

FIGURE 10 | Comparison between observed and predicted drought severity.

FIGURE 12 | Comparison between observed and predicted drought intensity.

FIGURE 11 | Comparison between observed and predicted drought duration.

the model are in good agreement with the real situation which the numerical indices of **Table 7** had previously emphasized.

By selecting the best proposed model, SARIMA (3,0,5) $(1,1,1)_6$, for the six-month drought index and addressing **Eqs 26–30**, the six-month drought index model is obtained according to

$$
\begin{aligned}
&\left(1 + 0.349B^6\right)\left(1 - 0.561B - 0.627B^2 - 0.305B^3 + 0.552B^4 \right.\\
&\left. + 0.026B^5\right)\left(1 - B^6\right)X(t) \\
&= \left(1 - 0.979B^6\right)\left(1 + 0.231B - 0.342B^2 - 0.607B^3\right)\varepsilon(t), \quad (35)
\end{aligned}
$$

where B represents the differential operator and $x(t)$ and $\varepsilon(t)$ are the drought index and residual series, respectively. In order to have a vision of the future, the selected model was used to evaluate the situation for the next 24 months. Applying **Eq. 35** to the

actual data of the six-month time series of the SPI drought index for 24 months creates a predicted series which is marked with a blue line in **Figure 9**.

Comparison Between Observed and Predicted Drought Characteristics

After modeling with the best proposed model and comparing the results of the drought index between the model and the observed data, the severity, duration, and intensity of the drought (SPI < −1) were also examined. Accordingly, the graphs in **Figures 10–12** show the comparison between severity, duration, and intensity of the SPI during droughts, respectively. As can be seen in these figures, there is a good agreement in the direction of the 45-degree axis between the points, which indicates the superiority of the proposed model.

CONCLUSION

Predicting hydrological variables, especially the drought index, has long been considered by many researchers, and various research studies have been conducted on this field, due to the importance and widespread use of the SPI in topics such as climate change and meteorology. The present study addresses the initial stationarity of drought index time series taken from rainfall statistics of Semnan meteorological station and then evaluates the effect of different non-seasonal, seasonal, and combined differencing on the time series stationarity, as well as the results of their selected models. For innovation in the research, we analyze the degree of increase in forecast accuracy and the effect of differencing operators on six-month drought index time series. The major findings can be summarized as follows. 1. Although both one- and six-month drought index time series are static, different differencing operations improve their static degree so that series with the combined differencing operator (non-seasonal and seasonal) provide the best

stationarity degree based on the results of the augmented Dickey–Fuller test. 2. Given the results of the ombrothermic curve and according to the precipitation conditions of the region, the seasonal period for modeling the drought index is considered 6 months. The best models from one- and six-month drought index time series are originated from seasonal differencing. Accordingly, SARIMA (2,0,2) $(1,1,1)_6$ and SARIMA (3,0,5) $(1,1,1)_6$ are the selected models for one- and six-month drought index time series, respectively. 3. The results indicate that the accuracy of models in calibration is significantly higher than that of validation for both selected series models resulting from seasonal differencing of one- and six-month drought index. Moreover, the six-month drought index has better modeling than the one-month drought index for both models. 4. For the selected time series model of one-month drought index SARIMA (2,0,2) (1,1,1), the results of RMSE, MAE, and R assessment criteria equal to 0.752, 0.510, and 0.218 in the calibration stage and 0.823, 0.589, and 0.039 in the validation stage, indicating poor performance of the time series in modeling and predicting the one-month drought index variable. 5. For the SARIMA (3,0,5) (1,1,1) model, the results of RMSE, MAE, and R equal to 0.58, 0.430, and 0.812 in the calibration stage and 910, 0.689, and 0.341 in the validation stage, respectively, highlighting a significant improvement (about 4 times increase in correlation coefficient in the calibration stage and 8 times in the

validation stage) compared to the one-month drought index. Also, the severity, duration, and intensity of the drought of the selected model and observed data were compared, and the results indicated a good agreement. The results of the present study have the potential to be used for similar regions in future research.

DATA AVAILABILITY STATEMENT

The original contributions presented in the study are included in the article/Supplementary Material, further inquiries can be directed to the corresponding authors.

AUTHOR CONTRIBUTIONS

• Conceptualization: SB, Y-WJ, AM, and K-WC. • Data curation: HK, SB, SF, MM, and SB. • Formal analysis: SF, SB, and HK. • Investigation: HK, SB, Y-WJ, AM, MM, K-WC, and SB. • Methodology: HK, SB, Y-WJ, SF, MM, SB, and SB. • Resources: HK, SF, MM, SB, and SB. • Software: SF, MM, SB, AM, and K-WC. • Supervision: SB and HK. • Validation: SB, HK, Y-WJ, SF, MM, K-WC, and SB. • Visualization: SB and HK. • Writing–original draft: HK, SF, MM, SB, and SB. • Writing–review and editing: HK, Y-WJ, SF, MM, SB, AM, and K-WC.

REFERENCES

Azimi, S., and Moghaddam, M. A. (2020). Modeling Short Term Rainfall Forecast Using Neural Networks, and Gaussian Process Classification Based on the SPI Drought Index. *Water Resour. Manage.* 34 (4), 1–37. doi:10.1007/s11269-020-02507-6

Bahrami, M., Bazrkar, S., and Zarei, A. R. (2019). Modeling, Prediction and Trend Assessment of Drought in Iran Using Standardized Precipitation index. *J. Water Clim. Change* 10 (1), 181–196. doi:10.2166/wcc.2018.174

Barua, S., Ng, A. W. M., and Perera, B. J. C. (2012). Artificial Neural Network-Based Drought Forecasting Using a Nonlinear Aggregated Drought Index. *J. Hydrol. Eng.* 17, 1408–1413. doi:10.1061/(asce)he.1943-5584.0000574

Bhunia, P., Das, P., and Maiti, R. (2020). Meteorological Drought Study through SPI in Three Drought Prone Districts of West Bengal, India. *Earth Syst. Environ.* 4 (1), 43–55. doi:10.1007/s41748-019-00137-6

Bong, C. H. J., and Richard, J. (2020). Drought and Climate Change Assessment Using Standardized Precipitation index (SPI) for Sarawak River Basin. *J. Water Clim. Change* 11 (4), 956–965. doi:10.2166/wcc.2019.036

Brito, S. S. B., Cunha, A. P. M. A., Cunningham, C. C., Alvalá, R. C., Marengo, J. A., and Carvalho, M. A. (2018). Frequency, Duration and Severity of Drought in the Semiarid Northeast Brazil Region. *Int. J. Climatol* 38 (2), 517–529. doi:10.1002/joc.5225

Cryer, J. D., and Chan, K. S. (2008). *Time Series Analysis with Applications in R*. Second Ed. NY: Springer.

Danandeh Mehr, A., Vaheddoost, B., and Mohammadi, B. (2020). ENN-SA: A Novel Neuro-Annealing Model for Multi-Station Drought Prediction. *Comput. Geosciences* 145, 104622. doi:10.1016/j.cageo.2020.104622

Diani, K., Kacimi, I., Zemzami, M., Tabyaoui, H., and Haghighi, A. T. (2019). Evaluation of Meteorological Drought Using the Standardized Precipitation Index (SPI) in the High Ziz River Basin, Morocco. *Limnol. Rev.* 19 (3), 125–135. doi:10.2478/limre-2019-0011

Hejazizadeh, Z., and Javizadeh, S. (2010). *Introduction to Drought and its Indices*. SMT Incorporated.

Hosseini-Moghari, S. M., and Araghinejad, S. (2015). Monthly and Seasonal Drought Forecasting Using Statistical Neural Networks. *Environ. Earth Sci.* 74 (1), 397–412. doi:10.1007/s12665-015-4047-x

Jalili, M., Gharibshah, J., Ghavami, S. M., Beheshtifar, M. R., and Farshi, R. (2013). Nationwide Prediction of Drought Conditions in Iran Based on Remote Sensing Data. *IEEE Trans. Comput.* 63 (1), 90–101. doi:10.1109/TC.2013.118

Johnson, D. E., Bhattacharyya, G. K., Johnson, R. A., and Bhattacharyya, G. (1977). *Statistical Concepts and Methods*. John Wiley & Sons Incorporated, 106.

Karamouz, M., and Araghinejad, S. (2010). *Advanced Hydrology*. Tehran, Iran: Industrial University of Amir Kabir Poly Technics.

Karimi, M., Melesse, A. M., Khosravi, K., Mamuye, M., and Zhang, J. (2019). "Analysis and Prediction of Meteorological Drought Using SPI index and ARIMA Model in the Karkheh River Basin, Iran," in *Extreme Hydrology and Climate Variability* (Karkheh River basin, Iran: Elsevier), 343–353. doi:10.1016/b978-0-12-815998-9.00026-9

Komasi, M., Alami, M. T., and Nourani, V. (2013). Drought Forecasting by SPI Index and ANFIS Model Using Fuzzy C-Mean Clustering. *J. Water Wastewater* 24 (4), 90–102. Available at http://www.wwjournal.ir/article_3196.html?lang=en.

Lee, S.-H., Yoo, S.-H., Choi, J.-Y., and Bae, S. (2017). Assessment of the Impact of Climate Change on Drought Characteristics in the Hwanghae Plain, North Korea Using Time Series SPI and SPEI: 1981-2100. *Water* 9 (8), 579. doi:10.3390/w9080579

Li, L., She, D., Zheng, H., Lin, P., and Yang, Z.-L. (2020). Elucidating Diverse Drought Characteristics from Two Meteorological Drought Indices (SPI and SPEI) in China. *J. Hydrometeorology* 21 (7), 1513–1530. doi:10.1175/jhm-d-19-0290.1

Mahmoudi, P., Rigi, A., and Kamak, M. M. (2019). Evaluating the Sensitivity of Precipitation-Based Drought Indices to Different Lengths of Record. *J. Hydrol.* 579, 124181. doi:10.1016/j.jhydrol.2019.124181

Malik, A., and Kumar, A. (2020). Meteorological Drought Prediction Using Heuristic Approaches Based on Effective Drought index: a Case Study in Uttarakhand. *Arab J. Geosci.* 13, 276. doi:10.1007/s12517-020-5239-6

Malik, A., Kumar, A., Salih, S. Q., Kim, S., Kim, N. W., Yaseen, Z. M., et al. (2020). Drought index Prediction Using Advanced Fuzzy Logic Model: Regional Case Study over Kumaon in India. *Plos one* 15 (5), e0233280. doi:10.1371/journal.pone.0233280

Malik, A., Tikhamarine, Y., Sammen, S. S., Abba, S. I., and Shahid, S. (2021a). Prediction of Meteorological Drought by Using Hybrid Support Vector Regression Optimized with HHO Versus PSO Algorithms. *Environ. Sci. Pollut. Res.* 28, 39139–39158. doi:10.1007/s11356-021-13445-0

Malik, A., Tikhamarine, Y., Souag-Gamane, D., Rai, P., Sammen, S. S., and Kisi, O. (2021b). Support Vector Regression Integrated with Novel Meta-Heuristic Algorithms for Meteorological Drought Prediction. *Meteorol. Atmos. Phys.* 133 (3), 891–909. doi:10.1007/s00703-021-00787-0

Marini, G., Fontana, N., and Mishra, A. K. (2019). Investigating Drought in Apulia Region, Italy Using SPI and RDI. *Theor. Appl. Climatol* 137 (1), 383–397. doi:10.1007/s00704-018-2604-4

Montaseri, M., Amiratee, B., and Khalili, K. (2016). Identification of Trend in Spatial and Temporal Dry and Wet Periods in Northwest of Iran Based on SPI and RAI Indices. *J. Water Soil* 30 (2), 655–671. Available at https://www.cabdirect.org/cabdirect/abstract/20173236578.

Negaresh, H., and Aramesh, M. (2012). Drought Forecasting in Khash City by Using Neural Network Model. *Arid Regions Geogr. Stud.* 2 (6), 33–50.

Niknam, H. H., Moghadam, M. A., and Khosravi, M. (2013). Drought Forecasting Using Adaptive Neuro-Fuzzy Inference Systems (ANFIS), Drought Time Series and Climate Indices for Next Coming Year, (Case Study: Zahedan). *Water and Wastewater* 2, 42–51. Available at http://www.wwjournal.ir/article_1642.html?lang=en.

Poornima, S., and Pushpalatha, M. (2019). Drought Prediction Based on SPI and SPEI with Varying Timescales Using LSTM Recurrent Neural Network. *Soft Comput.* 23 (18), 8399–8412. doi:10.1007/s00500-019-04120-1

Pramudya, Y., and Onishi, T. (2018). Assessment of the Standardized Precipitation Index (SPI) in Tegal City, Central Java, Indonesia. *IOP Conf. Ser. Earth Environ. Sci.* 129 (1), 012019. doi:10.1088/1755-1315/129/1/012019

Sadeghian, M., Karami, H., and Mousavi, S. F. (2020). Evaluating the Performance of Time-Series, Neural Network and Neuro-Fuzzy Models in Prediction of Meteorological Drought (Case Study: Semnan Synoptic Station). *Irrigation Sci. Eng.* 43 (2), 1–18. doi:10.22055/jise.2017.17729.1283

Sadeghian, M., Karami, H., and Mousavi, S. F. (2018). Selection of a Proper Model to Predict Monthly Drought in Semnan Using Weather Data and Linear and Nonlinear Models. *J. Water Soil Sci.* 21 (4), 57–70. doi:10.29252/jstnar.21.4.57

Salas, J. D., Delleur, J. W., Yevjevich, V., and Lane, W. L. (1980). *Applied Modeling of Hydrologic Time Series*. Colorado: Water Resources Publication.

Shirmohammadi, B., Moradi, H., Moosavi, V., Semiromi, M. T., and Zeinali, A. (2013). Forecasting of Meteorological Drought Using Wavelet-ANFIS Hybrid Model for Different Time Steps (Case Study: Southeastern Part of East Azerbaijan Province, Iran). *Nat. Hazards* 69, 389–402. doi:10.1007/s11069-013-0716-9

Sobhani, B., Safarian Zengir, V., and Kianian, M. K. (2019). Modeling, Monitoring and Prediction of Drought in Iran. *Iranian (Iranica) J. Energ. Environ.* 10 (3), 216–224. doi:10.5829/IJEE.2019.10.03.09

Sobral, B. S., Oliveira-Júnior, J. F., de Gois, G., and Pereira-Júnior, E. R. (2018). Spatial Variability of SPI and RDIstdrought Indices Applied to Intense Episodes of Drought Occurred in Rio de Janeiro State, Brazil. *Int. J. Climatol* 38 (10), 3896–3916. doi:10.1002/joc.5542

Spinoni, J., Naumann, G., and Vogt, J. V. (2017). Pan-European Seasonal Trends and Recent Changes of Drought Frequency and Severity. *Glob. Planet. Change* 148, 113–130. doi:10.1016/j.gloplacha.2016.11.013

Tan, C., Yang, J., and Li, M. (2015). Temporal-Spatial Variation of Drought Indicated by SPI and SPEI in Ningxia Hui Autonomous Region, China. *Atmosphere* 6 (10), 1399–1421. doi:10.3390/atmos6101399

Tirivarombo, S., Osupile, D., and Eliasson, P. (2018). Drought Monitoring and Analysis: Standardised Precipitation Evapotranspiration index (SPEI) and Standardised Precipitation Index (SPI). *Phys. Chem. Earth, Parts A/B/C* 106, 1–10. doi:10.1016/j.pce.2018.07.001

Vaziri, H. R., Karami, H., Mousavi, S. F., and Hadiani, O. (2018). Optimizing Reservoirs Exploitation with a New Crow Search Algorithm Based on a Multi-Criteria Decision-Making Model. *J. Water Soil Sci.* 22 (1), 279–290. doi:10.29252/jstnar.22.1.279

Wang, H., Chen, Y., Pan, Y., Chen, Z., and Ren, Z. (2019). Assessment of Candidate Distributions for SPI/SPEI and Sensitivity of Drought to Climatic Variables in China. *Int. J. Climatol* 39 (11), 4392–4412. doi:10.1002/joc.6081

Won, J., Choi, J., Lee, O., and Kim, S. (2020). Copula-Based Joint Drought Index Using SPI and EDDI and its Application to Climate Change. *Sci. Total Environ.* 744, 140701. doi:10.1016/j.scitotenv.2020.140701

Xu, D., Zhang, Q., Ding, Y., and Huang, H. (2020). Application of a Hybrid ARIMA-SVR Model Based on the SPI for the Forecast of Drought-A Case Study in Henan Province, China. *J. Appl. Meteorology Climatology* 59 (7), 1239–1259. doi:10.1175/jamc-d-19-0270.1

Zhang, S., Ali, S., Wang, X., Wang, G., Pan, Z., and Zhang, J. (2019). The Evolutionary Game Analysis and Simulation with System Dynamics of Manufacturer's Emissions Abatement Behavior under Cap-And-Trade Regulation. *Appl. Maths. Comput.* 355, 343–355. doi:10.1016/j.amc.2019.02.080

Spatial and Temporal Global Patterns of Drought Propagation

Ignacio Fuentes [1,2]*, José Padarian [1] and R. Willem Vervoort [1,3]

[1]*School of Life and Environmental Sciences, The University of Sydney, Sydney, NSW, Australia,* [2]*WaterTechnology Pty, Ltd., Melbourne, VIC, Australia,* [3]*ARC ITTC Data Analytics for Resources and the Environment, The University of Sydney, Sydney, NSW, Australia*

Drought is the most expensive natural hazard and one of the deadliest. While drought propagation through standardised indices has been extensively studied at the regional scale, global scale drought propagation, and particularly quantifying the space and time variability, is still a challenging task. Quantifying the space time variability is crucial to understand how droughts have changed globally in order to cope with their impacts. In particular, better understanding of the propagation of drought through the climate, vegetation and hydrological subsystems can improve decision making and preparedness. This study maps spatial temporal drought propagation through different subsystems at the global scale over the last decades. The standardised precipitation index (SPI) based on the gamma distribution, the standardised precipitation evapotranspiration index (SPEI) based on the log-logistic distribution, the standardised vegetation index (SVI) based on z-scores, and the standardised runoff index (SRI) based on empirical runoff probabilities were quantified. Additionally, drought characteristics, including duration, severity and intensity were estimated. Propagation combined the delay in response in the subsystems using drought characteristics, and trends in time were analysed. All these were calculated at 0.05 to 0.25 arc degree pixels. In general, drought propagates rapidly to the response in runoff and streamflow, and a with longer delay in the vegetation. However, this response varies spatially across the globe and depending on the observation scale, and amplifies progressively in duration and severity across large regions from the meteorological to the agricultural/ecological and hydrologic subsystems, while attenuating in intensity. Significant differences exist between major Köppen climate groups in drought characteristics and propagation. Patterns show intensification of drought severity and propagation affecting vegetation and hydrology in regions of southern South America, Australia, and South West Africa.

Keywords: drought propagation, meteorological drought, agricultural drought, hydrologic drought, trend analysis

1 INTRODUCTION

Drought corresponds to a sequence of climate events triggered by ocean or atmospheric circulation conditions which results in rainfall deficits (Zargar et al., 2011; Yuan et al., 2017), leading to a landscape imbalance between water supply and demand (Ault, 2020). Drought conditions can extend in time having large environmental and socio-economical consequences (Apurv et al., 2017). Droughts have been identified as one of the most costly and deadly natural hazards (Ault, 2020), and could be one of the reasons for the collapse of ancient civilizations (Kerr, 1998; Gill

et al., 2007). In recent decades, large drought episodes have occurred in different regions and have received different names, such as the millennium drought that occurred in Australia between 2001 and 2009 (Van Dijk et al., 2013) or the megadrought that has affected Chile since 2010 (Garreaud et al., 2020).

Drought can occur due multiple different atmospheric drivers. Atmospheric/oceanic circulation cycles strongly impact the development of dry/wet conditions, leading to interannual/interdecadal climate variability (Vicente-Serrano et al., 2011). Some examples of this are the El Niño Southern Oscillation (ENSO), the Pacific Decadal Oscillation (PDO), or the Indian Ocean Dipole (IOD), which all cause an oscillation in surface ocean temperatures (Mantua and Hare, 2002; Xiao et al., 2015). Other processes, like the Subtropical Ridge (STR) or the North Atlantic Oscillation (NAO), are mainly driven by atmospheric conditions that affect the atmospheric pressure at sea level (Hurrell et al., 2003; Grose et al., 2015). All these cycles strongly impact weather conditions across different time scales. However, anthropogenic impacts on the interannual climate variability as part of "climate change" are still difficult to quantify. Despite this, He and Li (2019) identified an overall increase in the interannual variability of rainfall associated with climate change across all longitudes between latitudes 20°S–50°N, while Zhu (2013) estimated an overall increase in rainfall intensities across the United States. In both cases, estimates were spatially variable. Additionally, climate change has decreased rainfall in Mediterranean regions, and an increase in temperatures is expected to increase evaporative demand, reduce snowfall and increase the ablation of glaciers, the soil water deficit and runoff, leading to an increase in drought risk and severity (Cook et al., 2018).

Drought conditions, triggered by oceanic/atmospheric circulation processes, propagate from the meteorologic subsystem, which is evident through a deficit in precipitation, to the hydrologic and agricultural subsystems (Wang et al., 2016), and therefore, referred to as a multi-scalar phenomenon (McKee, 1995). In terms of hydrology, drought may cause reduced discharge in streams, lower groundwater levels, and a reduction in reservoir storage (Maity et al., 2013). However in the hydrologic subsystem alone, drought may have different propagation rates. For example, in the surface drainage network, propagation may be relatively fast compared to the groundwater system, which depending on variables such as recharge rate and aquifer transmissivity, can have a substantial lagged response, which can also vary significantly across sites (Bloomfield and Marchant, 2013; Lorenzo-Lacruz et al., 2017; Han et al., 2019). Focusing on the surface drainage system, propagation rates can further depend on climate and catchment characteristics (Barker et al., 2016), and may be additionally modulated by water consumption in different reaches and water management (Yuan et al., 2017). Reservoirs, in particular, may play an important role in delaying drought impacts (Lorenzo-Lacruz et al., 2013). Water deficit conditions also lead to a propagation of drought in the agricultural/ecological subsystem, which results in less water in soils and consequently, vegetation stress conditions due to the water deficit (Son et al.,

2012). These may additionally translate into economic deficits due to reductions in crop yields, and subsequently into societal distress and starvation, which may cause political instability (Sternberg, 2012). However, in each subsystem the propagation is modulated by different factors that exacerbate/attenuate their impacts.

One of the difficulties in evaluating drought, is related to the methods to characterise and quantify drought, given limitations in the length of historic data and the spatial coverage (Ault, 2020). Water deficits can be evaluated through water budget anomalies, and several standardised indices have been developed to characterize the magnitude of drought (Zargar et al., 2011; Ault, 2020). For instance, meteorologic drought can be quantified through the standardised precipitation index (SPI) (McKee et al., 1993), which has been further modified to include evapotranspiration (standardised precipitation evapotranspiration index; SPEI) (Vicente-Serrano et al., 2010; Guenang and Kamga, 2014). From a hydrologic perspective, indices may include runoff (standardised runoff index, SRI) (Shukla and Wood, 2008), the streamflow in channels (standardised streamflow index, SSI) (Vicente-Serrano et al., 2012), groundwater levels, or storage volumes in reservoirs (Bhuiyan et al., 2006; Nalbantis and Tsakiris, 2009). Likewise, drought has been monitored in agricultural/ecological systems by studying the impacts on vegetation trough the standardised vegetation index (SVI) (Peters et al., 2002), which uses the normalised difference vegetation index (NDVI) as a proxy for vegetation health, or through the standardised soil moisture index (SSMI) (Sohrabi et al., 2015).

The main advantage of these indices is that standardisation is based on simple methodologies which can be used to draw conclusions on the drought severity from the observed anomalies and allows comparison across different sites and scales. This may facilitate the communication of drought research results between institutions (Zargar et al., 2011). However, to have a better understanding of drought effects at different time and space scales, diverse data sources for drought monitoring involving different variables are needed, as well as a critical evaluation of how these indices are estimated and how they may relate with each other (Wanders et al., 2017; Trnka et al., 2018). In this regard, Lorenzo-Lacruz et al. (2010) found changes in the hydrologic response to droughts in regulated systems of the Tangus catchment, in Spain, due to the external demand after the implementation of a water transfer system to other basins. Van Loon et al. (2012) found drought events to become fewer and longer as these propagate through different subsystems, and also concluded that the drought propagation processes were reasonably well reproduced in some European catchments using an ensemble mean of large-scale hydrological models. Vicente-Serrano et al. (2013), studying the vegetation response to drought, found that different biomes vary in the time-scale response to drought due to vegetation adaptation characteristics. Barker et al. (2016) studied the variability in the drought propagation from the meteorological to the hydrological subsystem using standardised indices across different catchments in the United Kingdom, while Barella-Ortiz and Quintana-Seguí (2019) found uncertainties in the

characterisation and propagation of drought in the hydrologic and soil moisture subsystems when evaluating regional climate models using standardised indices including SPI, SRI, SSI, and SSMI across Spain. Similarly, Peña-Gallardo et al. (2019) studied the relationships between meteorological and hydrological droughts in the conterminous United States and found a response of SSI to SPEI at short time scales, suggesting that elevation and vegetation play an important role in modulating this response. The authors also found a higher correlation between both indices in natural systems compared to regulated systems.

Given the importance of drought for society, the study of drought has led to an entire sub-discipline where different fields of science converge (Stahl et al., 2020). As a result of this, several unanswered questions for drought research have been identified (Trnka et al., 2018; Ault, 2020). This reinforces that there is still a need to better understand drought propagation, particularly in relation to time lags of propagation across the different hydroclimatic subsystems, and the factors that determine drought propagation (Wang et al., 2016; Trnka et al., 2018). Finally, changes in drought intensity and duration as drought transitions from one subsystem to another need to be studied.

While drought propagation analysis using standardised indices has been widely used at both local and regional scales (Bhuiyan et al., 2006; Barker et al., 2016; Loon et al., 2017; Xu et al., 2019; Zhou et al., 2019; Chen et al., 2020), few studies have addressed this at the global scale, and particularly in reference to the vegetation response to drought (Vicente-Serrano et al., 2013). Investigating the global scale is important, as the shifts and similarities in patterns at the global scale can deliver insights that are not visible at the local and regional scale. This study therefore aims to: 1) Characterise global drought through standardised indices using common average drought metrics (duration-severity-intensity), which evaluates how drought amplifies or diminishes across different subsystems. These include the meteorological subsystem through the evaluation of rainfall-evapotranspiration, the agricultural/ecological subsystem by assessing the vegetation, and the hydrological subsystem by studying modelled runoff and observed discharge. The groundwater subsystem was not included in this study because of the lack of information from global datasets that allows to differentiate monitoring wells dug in shallow alluvial aquifers from deeper aquifers, and the effect that active pumping from surrounding wells may have on the piezometric level of monitoring sites. Therefore, we prioritised surface water in the hydrological subsystem; 2) Quantify the global propagation of drought, i.e., the delay in response to drought across the different subsystems (meteorological, agricultural/ecological, and hydrological), and identify the spatial variation in this delay; 3) Discuss the implications of spatio-temporal changes of the drought characteristics across the last decades (1982–2019) for drought management and future global drought preparedness. It is clear that the 37 years selected for this study may constitute a limitation for the characterisation of drought variability on multidecadal time scales (Ault, 2020). However, this period might shed some light on average drought characteristics among subsystems and on drought propagation.
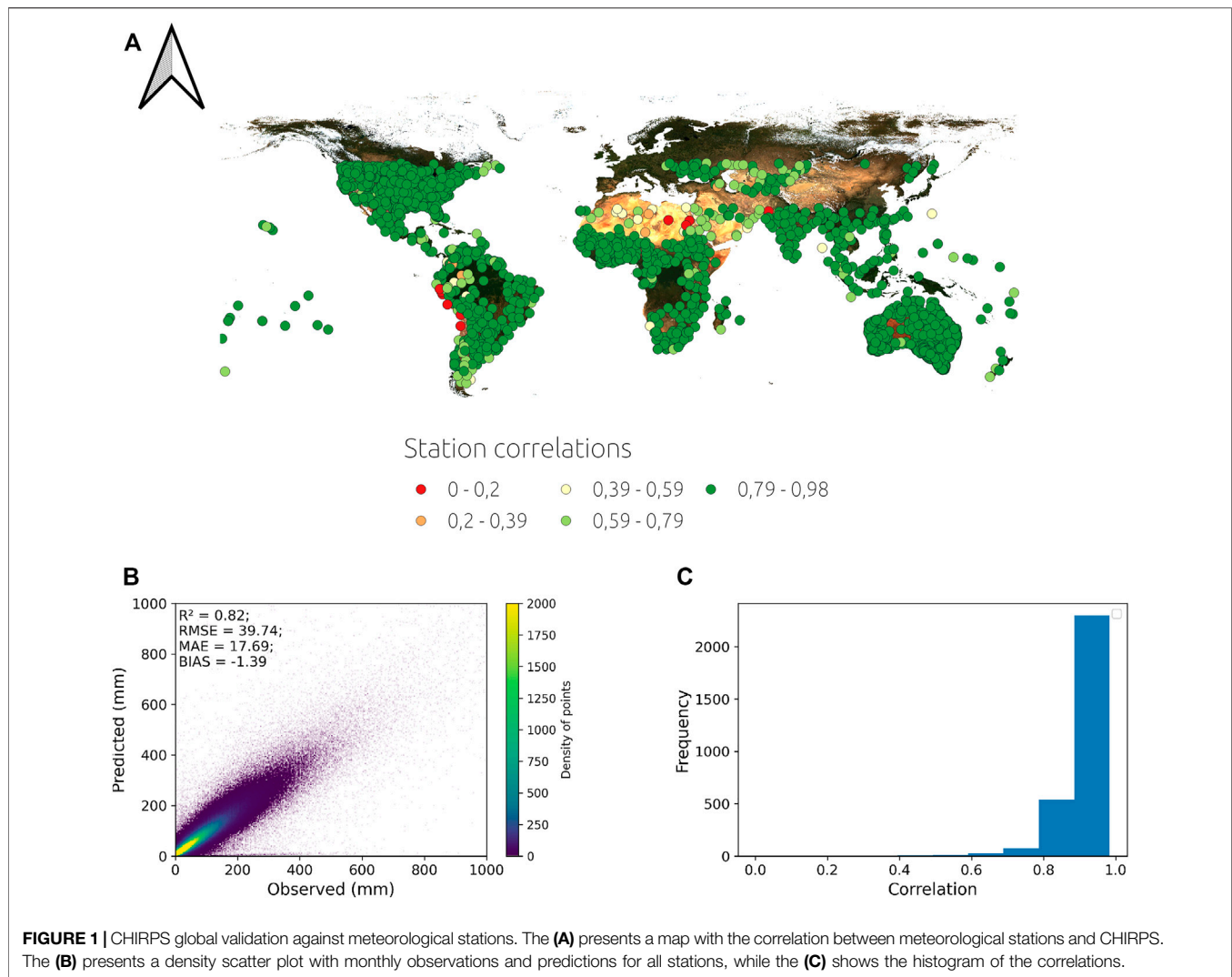
2 MATERIALS AND METHODS

2.1 Datasets Used

Because this study has a global extent, several data sets at that scale are used for the analysis. Climate variables and vegetation were based on remote sensing products. Rainfall daily data was based on the Climate Hazards Group InfraRed Precipitation with Station Data (CHIRPS version 2.0) (Funk et al., 2015). CHIRPS daily data was monthly aggregated, with a spatial resolution of 0.05°, covering 1981 to the present. However, this coverage excludes the Northern Arctic regions. CHIRPS data has been validated in many regional studies, which in general indicate a good agreement between estimates and observed data (average r of 0.94 and 0.85 in Northeast Brazil and Cyprus, respectively) (Katsanos et al., 2016; Paredes-Trejo et al., 2017). However the data can have under- and over-predictions in extreme wet and dry events and the data can have a lower performance in mountainous regions (Dinku et al., 2018). Given possible discrepancies beyond those discussed in Funk et al. (2015), monthly observations from 3,301 weather stations across the world were obtained from the World Meteorological Organization (https://climexp.knmi.nl/). These were filtered to the CHIRPS coverage period and extent, which reduced their number to 2,978, and compared against CHIRPS predictions (**Figure 1**).

At the global scale CHIRPS rainfall estimates are good, presenting globally on average an R^2 of 0.82 (r > 0.9). Additionally, over 95% of stations presented a correlation greater than 0.8, confirming the results in Funk et al. (2015). However, in some locations, such as in the Peruvian and Atacama deserts in South America, or in the Sahara desert, few stations show moderate to low correlations (a total of 18 stations have r < 0.4), which should be taken into account in the drought analysis.

Monthly temperature, wind and surface pressure were based on the 0.25° European Centre for Medium-Range Weather Forecasts (ECMWF) Reanalysis v5 (ERA5) dataset, which is associated with the fifth generation ECMWF atmospheric reanalysis of the global climate (Hoffmann et al., 2019). Several of the ERA5 variables have been compared to other datasets, and have been described as equivalent to using observational data for large areas in North America (Tarek et al., 2020). Compared with the Modern-Era Retrospective analysis for Research and Applications, Version 2 (MERRA-2 reanalysis data), it outperforms that data set in all aspects related to wind (Olauson, 2018). Monthly incoming shortwave radiation from the Famine Early Warning Systems Network (FEWS NET) Land Data Assimilation System (FLDAS) was obtained at a 0.1° resolution (McNally et al., 2017).

The third generation Global Inventory Modeling and Mapping Studies (GIMMS) normalized difference vegetation index (NDVI) from the Advanced Very High Resolution Radiometer (AVHRR) sensors at five arc minute resolution was aggregated to monthly data for 1981 to 2014 (Pinzon and Tucker, 2014). We added the Moderate Resolution Imaging Spectroradiometer (MODIS) NDVI from Terra instruments (MOD13A2), which is available from 2001 to

FIGURE 1 | CHIRPS global validation against meteorological stations. The **(A)** presents a map with the correlation between meteorological stations and CHIRPS. The **(B)** presents a density scatter plot with monthly observations and predictions for all stations, while the **(C)** shows the histogram of the correlations.

the present, but at a much higher resolution (1,000 m) (Didan, 2015).

Modelled mean monthly runoff rasters from the ERA5 collection were also included in the analysis to account for hydrological variables. Runoff corresponds to the fraction of water that flows through the surface or subsurface, which does not stay stored in the soils. Additionally, to evaluate hydrologic droughts using point measurements, level 4 basins from the HydroSHEDS dataset (Lehner and Grill, 2013) were combined with reference stations from the Global Runoff Data Centre (GRDC; https://www.bafg.de/GRDC/). These stations (and basins) were filtered based on drained areas of at least 10,000 km^2, and discharge data was filtered from 1981. From the combined basins and gauging stations, stations located furthest downstream within each basin were selected for further analysis. Additionally, the degree of regulation attribute of the basins contained in the HydroATLAS version 1.0 dataset (Lehner et al., 2011) was appended to the stations to differentiate between regulated and natural systems.

The raster datasets were all accessed, pre-processed, and analysed using Google Earth Engine (Gorelick et al., 2017), while observational data was processed using Python libraries.

2.2 Pre-processing and Drought Indices

As discussed, there are several drought indices. In this study, we used the Standardised Precipitation Index (SPI), the Standardised Precipitation Evapotranspiration Index (SPEI), the Standardised Vegetation Index (SVI), and we also standardised the runoff to get a Standardised Runoff Index (SRI). These indices can be calculated for different time scales based on the sum of observations in a selected time window (Zhang and Li, 2020):

$$x_{i,j}^k = \sum_{t=0}^{k-1} x_{i,j-t} \qquad (1)$$

where $x_{i,j}^k$ is the record of the variable used in any index evaluated in the ith year and jth month using the k time scale, which in this study was set to 1, 3, 6, and 12 months. These different time scales aggregate the data with increasing periods, which in some cases

have been reported to take into account the meteorological (1 month), agricultural (3–6 months), and hydrological aspects (12 months) of droughts (Tirivarombo et al., 2018). The observations for the different drought indices correspond to rainfall for SPI, rainfall minus evapotranspiration for SPEI, NDVI for SVI, and runoff/discharge for SRI.

2.2.1 Standardised Precipitation Index

The SPI was standardised assuming a gamma distribution, as this distribution has been used as the benchmark for studying drought using positive hydroclimatic variables and is recommended for use at large scales (Stagge et al., 2015), which was implemented in Google Earth Engine (Guenang and Kamga, 2014):

$$g(x) = \frac{1}{\beta^\alpha \Gamma(\alpha)} - x^{\alpha-1} e^{x/\beta} \ for \ x > 0 \tag{2}$$

where α and β are the shape and scale parameters.

2.2.2 Standardised Precipitation Evapotranspiration Index

Since SPEI requires the subtraction of rainfall and evapotranspiration, this last was calculated in Google Earth Engine by combining the ERA5 dataset with the FLDAS forcing radiation using the Food and Agriculture Organization (FAO) Penman Monteith equation (Pereira et al., 2015):

$$ET_r = \frac{0.408\Delta(R_n - G) + \gamma\frac{900}{T+273} u_2 (e_s - e_a)}{\Delta + \gamma(1 + 0.34u_2)} \tag{3}$$

where ET_r is the monthly reference evapotranspiration, R_n is the net radiation, G is the soil heat flux, Δ is the slope vapour pressure, T the mean temperature, e_s the saturation vapour pressure, e_a the actual vapour pressure, γ the psychrometric constant, and u_2 the wind speed at 2 m height.

The subtraction of precipitation and ET_r can result in negative values. As a result, and based on earlier comparisons (Vicente-Serrano and Beguería, 2016), SPEI was standardised using a log-logistic distribution with three parameters (Beguería et al., 2010) in Google Earth Engine. The probability distribution function for the log-logistic distribution is:

$$F(x) = \left[1 + \left(\frac{\alpha}{x - \gamma} \right)^\beta \right]^{-1} \tag{4}$$

where α, β, and γ are the parameters of the function that can be estimated from a probability weighted moments calculation. From this, P, i.e., the probability of exceeding a value of D (D stands for difference between rain and evapotranspiration), is calculated as $1-F(x)$. Finally, SPEI is calculated as:

$$SPEI = W - \frac{C_0 + C_1 W + C_2 W^2}{1 + d_1 W + d_2 W^2 + d_3 W^3} \tag{5}$$

where $W = \sqrt{-2\ln P}$ if $P \leq 0.5$ and $W = \sqrt{-2\ln(1 - P)}$ if $P > 0.5$. Additionally, when $P > 0.5$ SPEI is multiplied by -1. In this case C_0, C_1, C_2, d_1, d_2, and d_3 are constants estimated to be 2.515517, 0.802853, 0.010328, 1.432788, 0.189269, and 0.001308, respectively (Abramowitz and Stegun, 1964).

2.2.3 Standardised Vegetation Index

Given that the GIMMS NDVI from the AVHRR sensors is discontinued after 2013, MODIS NDVI was used to generate a monthly continuous series from 1981 to the present. However, MODIS data had to be re-projected and re-scaled to the GIMMS projection and resolution. Additionally, since some artifacts arise from the difference between sensors, which are evident even when re-projecting and re-scaling MODIS, a correction using ordinary least squares (OLS) between sensors was used. Thus, GIMMS NDVI was modelled from MODIS NDVI based on a modification of the Mao et al. (2012) methodology, which is needed because of the seasonal NDVI variability. The modification consisted of using OLS on both datasets for each month using 10 years (2001–2010) of observations. A validation was carried out on 1,000 randomly distributed points sampled from 14 polygons drawn in different continents, comparing the predictions against the monthly GIMMS NDVI observations from 2011 to 2013 (36 months), which results in a total of 36,000 observations.

Validation results of merging AVHRR and MODIS NDVI are in **Figure 2**. The validation of the modelled NDVI has an error of around 5%, with a small bias of 0.003, and a determination coefficient of 0.96, which was considered acceptable for subsequent analysis.

The SVI was then calculated following the original calculation described in Peters et al. (2002) based on a z-scores estimation, which is the deviation from mean values in standard deviation units:

$$SVI = \frac{NDVI_{i,k} - \overline{NDVI}_k}{\sigma_k} \tag{6}$$

where $NDVI_{i,k}$ is the NDVI for observation i at the time period k, $\overline{NDVI}_k$ and σ_k are the mean and standard deviation of NDVI for period k.

2.2.4 Standardised Runoff Index

Lastly, SRI was calculated using empirical probabilities that lead to non-parametric standardised indices based on the Gringorten plotting position (Farahmand and AghaKouchak, 2015; Wu et al., 2018):

$$p(x_i) = \frac{i - 0.44}{n + 0.12} \tag{7}$$

being n the length of observations and i the rank of event x in the collection. Then, the inverse normal function needs to be applied to standardise the range of values:

$$SRI = \text{erfinv}(2p(x_i) - 1)\sqrt{2} \tag{8}$$

where erfinv corresponds to the inverse error function. SRI was estimated for the ERA5 runoff rasters and the GRDC gauging stations. In this case, SRI was used because it allows to relax the assumption of representative parametric distribution types assigned to the data (Farahmand and AghaKouchak, 2015).

2.3 Calculations of Drought Characteristics

Drought indices describe wet and dry conditions based on time series records of different variables, and can be separated in dry/wet classes (**Table 1**) (Jain et al., 2015; Potopová et al., 2015).
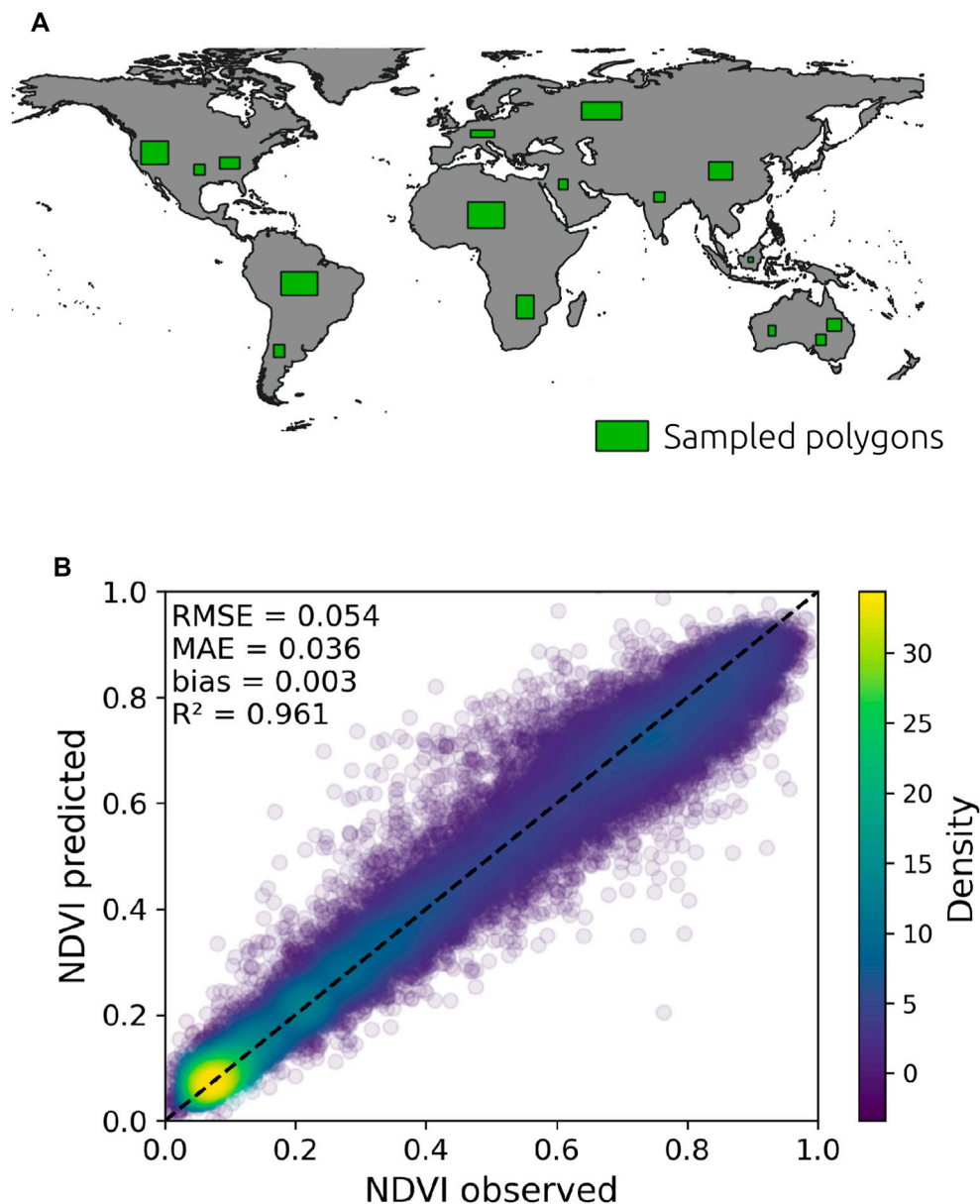
FIGURE 2 | Validation of the combination of the GIMMS AVHRR NDVI and MODIS NDVI using monthly observations of GIMMS NDVI from 2011 to 2013. Polygons where random samples were taken for validation are presented in the **(A)**, while the **(B)** shows a density scatter plot of the validation and associated statistics.

While drought propagation can be defined as the delay in the drought response in the different subsystems, a characterisation of drought in each subsystem was calculated in Google Earth Engine to evaluate the amplification or diminishing of drought effects during drought conditions through subsystems.

Thus, based on a threshold defined at −1 (Van Loon and Van Lanen, 2013; Li et al., 2020), a drought period was assumed to be any period where the drought index goes below −1,

corresponding to moderately to extremely dry conditions (Potopová et al., 2015). Drought duration has been defined in different ways (Halwatura et al., 2015; Cavus and Aksoy, 2020). For simplicity, drought duration was defined as the consecutive months of drought indices below −1, which are preceded and followed by values above −1. Severity, considered as the strength of droughts, refers to the cumulative effects of drought and is calculated as:

TABLE 1 | Drought indices and wet/dry classes.

Classes	Range of values
Extremely dry	≤−2.00
Severely dry	−1.99 to −1.50
Moderately dry	−1.49−−1.00
Mild dry	−0.99 to 0.00
Mild wet	0.00 to 0.99
Moderately wet	1.00 to 1.49
Severely wet	1.50 to 1.99
Extremely wet	≥2.00

$$S_e = \sum_{i=1}^{D} |SI| \qquad (9)$$

where S_e corresponds to the drought severity for the e drought event, with D the drought duration (in months) and SI the estimate of the respective standardised drought index. The intensity of the drought was also estimated as the ratio of the drought severity and the drought duration.

2.4 Spatial and Temporal Analysis of Drought Characteristics

To study the lag response between meteorological, agricultural, and hydrological drought, the lag at the maximum cross correlation between the meteorological and the agricultural, and between the meteorological and hydrological drought indices was estimated at each pixel. Additionally, this analysis was evaluated at the basin scale by combining the hydrologic drought calculated from GRDC stations and mean meteorologic—agricultural/ecological droughts in the filtered basins. This was done because pixel values refer to surface estimations at a particular scale, but point observations such as terminal gauges in a catchment or pixels aggregated within the catchment refer to hydrologic/vegetational values representative of the catchment scale, and different study scales may lead to different conclusions (Joao, 2002). In addition, runoff corresponds to a modelled variable, while GRDC stations correspond to observational data, which might be useful as a source of comparison to evaluate the drought propagation using modelled data in the hydrologic subsystem.

However, since the time series are in general serially correlated, these were first prewhitened to convert at least one of them into white noise (Shumway and Stoffer, 2017). Therefore, multiband raster grids were downloaded and converted into arrays. The prewhitening used the auto-ARIMA function from the pmdarima library (Smith 2017) along the 0 axis (time) of the independent array (x-variable in the cross correlation analysis) and setting minimum and maximum autoregressive (p) and moving average (q) terms to 0 and 5 respectively, and a minimum and maximum differencing (d) of 0 and 2. The auto-ARIMA function fits an ARIMA model to the time series:

$$Y_t = -\left(\Delta^d Y_t - Y_t\right) + \phi_0 + \sum_{i=1}^{p} \phi_i \Delta^d Y_{t-i} - \sum_{i=1}^{q} \theta_i \epsilon_{t-i} + \epsilon_t \qquad (10)$$

where ϕ are the constants associated with the autoregressive behaviour, θ corresponds to the parameters associated with the moving average in the model, and ϵ corresponds to the error terms, being:

$$\Delta Y = Y_t - Y_{t-1} \qquad (11)$$

The auto-ARIMA function identifies the (p, d, q) model parameters of ARIMA optimizing (minimizing) the Akaike Information Criterion (AIC). The x-variable to use in the cross correlation corresponds then to the residuals of the ARIMA model. Stationarity in the series is evaluated based on the d parameter from the ARIMA model. Subsequently, the selected ARIMA model is also fitted to the cross correlation y-variable and the residuals are used for the cross correlation. This makes the series stationary and removes serial correlation before the cross correlation analysis. The significance of the cross correlation was based on:

$$r_k > \left| \frac{1.96}{\sqrt{n}} \right| \qquad (12)$$

being r the correlation coefficient at lag k and n the length of the series.

A further hypothesis is that continued climate change would introduce a trend in the drought characteristics. Therefore a trend analysis using Ordinary Least Squares (OLS) was applied to the drought characteristics, rather than directly to the standardised indices since drought events are considered independent. The significance of the trend (p-value) was estimated using Google Earth Engine.

2.5 Major Köppen Climate Groups and Drought Propagation

Different climate characteristics might result in variations in drought, especially if droughts are calculated globally in a standardised way. Vectorial information of major Köppen climate groups from Rubel and Kottek (2010) was used to aggregate drought characteristics from the SPEI, SRI, and SVI and propagation characteristics (**Figure 3**). Thus, drought rasters were sampled using all groups and were compared using analysis of variance or the non-parametric Kruskal Wallis test to evaluate if major climate groups indicate drought differences and drought propagation differences. Additionally, a multiple comparison to evaluate differences between groups was carried out through the non-parametric Dunn's multiple comparison test, setting a step-down method that uses Bonferroni to adjust the p-values (Glantz, 2002). For all these tests, a p-value < 0.05 was assumed to lead to strong evidence of differences between major climate groups.

3 RESULTS

3.1 Meteorological Drought

Since drought is associated with atmospheric and oceanic circulation patterns, and these are dynamic in time and space around the world, it is possible to observe large spatial differences in dry/wet conditions on any specific date. This is what can be observed in the **Figure 4A** for SPI and SPEI maps in July 2019.
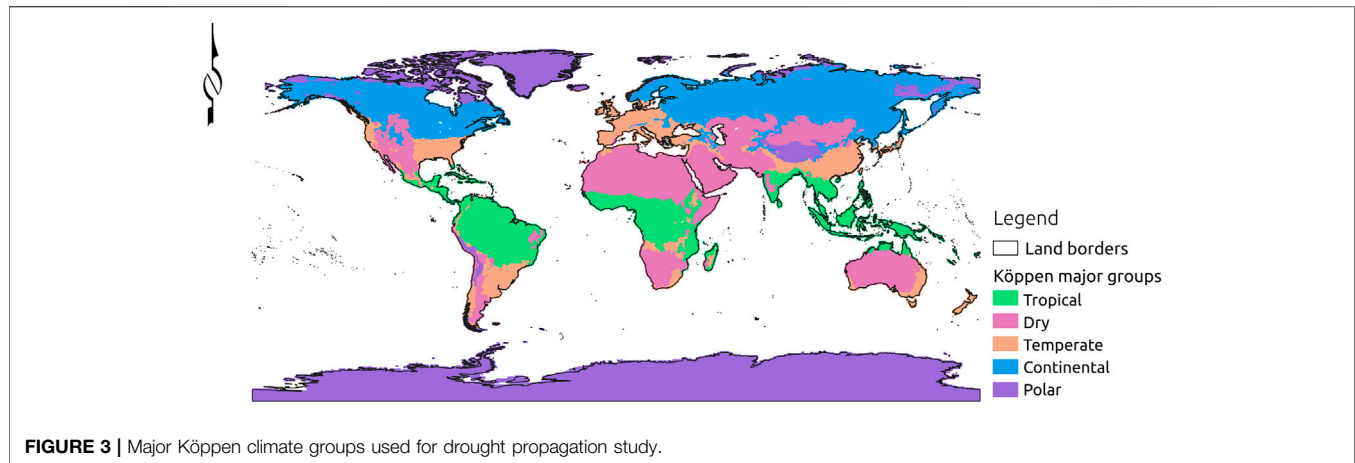
FIGURE 3 | Major Köppen climate groups used for drought propagation study.
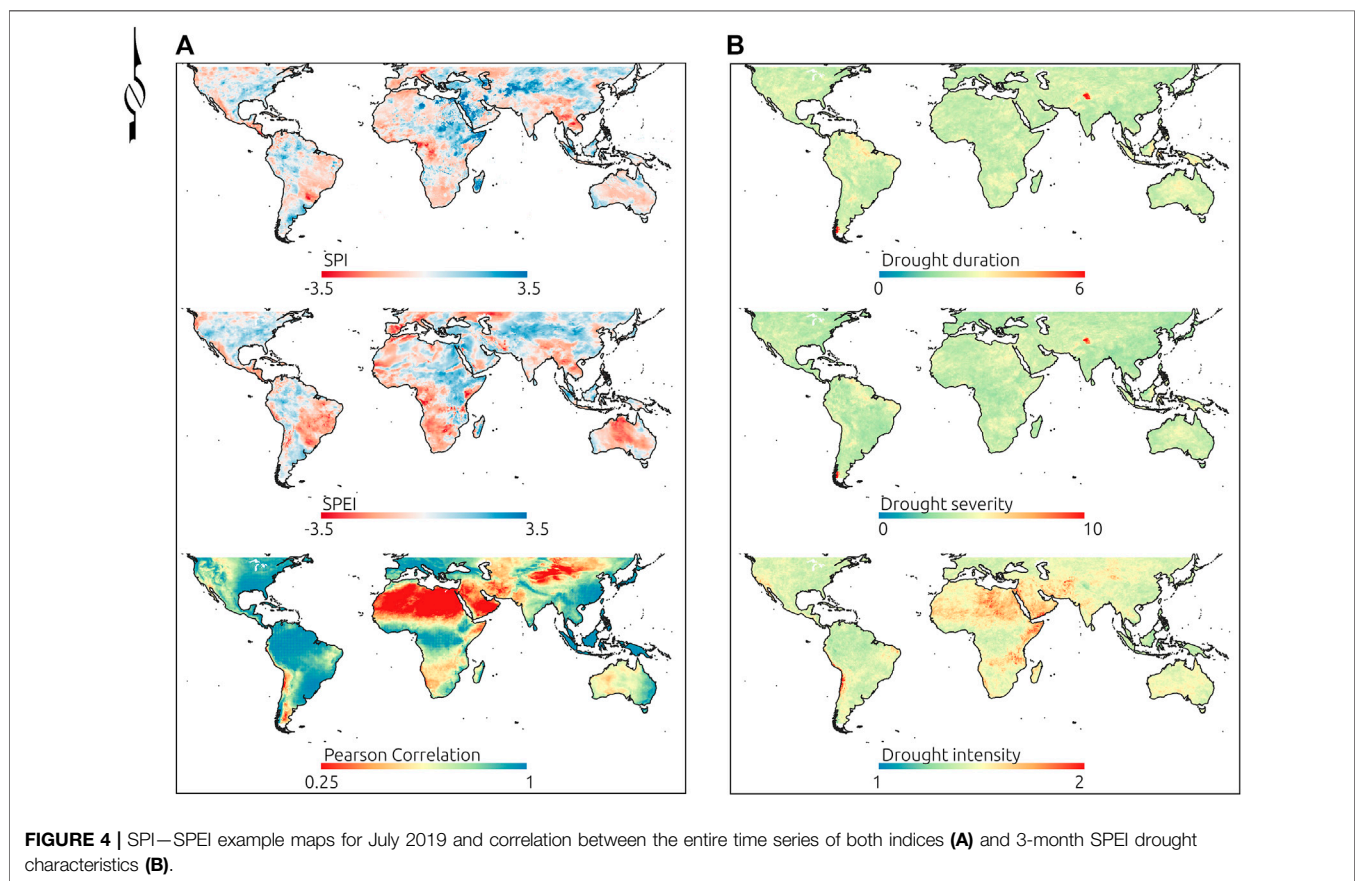
FIGURE 4 | SPI—SPEI example maps for July 2019 and correlation between the entire time series of both indices **(A)** and 3-month SPEI drought characteristics **(B)**.

The upper and middle panels correspond to a graphical representation of a single SPI/SPEI record. The lower panel indicates the Pearson correlation between both series for 1981–2019 at each pixel, which shows high correlation in South America and the tropics, and more generally in high rainfall areas.

Average meteorological drought characteristics estimated from the 3-month SPEI series are in **Figure 4B**. While the

lowest drought duration regions are in northern latitudes (western Europe and Asiatic Russia), low duration can also be found in southern and eastern Asia. On the other hand, regions showing the largest drought duration seem to be constrained, in some cases, to areas with high annual rainfall, including some countries of Oceania such as Indonesia, Philippines, and Papua New Guinea, which can reach in average to more than 5 months of continuous drought (SPEI < −1). However, northeastern

FIGURE 5 | Average 3-month SVI **(A)** and 3-month SRI **(B)** drought characteristics.
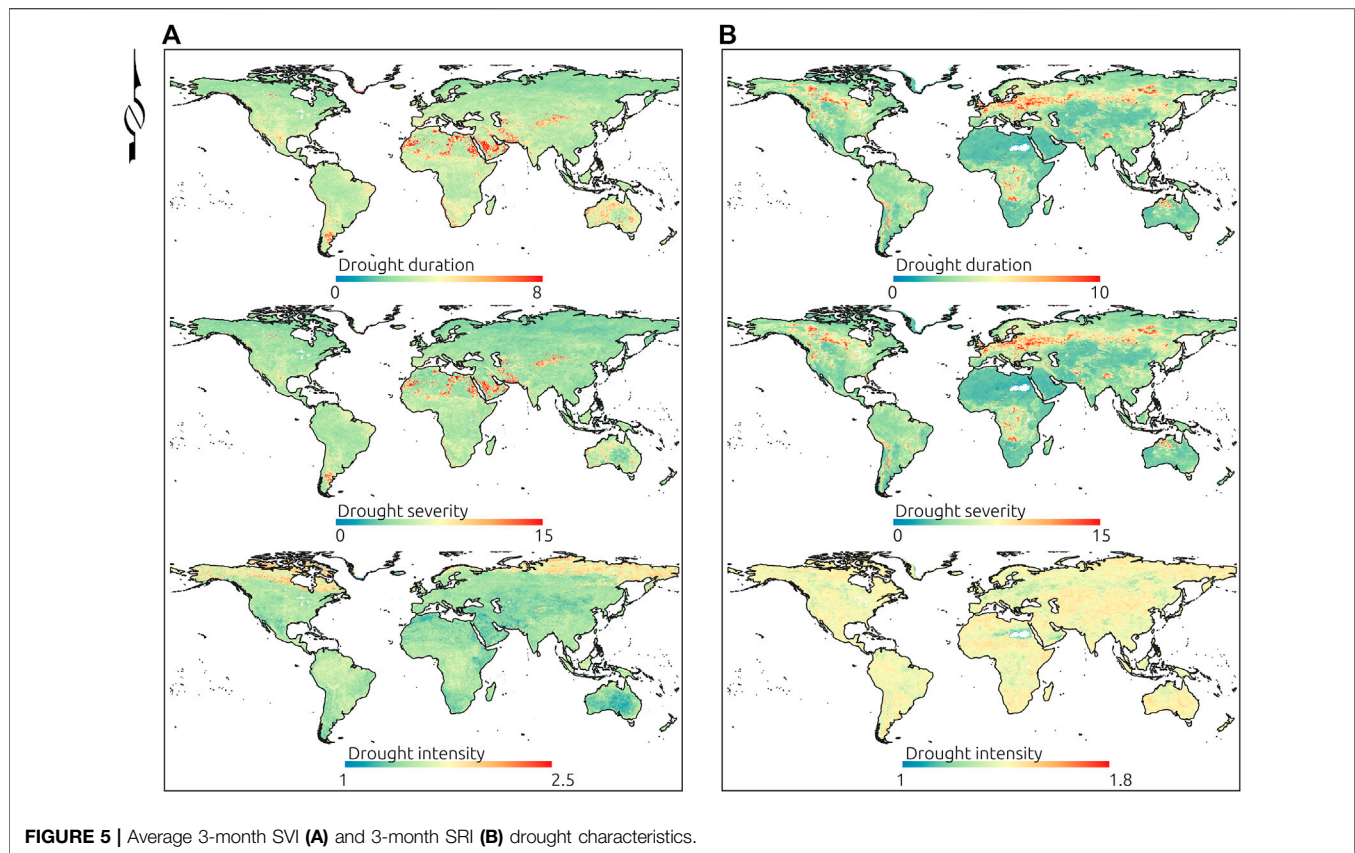
South America also presents a large mean drought duration. Highlights the Kashmir region, which presents the largest drought duration, reaching on average over 9 months. No significant correlation was found between average rainfall and mean drought duration derived from SPEI (not shown). Drought severity follows a similar pattern compared to drought duration since it corresponds to the accumulated drought severity (in standardised units) during drought events.

In terms of drought intensity, northern Africa and western Asia have on average the largest values. In contrast, on average, lower intensities are found in the Amazon, Micronesia, Polynesia, and Melanesia regions. However, the lowest drought intensity also occurs around the Kashmir region, but neighbour areas of very high intensity are also visible.

3.2 Agricultural/Ecological and Hydrologic Drought

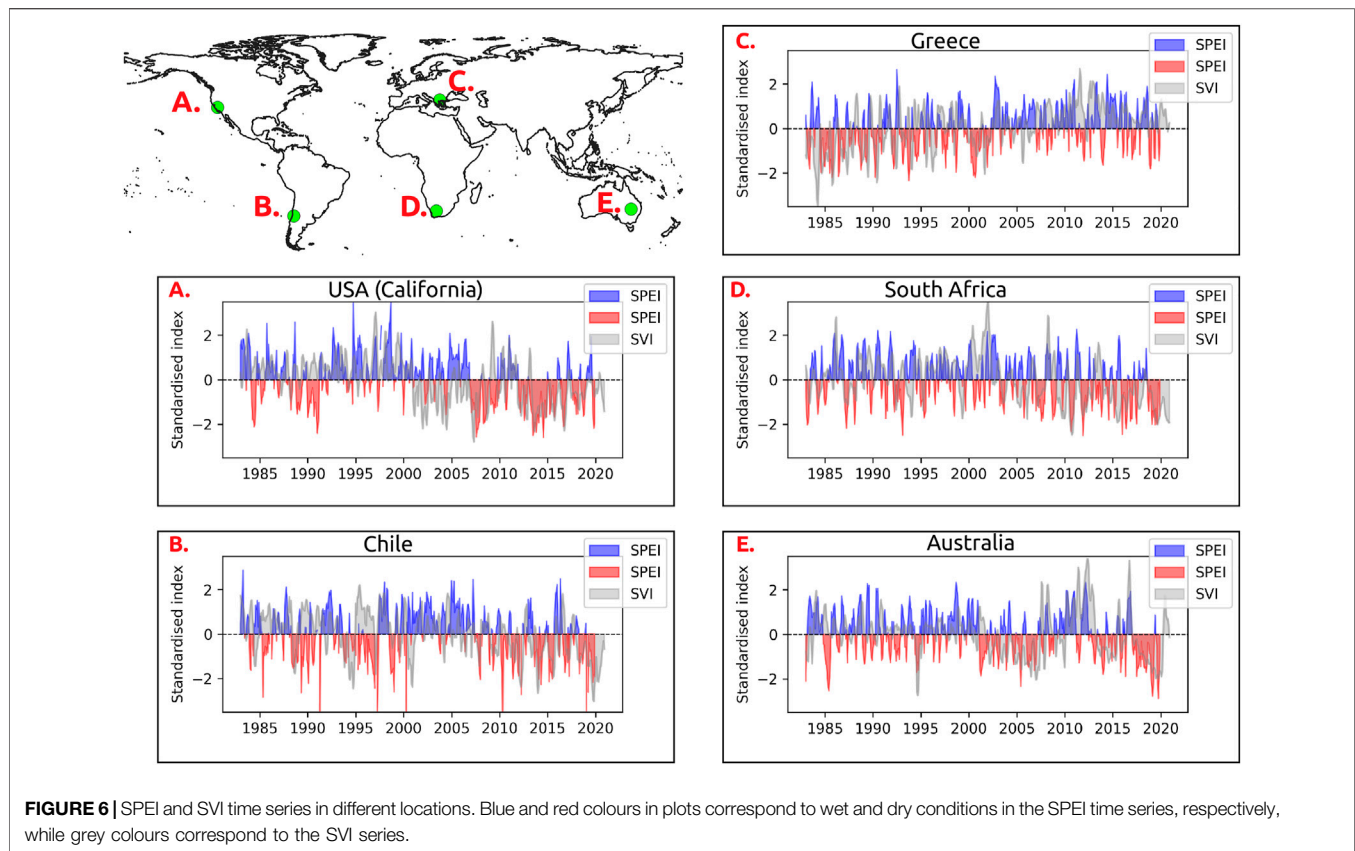An example map of SVI for July 2019 is in the Supplementary materials (**Supplementary Figure S1**), while average agricultural drought characteristics are in the **Figure 5A** calculated using the entire series of 3-month SVI. Agricultural drought duration and severity increases in most regions compared to the meteorological drought using SPEI (**Figure 4**), except in Melanesia. For instance, while the mean meteorological drought duration in southern Africa is 2.1 months, its mean agricultural drought duration

increases up to 2.4 months using SVI. In central Asia the mean drought duration increases from 2.4 to 3.1 months, in North America from 2.3 to 3 months, and in Australia and New Zealand from 2.5 to 3.7 months. Additionally, there is a general increase in spatial variability of drought duration in different regions using SVI, except in South America. The increase in variability is stronger in western Europe and Polynesia. The intensity of agricultural drought using SVI is in the lower **Figure 5A**. Higher intensities can be found in northern regions which can be associated with large severity of short duration events, since the intensity refers to the ratio between severity and duration.

An example map of the SRI index calculated for July 2019 and its correlation with SPEI are in the Supplementary materials (**Supplementary Figure S2**). Higher correlations between both indices occur in large areas of the United States, eastern sectors of Australia and Southern Africa when considering the entire time series. Similar to the other indices, average SRI characteristics are in the **Figure 5B**. Low duration and severity of drought occur in the Saharan and Middle East regions, where dry climates occur, but this is not extensive for Australian deserts, and low duration and severity also occur in central Asia and southern Africa. On the other hand, large values can be found in central Africa, to the east of the Andes mountain range in South America, in north western Australia and in western and eastern Europe. Intensities, in general, indicate an opposite behaviour relative to duration and severity.

FIGURE 6 | SPEI and SVI time series in different locations. Blue and red colours in plots correspond to wet and dry conditions in the SPEI time series, respectively, while grey colours correspond to the SVI series.
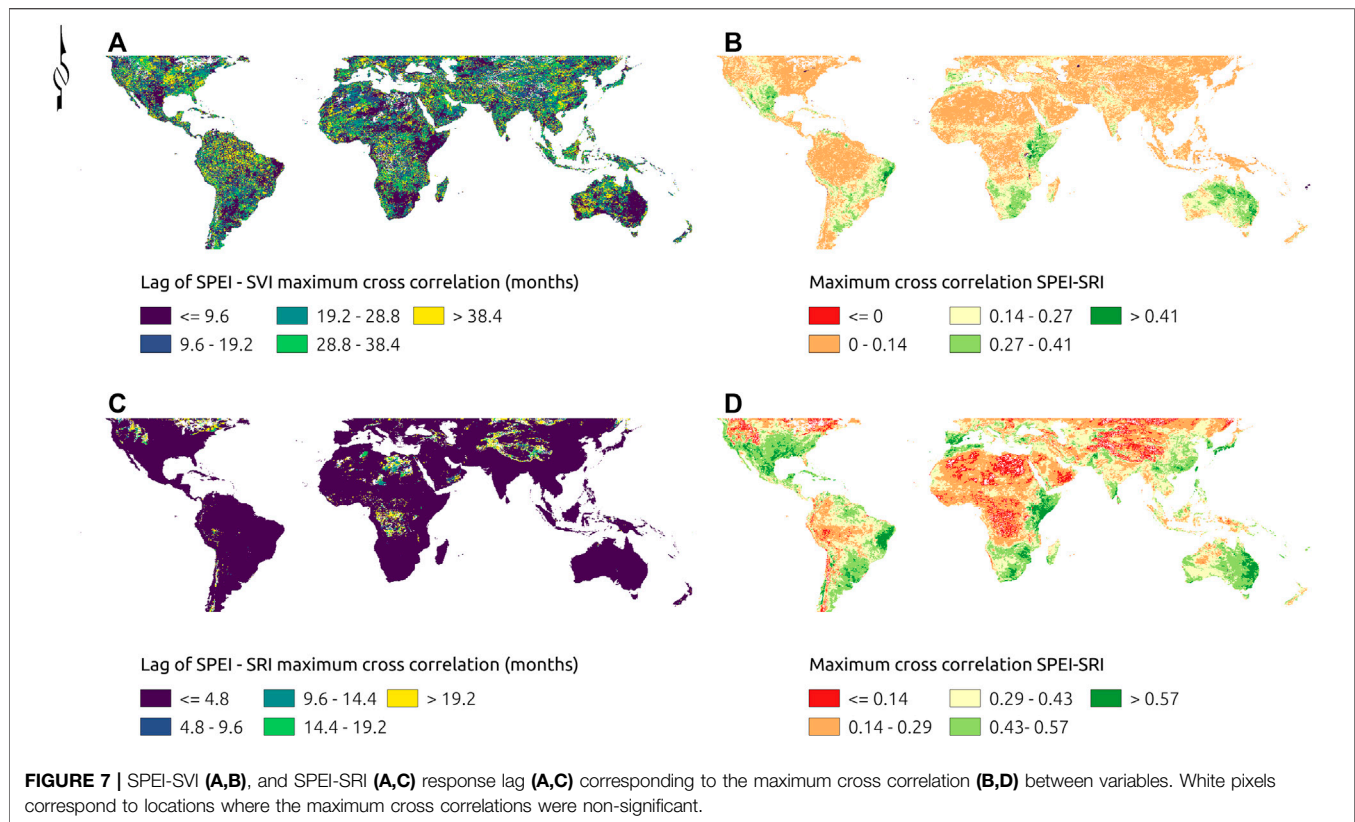
3.3 Drought Propagation

Apart from the drought characteristics, which may describe how the drought affects the different subsystems in terms of duration, severity and intensity, the propagation was identified as the lag in the peak of correlation between drought time series in different subsystems.

Theoretically, drought propagation progresses from the meteorological subsystem (SPEI) to the hydrologic subsystem (SRI), passing through the agricultural subsystem (SVI) (Wang et al., 2016). **Figure 6** shows the time series of SPEI (red and blue colours) and the SVI propagation (grey colour) at different global locations. Different patterns are visible at each of these locations. For instance, Australia (New South Wales) (E) shows a pattern with clear drought events after 2012, characterised by low SPEI, which amplifies the duration in the SVI series. A similar pattern can be observed in California, United States (A), and in central Chile (B), especially after 2008, while an opposite behaviour can be detected in Greece (C).

The lagged responses from the meteorological (SPEI) to the other subsystems (**Figures 7A,C**) indicate how these vary depending on the location and the subsystem being evaluated. The vegetation subsystem response (SVI) can be direct with maximum cross correlation with SPEI at lag 0. This seems to occur especially in Temperate and Dry climates such as in the eastern part of Australia, the pampas area (Argentina) in South America, southern and eastern Africa, and south central United States. These regions also tend to present larger

maximum cross correlation values between both indices (**Figures 7B,D**). However, in most cases the response is delayed several months. In equatorial forest areas like the Amazon and central Africa, a large lag can be observed, but this also occurs in mid latitude regions, such as northern North America. In contrast to what is generally described in the literature (Zargar et al., 2011; Wang et al., 2016), the response in the hydrologic subsystem, through runoff, is mainly direct and minima and maxima are at the same time as the SPEI, but this occurs on a pixel basis. However, there are also some patches where large lags occur between SPEI and SRI, for instance in the Mountainous western region of United States, or surrounding the Great lakes in the United States and Canada, to the west of the Andes mountain range in South America, and spread out in several regions of Europe, and across eastern and central Asia.

Basin aggregated lagged responses in the agricultural/ecologic and hydrological subsystems are in **Figure 8** and tend to confirm the results found on a pixel basis. Again, it is evident that the hydrological response tends to be faster than the vegetation response, except in some particular basins, such as the Great Plains in North America, to the east of the Andes in South America, or downstream of the Tsimlyanskoya reservoir in Russia and the Guanting reservoir in China. These are most likely all snow/glacier driven systems. From the 403 basins filtered in the preprocessing steps, 302 and 233 had significant SVI-SPEI and SRI-SPEI cross correlation values, respectively. For the maximum SRI-SPEI cross correlation at lag (month) 0 there

FIGURE 7 | SPEI-SVI **(A,B)**, and SPEI-SRI **(A,C)** response lag **(A,C)** corresponding to the maximum cross correlation **(B,D)** between variables. White pixels correspond to locations where the maximum cross correlations were non-significant.

were 101 basins, while 121 basins indicate lags between 1 and 3, and 11 basins indicate lags greater than 3. On the other hand, 49 basins indicate a maximum SVI-SPEI cross correlation at lag 0, while 48 basins were between 1 and 3 months, 39 basins between 3 months and 1 year, and 166 longer than 1 year.

Differences between regulated and natural basins are in **Figure 9**. Natural drainage systems indicate higher and more significant correlations between SPEI and SRI, which was confirmed using the Kruskal Wallis test (*p*-value < 0.05). Additionally, unregulated basins tend to respond to meteorological droughts at shorter time scales. No significant differences in the lagged response were found between natural and unregulated basins. However, regulated systems have a larger dispersion in the lagged response, with some basins indicating a delay of over 19 months after the beginning of meteorological droughts.

Additionally, by subtracting the average drought characteristics in each subsystem, the change in duration and intensity can be evaluated (amplification or attenuation of drought) in the different subsystems. **Figure 10** shows the difference between SVI and SPEI in terms of duration (months), severity and intensity (left panel).

Drought duration and severity amplify in large regions of the mid-latitudes. In contrast, smaller patches of attenuation can be observed in between those areas, probably associated with vegetation patches. Small areas in the northern South America, around the Great Lakes in North America, in the Malay Archipelago, and in the Kashmir region indicate drought

duration/severity attenuation in the agricultural/ecological subsystem. Drought intensity, on the other hand, attenuates in several regions. It also shows an opposite behaviour compared to duration and severity in dry regions where these strongly amplify, such as in the Argentinian Patagonia, western Australia, some regions in northern Africa and middle East. In these regions agricultural/ecological drought intensity reduces to about half of the magnitude of meteorological drought intensity.

The difference of drought characteristics between SRI and SPEI are in the right panel of **Figure 10**. In general, duration and severity indicate a larger heterogeneity compared to the difference between SVI and SPEI. Drought duration/severity attenuation in the hydrological subsystem can be seen in the Saharan and sub-Saharan regions, Middle East, central Australia, southern Africa, and the Patagonia, while amplification can be found to the west of Los Andes and in large extents of Brazil, in eastern North America, Europe, central Africa, and eastern Asia, among others. Similar heterogeneity between drought intensity amplification/attenuation regions can be observed across the world.

3.4 Spatial and Temporal Drought Patterns
The trends based on the OLS analysis and associated levels of significance for the 3-month SPEI drought characteristics are in **Figure 11**. Trends in the duration, severity and intensity of meteorological drought are quite variable across the globe. Concerning are increases in drought characteristic trends which can be observed in western Europe (Portugal and

FIGURE 8 | Basin aggregated SPEI-SVI (A,B), and SPEI-SRI (A,C) response lags (A,C) corresponding to the maximum cross correlation (B,D) between prewhitened average aggregated SPEI/SVI and SRI calculated from gauging stations. Basins with non-significant cross correlations were masked out.

FIGURE 9 | Maximum cross correlation coefficient distributions (A) and significant lagged response categories [months; (B)] between 3-month SPEI and 3-month SRI for regulated and unregulated basins.

Spain), western regions of North America, Central America, Australia, southern South America, south west Africa, and eastern Russia. In all those regions droughts are increasing, either in duration, severity, or intensity, or in all of these.

Similarly, 3-month trends in SVI drought characteristics follow slightly different patterns, but again increasing trends occur in southern South America, the Northern Territory and Western Australia, south west Africa, and regions in central and

FIGURE 10 | Duration **(A,B)**, severity **(C,D)** and intensity **(E,F)** mean differences between SVI and SPEI **(A,C,E)** and between SRI and SPEI **(B,D,F)**.
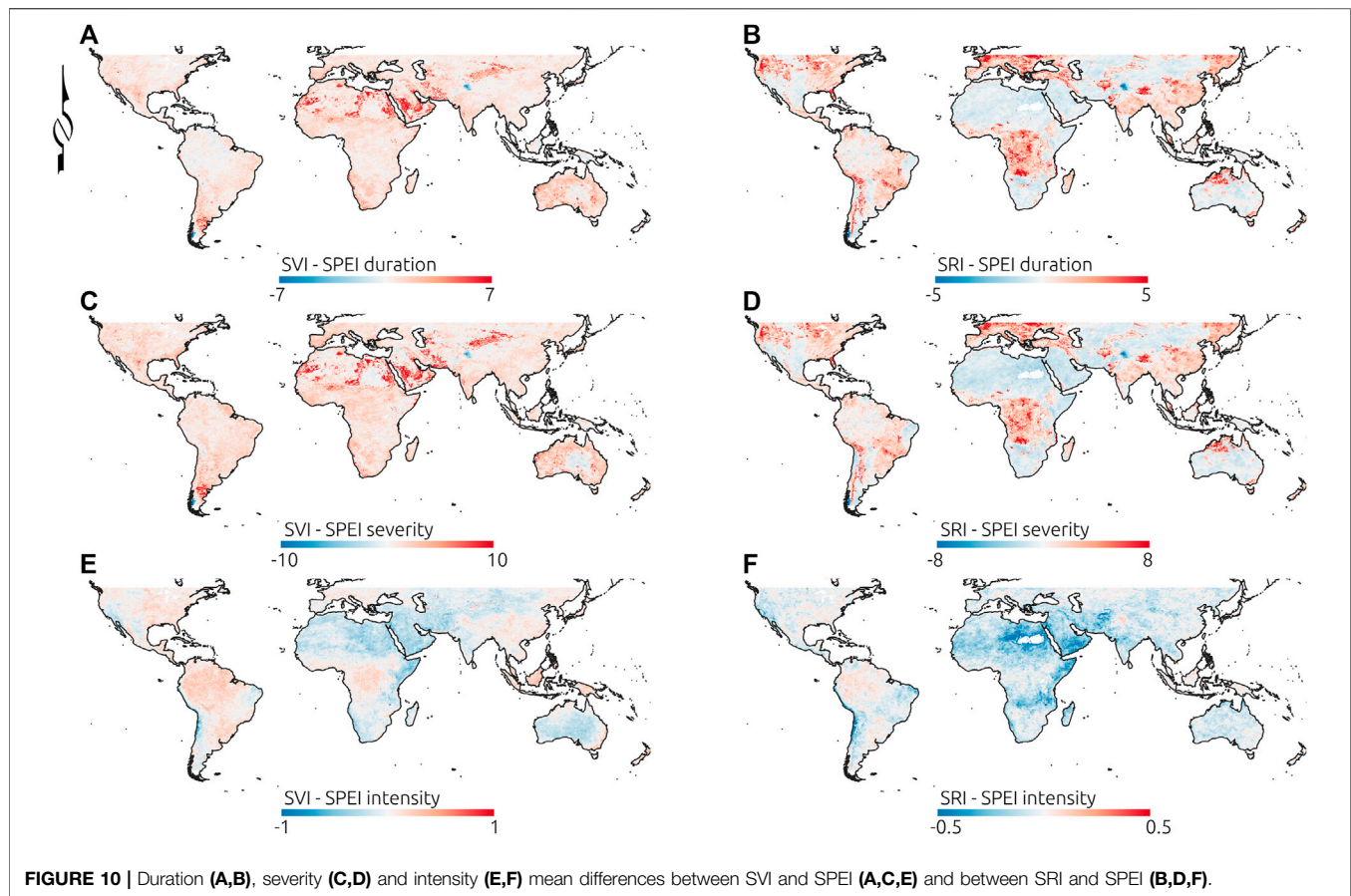
eastern Asia (**Supplementary Figure S3**). On the other hand, strong and significant increasing trends in drought effects for runoff can be detected in central Africa, central Australia, to the east of the Andes mountain range in South America and in central and eastern Europe (**Supplementary Figure S4**).

Heat maps of the severity of drought based on the 3-month SPEI for latitude and longitude are in **Figure 12**. About four severe global drought events can be observed surrounding the equator (mean SPEI severity > 8), but extending to the north and south latitudes in 1983, 1993, 1998, and 2016. Some of these tend to propagate in time and tend to cover a large extent of the continental surface (above right panels). In between the 30–40°parallels, a rela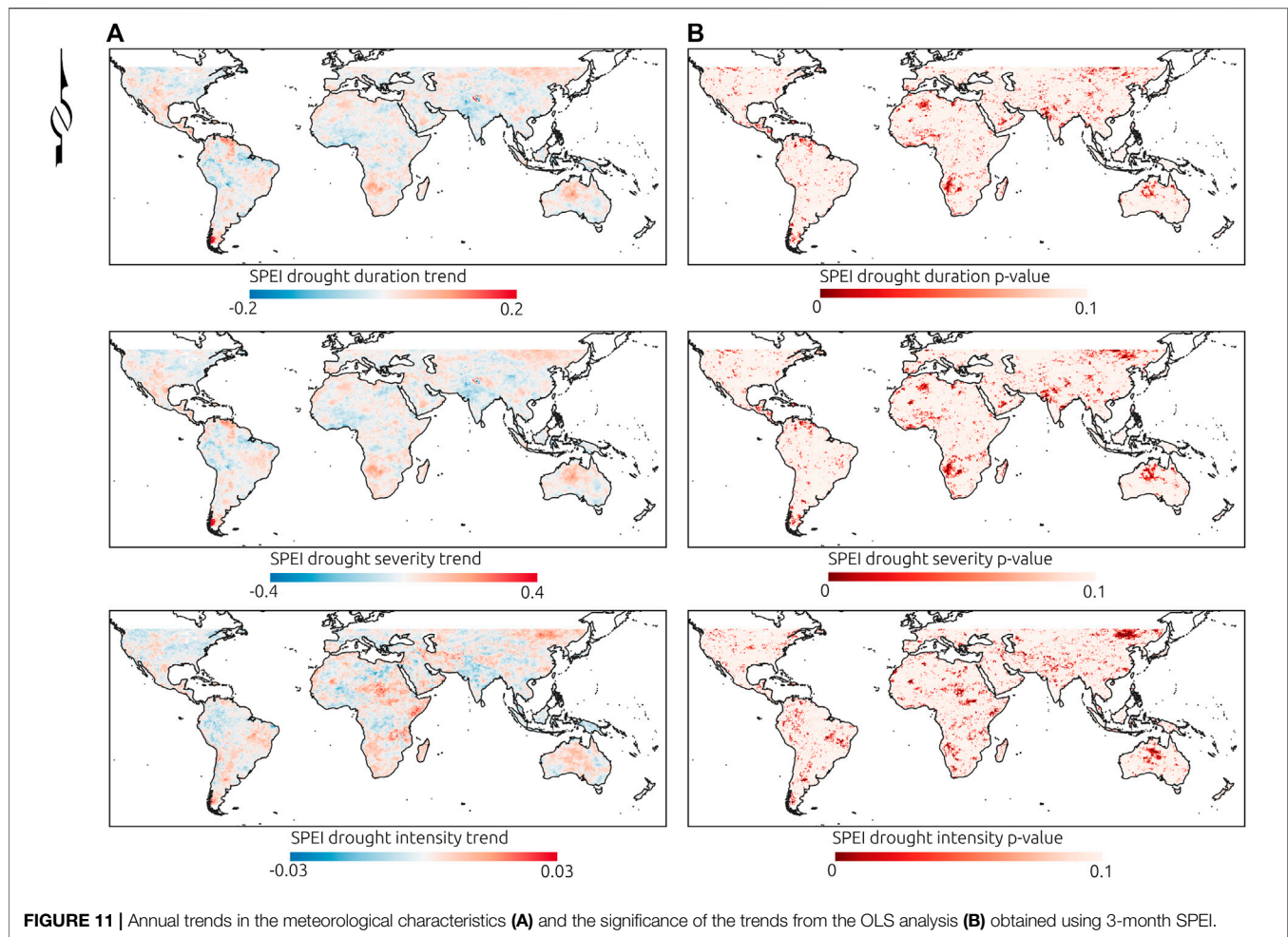tively large drought event can be observed, lasting at least 1 year. In between the −25 to −50°latitude several drought events of large severity can also be observed. Additionally, the propagation of a long lasting drought event can be observed in the 80°meridian, yet it seems to be spatially constrained.

The heat map for SVI (**Figure 13A**) indicates quite a different behaviour. The drought observed in 1983 through SPEI record can also be detected in the SVI heat map. During the 1994–1995 a large drought is evident in the vegetation based index, covering a large extent of continental surface, but with the largest severity close to the equator. Then, after a long gap (1995–2000), some drought events are observed through the vegetation index which increase in severity and propagate longer in time, especially after 2005. Another obvious

drought event occurs around the 25°parallel, which propagates over 3–4 years. The same can be observed surrounding the -25°parallel, which would be consistent with the millennium drought described in Australia (Van Dijk et al., 2013).

The largest severity in SRI occurs above the 50°parallel (**Figure 13B**). However, severe hydrological drought events can also be seen in equatorial and southern latitudes. Again, the drought events detected surrounding the equator (1983, 1993, 1998, 2016) can be also detected in the SRI severity. But one thing that stands out is the increase over time in SRI severity and its propagation period, especially after 2008, in northern latitudes, and the increase and spread in the continental coverage with time, which means that droughts are extending in space in the hydrologic subsystem.

Spatial patterns in the difference of drought impacts between subsystems are in the Supplementary materials (**Supplementary Figure S5**). While in the meteorological subsystem drought severity tends to follow some sort of interannual variability, which is especially evident surrounding the equator, with a limited propagation period, such events extend to northern and southern parallels in the vegetation subsystem, but also increasing in severity and with longer propagation from 2005. The propagation also occurs in the hydrological subsystem, but not as severe as in vegetation, and tend to increase in continental coverage in low and high latitudes, while diminishing in extent surrounding the −25 and 25°parallels.

FIGURE 11 | Annual trends in the meteorological characteristics **(A)** and the significance of the trends from the OLS analysis **(B)** obtained using 3-month SPEI.

3.5 Major Köppen Climate Groups and Drought

The distribution of pixels sampled from the mean SPEI, SVI, and SRI drought characteristics based on the major Köppen climate groups are in the Supplementary materials (**Supplementary Figure S6**). In general, greater homogeneity can be observed through more compact violins and smaller y-scale range of values. Even though distributions appear quite homogeneous in some cases, the Kruskal Wallis test indicated significant differences (*p* value < 0.05) in all drought characteristics between Köppen major groups, for all indices. Likewise, the Dunn's multiple comparison test showed strong evidence of drought differences between all major Köppen climate groups (**Supplementary Tables S1–S9**). In fact, the largest drought effects occur in different climate groups depending on the drought index. For instance, drought severity effects tend to be the strongest for Polar climates in the meteorological subsystem (using SPEI), while these are the strongest in Dry and Continental climates for the vegetation (SVI) and runoff (SRI), respectively.

Additionally, **Figure 14** highlights the difference between SVI and SPEI (left panel), and between the SRI and SPEI mean characteristics (right panel). The Polar climate group has the lowest drought duration difference between SVI and SPEI, while the largest differences occur in Dry climates, which show larger variations, but also the lowest intensity differences. Significant differences using Kruskal Wallis were found between Köppen climate groups, and in most cases, these differences were significant comparing between groups (**Supplementary Tables S10–S15**).

The largest differences between SRI and SPEI occur in Continental climates, while the Polar and Dry climate groups contain the smallest differences. Differences between SRI and SPEI differ in magnitude relative to SVI—SPEI differences, especially conditional on climate groups. Thus, for instance, the median difference in duration between SVI and SPEI is 0.5 for the Tropical, 1.0 for the Dry, 0.7 for the Temperate, 0.5 for the Continental, and 0.2 months for the Polar climates. However, these differences change to 0.6, −0.3, 0.9, 1.0, and 0.1 months for the difference between SRI and SPEI.

4 DISCUSSION

Drought propagation and temporal changes are spatially variable across the globe and linked to climate groups. Correlations
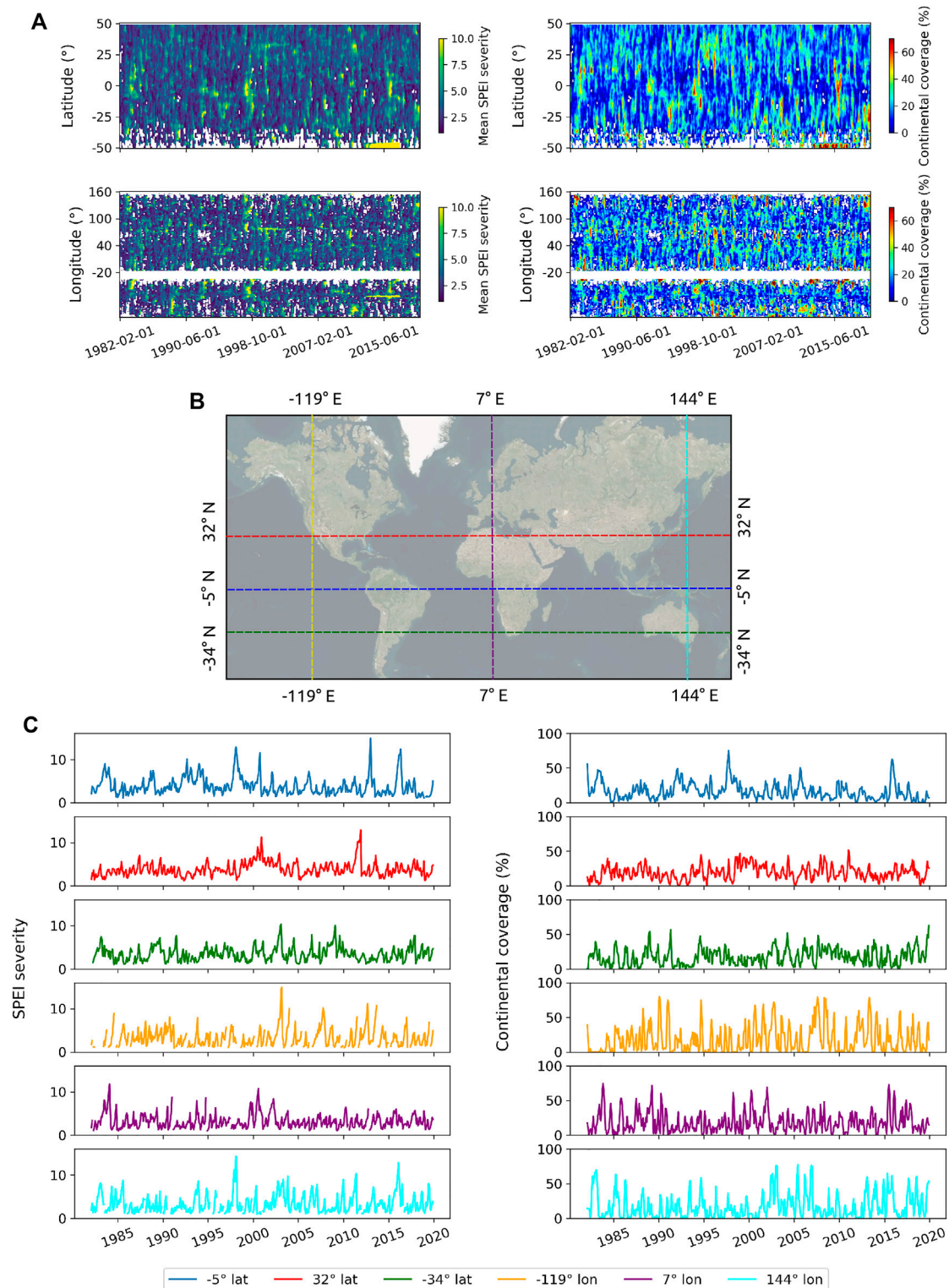
FIGURE 12 | Heat maps **(A)** of mean 3-month SPEI severity by latitude and longitude **(B)** with the corresponding latitudinal and longitudinal continental coverage [percentage of latitudinal/longitudinal continental extent affected by drought; **(C)**]. Examples of three parallel and meridian mean SPEI severity time series and their corresponding continental extents (%) are in the middle and lower panels.

FIGURE 13 | Heat maps of mean 3-month SVI severity **(A)** and 3-month SRI severity **(B)** by latitude and longitude with the corresponding latitudinal and longitudinal continental coverage (right panels).

FIGURE 14 | Differences of drought characteristics between SVI and SPEI **(A)** and between SRI and SPEI **(B)** for major Köppen climate groups.
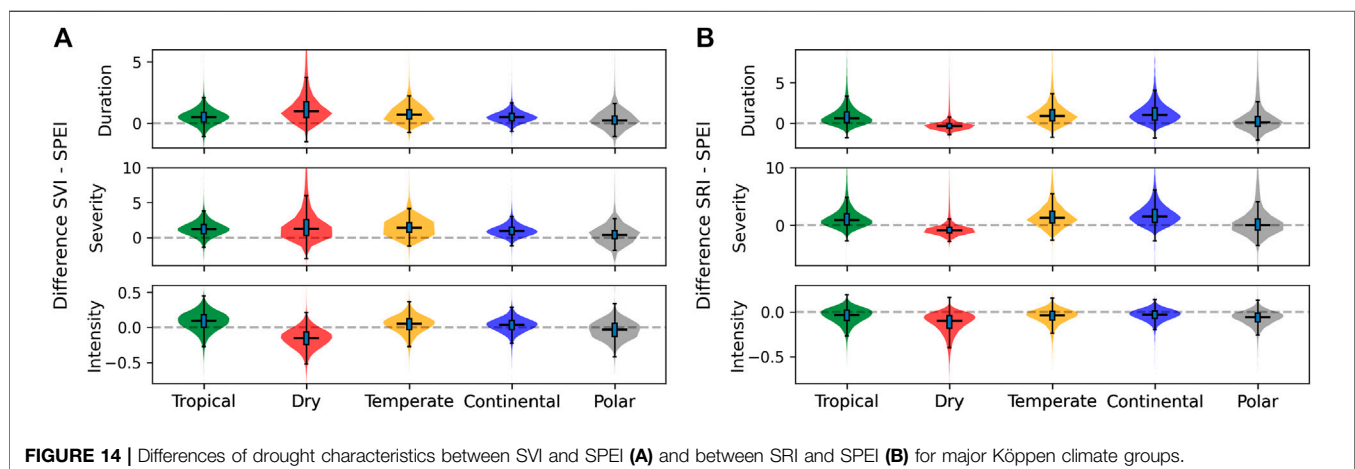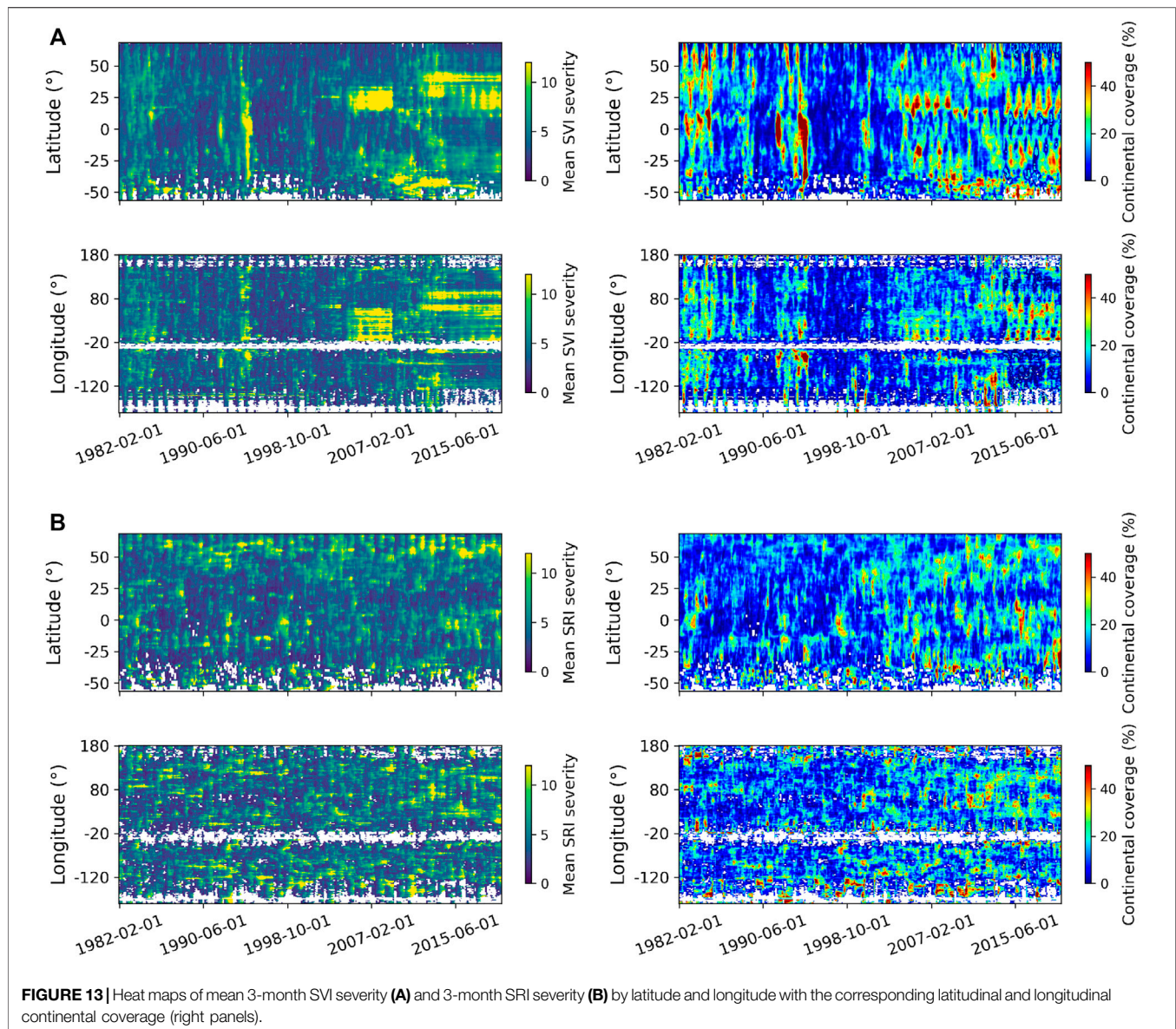
between meteorological indices (SPI and SPEI) depend on the precipitation abundance or the dominance of precipitation relative to evapotranspiration. For example, lower correlations can be observed in mid latitudes associated with areas with arid and desert climates, characterised by low rainfall and elevated evapotranspiration. Generally speaking, drought progresses through the subsystems and, as in Peña-Gallardo et al. (2019), this varies by location. The propagation lag increases from the runoff to the vegetation subsystems. Similar to other studies (Lorenzo-Lacruz et al., 2013; Sattar et al., 2019), runoff or streamflow, in most cases, have a maximum response to meteorological droughts at short time lags, e.g., in the same month on a pixel basis, or during the next few months if aggregated to a larger scale. Additionally, the severity and duration of drought tend to amplify across large regions moving from meteorological to the agricultural and the hydrological subsystems, but attenuating in intensity on dry and polar climates. However, the dominant idea that drought progresses following the meteorological-agricultural-hydrologic order (Zargar et al., 2011; Wang et al., 2016) does not necessarily apply to all regions, at least in terms of the time lag of response among subsystems (start of drought event in subsystems). In some places, the hydrological response to rainfall through runoff is almost immediate and may precede the vegetation response to drought. Differences in this lagged response would depend on catchment characteristics, land cover, vegetation, climate, and water management (Lorenzo-Lacruz et al., 2010; Vicente-Serrano et al., 2013; Barker et al., 2016; Yuan et al., 2017; Ding et al., 2021). For example, runoff/discharge may proceed faster in areas with large rainfall and with a large slope gradient, while vegetation in semiarid and subhumid biomes may take several months to respond to meteorological droughts (Vicente-Serrano et al., 2013). Yet the streamflow response to meteorological droughts may be delayed/affected by geologic/geomorphic features, the location of the gauging station relative to the basin, water storage, and water usage (Lorenzo-Lacruz et al., 2013), which may explain the drop in stations that had significant cross correlation values between SRI and SPEI, clearly distinguished among regulated river systems as in Peña-Gallardo et al. (2019).

Vegetation, on the other hand, may have drought adaptation strategies (Vicente-Serrano et al., 2013), and can strongly rely on groundwater either by irrigation (Siebert et al., 2010) or due to root growth exploring the vadose zone and even reaching aquifers (Miller et al., 2010). In this case, groundwater has been reported to have a delayed response to meteorological droughts of on average 20.1 months in the United States (Schreiner-McGraw and Ajami, 2021), which might translate into a delayed response of vegetation in areas that rely extensively on groundwater resources. Additionally, different indices can lead to different results in the lagged response of subsystems. For instance, if soil moisture is used as an indicator of agricultural drought as proposed by (Zargar et al., 2011) instead of vegetation, it might lead to a faster response than the hydrological subsystem (runoff and streamflow).

While the characterisation of meteorological drought through SPEI and SPI is widely accepted (Hayes et al., 2011; Zargar et al., 2011; Wang et al., 2016; Ault, 2020), agricultural drought indices based on NDVI are less well accepted (Hayes et al., 2011). In this case, SVI, as any vegetation standardised drought index, can be questionable, since land cover changes affect the continuity of the NDVI series, which may translate into abrupt changes, causing non-stationary behaviour (Karnieli et al., 2010; De Keersmaecker et al., 2017). Additionally, NDVI can also be affected by natural hazards, such as fires and floods (Zargar et al., 2011) and agricultural practices (harvesting). These changes can obscure the real drought response and might affect time series analysis as well as trend detection (Peters et al., 2002). However, while at the local scale these are considered relevant, at a global scale these effects may attenuate. Other indices, such as those using soil moisture, have a shorter data length, which limits their applicability (Ault, 2020).

The global drought characteristic and propagation analysis presented here can be also extrapolated to include other hydrological and economic subsystems (Wang et al., 2016; Jehanzaib and Kim, 2020). However, a clear identification of the targets for drought evaluation need to be defined. Additionally, the spatial representation of the relevant data needs to be addressed. For instance, gauging stations, monitoring wells and reservoirs refer to point estimates that, in some limited cases, can be representative of catchment conditions. This means boundaries of the spatial units for the properties being evaluated and the aggregation of meteorological or agricultural/ecological data to be used needs to be considered. Additionally, while raster data is commonly available at the global scale, hydrological streamflow data cannot really be represented well at the global scale. More general hydrological variables, such as GRACE records, have disadvantages, including low spatial resolution and relatively short length of records (Li et al., 2019). In the present study, we choose to use runoff, which is frequently available as a modelled variable in a gridded format. However, using other variables, such as streamflow or groundwater, may lead to a different propagation behaviour given the lagged response of these variables (Kuss and Gurdak, 2014; Lorenzo-Lacruz et al., 2017), which was observed in a slight increase in the lagged response using catchment discharge.

Additionally, a multi-scale analysis should be considered when studying drought and the potential effect of water usage (McKee, 1995; Lorenzo-Lacruz et al., 2010), because it requires of a regional/local component for water withdrawals (Loon et al., 2019; Rangecroft et al., 2019). As stated by Barker et al. (2016), different catchment characteristics may be responsible for the drought propagation, but also different reaches within the same river might vary in the drought propagation and response given water withdrawals (Yuan et al., 2017). This means quantifying drought may require a nested scale analysis given the complexity of processes.

Mitigation plans for drought require consideration of local/regional climate characteristics and drought impacts in different subsystems by policy makers and planners (Wilhite, 2016) given the clear spatial variation in drought propagation observed here. Drought monitoring and knowledge of drought propagation characteristics and trends give governments further tools to develop national scale drought preparedness plans. This means resources can be prioritised to cope with drought based on the

likelihood drought will amplify in the agricultural/hydrological subsystems and in time at certain locations. Additionally, the lagged drought response between subsystems can be used as an early warning by decision makers to trigger drought mitigation actions and reduce socioeconomic impacts. Similarly, at the global scale, the study of drought propagation can help to identify spatially connected regions prone to drought impacts. Overall this study maps the global temporal changes in drought and the regional extent, likely partly associated with climate change. This can help global aid and development organizations to delineate strategies for drought impact mitigation and water and food security improvement. For instance, the definition of drought resistant crops and promotion in regions/countries where drought strongly amplifies in the agricultural/ecological subsystem can reduce drought effects (Wang et al., 2014). Groundwater storage is an important subsystem to consider for drought mitigation at regional scales (Wendt et al., 2021). In drought prone regions, replenishing groundwater and soil water stocks in wet periods should be further promoted to increase water security in dry periods (Zhang et al., 2020), as groundwater reduces the large evaporation losses associated with water storage in dams (Zhao and Gao, 2019; Fuentes et al., 2020). On the other hand, a clear global concern is the increasing hydrological drought extent observed in the last years (**Figure 13B**) and its severity increase in northern latitudes. Drought effects in the hydrological and agricultural/ecological subsystems are clearly increasing in some regions, which can also be observed in trend analysis. This increase in the drought effects in these subsystems may arise as a response to a loss in catchment memory caused by a reduction in storage capacity due to climate change, which needs to be addressed.

Different drivers can lead to spatially variable dry/wet conditions (Schubert et al., 2016) such as those evaluated here. Here we observed that major climate groups lead to differences in the drought characteristics and in the propagation of drought. However, no evaluation of changes in atmospheric/oceanic circulation patterns was carried out such as in Van Dijk et al. (2013) at a smaller scale. Additionally, there is no clarity on where different drivers have preeminence at the global scale, nor the interaction between these and their hierarchical importance. Since differences in drought propagation arise, it is necessary to understand why such differences occur. These are questions that we will address in future research.

5 CONCLUSION

Drought differs in average characteristics based on different standardised drought indices. Its effects vary spatially and lead to a propagation from the meteorological subsystem towards the agricultural/ecological and hydrologic subsystems. However, the lag in the response from the meteorologic subsystem to other subsystems is also spatially variable but in general faster towards the hydrological subsystem, while this propagation is much slower reflected in the vegetation subsystem. Drought can both amplify and attenuate from one subsystem to the other, driven by differences in major Köppen climate groups. However, drought duration and severity tend to amplify progressively into the agricultural/ecologic subsystem, especially under Dry and Temperate climates, and into the hydrological subsystem, especially under Continental and Temperate climates, while attenuating in intensity in Dry and Polar climates. Drought characteristics have intensified in the last decades in several regions of the world, including areas in southern South America, central Australia, south west Africa, and central and eastern Asia, and these changes are much more evident in the vegetation and hydrological subsystems, which may be explained by a decrease in catchment memory as a consequence of climate change. The results of this study highlight the need for policy and decision makers to consider the global space and time relationships to prioritise resources for drought mitigation plans.

DATA AVAILABILITY STATEMENT

The datasets presented in this study can be found in online repositories. The names of the repository/repositories and accession number(s) can be found below: https://github.com/IFuentesSR/FES_drought/.

AUTHOR CONTRIBUTIONS

The original idea was developed by IF, and discussed with RV and JP; IF carried out the analysis and wrote the original draft, which was reviewed by RV and JP; IF wrote the final manuscript based on RV and JP suggested changes.

FUNDING

SUPPLEMENTARY MATERIAL

The Supplementary Material for this article can be found online at: https://www.frontiersin.org/articles/10.3389/fenvs.2022.788248/full#supplementary-material

REFERENCES

Abramowitz, M., and Stegun, I. A. (1964). *Handbook of Mathematical Functions with Formulas, Graphs, and Mathematical Tables*, 55. Washington: US Government printing office.

Apurv, T., Sivapalan, M., and Cai, X. (2017). Understanding the Role of Climate Characteristics in Drought Propagation. *Water Resour. Res.* 53 (11), 9304–9329. doi:10.1002/2017wr021445

Ault, T. R. (2020). On the Essentials of Drought in a Changing Climate. *Science* 368 (6488), 256–260. doi:10.1126/science.aaz5492

Barella-Ortiz, A., and Quintana-Seguí, P. (2019). Evaluation of Drought Representation and Propagation in Regional Climate Model Simulations across spain. *Hydrol. Earth Syst. Sci.* 23 (12), 5111–5131. doi:10.5194/hess-23-5111-2019

Barker, L. J., Hannaford, J., Chiverton, A., and Svensson, C. (2016). From Meteorological to Hydrological Drought Using Standardised Indicators. *Hydrol. Earth Syst. Sci.* 20 (6), 2483–2505. doi:10.5194/hess-20-2483-2016

Beguería, S., Vicente-Serrano, S. M., and Angulo-Martínez, M. (2010). A Multiscalar Global Drought Dataset: the Speibase: a New Gridded Product for the Analysis of Drought Variability and Impacts. *Bull. Amer. Meteorol. Soc.* 91 (10), 1351–1356. doi:10.1175/2010bams2988.1

Bhuiyan, C., Singh, R. P., and Kogan, F. N. (2006). Monitoring Drought Dynamics in the Aravalli Region (india) Using Different Indices Based on Ground and Remote Sensing Data. *Int. J. Appl. Earth Observation Geoinformation* 8 (4), 289–302. doi:10.1016/j.jag.2006.03.002

Bloomfield, J. P., and Marchant, B. P. (2013). Analysis of Groundwater Drought Building on the Standardised Precipitation index Approach. *Hydrol. Earth Syst. Sci.* 17 (12), 4769–4787. doi:10.5194/hess-17-4769-2013

Cavus, Y., and Aksoy, H. (2020). Critical Drought Severity/intensity-Duration-Frequency Curves Based on Precipitation Deficit. *J. Hydrol.* 584, 124312. doi:10.1016/j.jhydrol.2019.124312

Chen, N., Li, R., Zhang, X., Yang, C., Wang, X., Zeng, L., et al. (2020). Drought Propagation in Northern china plain: A Comparative Analysis of Gldas and Merra-2 Datasets. *J. Hydrol.* 588, 125026. doi:10.1016/j.jhydrol.2020.125026

Cook, B. I., Mankin, J. S., and Anchukaitis, K. J. (2018). Climate Change and Drought: From Past to Future. *Curr. Clim. Change Rep.* 4 (2), 164–179. doi:10.1007/s40641-018-0093-2

De Keersmaecker, W., Lhermitte, S., Hill, M., Tits, L., Coppin, P., and Somers, B. (2017). Assessment of Regional Vegetation Response to Climate Anomalies: A Case Study for australia Using Gimms Ndvi Time Series between 1982 and 2006. *Remote Sensing* 9 (1), 34. doi:10.3390/rs9010034

Didan, K. (2015). *Mod13a2 Modis/terra Vegetation Indices 16-day L3 Global 1km Sin Grid V006*. doi:10.5067/MODIS/MOD13A2.006

Ding, Y., Xu, J., Wang, X., Cai, H., Zhou, Z., Sun, Y., et al. (2021). Propagation of Meteorological to Hydrological Drought for Different Climate Regions in china. *J. Environ. Manage.* 283, 111980. doi:10.1016/j.jenvman.2021.111980

Dinku, T., Funk, C., Peterson, P., Maidment, R., Tadesse, T., Gadain, H., et al. (2018). Validation of the Chirps Satellite Rainfall Estimates over Eastern Africa. *Q. J. R. Meteorol. Soc.* 144, 292–312. doi:10.1002/qj.3244

Farahmand, A., and AghaKouchak, A. (2015). A Generalized Framework for Deriving Nonparametric Standardized Drought Indicators. *Adv. Water Resour.* 76, 140–145. doi:10.1016/j.advwatres.2014.11.012

Fuentes, I., van Ogtrop, F., and Vervoort, R. W. (2020). Long-term Surface Water Trends and Relationship with Open Water Evaporation Losses in the Namoi Catchment, australia. *J. Hydrol.* 584, 124714. doi:10.1016/j.jhydrol.2020.124714

Funk, C., Peterson, P., Landsfeld, M., Pedreros, D., Verdin, J., Shukla, S., et al. (2015). The Climate Hazards Infrared Precipitation with Stations-Aa New Environmental Record for Monitoring Extremes. *Sci. Data* 2 (1), 1–21. doi:10.1038/sdata.2015.66

Garreaud, R. D., Boisier, J. P., Rondanelli, R., Montecinos, A., Sepúlveda, H. H., and Veloso-Aguila, D. (2020). The central chile Mega Drought (2010-2018): A Climate Dynamics Perspective. *Int. J. Climatol* 40 (1), 421–439. doi:10.1002/joc.6219

Gill, R. B., Mayewski, P. A., Nyberg, J., Haug, G. H., and Peterson, L. C. (2007). Drought and the Maya Collapse. *Ancient Mesoam* 18 (2), 283–302. doi:10.1017/s0956536107000193

Glantz, S. A. (2002). *Primer of Biostatistics*. New York: McGraw-Hill.

Gorelick, N., Hancher, M., Dixon, M., Ilyushchenko, S., Thau, D., and Moore, R. (2017). Google Earth Engine: Planetary-Scale Geospatial Analysis for Everyone. *Remote sensing Environ.* 202, 18–27. doi:10.1016/j.rse.2017.06.031

Grose, M., Timbal, B., Wilson, L., Bathols, J., and Kent, D. (2015). The Subtropical ridge in Cmip5 Models, and Implications for Projections of Rainfall in Southeast australia. *Amoj* 65 (1), 90–106. doi:10.22499/2.6501.007

Guenang, G. M., and Kamga, F. M. (2014). Computation of the standardized precipitation index (spi) and its use to assess drought occurrences in cameroon over recent decades. *Journal of Applied Meteorology and Climatology* 53 (10), 2310–2324. doi:10.1175/jamc-d-14-0032.1

Halwatura, D., Lechner, A. M., and Arnold, S. (2015). Drought Severity-Duration-Frequency Curves: a Foundation for Risk Assessment and Planning Tool for Ecosystem Establishment in post-mining Landscapes. *Hydrol. Earth Syst. Sci.* 19 (2), 1069–1091. doi:10.5194/hess-19-1069-2015

Han, Z., Huang, S., Huang, Q., Leng, G., Wang, H., Bai, Q., et al. (2019). Propagation Dynamics from Meteorological to Groundwater Drought and Their Possible Influence Factors. *J. Hydrol.* 578, 124102. doi:10.1016/j.jhydrol.2019.124102

Hayes, M., Svoboda, M., Wall, N., and Widhalm, M. (2011). The lincoln Declaration on Drought Indices: Universal Meteorological Drought index Recommended. *Bull. Am. Meteorol. Soc.* 92 (4), 485–488. doi:10.1175/2010bams3103.1

He, C., and Li, T. (2019). Does Global Warming Amplify Interannual Climate Variability? *Clim. Dyn.* 52 (5), 2667–2684. doi:10.1007/s00382-018-4286-0

Hoffmann, L., Günther, G., Li, D., Stein, O., Wu, X., Griessbach, S., et al. (2019). From ERA-Interim to ERA5: the Considerable Impact of ECMWF's Next-Generation Reanalysis on Lagrangian Transport Simulations. *Atmos. Chem. Phys.* 19 (5), 3097–3124. doi:10.5194/acp-19-3097-2019

Hurrell, J. W., Kushnir, Y., Ottersen, G., and Visbeck, M. (2003). An Overview of the North Atlantic Oscillation. *Geophys. Monograph-American Geophys. Union* 134, 1–35. doi:10.1029/134gm01

Jain, V. K., Pandey, R. P., Jain, M. K., and Byun, H.-R. (2015). Comparison of Drought Indices for Appraisal of Drought Characteristics in the Ken River basin. *Weather Clim. Extremes* 8, 1–11. doi:10.1016/j.wace.2015.05.002

Jehanzaib, M., and Kim, T.-W. (2020). Exploring the Influence of Climate Change-Induced Drought Propagation on Wetlands. *Ecol. Eng.* 149, 105799. doi:10.1016/j.ecoleng.2020.105799

João, E. (2002). How Scale Affects Environmental Impact Assessment. *Environ. impact Assess. Rev.* 22 (4), 289–310. doi:10.1016/s0195-9255(02)00016-1

Karnieli, A., Agam, N., Pinker, R. T., Anderson, M., Imhoff, M. L., Gutman, G. G., et al. (2010). Use of Ndvi and Land Surface Temperature for Drought Assessment: Merits and Limitations. *J. Clim.* 23 (3), 618–633. doi:10.1175/2009jcli2900.1

Katsanos, D., Retalis, A., and Michaelides, S. (2016). Validation of a High-Resolution Precipitation Database (Chirps) over cyprus for a 30-year Period. *Atmos. Res.* 169, 459–464. doi:10.1016/j.atmosres.2015.05.015

Kerr, R. A. (1998). Sea-floor Dust Shows Drought Felled Akkadian empire. *Science* 279 (5349), 325–326. doi:10.1126/science.279.5349.325

Kuss, A. J. M., and Gurdak, J. J. (2014). Groundwater Level Response in U.S. Principal Aquifers to ENSO, NAO, PDO, and AMO. *J. Hydrol.* 519, 1939–1952. doi:10.1016/j.jhydrol.2014.09.069

Lehner, B., and Grill, G. (2013). Global River Hydrography and Network Routing: Baseline Data and New Approaches to Study the World's Large River Systems. *Hydrol. Process.* 27 (15), 2171–2186. doi:10.1002/hyp.9740

Lehner, B., Liermann, C. R., Revenga, C., Vörösmarty, C., Fekete, B., Crouzet, P., et al. (2011). High-resolution Mapping of the World's Reservoirs and Dams for Sustainable River-flow Management. *Front. Ecol. Environ.* 9 (9), 494–502. doi:10.1890/100125

Li, B., Rodell, M., Kumar, S., Beaudoing, H. K., Getirana, A., Zaitchik, B. F., et al. (2019). Global grace Data Assimilation for Groundwater and Drought Monitoring: Advances and Challenges. *Water Resour. Res.* 55 (9), 7564–7586. doi:10.1029/2018wr024618

Li, L., She, D., Zheng, H., Lin, P., and Yang, Z.-L. (2020). Elucidating Diverse Drought Characteristics from Two Meteorological Drought Indices (Spi and Spei) in china. *J. Hydrometeorology* 21 (7), 1513–1530. doi:10.1175/jhm-d-19-0290.1

Lorenzo-Lacruz, J., Garcia, C., and Morán-Tejeda, E. (2017). Groundwater Level Responses to Precipitation Variability in Mediterranean Insular Aquifers. *J. Hydrol.* 552, 516–531. doi:10.1016/j.jhydrol.2017.07.011

Lorenzo-Lacruz, J., Vicente-Serrano, S., González-Hidalgo, J., López-Moreno, J., and Cortesi, N. (2013). Hydrological Drought Response to Meteorological Drought in the Iberian peninsula. *Clim. Res.* 58 (2), 117–131. doi:10.3354/cr01177

Lorenzo-Lacruz, J., Vicente-Serrano, S. M., López-Moreno, J. I., Beguería, S., García-Ruiz, J. M., and Cuadrat, J. M. (2010). The Impact of Droughts and Water Management on Various Hydrological Systems in the Headwaters of the Tagus River (central spain). *J. Hydrol.* 386 (1-4), 13–26. doi:10.1016/j.jhydrol.2010.01.001

Maity, R., Ramadas, M., and Govindaraju, R. S. (2013). Identification of Hydrologic Drought Triggers from Hydroclimatic Predictor Variables. *Water Resour. Res.* 49 (7), 4476–4492. doi:10.1002/wrcr.20346

Mantua, N. J., and Hare, S. R. (2002). The pacific Decadal Oscillation. *J. oceanography* 58 (1), 35–44. doi:10.1023/a:1015820616384

Mao, D., Wang, Z., Luo, L., and Ren, C. (2012). Integrating Avhrr and Modis Data to Monitor Ndvi Changes and Their Relationships with Climatic Parameters in Northeast china. *Int. J. Appl. Earth Observation Geoinformation* 18, 528–536. doi:10.1016/j.jag.2011.10.007

McKee, T. B., Doesken, N. J., and Kleist, J. (1993). "The Relationship of Drought Frequency and Duration to Time Scales," in Proceedings of the 8th Conference on Applied Climatology (Boston, 179–183.17

McKee, T. B. (1995). Drought Monitoring with Multiple Time Scales. Proceedings of 9th Conference on Applied Climatology. Boston.

McNally, A., Arsenault, K., Kumar, S., Shukla, S., Peterson, P., Wang, S., et al. (2017). A Land Data Assimilation System for Sub-saharan Africa Food and Water Security Applications. *Sci. Data* 4 (1), 170012–170019. doi:10.1038/sdata.2017.12

Miller, G. R., Chen, X., Rubin, Y., Ma, S., and Baldocchi, D. D. (2010). Groundwater Uptake by Woody Vegetation in a Semiarid Oak savanna. *Water Resour. Res.* 46 (10). doi:10.1029/2009wr008902

Nalbantis, I., and Tsakiris, G. (2009). Assessment of Hydrological Drought Revisited. *Water Resour. Manage.* 23 (5), 881–897. doi:10.1007/s11269-008-9305-1

Olauson, J. (2018). Era5: The New champion of Wind Power Modelling? *Renew. Energ.* 126, 322–331. doi:10.1016/j.renene.2018.03.056

Paredes-Trejo, F. J., Barbosa, H. A., and Lakshmi Kumar, T. V. (2017). Validating Chirps-Based Satellite Precipitation Estimates in Northeast brazil. *J. arid environments* 139, 26–40. doi:10.1016/j.jaridenv.2016.12.009

Peña-Gallardo, M., Vicente-Serrano, S. M., Hannaford, J., Lorenzo-Lacruz, J., Svoboda, M., Domínguez-Castro, F., et al. (2019). Complex Influences of Meteorological Drought Time-Scales on Hydrological Droughts in Natural Basins of the Contiguous Unites States. *J. Hydrol.* 568, 611–625. doi:10.1016/j.jhydrol.2018.11.026

Pereira, L. S., Allen, R. G., Smith, M., and Raes, D. (2015). Crop Evapotranspiration Estimation with Fao56: Past and Future. *Agric. Water Management* 147, 4–20. doi:10.1016/j.agwat.2014.07.031

Peters, A. J., Walter-Shea, E. A., Ji, L., Vina, A., Hayes, M., and Svoboda, M. D. (2002). Drought Monitoring with Ndvi-Based Standardized Vegetation index. *Photogrammetric Eng. remote sensing* 68 (1), 71–75.

Pinzon, J., and Tucker, C. (2014). A Non-stationary 1981-2012 Avhrr Ndvi3g Time Series. *Remote sensing* 6 (8), 6929–6960. doi:10.3390/rs6086929

Potopová, V., Štěpánek, P., Možný, M., Türkott, L., and Soukup, J. (2015). Performance of the Standardised Precipitation Evapotranspiration index at Various Lags for Agricultural Drought Risk Assessment in the Czech republic. *Agric. For. Meteorology* 202, 26–38. doi:10.1016/j.agrformet.2014.11.022

Rangecroft, S., Van Loon, A. F., Maureira, H., Verbist, K., and Hannah, D. M. (2019). An Observation-Based Method to Quantify the Human Influence on Hydrological Drought: Upstream-Downstream Comparison. *Hydrological Sci. J.* 64 (3), 276–287. doi:10.1080/02626667.2019.1581365

Rubel, F., and Kottek, M. (2010). Observed and Projected Climate Shifts 1901-2100 Depicted by World Maps of the Köppen-Geiger Climate Classification. *metz* 19 (2), 135–141. doi:10.1127/0941-2948/2010/0430

Sattar, M. N., Lee, J.-Y., Shin, J.-Y., and Kim, T.-W. (2019). Probabilistic Characteristics of Drought Propagation from Meteorological to Hydrological Drought in south korea. *Water Resour. Manage.* 33 (7), 2439–2452. doi:10.1007/s11269-019-02278-9

Schreiner-McGraw, A. P., and Ajami, H. (2021). Delayed Response of Groundwater to Multi-Year Meteorological Droughts in the Absence of Anthropogenic Management. *J. Hydrol.* 603, 126917. doi:10.1016/j.jhydrol.2021.126917

Schubert, S. D., Stewart, R. E., Wang, H., Barlow, M., Berbery, E. H., Cai, W., et al. (2016). Global Meteorological Drought: A Synthesis of Current Understanding with a Focus on Sst Drivers of Precipitation Deficits. *J. Clim.* 29 (11), 3989–4019. doi:10.1175/jcli-d-15-0452.1

Shukla, S., and Wood, A. W. (2008). Use of a Standardized Runoff index for Characterizing Hydrologic Drought. *Geophys. Res. Lett.* 35 (2). doi:10.1029/2007gl032487

Shumway, R. H., and Stoffer, D. S. (2017). *Time Series Analysis and its Applications with R Examples.* Fourth Edition. Springer.

Siebert, S., Burke, J., Faures, J. M., Frenken, K., Hoogeveen, J., Döll, P., et al. (2010). Groundwater Use for Irrigation - a Global Inventory. *Hydrol. Earth Syst. Sci.* 14 (10), 1863–1880. doi:10.5194/hess-14-1863-2010

Smith, T. G. (2017), 'Pmdarima: Arima Estimators for Python'. Availableat: http://www.alkaline-ml.com/pmdarima

Sohrabi, M. M., Ryu, J. H., Abatzoglou, J., and Tracy, J. (2015). Development of Soil Moisture Drought index to Characterize Droughts. *J. Hydrol. Eng.* 20 (11), 04015025. doi:10.1061/(asce)he.1943-5584.0001213

Son, N. T., Chen, C. F., Chen, C. R., Chang, L. Y., and Minh, V. Q. (2012). Monitoring Agricultural Drought in the Lower Mekong basin Using Modis Ndvi and Land Surface Temperature Data. *Int. J. Appl. Earth Observation Geoinformation* 18, 417–427. doi:10.1016/j.jag.2012.03.014

Stagge, J. H., Tallaksen, L. M., Gudmundsson, L., Van Loon, A. F., and Stahl, K. (2015). Candidate Distributions for Climatological Drought Indices (SPI and SPEI). *Int. J. Climatol.* 35 (13), 4027–4040. doi:10.1002/joc.4267

Stahl, K., Vidal, J.-P., Hannaford, J., Tijdeman, E., Laaha, G., Gauster, T., et al. (2020). The Challenges of Hydrological Drought Definition, Quantification and Communication: an Interdisciplinary Perspective. *Proc. IAHS* 383, 291–295. doi:10.5194/piahs-383-291-2020

Sternberg, T. (2012). Chinese Drought, Bread and the arab spring. *Appl. Geogr.* 34, 519–524. doi:10.1016/j.apgeog.2012.02.004

Tarek, M., Brissette, F. P., and Arsenault, R. (2020). Evaluation of the Era5 Reanalysis as a Potential Reference Dataset for Hydrological Modelling over north america. *Hydrol. Earth Syst. Sci.* 24 (5), 2527–2544. doi:10.5194/hess-24-2527-2020

Tirivarombo, S., Osupile, D., and Eliasson, P. (2018). Drought Monitoring and Analysis: Standardised Precipitation Evapotranspiration index (Spei) and Standardised Precipitation index (Spi). *Phys. Chem. Earth, Parts A/B/C* 106, 1–10. doi:10.1016/j.pce.2018.07.001

Trnka, M., Hayes, M., Jurečka, F., Bartošová, L., Anderson, M., Brázdil, R., et al. (2018). Priority Questions in Multidisciplinary Drought Research. *Clim. Res.* 75 (3), 241–260. doi:10.3354/cr01509

Van Dijk, A. I. J. M., Beck, H. E., Crosbie, R. S., de Jeu, R. A. M., Liu, Y. Y., Podger, G. M., et al. (2013). The Millennium Drought in Southeast australia (2001-2009): Natural and Human Causes and Implications for Water Resources, Ecosystems, Economy, and Society. *Water Resour. Res.* 49 (2), 1040–1057. doi:10.1002/wrcr.20123

Van Loon, A. F., Kumar, R., and Mishra, V. (2017). Testing the Use of Standardised Indices and grace Satellite Data to Estimate the European 2015 Groundwater Drought in Near-Real Time. *Hydrol. Earth Syst. Sci.* 21 (4), 1947–1971. doi:10.5194/hess-21-1947-2017

Van Loon, A. F., Rangecroft, S., Coxon, G., Breña Naranjo, J. A., Van Ogtrop, F., and Van Lanen, H. A. J. (2019). Using Paired Catchments to Quantify the Human Influence on Hydrological Droughts. *Hydrol. Earth Syst. Sci.* 23 (3), 1725–1739. doi:10.5194/hess-23-1725-2019

Van Loon, A. F., Van Huijgevoort, M. H. J., and Van Lanen, H. A. J. (2012). Evaluation of Drought Propagation in an Ensemble Mean of Large-Scale Hydrological Models. *Hydrol. Earth Syst. Sci.* 16 (11), 4057–4078. doi:10.5194/hess-16-4057-2012

Van Loon, A. F., and Van Lanen, H. A. J. (2013). Making the Distinction between Water Scarcity and Drought Using an Observation-Modeling Framework. *Water Resour. Res.* 49 (3), 1483–1502. doi:10.1002/wrcr.20147

Vicente-Serrano, S. M., and Beguería, S. (2016). Comment on 'Candidate Distributions for Climatological Drought Indices (SPI and SPEI)' by James H. Staggeet Al. *Int. J. Climatol.* 36 (4), 2120–2131. doi:10.1002/joc.4474

Vicente-Serrano, S. M., Beguería, S., and López-Moreno, J. I. (2010). A Multiscalar Drought index Sensitive to Global Warming: the Standardized Precipitation Evapotranspiration index. *J. Clim.* 23 (7), 1696–1718. doi:10.1175/2009jcli2909.1

Vicente-Serrano, S. M., Gouveia, C., Camarero, J. J., Beguería, S., Trigo, R., López-Moreno, J. I., et al. (2013). Response of Vegetation to Drought Time-Scales across Global Land Biomes. *Proc. Natl. Acad. Sci.* 110 (1), 52–57. doi:10.1073/pnas.1207068110

Vicente-Serrano, S. M., López-Moreno, J. I., Beguería, S., Lorenzo-Lacruz, J., Azorin-Molina, C., and Morán-Tejeda, E. (2012). Accurate Computation of a Streamflow Drought index. *J. Hydrol. Eng.* 17 (2), 318–332. doi:10.1061/(asce)he.1943-5584.0000433

Vicente-Serrano, S. M., López-Moreno, J. I., Gimeno, L., Nieto, R., Morán-Tejeda, E., Lorenzo-Lacruz, J., et al. (2011). A Multiscalar Global Evaluation of the Impact of Enso on Droughts. *J. Geophys. Res. Atmospheres* 116 (D20). doi:10.1029/2011jd016039

Wanders, N., Loon, A. F. V., and Van Lanen, H. A. (2017). *'Frequently Used Drought Indices Reflect Different Drought Conditions on Global Scale'*, Hydrology And Earth System Sciences Discussions, 1–16. doi:10.5194/hess-2017-512

Wang, Q., Wu, J., Lei, T., He, B., Wu, Z., Liu, M., et al. (2014). Temporal-spatial Characteristics of Severe Drought Events and Their Impact on Agriculture on a Global Scale. *Quat. Int.* 349, 10–21. doi:10.1016/j.quaint.2014.06.021

Wang, W., Ertsen, M. W., Svoboda, M. D., and Hafeez, M. (2016). 'Propagation of Drought: from Meteorological Drought to Agricultural and Hydrological Drought'. *Hindawi* 2016, 6547209.

Wendt, D. E., Van Loon, A. F., Scanlon, B. R., and Hannah, D. M. (2021). Managed Aquifer Recharge as a Drought Mitigation Strategy in Heavily-Stressed Aquifers. *Environ. Res. Lett.* 16 (1), 014046. doi:10.1088/1748-9326/abcfe1

Wilhite, D. A. (2016). "Drought-management Policies and Preparedness Plans: Changing the Paradigm from Crisis to Risk Management," in *Land Restoration* (Elsevier), 443–462. doi:10.1016/b978-0-12-801231-4.00007-0

Wu, J., Miao, C., Tang, X., Duan, Q., and He, X. (2018). A Nonparametric Standardized Runoff index for Characterizing Hydrological Drought on the Loess Plateau, china. *Glob. Planet. Change* 161, 53–65. doi:10.1016/j.gloplacha.2017.12.006

Xiao, M., Zhang, Q., and Singh, V. P. (2015). Influences of Enso, Nao, Iod and Pdo on Seasonal Precipitation Regimes in the Yangtze River basin, china. *Int. J. Climatol* 35 (12), 3556–3567. doi:10.1002/joc.4228

Xu, Y., Zhang, X., Wang, X., Hao, Z., Singh, V. P., and Hao, F. (2019). Propagation from Meteorological Drought to Hydrological Drought under the Impact of Human Activities: A Case Study in Northern china. *J. Hydrol.* 579, 124147. doi:10.1016/j.jhydrol.2019.124147

Yuan, X., Zhang, M., Wang, L., and Zhou, T. (2017). Understanding and Seasonal Forecasting of Hydrological Drought in the Anthropocene. *Hydrol. Earth Syst. Sci.* 21 (11), 5477–5492. doi:10.5194/hess-21-5477-2017

Zargar, A., Sadiq, R., Naser, B., and Khan, F. I. (2011). A Review of Drought Indices. *Environ. Rev.* 19, 333–349. doi:10.1139/a11-013

Zhang, H., Xu, Y., and Kanyerere, T. (2020). A Review of the Managed Aquifer Recharge: Historical Development, Current Situation and Perspectives. *Phys. Chem. Earth, Parts A/B/CParts A/B/C* 118-119, 102887. doi:10.1016/j.pce.2020.102887

Zhang, Y., and Li, Z. (2020). Uncertainty Analysis of Standardized Precipitation Index Due to the Effects of Probability Distributions and Parameter Errors. *Front. Earth Sci.* 8, 76. doi:10.3389/feart.2020.00076

Zhao, G., and Gao, H. (2019). Estimating Reservoir Evaporation Losses for the united states: Fusing Remote Sensing and Modeling Approaches. *Remote Sensing Environ.* 226, 109–124. doi:10.1016/j.rse.2019.03.015

Zhou, J., Li, Q., Wang, L., Lei, L., Huang, M., Xiang, J., et al. (2019). Impact of Climate Change and Land-Use on the Propagation from Meteorological Drought to Hydrological Drought in the Eastern Qilian Mountains. *Water* 11 (8), 1602. doi:10.3390/w11081602

Zhu, J. (2013). Impact of Climate Change on Extreme Rainfall across the united states. *J. Hydrol. Eng.* 18 (10), 1301–1309. doi:10.1061/(asce)he.1943-5584.0000725

Assessing the Joint Impact of Climatic Variables on Meteorological Drought Using Machine Learning

Yuexin Zheng, Xuan Zhang, Jingshan Yu *, Yang Xu, Qianyang Wang, Chong Li and Xiaolei Yao

College of Water Sciences, Beijing Normal University, Beijing, China

With the intensification of climate change, the coupling effect between climate variables plays an important role in meteorological drought identification. However, little is known about the contribution of climate variables to drought development. This study constructed four scenarios using the random forest model during 1981–2016 in the Luanhe River Basin (LRB) and quantitatively revealed the contribution of climate variables (precipitation; temperature; wind speed; solar radiation; relative humidity; and evaporative demand) to drought indices and drought characteristics, that is, the Standard Precipitation Evapotranspiration Index (SPEI), Standard Precipitation Index (SPI), and Evaporative Demand Drought Index (EDDI). The result showed that the R^2 of the model is above 0.88, and the performance of the model is good. The coupling between climate variables can not only amplify drought characteristics but also lead to the SPEI, SPI, and EDDI showing different drought states when identifying drought. With the decrease in timescale, the drought intensity of the three drought indices became stronger and the drought duration shortened, but the drought frequency increased. For short-term drought (1 mon), four scenarios displayed that the SPEI and SPI can identify more drought events. On the contrary, compared with the SPEI and SPI, the EDDI can identify long and serious drought events. This is mainly due to the coupling of evaporative demand, solar radiation, and wind speed. Evaporation demand also contributed to the SPEI, but the contribution (6–13%) was much less than the EDDI (45–85%). For SPEI-1, SPEI-3, and SPEI-6, the effect of temperature cannot be ignored. These results are helpful to understand and describe drought events for drought risk management under the condition of global warming.

Keywords: meteorological drought, quantification, climate variables, coupling effect, random forest

INTRODUCTION

Drought is one of the most serious natural disasters affecting the development of human society (Deb et al., 2019). Droughts are generally classified into meteorological droughts, agricultural droughts, hydrological droughts, and socioeconomic droughts (Wilhite and Glantz, 1985; Esfahanian et al., 2017). Meteorological drought, in general, precedes other droughts and is defined according to the degree of the lack of precipitation in an area over some time. One of the most prominent and widespread concerns is regional drought caused by climate warming and precipitation change, which has caused serious disasters worldwide (Zhai et al., 2010). For example, in 2014, California experienced a serious drought event that was mainly caused by an extreme lack of precipitation

and high temperature and was a record-breaking event in the last century (Griffin and Anchukaitis, 2014). In 2011, high temperatures and low soil moisture in Texas aggravated drought events, and rainfall was extremely scarce (Karl et al., 2012). It is estimated that drought in California and Texas caused economic losses of $2.7 billion and $7.7 billion, respectively (Shukla et al., 2015). Therefore, a better understanding of drought characteristics and their physical variable is significant for monitoring and forecasting drought.

The drought indices are the basis of the quantitative analysis of drought (Richard and Heim, 2002). In different regions, the different meteorological, hydrological, and underlying surface conditions lead to the complexity of drought formation (Ojha et al., 2013; Wang et al., 2013; Kousari et al., 2014). This is due to different drought indices having different physical meanings. For example, the Standard Precipitation Index (SPI) is characterized by multiple timescales, but it only considers the impact of precipitation deficit on drought (Yerdelen et al., 2021). The Palmer drought severity index (PDSI) is a representative drought index based on the principle of water balance (Zhang et al., 2019). However, the indices mainly reflect the comprehensive changes in precipitation and temperature and do not fully reflect the evaporation response under the background of climate change, which may lead to deviation of drought assessment results. Vicente-Serrano et al. (2010) further proposed the Standard Precipitation Evapotranspiration Index (SPEI) and introduced the potential evapotranspiration term, based on the advantages and disadvantages of the PDSI and SPI (Yang et al., 2020). This index not only has the characteristics of the SPI index with multiple timescales but also considers the effect of temperature change on drought. In recent decades, it has been a widespread tradition to monitor and understand drought using factors driven by precipitation and temperature only (Gocic and Trajkovic, 2013; Li et al., 2019). Among the available indices, the SPEI and SPI are two of the most widely used ones (He et al., 2011).

Many studies have found that most drought indices are driven by precipitation alone or affected by both precipitation and evaporation (Farahmand and AghaKouchak, 2015; Wen et al., 2020). Additionally, many researchers considered that the alterability of precipitation was even more obvious than that of other variables (McEvoy et al., 2012; Vicente–Serrano et al., 2014; Wang et al., 2015). However, under climate variation, this supposition is challenged because of the increasing demand for temperature and evaporation (Sheffield and Wood, 2008; Milly and Dunne, 2016). Meanwhile, the research focus in the field of drought monitoring is turning to the demand of water imbalance. The most typical work is the evaporative demand drought index (EDDI) proposed by Hobbins et al. (2012), which considers the radiative forcing term and the advection forcing term in the evaporation process (Blonquist et al., 2010). This index can provide near real-time information about the occurrence or persistence of abnormal evaporative demand in an area and can ignore the influence of underlying surface types in drought monitoring and assessment (Mo and Lettenmaier, 2015). Therefore, many people are committed to assessing the occurrence of drought from the perspective of insufficient

precipitation and increased evaporation (Liu et al., 2017; Rehana and Monish, 2021).

On the whole, most studies only emphasize the impact of precipitation on drought change or consider the flash drought caused by evaporation anomalies affected by temperature, wind speed, and radiation (Wang et al., 2016; Chen et al., 2019; Wang et al., 2020). The reduction of sunshine hours and wind speed is the main reason for the evaporation reduction; especially, evaporation plays an important role in soil water balance (Abramopoulos et al., 1988). The increase in temperature and the limited decrease in precipitation may aggravate the drought occurrence (Sheffield et al., 2012; Sun and Ma, 2015; Song et al., 2019). It is necessary to consider the coupling effect of multiple climate variables on drought, such as precipitation; evaporative demand; wind speed; temperature; solar radiation; and relative humidity, which may reduce uncertainty to the process of drought analysis and accurate prediction (Sun et al., 2017). Nevertheless, so far, due to the different responses of different drought indices to climate variables, there are still challenges in quantifying the impact of climate variables on drought. Most studies used multiple regression, canonical correlation, and principal component analysis to analyze the driving factors of climate change (Luedeling et al., 2013; Kaiwei Li et al., 2020). These methods are mainly analyzed from a qualitative point of view, but cannot quantitatively evaluate the importance of each factor. In recent years, with the progress of artificial intelligence, machine learning technology has been widely used in the assessment of climate change (Leroux et al., 2017; Masroor et al., 2021). Random forest (RF) algorithm is an integrated learning algorithm based on the decision tree proposed. The learning effect of this integration method is often greater than the sum of its parts (Jiangyu Wang et al., 2019). The RF does not need to consider the multicollinearity problem faced by general regression analysis (Wang et al., 2018). At the same time, it can calculate the nonlinear interaction between variables and reflect the interaction between variables and is not sensitive to outliers. In the existing algorithms, the RF can evaluate the importance of each feature in classification.

With these considerations, this study focuses on quantifying the response of drought change to climate variables. Specifically, the study aims to 1) analyze the temporal distinctions of the SPI, SPEI, and EDDI with 1-, 3-, 6-, and 12-month timescales of the Luanhe River Basin (LRB); 2) reveal the characteristics of the drought intensity, drought duration, and drought frequency of the SPI, SPEI, and EDDI at different timescales; and 3) quantify the contribution of climate variables to drought indices and drought characteristics at different timescales by setting different scenarios based on the RF model. The findings from this study can provide a reference for the development of drought early warning systems in arid and semiarid areas.

STUDY AREA

This study assessed changes in drought indices in the LRB, northern part of the North China Plain (**Figure 1**). The LRB comprises a large portion of the Haihe River Basin. The

FIGURE 1 | Topography of the study domain and spatial distribution of meteorological stations.
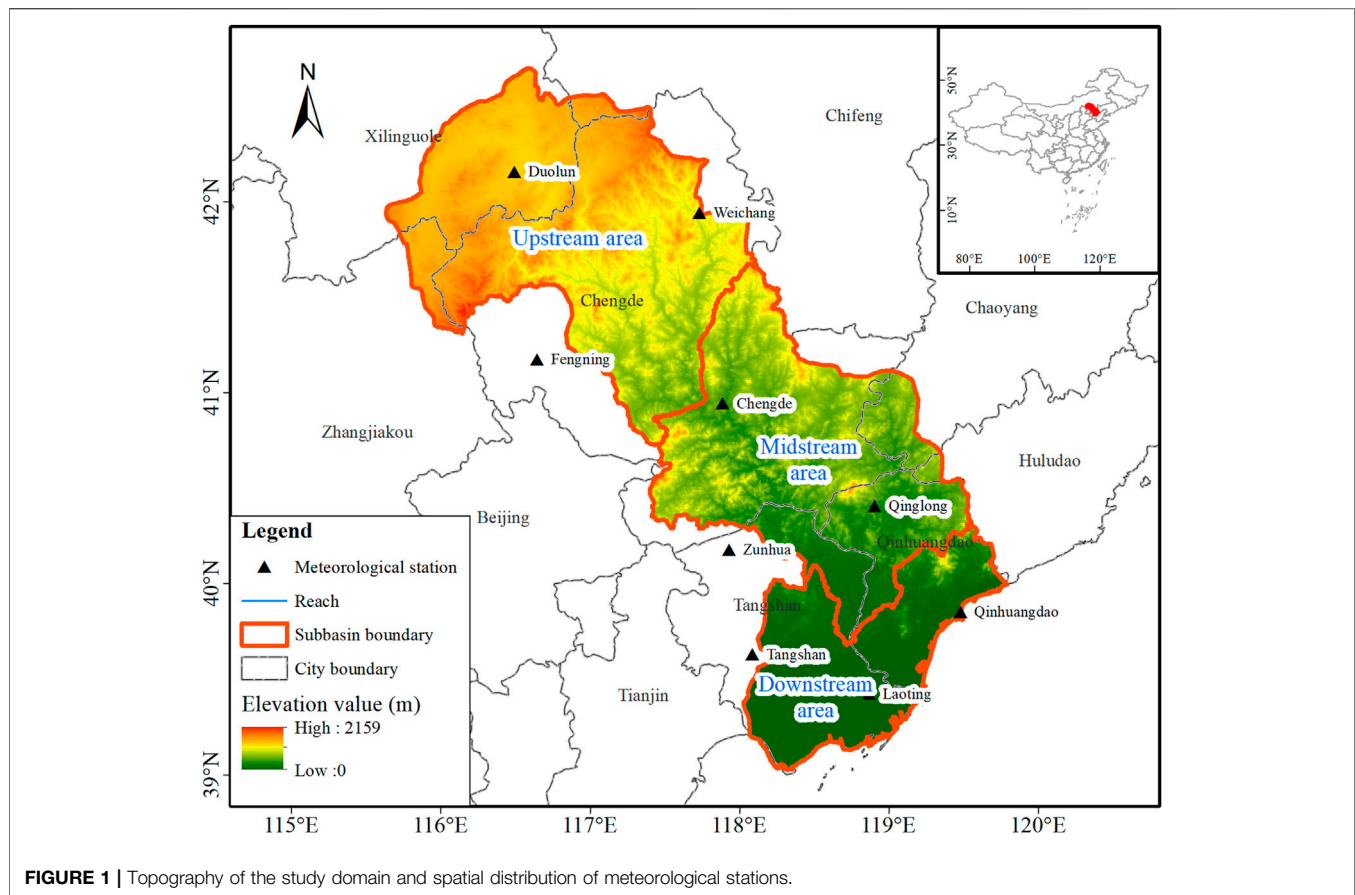
latitude ranges from 39.04°N to 42.73°N, and the longitude ranges from 115.56°E to 119.84°E. The Luanhe River, with a length of 888 km and a drainage area of 44,750 km², derives from Bayanguertu Mountain and flows into the Bohai Bay (Yang et al., 2019; Wu et al., 2020). The basin topography rises obviously from southeast to northwest. The LRB is in a semiarid area with a temperate continental monsoon climate. The annual temperature decreases from 11 to 1°C from southeast to northwest (Xu et al., 2019). The region has an average annual precipitation of 560 mm, approximately 80% of which occurs from July to August. The uneven spatial and temporal distribution leads to the occurrence of drought. The elevation of the basin reaches 2,159 m, with the terrain decreasing from northwest to southeast.

The LRB is one of the most important ecological barriers of Beijing, Tianjin, and Hebei and is also a water source and water retention area in Tianjin and Tangshan. Saihanba Forest Plain, a famous afforestation project worldwide, is located in this region (Wu et al., 2020). In recent decades, runoff and meteorological conditions have been altered, resulting in water resource shortages and severe drought events. Due to the increasing impact of global climate change, drought in the LRB occurs frequently, especially after 2000. It not only caused large-scale disasters in the basin but also caused serious losses. Furthermore, from 1981 to 2016, there was no significant change in

precipitation, while evaporative demand showed a significant decreasing trend ($p < 0.01$) and the temperature increased significantly ($p < 0.01$). The effect of climate change caused by evaporative demand and temperature on drought should not be ignored.

MATERIALS AND METHODS

Data Collection

This study focuses on a comparative analysis of drought indices in the LRB. The daily observation meteorological records of nine stations for 1981–2016 were collected from the National Meteorological Information Center (http://data. cma.cn/) with strict quality control, including precipitation; maximum, average, and minimum temperatures; wind speed; solar radiation; relative humidity; and pan evaporation. The time coverage of weather data can be as high as 99.6%. The missing data were interpolated using the arithmetic mean of adjacent days. The data quality and credibility were cross validated using nonparametric tests, involving the Mann–Whitney homogeneity tests and Kendall autocorrelation test (Heim, 2002; Yao et al., 2018). The results showed that the stability and randomness of weather data are fixed in the critical range of the data, and the statistical significance level was 5%.

Computation of Drought Indices

This study considered three drought indices including the SPI, SPEI, and EDDI. The SPI utilized the Gamma distribution to fit the cumulative monthly precipitation time series to quantify the meteorological drought (Vicente–Serrano et al., 2010). For the SPI value, when the timescale is k months, the water surplus/deficit accumulation of a month is the sum of the water surplus/deficit of the previous k–1 month and the current month. Compared with the SPI, the SPEI, the calculation of which was similar to that of the SPI, considered the influence of evaporative demand. Among them, evaporative demand is the ability to control the evaporation process of various surfaces underlying the atmosphere. This study used the Penman–Monteith formula to approximately estimate evaporative demand, which was provided by the Food and Agricultural Organization (FAO) in 1965 (Frank et al., 2017). The calculation formula is as follows:

$$E_0 = \frac{0.408\Delta\left(R_n + L_n - G\right)}{\Delta + \gamma\left(1 + 0.34U\right)}\frac{86400}{10^6}$$
$$+ \frac{\gamma\frac{900}{T_{air}}}{\Delta + \gamma\left(1 + 0.34U\right)}\frac{U\left(e_{sat} - e_a\right)}{10^3} \quad (1)$$

where E_0 is the evaporative demand in mm day^{-1}; Δ is the slope of saturated vapor pressure for 2 m in Pa K^{-1}; γ represents the psychrometric constant in Pa K^{-1}; R_n and L_n represent the solar radiation and short-wave radiation, respectively, in W m^{-2}; G is the downward ground heat flux in W m^{-2}; U is the wind speed for 2 m in m s^{-1}; T_{air} is the average of T_{max} and T_{min} in °C; and e_{sat} and e_a represent the saturated and actual vapor pressures, respectively, in Pa.

The relationship between evaporative demand and pan evaporation in the LRB from 1981 to 2016 was analyzed by using the existing meteorological data, and the correlation coefficient was 0.906 (see **Supplementary Materials**; **Supplementary Figure. S1**), which illustrated that the calculation results of evaporative demand can represent the average E_0 of the study area. The SPEI used the cumulative change between the monthly precipitation and evaporative demand to replace the variation in precipitation. The cumulative change meant the surplus and deficit of climatic water. The inverse standard normal distribution is used to convert the cumulative probability density functions to the value of the SPEI and SPI.

The EDDI uses a nonparametric method that is different from the SPEI and SPI (Hobbins et al., 2016). The EDDI is obtained by sorting the accumulated value of evaporative demand every day within a set timescale to construct the distribution probability of E_0 and normalize it. This probability-based method permits more comparisons of consistency between the EDDI and the SPEI, SPI, and other standard indices (Farahmand and AghaKouchak, 2015; Hobbins et al., 2016).

The EDDI is multi-scale in space and time. This index can be estimated at a point (or pixel) by applying the spatial average evaporative demand of a region. The aggregation periods might differ from 1 day to 1 month or more. The cumulative

TABLE 1 | Drought level based on the EDDI, SPEI, and SPI.

Drought level	EDDI	SPEI	SPI
Normal	(0–0.5]	(-0.5–0]	(-0.5–0]
Light drought	(0.5–1]	(-1, -0.5]	(-1, -0.5]
Moderate drought	(1.0–1.5]	(-1.5, -1]	(-1.5, -1]
Severe drought	(1.5–2]	(-2, -1.5]	(-2, -1.5]
Extreme drought	≥2	≤-2	≤-2

distribution probability of evaporative demand on a research timescale is calculated as follows:

$$P\left(E_{0_i}\right) = \frac{i - 0.33}{n + 0.33} \quad (2)$$

where $P\left(E_{0i}\right)$ is the empirical probability of E_{0i}; i is 1 for maximum E_0, which represents the rank of accumulated E_0 in the study period; and n is the number of observations in the series being ranked. Based on the reverse normal distribution described by Vicente–Serrano et al. (2010), the EDDI is calculated as follows:

$$EDDI = W - \frac{C_0 + C_1 W + C_2 W}{1 + d_1 W + d_2 W^2 + d_3 W^3} \quad (3)$$

The constants in the formula are defined as follows: $C_0 = 2.515517$, $C_1 = 0.802853$, $C_2 = 0.010328$, $d_1 = 1.432788$, $d_2 = 0.189269$, and $d_3 = 0.001308$. When $P\left(E_{0i}\right) \leq 0.5$, $W = \sqrt{-2\ln\left[P(E_{0i})\right]}$, and when $P\left(E_{0i}\right) > 0.5$, $W = \sqrt{-2\ln\left[1 - P(E_{0i})\right]}$, and the sign of the EDDI needs to be reversed.

We divided the drought indices into five grades, which were based on the classification system to define drought or wet intensities (McEvoy et al., 2016; Yao et al., 2018) (**Table 1**). The positive or negative SPI and SPEI values represented wet or dry conditions, respectively. The value of −0.5 was used as the division standard, while for the EDDI, it was reversed. The negative EDDI value (less than 0.5) indicated that it was wetter than normal, and a positive value (more than 0.5) indicated that it was more arid than normal. Drought intensity increased with increasing EDDI value.

Definition of Drought Characteristics

We first compared the variation characteristics of the SPI, SPEI, and EDDI on 1-, 3-, 6-, 12-month scales from 1981 to 2016. Second, this study used drought duration, drought intensity, and drought frequency to identify and assess the underlying drought characteristics of the SPEI, SPI, and EDDI at 1-, 3-, 6-, and 12-month scales. Generally, the run theory is used to identify and describe drought events (Yevjevich, 1967). The run is defined as a part of the time series X_t, in which all values are lower or higher than the selected threshold X_0 (**Supplementary Figure S2**). The run theory is used to express the drought duration and drought intensity (Montaseri and Amiratee, 2017). When the drought index value is less than −0.5, it is considered that the month is the beginning of the drought event. However, the drought event is considered over until the value of the drought index is greater

TABLE 2 | Information of the four scenarios for the contribution of drought change.

Scenarios	Schemes	Variable	Impact indicators	Drought indices	Sample points
Scenario 1	a	Precipitation (P); evaporative demand (E_0); wind speed (Ws); temperature (T); relative humidity (Rh); solar radiation (Sr)	E_0; Ws; T; Rh; Sr for 1-month scale	EDDI-1	432
	b		P; Ws; T; Rh; Sr for 1-month scale	SPI-1	432
	c		P; E_0; Ws; T; Rh; Sr for 1-month scale	SPEI-1	432
Scenario 2	d		E_0; Ws; T; Rh; Sr for 3-month scale	EDDI-3	430
	e		P; Ws; T; Rh; Sr for 3-month scale	SPI-3	430
	f		P; E_0; Ws; T; Rh; Sr for 3-month scale	SPEI-3	430
Scenario 3	g		E_0; Ws; T; Rh; Sr for 6-month scale	EDDI-6	427
	h		P; Ws; T; Rh; Sr for 6-month scale	SPI-6	427
	i		P; E_0; Ws; T; Rh; Sr for 6-month scale	SPEI-6	427
Scenario 4	j		E_0; Ws; T; Rh; Sr for 12-month scale	EDDI-12	421
	k		P; Ws; T; Rh; Sr for 12-month scale	SPI-12	421
	l		P; E_0; Ws; T; Rh; Sr for 12-month scale	SPEI-12	421

than −0.5. Drought duration is defined as the sum of consecutive months of all drought events. Drought intensity refers to the average of the indices' values from the beginning to the end of the drought. The drought intensity is used to assess the severity of the drought. The drought frequency is the mean number of drought events per year.

Quantitative Evaluation Based on the RF Model

To reveal the response of drought change to climate variables, the RF model is applied to quantify the contribution of each climate variable (precipitation; evaporative demand; wind speed; temperature; solar radiation; and relative humidity) to the SPEI, SPI, and EDDI. The RF is an integrated model which can achieve classification or regression goals. On the whole, in the training set, the RF is not responsive to the noise, which makes it more beneficial to obtaining a robust model and avoiding overfitting conditions (Prasad et al., 2019). The RF is widely used in hydrometeorology to extract relative features (Amiri et al., 2019). For more information about the RF, see the work of Chen et al. (2020) and Kursa and Rudnicki (2010).

Construction of RF Model Under Different Scenarios

In this study, we set up 4 scenarios and 12 schemes to quantitatively evaluate the influence degree between drought change and climate variables based on the RF model from 1981 to 2016. Considering that the SPI is not affected by evaporative demand, only the contribution of precipitation; wind speed; temperature; solar radiation; and relative humidity to the SPI is explored. The SPEI considered these six variables. At

TABLE 3 | The performance evaluation of the RF model.

| Scenarios	Schemes	Training		Validation	
		R^2	MSE	R^2	MSE
Scenario 1	a	0.98	0.02	0.90	0.04
	b	0.97	0.03	0.89	0.03
	c	0.97	0.02	0.88	0.03
Scenario 2	d	0.95	0.01	0.94	0.08
	e	0.97	0.05	0.91	0.09
	f	0.91	0.01	0.90	0.04
Scenario 3	g	0.96	0.03	0.95	0.10
	h	0.96	0.06	0.91	0.08
	i	0.96	0.01	0.88	0.03
Scenario 4	j	0.97	0.05	0.88	0.05
	k	0.98	0.01	0.96	0.04
	l	0.98	0.04	0.97	0.07

the same time, the EDDI ignored the impact of precipitation. The number of samples obtained was randomly assigned according to the ratio of 7:3 into the training set and the testing set. The maximum depth of decision trees is 10, and the number of decision trees is 2000. The specific scenario information is shown in **Table 2**.

Verification of the RF Model

The R^2 and mean absolute error (MSE) coefficients were used to evaluate the results of the model (Guo et al., 2021). Among them, MAE evaluated the deviation between the real value and the predicted value, that is, the actual size of the prediction error. The
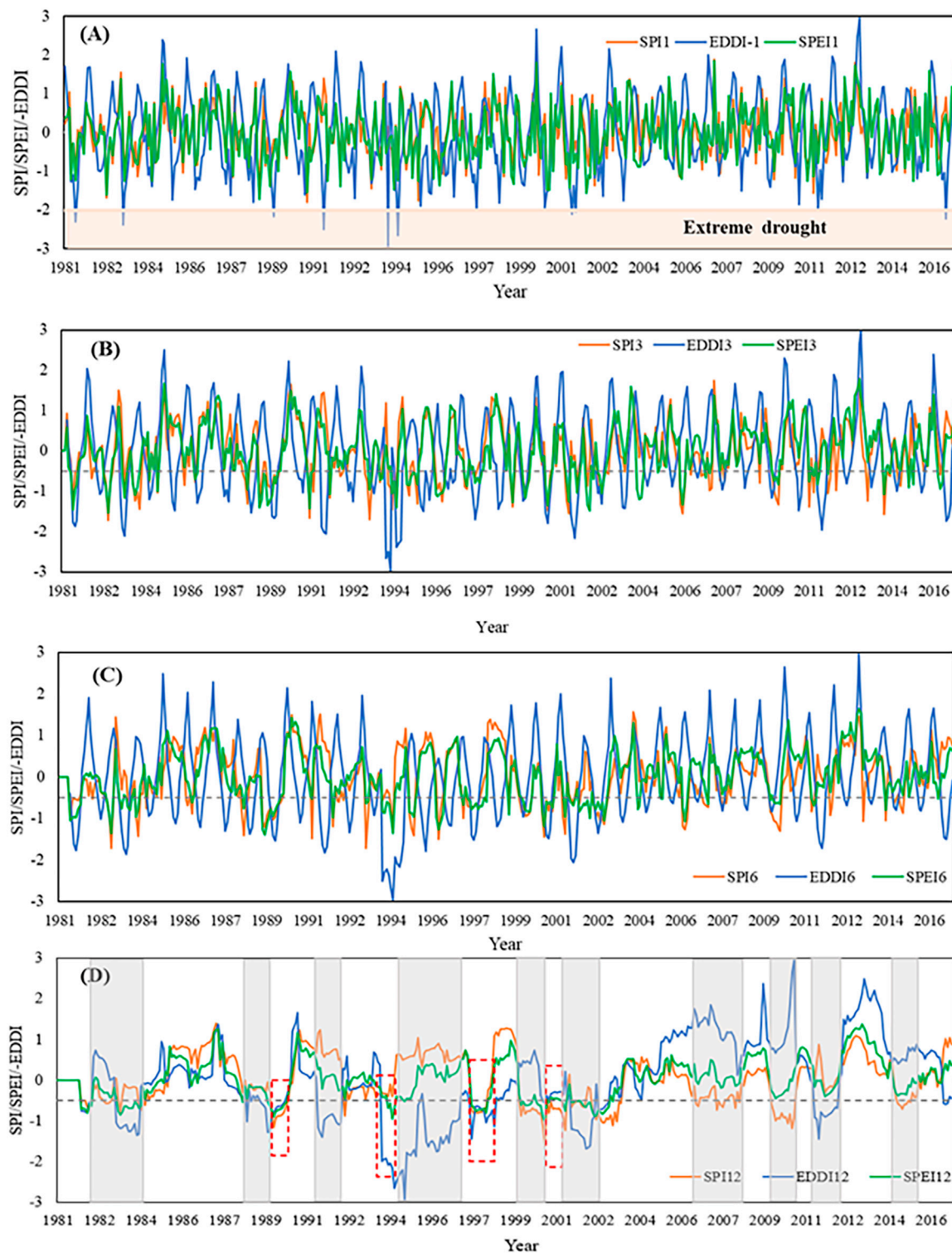
FIGURE 2 | Temporal evolution of the SPI, SPEI, and EDDI for 1-month **(A)**, 3-month **(B)**, 6-month **(C)**, and 12-month **(D)** timescales. It is noted that the shaded area represents the range of the extreme drought conditions (SPEI, SPI, and EDDI ≤ -2); the black dotted lines represent the dividing line between wet and drought states (the value is −0.5); the grey shaded areas highlight when the three indices have opposite states; and the red wireframe indicates when the three indices identify different drought levels.
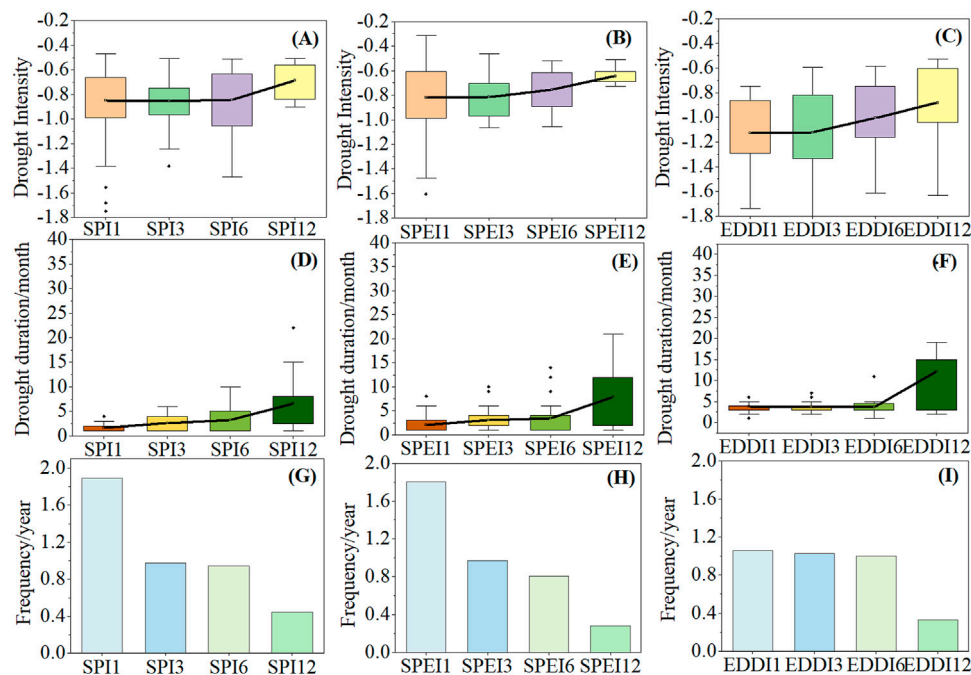
FIGURE 3 | Drought intensity **(A–C)**, duration **(D–F)**, and frequency **(G–I)** of the SPEI, EDDI, and SPI at 1-, 3-, 6-, and 12-month timescales in the LRB between 1981 and 2016 (it is noted that the black horizontal line represents the average value of drought characteristics at different scales; black dots mean outliers; the range of boxes represents the 75% quantile and the 25% quantile; and the whiskers mean the 75% quantile and 25% quantile of 1.5 times, respectively.)

smaller the MAE value, the better the model quality and the more accurate the prediction. **Table 3** shows the performances of the RF model. The results showed that the R^2 of the training set is between 0.91–0.98. In addition, the validation set is above 0.88. The value of the MAE is below 0.1, indicating that the model can calculate the contribution of climate variables better.

RESULTS

Temporal Variation in Drought Indices

Figure 2 presents the evolution characteristics of the SPI, SPEI, and EDDI at the 1-, 3-, 6-, and 12-month timescales over the LRB from 1981–2016. The three drought indices showed similarities and differences with the different timescales. For the convenience of comparison, we took the value of the EDDI as the opposite number, and less than −0.5 in the figure represented drought. The shaded area identified extreme drought states of the SPEI, SPI, and EDDI (**Figure 2A**). We found that extreme drought events occurred in 1981, 1983, 1989, 1991, 1994, 1997, 2001, and 2016, as in **Figure 2A**, which was similar to the historical drought years in the LRB (Yixuan Wang et al., 2019). Compared with the 3-, 6-, and 12-month timescales (**Figures 2B–D**), the EDDI, SPEI, and SPI curves fluctuated more abruptly at the 1-month timescale. Moreover, the SPI curve was similar with the SPEI (**Figures 2B,C**). However, the EDDI was different from the SPEI and SPI.
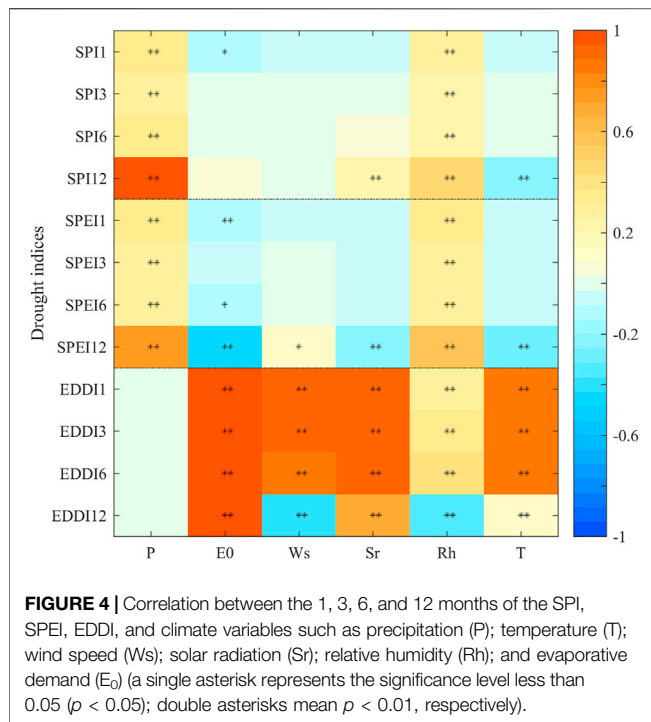
At the 12-month timescale, the grey shaded areas indicate when the SPEI, SPI, and EDDI have opposite states (**Figure 2D**). In 1983, 1988, 1990–1991, 1994–1996, 2002, and 2011, the EDDI

showed drought states (values less than −0.5), while the SPEI and SPI displayed wet states (values more than −0.5). However, the SPEI and SPI showed drought states, while the EDDI showed wet states in 1982, 1992, 1999–2000 and 2002, 2006–2007, 2008–2009, and 2014. Under drought conditions, the red wireframe highlights when the three indices had different abilities to identify drought. In 1989 and 1997, the SPI and SPEI performed better than the EDDI. Especially in 1989, the SPI and SPEI showed moderate drought states, while the EDDI showed a light drought state. In 1993 and 2001, the EDDI performed better than the SPEI and SPI. Especially in 1993, the EDDI showed extreme drought states, while the SPI and SPEI showed light drought and moderate drought states, respectively. This meant that the three drought indices were different in identifying drought severity. However, the SPI, SPEI, and EDDI showed the same wet/drought states for the other years, which indicated that the SPI, SPEI, and EDDI were consistent.

Drought Characteristics at Different Time Scales

Due to the complexity of drought, the drought intensity, frequency, and duration under different timescales were studied to have a comprehensive understanding of drought. **Figures 3A–C** displayed that the shorter the timescale, the greater the drought intensity. In particular, the average drought intensity of the EDDI was greater than that of the SPEI and SPI at 1-, 3-, 6-, and 12-month scales. This illustrated that the EDDI can identify more severe drought

FIGURE 4 | Correlation between the 1, 3, 6, and 12 months of the SPI, SPEI, EDDI, and climate variables such as precipitation (P); temperature (T); wind speed (Ws); solar radiation (Sr); relative humidity (Rh); and evaporative demand (E$_0$) (a single asterisk represents the significance level less than 0.05 ($p < 0.05$); double asterisks mean $p < 0.01$, respectively).

than the SPEI and SPI, especially in short-term drought. The drought intensity of the SPI did not change significantly in 1-, 3-, 6-mon scales. From SPEI-3 to SPEI-12, the average drought intensity decreased from −0.81 to −0.64.

Figure 3D–F showed that, with the increase in timescale, the drought duration became longer. Especially for EDDI-12, the average duration of drought (more than 12 months) was higher than that for SPEI-12 (7.9 months) and SPI-12 (6.5 months). Furthermore, the drought duration for EDDI-1 (3.7 months) was longer than that for SPEI-1 (2.1 months) and SPI-1 (1.7 months). This indicated that the EDDI was better than the SPEI and SPI in identifying short-term drought (1 mon) and long-term drought (12 mon). For seasonal drought (3 mon) and semiannual drought (6 mon), the SPEI was better than the SPI.

The drought frequency decreased with the increase in timescale (**Figures 3G–I**), especially SPEI-3 and SPI-3. The drought frequency of SPI-1 (1.8 times/year) and SPEI-1 (1.8 times/year) was higher than that of EDDI-1 (1.0 times/ year). For 3 months, there was no significant difference among the three drought indices. For 6 months, the drought frequency of SPI-6 was less than that of SPEI-6 and EDDI-6. On the contrary, for long-term drought, SPI-12 can identify more drought events than SPEI-12 and EDDI-12.

## Correlation Between Drought Indices and Climate Variables

Although drought variations of the EDDI, SPEI, and SPI were mainly influenced by precipitation and evaporative demand, other climate variables cannot be ignored. **Figure 4** showed the Spearman correlation among the three drought indices

and climate variables at 1-, 3-, 6-, 12- month scales. We found that the SPEI and SPI were positively correlated not only with precipitation ($p < 0.01$) but also the relative humidity ($p < 0.01$), although the correlation coefficient was low. Surprisingly, the correlation of SPI-12 and SPEI-12 with precipitation reached 0.98 ($p < 0.01$) and 0.77 ($p < 0.01$), respectively. In the meantime, the SPEI also displayed a significant positive correlation with evaporative demand (Spearman correlation coefficient is −0.47, $p < 0.01$) and a negative correlation with temperature and solar radiation (Spearman correlation coefficient is −0.23 and 0.29, $p < 0.01$).

Generally, under the different timescales, the correlation between the EDDI and evaporative demand is the highest, fluctuating from 0.92 to 0.98 ($p < 0.01$). Moreover, wind speed, solar radiation, and temperature were also highly related to EDDI at 1-, 3-, 6-month scales, indicating that these variables were also main factors affecting the change of the EDDI. Yet, at the 12-month scale, the correlation between solar radiation and temperature with drought indices was weakened. The correlation between wind speed and relative humidity with the EDDI changed from positive correlation to negative correlation, and the value of the correlation coefficient also decreased. Compared with other variables, relative humidity has little effect on the EDDI under the different timescales.

Contributions of the Climate Variables to the Drought Index Variation

This study set up four scenarios and twelve schemes under the different timescales, to quantitatively characterize the impact of climate variables on drought index changes based on the RF model. **Figure 5** shows that the contribution of evaporative demand, wind speed, and solar radiation to the EDDI reaches more than 87%. It was obvious that evaporative demand contributed the most to the EDDI, up to 45–85%, and the contribution was higher than that of wind speed and solar radiation. Nevertheless, it is not worth mentioning the contribution of relative humidity and temperature to the
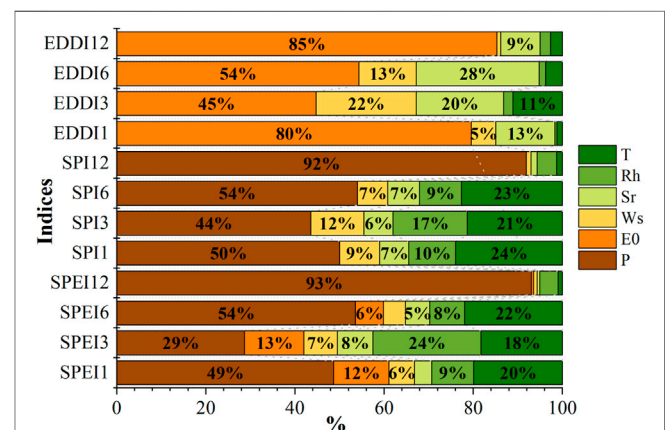
FIGURE 5 | Contribution of climate variables to drought indices are based on the RF model at 1-, 3-, 6-, 12-month timescales.
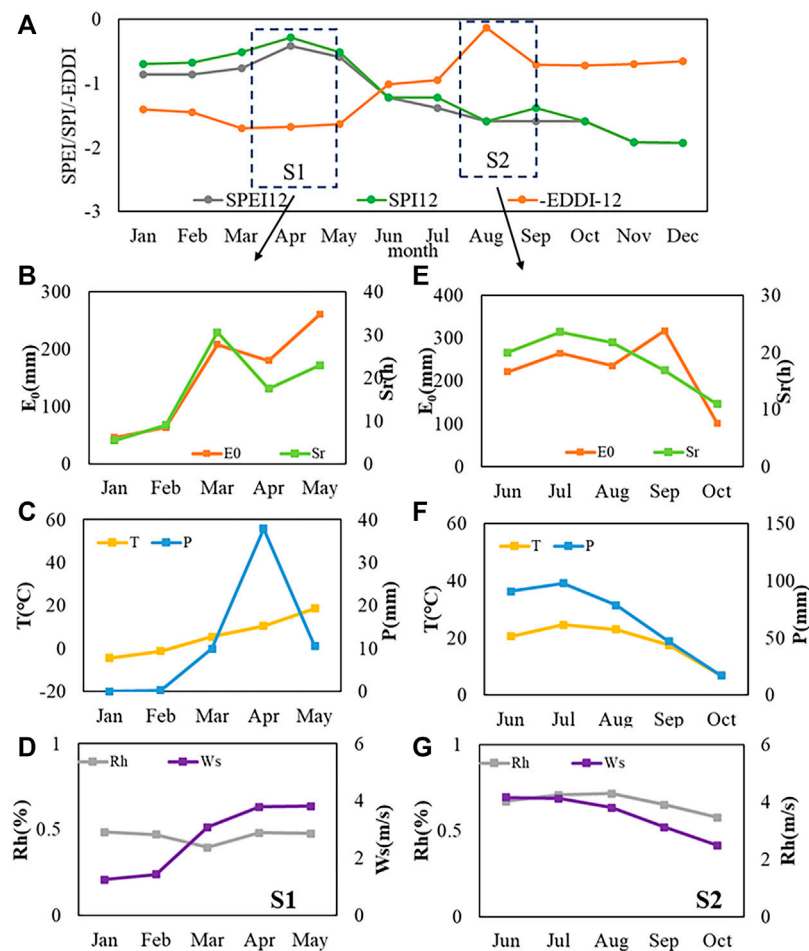
FIGURE 6 | Temporal variations in the SPEI, SPI, EDDI **(A)**, and driving factors in different situations (situation 1 (S1) and situation 2 (S2)) in 2002. Among them, **(B–D)** and **(E–G)** represent Evaporation demand(E0) and Solar radiation (Sr); Temperature (T) and Precipitation (P); Relative humidity (Rh) and Wind speed (Ws) in S1 and S2 respectively.

EDDI. For EDDI-3 and EDDI-6 in scenarios 3 and 4, the coupling contribution of wind speed and solar radiation was close to that of evaporative demand, and the solar radiation was greater than wind speed.

For SPI-12 in scenario 4, the precipitation was the dominant factor, contributing 92%. However, for short-term drought (SPI-1) in scenario 1, the contribution of precipitation decreased significantly. By contrast, the wind speed, solar radiation, temperature, and relative humidity increased in varying degrees at a 1-mon scale. The temperature contribution to the SPI increased from 1% (SPI-12) to 24% (SPI-1), which indicated that the shorter the timescale, the more intense the impact of climate variables other than precipitation on the SPI.

For the SPEI, the contribution of precipitation is much higher than that of evaporative demand. Besides, the contribution of temperature to the SPEI should not be neglected, especially for SPEI-1, SPEI-3, and SPEI-6, with a contribution of 20, 18, and 22%. So far , the wind speed and solar radiation contribution to

the SPEI has been weak, which indicated to a certain extent that the precipitation and temperature have a great impact on the SPEI.

DISCUSSION

Climate Variables Lead to the Differences Among the Drought Indices

We found that the EDDI, SPEI, and SPI showed the opposite states when it came to drought recognition (**Figure 2D**). Especially in 2002, a severe drought year, the drought indices showed two opposite states. The occurrence of this phenomenon can be explicated by the fact that climate variables cause the differences among the EDDI, SPEI, and SPI. Most of the results were consistent with ours (Nam et al., 2015; Noguera et al., 2021). Tirivarombo et al. (2018) believed that the difference between the SPEI and SPI was mainly due to the temperature which increased
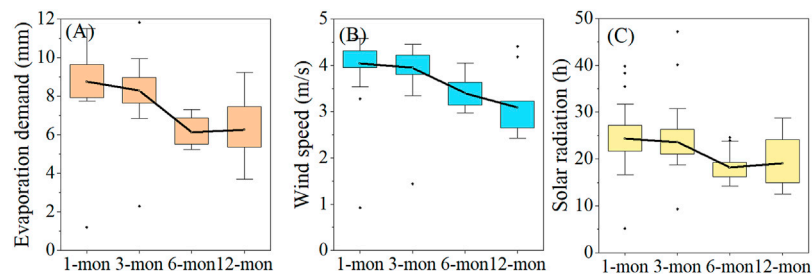
FIGURE 7 | Differences in the values of different contributing variables ((**A**) Evaporation demand(E0); (**B**) Wind speed (Ws); (**C**) Solar radiation (Sr)) to the EDDI at different timescales.

the evapotranspiration rate, which in turn increased the evaporative demand, while the SPI only considered the single input variable of precipitation. In addition, their study differed from ours in that it only thought about the effects of precipitation, temperature, and evaporative demand, while not introducing variables such as wind speed, solar radiation, and relative humidity. In 2002, situation 1 (S1) of **Figure 2D** showed that the EDDI identified the dry state, while the SPEI and SPI identified the wet state in April (**Figure 6A**). This result is mainly because precipitation and temperature have a large upward trend starting in March (**Figures 6A,C**), with an increase of 73.6 and 48.4%, respectively. However, relative humidity and wind speed also have different degrees of increase. Although relative humidity is positive, the sensitivity of the EDDI to the relative humidity in this region is small, which leads to little contribution to the EDDI in S1. Therefore, the SPEI and SPI identify the wet state in April. In addition, when evaporative demand (69.6%), solar radiation (70.5%), and wind speed (53.2%) began to increase in February, the drought identified by the EDDI increased from moderate drought to severe drought (**Figure 6A**).

In contrast, situation 2 (S2) showed that the SPEI and SPI identified the dry state, while the EDDI identified the wet state in August (**Figure 6A**). The driving factors evaporative demand (12.5%), solar radiation (8.3%), and wind speed (8.3%) provided negative contributions to the EDDI (**Figures 6E,G**). However, from June to August, compared with evaporative demand and solar radiation, the contribution of relative humidity and temperature to the EDDI was small despite fluctuations (**Figures 6F,G**). This led the EDDI to identify the wet state in August. The decrease in precipitation (24.3%) led to the aggravation of drought identified by the SPEI and SPI in July. After August, the rapid increase in evaporative demand (34.9%) led to a decrease in the EDDI, which resulted in the EDDI showing a drought state. Consequently, the influence of these variables on the drought index should not be ignored.

The Response of the Drought Characteristics to Climate Variables

Drought intensity, drought duration, and drought frequency are affected by different timescales (Satish Kumar et al., 2021). We

found that compared with the SPEI and SPI, the EDDI can identify drought events with higher drought intensity and longer
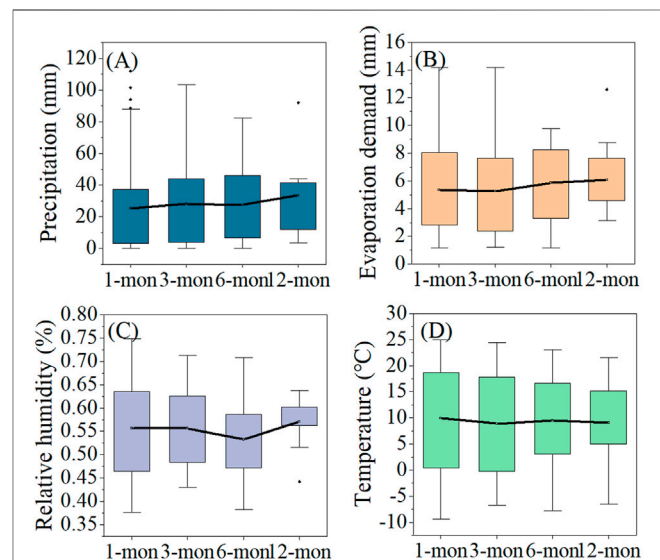
FIGURE 8 | Differences in the values of different contributing variables ((**A**) Precipitation (P); (**B**) Evaporation demand (E0); (**C**) Relative humidity (Rh); (**D**) Temperature (T)) to the SPEI at different timescales.

duration (**Figure 2**). However, the SPEI and SPI can identify drought events more frequently than the EDDI, especially short-term drought (1 mon). From 1981 to 2016, the alteration of precipitation was not obvious at any scale, while evaporative demand did not. Generally, when the change of evaporative demand is greater than that of precipitation, drought is more sensitive to evaporative demand than precipitation (Qin et al., 2015), which indicates that evaporative demand plays a relativity important role in the drought of the LRB. This further proved that the drought intensity and drought duration of the EDDI were higher than those of the SPEI and SPI, which was mainly due to the joint effect of evaporation, wind speed, and solar radiation. Compared with EDDI-12, the drought intensity of EDDI-1 increased by 28%, the average drought duration increased by 8 months, and the evaporation, wind speed, and radiation
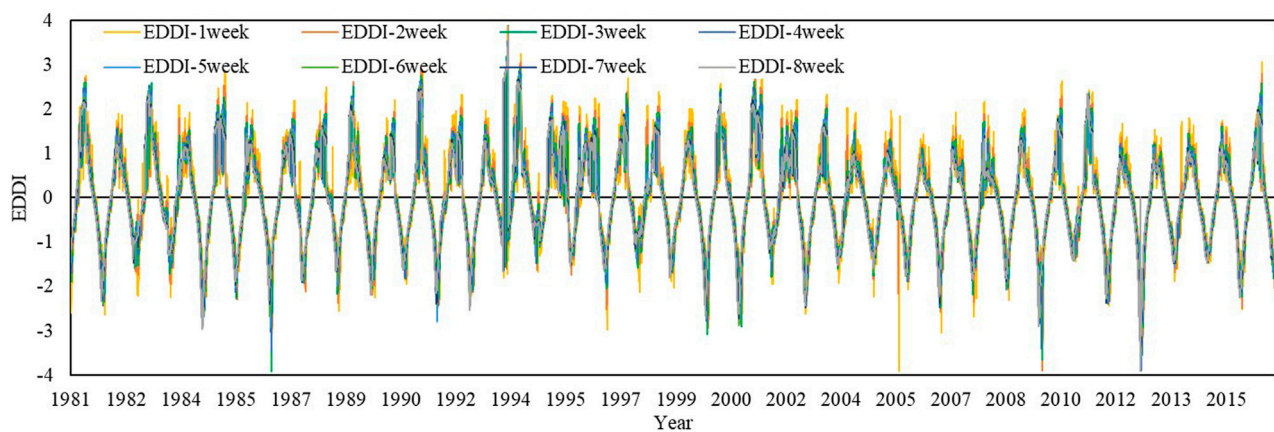
FIGURE. 9 | Temporal variations in the EDDI with 1–8-week timescales during 1981–2016.

increased by 40, 33, and 27%, respectively (**Figure 7**). Evaporation demand also contributed to the SPEI, but the contribution (6–13%) was much less than the EDDI (45–85%) (**Figure 5**). In addition, we found that there was no significant difference in drought intensity between SPEI-1 and SPEI-3. However, for SPEI-6, the drought intensity began to weaken (**Figure 3**), which was caused by the 18.3% increase in precipitation, 15.6% increase in evaporation, 2.5% increase in temperature, and 3.6% increase in humidity from SPEI-3 to SPEI-6 (**Figure 8**). This also confirmed that, in addition to precipitation and evaporation demand, temperature and relative humidity have a certain impact on the SPEI in identifying drought.

Although the temperature increase can promote the generation of wind speed and increase the evaporative demand, thus aggravating the occurrence of drought (Zhao et al., 2019), the temperature contribution is far less than that of evaporative demand (80%), which further explains the phenomenon that the drought intensity of the EDDI is stronger than that of the SPEI and SPI. This finding is related to seasonality (Van Loon and Van Lanen, 2013; Bisht et al., 2018). Especially in winter, the precipitation was low, and the change was not obvious. Other studies also explained roughly similar results; that is, snow melting in winter increased soil moisture, and evaporation increased gradually under the condition of lack of rainfall, which led to the continuous increase in the EDDI (Narasimhan and Srinivasan, 2005; Sheffield et al., 2012). Although evaporation demand has a certain contribution to the EDDI and SPEI, it showed a significant decreasing trend in the study area, which was the main reason for the alleviation of drought. Other studies also illustrated roughly similar results (Yao et al., 2018; Lingcheng Li et al., 2020). In this period, not only did evaporative demand decrease significantly but also the solar radiation had a similar trend, and the temperature increased significantly ($p < 0.01$). The significant reduction of solar radiation is the main reason for the reduction of evaporative demand, which is further proved by the research results of Roderick and Farquhar (2002). It is mainly caused by the wide-range reduction of solar radiation caused by the increase in cloud cover and aerosol concentration, which also reduces evaporative demand to varying degrees.

Moreover, the smallest timescale for both the SPI and SPEI was 1 month, while for the EDDI, it was 1 week (McEvoy et al., 2012; Yao et al., 2018). For example, **Figure 9** illustrates the variation characteristics of the EDDI with 1- to 8-week timescales. We found that the shorter the timescale was, the more the peaks and valleys the curve had. In particular, the 1-week EDDI curve was steeper than the longer timescales. Therefore, the EDDI can identify more serious drought events and is especially suitable for early warning and rapid drought detection.

Study Limitations

Although this study quantifies the impact of climate variables on drought, it still ignores some factors, such as human activities and soil properties. Solar radiation is related to air pollution caused by rapid urbanization (Qian et al., 2007; Zongxing et al., 2012). Therefore, land use and cover change will have a certain impact on drought. The same is true of deforestation, which will cause soil erosion and reduce soil water content, further increase evaporation, and lead to more droughts (Sun et al., 2017). Generally, soil properties are closely related to soil moisture. Different soil properties directly affect the water holding capacity of the soil (Park et al., 2004). It is necessary to explore the impact of soil properties on drought, which plays an important role in monitoring drought.

CONCLUSION

In this study, we compared the differences of meteorological drought indices (SPI, SPEI, and EDDI) at different timescales in the LRB, northern China, and further carried out quantifying the contribution of climate variables to drought change. To sum up, this study emphasized the necessity for adequate attention to the coupling effect between climate variables in drought studies. The conclusions are as follows.

The temporal fluctuations of the EDDI, SPEI, and SPI were increasingly acute when the timescale decreased. Besides, the

drought indices showed opposite states in 2002. This is mainly because of the positive contribution of evaporative demand and solar radiation to the EDDI, which made it show severe drought in April. In the meantime, the SPEI and SPI identified the wet state under the coupling effect of precipitation and temperature, respectively. The smallest timescale for both the SPI and SPEI was 1 month, while for the EDDI, it was 1 week. The weekly EDDI illustrated the potential to bring to light early warnings of the drought that occurred, which was not accomplished by the SPEI and SPI.

The results of four scenarios and twelve schemes based on the RF model showed that the R^2 of the model was greater than 0.88 and the MSE was small, indicating that the performance of the model was good. For the EDDI, the contributions are evaporative demand > Rn > U, respectively. Precipitation and evaporative demand are not the only variables affecting the SPEI, and the temperature (22%) contribution to the SPEI is greater than that of evaporative demand (6%), especially in SPEI-6.

With the decrease in timescale, the drought intensity of the three drought indices became stronger, the drought duration shortened, but the drought frequency increased. Especially, the drought intensity and duration of the EDDI were significantly higher than those of the SPEI and SPI. This is mainly due to the coupling effect of evaporative demand, wind speed, and solar radiation on the EDDI. The contribution of evaporative demand to the SPEI was less than that of precipitation, but the contribution of temperature cannot be ignored. This is also the main reason that the SPEI and SPI can identify more short-term drought events.

The information gained from this study may have useful implications not only for the LRB but also for other areas with strong evaporation change in the world. We cannot ignore the joint response of climate variables other than precipitation and evaporative demand in drought disasters. The spatial differences of climate variables may have a certain impact on the evolution of drought. Therefore, a quantitative model selected through the comparative optimization of multiple machine learning models can be established to explore the effects of climate variables on drought at a spatial scale, which will be conducted in our further studies.

REFERENCES

Abramopoulos, F., Rosenzweig, C., and Choudhury, B. (1988). Improved Ground Hydrology Calculations for Global Climate Models (GCMs): Soil Water Movement and Evapotranspiration. *J. Clim.* 1, 921–941. doi:10.1175/1520-0442(1988)001<0921:ighcfg>2.0.co;2

Amiri, M., Pourghasemi, H. R., Ghanbarian, G. A., and Afzali, S. F. (2019). Assessment of the Importance of Gully Erosion Effective Factors Using Boruta Algorithm and its Spatial Modeling and Mapping Using Three Machine Learning Algorithms. *Geoderma* 340, 55–69. doi:10.1016/j.geoderma.2018.12.042

Bisht, D. S., Chatterjee, C., Raghuwanshi, N. S., and Sridhar, V. (2018). An Analysis of Precipitation Climatology over Indian Urban Agglomeration. *Theor. Appl. Climatol.* 133, 421–436. doi:10.1007/s00704-017-2200-z

Blonquist, J. M., Allen, R. G., and Bugbee, B. (2010). An Evaluation of the Net Radiation Sub-model in the ASCE Standardized Reference Evapotranspiration Equation: Implications for Evapotranspiration Prediction. *Agric. Water Manage.* 97, 1026–1038. doi:10.1016/j.agwat.2010.02.008

DATA AVAILABILITY STATEMENT

The original contributions presented in the study are included in the article/**Supplementary Material**; further inquiries can be directed to the corresponding author.

AUTHOR CONTRIBUTIONS

All authors contributed to the study conception and design. Material preparation, data collection, and analysis were performed by YZ, XZ,JY, and YX. The first draft of the manuscript was written by YZ, and all authors commented on the previous versions of the manuscript. All authors read and approved the final manuscript.

FUNDING

ACKNOWLEDGMENTS

SUPPLEMENTARY MATERIAL

The Supplementary Material for this article can be found online at: https://www.frontiersin.org/articles/10.3389/feart.2022.835142/full#supplementary-material

Chen, L. G., Gottschalck, J., Hartman, A., Miskus, D., Tinker, R., and Artusa, A. (2019). Flash Drought Characteristics Based on U.S. Drought Monitor. *Atmosphere* 10, 498. doi:10.3390/atmos10090498

Chen, H., Liu, H., Chen, X., and Qiao, Y. (2020). Analysis on Impacts of Hydro-Climatic Changes and Human Activities on Available Water Changes in Central Asia. *Sci. Total Environ.* 737, 139779. doi:10.1016/j.scitotenv.2020.139779

Deb, P., Kiem, A. S., and Willgoose, G. (2019). A Linked Surface Water-Groundwater Modelling Approach to More Realistically Simulate Rainfall-Runoff Non-stationarity in Semi-arid Regions. *J. Hydrol.* 575, 273–291. doi:10.1016/j.jhydrol.2019.05.039

Esfahanian, E., Nejadhashemi, A. P., Abouali, M., Adhikari, U., Zhang, Z., Daneshvar, F., et al. (2017). Development and Evaluation of a Comprehensive Drought index. *J. Environ. Manage.* 185, 31–43. doi:10.1016/j.jenvman.2016.10.050

Farahmand, A., and AghaKouchak, A. (2015). A Generalized Framework for Deriving Nonparametric Standardized Drought Indicators. *Adv. Water Resour.* 76, 140–145. doi:10.1016/j.advwatres.2014.11.012

Frank, A., Armenski, T., Gocic, M., Popov, S., Popovic, L., and Trajkovic, S. (2017). Influence of Mathematical and Physical Background of Drought Indices on

Their Complementarity and Drought Recognition Ability. *Atmos. Res.* 194, 268–280. doi:10.1016/j.atmosres.2017.05.006

Gocic, M., and Trajkovic, S. (2013). Analysis of Changes in Meteorological Variables Using Mann-Kendall and Sen's Slope Estimator Statistical Tests in Serbia. *Glob. Planet. Change* 100, 172–182. doi:10.1016/j.gloplacha.2012.10.014

Griffin, D., and Anchukaitis, K. J. (2014). How Unusual Is the 2012-2014 California Drought? *Geophys. Res. Lett.* 41, 9017–9023. doi:10.1002/2014GL062433

Guo, Y., Fu, Y., Hao, F., Zhang, X., Wu, W., Jin, X., et al. (2021). Integrated Phenology and Climate in rice Yields Prediction Using Machine Learning Methods. *Ecol. Indicators* 120, 106935. doi:10.1016/j.ecolind.2020.106935

He, B., Lü, A., Wu, J., Zhao, L., and Liu, M. (2011). Drought hazard Assessment and Spatial Characteristics Analysis in China. *J. Geogr. Sci.* 21, 235–249. doi:10.1007/s11442-011-0841-x

Heim, R. R. (2002). A Review of Twentieth-Century Drought Indices Used in the United States. *Bull. Amer. Meteorol. Soc.* 83, 1149–1166. doi:10.1175/1520-0477-83.8.1149

Hobbins, M., Wood, A., Streubel, D., and Werner, K. (2012). What Drives the Variability of Evaporative Demand across the Conterminous United States? *J. Hydrometeorol.* 13, 1195–1214. doi:10.1175/JHM-D-11-0101.1

Hobbins, M. T., Wood, A., McEvoy, D. J., Huntington, J. L., Morton, C., Anderson, M., et al. (2016). The Evaporative Demand Drought Index. Part I: Linking Drought Evolution to Variations in Evaporative Demand. *J. Hydrometeorol.* 17, 1745–1761. doi:10.1175/JHM-D-15-0121.1

Wang, J., Li, S., Chen, H., Yuan, Y., and Huang, Y. (2019). Data-driven Model Predictive Control for Building Climate Control: Three Case Studies on Different Buildings. *Build. Environ.* 160, 106204. doi:10.1016/j.buildenv.2019.106204

Li, K., Tong, Z., Liu, X., Zhang, J., and Tong, S. (2020). Quantitative Assessment and Driving Force Analysis of Vegetation Drought Risk to Climate change: Methodology and Application in Northeast China. *Agric. For. Meteorol.* 282-283, 107865. doi:10.1016/j.agrformet.2019.107865

Karl, T. R., Gleason, B. E., Menne, M. J., McMahon, J. R., Heim, R. R., Brewer, M. J., et al. (2012). U.S. Temperature and Drought: Recent Anomalies and Trends. *Eos Trans. AGU* 93, 473–474. doi:10.1029/2012EO470001

Kousari, M. R., Dastorani, M. T., Niazi, Y., Soheili, E., Hayatzadeh, M., and Chezgi, J. (2014). Trend Detection of Drought in Arid and Semi-arid Regions of Iran Based on Implementation of Reconnaissance Drought Index (RDI) and Application of Non-parametrical Statistical Method. *Water Resour. Manage.* 28, 1857–1872. doi:10.1007/s11269-014-0558-6

Kursa, M. B., and Rudnicki, W. R. (2010). Feature Selection with the Boruta Package. *J. Stat. Soft.* 36, 1–13. doi:10.18637/jss.v036.i11

Leroux, L., Bégué, A., Lo Seen, D., Jolivot, A., and Kayitakire, F. (2017). Driving Forces of Recent Vegetation Changes in the Sahel: Lessons Learned from Regional and Local Level Analyses. *Remote Sens. Environ.* 191, 38–54. doi:10.1016/j.rse.2017.01.014

Li, X., Li, Y., Chen, A., Gao, M., Slette, I. J., and Piao, S. (2019). The Impact of the 2009/2010 Drought on Vegetation Growth and Terrestrial Carbon Balance in Southwest China. *Agric. For. Meteorol.* 269-270, 239–248. doi:10.1016/j.agrformet.2019.01.036

Li, L., She, D., Zheng, H., Lin, P., and Yang, Z.-L. (2020). Elucidating Diverse Drought Characteristics from Two Meteorological Drought Indices (SPI and SPEI) in China. *J. Hydrometeorol.* 21, 1513–1530. doi:10.1175/JHM-D-19-0290.1

Liu, M., Xu, X., Xu, C., Sun, A. Y., Wang, K., Scanlon, B. R., et al. (2017). A New Drought index that Considers the Joint Effects of Climate and Land Surface Change. *Water Resour. Res.* 53, 3262–3278. doi:10.1002/2016WR020178

Luedeling, E., Guo, L., Dai, J., Leslie, C., and Blanke, M. M. (2013). Differential Responses of Trees to Temperature Variation during the Chilling and Forcing Phases. *Agric. For. Meteorol.* 181, 33–42. doi:10.1016/j.agrformet.2013.06.018

Masroor, M., Rehman, S., Sajjad, H., Rahaman, M. H., Sahana, M., Ahmed, R., et al. (2021). Assessing the Impact of Drought Conditions on Groundwater Potential in Godavari Middle Sub-Basin, India Using Analytical Hierarchy Process and Random forest Machine Learning Algorithm. *Groundwater Sustain. Dev.* 13, 100554. doi:10.1016/j.gsd.2021.100554

McEvoy, D. J., Huntington, J. L., Abatzoglou, J. T., and Edwards, L. M. (2012). An Evaluation of Multiscalar Drought Indices in Nevada and Eastern California. *Earth Interact.* 16, 1–18. doi:10.1175/2012EI000447.1

McEvoy, D. J., Huntington, J. L., Hobbins, M. T., Wood, A., Morton, C., Anderson, M., et al. (2016). The Evaporative Demand Drought Index. Part II: CONUS-wide Assessment against Common Drought Indicators. *J. Hydrometeorol.* 17, 1763–1779. doi:10.1175/JHM-D-15-0122.1

Milly, P. C. D., and Dunne, K. A. (2016). Potential Evapotranspiration and continental Drying. *Nat. Clim Change* 6, 946–949. doi:10.1038/nclimate3046

Mo, K. C., and Lettenmaier, D. P. (2015). Heat Wave Flash Droughts in Decline. *Geophys. Res. Lett.* 42, 2823–2829. doi:10.1002/2015GL064018

Montaseri, M., and Amirataee, B. (2017). Comprehensive Stochastic Assessment of Meteorological Drought Indices. *Int. J. Climatol.* 37, 998–1013. doi:10.1002/joc.4755

Nam, W.-H., Hayes, M. J., Svoboda, M. D., Tadesse, T., and Wilhite, D. A. (2015). Drought hazard Assessment in the Context of Climate Change for South Korea. *Agric. Water Manage.* 160, 106–117. doi:10.1016/j.agwat.2015.06.029

Narasimhan, B., and Srinivasan, R. (2005). Development and Evaluation of Soil Moisture Deficit Index (SMDI) and Evapotranspiration Deficit Index (ETDI) for Agricultural Drought Monitoring. *Agric. For. Meteorol.* 133, 69–88. doi:10.1016/j.agrformet.2005.07.012

Noguera, I., Domínguez-Castro, F., and Vicente-Serrano, S. M. (2021). Flash Drought Response to Precipitation and Atmospheric Evaporative Demand in Spain. *Atmosphere* 12, 165. doi:10.3390/atmos12020165

Ojha, R., Nagesh Kumar, D., Sharma, A., and Mehrotra, R. (2013). Assessing Severe Drought and Wet Events over India in a Future Climate Using a Nested Bias-Correction Approach. *J. Hydrol. Eng.* 18, 760–772. doi:10.1061/(asce)he.1943-5584.0000585

Park, S., Feddema, J. J., and Egbert, S. L. (2004). Impacts of Hydrologic Soil Properties on Drought Detection with MODIS thermal Data. *Remote Sens. Environ.* 89, 53–62. doi:10.1016/j.rse.2003.10.003

Prasad, R., Deo, R. C., Li, Y., and Maraseni, T. (2019). Weekly Soil Moisture Forecasting with Multivariate Sequential, Ensemble Empirical Mode Decomposition and Boruta-Random forest Hybridizer Algorithm Approach. *CATENA* 177, 149–166. doi:10.1016/j.catena.2019.02.012

Qian, Y., Wang, W., Leung, L. R., and Kaiser, D. P. (2007). Variability of Solar Radiation under Cloud-free Skies in China: The Role of Aerosols. *Geophys. Res. Lett.* 34, 1–5. doi:10.1029/2006GL028800

Qin, N., Wang, J., Yang, G., Chen, X., Liang, H., and Zhang, J. (2015). Spatial And Temporal Variations Of Extreme Precipitation And Temperature Events For The Southwest China In 1960-2009. *Geoenviron. Disasters* 2, 1–14. doi:10.1186/s40677-015-0014-9

Rehana, S., and Monish, N. T. (2021). Impact of Potential and Actual Evapotranspiration on Drought Phenomena over Water and Energy-Limited Regions. *Theor. Appl. Climatol.* 144, 215–238. doi:10.1007/s00704-021-03521-3

Richard, R., and Heim, Jr (2002). A Review of Twentieth-Century Drought Indices Used in the United States. *Bull. Am. Meteorol. Soc.* 83, 1149–1165. doi:10.1175/1520-0477-83.8.1149

Roderick, M. L., and Farquhar, G. D. (2002). The Cause of Decreased pan Evaporation over the Past 50 Years. *Science (New York, N.Y.)* 298, 1410–1411. doi:10.1126/science.1075390-a

Satish Kumar, K., Venkata Rathnam, E., and Sridhar, V. (2021). Tracking Seasonal and Monthly Drought with GRACE-based Terrestrial Water Storage Assessments over Major River Basins in South India. *Sci. Total Environ.* 763, 142994. doi:10.1016/j.scitotenv.2020.142994

Sheffield, J., and Wood, E. F. (2008). Global Trends and Variability in Soil Moisture and Drought Characteristics, 1950-2000, from Observation-Driven Simulations of the Terrestrial Hydrologic Cycle. *J. Clim.* 21, 432–458. doi:10.1175/2007JCLI1822.1

Sheffield, J., Wood, E. F., and Roderick, M. L. (2012). Little Change in Global Drought over the Past 60 Years. 027Z. Available at: https://www.nature.com/articles/nature11575 (Accessed October 26, 2020).

Shukla, S., Safeeq, M., AghaKouchak, A., Guan, K., and Funk, C. (2015). Temperature Impacts on the Water Year 2014 Drought in California. *Geophys. Res. Lett.* 42, 4384–4393. doi:10.1002/2015GL063666

Song, H., Tian, J., Huang, J., Guo, P., Zhang, Z., and Wang, J. (2019). Hybrid Causality Analysis of ENSO's Global Impacts on Climate Variables Based on Data-Driven Analytics and Climate Model Simulation. *Front. Earth Sci.* 7, 1–15. doi:10.3389/feart.2019.00233

Sun, C., and Ma, Y. (2015). Effects of Non-linear Temperature and Precipitation Trends on Loess Plateau Droughts. *Quat. Int.* 372, 175–179. doi:10.1016/j.quaint.2015.01.051

Sun, S., Chen, H., Ju, W., Wang, G., Sun, G., Huang, J., et al. (2017). On the Coupling between Precipitation and Potential Evapotranspiration: Contributions to Decadal Drought Anomalies in the Southwest China. *Clim. Dyn.* 48, 3779–3797. doi:10.1007/s00382-016-3302-5

Tirivarombo, S., Osupile, D., and Eliasson, P. (2018). Drought Monitoring and Analysis: Standardised Precipitation Evapotranspiration Index (SPEI) and Standardised Precipitation Index (SPI). *Phys. Chem. Earth, Parts A/B/C* 106, 1–10. doi:10.1016/j.pce.2018.07.001

Van Loon, A. F., and Van Lanen, H. A. J. (2013). Making the Distinction between Water Scarcity and Drought Using an Observation-Modeling Framework. *Water Resour. Res.* 49, 1483–1502. doi:10.1002/wrcr.20147

Vicente-Serrano, S. M., Beguería, S., and López-Moreno, J. I. (2010). A Multiscalar Drought Index Sensitive to Global Warming: The Standardized Precipitation Evapotranspiration Index. *J. Clim.* 23, 1696–1718. doi:10.1175/2009JCLI2909.1

Vicente-Serrano, S. M., Lopez-Moreno, J.-I., Beguería, S., Lorenzo-Lacruz, J., Sanchez-Lorenzo, A., García-Ruiz, J. M., et al. (2014). Evidence of Increasing Drought Severity Caused by Temperature Rise in Southern Europe. *Environ. Res. Lett.* 9, 44001. doi:10.1088/1748-9326/9/4/044001

Wang, B., Zhang, M., Wei, J., Wang, S., Li, S., Ma, Q., et al. (2013). Changes in Extreme Events of Temperature and Precipitation over Xinjiang, Northwest China, during 1960-2009. *Quat. Int.* 298, 141–151. doi:10.1016/j.quaint.2012.09.010

Wang, H., Rogers, J. C., and Munroe, D. K. (2015). Commonly Used Drought Indices as Indicators of Soil Moisture in China. *J. Hydrometeorol.* 16, 1397–1408. doi:10.1175/JHM-D-14-0076.1

Wang, S.-p., Wang, J.-s., Zhang, Q., Li, Y.-p., Wang, Z.-l., and Wang, J. (2016). Cumulative Effect of Precipitation Deficit Preceding Severe Droughts in Southwestern and Southern China. *Discrete Dyn. Nat. Soc.* 2016, 1–10. doi:10.1155/2016/2890852

Wang, W., Ma, X., Moazzam Nizami, S., Tian, C., and Guo, F. (2018). Anthropogenic and Biophysical Factors Associated with Vegetation Restoration in Changting, China. *Forests* 9, 306. doi:10.3390/f9060306

Wang, K., Niu, J., Li, T., and Zhou, Y. (2020). Facing Water Stress in a Changing Climate: A Case Study of Drought Risk Analysis under Future Climate Projections in the Xi River Basin, China. *Front. Earth Sci.* 8, 1–12. doi:10.3389/feart.2020.00086

Wen, X., Pan, W., Sun, X., Li, M., Luo, S., Cao, B., et al. (2020). Study on the Variation Trend of Potential Evapotranspiration in the Three-River Headwaters Region in China over the Past 20 Years. *Front. Earth Sci.* 8, 1–12. doi:10.3389/feart.2020.582742

Wilhite, D. A., and Glantz, M. H. (1985). Understanding: the Drought Phenomenon: The Role of Definitions. *Water Int.* 10, 111–120. doi:10.1080/02508068508686328

Wu, L., Zhang, X., Hao, F., Wu, Y., Li, C., and Xu, Y. (2020). Evaluating the Contributions of Climate Change and Human Activities to Runoff in Typical Semi-arid Area, China. *J. Hydrol.* 590, 125555. doi:10.1016/j.jhydrol.2020.125555

Xu, Y., Zhang, X., Wang, X., Hao, Z., Singh, V. P., and Hao, F. (2019). Propagation from Meteorological Drought to Hydrological Drought under the Impact of Human Activities: A Case Study in Northern China. *J. Hydrol.* 579, 124147. doi:10.1016/j.jhydrol.2019.124147

Yang, W., Long, D., and Bai, P. (2019). Impacts of Future Land Cover and Climate Changes on Runoff in the Mostly Afforested River basin in North China. *J. Hydrol.* 570, 201–219. doi:10.1016/j.jhydrol.2018.12.055

Yang, P., Zhang, Y., Xia, J., and Sun, S. (2020). Identification of Drought Events in the Major Basins of Central Asia Based on a Combined Climatological Deviation index from GRACE Measurements. *Atmos. Res.* 244, 105105. doi:10.1016/j.atmosres.2020.105105

Yao, N., Li, Y., Lei, T., and Peng, L. (2018). Drought Evolution, Severity and Trends in mainland China over 1961-2013. *Sci. Total Environ.* 616-617, 73–89. doi:10.1016/j.scitotenv.2017.10.327

Yerdelen, C., Abdelkader, M., and Eris, E. (2021). Assessment of Drought in SPI Series Using Continuous Wavelet Analysis for Gediz Basin, Turkey. *Atmos. Res.* 260, 105687. doi:10.1016/j.atmosres.2021.105687

Yevjevich, V. M. (1967). An Objective Approach to Definitions and Investigations of continental Hydrologic Droughts. *J. Hydrol.* 7, 353. doi:10.1016/0022-1694(69)90110-3

Wang, Y., Li, J., Zhang, T., and Wang, B. (2019). Changes in Drought Propagation under the Regulation of Reservoirs and Water Diversion. *Theor. Appl. Climatol,* 138, 701–711. doi:10.1007/s00704-019-02839-3

Zhai, J., Su, B., Krysanova, V., Vetter, T., Gao, C., and Jiang, T. (2010). Spatial Variation and Trends in PDSI and SPI Indices and Their Relation to Streamflow in 10 Large Regions of China. *J. Clim.* 23, 649–663. doi:10.1175/2009JCLI2968.1

Zhang, X., Xu, Y., Hao, F., Li, C., and Wang, X. (2019). Hydrological Components Variability under the Impact of Climate Change in a Semi-arid River Basin. *Water* 11, 1122. doi:10.3390/w11061122

Zhao, H., Zhou, Y., Li, X., Liu, C., and Chen, X. (2019). The Influence of Wind Speed on Infrared Temperature in Impervious Surface Areas Based on *In Situ* Measurement Data. *GISci. Remote Sens.* 56, 843–863. doi:10.1080/15481603.2019.1572322

Zongxing, L., Qi, F., Wei, Z., Yuanqing, H., Xufeng, W., Catto, N., et al. (2012). Decreasing Trend of sunshine Hours and Related Driving Forces in Southwestern China. *Theor. Appl. Climatol.* 109, 305–321. doi:10.1007/s00704-012-0583-4

Spatio-Temporal Differentiation Characteristic and Evolution Process of Meteorological Drought in Northwest China From 1960 to 2018

Hui Li*, Enke Hou and Jiawei Deng

College of Geology and Environment, Xi'an University of Science and Technology, Xi'an, China

Against the backdrop of global climate change, the response characteristic of meteorological drought is of great concern, especially in the arid or semi-arid regions. By employing the Standardized Precipitation Index (SPI), TPFW-MK test, Run Theory, Moran's *I*, and General *G*, the spatio-temporal evolution characteristic of drought was clarified and the spatial autocorrelation of local and global drought characteristic variables was explored based on the meteorological data from 122 stations in Northwest China (NWC) during 1960–2018. The results indicated that the drought situation of NWC was improving regardless of annual or seasonal scale. According to the Z-statistics by the TPFW-MK test, there existed an obvious wet trend in west NWC and a slight dry trend in east NWC. The center of gravity migration model revealed that the gravity center of SPI moved towards higher latitude over the last decades, there was a northwest (1960–1990) and northeast (1990–2018) variation in the covering shapes of the standard deviational ellipses of SPI, and the spatial distribution of SPI tended to be concentrated. Meanwhile, the distribution pattern of drought characteristics suggested that more droughts occurred in east of NWC, which were less harmful while fewer droughts happened in west NWC, which brought greater drought damage. The results of global Moran's *I* (GMI) indicated that both annual and seasonal drought variables were characterized with significant spatial autocorrelation, the spatial distribution of winter drought variables was more disperse than other seasons, while the damage of summer and autumn drought was bigger than that in spring and winter. Besides, the results of local Moran's *I* (LMI) showed that there was obvious agglomeration in the overall distribution of drought characteristic variables, which had a seesaw effect. The spatial distribution of hot spots and cold spots at different confidence levels indicated that Shaanxi Province experienced the most droughts but with shortest duration and lowest severity while northwest Xinjiang had the fewest droughts with longest duration and highest severity. The results of revealing the drought development process and identifying the location of drought aggregation will provide references for supporting climate adaptation strategies and preventing drought-related loss.

Keywords: meteorological drought, Run Theory, differentiation characteristic, spatial similarity, evolution process, Northwest China

1 INTRODUCTION

Global warming is expected to accelerate the global hydrological cycle and change the spatio-temporal patterns of precipitation, which will give rise to weather-related hazards such as droughts and floods, and aggravate the contradiction between water resource and the distribution of geographic productivity (Shi et al., 2015; Chen et al., 2016; Naumann et al., 2018; Hu et al., 2019). Therefore, water planning and management are far more complex during drought periods, particularly against the backdrop of serious concerns about water security, socioeconomic development, and ecological sustainability.Drought is a natural and recurring meteorological disaster that mainly resulted from prolonged precipitation deficit (Mishra et al., 2015; Deng et al., 2018; Campozano et al., 2020). As the initial stage of a drought, the meteorological drought determines the scale of a drought episode and has presented a great challenge to regional agriculture, ecological environment, and livelihoods (Mondal and Mujumdar, 2015; Spinoni et al., 2019). In fact, the global economic losses caused by meteorological drought was up to 6–8 billion dollars a year, far more than other meteorological disasters (Udmale et al., 2014; Montaseri and Amirataee, 2017; Lin and Shelton, 2020). China has an instable monsoon climate and a complex terrain, which result in maldistribution of water-heat and frequent droughts. Statistics showed that from 1981 to 2014, about 23 million hectares of crop area per year in China have been suffering from droughts (MWR, 2015; National Bureau of Statistics of China, 2015; Wang et al., 2017).

Given the damage that drought causes, attention has been paid to drought identification or the calculation of basic drought characteristic. Huang et al. (2015) proposed a Nonparametric Multivariate Standardized Drought Index (NMSDI) to investigate the spatial and temporal features of drought structure in the Yellow River Basin (YRB) of China, and found that the drought structure in terms of drought duration, onset, and termination transition periods in the YRB is stable and no significant change trend was detected. By comparing the SPI and the SPEI, Tirivarombo et al. (2018) and Oikonomou et al. (2020) respectively assessed the drought characteristics of Kafue basin and Europe. Kalisa et al. (2020) analyzed the spatio-temporal characteristics of drought and its return periods over the East African region. A detailed description of drought events contains multiple characteristic variables, such as drought duration, severity, and frequency, which have important implications for drought identification and can explain the complexity and extensive influence of drought events (Yusof et al., 2013; Brito et al., 2018; Sun et al., 2019; Oikonomou et al., 2020). For example, Guo et al. (2018) discussed the spatial and temporal drought characteristic variables such as drought duration and severity in Central Asia by using Run Theory. Xu et al. (2015) analyzed the variation of drought frequency in Southwest China by integrating the effects of drought duration, affected area, and severity into the 3-D joint probability distribution with a trinary function. In order to provide references for making adaption strategies, drought hazards using statistical methods have also been analyzed in some research. Azimi et al. (2020) studied the

spatial interpolation of drought steady-state probabilities based on a Markov chain model, and the results showed an average drought increase of 62% in the steady-state condition in Iran. Ayantobo et al. (2017) evaluated drought hazards of mainland China from 1961 to 2013 based on a univariate frequency analysis, and found that the distribution of drought frequency in China decreased both from west of east and from north to west. Ogunrinde et al. (2021) explored the variation of drought severity and its correlation with climate change in the Sahel region of Nigeria from 1981 to 2015 by Mann–Kendall test, the findings demonstrated that the drought severity exhibited an increasing trend, and a slight change of rainfall will not have a significant effect on drought or the severity of drought increase.

Northwest China (NWC) is widely regarded as one of the driest areas in the world, which mainly depend on eco-agricultural economy. Situated in the inland with extremely fragile ecological environment, drought has been considered as the one of the major factors limiting the social and economic development in NWC (Sternberg, 2018; Wei et al., 2021). Against the backdrop of global warming, the precipitation of NWC has exhibited an upward trend over the last 20 years, which offered some relief to drought conditions (Liu et al., 2016a; Yang et al., 2018; Li et al., 2021).According to Wang and Qin (2017) and Yang et al. (2018a), the climate of NWC tended to be more humid and warmer from the 1960s to the 2010s, as well as the drought severity was relieved. However, due to the complex territory and nonlinear nature in different climate conditions, water scarcity and the uneven distribution of water resource are still the major factors affecting ecosystem and economy (Hu et al., 2021). Meanwhile, the redistribution of water-heat caused by global climate change has exerted a great effect on the spatial and temporal distribution characteristic of drought in NWC (Chen and Sun, 2015; Mo et al., 2018; Li et al., 2020). Gu et al. (2018) found that the drought frequency and drought duration are projected to decrease in NWC while the drought severity will be heavier in the next 30 years based on the bias-corrected CESM1 and CSIRO ensembles.

Influenced by the underlying surface conditions, drought frequency, duration, and intensity will change during the spread of a drought event (Burke et al., 2010; Naumann et al., 2015; Liu et al., 2016b). Previous studies were mainly focused on the spatio-temporal variation of drought events or the characteristic of drought variables such as drought frequency and drought duration, which failed to describe the whole process of drought evolution characteristic and the spatial autocorrelation of multiple drought events. Besides, every drought event has a certain duration and a range of influence; drought indexes used in past research were based on single rain gauges that could not explore the influence area of a single drought event. Considering the calculated drought indexes are affected by topography, elevation, and climate, the variation of drought characteristic variables in adjacent sites or regions would exhibit similar characteristics. Therefore, analyzing the correlation of drought events in different distances is important for identifying the spatial similarity and heterogeneity of drought.

Accordingly, the primary objectives of this paper are (1) to explore the spatio-temporal variation characteristic of drought
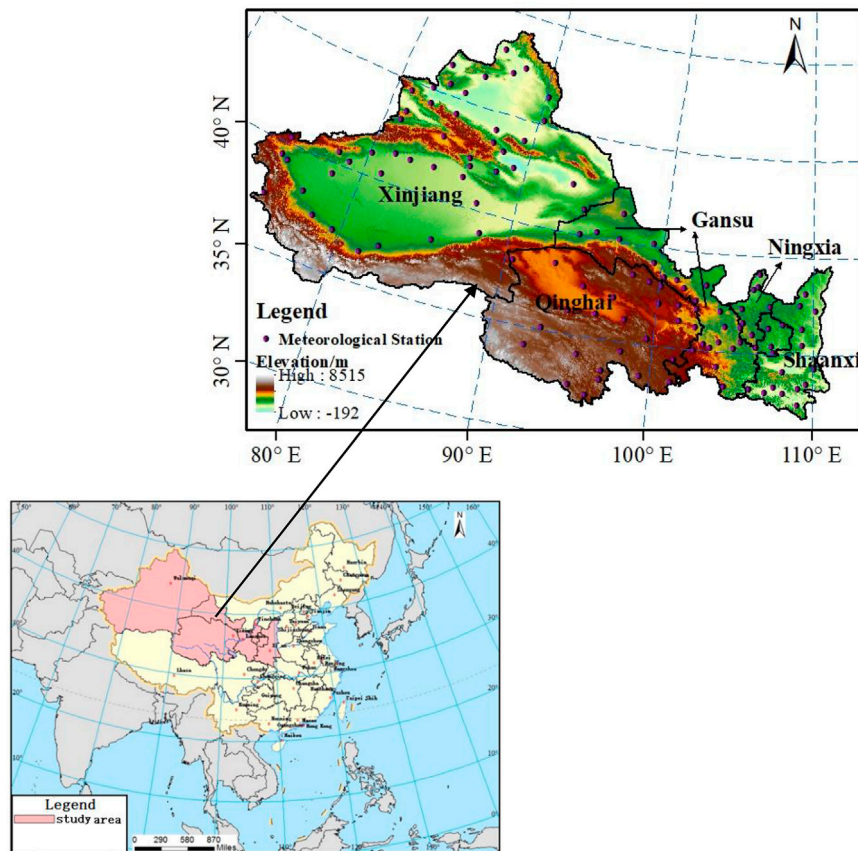
FIGURE 1 | Location and the meteorological details of the study area.

in NWC based on the SPI values of 123 rain gauges; (2) to identify the drought events from hydrometeorological series and to reveal the spatial evolution features of drought characteristic variables; (3) to visualize the development process of drought in NWC; and (4) to investigate the spatial heterogeneity and similarity of drought variables.

2 STUDY AREA

NWC is in the hinterland of Eurasia, which accounts for 31.7% of the total land area of China and geographically includes five administrative provinces (Xinjiang, Qinghai, Gansu, Shaanxi, and Ningxia) (**Figure 1**). Because of its geographic position and the topographic features with high mountains all around, it is difficult for the water vapor to transport from the ocean to the study area; thus, NWC is one of the driest places in the same latitude, which is characterized by cold winters and hot summers with low precipitation; the annual average temperature and precipitation from 1960 to 2018 were 6.3°C and 248.2 mm, respectively. Besides, the terrain and physical geographical features of NWC varied greatly (the landscape includes deserts, basins, plateaus, plains, and mountains), which result

in different climatic characteristics, and the precipitation gradually decreases from southeast to northwest.

3 DATASET AND METHODOLOGY

3.1 Data Availability
The precipitation data are obtained from China Meteorological Data Sharing Service System (http://www.cma.gov.cn) for the 1960–2018 periods from 122 meteorological stations. In order to ensure high-quality series, data series with a cumulative absence of more than 1 year were excluded, and the homogeneity of the dataset was checked and corrected by using the standardized toolkit RHtestsV4. The geographical distribution of the rain gauges is shown in **Figure 1**.

3.2 Methodology
3.2.1 SPI
The Standardized Precipitation Index (SPI) and the Standardized Precipitation Evapotranspiration Index (SPEI) are the most commonly used indices for drought assessment, which are able to detect drought events at different time scales (Kalisa et al., 2020; Bonaccorso et al., 2015). The SPI employs precipitation to calculate the drought index while the SPEI incorporates both
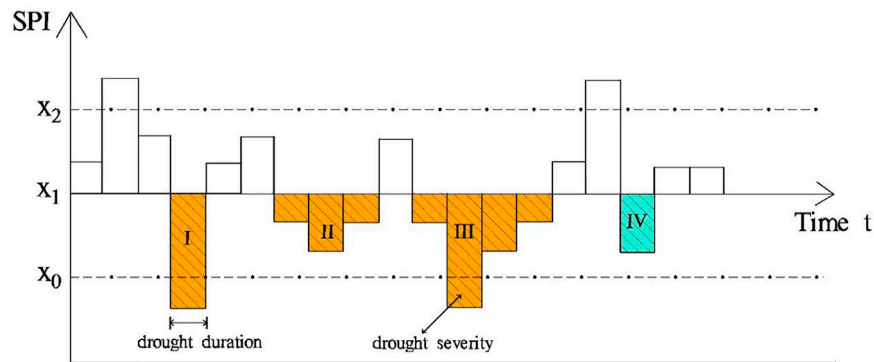
FIGURE 2 | Drought event identification process by Run Theory.

temperature and precipitation to identify drought (Fung et al., 2020). Though the temperature has played an important role on drought identification especially in arid regions, the climate conditions with lower variability of temperature than the variability in precipitation indicated that the precipitation is the major driver of droughts (Tirivarombo et al., 2018; Begueria et al., 2014). Besides, the near-zero potential evapotranspiration in winter of some regions and the calculation of potential evapotranspiration by empirical formula may add to the uncertainty of the results.Therefore, considering this paper is mainly aimed at studying the spatio-temporal differentiation characteristic and evolution process of meteorological drought in NWC, the evapotranspiration has more spatio-temporal effects on soil moisture availability and water resources planning in the face of agriculture drought, and for simplicity of calculation, this study employed the SPI to analyze the variation characteristic of drought in NWC. Based on the theory, the SPI is determined as follows (Raziei et al., 2014; Haroon et al., 2016):

$$SPI = -t + \frac{C_0 + C_1 t + C_2 t^2}{1 + d_1 t + d_2 t^2 + d_3 t^3} \ (0 < G(x) \le 0.5) \quad (1)$$

or

$$SPI = t - \frac{C_0 + C_1 t + C_2 t^2}{1 + d_1 t + d_2 t^2 + d_3 t^3} \ (0.5 < G(x) \le 1) \quad (2)$$

where: $t = \sqrt{ln 1/(G(x))^2} \ (0 < G(x) \le 0.5)$; $t = \sqrt{ln 1/(1 - G(X))^2}$ $(0.5 < G(x) \le 1)$; x is the precipitation time series; $G(x)$ is the Cumulative Gamma function of precipitation:

$$G(x) = \frac{1}{\alpha^\beta \Gamma(\beta)} \int_0^x x^{\beta-1} e^{x/\alpha} dx \quad (3)$$

where α, β are the scale and shape parameter of Gamma function:

$$\beta = \frac{1}{4[ln(x) - ln(x)/n]} \left[1 + \sqrt{\frac{4[ln(x) - ln(x)/n]}{3}} \right] \quad (4)$$

$$\alpha = \frac{\bar{x}}{\beta} \quad (5)$$

where $\bar{x} = \frac{\sum x}{n}$, n is the length of data records.

The constants in **Eq. 1** and **Eq. 2** are given as follows: $C_0 = 2.515517$; $d_1 = 1.432788$; $C_1 = 0.802853$; $d_2 = 0.189269$; $C_2 = 0.010328$, $d_3 = 0.001308$.

The positive values of SPI indicate greater than mean precipitation and are related to wet conditions, while the negative values suggest less than mean precipitation and are related to dry conditions. SPI-1, SPI-3, SPI-6, and SPI-12 represent monthly, seasonal, semi-annual, and annual accumulated drought condition, respectively. Therefore, SPI-3 and SPI-12 were selected to monitor drought in this research.

3.2.2 Run Theory

SPI was mainly adopted to demonstrate the spatial and temporal variation of drought events, which limited the identification the multiple attributes of drought events. Therefore, Run Theory was employed to separate drought characteristic variables (drought frequency, duration, and severity) from SPI series and reveal the basic attributes of drought (Amirataee et al., 2020; Wu et al., 2020; Leng et al., 2020). According to the theory, three truncation levels $X_0 = -0.5$ (light drought occurs when SPI < −0.5), $X_1 = -0.3$ (drought is also expected when the SPI values of one period or multiple time periods are kept between −0.5 and −0.3), and $X_2 = 0$ (drought may happen when the run length of SPI is negative) were set to identify drought events; the identification process of drought events is as follows:

1) If the SPI value is less than x_1, it would be preliminarily considered that a drought event occurs (**Figure 2** shows four droughts, I, II, III and IV).
2) If the drought event lasts only 1 month (I, IV) and the corresponding SPI value is less than x_0, it would be considered that a drought event occurs (I); otherwise, there is no drought in this month (IV).
3) If the time interval between two adjacent drought events (II and III) is 1 month and the corresponding SPI value is less than x_2, the two adjacent drought events would be merged as one drought event, and then the drought duration $D = D_{II} + D_{III}+1$ and the drought severity $S = S_{II} + S_{III}$. Otherwise, they would be considered as two independent drought events.

3.2.3 TFWP-MK

Since the positive correlation of time series may cause the major source of uncertainty by Mann–Kendall test, trend-free pre-
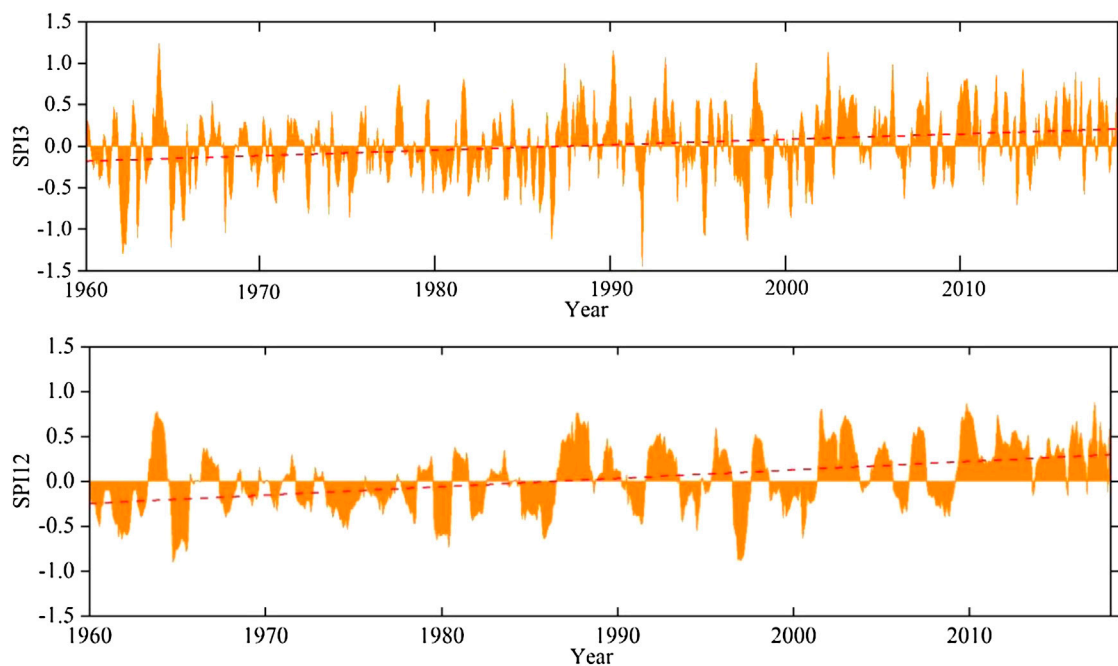
FIGURE 3 | Variation of SPI series from 1960 to 2018 in NWC.

whitening (TFWP-MK) was employed to eliminate the effect of serial correlation (Dinpashoh et al., 2011; Gocic and Trajkovic, 2013; Ji et al., 2014). The procedure of TFPW-MK can be represented as:

$$Y_i = X_i \beta i \qquad (6)$$

The slope, an index indicating the direction and quantity of the trend, was estimated using the Theil–Sen regression estimator by:

$$\beta = Median\left[\frac{(X_j - X_i)}{(t_j - t_i)}\right] \forall i < j \qquad (7)$$

where X_j and X_i are the data values at time i and j.

Then the lag-1 serial correlation coefficient of the sample data is obtained by:

$$r_1 = \frac{1/n - 1 \sum_{i=1}^{n-1} [X_i - E(X_i)][X_{i+1} - E(X_i)]}{1/n \sum_{i=1}^{n} [X_i - E(X_i)]^2} \qquad (8)$$

$$E(X_i) = \frac{1}{n} \sum_{i=1}^{n} X_i \qquad (9)$$

where r_1 is the X_t and $E(X_t)$ is the mean of the sample data.

If r_i is not significantly different from zero, the time series are considered to be independent and the Mann–Kendall test can be used directly. Otherwise, it should be pre-whitened by:

$$Y_i' = Y_i - r_i \times Y_{i-1} \qquad (10)$$

Then, β_i is added again to the residual dataset of **Eq. 10**.

$$Y_i'' = Y_i' - \beta i \qquad (11)$$

where Y_i'' is the pre-whitened series (final series).

Finally, the Mann–Kendall test is used to detect the trend of the pre-whitened time series (Jhajharia et al., 2011; Machiwal et al., 2017).

3.2.4 Geostatistical Methods

In this research, we use Moran's I, General G, and Gravity Migration Model to explore the spatial correlation drought characteristic variables, and identify the evolution characteristic of drought in NWC.

3.2.4.1 Center of Gravity Migration Model

The temporal and spatial evolution features of drought were investigated by the center of gravity migration model:

$$X_j = \frac{\sum_{i=1}^{n}(C_{ij}X_i)}{\sum_{i=1}^{n}C_{ij}} \qquad (12)$$

$$Y_j = \frac{\sum_{i=1}^{n}(C_{ij}Y_i)}{\sum_{i=1}^{n}C_{ij}} \qquad (13)$$

where X_j, Y_j are the longitude and latitude coordinate of SPI gravity center of j year, C_{ij} is the SPI value of unit i in year j, X_i and Y_i are the longitude and latitude coordinate of geometrical center of unit i, and n is the number of research units.
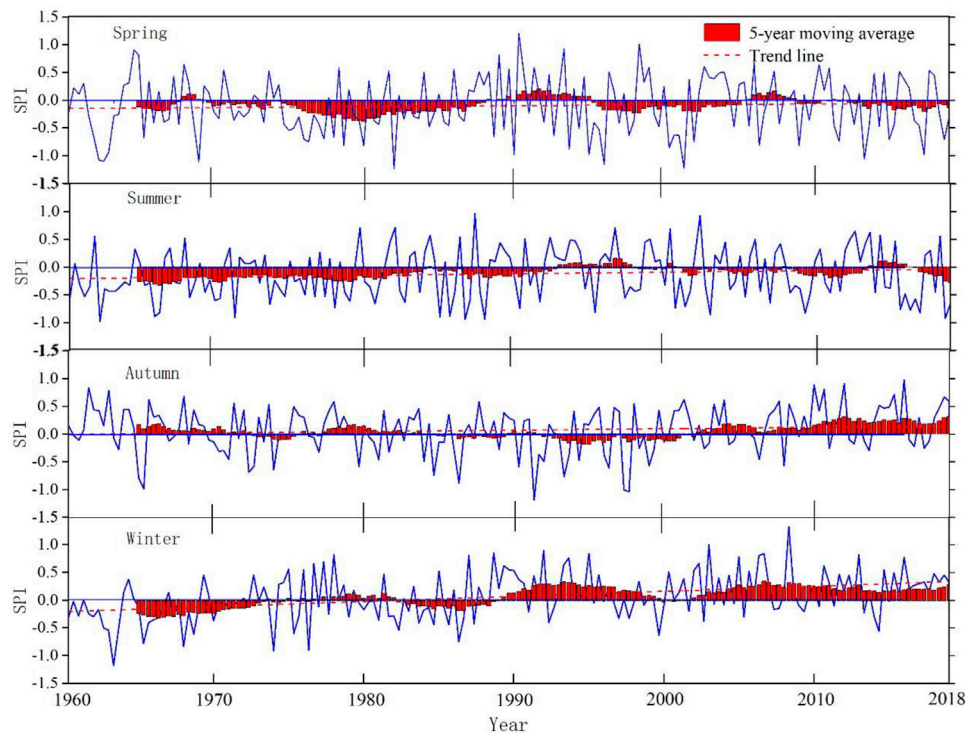
FIGURE 4 | Variation of seasonal SPI series from 1960 to 2018 in NWC.

3.2.4.2 Moran's I

Moran's *I* is used to identify the autocorrelation of spatial elements or the similarity of neighboring data, which can be classified as Global Moran's *I* index (GMI) and Local Moran's *I* index (LMI) (Sheng et al., 2002; Wang et al., 2016). This research employed the GMI to determine whether there existed spatial autocorrelation of drought characteristic variables, and the LMI was used to identify the property of the cluster or the disperse variables. The GMI is given as:

$$GMI = \frac{n}{S_0} \frac{\sum\limits_{i=1}^{n}\sum\limits_{j=1}^{n} w_{ij}(x_i - \bar{x})(x_j - \bar{x})}{\sum\limits_{i=1}^{n}(x_i - \bar{x})^2} \quad (14)$$

$$S_0 = \sum\limits_{i=1}^{n}\sum\limits_{j=1}^{n} w_{ij} \quad (15)$$

where *n* is the number of research units; x_i is the drought variable value of unit *i*; x_j is the drought variable value of unit *j*; $\bar{x}$ is the average drought variable value of the study area; and w_{ij} is the spatial weight matrix that is defined by the inverse distance weighted method. The GMI ranges from −1 to 1. If GMI > 0, the spatial distribution of drought variable is considered positively autocorrelated, and the drought variable is characterized with a cluster type. If GMI < 0, the spatial distribution of drought variable is identified as negatively autocorrelated, and the drought variable is defined as a

disperse type. If GMI = 0, the drought variable is defined as a random spatial pattern.

Additionally, the LMI is computed as the following:

$$LMI = \frac{n^2}{S_0} (x_i - \bar{x}) \frac{\sum\limits_{j=1}^{n}(x_j - \bar{x})}{\sum\limits_{j=1}^{n}(x_j - \bar{x})^2} \quad (16)$$

The meaning of the parameters were the same as that in **Eq. 14** and **Eq. 15**.

3.2.4.3 General G

Though the GMI can be used to classify the cluster pattern, it cannot figure out whether the property of the clustered variable are hot spots (have high values) or cold spots (have low values). Thus, the Getis-Ord General *G* is applied to identify locations that spatially clustered with either high or low values (Chen, 2021).

$$G_i(d) = \frac{\left[\sum\limits_{j=1}^{n} w_{ij}(d) w_j\right]}{\sum\limits_{j=1}^{n} x_j (j \neq i)} \quad (17)$$

where *d* is the distance between the unit *i* and unit *j*, and w_{ij} is the same spatial weight used for obtaining GMI as **Eq. 14** and **Eq. 15**. High positive values of $G_i(d)$ indicate that the locations are
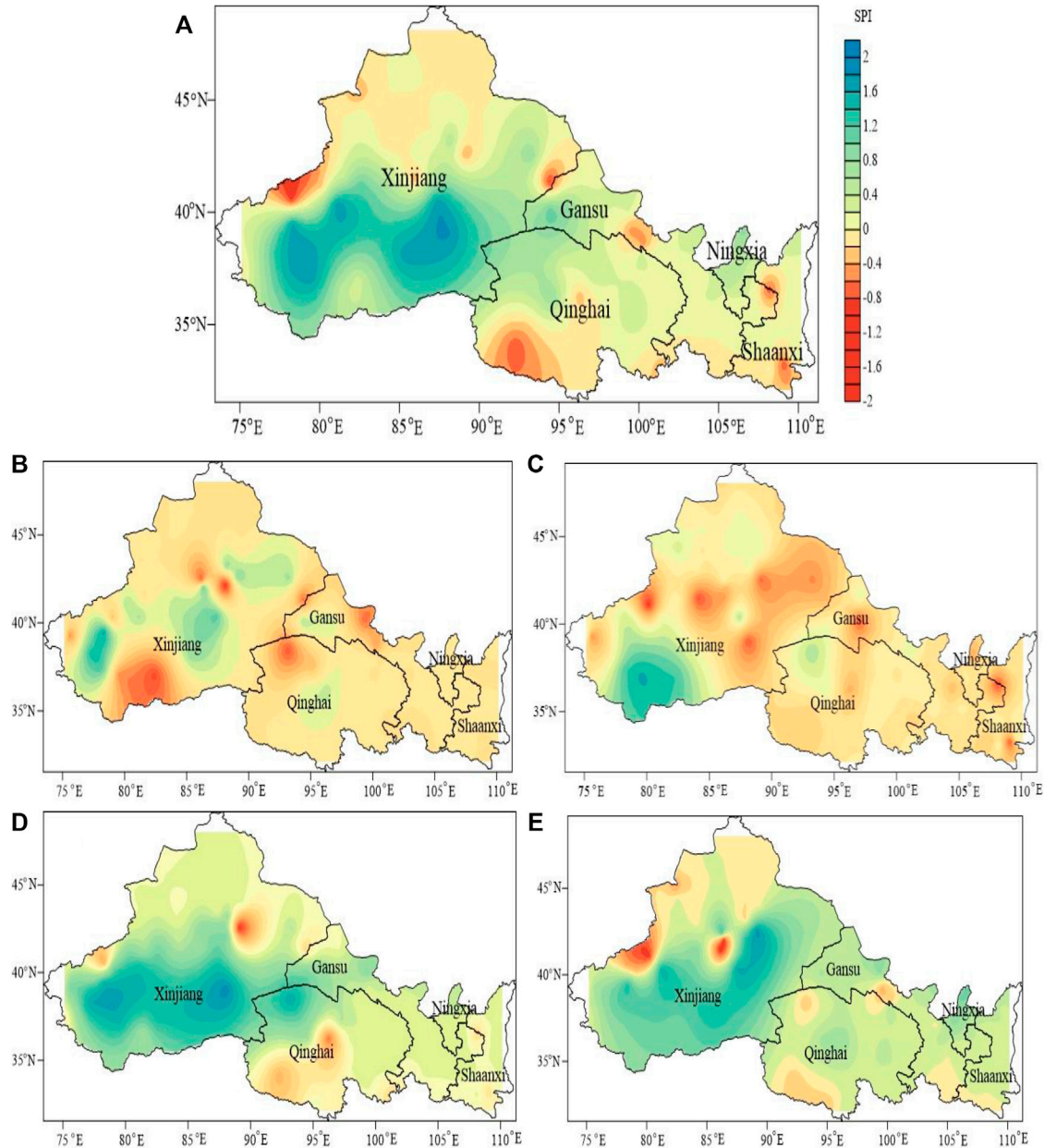
FIGURE 5 | Spatial distribution of average SPI from 1960 to 2018 in NWC.

clustered with hot spots while negative values indicate a spatial cluster with cold spots.

For the purpose of statistically identifying the hot spots or cold spots, the Z score of $G_i(d)$ is calculated by:

$$Z(G_i) = \frac{G_i - E(G_i)}{SD(G_i)} \, (j \neq i) \tag{18}$$

where $E(G_i)$ is the expected value of G_i; $SD(G_i)$ is the standard deviation of G_i. To decide whether the Z score is statistically significant, the absolute value would have to be greater than 1.65,

1.96, and 2.57, which were the significant level of 0.1, 0.05, and 0.01, respectively (Huang et al., 2013).

4 RESULTS

4.1 Spatio-Temporal Variation of Drought

As shown in **Figure 3**, both SPI-3 series and SPI-12 series have been in a significant fluctuation, droughts and floods alternated frequently, and both series exhibited slightly increasing trends,
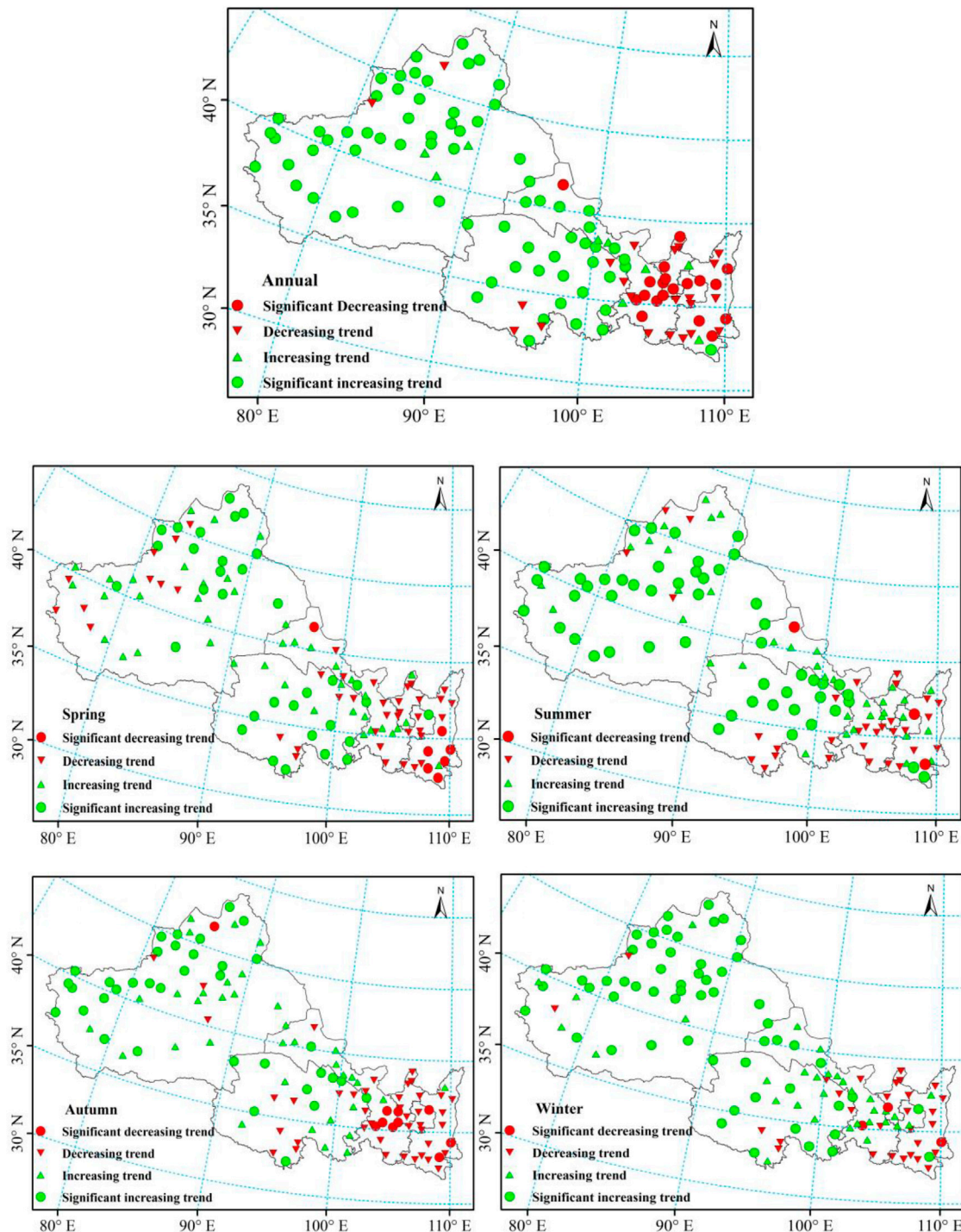
FIGURE 6 | Spatial distribution of annual and seasonal Z-statistics of SPI by TFPW-MK.

suggesting a weakening drought in the NWC. Late 1980s was the turning point of drought, after which positive values were dominant and this trend was more prominent in the 2010s.

Figure 4 illustrated the temporal variation characteristics of seasonal drought based on the SPI-3 in NWC from 1960 to 2018. All the SPI series presented with upward trends, which indicated

that the drought situation of all seasons in NWC was relieved. According to the Z-statistic test by TFPW-MK, the SPI series of winter passed the significant test at level 0.05 while the series of spring, summer, and autumn did not, suggesting that the SPI series of winter presented a significant increasing trend while the SPI series of spring, summer, and autumn slightly increased.

FIGURE 7 | Migration of gravity center of SPI.
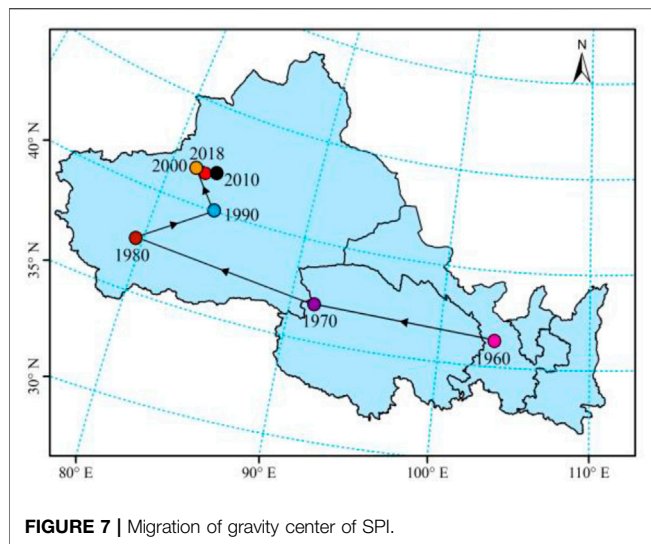
Besides, as can be seen from **Figure 4**, the SPI values of spring and summer varied greatly; prolonged droughts of spring and summer were detected before the 1990s. No significant change of autumn drought series was observed until the 2010s. Winter humidification was identified after the late 1980s.

Figure 5 demonstrated the spatial distribution characteristics of annual and seasonal SPI values in NWC. The annual and seasonal SPI were the average station-based SPI values from 1960 to 2018. Affected by the geography, topography, vegetation, and other factors, the spatial distribution of SPI exhibited significant spatial differences. For annual scale (**Figure 5A**), except for southern Xinjiang, most areas of NWC experienced dry conditions. The minimum SPI values mainly occurred in east Xinjiang and south Qinghai, suggesting that these areas had more severe droughts. The distribution of SPI values in spring and summer showed that the NWC has suffered extensive summer and spring droughts (**Figures 5B,C**). Autumn and winter droughts in NWC were much lighter than that of spring and summer. Autumn drought mainly appeared at south Qinghai and northwest Xinjiang (**Figure 5D**), and winter drought mainly occurred in local areas of west Xinjiang (**Figure 5E**).

4.2 Trend Analysis

Figure 6 shows the geographical distribution of annual and seasonal test Z-statistics of SPI series. According to the results, both annual and seasonal drought series of NWC exhibited a typical distribution pattern—positive trends in the west and negative trends in the east. In fact, Z-statistics by the TFPW-MK test of annual SPI values revealed that 89 stations (73.0%) had increasing trends while 33 stations (27.0%) had decreasing trends, of which 72 stations have passed the positive significant test at level 0.05 while 19 stations have passed the negative significant test, indicating an obvious wet tendency in west NWC and a slight dry tendency in east NWC.

The spring drought series showed positive trends at 68.9% of the stations, and 33 stations of these passed the significant test at level 0.05. South Qinghai and northwest Xinjiang experienced

distinct wetting conditions. Significant decreasing trends were detected in south Shaanxi, suggesting a remarkable aggravation of spring drought in such area. In summer, 98 stations (80.3%) showed positive trends, 51 stations of which have passed the significant test at 0.05 level and these stations mainly occurred in Xinjiang and Qinghai, which indicated that the summer drought in Xinjiang and Qinghai were greatly relieved from 1960 to 2018. The results obtained by elaborating the autumn droughts were similar to those relative to spring and summer. In this case, 81 out of 122 stations presented positive trends, 36 stations passed the significant tests and these stations were presented at Tianshan Mountain area in western Xinjiang. The significant decreasing trends of south Gansu indicated that these areas have experienced an obvious intensifying autumn drought. The results of winter Z-statistics demonstrated that 81.9% of the stations had increasing trends and the significant positive trends mostly occurred in Xinjiang and south Qinghai and east Gansu.

In addition, the droughts in eastern regions, such as Shaanxi, Ningxia, and west Gansu, were aggravating while the droughts in west NWC, such as Xinjiang and Qinghai, were alleviating or tended to be wet. Besides, in winter and summer, more than 50% of the stations passed the significant test, suggesting that the winter and summer drought experienced greater change compared with spring and autumn droughts.

4.3 Migration Characteristic of Drought

Based on the model of Gravity Migration, the spatial evolution of annual SPI values in NWC was revealed. The results showed that the distribution center of SPI in 1960 was (103.54°E, 36.38°N), while the center in 2018 was (82.32°E, 41.64°N), suggesting a great climate change in NWC. According to the gravity migration paths (**Figure 7**), the gravity center of SPI moved from southeast to northwest and then turned from southwest Xinjiang to northeast Xinjiang, which indicated that the drought in NWC was alleviating from southeast to northwest during 1960–2018. Moreover, the average migration distances (57.32 km.year^{-1}) of SPI centers in NWC from 1960 to 1990 were much greater than

FIGURE 8 | Standard deviation ellipse of SPI.
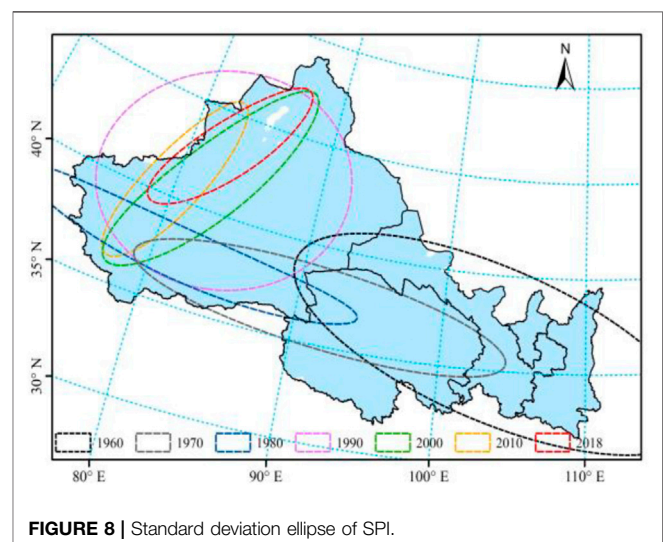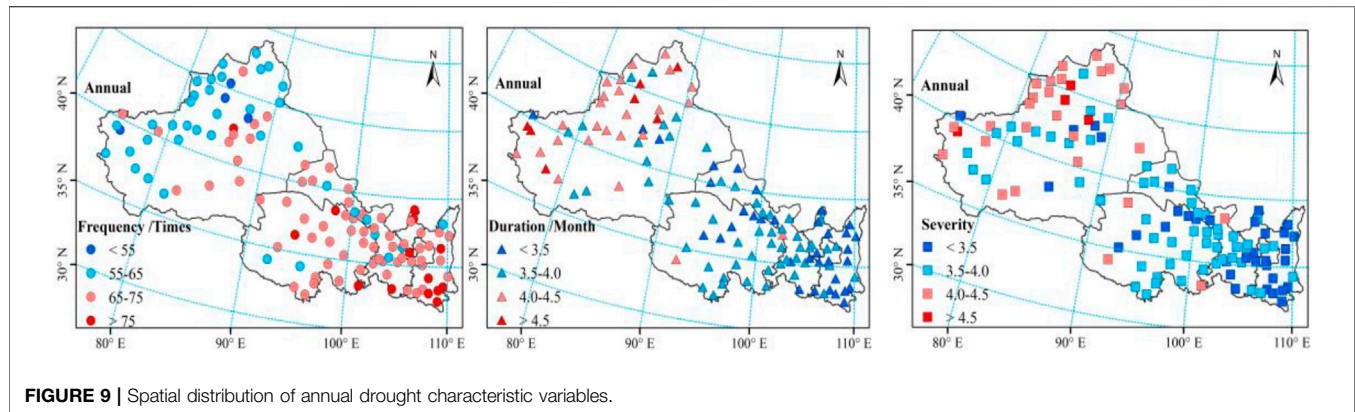
FIGURE 9 | Spatial distribution of annual drought characteristic variables.

that from 1990 to 2018 (16.08 km.year^{-1}), suggesting that the wetting area in west NWC was much larger than the drying area in east NWC. The reason why the SPI centers moved towards high latitudes in NWC may be related to the strengthened moisture current from south for the past few years especially in Xinjiang.

As **Figure 8** showed, the standard deviation ellipse of SPI values in 1960 almost covered the middle and east regions of NWC, suggesting that the droughts had large spatial differences in 1960. After then, the coverage of ellipse exhibited a decreased trend, indicating that the spatial distribution of SPI values has turned from disperse to concentrated. That is, the spatial distribution of drought in NWC tended to be concentrated during 1960–2018. Meanwhile, from 1960 to 1980, the ellipses flattened and moved towards northwest, further illustrating that the variation of SPI values had exhibited a direction of northwest–southeast. Besides, the difference between the ellipsoidal shape of 1980 and the ellipse of 1990 was much greater compared with other adjacent decades, which was consistent with the previous reports that the climate in NWC has turned from dry to wet since 1986.

4.4 Spatial Evolution Characteristic of Drought Variables

Based on Run Theory, the drought characteristic variables (drought frequency, drought duration, and drought severity) were separated from SPI series and are shown in **Figure 9** and **Figure 10**. As can be seen from **Figure 9**, the annual drought frequency in most areas of NWC was between 65 and 75 times from 1960 to 2018. The highest drought frequency (85 times) occurred in Ankang of Shaanxi Province; the minimum value (51 times) happened in Wusu of Xinjiang, with a difference of 34 times. Annual drought duration in most areas of NWC from 1960 to 2018 lay in the range of 3.1–4.7 months; Shaanxi experienced the shortest drought duration (3.3 months in average) while west Xinjiang had the longest duration (4.2 months in average). The spatial distribution of annual drought severity was similar to drought duration, and the highest drought severity (4.5) happened in Kelamayi of Xinjiang, suggesting that it went through the worst drought in NWC. The lowest drought

severity (3.1) appeared at Huinong of Ningxia. Overall, on an annual scale, drought frequency decreased from southeast to northwest, while drought duration and severity increased from southeast to northwest, suggesting that more droughts occurred in east of NWC, which were less harmful, while less drought presented at west NWC, which brought greater drought damage.

Except for autumn, the distribution patterns of seasonal drought characteristics were similar to that of annual drought characteristics (**Figure 10**). The drought frequency of spring, summer, and winter showed a downward trend from east to west while drought duration and severity exhibited an upward trend from east to west, and the drought characteristics of autumn presented with opposite trends. In spring and winter, most areas experienced more frequent droughts with shorter duration and lower severity. Serious spring and winter droughts appeared at northwest Xinjiang. Meanwhile, Shaanxi, Ningxia, and Gansu endured the most frequent winter droughts. In summer, the distribution boundary of drought variables between east and west was more clear than others'; more summer droughts occurred in east NWC with shorter duration and lighter severity, while fewer summer droughts with longer duration and higher severity were found in west NWC. Autumn drought with longer duration and higher severity mainly happened in Ningxia, south Shaanxi, and west Xinjiang. The average drought frequency of spring, summer, autumn, and winter was 22.5, 20.8, 21.1, and 22.8 times, respectively. Seasonal drought duration varied from 2.1 to 4.6 months; 35 stations in spring and winter experienced longer drought duration above 3 months, 54 stations' drought duration in summer were longer than 3 months, and 64 stations in autumn went through more than 3 months of drought duration. Seasonal drought severity of the study area ranged from 1.7 to 6.3; the average values of spring, summer, autumn, and winter were 2.9, 3.1, 3.0, and 2.7, respectively.

The statistics of seasonal drought frequency, duration, and severity of 122 meteorological stations were shown as violin box plots. As can be seen from **Figure 11**, winter drought variables of different stations had the greatest differences, while autumn drought variables had the smallest differences. Though the average drought frequency of summer and autumn was smaller, the drought duration and severity of summer and

FIGURE 10 | Spatial distribution of seasonal drought characteristic variables.
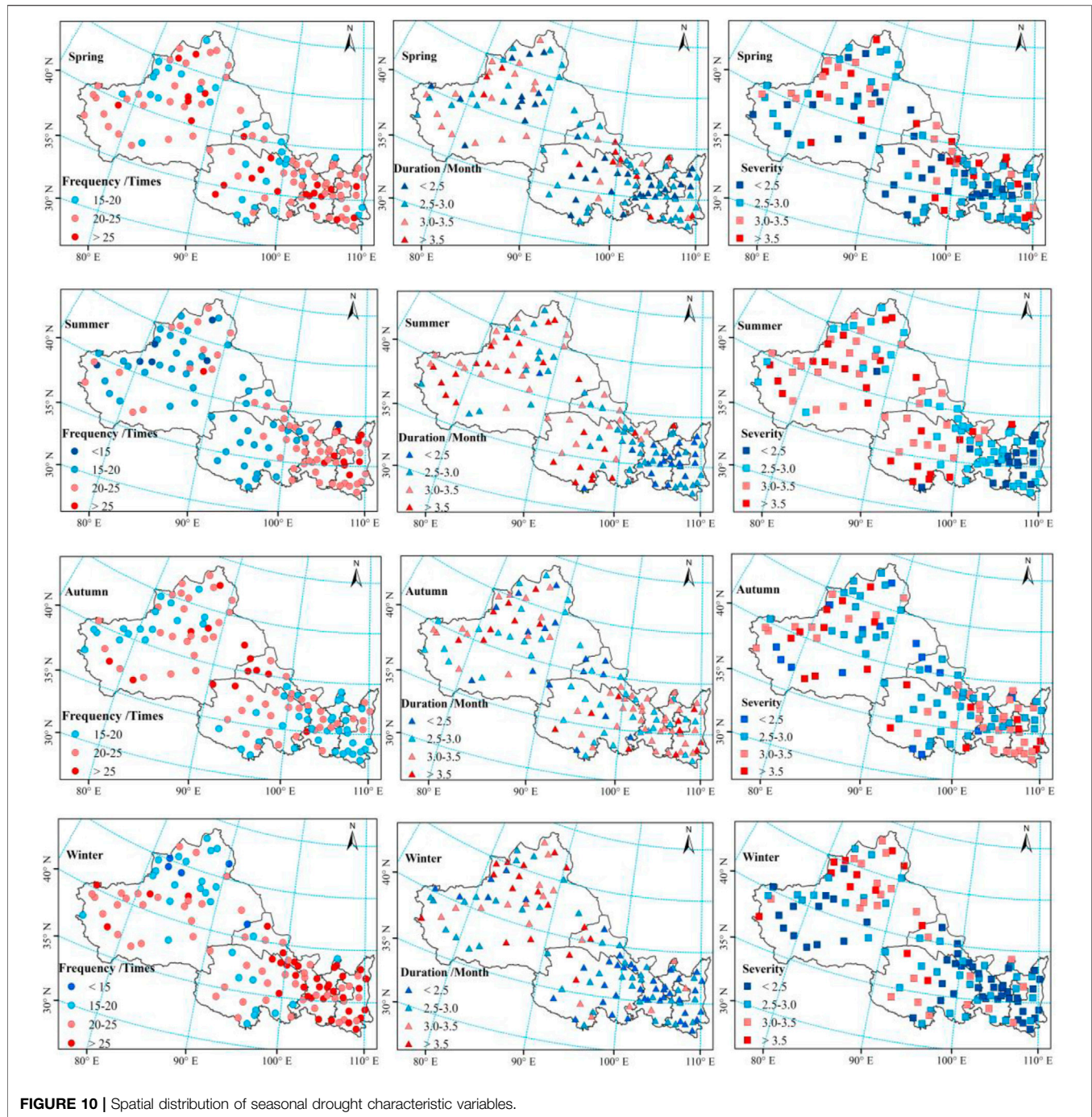
autumn were greater than that of spring and winter, demonstrating that the damage of a drought event in autumn and summer was bigger than in spring and winter; a summer and autumn drought would be more severe and widespread.

In conclusion, the spatial distribution of seasonal drought characteristic variables in NWC had much difference. Winter droughts were the most frequent. Summer drought situation in west of NWC was more severe than other seasons, while autumn drought situation in east of NWC was more severe

than other seasons, suggesting that the contradiction between supply and demand of water resources was more prominent in these areas. Drought duration and drought severity had the same varying tendency, which indicated that a longer drought duration tend to cause a severe drought event. Meanwhile, the contrasting distribution patterns between drought frequency, drought duration, and drought severity demonstrated that the drought duration and drought severity tended to be weakened with the increasing number of drought. That is, the drought situation of NWC exhibited as low frequency with long
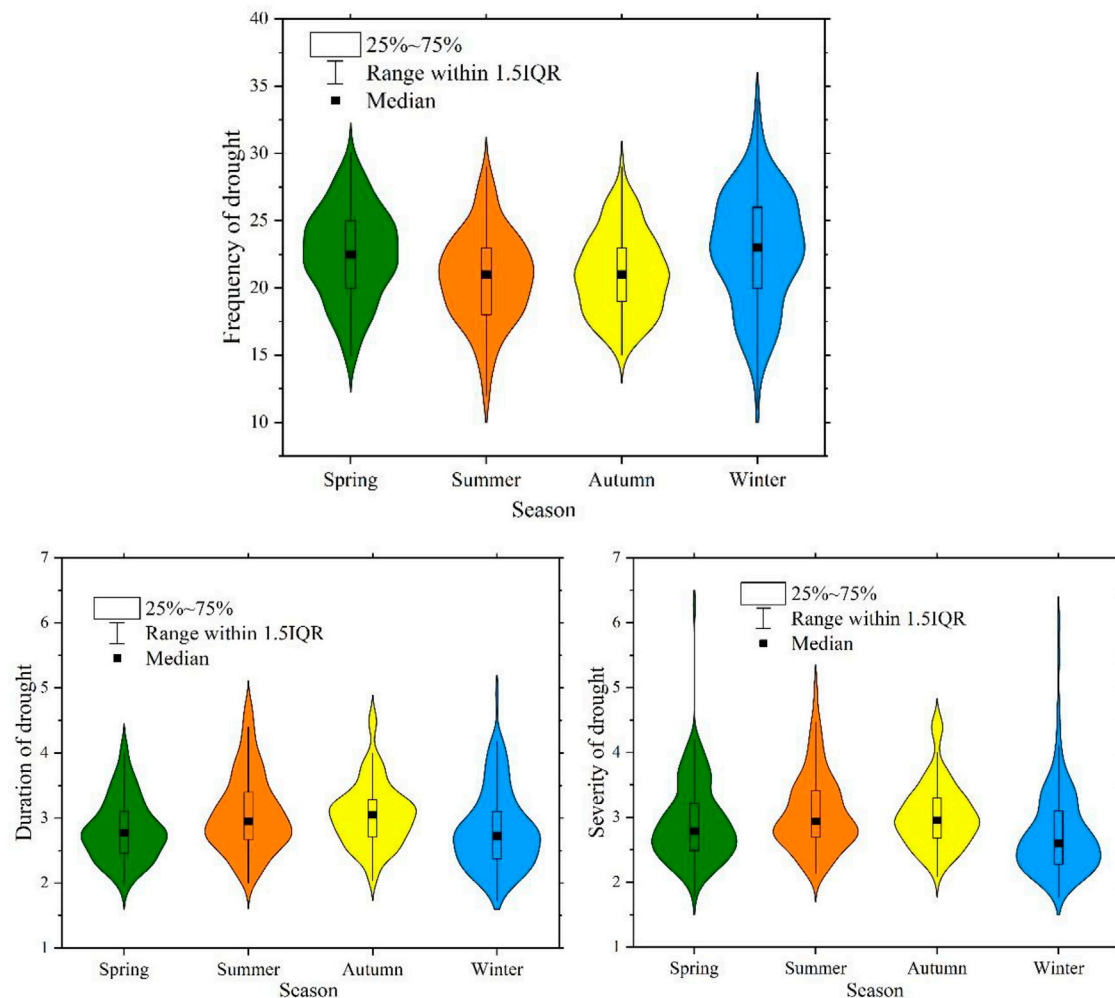
FIGURE 11 | Statistics of seasonal drought variables of 122 meteorological stations.
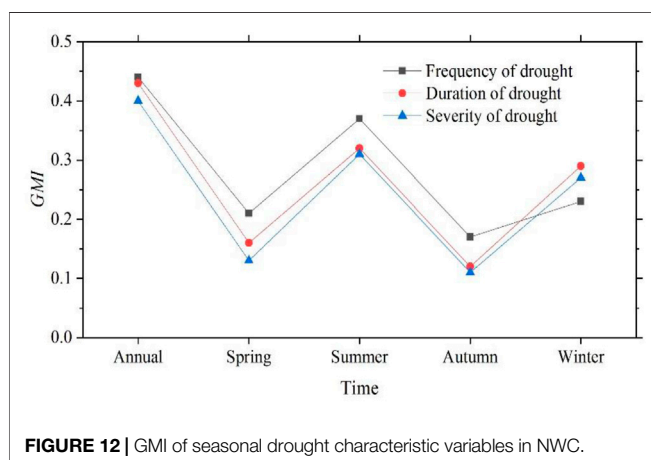
FIGURE 12 | GMI of seasonal drought characteristic variables in NWC.

suggesting a potential interdependence. Therefore, it is of great significance to identify the spatial correlation of drought factors.

4.5 Spatial Autocorrelation of Drought Variables
4.5.1 Analysis of Global Spatial Autocorrelation
As shown in **Figure 12**, all the GMI values of drought variables were above zero and passed the confidence test at level 95%, suggesting that the spatial distributions of annual or seasonal drought variables in NWC were significantly autocorrelated. That is, the drought variables were characterized with regional similarity. The higher GMI values of annual drought variables indicated a better spatial autocorrelation than that of seasonal drought variables. Except for the winter GMI, the GMI of seasonal drought frequency in spring, summer, and autumn was greater than that of drought duration and severity, which demonstrated that the spring, summer, and autumn drought frequency had stronger spatial autocorrelation than their drought

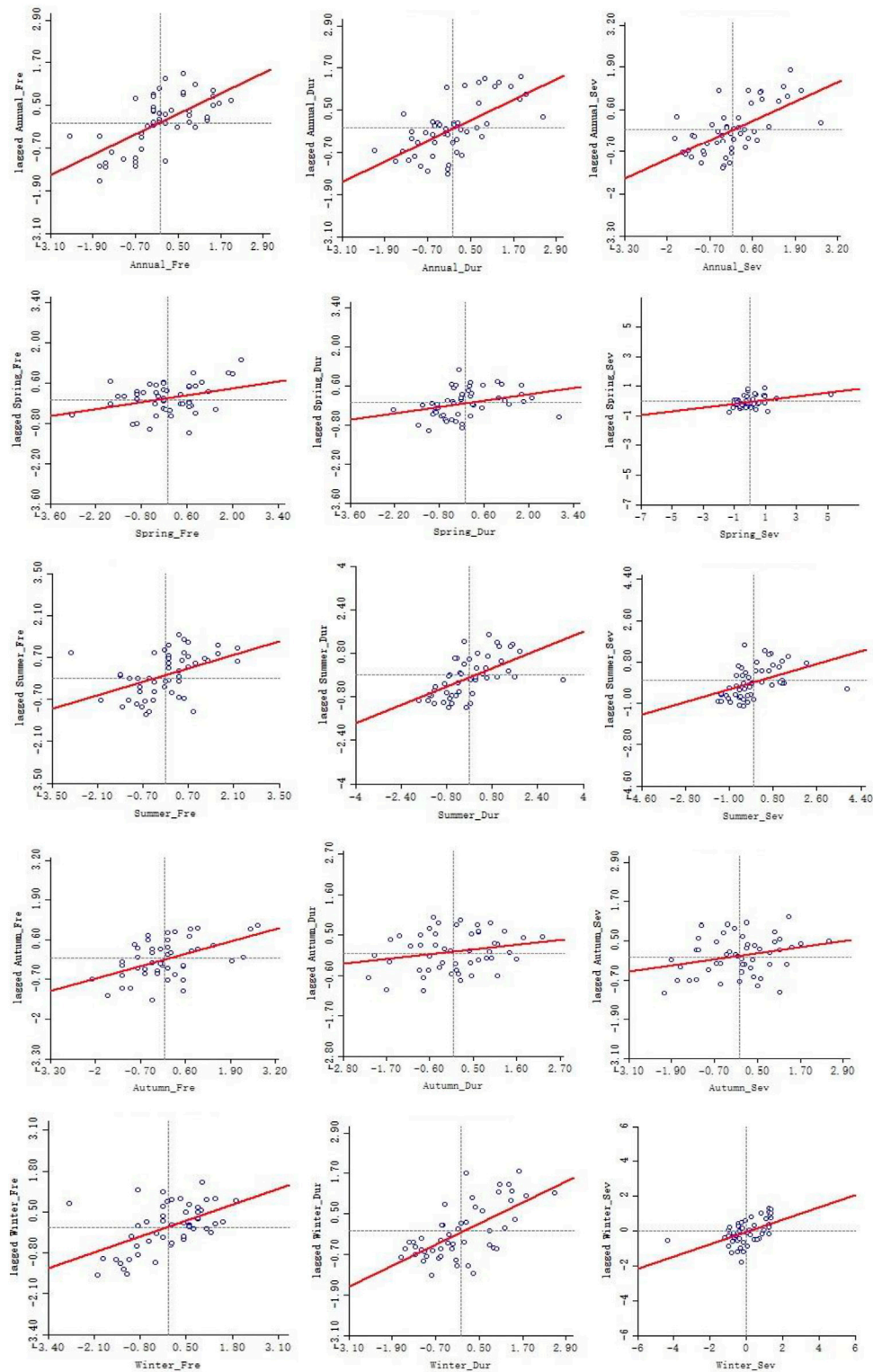duration and strong severity, or high frequency with short duration and light severity. Besides, the drought variables presented a characteristic of spatial concentration,

FIGURE 13 | Scatter plots of LMI for the drought characteristic variables.

FIGURE 14 | Spatial autocorrelation pattern of annual drought variables.
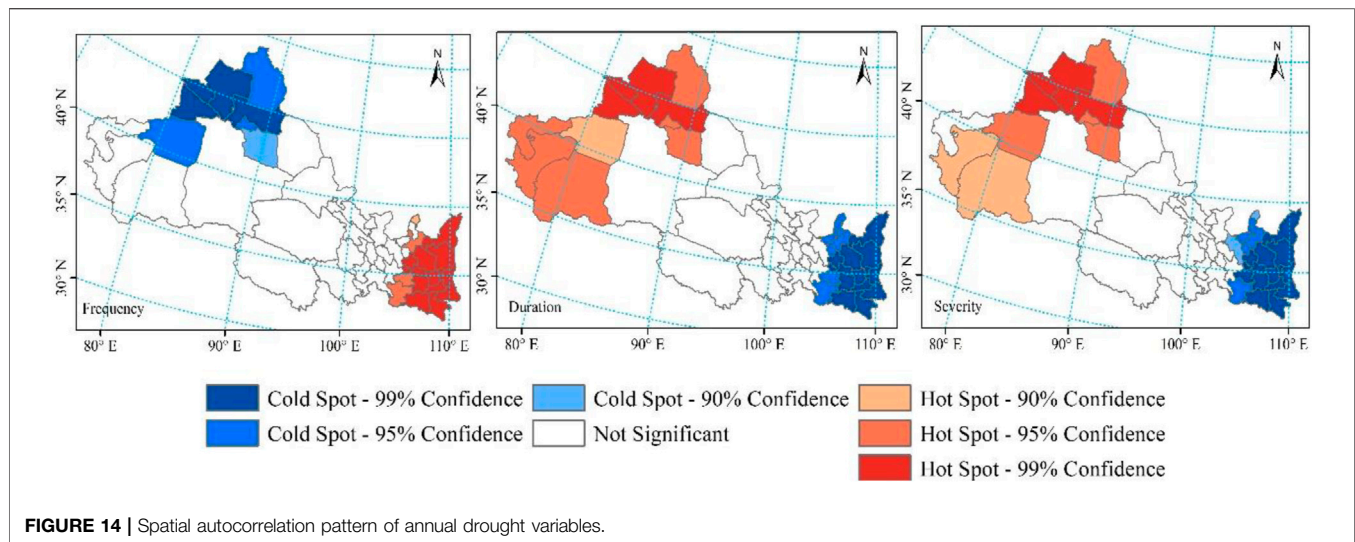
duration and severity while the spatial autocorrelation of drought frequency in winter was weaker than its duration and severity. The greater GMI (0.21–0.43) of drought frequency demonstrated a higher spatial correlation of drought frequency in NWC; a local drought may increase the risk of drought occurrence in adjacent regions. Furthermore, the similar variation trend and the small difference between drought duration and drought severity further verified their good long-range correlations.

4.5.2 Analysis of Local Spatial Autocorrelation
According to the scatter plots of LMI for annual and seasonal drought variables (**Figure 13**), the points in the first and third quadrant were much more than that in the second and fourth quadrant, suggesting that drought variables of most areas in NWC showed an aggregation state of High–High value or Low–Low value; the areas with High–Low value or Low–High value were relatively small.

The spatially clustered locations with features of either high or low values (hot or cold spots) were identified by General *G.*As can be seen from **Figures 14**, **15**, the hot and cold spots of drought characteristic variables in NWC were obviously spatial distribution features. On an annual scale, Shaanxi, Ningxia, and southeast Gansu presented with hot spots of drought frequency and cold spots of drought duration and severity, while northwest Xinjiang (Tacheng, Yili, Aletai, Akesu, Changji, and Tulufan) was characterized with cold spots of drought frequency and hot spots of drought duration and severity, which indicated that the drought frequency of Shaanxi, Ningxia, and southeast Gansu was more than the average values of adjacent areas while the duration and severity of such areas were shorter and milder than their nearby regions, and that the drought frequency of northwest Xinjiang was less than its neighboring area while the duration and severity were longer and more intense than the adjacent areas. Meanwhile, the distribution of hot spots and cold spots at 99% confidence level suggested that Shaanxi experienced the most droughts with shortest duration and lowest severity, while

northwest Xinjiang had the fewest droughts with longest duration and highest severity.

The hot spots of drought frequency in spring mainly occurred in southeast Gansu, indicating that the frequency of spring drought in such areas was more than its nearby regions. As for spring drought duration, the cold spots were scattered in local areas of south Gansu and east Qinghai, and only the hot spot at 95% confidence level was discovered in Akesu of Xinjiang. The hot spots of spring drought severity appeared at Jiuquan and Zhangye, suggesting a higher drought severity in such regions.

In summer, south-central Shaanxi and southeast Gansu presented with cold spots of drought duration and severity at 99% confidence level, suggesting a much lighter summer drought in these areas. The hot spots of drought duration and severity in west Xinjiang indicated a regional heavier summer drought.

In autumn, the hot spots of drought frequency happened in Hexi Corridor and north Qinghai, which also exhibited with cold spots of drought duration and severity, demonstrating that these areas were characterized with more autumn droughts, which were in a lighter situation. Likewise, Shaanxi appeared with cold spots of drought frequency and hot spots with drought duration and severity, which means that these areas suffered a more severe autumn drought but with less frequency.

The spatial distributions of hot and cold spots of the three drought variables in winter were similar to that in summer, but the area presented with significant correlation expanded. Most areas of east NWC (including Shaanxi, Ningxia, and central-south Gansu) exhibited hot spots of drought frequency and cold spots of drought duration and severity while northwest Xinjiang (Changji, Tacheng, Kelamayi) showed cold spots of drought frequency and hot spots of drought duration and severity, indicating a light winter drought in east NWC and a more severe winter drought in northwest Xinjiang. Besides, the hot spots of drought duration and severity in Tacheng and Changji were at a confidence level of 99%, suggesting a much more serious winter drought in such areas.

FIGURE 15 | Spatial autocorrelation pattern of cold hot spots of seasonal drought variables.
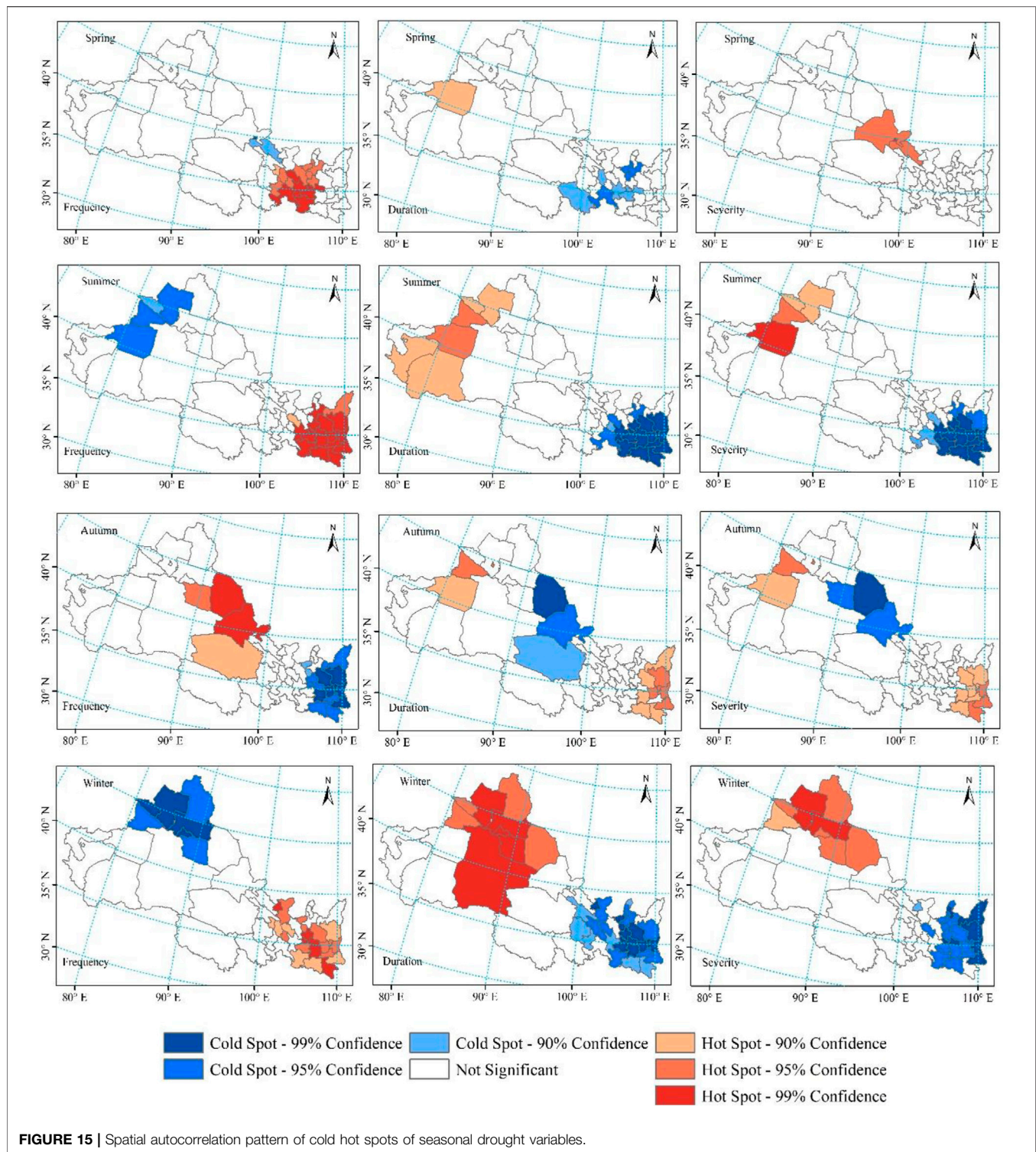
On the whole, *G* values of the three drought variables in east NWC were opposite to the west. Shaanxi and Xinjiang were at the highest confidence level regardless of cold or hot spots, suggesting that the climate conditions in this area were complicated; more drought monitoring should be conducted in such areas in order to investigate causes and improve drought resistance.

5 CONCLUSION AND DISCUSSION

As drought in NWC is partially a large-scale phenomenon and exhibited regional characteristics, it is necessary to provide a comprehensive assessment of drought in terms of drought indexes, the distribution of drought characteristic variables

(frequency, duration, and severity), the spatio-temporal evolution features of drought, and the spatial similarity of drought characteristic variables. This research analyzed the spatio-temporal variation of SPI in NWC during 1960–2018; characteristic variables of drought (including drought frequency, drought duration, and drought severity) were identified and their distribution patterns were studied based on Run Theory; the evolution process of drought was discussed and spatial autocorrelation of drought characteristic variables was revealed by TFPW-MK, GMI, LMI, and General *G*.

From 1960 to 2018, the drought in NWC was alleviating, which was in accordance with the previous reports that the climate in NWC has turned from warm dry to warm wet (Yuan et al., 2017; Huang et al., 2019; Cao et al., 2020). Affected by the complicated topography and various climate conditions, the variation of drought had obvious regional differences; west NWC with an arid or semi-arid climate was presented with significant wet tendency, while east NWC with a semi-humid climate experienced an increasing trend in dryness. The migration path of the gravity center of SPI showed that SPI moved towards higher latitude in NWC. On an annual scale, the average drought frequency in NWC from 1960 to 2018 was 71 times, while the average drought duration and severity were 3.8 months and 4.0, respectively. The spatial distribution of drought frequency decreased from southeast to northwest, while drought duration and severity increased from southeast to northwest, illustrating that east NWC experienced more frequent droughts that were less harmful while west NWC experienced fewer droughts that brought greater drought damage. Regardless of time scale, drought duration was positively correlated to drought severity; a longer drought duration tends to cause a severer drought event. Summer and autumn were characterized with longer duration and higher severity while spring and winter were characterized with shorter duration and lower severity. According to GMI, all the seasonal drought variables presented with significant positive spatial correlation. The results of LMI showed that there was a significant difference in the local spatial autocorrelation of seasonal drought variables. The hotspots of annual drought frequency mainly concentrated in Shaanxi while the hotspots of annual drought duration and severity mainly occurred in northwest Xinjiang, suggesting that there was significant positive correlation between Shaanxi and its surrounding areas, and between northwest Xinjiang and its adjacent areas. That is, there existed regional similarity of drought characteristics in Shaanxi and surrounding areas (more droughts, shorter duration, and lower severity), while northwest Xinjiang and adjacent areas exhibited the same drought characteristic with fewer but more severe droughts.

Compared with previous studies, this study considered the spatial heterogeneity and similarity of drought, the combination of the drought index map, drought characteristic variable map, Z-statistics of SPI by TFPW-MK, the barycenter model, and standard deviation ellipse, and the spatial autocorrelation analysis can be expected to explore the spatio-temporal evolution characteristics of meteorological drought in NWC. However, though the drought of NWC has been relieved, the average precipitation (less than 300 mm year^{-1}) increased only by 10%, which was not enough to change the basic state of climate in NWC; the drought issue is still a major factor limiting the economic development of NWC. Meanwhile, the cause mechanism of drought evolution characteristics in NWC was simply mentioned due to space constraints; root cause analysis and how long can the wetting tendency last in NWC will be the next research topics.

This study employed SPI for drought identification without considering the effects of potential evapotranspiration, which may have an impact on the results. Further study on the application conditions of SPEI and SPI for drought assessment in NWC should be conducted.

DATA AVAILABILITY STATEMENT

The data analyzed in this study are subject to the following licenses/restrictions: The datasets analyzed in this study are only available upon request directed to the China Meteorological Data Sharing Service System (http://www.cma.gov.cn). Requests to access these datasets should be directed to http://www.cma.gov.cn.

AUTHOR CONTRIBUTIONS

HL: Data curation, Funding Acquisition, Writing—original draft, Methodology, and Validation. EH: Validation and Writing—review and editing. JD: Methodology and Writing—review and editing.

FUNDING

ACKNOWLEDGMENTS

REFERENCES

Amirataee, B., Montaseri, M., and Rezaie, H. (2020). An Advanced Data Collection Procedure in Bivariate Drought Frequency Analysis. *Hydrological Process.* 34 (21), 4067–4082. doi:10.1002/hyp.13866

Ayantobo, O. O., Li, Y., Song, S., and Yao, N. (2017). Spatial Comparability of Drought Characteristics and Related Return Periods in mainland China over 1961-2013. *J. Hydrol.* 550, 549–567. doi:10.1016/j.jhydrol.2017.05.019

Azimi, S., Hassannayebi, E., Boroun, M., and Tahmoures, M. (2020). Probabilistic Analysis of Long-Term Climate Drought Using Steady-State Markov Chain Approach. *Water Resour. Manag.* 34 (15), 4703–4724. doi:10.1007/s11269-020-02683-5

Beguería, S., Vicente-Serrano, S. M., Reig, F., and Latorre, B. (2014). Standardized Precipitation Evapotranspiration index (SPEI) Revisited: Parameter Fitting, Evapotranspiration Models, Tools, Datasets and Drought Monitoring. *Int. J. Climatol.* 34, 3001–3023. doi:10.1002/joc.3887

Bonaccorso, B., Peres, D. J., Castano, A., and Cancelliere, A. (2015). SPI-based Probabilistic Analysis of Drought Areal Extent in Sicily. *Water Resour. Manage.* 29 (2), 459–470. doi:10.1007/s11269-014-0673-4

Brito, S. S. B., Cunha, A. P. M. A., Cunningham, C. C., Alvalá, R. C., Marengo, J. A., and Carvalho, M. A. (2018). Frequency, Duration and Severity of Drought in the Semiarid Northeast Brazil Region. *Int. J. Climatol* 38, 517–529. doi:10.1002/joc.5225

Burke, E. J., Perry, R. H. J., and Brown, S. J. (2010). An Extreme Value Analysis of UK Drought and Projections of Change in the Future. *J. Hydrol.* 388, 131–143. doi:10.1016/j.jhydrol.2010.04.035

Campozano, L., Ballari, D., Montenegro, M., and Avilés, A. (2020). Future Meteorological Droughts in Ecuador: Decreasing Trends and Associated Spatio-Temporal Features Derived from CMIP5 Models. *Front. Earth Sci.* 8, 17. doi:10.3389/feart.2020.00017

Cao, D., Zhang, J., Yan, H., Xun, L., Yang, S., Bai, Y., et al. (2020). Regional Assessment of Climate Potential Productivity of Terrestrial Ecosystems and its Responses to Climate Change over China from 1980-2018. *IEEE Access* 8, 11138–11151. doi:10.1109/access.2019.2963458

Chen, H., and Sun, J. (2015). Changes in Drought Characteristics over China Using the Standardized Precipitation Evapotranspiration index. *J. Clim.* 28 (13), 5430–5447. doi:10.1175/jcli-d-14-00707.1

Chen, Y. D., Zhang, Q., Xiao, M., Singh, V. P., and Zhang, S. (2016). Probabilistic Forecasting of Seasonal Droughts in the Pearl River basin, China. *Stoch Environ. Res. Risk Assess.* 30 (7), 2031–2040. doi:10.1007/s00477-015-1174-6

Chen, Y. G. (2021). An Analytical Process of Spatial Autocorrelation Functions Based Moran's index. *Plos One* 16 (4), e0249589. doi:10.1371/journal.pone.0249589

Deng, S., Chen, T., Yang, N., Qu, L., Li, M., and Chen, D. (2018). Spatial and Temporal Distribution of Rainfall and Drought Characteristics across the Pearl River basin. *Sci. Total Environ.* 619-620, 28–41. doi:10.1016/j.scitotenv.2017.10.339

Dinpashoh, Y., Jhajharia, Fakheri-Fard, D. A., Vijay, P. S., and Ercan, K. (2011). Trends in Reference Crop Evapotranspiration over Iran. *J. Hydrol.* 399, 422–433. doi:10.1016/j.jhydrol.2011.01.021

Fung, K. F., Huang, Y. F., and Koo, C. H. (2020). Assessing Drought Conditions through Temporal Pattern, Spatial Characteristic and Operational Accuracy Indicated by SPI and SPEI: Case Analysis for Peninsular Malaysia. *Nat. Hazards* 103, 2071–2101. doi:10.1007/s11069-020-04072-y

Gocic, M., and Trajkovic, S. (2013). Analysis of Changes in Meteorological Variables Using Mann-Kendall and Sen's Slope Estimator Statistical Tests in Serbia. *Glob. Planet. Change* 100, 172–182. doi:10.1016/j.gloplacha.2012.10.014

Gu, L., Chen, J., Xu, C. Y., Wang, H. M., and Zhang, L. P. (2018). Synthetic Impacts of Internal Climate Variability and Anthropogenic Change on Future Meteorological Droughts over China. *Water* 10 (11), 1702. doi:10.3390/w10111702

Guo, H., Bao, A., Liu, T., Jiapaer, G., Ndayisaba, F., Jiang, L., et al. (2018). Spatial and Temporal Characteristics of Droughts in Central Asia during 1966-2015. *Sci. Total Environ.* 624, 1523–1538. doi:10.1016/j.scitotenv.2017.12.120

Haroon, M. A., Zhang, J., and Yao, F. (2016). Drought Monitoring and Performance Evaluation of MODIS-Based Drought Severity index (DSI) over Pakistan. *Nat. Hazards* 84 (2), 1349–1366. doi:10.1007/s11069-016-2490-y

Hu, Z., Chen, X., Chen, D., Li, J., Wang, S., Zhou, Q., et al. (2019). "Dry Gets Drier, Wet Gets Wetter": A Case Study over the Arid Regions of central Asia. *Int. J. Climatol* 39 (2), 1072–1091. doi:10.1002/joc.5863

Hu, Z., Chen, X., Li, Y., Zhou, Q., and Yin, G. (2021). Temporal and Spatial Variations of Soil Moisture over Xinjiang Based on Multiple GLDAS Datasets. *Front. Earth Sci.* 9, 654848. doi:10.3389/feart.2021.654848

Huang, J. Q., Ma, J. R., Guan, X. D., Li, Y., and He, Y. L. (2019). Progress in Semi-arid Climate Change Studies in China. *Adv. Atmos. Sci.* 36 (9), 922–937. doi:10.1007/s00376-018-8200-9

Huang, J., Sun, S., and Zhang, J. (2013). Detection of Trends in Precipitation during 1960–2008 in Jiangxi Province, Southeast China. *Theor. Appl. Climatol* 114 (1–2), 237–251. doi:10.1007/s00704-013-0831-2

Huang, S. Z., Huang, Q., Chang, J. X., Zhu, Y. L., Leng, G. Y., and Xing, L. (2015). Drought Structure Based on a Nonparametric Multivariate Standardized Drought index across the Yellow River basin, China. *J. Hydrol.* 530, 127–136. doi:10.1016/j.jhydrol.2015.09.042

Jhajharia, D., Dinpashoh, Y., Kahya, E., Singh, V. P., and Fakheri-Fard, A. (2011). Trends in Reference Evapotranspiration in the Humid Region of Northeast India. *Hydrol. Process.* 26 (3), 421–435. doi:10.1002/hyp.8140

Ji, F., Wu, Z., Huang, J., and Chassignet, E. P. (2014). Evolution of Land Surface Air Temperature Trend. *Nat. Clim Change* 4 (4), 462–466. doi:10.1038/nclimate2223

Kalisa, W., Zhang, J., Igbawua, T., Ujoh, F., Ebohon, O. J., Namugize, J. N., et al. (2020). Spatio-temporal Analysis of Drought and Return Periods over the East African Region Using Standardized Precipitation Index from 1920 to 2016. *Agric. Water Manage.* 237, 106195. doi:10.1016/j.agwat.2020.106195

Leng, X., Liu, X., Gao, Y., Liu, Y., Yang, Q., Sun, G., et al. (2020). Drought Assessment of Southwestern China Based on HadGEM2-ES Model under Representative Concentration Pathway 4.5 Scenario. *Nat. Hazards* 102, 307–334. doi:10.1007/s11069-020-03928-7

Li, H., Gao, Y., and Hou, E. (2021). Spatial and Temporal Variation of Precipitation during 1960-2015 in Northwestern China. *Nat. Hazards* 109 (3), 2173–2196. doi:10.1007/s11069-021-04915-2

Li, S.-Y., Miao, L.-J., Jiang, Z.-H., Wang, G.-J., Gnyawali, K. R., Zhang, J., et al. (2020). Projected Drought Conditions in Northwest China with CMIP6 Models under Combined SSPs and RCPs for 2015-2099. *Adv. Clim. Change Res.* 11 (3), 210–217. doi:10.1016/j.accre.2020.09.003

Lin, Z., and Shelton, S. (2020). Interdecadal Change of Drought Characteristics in Mahaweli River Basin of Sri Lanka and the Associated Atmospheric Circulation Difference. *Front. Earth Sci.* 8, 306. doi:10.3389/feart.2020.00306

Liu, Z., Menzel, L., Dong, C., and Fang, R. (2016a). Temporal Dynamics and Spatial Patterns of Drought and the Relation to ENSO: a Case Study in Northwest China. *Int. J. Climatol.* 36, 2886–2898. doi:10.1002/joc.4526

Liu, Z., Wang, Y., Shao, M., Jia, X., and Li, X. (2016b). Spatiotemporal Analysis of Multiscalar Drought Characteristics across the Loess Plateau of China. *J. Hydrol.* 534, 281–299. doi:10.1016/j.jhydrol.2016.01.003

Machiwal, D., Kumar, S., Dayal, D., and Mangalassery, S. (2017). Identifying Abrupt Changes and Detecting Gradual Trends of Annual Rainfall in an Indian Arid Region under Heightened Rainfall Rise Regime. *Int. J. Climatol.* 37 (5), 2719–2733. doi:10.1002/joc.4875

Ministry of Water Resources, P.R. China (MWR) (2015). *Bulletin of Flood and Drought Disaster in China 2015*. Beijing: China Water Power Press.

Mishra, A. K., Sivakumar, B., and Singh, V. P. (2015). Drought Processes, Modeling, and Mitigation. *J. Hydrol.* 526, 1–2. doi:10.1016/j.jhydrol.2015.03.054

Mo, X. G., Hu, S., Lu, H. J., Lin, Z. H., and Liu, S. X. (2018). Drought Trends over the Terrestrial China in the 21st century in Climate Change Scenarios with Ensemble GCM Projections. *J. Nat. Resour.* 33 (7), 1244–1256. (in Chinese). doi:10.31497/zrzyxb.20170666

Mondal, A., and Mujumdar, P. P. (2015). Return Levels of Hydrologic Droughts under Climate Change. *Adv. Water Resour.* 75, 67–79. doi:10.1016/j.advwatres.2014.11.005

Montaseri, M., and Amirataee, B. (2017). Comprehensive Stochastic Assessment of Meteorological Drought Indices. *Int. J. Climatol.* 37, 998–1013. doi:10.1002/joc.4755

National Bureau of Statistics of China, P.R. China (NBS) (2015). *China Statistical Yearbook 2014*. Xicheng District, Beijing: NBS.

Naumann, G., Alfieri, L., Wyser, K., Mentaschi, L., Betts, R. A., Carrao, H., et al. (2018). Global Changes in Drought Conditions under Different Levels of Warming. *Geophys. Res. Lett.* 45, 3285–3296. doi:10.1002/2017gl076521

Naumann, G., Spinoni, J., Vogt, J. V., and Barbosa, P. (2015). Assessment of Drought Damages and Their Uncertainties in Europe. *Environ. Res. Lett.* 10, 124013. doi:10.1088/1748-9326/10/12/124013

Ogunrinde, A. T., Enaboifo, M. A., Olotu, Y., Bao, P., and Tayo, A. B. (2021). Characterization of Drought Using Four Drought Indices under Climate Change in the Sahel Region of Nigeria: 1981–2015. *Theor. Appl. Climatol* 143 (1-2), 843–860. doi:10.1007/s00704-020-03453-4

Oikonomou, P. D., Karavitis, C. A., Tsesmilis, D. E., Kolokytha, E., and Maia, R. (2020). Drought Characteristics Assessment in Europe over the Past 50 Years. *Water Resour. Manag.* 34 (15), 4757–4772. doi:10.1007/s11269-020-02688-0

Razie, T., Martins, D. S., Bordi, I., Santos, J. F., Portela, M. M., Pereira, L. S., et al. (2014). SPI Modes of Drought Spatial and Temporal Variability in Portugal: Comparing Observations, PT02 and GPCC Gridded Datasets. *Water Resour. Manage.* 29, 487–504. doi:10.1007/s11269-014-0690-3

Shi, P., Wu, M., Qu, S., Jiang, P., Qiao, X., Chen, X., et al. (2015). Spatial Distribution and Temporal Trends in Precipitation Concentration Indices for the Southwest China. *Water Resour. Manage.* 29 (11), 3941–3955. doi:10.1007/s11269-015-1038-3

Spinoni, J., Barbosa, P., De Jager, A., McCormick, N., Naumann, G., Vogt, J. V., et al. (2019). A New Global Database of Meteorological Drought Events from 1951 to 2016. *J. Hydrol. Reg. Stud.* 22, 100593. doi:10.1016/j.ejrh.2019.100593

Sternberg, T. (2018). Moderating Climate hazard Risk through Cooperation in Asian Drylands. *Land* 7 (1), 1–13. doi:10.3390/land7010022

Sun, F., Mejia, A., Zeng, P., and Che, Y. (2019). Projecting Meteorological, Hydrological and Agricultural Droughts for the Yangtze River basin. *Sci. Total Environ.* 696, 134076. doi:10.1016/j.scitotenv.2019.134076

Tirivarombo, S., Osupile, D., and Eliasson, P. (2018). Drought Monitoring and Analysis: Standardised Precipitation Evapotranspiration Index (SPEI) and Standardised Precipitation Index (SPI). *Phys. Chem. Earth, Parts A/B/C* 106, 1–10. doi:10.1016/j.pce.2018.07.001

Udmale, P., Ichikawa, Y., Manandhar, S., Ishidaira, H., and Kiem, A. S. (2014). Farmers′ Perception of Drought Impacts, Local Adaptation and Administrative Mitigation Measures in Maharashtra State, India. *Int. J. Disaster Risk Reduction* 10, 250–269. doi:10.1016/j.ijdrr.2014.09.011

Wang, H., Zhang, J. F., Zhu, F. B., and Zhang, W. W. (2016). Analysis of Spatial Pattern of Aerosol Optical Depth and Affecting Factors Using Spatial Autocorrelation and Spatial Autoregressive Model. *Environ. Earth Sci.* 75 (9), 822. doi:10.1007/s12665-016-5656-8

Wang, Y.-J., and Qin, D.-H. (2017). Influence of Climate Change and Human Activity on Water Resources in Arid Region of Northwest China: an Overview. *Adv. Clim. Change Res.* 8 (4), 268–278. in Chinese. doi:10.1016/j.accre.2017.08.004

Wang, Z., Li, J., Lai, C., Zeng, Z., Zhong, R., Chen, X., et al. (2017). Does Drought in China Show a Significant Decreasing Trend from 1961 to 2009? *Sci. Total Environ.* 579, 314–324. doi:10.1016/j.scitotenv.2016.11.098

Wei, W., Zhang, H., Zhou, J., Zhou, L., Xie, B., and Li, C. (2021). Drought Monitoring in Arid and Semi-arid Region Based on Multi-Satellite Datasets in Northwest, China. *Environ. Sci. Pollut. Res.* 28, 51556–51574. doi:10.1007/s11356-021-14122-y

Wu, J., Chen, X., Yao, H., and Zhang, D. (2021). Multi-timescale Assessment of Propagation Thresholds from Meteorological to Hydrological Drought. *Sci. Total Environ.* 765, 144232. doi:10.1016/j.scitotenv.2020.144232

Xu, K., Yang, D., Xu, X., and Lei, H. (2015). Copula Based Drought Frequency Analysis Considering the Spatio-Temporal Variability in Southwest China. *J. Hydrol.* 527, 630–640. doi:10.1016/j.jhydrol.2015.05.030

Yang, S. Y., Meng, D., Li, X. J., and Wu, X. L. (2018). Multi-scale Responses of Vegetation Changes Relative to the SPEI Meteorological Drought index in North China in 2001-2014. *Acta Ecol. Sin* 38, 1028–1039. doi:10.5846/stxb201611242398

Yang, X., Wood, E. F., Sheffield, J. L., Ren, L., Zhang, M., and Wang, Y. (2018a). Bias Correction of Historical and Future Simulations of Precipitation and Temperature for China from CMIP5 Models. *J. Hydrometeorol* 19 (3), 609–623. doi:10.1175/jhm-d-17-0180.1

Yuan, Q., Wu, S., Dai, E., Zhao, D., Zhang, X., and Ren, P. (2017). Spatio-temporal Variation of the Wet-Dry Conditions from 1961 to 2015 in China. *Sci. China Earth Sci.* 60 (11), 2041–2050. doi:10.1007/s11430-017-9097-1

Yue, S., Pilon, P., Phinney, B., and Cavadias, G. (2002). The Influence of Autocorrelation on the Ability to Detect Trend in Hydrological Series. *Hydrol. Process.* 16 (9), 1807–1829. doi:10.1002/hyp.1095

Yusof, F., Hui-Mean, F., Suhaila, J., and Yusof, Z. (2013). Characterisation of Drought Properties with Bivariate Copula Analysis, Properties with Bivariate Copula Analysis. *Water Resour. Manage.* 27 (12), 4183–4207. doi:10.1007/s11269-013-0402-4

Check for updates

Precipitation Moisture Sources of Ethiopian River Basins and Their Role During Drought Conditions

Milica Stojanovic[1,2]*, Getachew Mehabie Mulualem[3], Rogert Sorí[1], Marta Vázquez[1], Raquel Nieto[1] and Luis Gimeno[1]

[1]Centro de Investigación Mariña, Environmental Physics Laboratory (EPhysLab), Universidade de Vigo, Ourense, Spain, [2]Department Meteorology and Geophysics, Faculty of Physics, Sofia University "St. Kliment Ohridski", Sofia, Bulgaria, [3]College of Science, Bahir Dar University, Bahir Dar, Ethiopia

In this study, we identified and investigated the annual climatological moisture sources for the Ethiopian river basins during 1980–2018. First, according to cluster analysis, the 12 river basins of this country were grouped into four regions: northeast (NE), southeast (SE), southwest (SW), and west (W), which were characterised by similar annual precipitation features. Global outputs from the Lagrangian FLEXPART model were used to investigate the air mass humidity gain before reaching each region. This revealed five main oceanic moisture sources located in the Mediterranean Sea, Red Sea, Indian Ocean, Persian Gulf, and the Arabian Sea, in addition to three main terrestrial moisture sources located in the African continent, Arabian Peninsula, and the regions themselves. Once the main climatological sources of moisture for each region were identified, a forward-in-time analysis of air masses over each source was performed to calculate the moisture contribution to precipitation (E – P) < 0 over the defined regions. The most important source at the annual scale for the NE, SW, and W regions is the African continent, while for the SE, it is the Indian Ocean. Indeed, terrestrial moisture sources are the major contributors (>50%) to the precipitation over the NE, SW, and W, whereas oceanic sources are the major contributors to the SE. Another analysis identified the years affected by drought conditions in the regions. The role of the sources was evaluated for those years affected by severe and extreme drought, revealing the heterogeneous and also direct influences on the regions. Finally, according to the normalised difference vegetation index, the impacts of annual severe and extreme droughts were more prominent in areas of the NE and SE, but also in the SW during 1984.

Keywords: drought, SPEI, moisture sources, Ethiopia, Lagrangian approach

1 INTRODUCTION

Drought is one of the most devastating natural phenomena related to a significant decrease in water availability owing to precipitation reduction over an extended period (Bayissa et al., 2015; Van Loon, et al., 2016; Stojanovic et al., 2020; Yirga, 2021). It is a relatively complex event, mainly because of the difficulty in defining its beginning, severity, and end (Wilhite, 1993; Belayneh et al., 2014). In addition, its effects can slowly accumulate over a substantial period, affecting a wide range of geographic areas and different sectors, such as agriculture, water management, and the environment (WMO, 2012; Trenberth et al., 2014; Ebi and Bowen, 2016; Van Loon, et al., 2016; Ionita et al., 2017).

Therefore, droughts can generally be classified as meteorological, agricultural, hydrological, and socioeconomic, according to their associated impacts (Wilhite and Glantz, 1985; Keyantash and Dracup, 2002; Dai, 2010). Meteorological drought implies below-average amounts of precipitation and represents the initial stage of all drought types. A lack of soil moisture is referred to as agricultural drought, as it reduces the quantity of water available for crops and affects the agricultural demands of a region. Hydrological drought occurs when sustained dry conditions cause a deficit in soil moisture content, low-level river flows, and a reduction in surface water and groundwater reserves. Finally, socioeconomic drought occurs when a deficit in water supply exceeds the demand for economic goods and social activities.

In Africa, drought is one of the most dangerous natural risks, which, in combination with high water consumption and low water quality, worsens existing water scarcity concerns (Mishra and Singh, 2010; El Kenawy et al., 2016). Among African countries, Ethiopia is frequently portrayed as a drought-stricken region because of anthropogenic activities and climate change (e.g., increased temperature, decreased precipitation, and reduced crop yield) (Belayneh et al., 2014; Bayissa et al., 2015; El Kenawy et al., 2016; Gezie, 2019; Temam et al., 2019; Alemu et al., 2021; Yirga, 2021). A trend analysis performed by Cheung et al. (2008) for annual and seasonal precipitation between 1960 and 2002 showed a remarkable decline in precipitation from June to September for most river basins situated in the southwest and central parts of Ethiopia (Baro-Akobo, Omo-Ghibe, Rift Valley, and Upper Blue Nile). Negash et al. (2013) also reported a significant decreasing trend in the northern, northwestern, and western parts of Ethiopia for the period 1951–2000. Mekonen and Berlie (2020) reported a decreasing trend in precipitation at a level of 6.5 mm/decade in the northeastern areas of Ethiopia from 1900 to 2016. In contrast, Gebrechorkos et al. (2019) recently showed that the climate of Ethiopia has changed over the last 4 decades, with temperatures increasing trends. In line with these findings, some researchers have illustrated that the frequency of drought in Ethiopia has increased over the past few decades (Edossa et al., 2010; Gebrehiwot et al., 2011; Asfaw et al., 2018).

Ethiopia is a highly populated country with 85% of the economy primarily depending on agriculture. Drought represents a major threat that mostly affects the agricultural and water sectors, particularly in regions where access to water supplies is limited (Funk et al., 2005; Mersha and van Laerhoven, 2018; Matewos, 2019; Hirko et al., 2021). The 1984/1985 drought that affected Ethiopia, caused crop failure and, consequently, the displacement of millions of people. Also, the drought that occurred in 2002/2003 led to the biggest food crisis that affected more than 13 million people and caused severe impacts on the economy (Gebrehiwot et al., 2011; Bayissa et al., 2015). According to Funk et al. (2005), the 1984 events stand as the worst years on the record, while 2002 received very low precipitation for the longest period of the year. The year 2009 has also been documented as a severely dry year, with more than six million people being affected (Sheffield et al., 2012; Viste et al., 2013; Mekonen and Berlie 2020). More recently, a severe drought in 2015 affected the northeast of Ethiopia, resulting in more than
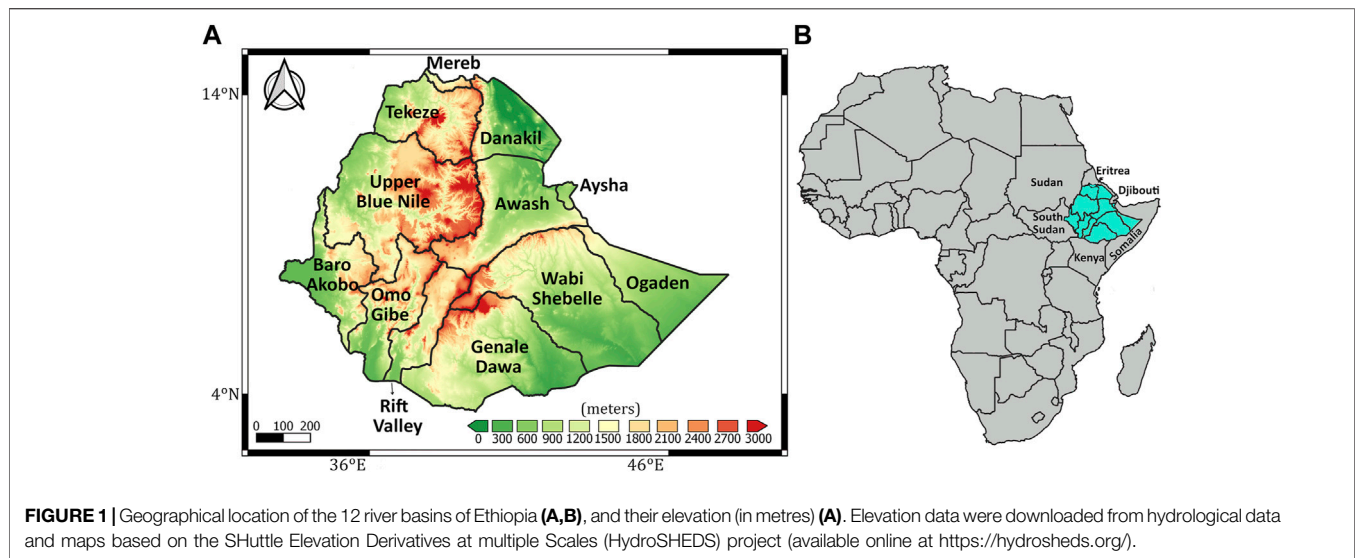
10 million people being affected and seeking humanitarian aid (Mekonen and Berlie 2020). These dry years have been the worst in the history of Ethiopia, with millions of people becoming displaced, and many being forced into further destitution (Bayissa et al., 2015).

The large spatial variability of precipitation over Ethiopia can cause spatial variations in drought severity (World Bank, 2006; Viste et al., 2013). Jjemba et al. (2017) and Philip et al. (2017) showed that a severely dry year in 2015 in the northern part of Ethiopia occurred due to the failure of the March–May (Belg) precipitation season, and the June–September (Kiremt) precipitation season was considerably delayed and below the long-term average. Rainfall in Ethiopia is the result of multi-weather systems that include the Subtropical Jet, Intertropical Convergence Zone (ITCZ), Red Sea Convergence Zone, Tropical Easterly Jet, Southwest Indian and South Atlantic Ocean anticyclones, and Somali Jet (NMA, 1996; Riddle and Cook, 2008; Aerts et al., 2016; Philip et al., 2017; Dubache et al., 2019; Alhamshry et al., 2020; Munday et al., 2021). The intensity, position, and direction of these weather systems lead to variability in the amount and distribution of rainfall in Ethiopia (Berhanu et al., 2014). Precipitation shortfall and its spatial variations are associated with changes in atmospheric moisture transport (Bisselink and Dolman, 2008; Gimeno et al., 2010; Viste and Sorteberg, 2011; Stojanovic et al., 2018; Drumond et al., 2019). Hence, the identification of moisture sources for precipitation is crucial for understanding rainfall variability, timing, and development of dry conditions in Ethiopia Indeed, it is nowadays considered a challenge for the atmospheric sciences (Gimeno et al., 2020). The moisture sources for precipitation over a certain region can be identified through different methods, such as analytical and box models, physical water vapour tracers (isotopes), and numerical water vapour tracers. A complete explanation and comparison of the methodologies used to study moisture transport have been reported by Gimeno et al. (2020).

The main objectives of this study were: 1) to identify the main climatological moisture sources for the four regions of grouped river basins of Ethiopia during the period 1980–2018 through a Lagrangian methodology; 2) to identify the occurrence of drought conditions in the target regions; and 3) to analyse the relationship between severely and/or extremely dry years and the anomalies of the moisture contribution to precipitation computed from their climatological oceanic and terrestrial sources of moisture.

1.1 Study Area

Ethiopia is a landlocked country located within the tropics (33°–48°E longitude and 3°–15°N latitude) of northeast Africa (**Figure 1**). It is bordered by Eritrea and Djibouti to the north and northeast, Somalia to the east, South Sudan and Sudan to the west and northwest, and Kenya to the south (Viste et al., 2013). With an area of approximately 1.11 million km^2, it is the second most populous country in Africa (Awulachew et al., 2005; Worqlul et al., 2017; Liou and Mulualem, 2019). Ethiopia is a country of geographical diversity with topography varying from approximately 4,500 m above sea level in the north and central parts to approximately 100 m below sea level over the lowlands in

FIGURE 1 | Geographical location of the 12 river basins of Ethiopia **(A,B)**, and their elevation (in metres) **(A)**. Elevation data were downloaded from hydrological data and maps based on the SHuttle Elevation Derivatives at multiple Scales (HydroSHEDS) project (available online at https://hydrosheds.org/).

the northeastern parts of the country (**Figure 1**) (Zeleke et al., 2013; Worqlul et al., 2017; Liou and Mulualem, 2019; Asefa et al., 2020). Approximately 35% of the central and northern parts of the country constitute the highlands, with elevations of 1,500 m or above (Seleshi and Zanke, 2004; Worqlul et al., 2017; Liou and Mulualem, 2019).

Ethiopia's proximity to the equator and the complexity of its topography play an essential role in regulating the annual cycle of precipitation and temperature (Asefa et al., 2020). Precipitation normally increases from north to south and from east to west, with a mean annual precipitation of 600 mm per year in the northeastern parts and 2,000 mm per year in the southwest parts of the country (Aerts et al., 2016; Asefa et al., 2020). The amount of precipitation over the mountainous regions is higher than that in the lowlands. The highland regions receive more than 1,200 mm per year, with a small temperature variation, while the lowland regions gain less than 500 mm per year with greater temperature variations (Aerts et al., 2016; Worqlul et al., 2017; Liou and Mulualem, 2019). Because of these complex topographical and geographical features, the climate of Ethiopia reveals strong spatial variations, and different parts of the country do not receive equal amounts of precipitation (Seleshi and Camberlin, 2005; Zeleke et al., 2013). The northeastern, eastern, and southeastern parts of Ethiopia receive less precipitation than the west of the country, and because of this, the three river basins located in these parts (Ogaden, Aysha, and Dinakle) are mostly dry. Likewise, most of the high-flow river basins, which occupy 80%–90% flow, are found in the west and southwestern parts of Ethiopia (Ayalew, 2018). Generally, Ethiopia has three climatic seasons: the main rainy season from June to September (Kiremt), a short rainy season from March to May (Belg), and a dry season from October to January (Bega) (Seleshi and Zanke, 2004; Diro et al., 2011; Fekadu, 2015; Dika, 2018; Alemayehu et al., 2020; Bayable et al., 2021). Kiremt is the major rainy season for most parts of the country (southwestern, northern, eastern, western, northwestern, and central parts), which represents up to 90% of the total

precipitation in a year. By contrast, in the south and southeastern parts of Ethiopia, the Belg season is the main rainy season (Seleshi and Zanke, 2004; Misganaw, 2014; Fekadu, 2015).

Considering population density, there are two region types where water availability is limited: semi-arid regions in the east and north, and wet, densely populated regions in the southern highlands and the Rift Valley (Funk et al., 2012; Berhanu et al., 2014). Ethiopia is considered the water tower of the Horn of Africa owing to its substantial number of water resources (Awulachew et al., 2007; Berhanu et al., 2014). The country has 12 major river catchments, eight of which are river basins (Upper Blue Nile [Abbay], Tekeze, Awash, Danakil, Genale Dawa, Wabi Shebelle, Omo-Gibe, and Baro-Akobo), one is a lake basin (Rift Valley), and the remaining three are considered dry river basins (Merebe, Aysha, and Ogaden) owing to insignificant flow from the drainage system (Berhanu et al., 2014). These river basins provide an estimated annual runoff of approximately 125 billion m^3, with the Upper Blue Nile (Abbay) accounting for approximately 45% of that volume (Asmamaw, 2015).

2 DATASETS AND METHODS

2.1 Datasets

Global outputs of atmospheric moisture changes for nearly 2 million parcels from the Lagrangian FLEXible PARTicle (FLEXPART) dispersion model (Stohl and James, 2004, 2005), with a resolution of 0.25° × 0.25° in latitude and longitude for a period of 39 years (1980–2018), were used in this study. Since the available model output data is for this period, analyses throughout the study were limited to this period. FLEXPART was forced using the ERA-Interim global reanalysis dataset from the European Centre for Medium-Range Weather Forecasts (Dee et al., 2011) with a spatial resolution of 1° × 1° on 61 vertical levels from the surface to 0.1 hPa.

The monthly integrated water vapour transport (IVT) is calculated as the composite of northward and eastward water vapour horizontal fluxes, both obtained from ERA-Interim reanalysis (Dee et al., 2011) at a horizontal resolution of 0.25°. From this source was also downloaded the vertically integrated moisture flux divergence (VIMF). These datasets are available at no cost from https://apps.ecmwf.int. The IVT represents the horizontal moisture transport in the atmosphere, while the VIMF is the horizontal divergence of moisture spreading outward from a point, per square metre, indicating whether atmospheric motions act to decrease due to divergence or increase because of the convergence of the vertical integral of moisture.

Monthly precipitation (PRE) and atmospheric evaporative demand (AED) values with a spatial resolution of 0.5° were obtained from the Climatic Research Unit (CRU) Time-Series version 4.05 (Harris et al., 2020). This dataset was used for this study since it was built from observational data, which ensures a reliable representation of climatic conditions in the study regions. In addition, this dataset has been previously assessed and used for hydrometeorological studies for Ethiopia, showing a good performance (e.g., Mulugeta et al., 2019; Reda et al., 2021; Degefu et al., 2022). Also, the modified version of the Penman-Monteith reference evapotranspiration equation was used in this dataset as a metric for AED, which has been recommended by the Food and Agriculture Organization (FAO), and is the most physical and reliable method among several methods that can be used to model AED (Allen et al., 1998).

The normalised difference vegetation index (NDVI) at a resolution of 0.05° derived from the NOAA Climate Data Record of the Advanced Very High-Resolution Radiometer was used for this study. This long-term record of remotely sensed vegetation observations permits a description of the health of vegetation in diverse regions around the world. Among various vegetation indices, NDVI is more sensitive to various vegetation covers (Leprieur et al., 2000; Roberts et al., 2011), especially in arid regions such as Ethiopia. Therefore, it is commonly used to identify and investigate the effects of drought on vegetation cover (Hassan et al., 2018).

2.2 Ward's Method

For hydroclimatological studies, categorising different river basins into homogeneous precipitation aggregates warrants further analysis because it can deliver very similar results. Therefore, we used Ward's hierarchical clustering method (Wilks, 2011; Bednorz et al., 2019) to determine the similarity in precipitation regimes between Ethiopia's 12 major drainage systems. Ward's method has been commonly used among several hierarchical clustering methods, and it has been widely applied by different researchers to define consistent precipitation zones (Munoz-Díaz and Rodrigo 2004; Ferreira and Hitchcock 2009; Murtagh and Legendre, 2014; Zhang et al., 2016; Sharghi et al., 2018; Stojanovic et al., 2021a; Beyene et al., 2021). Ward's method was employed with Euclidean distance used as similarity measurement. The hierarchical clustering technique classifies data into a hierarchical structure based on the Euclidean

distance between two groups (Murtagh and Legendre 2014; Tian et al., 2014). The Euclidean distance (D) is the length of the line segment between i number of two points (x, y) in the euclidean space, as indicated in **Eq. 1**.

$$D(x, y) = \sqrt{\sum_i (x_i - y_i)^2} \tag{1}$$

It differs from other methods because it is designed to generate which pairs of groups (e.g., A and B) will merge at each step by minimising the sum of squared distances between the points and the centroids of their groups (Unal et al., 2003; Zhang et al., 2016; Beyene et al., 2021), according to **Eq. 2**.

$$\Delta(A, B) = \sum_{i \in A \cup B} \left\| \vec{x}_i - \vec{m}_{A \cup B} \right\|^2 - \sum_{i \in A} \left\| \vec{x}_i - \vec{m}_A \right\|^2 - \sum_{i \in B} \left\| \vec{x}_i - \vec{m}_B \right\|^2$$
$$= \frac{n_A n_B}{n_A + n_B} \left\| \vec{m}_A - \vec{m}_B \right\|^2 \tag{2}$$

where Δ represents the merging cost of combining the clusters A and B; $\vec{m}_j$ the centre of the cluster j, and n_j is the number of points in it (Distances between Clustering, 2009). The two most similar data would be clustered into one bough in the first step, and then in the next step, it will be used as a new unit. In each step, the two units are combined. Once a unit is assigned to a bough, it cannot be separated, and the algorithm continues until the last two units are joined. The outcome is a tree diagram showing the final number of clusters (Zhang et al., 2016).

An advantage of using cluster analysis is that can be generally easily implemented and further interpret the results. In the process, it is also not necessary to specify the number of clusters for the algorithm and a final dendrogram allows to select the optimum number of clusters for analysis. One advantage of Ward's method compared with other hierarchical clustering methods is that it usually does not leave single-member clusters after a reasonable number of stages, and it tends to produce clusters with approximately the same number of entities (Dezfuli, 2011; Bu et al., 2020). However, one limitation of Ward's method is that is computationally intensive and struggles to handle large datasets with more than a thousand observations because of that it is not recommended to be used with large datasets since it will take a lot of time to calculate (Tsiptsis and Chorianopoulos, 2009). In addition, the analysis and decisions on dendrograms may result difficult, leading to possible bad decisions, for which is necessary to analyse if the result makes sense or not.

2.3 Standardised Precipitation Evapotranspiration Index

Many drought indices have been developed and used by researchers worldwide to detect, analyse, and understand the characteristics of droughts on global, regional, and local scales (Saravi et al., 2009; Dai 2010; Hadish, 2010; Gebrehiwot et al., 2011; Herring et al., 2014; El Kenawy et al., 2016; Mohammed et al., 2018; Drumond et al., 2019). In general, precipitation is used to compute the indices. The standardised precipitation index (SPI) (McKee et al., 1993), for instance, is one of the most

SPEI	Category
0; −0.99	Mild dry
−1.00; −1.49	Moderately dry
−1.50; −1.99	Severely dry
≤−2.0	Extremely dry

frequently used drought indices worldwide, as recommended by the World Meteorological Organization (Svoboda et al., 2012; WMO, 2012). However, several studies (Labedzki, 2007; Livada and Assimakopoulos, 2007; Naresh Kumar et al., 2009; Vicente-Serrano et al., 2010; Zarch et al., 2015) have indicated that SPI relying only on precipitation as input data for assessing drought is a major loophole. Although precipitation is the primary cause in controlling the occurrences of drought, the impact of other variables such as temperature in the context of global warming cannot be overlooked (Vicente-Serrano et al., 2012). For this reason, the SPEI (Vicente-Serrano et al., 2010) was utilised, which includes the role of temperature through AED in the assessment of drought. Besides, the SPEI has been widely used, demonstrating its usefulness for the most realistic representation of dry conditions that affect a given region (Hernandez and Uddameri, 2014; Wang et al., 2015; Ghebrezgabher et al., 2016; Delbiso et al., 2017; Stojanovic et al., 2018; Drumond et al., 2019; Tefera et al., 2019; Sorí et al., 2020; Stojanovic et al., 2021b).

The calculation of the SPEI is based on the original procedure used to calculate the SPI but includes the influence of the AED to estimate the severity of drought while maintaining the multiscale characteristics of the SPI (Beguería et al., 2014). The SPEI is computed using the monthly climatic water balance (precipitation minus AED) calculated at various timescales (i.e., accumulation periods) (Vicente-Serrano et al., 2010; Lweendo et al., 2017; Abara et al., 2020). These accumulation periods can be related to different drought types, such as 1-month SPEI for meteorological drought, 1–6 months SPEI for agricultural drought, and 6–24 months SPEI for hydrological drought (WMO, 2012). Detailed information for calculating SPEIs can be found in Beguería et al. (2014). In this study we calculated the 12-month SPEI (SPEI12) and was particularly used the SPEI12 of December, which provides the diagnoses of wet or dry conditions for December and the previous 11 months, permitting us to identify those years affected by severely and/or extremely dry conditions in the four aggrupations of major river basins of Ethiopia. The 1-month SPEI (SPEI1) SPEI1 was also used to understand the behaviour of dry conditions during years affected by severe and extreme drought conditions. Finally, the identification of the severely and/or extremely dry conditions during 1980–2018 follows the criteria of McKee et al. (1993) (**Table 1**).

2.4 Lagrangian Methodology

The Lagrangian dispersion model, FLEXPART, allows the investigation of atmospheric moisture changes combined with the motion of air masses. Therefore, global outputs from this

model were used to initially identify the annual climatological moisture sources of the four river basin groups that cover Ethiopia (**Figure 2**). This model considers an atmosphere divided into nearly two million particles or parcels of equal mass (m) that can be tracked backward or forward using three-dimensional wind field. For each tracked parcel, the changes of specific humidity (q) every 6 h (dt) are calculated along the trajectory, which can be adopted as the budget of evaporation (e) minus the precipitation (p) in the parcel, according to **Eq. 3**:

$$(e - p) = m\left(\frac{dq}{dt}\right) \quad (3)$$

By integrating the ($e − p$) values for all parcels (K) residing in the atmospheric column over the unit area (A), it is possible to estimate the total budget of atmospheric humidity ($E − P$), where E represents evaporation and P represents precipitation, as indicated in **Eq. 4**:

$$(E - P) = \frac{\sum_{k=1}^{k}(e - p)}{A} \quad (4)$$

The computation of ($E − P$) in a backward experiment from the target regions allows us to identify regions where air masses gained (($E − P$) > 0)) rather than lost atmospheric moisture before arriving at the target region. Areas with positive values were then considered as sources of moisture, whereas those where air masses lost moisture (($E − P$) < 0)) are considered moisture sinks. If parcels are tracked forward in time for a delimited region, it is possible to estimate areas where air masses will lose moisture, which can be assumed to contribute to precipitation. For both the backward and forward experiments, the optimum integration times (in days) proposed by Nieto and Gimeno (2019) provide the optimal days, in which the Lagrangian precipitation is a better fit for precipitation in grids with a resolution of 0.25° latitude and longitude. The average integration times for the grouped river basins resulted from the cluster analysis were calculated.

Finally, to determine the most important sources of moisture for each region, the 95th percentile (p95) for ($E − P$) > 0 was obtained in the backward climatological experiment performed from the final study regions. This approach has been widely used to achieve similar objectives previously. The use of FLEXPART for the identification of sources of moisture has been widespread. This is because, compared to other methods such as Eulerian models and using isotopes, the Lagrangian approach provides a more robust assessment (Gimeno et al., 2020).

3 RESULTS

3.1 Spatial Regionalisation of Precipitation

Due to its geographic position near the equator and topography, the distribution of the mean annual precipitation in Ethiopia is subject to large spatial variations (Seleshi and Camberlin, 2005; Zeleke et al., 2013; Fazzini et al., 2015; Suryabhagavan, 2017). The regionalisation of precipitation by Ward's method provided four major drainage systems groups (**Figure 2A**); the graphical representation of the 12

FIGURE 2 | (A) Graphical illustration of Ward's method: tree diagram showing the assigned clusters, and (B) schematic representation of the clusters, named as: northeast (NE), southeast (SE), southwest (SW), and west (W).
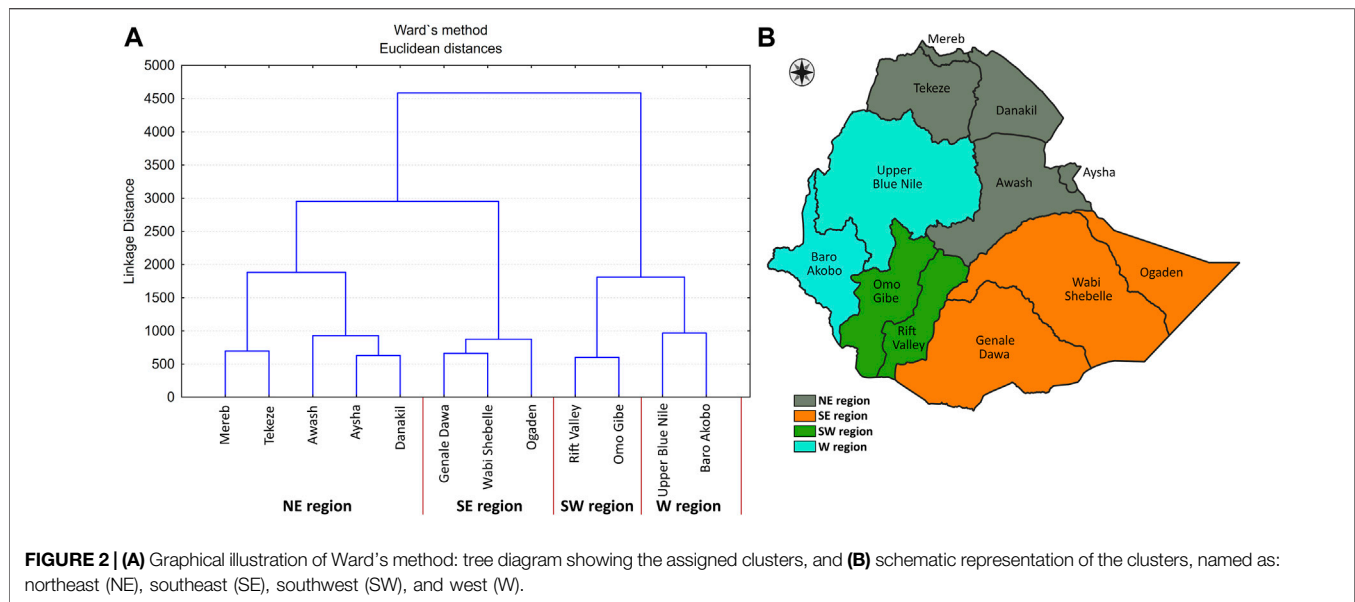
river basins that constitute each region is shown in **Figure 2B**. We based our decision on the analysis of the cluster analysis through the output of the tree diagram (dendrogram), which makes possible to hierarchically depict the groups of clusters and their combinations, indicating the level of similarity/dissimilarity in the vertical scale and the sample elements in clustering order on the horizontal axis. In the Dendrogram appears at first two well defined groups (dissimilar) that later are divided into other pairs of groups that indeed are also quite far. Thus, we decided to select these main four aggrupations from the Dendrogram obtained through Ward's algorithm. For this, a subjective criterion based on the interest of our research was also taken into account. The selection of two groups seemed small to us, considering that the association distances between the four groups are appreciable, which allows us to focus the study on more study regions without compromising the distance of dissimilarity. According to Wilks (2011), the best number of clusters could be sometimes not obvious, and establishing the number of groups necessitates a subjective choice that depends on the objectives of the analysis. The results show that Mereb, Tekeze, Danakil Awash, and Aysha represent river basins with similar precipitation regimes and are classified here as the northeast (NE) region. Genale Dawa, Wabi Shebelle, and Ogaden belong to the southeast (SE) region. The southwest (SW) region includes the Omo-Gibe and Rift Valley catchments, and the Upper Blue Nile and Baro Akobo River basins belong to the western (W) region. These results differ from previous classifications: the National Meteorology Agency of Ethiopia categorised homogeneous rainfall regions into three clusters, Diro et al. (2011) into six clusters, and Gissila et al. (2004) into four clusters. Our selection of four regions is in agreement with the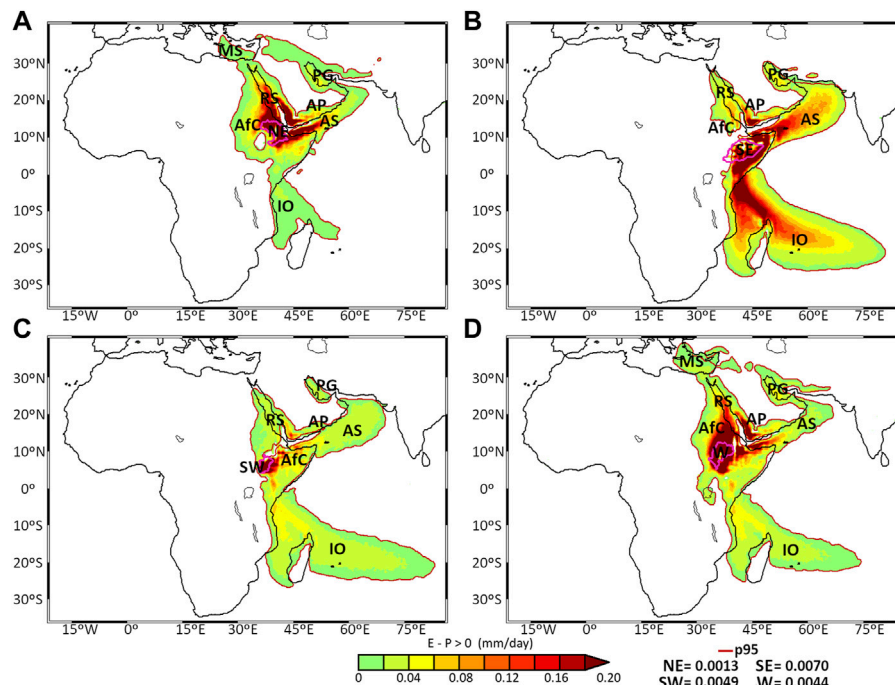 geographical characteristics of the country. The configuration of the SE region appears to be determined by river basins delimited by a rift valley that extends from the southwest of the country until the northeast coast, occupying the Hararge and Arsi Bale highlands and the southeastern lowlands. Similarly, the SW occupies the southwest highlands; the W is formed by river basins that occupy the Gojjam
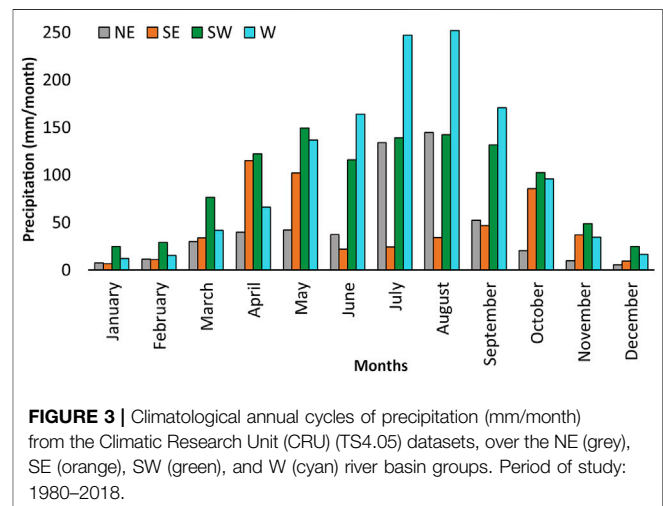
and Wollo highlands and the Western lowlands; and finally, the NE covers the northeast rift valley and the northern Simen mountains region.

3.1.2 Precipitation Regimes

The annual climatological cycle of precipitation for 1980–2018 for each of the four regions under study is shown in **Figure 3**. Visual analysis revealed great differences among the annual cycles, confirming the great spatial variability of the precipitation documented for Ethiopia. However, the annual precipitation cycle over the NE and W regions seemed very similar, with a predominantly unimodal behaviour, with the maximum precipitation occurring in August (145 and 251 mm/month, respectively) and July (133 and 247 mm/month, respectively). Precipitation decreased over the NE and W regions in the rest of the months until reaching minimum

FIGURE 3 | Climatological annual cycles of precipitation (mm/month) from the Climatic Research Unit (CRU) (TS4.05) datasets, over the NE (grey), SE (orange), SW (green), and W (cyan) river basin groups. Period of study: 1980–2018.

FIGURE 4 | Annual patterns of (E – P) > 0 obtained in a backward experiment for the **(A)** NE, **(B)** SE, **(C)** SW, and **(D)** W river basin groups. The extensions of the sources were delimited using percentile 95 (represented by a pink line). Period: 1980–2018.

TABLE 2 | Mean water vapour optimal annual integration time for each of the four river basin groups of Ethiopia; the northeast (NE), southeast (SE), southwest (SW), and west (W). Period 1980–2018.

Regions	Optimal integration time (days)
NE	5
SE	6
SW	9
W	8

values in December (5 and 25 mm/month, respectively) and January (8 and 12 mm/month, respectively). The SE and SW regions were characterised by a bimodal precipitation pattern that was more pronounced over the SE region, while the maximum precipitation in every region occurred in different months. The rainiest months over the SE were April (115 mm/month) and May (102 mm/month), while those over the SW were May (149 mm/month) and August (142 mm/month). Similar to the NE and W regions, the lowest mean monthly precipitation values occurred in the Northern Hemisphere winter months, which is in agreement with previous studies (Seleshi and Zanke, 2004; Abebe, 2010).

3.2 Identification of Moisture Sources for Each Region

The annual climatological pattern of (E – P) > 0 obtained in a backward experiment for each of the four regions identified

through the cluster analysis of each catchment's precipitation during 1980–2018 is shown in **Figure 4**. For this analysis was considered the mean water vapour optimal annual integration times (in days) listed in **Table 2**.

The areas shaded by reddish colours represent regions where air masses gained humidity rather than losing humidity before reaching each region. The p95 used as a threshold for delimiting the most important moisture sources reveals a very similar pattern of (E – P) > 0 for the four regions, which extend over northeast Africa and west of the Indian Ocean (IO). However, some differences among the (E – P) > 0 patterns can be explained by the geographical location of the regions. For example, the moisture sources for the NE and W regions were more extended and intense over continental areas than over oceanic areas, covering a large part of northeast Africa (AfC), including the whole NE group, and part of the Arabian Peninsula (AP). With respect to oceanic sources, the NE receives moisture from the Mediterranean Sea (MS), Red Sea (RS), western IO, Persian Gulf (PG) and Arabian Sea (AS). For the SE and SW catchment regions, the spatial extension of the (E – P) > 0 patterns covered less extension of northeast Africa but were more extended over the IO. In addition, for both SE and SW, the p95 line does not include the MS source. Finally, the most intense values of moisture uptake were usually observed in and around the study regions, although for the SE region, the intensity of the pattern was also high over the western IO and AS regions. The mechanisms associated with moisture transport from the sources to the precipitation over Ethiopia are crucial to the contribution of each source. During the boreal spring, the Somali Jet begins to

FIGURE 5 | Average pattern and direction of the IVT (kg m^{-1} s^{-1}). Period: 1980–2018. The borders of Ethiopia are delimited in red.
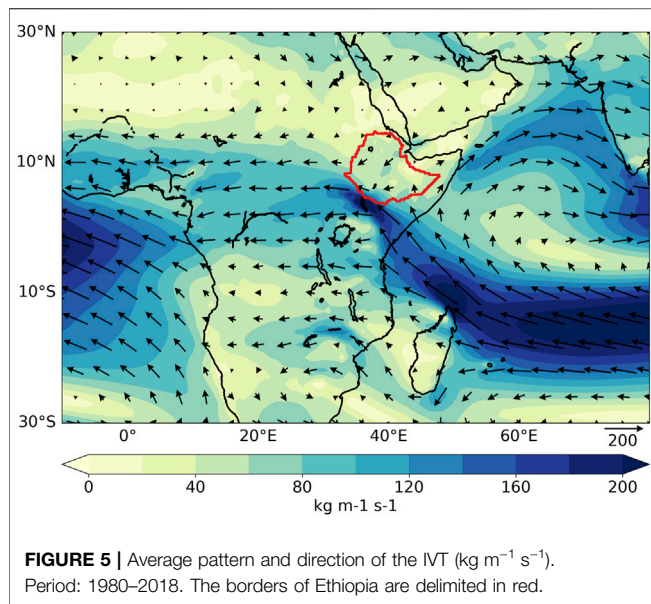
form as a low-level cross-equatorial one, bringing moist air from the southern IO to the southern escarpment of the Ethiopian highlands (Riddle and Cook, 2008; Riddle and Wilks, 2013).
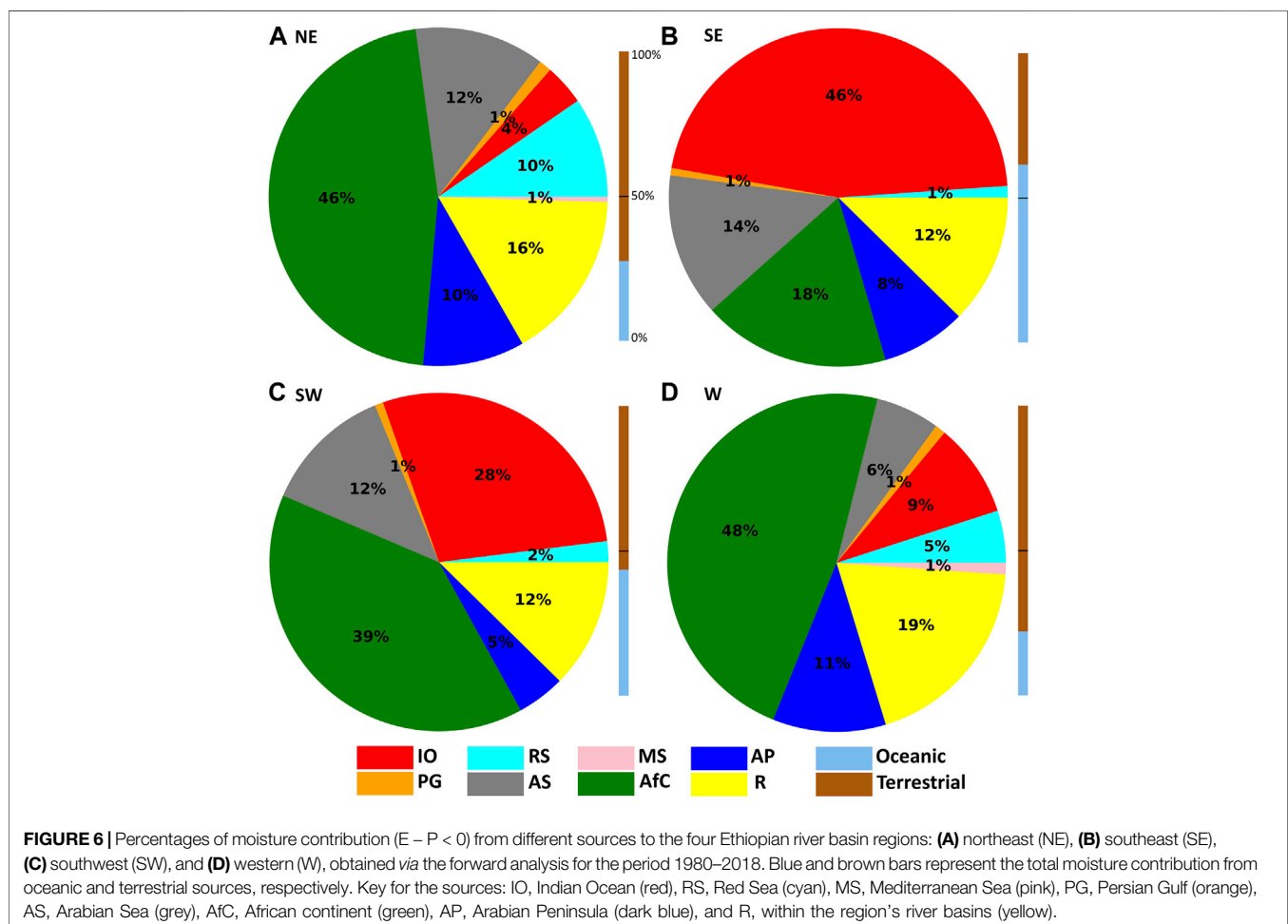
During the boreal summer, low-level flows from the Congo Basin to the southwest and the RS to the northeast converge over Ethiopian highlands, fuelling the Ethiopian summer rainy season (Jury, 2011; Viste and Sorteberg, 2011; Jury and Chiao, 2014). An analysis of the annual mean value of the IVT and its direction for the study period (**Figure 5**) reveals the predominant IVT entering Ethiopia predominantly by the southeast, arriving from the IO, where the magnitude of the IVT is very high (>200 kg m^{-1} s^{-1}). The IVT also enters Ethiopia from the northeast, but to a lesser extent. These results based on an eulerian approach confirm the importance of the IO and the AR as sources of moisture for precipitation over Ethiopia, as revealed by the location and extension of sources in **Figure 4**.

3.2.1 Moisture Contribution for Precipitation From the Sources for Each River Basin Group

Once the sources of moisture were identified for each group of river basins, a forward analysis was performed from each of the sources to calculate the moisture contribution to precipitation ((E − P) < 0)) over each of the respective regions. The results are expressed as percentages and shown in **Figure 6**. For the basins grouped in the NE and W regions, the sources of moisture that most contribute to precipitation are the AfC (46%, 48%), while the second most important sources are the regions themselves (16% and 19%, respectively) (**Figures 6A,D**).

FIGURE 6 | Percentages of moisture contribution (E − P < 0) from different sources to the four Ethiopian river basin regions: **(A)** northeast (NE), **(B)** southeast (SE), **(C)** southwest (SW), and **(D)** western (W), obtained *via* the forward analysis for the period 1980–2018. Blue and brown bars represent the total moisture contribution from oceanic and terrestrial sources, respectively. Key for the sources: IO, Indian Ocean (red), RS, Red Sea (cyan), MS, Mediterranean Sea (pink), PG, Persian Gulf (orange), AS, Arabian Sea (grey), AfC, African continent (green), AP, Arabian Peninsula (dark blue), and R, within the region's river basins (yellow).

FIGURE 7 | Pearson correlation values obtained between the series of precipitation over the NE, SE, SW, and W regions from the Climatic Research Unit and the $|(E − P) < 0|$ computed over these regions on air masses tracked forward in time from all the sources (MS, RS; IO; PG; AS; AfC, AP, and R).

As Ethiopia is located in the north of Africa and close to the equator, the annual rainfall is dominated by the migration of the ITCZ (Segele et al., 2009; Fazzini et al., 2015; Seregina et al., 2019), which supports the results explained earlier. **Figure 4** shows that the NE also receives air masses that gain humidity from oceanic sources, such as the IO, PG, and RS, and their contributions to the total moisture loss are 4%, 1%, and 10%, respectively (**Figure 6**). Nevertheless, according to Viste and Sorteberg, 2011, the Ethiopian highlands receive a small contribution of moisture transported from the Gulf of Guinea. In addition, Mohamed et al. (2005) described the predominant influence of moisture flux of Atlantic origin over the northern Ethiopian Plateau. However, we did not identify any moisture sources from the Atlantic Ocean causing precipitation over the NE and W basins of Ethiopia. For the SW region, the AfC remains the most important moisture source, supplying 39% of the total moisture contribution to precipitation, followed by the IO (28%). However, because the SE region is closer to the IO, it receives a major contribution from this oceanic source, followed by the AfC (18%), AS (14%), SE itself (12%), and AP (8%). Thus, SE region is the only region that receives more than 50% of the moisture supply, which contributes to rainfall from oceanic sources. This is in agreement with the findings of Viste and Sorteberg, 2011, who reported that most of the moisture entering Ethiopia is via the African continent.

Figure 7 presents the correlation analysis between the series of precipitation over each region of study, and the corresponding series of $|(E − P) < 0|$ computed through the forward experiment from the respective moisture sources. For NE, the correlations were positive, except for that obtained with the moisture contribution from AS, which was negative. Similarly, the moisture contribution to precipitation from AS and precipitation over the other regions had an inverse relationship, which may depend on the influence of the position and intensity of the Somali low-level jet during the boreal summer months. In the remaining regions, the correlations were predominantly positive, particularly for the W region, which confirms a direct relationship.

3.3 Assessment of Drought Conditions
### 3.3.1 Anomaly of Vertically Integrated Moisture Flux
The SPEI12 values for December were used to investigate the annual evolution of dry and wet conditions in each region during

the study period (**Figure 8**). At this time scale, the SPEI permits the assessment of the occurrence of long-term drought, which can be associated with a combination of accumulated impacts on agriculture, streamflows, and reservoir levels. The negative (positive) SPEI12 values for December revealed a predominance of annual dry (wet) conditions for each year from 1980 to 2018, respectively. The dashed green line marks the threshold (−1.5), below which the SPEI indicates the occurrence of severe and extremely dry conditions. In 1984, the NE region was affected by extreme drought conditions, while in 2009 and 2015, it was affected by severe conditions. Philip et al. (2018) also described 2015 as a very dry year in northern and central Ethiopia. Extreme drought conditions affected the SE and SW regions in 1984, when in the W region, the SPEI12 almost reached the threshold of −1.5. This indicated that it was a dry year in all river basins throughout the country. This drought was associated with devasting famine and mortality that affected the entire Ethiopian economy and population in 1984, requiring support from global institutions and developed countries (Vestal, 1985; Dercon and Porter, 2014). The SE region was also affected by severe drought conditions in 1980 and 1999, the SW region in 1999 and 2002, and the W region in 1995 and 2009. Finally, the worst year in the W region was 2009, with severe drought conditions; this was also the most affected region that year. A report from the United Union in 2009 (UN, 2009) associated the successive failure of precipitation in this year and a substantial food shortfall and high prices globally with over six million drought victims. The temporal evolution of annual dry/wet conditions in the four study regions reveals that in some years (e.g., 1984, 2009), there was a simultaneous occurrence of drought that affected the four regions, although with different severity in each of them. However, this does not ensure that the phenomenon of drought occurs simultaneously in all the study regions that make up the country. In some years such as 1987, three regions were affected by dry conditions while the SE experienced wet conditions; in 1985 the W and SE regions were affected by wet conditions but negative SPEI12 indicate dry conditions in the NE and SW, or the year 2000, when the W region experienced extremely wet conditions but the other regions dry conditions.

Annual (in percentages) and monthly (in mm/day) anomalies of the moisture contribution for those years in which severe and extreme drought affected the study regions were calculated, as shown in **Figures 9A,B** respectively. The number of months with negative anomalies of $|(E − P) < 0|$ are summarised on the bars representing the annual anomalies from the sources (**Figure 9A**). In addition, the SPEI1 is also over plotted to the monthly anomalies of $|(E − P) < 0|$ (**Figure 9B**); the visual analysis of both series allows characterising the behaviour of the SPEI1 and the contribution of the sources for each month of the years affected by severe and/or extreme drought conditions. Besides, it allows inferring the possible influence of peaks of the moisture contribution during a particular month on the value of the annual anomaly also plotted in the panel a of this figure. For the NE region, we analysed the anomalies over 3 years: 1984, 2009, and 2015. The annual anomaly values show that only the contribution from the PG experiences a decrease (30%); however, the
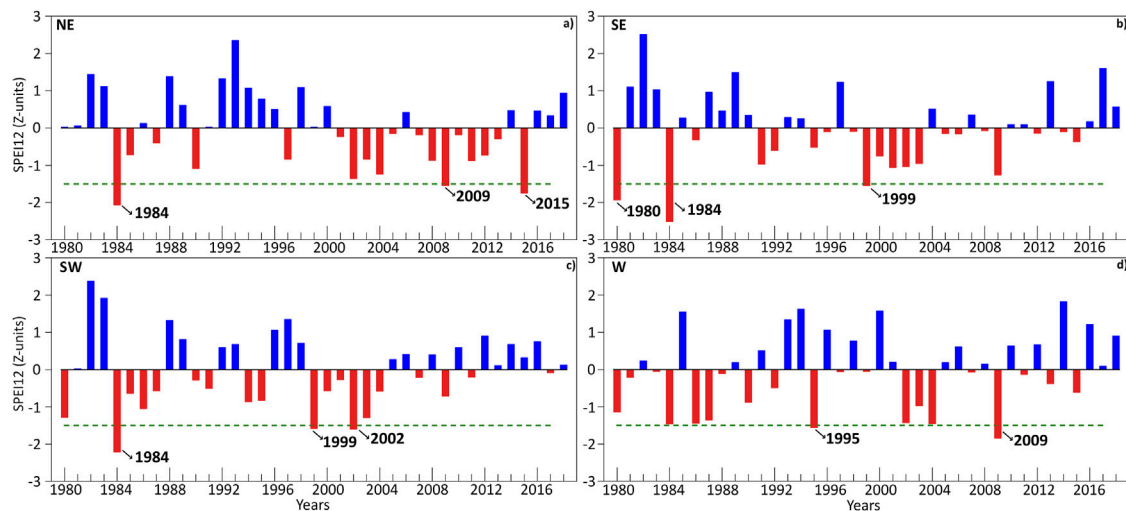
FIGURE 8 | Annual standardised precipitation evapotranspiration index (December‑SPEI12) for the NE **(A)**, SE **(B)**, SW **(C)**, and W **(D)** groups. Period: 1980–2018. The green dashed line indicates years where SPEI12 values were lower than −1.50 (severely dry conditions).
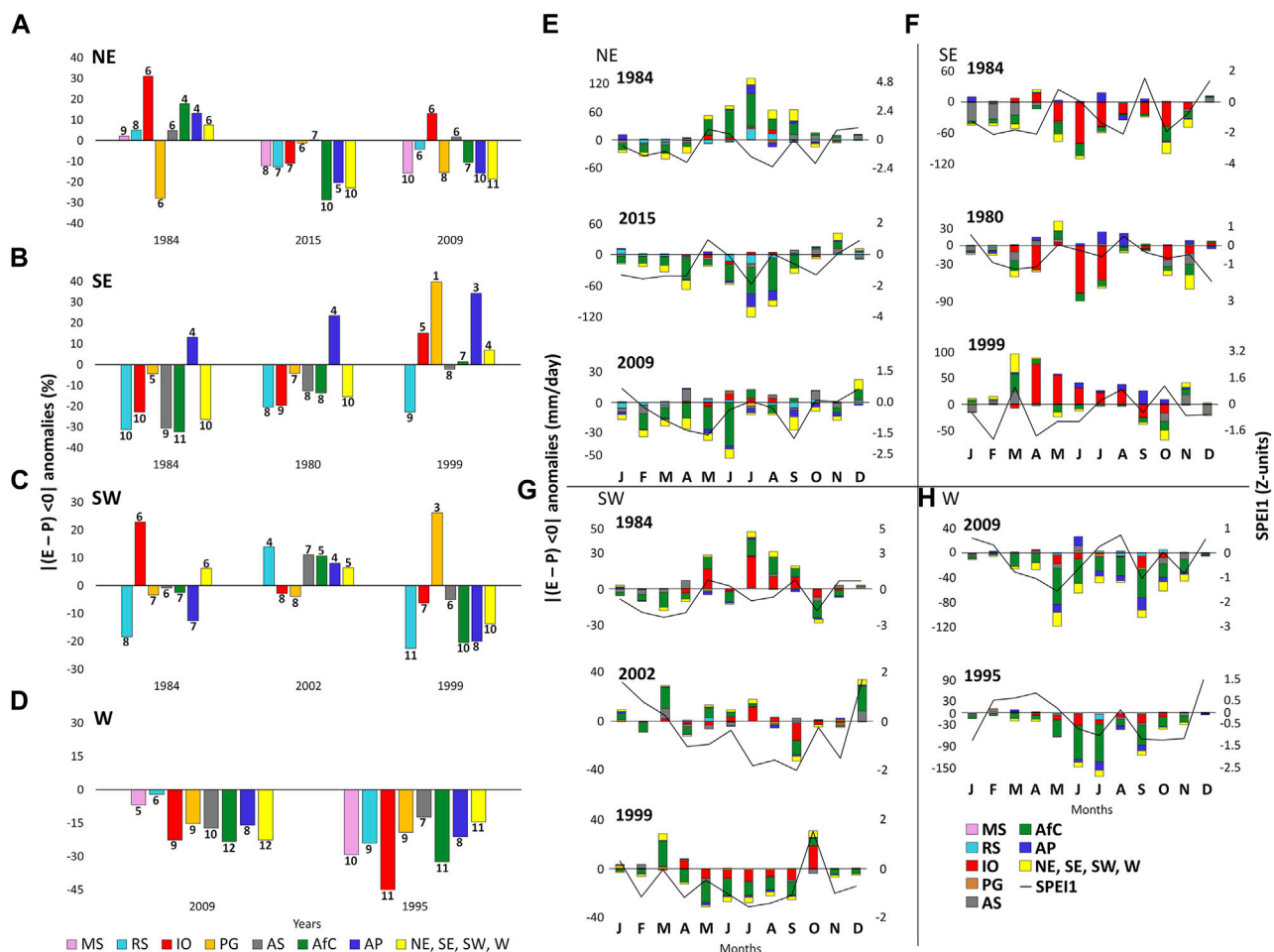
FIGURE 9 | Left panel: Anomalies on the moisture contribution to precipitation |(E − P) < 0| (expressed in percentage) from every source during years affected by severe or extreme drought conditions in the study regions; NE **(A)**, SE **(B)**, SW **(C)**, and W **(D)**; and the number of months with a negative anomaly on the moisture contribution from each source (expressed in numbers). Right panels: SPEI1 and monthly anomalies of |(E − P) < 0| during each year in the study regions; NE **(E)**, SE **(F)**, SW **(G)**, and W **(H)**.

FIGURE 10 | Anomalies of vertically integrated moisture flux (VIMF, unit: mm/day) for severe annual drought in each of the four [NE **(A)**, SE **(B)**, SW **(C)**, and W **(D)**] regions of study (shown in **Figure 2**).
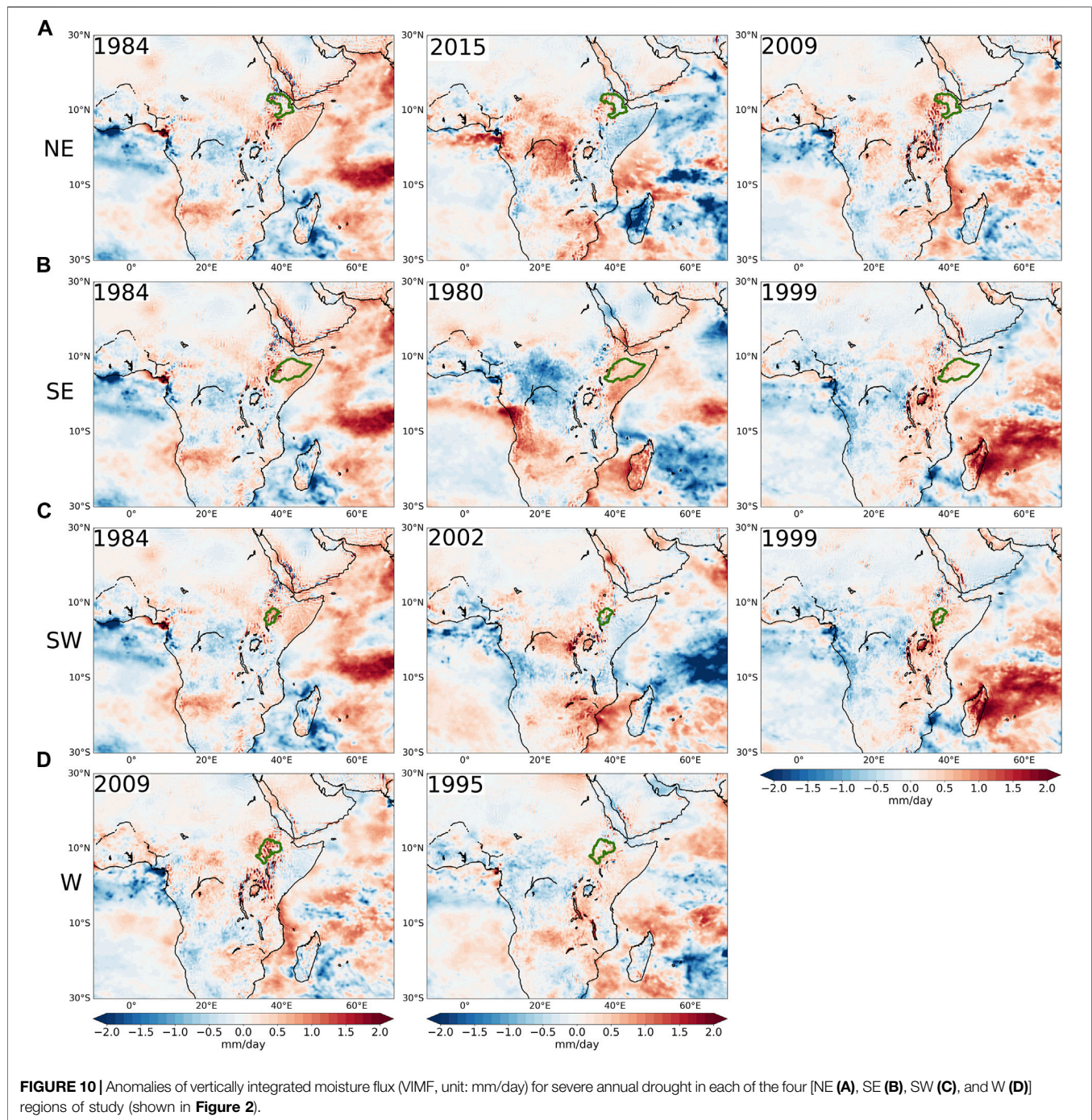
climatological contribution from this source represents only 1% of the total contribution from the main moisture sources in the NE region. An analysis of the monthly anomalies in the contribution of each source showed that in most months, the negative anomalies coincided with negative values of SPEI1; however, in July 1984 there were high positive values in the contributions but negative values in SPEI1 (**Figure 9B**). Although most sources contributed more than the annual average in this year, the effect of the contribution in specific months masked what happened during the rest of the year. For example, for

8–9 months of 1984, the anomalies in the contribution from the MS and RS were negative, although, these are not the most important sources. In 2015, there was a reduction in the moisture contribution to precipitation from all sources in the NE region, except for a negligible percentage from the PG. In 1984, there was also a decrease in the moisture contribution from most of the sources to the precipitation over the NE region, including two of the most important sources, the AfC and AP, which prevailed in almost all months of the year. To support the understanding of the role of moisture contribution anomalies in

FIGURE 11 | Anomalies in the normalised difference vegetation index (NDVI) for the NE **(A)**, SE **(B)**, SW **(C)**, and W **(D)** regions under study during severe and extreme drought years.
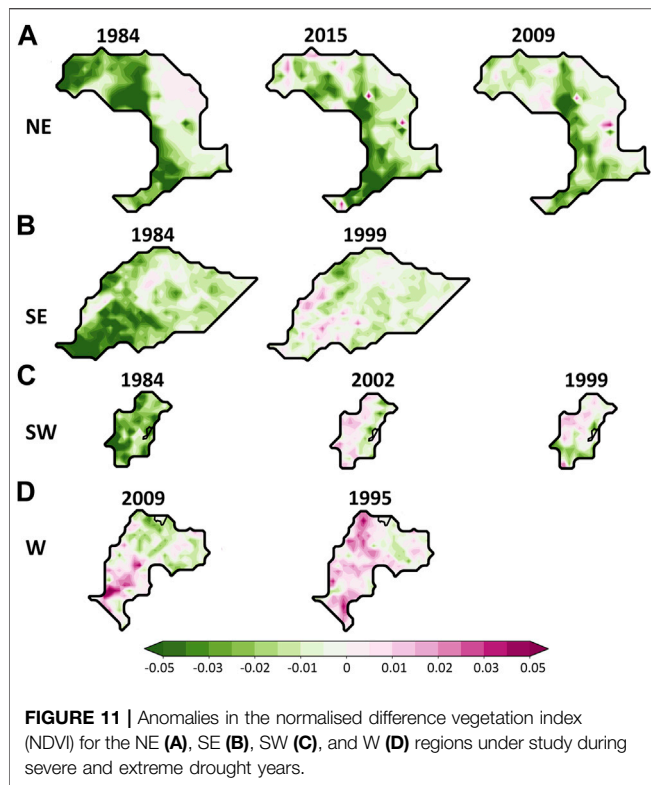
the occurrence of severe and extreme drought conditions, VIMF anomalies were calculated (**Figure 10**). In 1984, 2015, and 2009, positive anomalies (red shades) of the VIMF prevailed over the NE region, which favoured the inhibition of convective movements and therefore precipitation. However, this analysis on an annual scale can frame the behaviour of a particular month in 1984, when the sources increased their contributions.

The years of extreme (1984) and severe (1980) droughts in the SE region witnessed a decrease in the moisture contribution from the sources to precipitation, except for the AP source. The monthly analysis of SPEI (SPEI1) for 1984 showed a possible temporal lag. Likewise, in both years, the number of months affected by negative anomalies of contributions was predominant. In another year affected by severe drought conditions (1999), the behaviour of the sources in terms of decreasing contribution was not as homogeneous. However, the deficit of moisture supplies from the RS and AS during 9 and 8 months of 1999, respectively. Here stand out that from the AS, taking into account that the average annual supply from this source represents a 14% of the total moisture lose over the SE region. The visual analysis results in **Figure 10** reveal the predominance of positive VIMF anomalies over the SE region, particularly in 1984, thereby confirming the importance of dynamic conditions in the final hydroclimatic conditions of the region. Although the number of years with severe and extreme drought conditions in this region is low, the results confirm a more direct relationship between the accumulated moisture contribution deficit and the impact of droughts in the W region. In summary, although the analysis done in **Figure 9** reveals the role of sources in the annual

occurrence of droughts, the monthly anomalies of the contribution from the sources reveal that a more detailed analysis at the seasonal scale is necessary to better characterize their role in the occurrence of droughts.

For the SW region, the anomaly analysis indicated that in the driest year (1984), there were 8 months with reduced moisture contribution to precipitation from the RS source, while there were 7 months with the same conditions from the AP, PG, and AfC sources. The annual reductions from the RS and AP represented almost 20% and 14% of the historical average, respectively. However, these sources are not the largest contributors. However The AfC source only experienced an annual reduction of 3% but is the most important from a climatological point of view for this region. The temporal evolution of SPEI1 during this year shows an inconsistency in July and August when the anomalies of $|(E − P) < 0|$ values were positive, but the SPEI1 was negative. In 2002, only two sources, the IO and PG, experienced a decrease in their contribution to the annual average, with negative SPEI1 values in 8 months of the year. It is worth highlighting the importance of the IO source, which is the second most important source for this region. The SW region was also affected by severe drought conditions in 1999, when the contribution from all sources, except the PG, decreased substantially. The temporal evolution of SPEI1 during this year reveals a good correlation between the evolution of the index and anomalies of moisture contributions from the different sources. The VIMF anomalies over the SW region during these years were mostly positive, mainly in 1984, which was the driest year. Finally, in the 2 years (2009 and 1995) affected by severe drought conditions in the W region, there was a negative anomaly in the contribution of moisture to precipitation from all moisture sources of this region, as well as unfavourable conditions for precipitation according to positive anomalies of the VIMF. The evolution of SPEI1 during these years was consistent with the monthly $|(E − P) < 0|$ anomalies.

3.3.2 Drought Impacts on Vegetation

The vegetation dynamics in each region were investigated during severe and extreme annual droughts. To this end, the NDVI anomalies were calculated (**Figure 11**). For the NE region under the extreme drought of 1984, the NDVI anomalies were predominantly negative. This confirms the marked reduction in vegetation cover in a region characterised by the prevalence of dry evergreen Afromontane forest and Combretum-Terminalia woodland and wooded grassland (Friis et al., 2010). In 2015 and 2009, lower vegetation activity was observed in a large part of the NE region, particularly in the north, and south, respectively. Vegetation stress was also observed in a major part of the SE region due to extreme drought conditions in 1984, particularly in the southwest of this region. The results are also consistent for 1999, when severe drought affected the SE region and negative anomalies of the NDVI prevailed, although they were less intense than those found for 1984. NDVI anomalies were not calculated for 1980 because the relevant data were unavailable.

For the SW region, negative NDVI anomalies were obtained for 1984, a year of extreme drought, which extended over the entire region. This is supported by the study conducted by

Dagnachew et al. (2020) for the Omo-Gibe basin (located in the SW region), which described vegetation degradation in 1984. The years 2002 and 1999, which were the second and third most severe dry years for the SW region, respectively, showed less pronounced negative NDVI anomalies that are mostly located to the east in 2002 and south in 1999. Finally, in the W region, a common contrast was observed in vegetation growing conditions between the northeast and southwest in 2009 and 1995, both years affected by severe drought. However, it was contradictory to find a prevalence of positive NDVI anomalies in the year 1995. A possible explanation for this could be the occurrence of two previous years (1993 and 1994) characterised by severe wet conditions (**Figure 8**). To confirm this, future studies should identify the optimal temporal lag in which dry and humid conditions affect the vegetation conditions in these regions.

4 CONCLUSION

This study revealed the most important sources of moisture for precipitation in Ethiopian river catchments. For this purpose, a cluster analysis was implemented to reduce the 12 river basins that make up the country into a smaller group of major drainage systems with similar pluviometry characteristics. This resulted in four study regions named N, SE, SW, and W, according to their geographical position in the country. The analysis was based on a Lagrangian approach using global outputs from the FLEXPART model for 39 years (1980–2018) for ensuring accrued climatological results. This model permitted to track backward in time air masses and computed the moisture gain over time, which allows the identification of the most important oceanic and terrestrial moisture sources. These were the western IO, AS, PG, MS, and RS as well as terrestrial sources from the adjacent AfC, AP, and R. However, the MS was not selected as one of the most important sources for the SE and SW regions. The size of the sources differs, even when they originated from the same geographical region. The moisture contribution from these sources to precipitation (E − P) < 0 over the target regions was calculated by forecasting air masses occurring over the sources and considering the optimum integration times of the Lagrangian precipitation proposed in previous studies. This analysis revealed the crucial role of moisture recycling and moisture export within the African continent according to the major moisture contribution supply from the AfC, R, and AP sources to the precipitation over the NW, W, and SW regions. In contrast, the IO and AS are responsible for supplying 46% and 14% of the moisture loss over the SE region, respectively; thus, the oceanic origin of precipitation is significant in this region. Correlation analysis confirmed the direct relationship between the |(E − P) < 0| series and precipitation over each region.

REFERENCES

Abara, M., Komariah, K., and Budiastuti, S. (2020). Drought Frequency, Severity, and Duration Monitoring Based on Climate Change in Southern and Southeastern Ethiopia. *IOP Conf. Ser. Earth Environ. Sci.* 477, 012011. doi:10.1088/1755-1315/477/1/012011

Drought assessment using the SPEI on a 12-month scale identified the years affected by severe and extreme drought conditions in each of the study regions. The years in order of severity for the NE regions were 1984, 2015, and 2009; for the SE, 1984, 1980, and 1989; for the SW, 1984, 2002, 1999; and for the W, 2009, and 1995. During these years, a significant reduction in the moisture contributions from the sources occurred in combination with positive anomalies of the VMIF, which confirmed the inhibition of convection and precipitation processes. In 1984 for the NE region, analysis at the annual scale did not provide wholly consistent results; however, a monthly analysis partially supported an explanation. Finally, annual severe and extreme drought conditions reduced the vegetation activity, particularly in the NE, SE, and SW regions. Our ongoing research is focused on a more detailed seasonal analysis, which will provide more comprehensive information regarding the variability of precipitation sources. Further, its impact on Ethiopian seasonal rainfall and the associated influence of drought on hydrological cycles and vegetation.

DATA AVAILABILITY STATEMENT

Publicly available datasets were analyzed in this study. This data can be found here: https://apps.ecmwf.int; https://crudata.uea.ac.uk/cru/data/hrg/cru_ts_4.05/; https://www.ncei.noaa.gov/access/metadata/landing-page/bin/iso?id=gov.noaa.ncdc:C01558.

AUTHOR CONTRIBUTIONS

MS and GM provided research ideas. MS, RS, and MV calculated, analysed and wrote the manuscript. RN, LG, and GM wrote and revisited the final version of the manuscript.

FUNDING

Abebe, D. (2010). Future Climate of Ethiopia from PRECIS Regional Climate Model Experimental Design. Ethiopia Available at: https://www.metoffice.gov.uk/binaries/content/assets/metofficegovuk/pdf/research/applied-science/precis/precis_experimental_design_dawit.pdf (accessed 04 18, 2022).

Aerts, R., Van Overtveld, K., November, E., Wassie, A., Abiyu, A., Demissew, S., et al. (2016). Conservation of the Ethiopian Church Forests: Threats,

Opportunities and Implications for Their Management. *Sci. Total Environ.* 551-552 (552), 404–414. doi:10.1016/j.scitotenv.2016.02.034

Alemayehu, A., Maru, M., Bewket, W., and Assen, M. (2020). Spatiotemporal Variability and Trends in Rainfall and Temperature in Alwero Watershed, Western Ethiopia. *Environ. Syst. Res.* 9, 22. doi:10.1186/s40068-020-00184-3

Alemu, Z. A., Dioha, E. C., Dioha, E. C., and Dioha, M. O. (2021). Hydrometeorological Drought in Addis Ababa: A Characterization Study. *AIMS Environ. Sci.* 8 (2), 148–168. doi:10.3934/environsci.2021011

Alhamshry, A., Fenta, A. A., Yasuda, H., Kimura, R., and Shimizu, K. (2020). Seasonal Rainfall Variability in Ethiopia and its Long-Term Link to Global Sea Surface Temperatures. *Water* 12, 1–19. doi:10.3390/w12010055

Allen, R. G., Pereira, L. S., Raes, D., and Smith, M. (1998). *FAO Irrigation and Drainage Paper No. 56*. Rome, Italy: Food and AgricultureOrganization of the United Nations.

Asadi Zarch, M. A., Sivakumar, B., and Sharma, A. (2015). Droughts in a Warming Climate: a Global Assessment of Standardized Precipitation Index (SPI) and Reconnaissance Drought Index (RDI). *J. Hydrology* 526, 183–195. doi:10.1016/j.jhydrol.2014.09.071

Asefa, M., Cao, M., He, Y., Mekonnen, E., Song, X., and Yang, J. (2020). Ethiopian Vegetation Types, Climate and Topography. *Plant Divers.* 42, 302–311. doi:10.1016/j.pld.2020.04.004

Asfaw, A., Simane, B., Hassen, A., and Bantider, A. (2018). Variability and Time Series Trend Analysis of Rainfall and Temperature in Northcentral Ethiopia: A Case Study in Woleka Sub-basin. *Weather Clim. Extrem.* 19, 29–41. doi:10.1016/j.wace.2017.12.002

Asmamaw, D. K. (2015). A Critical Review of Integrated River Basin Management in the Upper Blue Nile River Basin: the Case of Ethiopia. *Int. J. River Basin Manag.* 13, 429–442. doi:10.1080/15715124.2015.1013037

Awulachew, S. B., Merrey, D. J., Kamara, A. B., Van Koppen, B., Penning de Vries, F., Boelee, E., et al. (2005). *Experiences and Opportunities for Promoting Small–Scale/micro Irrigation and Rainwater Harvesting for Food Security in Ethiopia.* Colombo, Sri Lanka: IWMI. v. 86p. (Working paper 98). Available at: https://www.iwmi.cgiar.org/Publications/Working_Papers/working/WOR98.pdf.

Awulachew, S. B., Yilma, A. D., Loulseged, M., Loiskandl, W., Ayana, M., and Alamirew, T. (2007). *Water Resources and Irrigation Development in Ethiopia.* Colombo, Sri Lanka: International Water Management Institute. (IWMI). 66p. (IWMI Working Paper 123). doi:10.3910/2009.305

Ayalew, D. W. (2018). Theoretical and Empirical Review of Ethiopian Water Resource Potentials, Challenges and Future Development Opportunities. *Int. J. Waste Resour.* 08, 353. doi:10.4172/2252-5211.1000353

Bayable, G., Amare, G., Alemu, G., and Gashaw, T. (2021). Spatiotemporal Variability and Trends of Rainfall and its Association with Pacific Ocean Sea Surface Temperature in West Harerge Zone, Eastern Ethiopia. *Environ. Syst. Res.* 10, 7. doi:10.1186/s40068-020-00216-y

Bayissa, Y., Semu, A., Yunqing, X., Schalk, A., Shreedhar, M., Dimitri, S., et al. (2015). Spatio-temporal Assessment of Meteorological Drought under the Influence of Varying Record Length: The Case of Upper Blue Nile Basin, Ethiopia. *Hydrol. Sci. J.* 60, 1927–1942. doi:10.1080/02626667.2015.1032291

Bednorz, E., Wrzesiński, D., Tomczyk, A. M., and Jasik, D. (2019). Classification of Synoptic Conditions of Summer Floods in Polish Sudeten Mountains. *Water* 11 (7), 1450. doi:10.3390/w11071450

Beguería, S., Vicente-Serrano, S. M., Reig, F., and Latorre, B. (2014). Standardized Precipitation Evapotranspiration Index (SPEI) Revisited: Parameter Fitting, Evapotranspiration Models, Tools, Datasets and Drought Monitoring. *Int. J. Climatol.* 34, 3001–3023. doi:10.1002/joc.3887

Belayneh, A., Adamowski, J., Khalil, B., and Ozga-Zielinski, B. (2014). Long-term SPI Drought Forecasting in the Awash River Basin in Ethiopia Using Wavelet Neural Network and Wavelet Support Vector Regression Models. *J. Hydrology* 508, 418–429. doi:10.1016/j.jhydrol.2013.10.052

Berhanu, B., Seleshi, Y., and Melesse, A. (2014). "Surface Water and Groundwater Resources of Ethiopia: Potentials and Challenges of Water Resources Development," in *Nile River Basin*. Editors A. Melesse, W. Abtew, and S. Setegn (Cham: Springer). doi:10.1007/978-3-319-02720-3_6

Beyene, T. K., Jain, M. K., Yadav, B. K., and Agarwal, A. (2021). Multiscale Investigation of Precipitation Extremes over Ethiopia and Teleconnections to Large-Scale Climate Anomalies. *Stoch. Environ. Res. Risk Assess.* 36, 1503–1519. doi:10.1007/s00477-021-02120-y

Bisselink, B., and Dolman, A. J. (2008). Precipitation Recycling: Moisture Sources over Europe Using ERA-40 Data. *J. Hydrometeorol.* 9, 1073–1083. doi:10.1175/2008jhm962.1

Bu, J., Liu, W., Pan, Z., and Ling, K. (2020). Comparative Study of Hydrochemical Classification Based on Different Hierarchical Cluster Analysis Methods. *Ijerph* 17, 9515. doi:10.3390/ijerph17249515

Cheung, W. H., Senay, G. B., and Singh, A. (2008). Trends and Spatial Distribution of Annual and Seasonal Rainfall in Ethiopia. *Int. J. Climatol.* 28, 1723–1734. doi:10.1002/joc.1623

Dagnachew, M., Kebede, A., Moges, A., and Abebe, A. (2020). Effects of Climate Variability on Normalized Difference Vegetation Index (NDVI) in the Gojeb River Catchment, Omo-Gibe Basin, Ethiopia. *Adv. Meteorol.* 2020, 8263246. doi:10.1155/2020/8263246

Dai, A. (2010). Drought under Global Warming: a Review. *WIREs Clim. Change* 2 (1), 45–65. doi:10.1002/wcc.81

Dee, D. P., Uppala, S. M., Simmons, A. J., Berrisford, P., Poli, P., Kobayashi, S., et al. (2011). The ERA-Interim Reanalysis: Configuration and Performance of the Data Assimilation System. *Q.J.R. Meteorol. Soc.* 137, 553–597. doi:10.1002/qj.828

Degefu, M. A., Bewket, W., and Amha, Y. (2022). Evaluating Performance of 20 Global and Quasi-Global Precipitation Products in Representing Drought Events in Ethiopia I: Visual and Correlation Analysis. *Weather Clim. Extrem.* 35, 100416. doi:10.1016/j.wace.2022.100416

Delbiso, T. D., Rodriguez-Llanes, J. M., Donneau, A.-F., Speybroeck, N., and Guha-Sapir, D. (2017). Drought, Conflict and Children's Undernutrition in Ethiopia 2000-2013: a Meta-Analysis. *Bull. World Health Organ.* 95 (2), 94–102. doi:10.2471/BLT.16.172700

Dercon, S., and Porter, C. (2014). Live Aid Revisited: Long-Term Impacts of the 1984 Ethiopian Famine on Children. *J. Eur. Econ. Assoc.* 12 (4), 927–948. doi:10.1111/jeea.12088

Dezfuli, A. K. (2011). Spatio-temporal Variability of Seasonal Rainfall in Western Equatorial Africa. *Theor. Appl. Climatol.* 104, 57–69. doi:10.1007/s00704-010-0321-8

Dika, G. (2018). Impacts of Climate Variability and Households Adaptation Strategies in Lare District of Gambella Region, South Western Ethiopia. *J. Earth Sci. Clim. Chang.* 9, 1–12. doi:10.4172/2157-7617.1000480

Diro, G. T., Grimes, D. I. F., and Black, E. (2011). "Large Scale Features Affecting Ethiopian Rainfall," in *African Climate and Climate Change*. Editors C. J. R. Williams and D. R. Kniveton (Netherlands, Vol. 43, 13–50. Advances in global change researchSpringer. doi:10.1007/978-90-481-3842-5_2

Distances between Clustering (2009). Distances between Clustering, Hierarchical Clustering 36-350, Data Mining (2009) by Unknown Authors. Available at: http://citeseerx.ist.psu.edu/viewdoc/download?doi=10.1.1.190.9886&rep=rep1&type=pdf

Drumond, A., Stojanovic, M., Nieto, R., Vicente-Serrano, S. M., and Gimeno, L. (2019). Linking Anomalous Moisture Transport and Drought Episodes in the IPCC Reference Regions. *BAMS* 100, 1481–1498. doi:10.1175/bams-d-18-0111.1

Dubache, G., Ogwang, B. A., Ongoma, V., and Towfiqul Islam, A. R. M. (2019). The Effect of Indian Ocean on Ethiopian Seasonal Rainfall. *Meteorol. Atmos. Phys.* 131, 1753–1761. doi:10.1007/s00703-019-00667-8

Ebi, K. L., and Bowen, K. (2016). Extreme Events as Sources of Health Vulnerability: Drought as an Example. *Weather Clim. Extrem.* 11, 95–102. doi:10.1016/j.wace.2015.10.001

Edossa, D. C., Babel, M. S., and Das Gupta, A. (2010). Drought Analysis in the Awash River Basin, Ethiopia. *Water Resour. manage.* 24, 1441–1460. doi:10.1007/s11269-009-9508-0

El Kenawy, A. M., McCabe, M. F., Vicente-Serrano, S. M., López-Moreno, J. I., and Robaa, S. M. (2016). Changes in the Frequency and Severity of Hydrological Droughts over Ethiopia from 1960 to 2013. *Cig* 42, 145–166. doi:10.18172/cig.2931

Fazzini, M., Bisci, C., and Billi, P. (2015). "The Climate of Ethiopia," in *Landscapes and Landforms of Ethiopia*. *World Geomorphological Landscapes*. Editor P. Billi (Dordrecht: Springer), 65–87. doi:10.1007/978-94-017-8026-1_3

Fekadu, K. (2015). Ethiopian Seasonal Rainfall Variability and Prediction Using Canonical Correlation Analysis (CCA). *Earth* 4, 112–119. doi:10.11648/j.earth.20150403.14

Ferreira, L., and Hitchcock, D. B. (2009). A Comparison of Hierarchical Methods for Clustering Functional Data. *Commun. Statistics - Simul. Comput.* 38, 1925–1949. doi:10.1080/03610910903168603

Friis, I., Sebsebe, D., and Breugel, P. (2010). "Atlas of the Potential Vegetation of Ethiopia," in *The Royal Danish Academy of Science and Letters.* Available at: https://www.royalacademy.dk/Publications/Low/3607_Friis,%20Ib,%20Demissew,%20Sebsebe%20and%20van%20Breugel,%20Paulo.pdf.

Funk, C. C., Rowland, J., Eilerts, G., Kebebe, E., Biru, N., Libby, W., et al. (2012). *A Climate Trend Analysis of Ethiopia.* Reston, VA: USGS Publications Warehouse, 1–6. Available at: http://pubs.er.usgs.gov/publication/fs20123053.

Funk, C. C., Senay, G., Asfaw, A., Verdin, J., Rowland, J., Michaelson, J., et al. (2005). *Recent Drought Tendencies in Ethiopia and Equatorial-Subtropical Eastern Africa.* Washington DC: FEWS-NET. Available at: https://pdf.usaid.gov/pdf_docs/PNADH997.pdf.

Gebrechorkos, S. H., Hülsmann, S., and Bernhofer, C. (2019). Changes in Temperature and Precipitation Extremes in Ethiopia, Kenya, and Tanzania. *Int. J. Climatol.* 39, 18–30. doi:10.1002/joc.5777

Gebrehiwot, T., Van Der Veen, A., and Maathuis, B. (2011). Spatial and Temporal Assessment of Drought in the Northern Highlands of Ethiopia. *Int. J. Appl. Earth Observation Geoinformation* 13, 309–321. doi:10.1016/j.jag.2010.12.002

Gezie, M. (2019). Farmer's Response to Climate Change and Variability in Ethiopia: A Review. *Cogent Food Agric.* 5 (1), 1–13. doi:10.1080/23311932.2019.1613770

Ghebrezgabher, M. G., Yang, T., and Yang, X. (2016). Long-term Trend of Climate Change and Drought Assessment in the Horn of Africa. *Adv. Meteorology* 2016, 1–12. doi:10.1155/2016/8057641

Gimeno, L., Drumond, A., Nieto, R., Trigo, R. M., and Stohl, A. (2010). On the Origin of Continental Precipitation. *Geophys. Res. Lett.* 37, L13804. doi:10.1029/2010gl043712

Gimeno, L., Vázquez, M., Eiras-Barca, J., Sorí, R., Stojanovic, M., Algarra, I., et al. (2020). Recent Progress on the Sources of Continental Precipitation as Revealed by Moisture Transport Analysis. *Earth-Sci. Rev.* 201, 1–25. doi:10.1016/j.earscirev.2019.103070

Gissila, T., Black, E., GrimesSlingo, D. I. F. J. M., and Slingo, J. M. (2004). Seasonal Forecasting of the Ethiopian Summer Rains. *Int. J. Climatol.* 24, 1345–1358. doi:10.1002/joc.1078

Hadish, L. (2010). Drought Risk Assessment using Remote Sensing and GIS: The Case of Southern Zone, Tigray Region, Ethiopia. *J. Nat. Sci. Res.* 4 (23), 87–95.

Harris, I., Osborn, T. J., Jones, P., and Lister, D. (2020). Version 4 of the CRU TS Monthly High-Resolution Gridded Multivariate Climate Dataset. *Sci. Data* 7, 109. doi:10.1038/s41597-020-0453-3

Hassan, M. A., Yang, M., Rasheed, A., Yang, G., Reynolds, M., Xia, X., et al. (2019). A Rapid Monitoring of NDVI across the Wheat Growth Cycle for Grain Yield Prediction Using a Multi-Spectral UAV Platform. *Plant Sci.* 282, 95–103. doi:10.1016/j.plantsci.2018.10.022

Hernandez, E. A., and Uddameri, V. (2014). Standardized Precipitation Evaporation Index (SPEI)-based Drought Assessment in Semi-arid South Texas. *Environ. Earth Sci.* 71 (6), 2491–2501. doi:10.1007/s12665-013-2897-7

Herring, S. C., Hoerling, M. P., Peterson, T. C., and Stott, P. A. (2014). Explaining Extreme Events of 2013 from a Climate Perspective. *Bull. Am. Meteorol. Soc.* 95 (9), S1–S104. doi:10.1175/1520-0477-95.9.S1.1

Hirko, A., Mergia, G., Nigussie, A., and Dandesa, T. (2021). Seasonal and Annual Meteorological Drought Frequency: Case Study West Hararge Province (Zone). *Int. J. Res. Environ. Sci.* 7, 1–10. doi:10.20431/2454-9444.0701001

Ionita, M., Tallaksen, L. M., Kingston, D. G., Stagge, J. H., Laaha, G., Van Lanen, H. A. J., et al. (2017). The European 2015 Drought from a Climatological Perspective. *Hydrol. Earth Syst. Sci.* 21, 1397–1419. doi:10.5194/hess-21-1397-2017

Jjemba, E., Singh, R., and Arrighi, J. (2017). *Extreme Drought in Ethiopia Stretches Drought Management Systems.* The Hague: Red Cross Red Crescent Climate Centre. Available at: https://cdkn.org/sites/default/files/files/Extreme-drought-in-Ethiopia-stretches-drought-management-systems.pdf.

Jury, M. R., and Chiao, S. (2014). Representation of Ethiopian Wet Spells in Global and Nested Models. *Adv. Meteorology* 2014 (4), 1–12. doi:10.1155/2014/237374

Jury, M. R. (2011). Meteorological Scenario of Ethiopian Floods in 2006-2007. *Theor. Appl. Climatol.* 104, 209–219. doi:10.1007/s00704-010-0337-0

Keyantash, J., and Dracup, J. A. (2002). The Quantification of Drought: An Evaluation of Drought Indices. *Bull. Amer. Meteor. Soc.* 83, 1167–1180. doi:10.1175/1520-0477-83.8.1167

Łabędzki, L. (2007). Estimation of Local Drought Frequency in Central Poland Using the Standardized Precipitation Index SPI. *Irrig. Drain.* 56 (1), 67–77. doi:10.1002/ird.285

Leprieur, C., Kerr, Y. H., Mastorchio, S., and Meunier, J. C. (2000). Monitoring Vegetation Cover across Semi-arid Regions: Comparison of Remote Observations from Various Scales. *Int. J. Remote Sens.* 21 (2), 281–300. doi:10.1080/014311600210830

Liou, Y.-A., and Mulualem, G. M. (2019). Spatio–temporal Assessment of Drought in Ethiopia and the Impact of Recent Intense Droughts. *Remote Sens.* 11, 1–19. doi:10.3390/rs11151828

Livada, I., and Assimakopoulos, V. D. (2007). Spatial and Temporal Analysis of Drought in Greece Using the Standardized Precipitation Index (SPI). *Theor. Appl. Climatol.* 89 (3–4), 143–153. doi:10.1007/s00704-005-0227-z

Lweendo, M., Lu, B., Wang, M., Zhang, H., and Xu, W. (2017). Characterization of Droughts in Humid Subtropical Region, Upper Kafue River Basin (Southern Africa). *Water* 9 (4), 242. doi:10.3390/w9040242

Matewos, T. (2019). Climate Change-Induced Impacts on Smallholder Farmers in Selected Districts of Sidama, Southern Ethiopia. *Climate* 7, 70. doi:10.3390/cli7050070

McKee, T. B., Doesken, N. J., and Kleist, J. (1993). "The Relationship of Drought Frequency and Duration to Time Scales," in Proceedings of the Eighth Conference on Applied Climatology, Anaheim, CA, USA, 17–22 January, 179–184.

Mekonen, A. A., and Berlie, A. B. (2020). Spatiotemporal Variability and Trends of Rainfall and Temperature in the Northeastern Highlands of Ethiopia. *Model. Earth Syst. Environ.* 6, 285–300. doi:10.1007/s40808-019-00678-9

Mersha, A. A., and van Laerhoven, F. (2018). The Interplay between Planned and Autonomous Adaptation in Response to Climate Change: Insights from Rural Ethiopia. *World Dev.* 107, 87–97. doi:10.1016/j.worlddev.2018.03.001

Mishra, A. K., and Singh, V. P. (2010). A Review of Drought Concepts. *J. Hydrology* 391, 202–216. doi:10.1016/j.jhydrol.2010.07.012

Mohamed, Y. A., van den Hurk, B. J. J. M., Savenije, H. H. G., and Bastiaanssen, W. G. M. (2005). Hydroclimatology of the Nile: Results from a Regional Climate Model. *Hydrol. Earth Syst. Sci.* 9, 263–278. doi:10.5194/hess-9-263-2005

Mohammed, Y., Yimer, F., Tadesse, M., and Tesfaye, K. (2018). Meteorological Drought Assessment in North East Highlands of Ethiopia. *Ijccsm* 10 (1), 142–160. doi:10.1108/ijccsm-12-2016-0179

Mulugeta, S., Fedler, C., and Ayana, M. (2019). Analysis of Long-Term Trends of Annual and Seasonal Rainfall in the Awash River Basin, Ethiopia. *Water* 11, 1498. doi:10.3390/w11071498

Munday, C., Washington, R., and Hart, N. (2021). African Low-Level Jets and Their Importance for Water Vapor Transport and Rainfall. *Geophys. Res. Lett.* 48, e2020GL090999. doi:10.1029/2020gl090999

Muñoz-Díaz, D., and Rodrigo, F. S. (2004). Spatio-temporal Patterns of Seasonal Rainfall in Spain (1912-2000) Using Cluster and Principal Component Analysis: Comparison. *Ann. Geophys.* 22, 1435–1448. doi:10.5194/angeo-22-1435-2004

Murtagh, F., and Legendre, P. (2014). Ward's Hierarchical Agglomerative Clustering Method: Which Algorithms Implement Ward's Criterion? *J. Classif.* 31, 274–295. doi:10.1007/s00357-014-9161-z

Naresh Kumar, M., Murthy, C. S., Sesha Sai, M. V. R., and Roy, P. S. (2009). On the Use of Standardized Precipitation Index (SPI) for Drought Intensity Assessment. *Met. Apps* 16 (3), 381–389. doi:10.1002/met.136

Nieto, R., and Gimeno, L. (2019). A Database of Optimal Integration Times for Lagrangian Studies of Atmospheric Moisture Sources and Sinks. *Sci. Data* 6, 59. doi:10.1038/s41597-019-0068-8

NMA (1996). Climatic and Agroclimatic Resources of Ethiopia. National Meteorological Services Agency of Ethiopia. *Meteorol. Res. Re.p Ser.* 1 (1), 137.

Philip, S., Kew, S. F., Jan van Oldenborgh, G., Otto, F., O'Keefe, S., Haustein, K., et al. (2017). *The Drought in Ethiopia.* Available at: https://cdkn.org/sites/default/files/files/Ethiopia-drought-science-summary.pdf (accessed on April 1,

2022).Climate and Development Knowledge Network and World Weather Attribution Initiative Raising Risk Awareness

Philip, S., Kew, S. F., Jan van Oldenborgh, G., Otto, F., O'Keefe, S., Haustein, K., et al. (2018). Attribution Analysis of the Ethiopian Drought of 2015. *J. Clim.* 31 (6), 2465–2486. doi:10.1175/JCLI-D-17-0274.1

Reda, K. W., Liu, X., Tang, Q., and Gebremicael, T. G. (2021). Evaluation of Global Gridded Precipitation and Temperature Datasets against Gauged Observations over the Upper Tekeze River Basin, Ethiopia. *J. Meteorol. Res.* 35, 673–689. doi:10.1007/s13351-021-0199-7

Riddle, E. E., and Cook, K. H. (2008). Abrupt Rainfall Transitions over the Greater Horn of Africa: Observations and Regional Model Simulations. *J. Geophys. Res.* 113, D15109. doi:10.1029/2007JD009202

Riddle, E. E., and Wilks, D. S. (2013). Statistical Indices of the Northward Rainfall Progression over Eastern Africa. *Int. J. Climatol.* 33, 356–375. doi:10.1002/joc.3429

Roberts, D., Roth, K., and Perroy, R. (2011). "Hyperspectral Vegetation Indices," in *Hyperspectral Remote Sensing of Vegetation*. Editors P. S. Thenkabail and J. G. Lyon (Boca Raton: CRC Press), 309–327. doi:10.1201/b11222-20

Saravi, M. M., Safdari, A. A., and Malekian, A. (2009). Intensity-Duration-Frequency and Spatial Analysis of Droughts Using the Standardized Precipitation Index. *Hydrol. Earth Syst. Sci. Discuss.* 6, 1347–1383. doi:10.5194/hessd-6-1347-2009

Segele, Z. T., Lamb, P. J., and Leslie, L. M. (2009). Large-scale Atmospheric Circulation and Global Sea Surface Temperature Associations with Horn of Africa June-September Rainfall. *Int. J. Climatol.* 29, 1075–1100. doi:10.1002/joc.1751

Seleshi, Y., and Camberlin, P. (2005). Recent Changes in Dry Spell and Extreme Rainfall Events in Ethiopia. *Theor. Appl. Climatol.* 83, 181–191. doi:10.1007/s00704-005-0134-3

Seleshi, Y., and Zanke, U. (2004). Recent Changes in Rainfall and Rainy Days in Ethiopia. *Int. J. Climatol.* 24, 973–983. doi:10.1002/joc.1052

Seregina, L. S., Fink, A. H., van der Linden, R., Elagib, N. A., and Pinto, J. G. (2019). A New and Flexible Rainy Season Definition: Validation for the Greater Horn of Africa and Application to Rainfall Trends. *Int. J. Climatol.* 39, 989–1012. doi:10.1002/joc.5856

Sharghi, E., Nourani, V., Soleimani, S., and Sadikoglu, F. (2018). Application of Different Clustering Approaches to Hydroclimatological Catchment Regionalization in Mountainous Regions, a Case Study in Utah State. *J. Mt. Sci.* 15, 461–484. doi:10.1007/s11629-017-4454-4

Sheffield, J., Wood, E. F., and Roderick, M. L. (2012). Little Change in Global Drought over the Past 60 Years. *Nature* 491 (7424), 435–438. doi:10.1038/nature11575

Sorí, R., Vázquez, M., Stojanovic, M., Nieto, R., Liberato, M. L. R., and Gimeno, L. (2020). Hydrometeorological Droughts in the Miño–Limia–Sil Hydrographic Demarcation (Northwestern Iberian Peninsula): the Role of Atmospheric Drivers. *Nat. Hazards Earth Syst. Sci.* 20, 1805–1832. doi:10.5194/nhess20-1805-2020

Stohl, A., and James, P. (2004). A Lagrangian Analysis of the Atmospheric Branch of the Global Water Cycle. Part I: Method Description, Validation, and Demonstration for the August 2002 Flooding in Central Europe. *J. Hydrometeor* 5, 656–678. doi:10.1175/1525-7541(2004)005<0656:alaota>2.0.co;2

Stohl, A., and James, P. (2005). A Lagrangian Analysis of the Atmospheric Branch of the Global Water Cycle. Part II: Moisture Transports between Earth's Ocean Basins and River Catchments. *J. Hydrometeorol.* 6, 961–984. doi:10.1175/jhm470.1

Stojanovic, M., Drumond, A., Nieto, R., and Gimeno, L. (2018). Anomalies in Moisture Supply during the 2003 Drought Event in Europe: A Lagrangian Analysis. *Water* 10 (4), 1–19. doi:10.3390/w10040467

Stojanovic, M., Gonçalves, A., Sorí, R., Vázquez, M., Ramos, A. M., Nieto, R., et al. (2021a). Consecutive Extratropical Cyclones Daniel, Elsa and Fabien, and Their Impact on the Hydrological Cycle of Mainland Portugal. *Water* 13, 1476. doi:10.3390/w13111476

Stojanovic, M., Liberato, M. L. R., Sorí, R., Vázquez, M., Phan-Van, T., Duongvan, H., et al. (2020). Trends and Extremes of Drought Episodes in Vietnam Sub-regions during 1980-2017 at Different Timescales. *Water* 12 (3), 813. doi:10.3390/w12030813

Stojanovic, M., Nieto, R., Liberato, M. L. R., Sorí, R., Vázquez, M., and Gimeno, L. (2021b). Tracking the Origins of Moisture over Vietnam: The Role of Moisture Sources and Atmospheric Drivers on Seasonal Hydroclimatic Conditions. *Int. J. Climatol.* 41 (13), 5843–5861. doi:10.1002/joc.7156

Suryabhagavan, K. V. (2017). GIS-based Climate Variability and Drought Characterization in Ethiopia over Three Decades. *Weather Clim. Extrem.* 15, 11–23. doi:10.1016/j.wace.2016.11.005

Svoboda, M., Hayes, M., and Wood, D. (2012). *Standardized Precipitation Index User Guide*. Geneva: World Meteorological Organization. Available at: https://library.wmo.int/doc_num.php?explnum_id=7768.

Tefera, A. S., Ayoade, J. O., and Bello, N. J. (2019). Comparative Analyses of SPI and SPEI as Drought Assessment Tools in Tigray Region, Northern Ethiopia. *SN Appl. Sci.* 1, 1265. doi:10.1007/s42452-019-1326-2

Temam, D., Uddameri, V., Mohammadi, G., Hernandez, E. A., and Ekwaro-Osire, S. (2019). Long-Term Drought Trends in Ethiopia with Implications for Dryland Agriculture. *Water* 11, 2571. doi:10.3390/w11122571

Tian, W., Zheng, Y., Yang, R., Ji, S., and Wang, J. (2014). A Survey on Clustering Based Meteorological Data Mining. *Ijgdc* 7 (6), 229–240. doi:10.14257/ijgdc.2014.7.6.19

Trenberth, K. E., Dai, A., Van Der Schrier, G., Jones, P. D., Barichivich, J., Briffa, K. R., et al. (2014). Global Warming and Changes in Drought. *Nat. Clim. Change* 4 (1), 17–22. doi:10.1038/nclimate2067

Tsiptsis, K., and Chorianopoulos, A. (2009). *Data Mining Techniques in CRM: Inside Customer Segmentation*. Chichester: John Wiley & Sons. Available at: https://www.academia.edu/9824899/Data_Mining_Techniques_in_CRM_Inside_Customer_Segmentation.

UN (2009). United Nations. Available at: https://news.un.org/en/story/2009/10/318562-ethiopia-faces-large-food-shortfall-over-6-million-drought-victims-un (accessed on 04 20, 2022).

Unal, Y., Kindap, T., and Karaca, M. (2003). Redefining the Climate Zones of Turkey Using Cluster Analysis. *Int. J. Climatol.* 23, 1045–1055. doi:10.1002/joc.910

Van Loon, A. F., Gleeson, T., Clark, J., Van Dijk, A. I. J. M., Stahl, K., Hannaford, J., et al. (2016). Drought in the Anthropocene. *Nat. Geosci.* 9, 89–91. doi:10.1038/ngeo2646

Vestal, T. M. (1985). Famine in Ethiopia: Crisis of Many Dimensions. *Afr. Today* 32, 7–28. Available at: https://www.jstor.org/stable/4186321.

Vicente-Serrano, S. M., Beguería, S., and López-Moreno, J. I. (2010). A Multiscalar Drought Index Sensitive to Global Warming: The Standardized Precipitation Evapotranspiration Index. *J. Clim.* 23, 1696–1718. doi:10.1175/2009jcli2909.1

Vicente-Serrano, S. M., Beguería, S., Lorenzo-Lacruz, J., Camarero, J. J., López-Moreno, J. I., Azorin-Molina, C., et al. (2012). Performance of Drought Indices for Ecological, Agricultural, and Hydrological Applications. *Earth Interact.* 16, 1–27. doi:10.1175/2012EI000434.1

Viste, E., Korecha, D., and Sorteberg, A. (2013). Recent Drought and Precipitation Tendencies in Ethiopia. *Theor. Appl. Climatol.* 112, 535–551. doi:10.1007/s00704-012-0746-3

Viste, E., and Sorteberg, A. (2011). Moisture Transport into the Ethiopian Highlands. *Int. J. Climatol.* 33, 249–263. doi:10.1002/joc.3409

Wagesho, N., Goel, N. K., and Jain, M. K. (2013). Temporal and Spatial Variability of Annual and Seasonal Rainfall over Ethiopia. *Hydrological Sci. J.* 58 (2), 354–373. doi:10.1080/02626667.2012.754543

Wang, Q., Shi, P., Lei, T., Geng, G., Liu, J., Mo, X., et al. (2015). The Alleviating Trend of Drought in the Huang-Huai-Hai Plain of China Based on the Daily SPEI. *Int. J. Climatol.* 35 (13), 3760–3769. doi:10.1002/joc.4244

Wilhite, D. A., and Glantz, M. H. (1985). Understanding: the Drought Phenomenon: The Role of Definitions. *Water Int.* 10, 111–120. doi:10.1080/02508068508686328

Wilhite, D. A. (1993). Understanding the Phenomenon of Drought. *Hydro. Rev.* 12 (5), 136–148.

Wilks, D. S. (2011). *Statistical Methods in the Atmospheric Sciences*. Amsterdam, The Netherlands: Elsevier.

World Bank (2006). *Ethiopia: Managing Water Resources to Maximize Sustainable Growth*. Washington, D.C: World Bank. Available at: https://openknowledge.worldbank.org/handle/10986/8170.

World Meteorological Organization (2012). *Standardized Precipitation Index User Guide*. Available at: http://www.wamis.org/agm/pubs/SPI/WMO_1090_EN.pdf (accessed on March 31, 2022).

Worqlul, A. W., Jeong, J., Dile, Y. T., Osorio, J., Schmitter, P., Gerik, T., et al. (2017). Assessing Potential Land Suitable for Surface Irrigation Using Groundwater in Ethiopia. *Appl. Geogr.* 85, 1–13. doi:10.1016/j.apgeog.2017.05.010

Yirga, S. A. (2021). Spatio-temporal Analysis of Drought Variability in Central Ethiopia. *J. Water Clim. Chang.* 12 (5), 1778–1787. doi:10.2166/wcc.2020.226

Zeleke, T., Giorgi, F., Mengistu Tsidu, G., and Diro, G. T. (2013). Spatial and Temporal Variability of Summer Rainfall over Ethiopia from Observations and a Regional Climate Model Experiment. *Theor. Appl. Climatol.* 111, 665–681. doi:10.1007/s00704-012-0700-4

Zhang, Y., Moges, S., and Block, P. (2016). Optimal Cluster Analysis for Objective Regionalization of Seasonal Precipitation in Regions of High Spatial-Temporal Variability: Application to Western Ethiopia. *J. Clim.* 29, 3697–3717. doi:10.1175/JCLI-D-15-0582.1

Drought- and heatwave-associated compound extremes: A review of hotspots, variables, parameters, drivers, impacts, and analysis frameworks

Mahnaz Afroz[1], Gang Chen[1] and Aavudai Anandhi[2]*

[1]Department of Civil and Environmental Engineering, FAMU FSU College of Engineering, Tallahassee, FL, United States, [2]Biological System Engineering Program, Florida A&M University, Tallahassee, FL, United States

Droughts and heatwaves are rising concerns with regard to the frequent formation of the compound or concurrent extremes (CEs), which can cause greater havoc than an individual event of a higher magnitude. Recently, they have been frequently detected to form CEs together or with other events (e.g., floods, aridity, and humidity events) concurrently or with spatiotemporal lags. Therefore, this systematic review assesses these CEs by reviewing the following aspects: CE hotspots, events, and variable combinations that form CEs; frequently analyzed CE parameters (e.g., frequency and severity); large-scale modes of climate variability (CV) as drivers alongside the approaches to relate them to CEs; and CE impacts (e.g., yield loss and fire risk) alongside the impact integration approaches from 166 screened publications. Additionally, three varied analysis frameworks of CEs are summarized to highlight the different analysis components of drought- and heatwave-associated CEs, which is the novelty of this study. The analysis frameworks vary with regard to the three major assessment objectives: only CE parameters (event−event), driver association (event−driver), and impacts (event−impact). According to this review, the most frequently reported hotspots of these CEs in global studies are southern Africa, Australia, South America, and Southeast Asia. In regional studies, several vital hotspots (e.g., Iberian Peninsula, Balkans, and Mediterranean Basin) have been reported, some of which have not been mentioned in global studies because they usually report hotspots as broader regions. In addition, different event combinations (e.g., drought and heatwave; and heatwave and stagnation) are analyzed by varying the combination of variables, namely, temperature, precipitation, and their derived indices. Thus, this study presents three major analysis frameworks and components of drought- and heatwave-associated CE analysis for prospective researchers.

1 Introduction

Concurrent or compound extremes (CEs), which can be defined as the simultaneous or sequential occurrence of more than two extremes at a single or multiple locations, may cause greater havoc than a single extreme of a higher magnitude (Kopp et al., 2017; Hao et al., 2018c). Although the primary idea of the joint probability of multiple extremes emerged decades ago, the explicit research on CEs has surged in the last few years (2018–2021). Especially on the verge of potential climate change, along with the plausible changes in meteorological variables such as temperature, precipitation, evapotranspiration, and wind speed, this research area has drawn more attention (Naveendrakumar et al., 2019). Examples of CEs may include drought and heatwave, drought and flood, temperature and precipitation extremes, and floods from storm surges and river discharges. Among these various combinations of CEs, one of the most explored is compound drought and heatwave. In addition, other combinations of CEs include either drought (dry event) or heatwave (hot event), for example, subsequent wet and dry events, concurrent day and nighttime heatwaves, and compound heatwave and stagnation.

Drought- and heatwave-associated CEs are among the most studied events and have significantly increasing temporal and spatial trends across various parts of the world. For instance, the global land and cropland areas affected by dry and hot CEs have reportedly increased 1.7–1.8 times in the last 50 years of the 20th and 21st centuries across different seasons, mostly in summer (Wu et al., 2021d). Such claims of increasing trends have also frequently been reported in many regional- and national-scale studies (Russo et al., 2019; Xu and Luo, 2019; Kong et al., 2020; Geirinhas et al., 2021). In China, hot and dry CEs have increased 2.3 times between 1957 and 2018, with 90% of the dry events being associated with hot events in 2010 (Ye et al., 2019b; Kong et al., 2020; Feng et al., 2021c). Similarly, Mishra et al. (2021) predicted a fivefold increase in the frequency of hot and dry CEs in India by the end of the 21st century compared with the 1951–2016 baseline. In the past 150 years, an increasing frequency of dry and hot months has been reported in Southeast Australia (Kirono et al., 2017). Additionally, the association of droughts with other events, such as pluvial floods, was reported in 5.9%–7.6% of global land areas between 1950 and 2016, with pluvial floods following approximately 11% of droughts during boreal spring–summer or fall–winter (He and Sheffield, 2020). For event combinations of heatwave and ozone (O_3), Ban et al. (2022) predicted an increase of 34.6 in annual mean CE days under high-emission scenarios (shared socioeconomic pathways (SSP): 3–7.0) in 2071–2090 compared with the historical baseline of 1995–2004 in a global analysis (Ban et al., 2022). Mukherjee and Mishra (2018) reported an increase of 2–12 times in the concurrent day and nighttime heatwaves using various representative concentration pathways (RCPs), namely, RCP

2.6–8.5 (Mukherjee and Mishra, 2018). Based on an analysis of the 2020 heatwave (concurrent day and nighttime temperatures) in central South America, the high magnitude and duration of this recent heatwave have been reported in many parts of South American countries, such as southeastern Brazil, northern Argentina, southeastern Paraguay, eastern Bolivia, and Pantanal wetland (Marengo et al., 2022). In addition, in a global analysis of the 1955–2014 period, the increasing frequency of compound day and nighttime warm-dry and warm-humid events caused by greenhouse gases have been reported to be elevated by 1.5–5 and 2–9 times, respectively (Chiang et al., 2022a).

Drought- and heatwave-associated CEs have not only been expanding in spatiotemporal extents across various parts of the world but have also severely affected impact variables and aspects such as crop yields, fire risk, vegetation productivity, air quality, and human health. A noticeable impact on global maize yield has been reported in compound drought and heatwave scenarios (31% decrease), whereas heatwaves (4% decrease) or drought (7% decrease) alone has a significantly lower impact (Feng et al., 2019). Feng and Hao (2020) associated the yield loss across the United States and France in 61% of cases with compound dry and hot conditions in a global study across top maize-growing countries (Feng and Hao, 2020). In another global study, He et al. (2022) reported that in each wheat-growing season, more than 92% of the global wheat-growing regions have faced at least one dry and hot CE during 1981–2020, along with increases of 28.2% and 33.2% in the CE frequency and duration, respectively. Furthermore, among the wheat-producing regions, Europe, eastern China, western United States, and northern Argentina have been identified as hotspots (He et al., 2022). The increasing frequency of hot and dry CEs in the top maize-producing regions has also been reported in a multi-index global analysis for the periods 1949–1980 and 1981–2012 (Feng et al., 2021a). Additionally, fire weather and burned areas have been associated with drought, heatwave, or both in global (Richardson et al., 2022) and several regional studies (e.g., Greece and Brazil) (Gouveia et al., 2016; Libonati et al., 2022), where fire risk may increase with increasing drought- and heatwave-associated CEs. In the case of vegetation productivity, an absence of extremes increased tree coverage by 10% compared with the control scenario in a global analysis (Tschumi et al., 2022b). A 26-fold increase in population exposure to the compound heatwave and ozone scenarios in the 1980s (under high emission scenario) compared with the 1995–2014 baseline has also been reported in another global study (Ban et al., 2022). Urbanization and population (e.g., exposure and mortality) have been reported to be significantly associated with CEs in China, indicating the need for potentially similar associations and research in other parts of the world (Wang et al., 2021; Zong et al., 2022).

The analysis frameworks of drought- and heatwave-associated CEs usually vary with the different objectives of

determining some of the direct spatial/temporal parameters (e.g., frequency, spatial extent, and probability) considering only event–event combinations, association with large-scale modes of climate variabilities (CVs) as drivers considering event–driver combinations, or the impact of such CEs on various aspects considering event–impact combinations. For example, while some studies reported the probability of joint occurrence of several event variables or indices, others reported the likelihood of large-scale CV or atmospheric circulation (AC), such as the El Niño–Southern Oscillation (ENSO), or agricultural impact indicators, such as the Standardized Crop Yield Index (SCI), given the occurrences of CEs. In these cases, the frameworks mainly varied due to variable types (event, driver, or impact variables), target parameters to be calculated, and associated methods (Hao et al., 2018b; Feng and Hao, 2020; Wu et al., 2021d).

A previous review on CE has addressed four categories of CEs: 1) preconditioned, in which the impact of hazard is worsened by a weather- or climate-driven precondition; 2) multivariate, in which the impact is aggravated by multiple hazards; 3) temporally compounding, in which the impact is aggravated by successive hazards; and 4) spatially compounding, in which the impact is worsened by hazards in multiple connected locations (Zscheischler et al., 2020). These categories mostly have common analysis frameworks and methods with slight variations in which temporally or spatially compounding data are used as inputs, other than in the case of concurrent multivariate events (Hao et al., 2018b; De Luca et al., 2020b; Sutanto et al., 2020). Furthermore, Zhang W. et al. 2021a discussed the drivers, mechanisms, and methods associated with these categories.

The quantitative methods to assess CEs parameters vary from a simple percentile-based peaks-over-threshold (POT) or an empirical approach to complex copula-based joint probability (JP) analysis, conditional probability (CP) analysis, pair copula construction (PCC), or developing a standardized compound event indicator (SCEI) (Hao et al., 2018a; 2020b; Cheraghalizadeh et al., 2018; Ribeiro et al., 2020b; Slater et al., 2020; Mishra et al., 2021). Some basic parameters used to convey the outcome of CE analysis are frequency, spatial extent, probability, duration, correlation, and severity. Occasionally, these same parameters are analyzed by separating the data using land cover (e.g., croplands and forests) and seasons (e.g., growing season) or by including an impact variable such as crop yield to assess the impacts in terms of several spatiotemporal extents or variables of interest, respectively (Lu et al., 2018; Manning et al., 2018; Wang et al., 2018; Feng et al., 2021c).

To date, various review articles have covered different aspects of CEs, such as definition, involved statistical procedures, upcoming CEs, dependence structure, and suggested framework (Leonard et al., 2014; Kopp et al., 2017; Hao et al., 2018c; Hao and Singh, 2020). For

instance, Hao et al. (2018c) discussed the processes associated with the statistical characterization and modeling of extremes in the hydroclimatic domain by discussing approaches such as multivariate distribution, empirical approach, Markov Chain Model, and quantile regression approach. Approaches for detecting and predicting hydroclimatic extremes (non-stationary cases) and the associated drivers and matrices were also discussed by Slater et al. (2020). In addition, some review articles focused on the potential CEs in the warming world, the associated drivers influencing the extremes, the potential risk associated with the extremes, and their frequency (Goodess, 2013; Kopp et al., 2017; AghaKouchak et al., 2020). While AghaKouchak et al. (2020) focused on most potential extremes (e.g., heatwaves, wildfires, extreme precipitation, and flooding), their interactions as compound events, associated drivers, and risk, Kopp et al. (2017) directly discussed various potential CEs such as simultaneous heat and drought, wildfires associated with hot and dry conditions, and flooding associated with high precipitation, as well as their associated risks and impacts of several shared large-scale modes of CVs along with atmospheric forcing factors such as ENSO and tipping elements such as Atlantic Meridional Overturning Circulation. In another review, CEs were mainly classified into four categories: preconditioned, multivariate, temporally compounding, and spatially compounding (Zscheischler et al., 2020). Most review articles have focused on associated analytical approaches, classification, driver assessment, and risk assessment, among others. In contrast, Raymond et al. (2020) primarily focused on a multidisciplinary (climatic, societal, and economic) argument for the concept of related extreme events, their impacts, and potential anthropogenic impacts on CEs (Raymond et al., 2020).

Despite covering many aspects of CEs, previous review articles have not discussed the analysis frameworks that vary with regard to analysis objectives. In addition, the already discovered hotspots, which are the most impacted or CE-frequent regions in the corresponding study area as claimed in many previous publications, have not been summarized in previous reviews (Ridder et al., 2020; Chiang et al., 2022b; He et al., 2022). Thus, this study aims to provide an overview of three major analysis frameworks, along with several aspects of CEs related to drought- and/or heatwave-associated events. This review focuses on the following aspects: 1) the already reported hotspots in previous publications; 2) the event combinations and associated variables to form CEs; and 3) three analysis frameworks that vary according to the objectives of assessing basic CE parameters (event–event), association with large-scale modes of CVs as drivers (event–driver), and impact on several aspects (event–impact) to showcase an overall breakdown of CE analysis focused on drought- and heatwave-associated CEs.
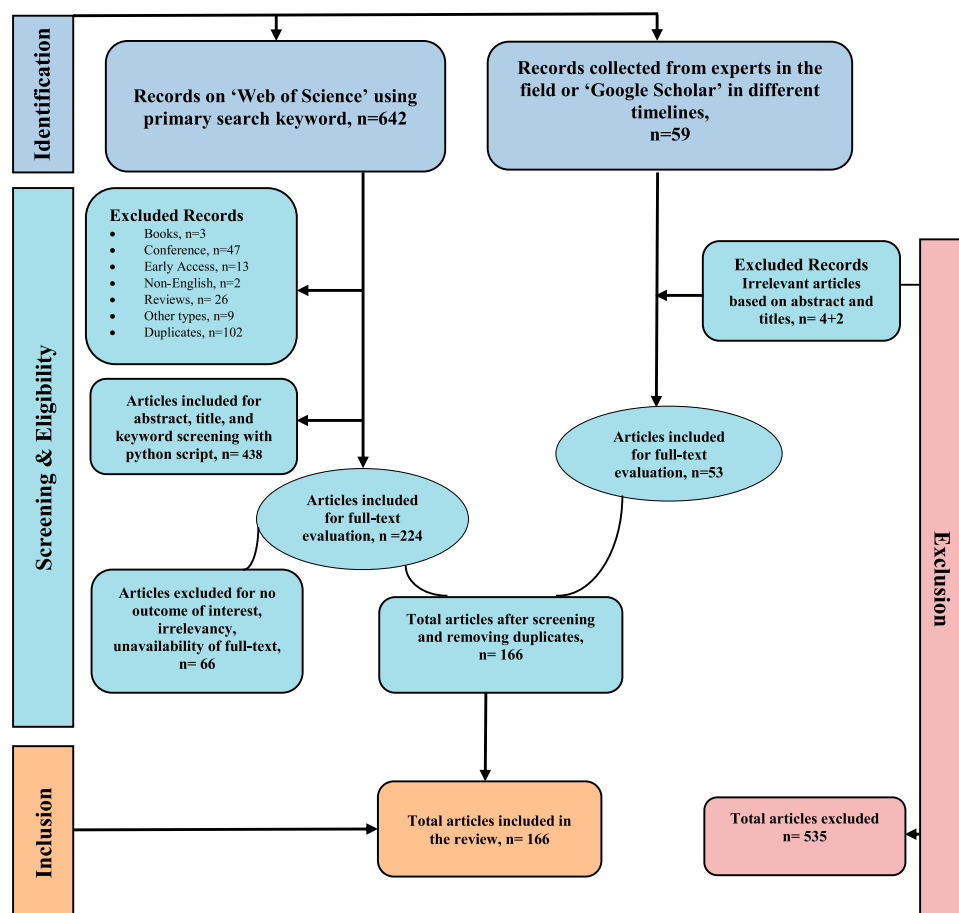
FIGURE 1
PRISMA diagram for article inclusion/exclusion in this systematic review.

2 Methodology

2.1 Article selection process

This systematic review includes 166 articles out of initially identified 701 records from the following sources: 1) "Web of Science" (WoS) on 2 September 2022 (642 records) and 2) "experts" and "Google Scholar" (59 records) for various timelines since September 2020. Herein, the term "experts" refers to colleagues, faculties, and reviewers in the field with whom the topic was discussed or consulted during the initial topic selection stage. Systematic literature identification, screening, eligibility, and exclusion/inclusion process are detailed in the PRISMA diagram (Figure 1).

The identification phase involves searching the WoS using search keywords. This phase results in 642 records for the following eight search keywords: "compound extremes" (73 records), "compound extreme" (75 records), "concurrent extremes" (22 records), "concurrent extreme" (31 records),

"compound events" (200 records), "compound event" (81 records), "concurrent events" (124 records), and "concurrent event" (36 records). Herein, the advanced search option "topic" (including the title, abstract, and keywords in the published literature) has been used for the last 10 years (1 January 2013 to 2 September 2022). Additionally, 59 records are identified from "Google Scholar" by searching the database and from discussions with "experts" at various timelines.

In the eligibility and screening phase of the systematic review, the WoS search records are directly exported to Excel files for processing with a Python script in the subsequent evaluation phase. The script is used to automate the subsequent evaluations, reducing eligible records to 540 articles. The filtering records' criteria for the excel files are "Language = English," "Publication Type = J," and "Document Type = Article." In this process, non-English language records (2), conference proceedings (47), books (3), review articles (26), early access (13), and other records (9)—all non-journal records and review articles—are screened. After

excluding duplicates within WoS, the number of records decreases to 438. Subsequently, the titles, abstracts, and keywords of these 438 articles from WoS are screened with a Python code to check for the presence of two sets of keywords of interest: set 1 comprises CE-defining words ("compound," "concurrent," "concurrently," "combined," "copula," "dependence," "dependences," "multivariate," "multi-variate," "multi," and "joint") and set 2 comprises drought- and heatwave-identifying words ("hot," "heat," "heatwave," "heatwaves," "heat waves," "heat wave," "warm," "dry," "dryness," "drought," "droughts," and "aridity"). These keywords are obtained from the 59 articles collected from "experts" and "Google Scholar" searches at different times from September 2020. Evidently, the aforementioned words are more likely to be present in the title, abstract, or keywords of an article if relevant to our topic of interest. During this process, the number of articles decreases to 224.

Subsequently, the full texts of 224 articles are reviewed to check relevancy and further eligibility criteria, with 10 articles unavailable to download with the available resources and 66 articles either irrelevant to the topic of interest or not containing adequate information on the targeted fields of this review. Eligible and relevant articles must have information about drought- and heatwave-associated CEs, mainly relevant to the domain of agriculture, hydrology, and topics of the review (hotspots, variables, parameters, drivers, impacts, and analysis framework).

Furthermore, the details of the percentage of excluded articles from WoS, where 148 articles are included after applying eligibility and inclusion criteria on 214 available full texts, are as follows:

- The article is written in a foreign language other than English (0.31%).
- The document type is not an article but a book, a report, or other (9.2%).
- The document is a review paper, not an original article (4.05%).
- The article is an early access version (2.02%).
- The article is simply a duplicated version of another article from the search (15.88%).
- The title, abstract, and keywords showcase no significant relevance to the topic of interest as per screening with CE-defining words and drought-heatwave relevant words (33.33%).
- The full-text article is unobtainable using the available access and resources, and only the title and abstract are accessible (1.56%).
- The overall article is not related to a topic of interest or does not contain significant data on the topics of review (10.30%).

Among the 59 records from "Google Scholar" and "experts," 6 records are excluded based on the evaluation criteria

incorporated after the screening and eligibility phase and 35 records are deemed as duplicates based on WoS. This results in 18 new articles.

The inclusion phase contains articles after the identification, screening and eligibility, and evaluation phases. A total of 166 (148 + 18) full-text articles are included in the final stage of the review by following the standard literature inclusion process for systematic reviews (Anandhi et al., 2018; Peng et al., 2020).

2.2 Data collection and processing

Based on the 166 collected articles, a data collection table is prepared, comprising 14 fields related to CEs, namely, "studied region," "study year," "study timeline," "hotspots," "studied event combinations of CE," "variable combinations," "scale of the data," "CE detection methods," "analyzed CE parameters or CE characteristics," "thresholds," "assessed impacts" (if any analyzed), "impact integration approach" (if applicable), "CVs as drivers" (if analyzed), and "methods to connect CVs and CEs" (if applicable). Subsequently, the collected data fields are organized into several sections, tables, and figures to represent the results associated with the objectives of this systematic review. The hotspot map (Section 3.1) is drawn in a GIS environment using the symbology option, namely, the "graduated symbol." Separate point shapefiles for each CE combination with hotspots reported in global studies are digitized using GIS. The number of studies that report a region as a hotspot is manually counted in the attribute table. After digitizing all reported hotspots and their counts in the attribute tables, the final dot density map is plotted by assigning different colors to different event combinations and by assigning different sizes of dots based on the number of studies that report a certain region as a hotspot. Data are obtained only from global studies (44) that report hotspots. The hotspots reported in the regional studies are plotted as stacked bar plots. Regional hotspots are not plotted on the map as different regions involve varying numbers of studies, and unlike global studies, the extents of the study areas are not similar. Consequently, regions with a higher number of studies reporting hotspots have higher dot densities, irrespective of whether a hotspot is more impacted by CEs compared to other regions of the world. The regional hotspots, distribution of publications by year, types of extreme studied for various study regions, and other figures and tables are prepared in the word processor.

Thus, the overall reviewed contents on drought- and heatwave-associated CEs are organized in the following workflow: 1) the hotspots of CEs found in reviewed publications; 2) the event combinations to form drought- and heatwave-associated CEs; 3) variables, associated data types, and thresholds to define different CEs; 4) CE analysis

FIGURE 2
Workflow to represent the outcome of the review from the collected data.
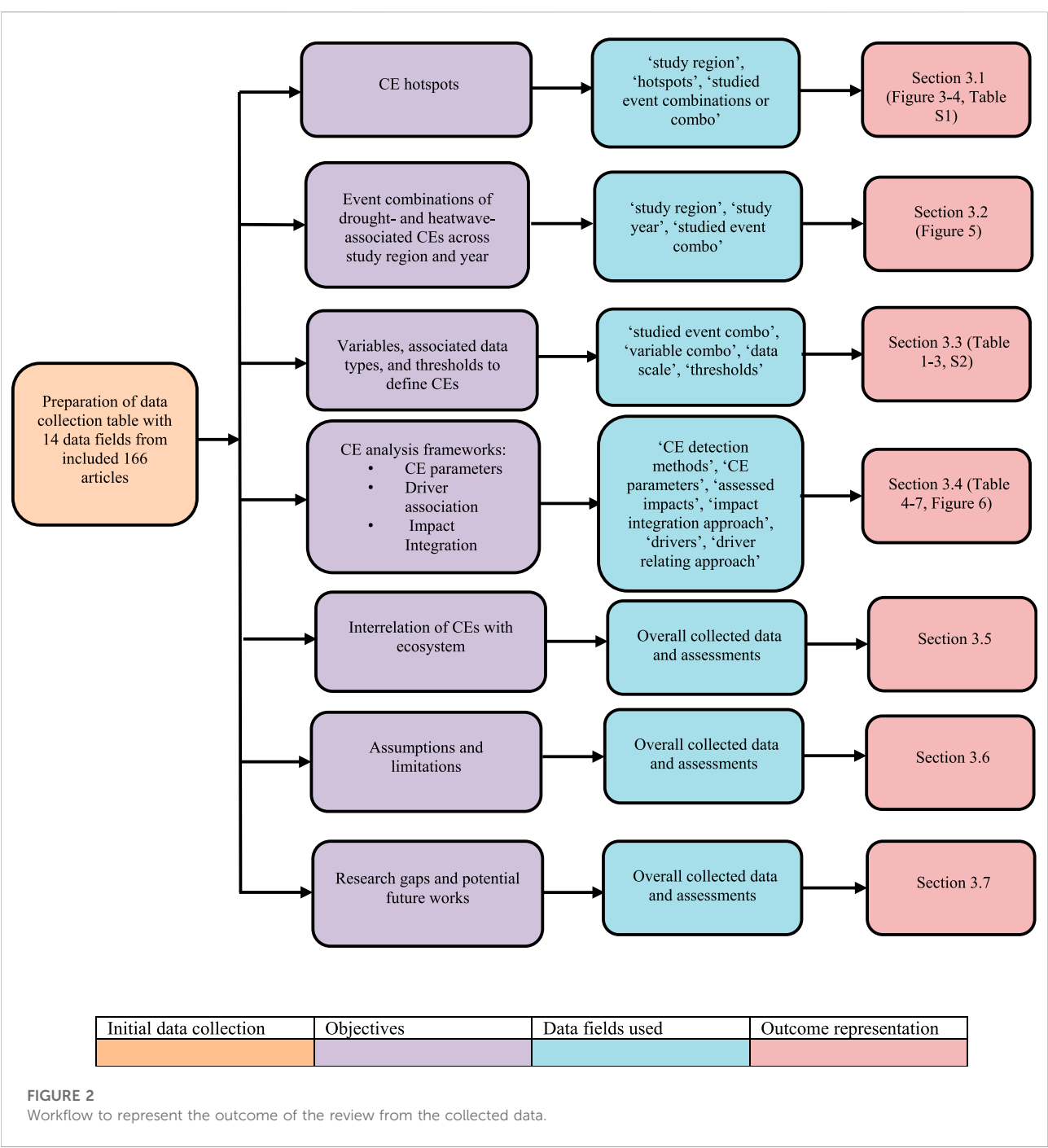
framework with frequently analyzed parameters, the association of large-scale modes of CVs as drivers, and the assessment of impacts with regard to several aspects; 5) interrelation of CEs with ecosystems; 6) assumption and limitations; and 7) research gaps and potential future work. The major objectives, associated data fields used to produce the results, associated sections, and related graphics (tables and figures) are represented as a workflow diagram of the review strategies in Figure 2.

3 Results and discussions

3.1 CE hotspots in reviewed publications

Most studies on CEs are conducted on global or national scales, with China, the United States, and India being the most studied countries. In global studies, South Africa, South America, Australia, southeastern Asia, South Asia, and the United States are evidently regarded as significantly impacted zones with
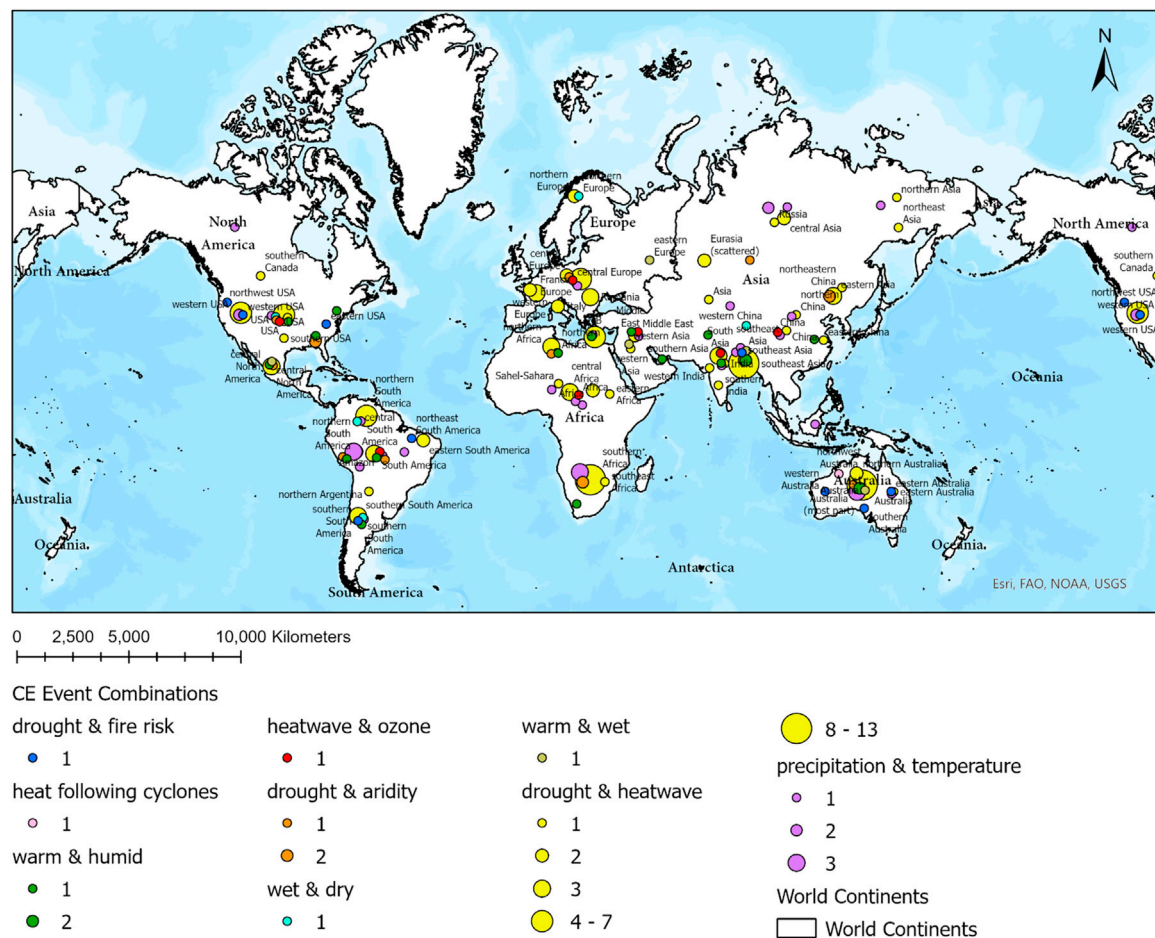
FIGURE 3
Graduated symbol plot to represent the hotspots detected in the 44 global publications. The number below each CE event combination indicates the number of studies that mentioned the location as a hotspot. The graduated point symbols are intended to represent the approximate locations of the broad regions found as hotspots in the global map, not the exact locations. The size of the graduated dot symbol is proportional to the count of global publications claiming a region as a hotspot.

regard to various CE combinations, especially compound drought and heatwave (Feng et al., 2019; Zhan et al., 2020; Wu et al., 2021d). In addition, hotspots for eight other drought- and heatwave-associated CEs (i.e., drought and fire risk, precipitation and temperature, wet and dry, warm and wet, warm and humid, heatwave and ozone, heatwave following cyclones, and drought and aridity) are included as reported in the global studies. Among these event combinations, drought and fire risk hotspots are situated in the western United States, various parts of South America, Australia, and Southeast Asia (Ridder et al., 2020; Richardson et al., 2022). A single hotspot for heat followed by a tropical cyclone has been reported in Australia (Matthews et al., 2019). For warm and humid events, hotspots are prevalent in various parts of the United States, South America, Southeast Asia, and Australia (Li et al., 2020; Raymond et al.,

2021; Chiang et al., 2022a). These hotspots for the aforementioned CE combinations are represented in Figure 3, where the dot densities indicate the number of publications that have reported the places as CE hotspots in 44 global studies. The associated data are listed in Supplementary Table S1 in the supplementary document.

In regional studies, various event combinations are assessed in different regions. Furthermore, the regions with higher numbers of studies (e.g., China and the United States) report the hotspots within such regions more frequently, even if the hotspots are not that frequently mentioned across the global studies. However, some important hotspots (e.g., Iberian Peninsula, Balkans, Mediterranean Basin, Pantanal, and Amazon) have significantly increasing trends concerning CEs in regional studies, whereas most global studies do not explicitly mention some of them and
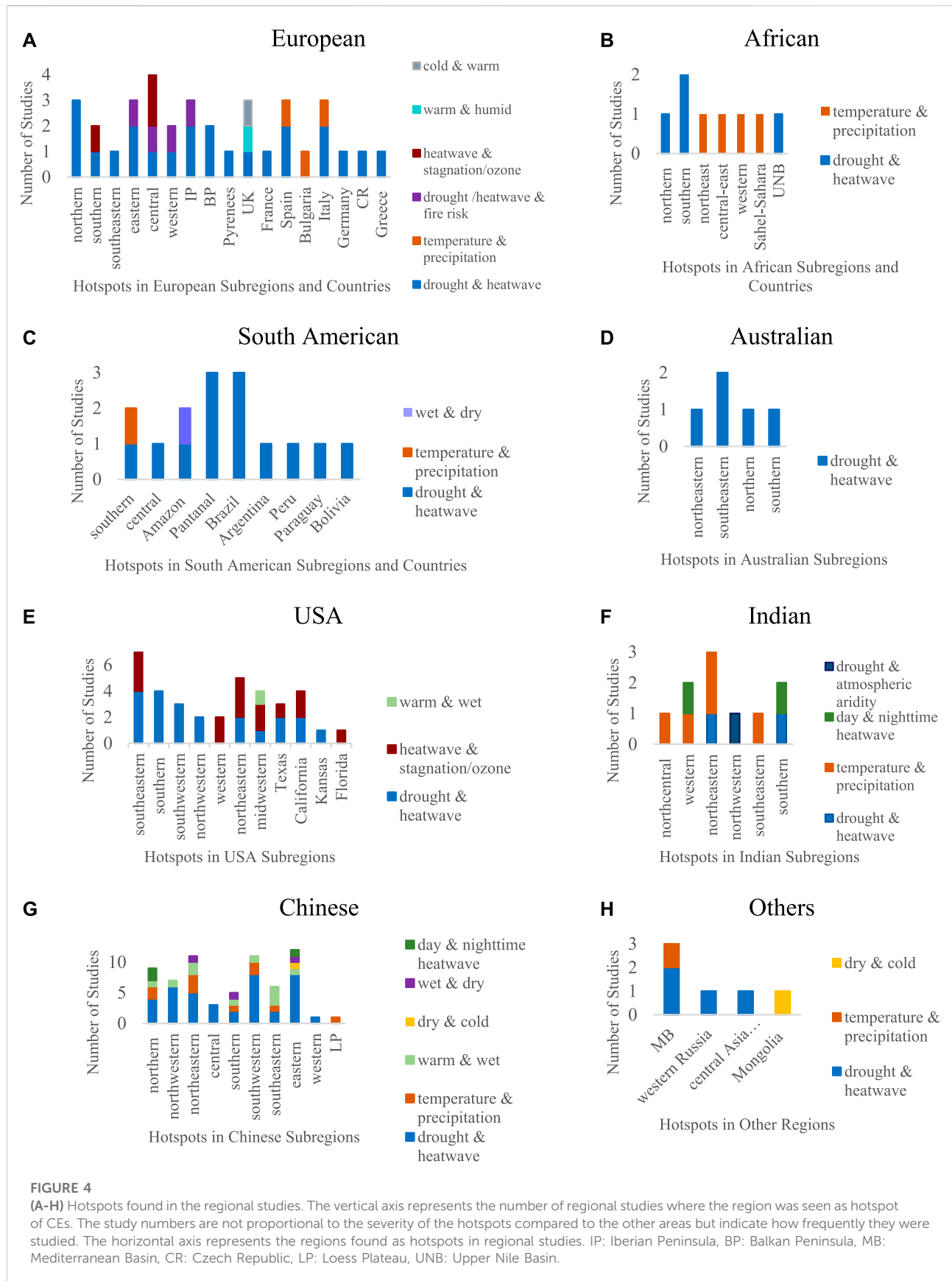
FIGURE 4
(A-H) Hotspots found in the regional studies. The vertical axis represents the number of regional studies where the region was seen as hotspot of CEs. The study numbers are not proportional to the severity of the hotspots compared to the other areas but indicate how frequently they were studied. The horizontal axis represents the regions found as hotspots in regional studies. IP: Iberian Peninsula, BP: Balkan Peninsula, MB: Mediterranean Basin, CR: Czech Republic, LP: Loess Plateau, UNB: Upper Nile Basin.
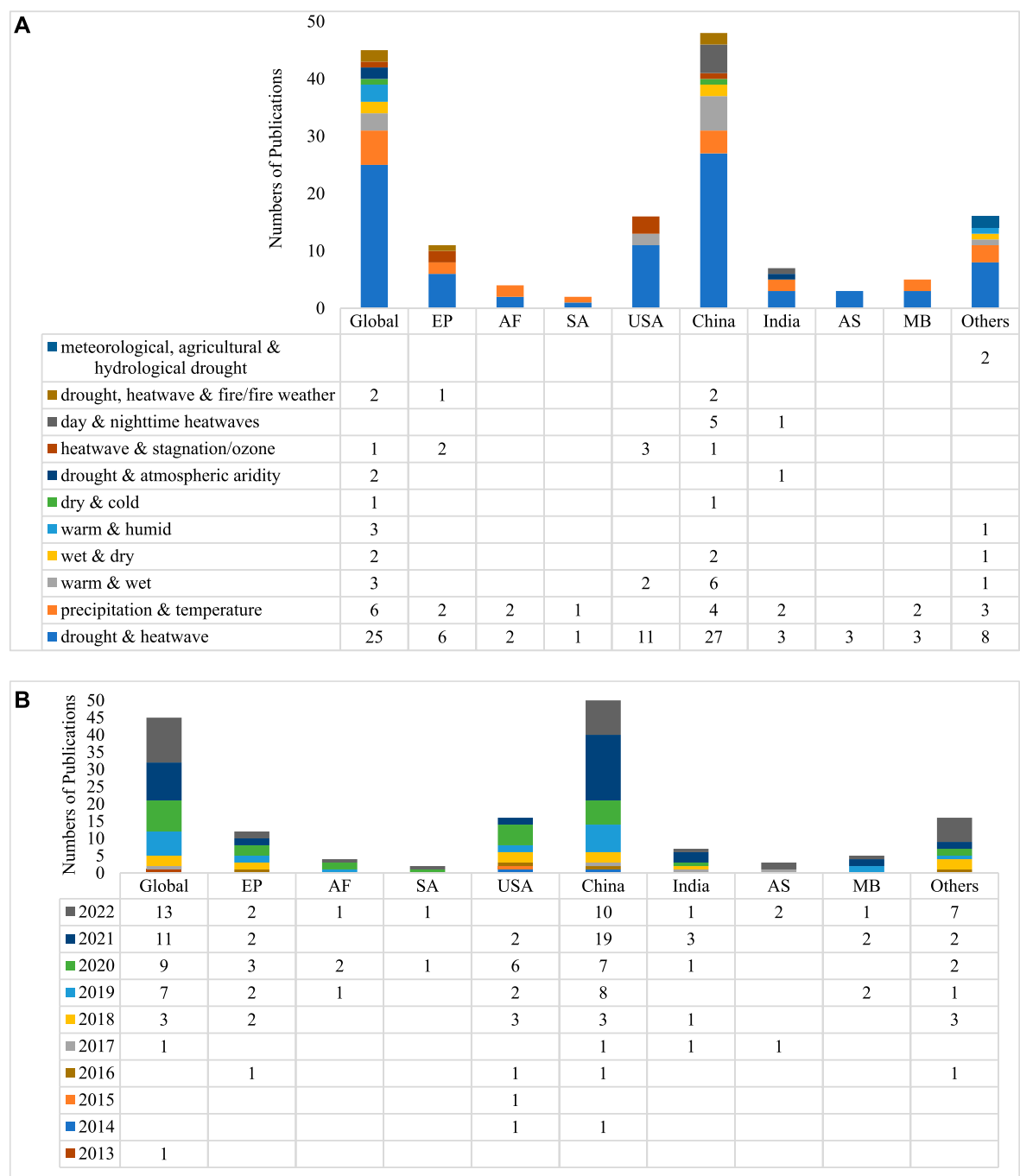
FIGURE 5
(A) Distribution of papers listing event combinations of drought and heatwave-associated extremes by study regions. **(B)** Distribution of papers listing publication years by the study regions (EP: Europe; AF: South Africa/Southern Africa/Africa; SA: South America; AS: Australia; MB: Mediterranean Basin; others: Germany, France, Canada, Mongolia, Nigeria, Russia, Upper Nile Basin, *etc.*).

rather report the hotspots as broader regions (Bezak and Mikoš, 2020; Vogel et al., 2021; Bento et al., 2022; Marengo et al., 2022). Figure 4 showcases the stacked bar plots that represent the regional hotspots across different event combinations. In these plots, the number of studies that report a regional hotspot is biased by the frequency of studies in the region.

3.2 Event combinations of drought- and heatwave-associated CEs with region and publication year distributions

In the reviewed studies, various combinations of several types of drought- and heatwave-associated CEs are found. The corresponding region-based distribution is presented in Figure 5A, representing the study gaps and the combinations of CEs explored in each region. In addition, for the event combinations mentioned in Figure 5A, a few other combinations of CEs are observed that have been rarely studied (one case). These include hot, dry, and windy events; drought and wind; and concurrent fire drivers (Ridder et al., 2020; Tavakol et al., 2020). Among the several temperature-, precipitation-, or drought-related extremes, compound drought and heatwave is the most studied joint extreme. Other types or combinations of CEs have been studied in different reviewed publications using several variables, indices, and thresholds to define them. In addition to hot and dry conditions, any of the other three combinations of temperature and precipitation extremes (cool and dry; hot and wet; and cool and wet) have been studied together in some studies (22 studies) (Wu et al., 2019c; Zhan et al., 2020; Camara et al., 2022).

Evidently, most studies on CEs, including drought- and heatwave-associated CEs, have been conducted since 2018 (Figure 5B). Many studies have been conducted on a global scale to focus on the frequency of CEs in different parts of the world and on various global issues (Feng et al., 2019; Mukherjee et al., 2020). In addition, more studies have been conducted in China and the United States.

3.3 Variables with associated datatypes and thresholds to define different CEs

Various publications have qualitatively and quantitatively explained compound drought- and heatwave-related extremes and their impacts with several variables and indices (Hao et al., 2018a; 2020c; Cheraghalizadeh et al., 2018; Brunner et al., 2021). However, the most common variables for assessing these CEs are temperature (maximum, minimum, and average) and precipitation, whereas the most widely used indices are the Standardized Precipitation Index (SPI) and Standardized Temperature Index (STI) derived from the corresponding variables (Zscheischler and Seneviratne, 2017; Mukherjee and Mishra, 2018; Hao et al., 2019a; Brunner et al., 2021). Stream flow and soil moisture are the most commonly used variables for predicting hydrological and agricultural droughts, respectively (Cheraghalizadeh et al., 2018; Zhou et al., 2019a; Mishra et al., 2021). Based on the study objective, various previous drought- and heatwave-associated CE articles have discussed the following variables: other climate variables, such as relative humidity (RH), vapor pressure, wind speed, and evapotranspiration; large-scale

modes of ACs or CVs, such as ENSO and Pacific Decadal Oscillation (PDO); impacted variables and aspects, such as crop yields, land use, vegetation vulnerability, and fire risk (Manning et al., 2018; Zhou et al., 2019b; Coffel et al., 2019; Hao et al., 2020c; Feng et al., 2021c; Vogel et al., 2021). In several cases, the following different indices have been used: single-variable dependent indices, such as SPI, STI, and SCI; multi-variable dependent indices, such as Standardized Precipitation Evapotranspiration Index (SPEI) and Palmer Drought Severity Index (PDSI); and copula-based compound event indicators, such as SCEI (Hao et al., 2018a; Cheraghalizadeh et al., 2018; De Luca et al., 2020b). The standardized indices and their defined ranges can illuminate the severity level of extreme events (e.g., drought) irrespective of the weather conditions in a region, enabling the severity in different regions to be compared. However, direct percentiles applied over variables are generally suitable for temporal comparison in a region, as the variables are compared with different percentiles of variables in the same region (Mishra et al., 2021). The variables or indices used to define drought, heatwave, and other associated CEs studied in the reviewed publications are summarized in Tables 1, 2, respectively. Herein, the impacted variables (i.e., SCI) or CVs (i.e., ENSO) are not included because the objective is to represent the participating variables/indices (meteorological, hydrological, and agricultural) as components of each combination of CEs. The variables/indices/aspects associated with the impacts and driving forces are explained in Section 3.4.

In a few instances, drought and heatwaves are explained with other inter-related variables such as RH and vapor pressure density (VPD) as well as temperature and precipitation. Chiang et al. (2018) proposed that drought, temperature, RH, and VPD are interdependent (Chiang et al., 2018). In the case of CEs with opposing phenomena, such as drought and pluvial flood in the same location, the lagged occurrences can be considered as the CE, and they may be indicated with the same dry/wet condition indices (PDSI and SPI) or variables (SM) (He and Sheffield, 2020).

In most cases, the articles use monthly data followed by daily data. Many articles use mixed cases, such as daily, monthly, or annual data, for different variables (Supplementary Table S2). A typical mixed case is the use of daily temperature data and either monthly precipitation total or SPI (Mazdiyasni and AghaKouchak, 2015; Wu et al., 2019c). Usually, in these cases, the days crossing a temperature threshold and falling within the same month, which crosses the precipitation threshold, are considered CE days. The most commonly used impacted variable (yield) data are always collected on an annual scale. In these cases, the growing season means or totals of other event variables (such as temperature and precipitation) are used as annual data points along with the annual yield data (Coffel et al., 2019; Feng and Hao, 2020). The variables are either handled as direct data or converted into indices.

In most articles, thresholds are defined beyond which variables/indices are considered extreme. A threshold is

TABLE 1 Variable (or index) combinations to be used to define drought (dry) and heatwave (hot) events.

CEs	Variable or index combinations	Variable 1/ index 1	Variable 2/ index 2	Subset of references
Event combinations		Drought	Heatwave	
Drought and heatwave	P-T/T$_{max}$	P	T/T$_{max}$	AghaKouchak et al. (2014), Hao et al. (2018b), Lu et al. (2018), Coffel et al. (2019), Ma et al. (2020a), Ribeiro et al. (2020a), Wu et al. (2021d)
	SPI-T	SPI	T	Mazdiyasni and AghaKouchak (2015), Sharma and Mujumdar (2017), Wu et al. (2019b), Hao et al. (2020b), Feng et al. (2021c)
	SPEI-T	SPEI	T	Ribeiro et al. (2020b)
	SM-PET-P	P, SM	PET	Manning et al. (2018)
	SPI-STI	SPI	STI	Feng et al. (2019), Hao et al. (2019a, 2019b), Feng and Hao (2020), Wu et al. (2020), Zhan et al. (2020), Brunner et al. (2021), Wu and Jiang (2022)
	(SPI, SM)-T	SPI, SM	T	Mishra et al. (2021)
	(P, SM)-T	P, SM	T	Cheng et al. (2019)
	(SPI, SPEI)-T	SPI, SPEI	T	Vogel et al. (2021)
	PDSI-T	PDSI	T	Ye et al. (2019a), Cheng et al. (2019), Mukherjee et al. (2020), Mukherjee and Mishra (2021)
	SPEI-EDD	SPEI	EDD	Wang et al. (2018)
	MCI-T	MCI	T	Yu and Zhai (2020b)
	EDI-T	EDI	T	Bezak and Mikoš (2020)

P: precipitation, T: temperature, T$_{max}$: maximum temperature, SM: soil moisture, SSI: Standardized Soil Moisture Index, SPI: Standardized Precipitation Index, STI: Standardized Temperature Index, EDI: Effective Drought Index, EDD: Extreme Degree Days, SPEI: Standardized Precipitation Evapotranspiration Index, PDSI: Palmar Drought Severity Index, MCI: Meteorological Drought Composite Index.

associated with the conditions linked to the framework for each variable. The threshold justification is attributed to "measurable" and "extreme," where a higher threshold may result in very few events being detected, and a lower threshold may result in too many events (Wu et al., 2019b). Therefore, different articles incorporate various levels of thresholds based on their objectives (Hao et al., 2018b; Wu et al., 2019b; Mukherjee et al., 2020). In an article, direct data of the variable, their derived standardized indices, or both can be used, which have been tagged as D type, I type, or D-I type, respectively, in this review article (Table 3). For direct data-based thresholds, percentile-based statistics are most commonly used, for example, the 90th percentile of June, July, and August daily temperatures for all baseline years (Wu et al., 2019a) or the 10th percentile of growing season precipitation of wet days during baseline years (Lu et al., 2018). For index-based fixed thresholds, standardized values of different severity levels are most commonly used; for example, Brunner et al. (2021) used SPI values of −1, −1.5, and −2 to define moderate, severe, and extreme conditions, respectively (Brunner et al., 2021). The collected information on data types and example thresholds for different event combinations is presented in Table 3, respectively.

3.4 CE analysis frameworks

The frameworks of analysis mainly vary based on the objectives of analyzing only CE events (e.g., drought and heatwave), the association of CE events with large-scale modes of CV drivers (e.g., the association of drought and heatwave with ENSO), or assessing the CE-induced impacts on various aspects (e.g., impacts of drought and heatwave on yield, varying CE parameters across different land covers). The components associated with each CE framework vary based on different variables (associated with events, drivers, or impacts); parameters (e.g., frequencies, spatial extents, probabilities, and correlations) to be analyzed as outcomes; and methods (e.g., POT, JP, and CP) used to calculate the parameters. Based on the analysis conducted in the reviewed articles, the major analysis frameworks have been summarized into three segments in this systematic review based on various analysis objectives: 1) event–event that involves quantification of CE parameters using the contributing event variables/indices; 2) event–driver that involves quantifying the association of CEs with large-scale modes of CVs as drivers using variables/indices that are representative of events and drivers; and 3) event–impact

TABLE 2 Variable (or index) combinations to be used to define other drought and heatwave associated CE combinations.

CEs	Variable or Index Combinations	Variable 1/ Index 1	Variable 2/ Index 2	Variable 3/ Index 3	Subset of References
Event Combinations		drought (meteorological)	drought (hydrological)	drought (agricultural)	
meteorological & hydrological drought	MDI-MHDI	SPI, SPEI, RDI	SDI		Cheraghalizadeh et al. (2018)
meteorological, hydrological & agricultural drought	SPI-SMI-SSI	SPI	SSI	SMI	Vorobevskii et al. (2022)
Event Combinations		drought	heatwave	fire	
heatwave, drought & fire	SM-T-FWI	SM	T	FWI	Sutanto et al. (2020)
drought & fire weather	Q-FFID	Q		FFDI	Ridder et al. (2020a)
heatwave & fire	T-FFID	T		FFDI	Ridder et al. (2020a)
Event Combinations		heatwave (day)	heatwave (night)		
day & nighttime heatwaves	T_{max}-T_{min}	T_{max}	T_{min}		Mukherjee and Mishra (2018), Wu et al. (2021b)
Event Combinations		heatwave	stagnation	O_3	
Heatwave & O_3	T- O_3 conc.	T		O_3 conc.	Ban et al. (2022), Zong et al. (2022)
Heatwave & stagnation	T-(WS, P)	T	P, WS		Gao et al. (2020)
Event Combinations		drought	aridity		
drought & atmospheric aridity	SM-VPD	SM	VPD		Zhou et al. (2019b), Ambika and Mishra (2021)
Event Combinations		warm	humid		
warm & humid	THI (T, RH)	THI	THI		Garry et al. (2021)
	WBGT	WBGT	WBGT		Li et al. (2020)
Event Combinations		dry/wet	hot/cool		
precipitation & temperature	P-T	P	T		Wu et al. (2019c), Zhan et al. (2020), Camara et al. (2022)
hot & wet/flood	P-T	P	T		Ben-Ari et al. (2018)
	WAP-T	WAP	T		Chen et al. (2021), Liao et al. (2021b)
dry & wet	CWD-CWE	CWD/CWE			Esteban et al. (2021)
	PDSI-PDSI	PDSI		De Luca et al. (2020b)	
	SPI-SM	SPI, SM		He and Sheffield (2020)	
cold & dry	Tmin-SPEI	SPEI	Tmin		Zhang et al. (2021b)
Event Combinations		heat	cyclone		
Heat following major tropical cyclone	HI-central pressure	HI	central pressure		Matthews et al. (2019)

VPD: Vapor Pressure Density, RH: Relative Humidity, MDI: Meteorological Drought Indicator, MDHI: Meteorological-Hydrological Drought Indicator, SMI: Standardized Soil Moisture Index, FWI: Fire Weather Index, WS: Wind Speed, RDI: Reconnaissance Drought Index, SDI: Standardized Drought Index, SSI: Standardized Streamflow Index, Q: Discharge, FFDI: Forest Fire Danger Index, CWD: Cumulative Water Deficit, CWE: Cumulative Water Excess, WBGT: Wet Bulb Globe Temperature, WAP: Weighted Average of Precipitation Index, THI: Temperature Humidity Index, HI: Heat Index.

that involves quantification of the impacts on various aspects using variables/indices that are representative of events and impacts. The summarized components of the three major analysis frameworks associated with CE analysis are presented in Figure 6.

In the reviewed publications, several parameters are quantified to convey the outcomes of the analyzed CEs. Herein, the most frequently assessed parameters associated with each type of analysis framework are presented. In the event–event framework, the analysis of basic CE parameters mainly includes basic outcome-indicating parameters such as frequency, spatial extent, probability, return periods (RPs), compound indicator-based magnitude/severity, and correlations. In the event–driver framework, the quantification of the association with large-scale modes of CVs is mainly assessed using parameters such as correlations and probabilities. Finally, in the event–impact framework, the impacts on other impacted variables or aspects are quantified using the following three major approaches: 1) spatial subsetting

of data followed by quantification of basic CE parameters with event–event framework components, 2) temporal subsetting of data followed by quantification of basic CE parameters with event–event framework components, and 3) integrating the impact variables/indices (i.e., crop yield, burned area, and mortality) directly into the equations/models with other event-indicating variables/indices (Wang et al., 2018; Feng et al., 2019; Gao et al., 2020; Feng et al., 2021c; Das et al., 2022; Ribeiro et al., 2022). Therefore, the parameters to be calculated for the aforementioned three approaches that assess the impacts are named region/land cover specific parameters, time/season specific parameters, and variable specific parameters, respectively, in this article.

The reviewed publications include one or more of these CE frameworks to represent the various outcomes of CE analysis (Hao et al., 2019b; Feng and Hao, 2020; Feng et al., 2021c). The associated methods and quantitative approaches regarding each type of analysis are described in the following three sections (3.4.1–3.4.3).
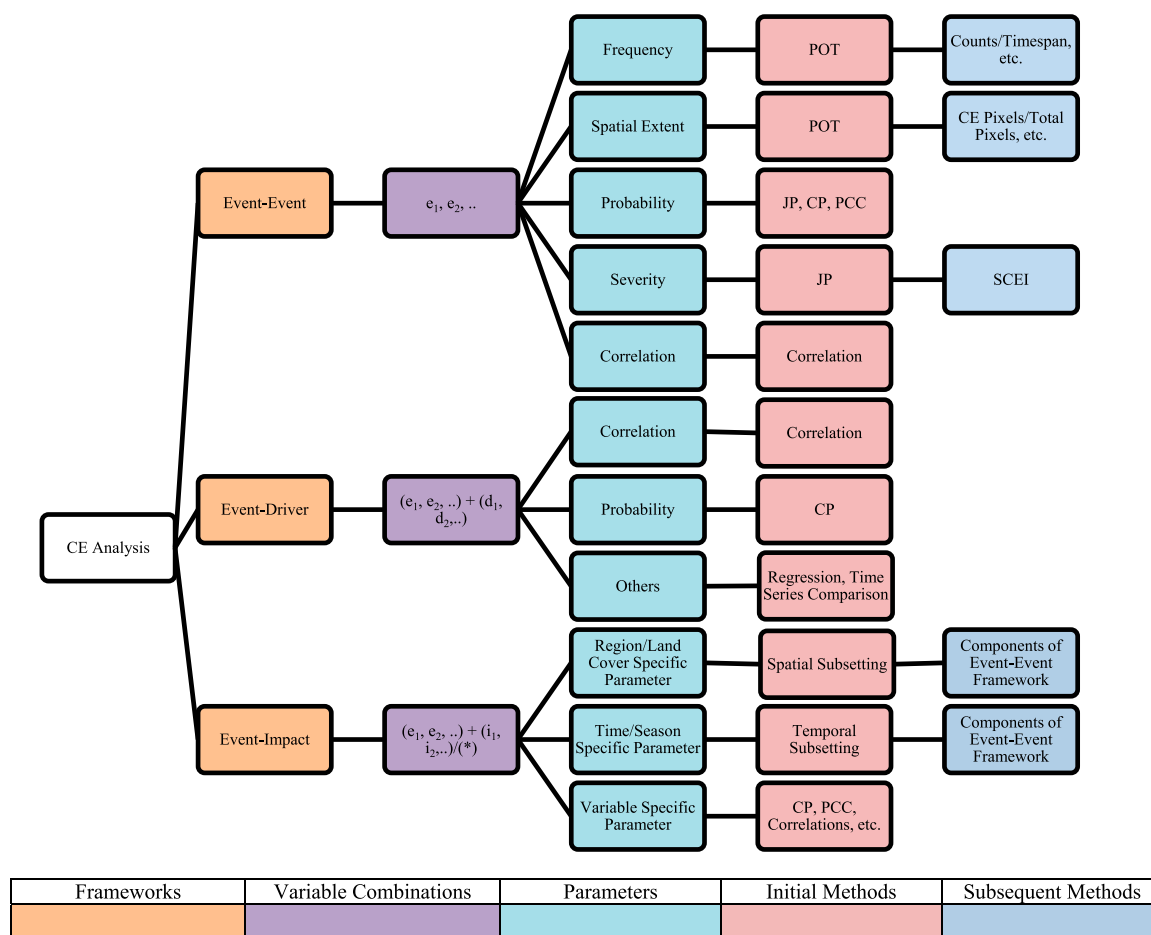

FIGURE 6
Summarized CE analysis components associated with three major analysis frameworks (event–event, event-driver, and event–impact) (here, e_n, d_n, and i_n refer to events, drivers (CVs), and impacts indicating variables/indices, respectively; (*) indicates seasonal or land use data in other forms.

TABLE 3 Some example threshold types: (D: data-based, D-I: data- and index-based, I: index-based).

References	CE event combinations	Variables	Indices	Threshold type (I/D)	Value	Stat.
Lu et al. (2018)	Drought and heatwave	P, T		D		$T \geq 90^{th}$ prctl (mean T of 21 days centered over the calendar day across all baseline years) $P \leq 10^{th}$ prctl (all growing season wet days during baseline years)
Vorobevskii et al. (2022)	Meteorological, hydrological, and agricultural drought		SPI, SSI, SMI	I	$SPI, SSI, SMI \leq -1, -1.5, -2$	
Sutanto et al. (2020)	Drought, heatwave, and fire weather	T_{min}, T_{max}, SM	FWI	D-I		$SM \leq 80^{th}$ prctl (monthly SM) of 30 days centered moving mean SM $T_{max}, T_{min} \geq 90^{th}$ prctl (T_{max}, T_{min} of 9 moving days centered around the day) for ≥ 3 consecutive days of JJA $FWI \geq 90^{th}$ prctl (FWI of 9 moving days centered around the day) for ≥ 3 consecutive days of JJA for a grid
Mukherjee and Mishra (2018)	Day and nighttime heatwaves	T_{min}, T_{max}		D		$T_{max} \geq 95^{th}$ prctl (daily T_{max} for 3 – day moving mean of AMJ for baseline) $T_{min} \geq 95^{th}$ prctl (daily T_{min} for 3 – day moving mean of AMJ for baseline)
Ban et al. (2022)	Heatwave and ozone (O_3)	T_{max}	O_3	D	$O_3 \geq 100$ mg/m³	$T_{max,} \geq 98^{th}$ prctl (daily T_{max} for baseline) for ≥ 2 consecutive days
Zhou et al. (2019b)	Drought and atmospheric aridity	SM, VPD		D		$SM \leq 10^{th}$ (daily SM of warm season) $VPD \geq 90^{th}$ (daily VPD of warm season) (1–10th and 90–99th are also used)
Garry et al. (2021)	Warm and humid		THI	I	$THI \geq 70, 68, 72, 75,$ and 77	
Wu et al. (2019c)	Precipitation and temperature	P, T		D		$P \leq (or \geq)$ 25th (or 75th) prctl (P over all years) $T \geq (or \leq)$ 755th (or 25th) prctl (T over all years)
Chen et al. (2021)	Hot and wet/flood	T-WAP		D-I		$T \geq 90^{th}$ prctl (daily $T_{max,}$ or T_{min} of baseline day) for ≥ 3 consecutive days $WAP \geq 95^{th}$ prctl (WAP for summer of baseline)
De Luca et al. (2020b)	Dry and wet		PDSI	I	$PDSI \leq -3, PDSI \geq 3$	
Matthews et al. (2019)	Heat following major tropical cyclone	Central pressure	HI	D-I	Central pressure ≥ 945 hPa, $HI \geq 40.6$ ℃	

prctl, Percentile; JJA, June-July-August; AMJ, April-May-June.

3.4.1 Frequently analyzed parameters of drought- and heatwave-associated CEs

The most analyzed parameter in previous studies is the frequency of CEs (Table 4). CEs are detected in these cases using the binary mapping technique expressed in Eq. 1, which is commonly called the "empirical approach" or "peaks-over-thresholds" (POT) (Lu et al., 2018; Wu et al., 2019c; Feng et al., 2021c). Subsequently, a comparison of frequencies between different time segments is conducted in some studies to detect the frequency changes between time periods. Occasionally, empirical RPs are also analyzed, which are the inverse of the frequency or empirical probability (Ridder et al., 2020; 2022a; 2022b). A typical example of frequency quantification is represented by the simplified Eq. 2 (Lu et al., 2018). In Eqs 1, 2, Z and $CEHD$ represent a binary response of 0 or 1 (based on whether a variable crosses its threshold) and compound extreme hot and dry days (determined from the summation of Z), respectively. Additionally, x (precipitation threshold) and y (temperature threshold) refer to the 10th percentile of all growing season wet days during baseline years and the 90th percentile of mean temperature centered over 21 calendar days across all baseline years, respectively.

$$Z = \frac{1\,(True),\ (P < x, T > y)}{0\,(False)} \quad (1)$$

$$Frequency = \frac{CEHD\,days}{total\,growing\,season\,days} \quad (2)$$

In addition to the detection of CE frequencies, the spatial extent (Mazdiyasni and AghaKouchak, 2015) and trend (Feng et al., 2021c) of CEs have been detected in some articles using the aforementioned binary detection approach (Eq. 1) followed by Eqs 3, 4 he following equations:

$$spatial\,counts = \frac{pixels\,with\,CEs}{total\,pixels} \quad (3)$$

$$spatial\,trend = \frac{\%CEHDs}{decade - station} \quad (4)$$

Another frequently analyzed parameter is the joint or conditional probability for two or more variables, such as temperature, precipitation, yield, and soil moisture (Feng et al., 2019; Ribeiro et al., 2020b). In addition, RPs are frequently analyzed along with or instead of probability (Miao et al., 2016; Zhou and Liu, 2018). Probability is commonly assessed using the copula-based method or meta-Gaussian model (Gaussian copula). The typical expressions of the joint and conditional probabilities can be expressed using Eqs 5, 6, respectively. In Eqs 5, 6, SPI, STI, and SCI thresholds were represented by x (e.g., −1.6, −1, and −0.8), y (e.g., 1.6, 1, and 0.8), and z (e.g., 0), respectively:

$$JP = P\left(SPI \le x, STI > y\right) \quad (5)$$

$$CP = P\left(SCI < z \,|\, SPI < x, STI > y\right) \quad (6)$$

Occasionally, a copula-based compound index, such as SCEI, can be used to indicate the severity or magnitude of CEs (Wu et al., 2020). Eq. 7 is a generalized expression of SCEI, where φ and F stand for standard normal distribution and marginal cumulative distribution, respectively. Additionally, the different severity levels mentioned by Wu et al. (2020) are summarized in Table 5:

$$SCEI = \varphi^{-1}\left[F\left(JP\right)\right] \quad (7)$$

Another important parameter proposed in CE publications is duration, which is basically the event span (Sedlmeier et al., 2018; Manning et al., 2019; Qiao et al., 2022). In some cases, the relation of CEs with another event (also lagged) can be indicated by analyzing the correlation. For instance, Hao et al. (2019a) determined the correlation between CE and standardized ENSO (Hao et al., 2019a). The details are presented in Section 3.4.2. The general equation of Spearman's correlation coefficient (r_R) is listed in Table 4, where n is the number of data points in the variables to be correlated and d_i is the difference in the rank of the ith element.

3.4.2 Large-scale modes of CVs as drivers of CEs

Different large-scale modes of CVs are evidently present during CEs or induced CEs as precursors or drivers in significant parts of the global land area (Hao et al., 2019a; 2019b; De Luca et al., 2020b). For instance, ENSO and PDO reportedly impact 18.1% and 12% of the global land area, respectively, whereas Atlantic Multi-decadal Oscillation (AMO) inversely affects 18.9% of the global land area. The effects of ENSO and PDO are reportedly significant in northern South America, the central United States, the western United States, the Middle East, eastern Russia, and eastern Australia. However, AMO substantially impacts Mexico, Brazil, central Africa, the Arabian Peninsula, China, and eastern Russia in different seasons (Table 6) (De Luca et al., 2020a). In most cases, the dependence between lagged or concurrent CVs is indicated using correlations. However, several other methods have also been associated with representing the relationships between CEs and CVs, as per previous studies (Table 7).

The dependence between different large-scale modes of CVs (i.e., ENSO and PDO) and CEs is most commonly assessed using correlation coefficients (e.g., Spearman's correlation test) (Wu et al., 2019c; Mukherjee et al., 2020; Shi et al., 2020). In some instances, the impact of a major CV must be discarded to assess the relationship between another CV and CE. For such instances, a partial correlation can be used (De Luca et al., 2020b). The relationship between two random variables can be represented by this method after discarding the effects of other variables; for example, De Luca et al. (2020) estimated the relationship between PDO and PDSI, given the ENSO-indicating index called Niño 3.4 (De Luca et al., 2020b). The partial correlation between CV to be correlated (x_i) and CE variable to be correlated (x_j) after

discarding the effect of another CV (x_k) can be assessed by Eq. 8, where r_{ij}, r_{jk}, r_{ik} refer to correlations between x_i and x_j, x_j and x_k, and x_i and x_k, respectively (De Luca et al., 2020):

$$r_{ij|k} = \frac{r_{ij} - r_{ik}r_{jk}}{\sqrt{1 - r_{ik}^2}\sqrt{1 - r_{jk}^2}} \qquad (8)$$

Evidently, ENSO has the most widespread impact on global land areas in terms of percent land area impacted; furthermore, ENSO interacts with other CV modes, such as PDO and Arctic Oscillation (AO) (Wu et al., 2019c; De Luca et al., 2020b). These complex interactions may induce uncertainties in correlation results. Therefore, the correlations are highly variable over seasons, regions, and event combinations of CEs (Wu et al., 2019c).

Large-scale modes of CVs can be used as predictors for determining the severity of upcoming CEs (Hao et al., 2019a; 2019b). According to Hao et al. (2019a), the upcoming severity of a CE after 1 month of period t ($W_{t+1} = SCEI_{t+1}$) can be determined using Eq. 9, given that the predictors W_t and X_t are the standardized CE indicator ($SCEI_t$) and standardized CV ($SNINO_t$), respectively:

$$P(W_{t+1}|W_t, X_t) \qquad (9)$$

Eq. 9 must have a normal distribution with mean μ and variance σ^2. The validity of the prediction can be assessed using Pearson's correlation coefficient between the observed and simulated CE indicators.

A logistic regression model (LRM) can also be used to predict CE occurrence (Hao et al., 2018b; 2019b). The regression model and 1-month leading probability can be expressed using Eqs 10, 11, respectively. In these two equations, x, π, α, and β stand for Niño 3.4 index, probability of CE given ENSO, regression constant, and regression coefficient, respectively. $P(Z_{t+1} = 1|x)$ represents 1-month leading probability of CE events:

$$\ln\left[\frac{\pi}{1-\pi}\right] = \alpha + \beta x \qquad (10)$$

$$P(Z_{t+1} = 1|x) = \frac{1}{1 + e^{\left[-\left(\alpha + \beta x_t\right)\right]}} \qquad (11)$$

The validity of the prediction can be determined using the Brier Skill Score in the case of LRM. The results showcase that lower SCEI values (more severe compound dry and hot events) are associated with higher SNINO (El Niño) values from December to February. In contrast, lower values of SNINO (La Niña) are associated with higher SCEI values in southern America (Hao et al., 2019b). Another expression of the relationship between compound events and ENSO is the odd ratio (= $\exp(\beta)$); a higher value (>1) of the odd ratio implies higher odds of CE occurrences with a higher Niño 3.4.

3.4.3 Assessment of CE impacts on several aspects

The impacts of various CEs have been assessed in several aspects, such as crop yield (Feng and Hao, 2020), crop growth season (Lu et al., 2018), phenological growth phases (Wang et al., 2018), land cover/land use (Feng et al., 2021c), urbanization (Wu et al., 2021b), fire risk (Richardson et al., 2022), and air quality (Gao et al., 2020). In order to assess the impacts on several aspects, the impacted parameters (region-, time-, or variable-specific) are integrated into the CE assessment framework using various approaches, such as temporal subsetting of time series for the growing season or growth stages, spatial subsetting of spatial data to include land cover/land use/region/station of interest, and directly integrating into the equations/model/method of assessment. The examples of these approaches are summarized in this section based on the major approaches to integrate impact variables or aspects. In the direct data integration approach, crop yield data or yield variables are directly included in the conditional probability or paired copula method in a few studies (Feng et al., 2019; Ribeiro et al., 2020a; Feng and Hao, 2020). In addition, the vegetation index is used as a direct variable in the vine copula model, and the burned area directly correlates with extremes. However, land cover and land use are integrated by spatial subsetting of the data by Feng et al. (2021c), with the stations or weather grids relating to different land covers, such as croplands, forests, and pastures (Feng et al., 2021c). Several other studies have followed a similar spatial subsetting approach with land use or land cover data to compare CEs for different land uses or land covers (Toreti et al., 2019; Wu et al., 2021d). In another case of spatial subsetting combined with direct variable integration, the population exposure to compound heatwave and ozone is spatially grouped across the spatial distribution of age and income (Ban et al., 2022). Examples of temporal subsettings can be found in Lu et al. (2018) and Wang et al. (2018), where CEs are compared by isolating them into the growing season and phenological stages, respectively (Lu et al., 2018; Wang et al., 2018). Additionally, assessed impacts are temporally sub-divided across CE magnitudes in the case of population mortality in Europe (Hertig et al., 2020) and vegetation vulnerability in southwest China (Liu et al., 2022), along with direct variable integration for both cases. In fact, both subsettings and variable integration approaches have been used in most cases to process spatiotemporal data used in the studies (Gao et al., 2021; Gazol and Camarero, 2022; Kroll et al., 2022). Examples of the major aspects/impact integration approaches are summarized in Table 8.

3.5 Interrelation between ecosystems and CEs

Ecosystems and vegetation productivity are closely inter-related with hydroclimatic extremes because they can affect

TABLE 4 Some key analyzed parameters of drought and heatwaves associated CEs assessed in reviewed publications (n = number of instances the parameter is evaluated in the reviewed articles, var_n = nth variable, t_n = threshold of nth variable).

Analyzed parameter	Example equation
Frequency/% change ($n = 102$)	$F = \dfrac{no.\ of\ CE\ days}{no.\ of\ days\ in\ a\ year/season}$
Spatial extent/trend ($n = 44$)	$Spatial\ extent = \dfrac{pixels\ with\ CEs}{total\ pixels}$
Probability or RPs ($n = 48$)	$JP = P(var1 \leq t_1, var2 \geq t_2)$
	$CP = P(var1 \leq t_1 \vert var2 \leq t_2, var3 \geq t_3)$
	$RPs = \dfrac{1}{Probability}$
Magnitude/severity indicators ($n = 45$)	$SCEI = \varphi^{-1}\{F(JP)\}$
Correlation ($n = 25$)	$r_R = 1 - \dfrac{6\sum_i d_i^2}{n(n^2 - 1)}$

each other. While CEs such as drought and heatwave can affect vegetation productivity in dry and hot regions, reduced vegetation productivity can affect evaporative cooling and soil moisture dynamics to alter surface fluxes and near-surface weather to induce CEs (Li et al., 2021; Kroll et al., 2022). Kroll et al. (2022) reported an association between vegetation productivity and hydroclimatic extremes in 50% of the global study area, with impacts varying across regions. Similarly, Li J. et al. (2022) reported varying impacts of CEs in different regions. For instance, CEs of temperature and precipitation (especially warm and dry or cold and dry events) can significantly reduce vegetation productivity in mid-latitude regions between 23.5°N and 50°N, whereas they may increase productivity in regions with latitude greater than 50°N (Li J. et al., 2022). Additionally, the abundance of dried vegetation caused by sequential wet and dry seasons can create fire weather, followed by fire hazards (Richardson et al., 2022). Moreover, reduced vegetation caused by CE can potentially affect terrestrial carbon dynamics and carbon sequestration, which may reduce crop yield and plant biomass and increase global warming potential (Afroz et al., 2021; Tschumi et al., 2022a; Kroll et al., 2022). Reduced vegetation in one season may also amplify drought in the next season, which can cause lower vegetation productivity with continued effects on the following seasons and productivity

(Li J. et al., 2022b). As vegetation potentially induces CEs, which may impact many other aspects (e.g., yield, air quality, livestock mortality, fire risk, and human health), the direct and indirect relationships among ecosystems, vegetation, and CEs are quite evident.

3.6 Assumptions and limitations of the current study

As this study is conducted by searching WoS with eight search keywords related to CEs, some studies might have been missed in which these keywords are not explicitly mentioned in the titles, abstracts, and keywords of the publications. However, the previously collected publications from "experts" and "Google Scholar" at different timelines did contain these keywords, with most being present in the title, abstract, or keywords of a relevant article of interest. Therefore, the used keywords are assumed to have resulted in a significant number of studies to conduct a systematic review and miss only a negligible number of relevant articles.

This study limits the scope to only the most frequently used approaches and divides the analysis types and frameworks accordingly. Other possible infrequent approaches have not been discussed in this study. Additionally, the hotspot map drawn in this study represents a study area as a more frequently claimed hotspot with dot densities based on the number of global studies claiming that region to be a hotspot. Local studies are excluded from the hotspot map because the study areas do not have similar extents as global studies. In addition, some regions have more relevant articles than others (e.g., United States and China), which would yield higher dot densities in the map, even if the region is not a global hotspot for a particular event combination of CE. Therefore, the regional hotspots are represented as stacked bar plots in this study, and the number of studies is biased by the varying numbers of studies in different regions. However, the hotspot map aims to represent the already reported hotspots from reviewed global publications and how frequently they were found more impacted. The bar plots drawn on regional hotspots aim to represent regional hotspots, which are not the focus of global studies as they report on broader regions. Thus, the study number frequency associated with regional hotspots should not be interpreted as an indicator of the severity of regional hotspots compared with other areas but rather as an

TABLE 5 Categories of compound severities (characterized by SCEI) of compound dry and hot conditions based on a previous publication.

Category	Compound dry and hot condition	Percentile chance	SCEI
1	Abnormal	20 to ≤ 30	−0.5 to −0.7
2	Moderate	10 to ≤ 20	−0.8 to −1.2
3	Severe	5 to ≤ 10	−1.3 to −1.5
4	Extreme	2 to ≤ 5	−1.6 to −1.9
5	Exceptional	≤ 2	−2.0 or less

TABLE 6 Regions detected with major CE-CV association in different seasons.

Drivers	Season/Months	Regions found with CE-CV association	References
ENSO	N/A	Northern South America, central United States, western United States, middle east, eastern Russia, eastern Australia	De Luca et al. (2020b)
	MAM	Central America, western Africa	Mukherjee et al. (2020)
	JJA	Central Europe, Asia	Mukherjee et al. (2020)
	JJA, JAS, ASO	South America, southern Africa, southeastern Asia, Australia	Hao et al. (2018b)
	SON	Southern Australia	Mukherjee et al. (2020),
	DJF	Amazon, southern Africa, and northern Australia, northern South America, northern North America, southeast Asia, Australia	Hao et al. (2019a; 2019b), Mukherjee et al. (2020)
	Summer	India	Mishra et al. (2020)
	Warm Season	Southern North America, northern South America, northern and southern Africa, southern and southeastern Asia, and Australia	Feng and Hao (2021)
	OND	Western and central Africa, the Maritime Continent and northeastern South America, western north America	Richardson et al. (2022)
PDO	N/A	Northern South America, central United States, western United States, middle east, eastern Russia, eastern Australia	De Luca et al. (2020b)
	JJA	Western North America, central North America, Sahara, Mediterranean, eastern Asia, and Tibet, Northern Hemisphere	Mukherjee et al. (2020)
AMO	N/A	Mexico, Brazil, central Africa, the Arabian Peninsula, China, and eastern Russia.	Wu et al. (2019c), De Luca et al. (2020b)
NAO	JJA	Northern Europe, eastern North America	Mukherjee et al. (2020)
EMI	N/A	Eastern China	Ma et al. (2020b)

MAM: March-April-May, JJA: June-July-August, JAS: July-August-September, ASO: August-September-October, SON: September-October-November, DJF: December-January-February, OND: October-November-December, PDO: Pacific Decadal Oscillation, AMO: Atlantic Multi-decadal Oscillation, NAO: North Atlantic Oscillation, EMI: El Niño Modoki Index (EMI).

indicator of the frequency with which they are studied. In addition, the term "hotspot" is used to indicate the most impacted or frequent CE zone in this study based on the reviewed articles, which might have other uses in other climate studies (De Luca et al., 2020a; Ridder et al., 2020; Chiang et al., 2022b; He et al., 2022).

Additionally, in this review, only the large-scale CVs are called "drivers." In contrast, other studies might have claimed that other events or impact variables/aspects are drivers of each other, as CEs, associated events, and impacts can influence each other (Slater et al., 2020; Zhang W. et al., 2021a). However, this study focuses on different analysis frameworks. As the large-scale modes of CVs are mainly assessed as driving forces with different framework components compared with other event–event or event–impact frameworks, they are mentioned as "drivers" in this study.

3.7 Research gaps and potential future works

Recent global and regional studies on CEs have analyzed several characteristics, driver associations, and impacts on several aspects (Hao et al., 2018b; Chiang et al., 2018; Wu et al., 2019b;

2019a). The assessment of frequency, spatial extent, correlations with variables and large-scale climate drivers, severity, probabilities of occurrence, RPs, and durations are among the most analyzed parameters either on a global scale or from a regional perspective in highly studied countries such as the United States, China, India, and Europe. However, global and regional research gaps exist on which future work should be planned.

Although Chinese studies have differentiated the impact on land-cover conditions and growth periods or growing seasons of major crops, the effect has not yet been directly assessed on yield data (Lu et al., 2018; Wang et al., 2018; Chen et al., 2021; Feng and Hao, 2021). The USA-based studies of CEs, as well as compound drought-related extremes, have already covered various aspects, including areas such as the likelihood of compound hot and drought extremes based on copula-based bivariate analysis (Hao et al., 2020b), RP analysis for California drought (AghaKouchak et al., 2014), analysis of statistically significant changes in the distribution of data (Mazdiyasni and AghaKouchak, 2015), the impact of compound drought and hot events on maize yield (Feng and Hao, 2020), analyzing shifts in temperature under various

TABLE 7 Methods to assess relations of large-scale modes of CVs as drivers.

References	Drivers	CEs	Relative variables	Study area	Study timeline	Methods to connect CVs and CEs
De Luca et al. (2020b)	ENSO, PDO, AMO	Concurrent wet and dry extremes	Monthly PDSI and CVs	Global	1950–2014	Spearman's rank correlation test, partial correlation
Wu et al. (2019c)	ENSO, AO, NAO, AMO, PDO, EA/WR	Wet/warm, dry/warm, wet/cold, dry/cold	Spatial extent of CE and CVs seasonal average	China	1961–2014	Pearson correlation coefficients
Ma et al. (2020b)	EMI	Concurrent dry and hot events	EMI and observed drought-related variables (V850, PW, VV500, P)	China (east)	1960–2019	Regression
Mukherjee et al. (2020)	ENSO, PDO, NAO	Compound drought and heatwave	Average seasonal CVs and (seasonal average T or P)	Global	1982–2016	Spearman's rank correlation test, Poisson GLM
Mishra et al. (2020)	ENSO	Hot and dry summer	Niño 3.4 anomaly and (T anomaly, SPEI)	India	1951–2018	Comparison of time series, correlation
Hao et al. (2019b)	ENSO, PDO, NAO	Compound dry and hot events	SCEI and lagged 1, 3-months Niño 3.4, post SCEI | prior SCEI, SNINO	Global	1980–2018	Correlation, conditional distribution model, LRM
Hao et al. (2018b)	ENSO	Compound dry and hot events	Niño 3.4 and (P, or T), CE| Niño 3.4: 0–2 months	Global	1951–2016	Correlation, LRM, odd ratio, CP empirical
Hao et al. (2019a)	ENSO	Compound dry and hot events	SCEI and Niño 3.4, post-SCEI | prior-SCEI, SNINO: 1 and 3 months	Southern Africa	1951–2016	Kendall's rank correlation, CP
Feng and Hao (2021)	ENSO	Compound dry and hot events	ONI and spatial extent of CEs, P-T correlation separation by ENSO, and neutral years	Global	1950–2018	Correlation, empirical probability, temporal subsetting across ENSO years
Richardson et al. (2022)	ENSO, DMI, SAM, PNA, GAR	Fire weather and meteorological drought	Niño 3.4, DMI, SAM, PNA, GAR, and BA	Global (western United States, eastern Australia)	1970–2020	Plotted comparison
Shi et al. (2020)	ENSO, AO	Dry and wet events	(ENSO, AO) and CE dynamics	China (YRB)	1952–2000	Correlation
Wu et al. (2021c)	NAO, PDO, ENSO	Compound dry and hot events	CVs and (P, T, SCEI)	China	1921–2016	Correlation, LR, composite analysis

AO: Arctic Oscillation, EA/WR: East Atlantic/Western Russia pattern, GLM: Poisson Generalized Linear Model, V850: meridional wind at 850 hPa, PW: precipitable water, VV500: vertical velocity at 500 hPa, ONI: Oceanic Niño Index, YRB: Yellow River Basin, DMI: Dipole Mode Index, PNA: Pacific North American Index; SAM, Southern Annular Mode Index; GAR, Gulf of Alaska Ridge Index.

dryness conditions (Chiang et al., 2018), the occurrence of windy events with dry and hot conditions in the Great Plains of the United States (Tavakol et al., 2020), and the impact of ozone due to heatwave and stagnation (Zhang et al., 2018, 2020). However, the impacts on other major field crops (e.g., cotton, peanut, and soybean) and vegetation vulnerability are yet to be addressed.

For Europe, impacts such as forest mortality resulting from drought and heatwave (Gazol and Camarero, 2022), compound ozone and heatwave (Hertig et al., 2020; Jahn and Hertig, 2022), and various temperature and precipitation combinations have been assessed (Sedlmeier et al., 2016, 2018). However, other event combinations and impacts on crops, urbanization, and other aspects also need to

be addressed in this region. For Australia, very few event combinations, such as drought and heatwave, strong winds, and heavy precipitation, are covered (Ridder et al., 2022a; Reddy et al., 2022); however, many other aspects (e.g., drought and fire risk, heatwave and ozone, warm and humid events, and drought and aridity), for which several parts of Australia have been deemed as global hotspots, have not yet been addressed from a regional perspective. The same is true for other hotspot regions, such as South Africa and South America (Tencer et al., 2016; Weber et al., 2020). In comparison to the United States and China, studies on other parts of the world have covered fewer aspects; however, they have included some local aspects that have not yet been covered in other regions, for example, the impact

TABLE 8 Examples of CE impacts assessed on several variables/aspects in reviewed publications and major impact integration approaches (there may be additional approaches and variables/aspects in the references listed under each integration approach; only some examples of each approach are listed here).

Major impact integration approaches	Study region	Variable/aspect integrated	Major methods	References
Spatial Subsetting	Global	Crop (maize) producing regions	POT	Feng et al. (2021a)
	China	LULC, land-surface conditions	POT	Feng et al. (2021c)
	China	Urban lands (from LULC)	POT, GFDL land model	Liao et al. (2021a)
	China	Urban lands (from LULC)	POT	Wu et al. (2021b)
	South China	Urban lands (from LULC, population density)	POT	Wu et al. (2021a)
Temporal Subsetting	China	Crop (maize and wheat) growing season	POT	Lu et al. (2018)
	China	Crop (maize) growing season (across phenological phases)	POT	Wang et al. (2018)
Direct Variable Integration	Global (maize producing countries)	Crop (maize) yield	meta-gaussian model	Feng et al. (2019a), Feng and Hao (2020), Feng et al. (2021b)
	Spain	Crop (wheat and barley) yield	Copula-based PCC	Ribeiro et al. (2020a)
	India	Crop yield	Correlation	Mishra et al. (2020)
	USA	Crop yield	Regression	Haqiqi et al. (2021)
	China (Xinjiang)	Vegetation biomass/indices	Copula-based CP, correlation	Li et al. (2021)
	IP	Fire risk variable (burned area)	POT, correlation	Bento et al. (2022)
Spatial and Temporal Subsettings	Global	Crop (maize and wheat) producing seasons, and regions	POT, statistical decomposition	Lesk and Anderson (2021)
	Global	Crop (wheat) producing seasons, and regions	IRMS	Toreti et al. (2019)
	Global	LULC (land, cropland)	POT, LMF	Wu et al. (2021d)
Subsettings and Variable Integration	Global	Crop yield (wheat), growing season, and region	POT, OLS regression	He et al. (2022)
	Global	Vegetation biomass/indices	POT, correlation	Kroll et al. (2022)
	Global	Vegetation biomass/indices	Copula, partial correlation	Li et al. (2022b)
	Global	Vegetation biomass/ indices	Meta-gaussian model	Wu and Jiang (2022)
	Global	Vegetation biomass/indices	DGVM, POT	Tschumi et al. (2022b)
	Global	Vegetation biomass/indices (carbon uptake)	Copula-based JP	Zhou et al. (2019b)
	Global	Population (exposure across age, income)	POT	Ban et al. (2022)
	Global	Fire risk variable (FFDI, burned area)	POT, plotting	Richardson et al. (2022)
	USA	Air quality variable (ozone)	POT, WRF/Chem model, Regression, Correlation	Zhang et al. (2018)
	USA	Air quality variable (ozone, PM 2.5), population (exposure, mortality, morbidity)	POT, WRF-chem, BenMAP-CE 1.3, pooled method	Zhang et al. (2020)
	Europe	SM	Copula-based PCC	Manning et al. (2018)
	Europe	vegetation biomass/ indices (tree mortality across CE magnitudes)	Copula	Gazol and Camarero (2022)
	Europe	Population (mortality, population)	POT	Hertig et al. (2020)

TABLE 8 (*Continued*) Examples of CE impacts assessed on several variables/aspects in reviewed publications and major impact integration approaches (there may be additional approaches and variables/aspects in the references listed under each integration approach; only some examples of each approach are listed here).

Major impact integration approaches	Study region	Variable/aspect integrated	Major methods	References
	Europe and MB	Vegetation biomass/indices (land degradation)	POT	Mulder et al. (2019)
	India	Population (exposure across CE combinations and SSPs)	POT, exposure Statistics	Das et al. (2022)
	China	Urban lands (from LULC)	POT, correlation, and regression	Yang et al. (2022)
	Eastern China	Urban lands (from population), population (exposure)	POT	Yu and Zhai (2020a)
	Southwest China	Vegetation biomass/indices	Copula-based RP	Liu et al. (2022)
	UK	Livestock mortality+ potato blight	POT, risk density	Garry et al. (2021)
	West Africa	LULC (reforestation)	RegCM4-model (vegetation on-off)	Camara et al. (2022)
	Southern Africa	Vegetation biomass/indices	Correlation, plotting	Hao et al. (2020a)
	Mongolia	Livestock mortality	POT, spatial clustering	Haraguchi et al. (2022)
	Northeast China	Crop (maize) yield	POT, APSIM model	Li et al. (2022a)
	Brazil (Pantanal, Xingu)	Fire risk variable (burned area)	Poisson regression, contours	Ribeiro et al. (2022)

LULC: Land Use and Land Cover, PCC: Pair Copula Construction, LMF: Likelihood Multiplication Factor, MVR: Multivariate Regression, RegCM4: Regional, WRF/Chem model: Weather Research and Forecasting model coupled with Chemistry, FFID: Forest Fire Danger Index, IRMS: Intensity-Reweighted Moment Stationarity, DGVM: Dynamic Global Vegetation Model, IP: Iberian Peninsula, UNB: Upper Nile Basin, OLS: Ordinary Linear Regression.

of reforestation on warm and dry, and warm and wet CEs in western Africa (Camara et al., 2022).

Other than drought and heatwave, the number of global studies has been limited for other event combinations (Figure 3). As the results are subjective to the studies identified in this literature review, a higher number of global studies can provide more hotspots produced from different data sources, timelines, and event/variable combinations, which are likely to provide more varied results. Even though global studies have covered various impacts and aspects such as population exposure to ozone and heatwave (Ban et al., 2022), maize yield vulnerability (Feng et al., 2019; 2021a), wheat growing season (He et al., 2022; Wu and Jiang, 2022), vegetation vulnerability (Kroll et al., 2022), population exposure to heat and humidity (Li et al., 2020), fire risk caused by drought and heatwaves (Ridder et al., 2020; Richardson et al., 2022), and various large-scale CVs related to CEs (Mukherjee et al., 2020; Mukherjee and Mishra, 2021), other potential aspects such as the effect of urbanization on CEs, concurrent day and nighttime heat extremes, and the impact of CEs on mortality/health are yet to be addressed on a global scale. These unexplored CEs and aspects on a global scale have been assessed in regional studies, showing significantly increasing trends and effects/impacts, respectively. Therefore, future research may

include studies on other event combinations besides drought and heatwave as well as on potential aspects that include further knowledge in the CE analysis field. More studies on these unexplored topics can help find more global hotspots, trends, events, and impacts across various regions, timelines, and different data sources.

Although an analysis framework has been suggested and proposed in a previous review along with definitions of CEs, three major analysis frameworks applied across related articles that focus on drought- and heatwave-associated CEs have been categorized and summarized in this systematic review (Leonard et al., 2014). The same applies to the included hotspots reported in recent studies. Previous reviews have covered several other topics, such as statistical approaches, upcoming CEs, categorization of CEs, and mutual dependence patterns (Supplementary Table S3). However, the components of analytical frameworks and hotspots for drought- and heatwave-associated CEs are unexplored areas that have been comprehensively covered in this review. However, considering scope, this review limitedly summarizes the most frequently used methods and parameters. Thus, future work can potentially focus on infrequent methods, parameters and upcoming machine-learning-based approaches (Feng et al., 2021d; Sweet and Zscheischler, 2022).

4 Conclusion

This novel review presents an overall breakdown of the quantitative assessment of drought- and heatwave-associated CEs by mainly focusing on their hotspots, variables, analysis frameworks, assessed parameters, association with large-scale CVs as drivers, and impacts of CEs on several aspects. While hotspot mapping reveals the most frequently reported regions with CEs as per the reviewed global studies, event and variable combinations represent the variables/indices most commonly used to define combinations of events to form CEs. The most reported hotspots worldwide are found in Southern Africa, several parts of South America, Southeast Asia, South Asia, and Australia for various CE combinations studied in several global studies. As per the review, the most analyzed parameters of the considered CEs are frequency, spatial extent, compound indicator-based severity/magnitude of CEs, probability, RPs, duration, and correlation. While the frequency and spatial extent are usually assessed with the binary counting approach in the POT method, probabilities are determined using copula-based joint probability, conditional probability, and empirical probability approaches (Ye et al., 2019a; Wu et al., 2019b; Hao et al., 2019c). The most assessed large-scale mode of CV is found to be ENSO, whereas the impacts are found to be yield loss of several globally important crops, vegetation vulnerability, fire risk, air quality, urbanization effect, and CE frequencies under different land-use conditions (Hao et al., 2018b; Feng and Hao, 2020; Gao et al., 2020; Feng et al., 2021c; Kroll et al., 2022; Richardson et al., 2022). Therefore, this study breaks down the components of CE analysis frameworks into variables/ indices, frequently calculated parameters, drivers, impacts, and associated methods. This study can aid future researchers in understanding the framework components of drought- and heatwave-associated CEs with reduced time and effort.

Data availability statement

The original contributions presented in the study are included in the article/Supplementary Material. Further inquiries can be directed to the corresponding author.

References

Author contributions

MA and AA conceptualized the study. The methodology design, data collection, and visualization were performed by MA. AA and GC supervised the research and acquired the funding. All authors contributed to the writing and editing of this manuscript.

Conflict of interest

The authors declare that the research was conducted in the absence of any commercial or financial relationships that could be construed as a potential conflict of interest.

Publisher's note

All claims expressed in this article are solely those of the authors and do not necessarily represent those of their affiliated organizations or those of the publisher, the editors, and the reviewers. Any product that may be evaluated in this article, or claim that may be made by its manufacturer, is not guaranteed or endorsed by the publisher.

Supplementary material

The Supplementary Material for this article can be found online at: https://www.frontiersin.org/articles/10.3389/feart.2022.914437/full#supplementary-material

Afroz, M., Li, R., Chen, G., and Anandhi, A. (2021). Agricultural greenhouse gas emissions in a data-scarce region using a scenario-based modeling approach: A case study in southeastern USA. *Agronomy* 11, 1323. doi:10.3390/agronomy11071323

AghaKouchak, A., Cheng, L., Mazdiyasni, O., and Farahmand, A. (2014). Global warming and changes in risk of concurrent climate extremes: Insights from the 2014 California drought: Global Warming and Concurrent Extremes. *Geophys. Res. Lett.* 41, 8847–8852. doi:10.1002/2014GL062308

AghaKouchak, A., Chiang, F., Huning, L. S., Love, C. A., Mallakpour, I., Mazdiyasni, O., et al. (2020). Climate extremes and compound hazards in a warming world. *Annu. Rev. Earth Planet. Sci.* 48, 519–548. doi:10.1146/annurev-earth-071719-055228

Ambika, A. K., and Mishra, V. (2021). Modulation of compound extremes of low soil moisture and high vapor pressure Deficit by irrigation in India. *Geophys. Res. Atmos.* 126. doi:10.1029/2021JD034529

Anandhi, A., Sharma, A., and Sylvester, S. (2018). Can meta-analysis be used as a decision-making tool for developing scenarios and causal chains in eco-hydrological systems? Case study in Florida. *Ecohydrology* 11, e1997.

Ban, J., Lu, K., Wang, Q., and Li, T. (2022). Climate change will amplify the inequitable exposure to compound heatwave and ozone pollution. *One Earth* 5, 677–686. doi:10.1016/j.oneear.2022.05.007

Ben-Ari, T., Boé, J., Ciais, P., Lecerf, R., Van der Velde, M., and Makowski, D. (2018). Causes and implications of the unforeseen 2016 extreme yield loss in the breadbasket of France. *Nat. Commun.* 9, 1627. doi:10.1038/s41467-018-04087-x

Bento, V. A., Russo, A., Gouveia, C. M., and DaCamara, C. C. (2022). Recent change of burned area associated with summer heat extremes over Iberia. *Int. J. Wildland Fire* 31, 658–669. doi:10.1071/WF21155

Bezak, N., and Mikoš, M. (2020). Changes in the compound drought and extreme heat occurrence in the 1961–2018 period at the European scale. *Water* 12, 3543. doi:10.3390/w12123543

Brunner, M. I., Gilleland, E., and Wood, A. W. (2021). Space-time dependence of compound hot-dry events in the United States: Assessment using a multi-site multi-variable weather generator. *Earth Syst. Dyn. Discuss.* 1–19. doi:10.5194/esd-2021-5

Camara, M., Diba, I., and Diedhiou, A. (2022). Effects of land cover changes on compound extremes over west Africa using the regional climate model RegCM4. *Atmosphere* 13, 421. doi:10.3390/atmos13030421

Chen, Y., Liao, Z., Shi, Y., Tian, Y., and Zhai, P. (2021). Detectable increases in sequential flood-heatwave events across China during 1961–2018. *Geophys. Res. Lett.* 48. doi:10.1029/2021GL092549

Cheng, L., Hoerling, M., Liu, Z., and Eischeid, J. (2019). Physical understanding of human-induced changes in U.S. Hot droughts using equilibrium climate simulations. *J. Clim.* 32, 4431–4443. doi:10.1175/JCLI-D-18-0611.1

Cheraghalizadeh, M., Ghameshlou, A. N., Bazrafshan, J., and Bazrafshan, O. (2018). A copula-based joint meteorological–hydrological drought index in a humid region (Kasilian basin, North Iran). *Arab. J. Geosci.* 11, 300. doi:10.1007/s12517-018-3671-7

Chiang, F., Cook, B. I., McDermid, S., Marvel, K., Schmidt, G. A., Nazarenko, L. S., et al. (2022a). Responses of compound daytime and nighttime warm-dry and warm-humid events to individual anthropogenic forcings. *Environ. Res. Lett.* 17, 084015. doi:10.1088/1748-9326/ac80ce

Chiang, F., Greve, P., Mazdiyasni, O., Wada, Y., and AghaKouchak, A. (2022b). Intensified likelihood of concurrent warm and dry months attributed to anthropogenic climate change. *Water Resour. Res.* 58. doi:10.1029/2021WR030411

Chiang, F., Mazdiyasni, O., and AghaKouchak, A. (2018). Amplified warming of droughts in southern United States in observations and model simulations. *Sci. Adv.* 4, eaat2380. doi:10.1126/sciadv.aat2380

Coffel, E. D., Keith, B., Lesk, C., Horton, R. M., Bower, E., Lee, J., et al. (2019). Future hot and dry years worsen Nile Basin water scarcity despite projected precipitation increases. *Earth's. Future* 7, 967–977. doi:10.1029/2019EF001247

Das, J., Manikanta, V., and Umamahesh, N. V. (2022). Population exposure to compound extreme events in India under different emission and population scenarios. *Sci. Total Environ.* 806, 150424. doi:10.1016/j.scitotenv.2021.150424

De Luca, P., Messori, G., Faranda, D., Ward, P. J., and Coumou, D. (2020a). Compound warm–dry and cold–wet events over the Mediterranean. *Earth Syst. Dynam.* 11, 793–805. doi:10.5194/esd-11-793-2020

De Luca, P., Messori, G., Wilby, R. L., Mazzoleni, M., and Di Baldassarre, G. (2020b). Concurrent wet and dry hydrological extremes at the global scale. *Earth Syst. Dynam.* 11, 251–266. doi:10.5194/esd-11-251-2020

Esteban, E. J. L., Castilho, C. V., Melgaço, K. L., and Costa, F. R. C. (2021). The other side of droughts: Wet extremes and topography as buffers of negative drought effects in an amazonian forest. *New Phytol.* 229, 1995–2006. doi:10.1111/nph.17005

Feng, S., and Hao, Z. (2020). Quantifying likelihoods of extreme occurrences causing maize yield reduction at the global scale. *Sci. Total Environ.* 704, 135250. doi:10.1016/j.scitotenv.2019.135250

Feng, S., and Hao, Z. (2021). Quantitative contribution of ENSO to precipitation-temperature dependence and associated compound dry and hot events. *Atmos. Res.* 260, 105695. doi:10.1016/j.atmosres.2021.105695

Feng, S., Hao, Z., Wu, X., Zhang, X., and Hao, F. (2021a). A multi-index evaluation of changes in compound dry and hot events of global maize areas. *J. Hydrology* 602, 126728. doi:10.1016/j.jhydrol.2021.126728

Feng, S., Hao, Z., Zhang, X., and Hao, F. (2021b). Changes in climate-crop yield relationships affect risks of crop yield reduction. *Agric. For. Meteorology* 304, 108401. doi:10.1016/j.agrformet.2021.108401

Feng, S., Hao, Z., Zhang, X., and Hao, F. (2019). Probabilistic evaluation of the impact of compound dry-hot events on global maize yields. *Sci. Total Environ.* 689, 1228–1234. doi:10.1016/j.scitotenv.2019.06.373

Feng, Y., Liu, W., Sun, F., and Wang, H. (2021c). Changes of compound hot and dry extremes on different land surface conditions in China during 1957–2018. *Int. J. Climatol.* 41, E1085–E1099. doi:10.1002/joc.6755

Feng, Y., Maulik, R., Wang, J., Balaprakash, P., Huang, W., Rao, V., et al. (2021d). Characterization of extremes and compound impacts: Applications of machine learning and interpretable neural networks. *Artif. Intell. Earth Syst. Predict. AI4ESP* 34, 176298.

Gao, H., Luo, Y., Jiang, X., Zhang, D.-L., Chen, Y., Wang, Y., et al. (2021). A statistical analysis of extreme hot characteristics and their relationships with urbanization in southern China during 1971–2020. *J. Appl. Meteorology Climatol.* 60, 1301–1317. doi:10.1175/jamc-d-21-0012.1

Gao, Y., Zhang, J., Yan, F., Leung, L. R., Luo, K., Zhang, Y., et al. (2020). Nonlinear effect of compound extreme weather events on ozone formation over the United States. *Weather Clim. Extrem.* 30, 100285. doi:10.1016/j.wace.2020.100285

Garry, F. K., Bernie, D. J., Davie, J. C. S., and Pope, E. C. D. (2021). Future climate risk to UK agriculture from compound events. *Clim. Risk Manag.* 32, 100282. doi:10.1016/j.crm.2021.100282

Gazol, A., and Camarero, J. J. (2022). Compound climate events increase tree drought mortality across European forests. *Sci. total Environ.* 816, 151604. doi:10.1016/j.scitotenv.2021.151604

Geirinhas, J. L., Russo, A., Libonati, R., Sousa, P. M., Miralles, D. G., and Trigo, R. M. (2021). Recent increasing frequency of compound summer drought and heatwaves in Southeast Brazil. *Environ. Res. Lett.* 16, 034036. doi:10.1088/1748-9326/abe0eb

Goodess, C. M. (2013). How is the frequency, location and severity of extreme events likely to change up to 2060? *Environ. Sci. Policy* 27, S4–S14. doi:10.1016/j.envsci.2012.04.001

Gouveia, C. M., Bistinas, I., Liberato, M. L. R., Bastos, A., Koutsias, N., and Trigo, R. (2016). The outstanding synergy between drought, heatwaves and fuel on the 2007 Southern Greece exceptional fire season. *Agric. For. Meteorology* 218–219, 135–145. doi:10.1016/j.agrformet.2015.11.023

Hao, Y., Hao, Z., Feng, S., Zhang, X., and Hao, F. (2020a). Response of vegetation to El Niño-Southern Oscillation (ENSO) via compound dry and hot events in southern Africa. *Glob. Planet. Change* 195, 103358. doi:10.1016/j.gloplacha.2020.103358

Hao, Z., Hao, F., Singh, V. P., Xia, Y., Shi, C., and Zhang, X. (2018a). A multivariate approach for statistical assessments of compound extremes. *J. Hydrology* 565, 87–94. doi:10.1016/j.jhydrol.2018.08.025

Hao, Z., Hao, F., Singh, V. P., and Zhang, X. (2018b). Quantifying the relationship between compound dry and hot events and El Niño–southern Oscillation (ENSO) at the global scale. *J. Hydrology* 567, 332–338. doi:10.1016/j.jhydrol.2018.10.022

Hao, Z., Hao, F., Singh, V. P., and Zhang, X. (2019a). Statistical prediction of the severity of compound dry-hot events based on El Niño-Southern Oscillation. *J. Hydrology* 572, 243–250. doi:10.1016/j.jhydrol.2019.03.001

Hao, Z., Hao, F., Xia, Y., Singh, V. P., and Zhang, X. (2019b). A monitoring and prediction system for compound dry and hot events. *Environ. Res. Lett.* 14, 114034. doi:10.1088/1748-9326/ab4df5

Hao, Z., Li, W., Singh, V. P., Xia, Y., Zhang, X., and Hao, F. (2020b). Impact of dependence changes on the likelihood of hot extremes under drought conditions in the United States. *J. Hydrology* 581, 124410. doi:10.1016/j.jhydrol.2019.124410

Hao, Z., Singh, V., and Hao, F. (2018c). Compound extremes in hydroclimatology: A review. *Water* 10, 718. doi:10.3390/w10060718

Hao, Z., and Singh, V. P. (2020). Compound events under global warming: A dependence perspective. *J. Hydrol. Eng.* 25, 03120001. doi:10.1061/(ASCE)HE.1943-5584.0001991

Hao, Z., Zhang, X., Singh, V. P., and Hao, F. (2020c). Joint modeling of precipitation and temperature under influences of El Niño Southern Oscillation for compound event evaluation and prediction. *Atmos. Res.* 245, 105090. doi:10.1016/j.atmosres.2020.105090

Haqiqi, I., Grogan, D. S., Hertel, T. W., and Schlenker, W. (2021). Quantifying the impacts of compound extremes on agriculture. *Hydrol. Earth Syst. Sci.* 25, 551–564. doi:10.5194/hess-25-551-2021

Haraguchi, M., Davi, N., Rao, M. P., Leland, C., Watanabe, M., and Lall, U. (2022). Estimating return intervals for extreme climate conditions related to winter disasters and livestock mortality in Mongolia. *Nat. Hazards Earth Syst. Sci.* 22, 2751–2770. doi:10.5194/nhess-22-2751-2022

He, X., and Sheffield, J. (2020). Lagged compound occurrence of droughts and pluvials globally over the past seven decades. *Geophys. Res. Lett.* 47, e2020GL087924. doi:10.1029/2020GL087924

He, Y., Fang, J., Xu, W., and Shi, P. (2022). Substantial increase of compound droughts and heatwaves in wheat growing seasons worldwide. *Intl. J. Climatol.* 42, 5038–5054. doi:10.1002/joc.7518

Hertig, E., Russo, A., and Trigo, R. M. (2020). Heat and ozone pollution waves in central and South europe—characteristics, weather types, and association with mortality. *Atmosphere* 11, 1271. doi:10.3390/atmos11121271

Jahn, S., and Hertig, E. (2022). Using clustering, statistical modeling, and climate change projections to analyze recent and future region-specific compound ozone and temperature burden over Europe. *GeoHealth* 6, e2021GH000561. doi:10.1029/2021gh000561

Kirono, D. G. C., Hennessy, K. J., and Grose, M. R. (2017). Increasing risk of months with low rainfall and high temperature in southeast Australia for the past 150years. *Clim. Risk Manag.* 16, 10–21. doi:10.1016/j.crm.2017.04.001

Kong, Q., Guerreiro, S. B., Blenkinsop, S., Li, X.-F., and Fowler, H. J. (2020). Increases in summertime concurrent drought and heatwave in Eastern China. *Weather Clim. Extrem.* 28, 100242. doi:10.1016/j.wace.2019.100242

Kopp, R., Easterling, D., Hall, T., Hayhoe, K., Horton, R., Kunkel, K., et al. (2017). Potential surprises – compound extremes and tipping elements. *Publ. Agencies Staff U.S. Dep. Commer.* Available at: https://digitalcommons.unl.edu/usdeptcommercepub/578.

Kroll, J., Denissen, J. M. C., Migliavacca, M., Li, W., Hildebrandt, A., and Orth, R. (2022). Spatially varying relevance of hydrometeorological hazards for vegetation productivity extremes. *Biogeosciences* 19, 477–489. doi:10.5194/bg-19-477-2022

Leonard, M., Westra, S., Phatak, A., Lambert, M., van den Hurk, B., McInnes, K., et al. (2014). A compound event framework for understanding extreme impacts. *WIREs Clim. Change* 5, 113–128. doi:10.1002/wcc.252

Lesk, C., and Anderson, W. (2021). Decadal variability modulates trends in concurrent heat and drought over global croplands. *Environ. Res. Lett.* 16, 055024. doi:10.1088/1748-9326/abeb35

Li, D., Yuan, J., and Kopp, R. E. (2020). Escalating global exposure to compound heat-humidity extremes with warming. *Environ. Res. Lett.* 15, 064003. doi:10.1088/1748-9326/ab7d04

Li, E., Zhao, J., Pullens, J. W., and Yang, X. (2022a). The compound effects of drought and high temperature stresses will be the main constraints on maize yield in Northeast China. *Sci. Total Environ.* 812, 152461. doi:10.1016/j.scitotenv.2021.152461

Li, H. W., Li, Y. P., Huang, G. H., and Sun, J. (2021). Quantifying effects of compound dry-hot extremes on vegetation in Xinjiang (China) using a vine-copula conditional probability model. *Agric. For. Meteorology* 311, 108658. doi:10.1016/j.agrformet.2021.108658

Li, J., Bevacqua, E., Chen, C., Wang, Z., Chen, X., Myneni, R. B., et al. (2022b). Regional asymmetry in the response of global vegetation growth to springtime compound climate events. *Commun. Earth Environ.* 3, 123–129. doi:10.1038/s43247-022-00455-0

Liao, W., Li, D., Malyshev, S., Shevliakova, E., Zhang, H., and Liu, X. (2021a). Amplified increases of compound hot extremes over urban land in China. *Geophys. Res. Lett.* 48, e2020GL091252. doi:10.1029/2020gl091252

Liao, Z., Chen, Y., Li, W., and Zhai, P. (2021b). Growing threats from unprecedented sequential flood-hot extremes across China. *Geophys. Res. Lett.* 48, e2021GL094505. doi:10.1029/2021gl094505

Libonati, R., Geirinhas, J. L., Silva, P. S., Russo, A., Rodrigues, J. A., Belém, L. B. C., et al. (2022). Assessing the role of compound drought and heatwave events on unprecedented 2020 wildfires in the Pantanal. *Environ. Res. Lett.* 17, 015005. doi:10.1088/1748-9326/ac462e

Liu, L., Jiang, Y., Gao, J., Feng, A., Jiao, K., Wu, S., et al. (2022). Concurrent climate extremes and impacts on ecosystems in southwest China. *Remote Sens.* 14, 1678. doi:10.3390/rs14071678

Lu, Y., Hu, H., Li, C., and Tian, F. (2018). Increasing compound events of extreme hot and dry days during growing seasons of wheat and maize in China. *Sci. Rep.* 8, 16700. doi:10.1038/s41598-018-34215-y

Ma, Q., Zhang, J., Game, A. T., Chang, Y., and Li, S. (2020a). Spatiotemporal variability of summer precipitation and precipitation extremes and associated large-scale mechanisms in Central Asia during 1979–2018. *J. Hydrology X* 8, 100061. doi:10.1016/j.hydroa.2020.100061

Ma, S., Zhu, C., and Liu, J. (2020b). Combined impacts of warm central equatorial pacific sea surface temperatures and anthropogenic warming on the 2019 severe drought in East China. *Adv. Atmos. Sci.* 37, 1149–1163. doi:10.1007/s00376-020-0077-8

Manning, C., Widmann, M., Bevacqua, E., Loon, A. F. V., Maraun, D., and Vrac, M. (2019). Increased probability of compound long-duration dry and hot events in Europe during summer (1950–2013). *Environ. Res. Lett.* 14, 094006. doi:10.1088/1748-9326/ab23bf

Manning, C., Widmann, M., Bevacqua, E., Loon, A. F. V., Maraun, D., and Vrac, M. (2018). Soil moisture drought in Europe: A compound event of precipitation and potential evapotranspiration on multiple time scales. *J. Hydrometeorol.* 19, 1255–1271. doi:10.1175/JHM-D-18-0017.1

Marengo, J. A., Ambrizzi, T., Barreto, N., Cunha, A. P., Ramos, A. M., Skansi, M., et al. (2022). The heat wave of October 2020 in central South America. *Intl. J. Climatol.* 42, 2281–2298. doi:10.1002/joc.7365

Matthews, T., Wilby, R. L., and Murphy, C. (2019). An emerging tropical cyclone–deadly heat compound hazard. *Nat. Clim. Chang.* 9, 602–606. doi:10.1038/s41558-019-0525-6

Mazdiyasni, O., and AghaKouchak, A. (2015). Substantial increase in concurrent droughts and heatwaves in the United States. *Proc. Natl. Acad. Sci. U. S. A.* 112, 11484–11489. doi:10.1073/pnas.1422945112

Miao, C., Sun, Q., Duan, Q., and Wang, Y. (2016). Joint analysis of changes in temperature and precipitation on the Loess Plateau during the period 1961–2011. *Clim. Dyn.* 47, 3221–3234. doi:10.1007/s00382-016-3022-x

Mishra, V., Aadhar, S., and Mahto, S. S. (2021). Anthropogenic warming and intraseasonal summer monsoon variability amplify the risk of future flash droughts in India. *npj Clim. Atmos. Sci.* 4, 1–10. doi:10.1038/s41612-020-00158-3

Mishra, V., Thirumalai, K., Singh, D., and Aadhar, S. (2020). Future exacerbation of hot and dry summer monsoon extremes in India. *npj Clim. Atmos. Sci.* 3, 10–19. doi:10.1038/s41612-020-0113-5

Mukherjee, S., Ashfaq, M., and Mishra, A. K. (2020). Compound drought and heatwaves at a global scale: The role of natural climate variability-associated synoptic patterns and land-surface energy budget anomalies. *J. Geophys. Res. Atmos.* 125, e2019JD031943. doi:10.1029/2019JD031943

Mukherjee, S., and Mishra, A. K. (2021). Increase in compound drought and heatwaves in a warming world. *Geophys. Res. Lett.* 48, e2020GL090617. doi:10.1029/2020GL090617

Mukherjee, S., and Mishra, V. (2018). A sixfold rise in concurrent day and night-time heatwaves in India under 2 °C warming. *Sci. Rep.* 8, 16922. doi:10.1038/s41598-018-35348-w

Mulder, V. L., van Eck, C. M., Friedlingstein, P., Arrouays, D., and Regnier, P. (2019). Controlling factors for land productivity under extreme climatic events in continental Europe and the Mediterranean Basin. *Catena* 182, 104124. doi:10.1016/j.catena.2019.104124

Naveendrakumar, G., Vithanage, M., Kwon, H.-H., Chandrasekara, S. S. K., Iqbal, M. C. M., Pathmarajah, S., et al. (2019). South asian perspective on temperature and rainfall extremes: A review. *Atmos. Res.* 225, 110–120. doi:10.1016/j.atmosres.2019.03.021

Peng, P., Lin, X., Ünal, Z. E., Lee, K., Namkung, J., Chow, J., et al. (2020). Examining the mutual relations between language and mathematics: A meta-analysis. *Psychol. Bull.* 146, 595–634. doi:10.1037/bul0000231

Qiao, Y., Xu, W., Wu, D., Meng, C., Qin, L., Li, Z., et al. (2022). Changes in the spatiotemporal patterns of dry/wet abrupt alternation frequency, duration, and severity in Mainland China, 1980–2019. *Sci. Total Environ.* 838, 156521. doi:10.1016/j.scitotenv.2022.156521

Raymond, C., Horton, R. M., Zscheischler, J., Martius, O., AghaKouchak, A., Balch, J., et al. (2020). Understanding and managing connected extreme events. *Nat. Clim. Chang.* 10, 611–621. doi:10.1038/s41558-020-0790-4

Raymond, C., Matthews, T., Horton, R. M., Fischer, E. M., Fueglistaler, S., Ivanovich, C., et al. (2021). On the controlling factors for globally extreme humid heat. *Geophys. Res. Lett.* 48, e2021GL096082. doi:10.1029/2021GL096082

Reddy, P. J., Perkins-Kirkpatrick, S. E., Ridder, N. N., and Sharples, J. J. (2022). Combined role of ENSO and IOD on compound drought and heatwaves in Australia using two CMIP6 large ensembles. *Weather Clim. Extrem.*, 100469.

Ribeiro, A. F., Brando, P. M., Santos, L., Rattis, L., Hirschi, M., Hauser, M., et al. (2022). A compound event-oriented framework to tropical fire risk assessment in a changing climate. *Environ. Res. Lett.* 17, 065015. doi:10.1088/1748-9326/ac7342

Ribeiro, A. F. S., Russo, A., Gouveia, C. M., Páscoa, P., and Zscheischler, J. (2020a). Risk of crop failure due to compound dry and hot extremes estimated with nested copulas. *Biogeosciences* 17, 4815–4830. doi:10.5194/bg-17-4815-2020

Ribeiro, A. F. S., Russo, A., Gouveia, C. M., and Pires, C. A. L. (2020b). Drought-related hot summers: A joint probability analysis in the iberian Peninsula. *Weather Clim. Extrem.* 30, 100279. doi:10.1016/j.wace.2020.100279

Richardson, D., Black, A. S., Irving, D., Matear, R. J., Monselesan, D. P., Risbey, J. S., et al. (2022). Global increase in wildfire potential from compound fire weather and drought. *npj Clim. Atmos. Sci.* 5, 23–12. doi:10.1038/s41612-022-00248-4

Ridder, N. N., Pitman, A. J., and Ukkola, A. M. (2022a). High impact compound events in Australia. *Weather Clim. Extrem.* 36, 100457. doi:10.1016/j.wace.2022.100457

Ridder, N. N., Pitman, A. J., Westra, S., Ukkola, A., Do, H. X., Bador, M., et al. (2020). Global hotspots for the occurrence of compound events. *Nat. Commun.* 11, 5956. doi:10.1038/s41467-020-19639-3

Ridder, N. N., Ukkola, A. M., Pitman, A. J., and Perkins-Kirkpatrick, S. E. (2022b). Increased occurrence of high impact compound events under climate change. *npj Clim. Atmos. Sci.* 5, 3–8. doi:10.1038/s41612-021-00224-4

Russo, A., Gouveia, C. M., Dutra, E., Soares, P. M. M., and Trigo, R. M. (2019). The synergy between drought and extremely hot summers in the Mediterranean. *Environ. Res. Lett.* 14, 014011. doi:10.1088/1748-9326/aaf09e

Sedlmeier, K., Feldmann, H., and Schädler, G. (2018). Compound summer temperature and precipitation extremes over central Europe. *Theor. Appl. Climatol.* 131, 1493–1501. doi:10.1007/s00704-017-2061-5

Sedlmeier, K., Mieruch, S., Schädler, G., and Kottmeier, C. (2016). Compound extremes in a changing climate – A Markov chain approach. *Nonlin. Process. Geophys.* 23, 375–390. doi:10.5194/npg-23-375-2016

Sharma, S., and Mujumdar, P. (2017). Increasing frequency and spatial extent of concurrent meteorological droughts and heatwaves in India. *Sci. Rep.* 7, 15582. doi:10.1038/s41598-017-15896-3

Shi, W., Huang, S., Liu, D., Huang, Q., Leng, G., Wang, H., et al. (2020). Dry and wet combination dynamics and their possible driving forces in a changing environment. *J. Hydrology* 589, 125211. doi:10.1016/j.jhydrol.2020.125211

Slater, L. J., Anderson, B., Buechel, M., Dadson, S., Han, S., Harrigan, S., et al. (2020). Nonstationary weather and water extremes: A review of methods for their detection, attribution, and management. *Hydrology Earth Syst. Sci. Discuss.*, 1–54. doi:10.5194/hess-2020-576

Sutanto, S. J., Vitolo, C., Di Napoli, C., D'Andrea, M., and Van Lanen, H. A. J. (2020). Heatwaves, droughts, and fires: Exploring compound and cascading dry hazards at the pan-European scale. *Environ. Int.* 134, 105276. doi:10.1016/j.envint. 2019.105276

Sweet, L., and Zscheischler, J. (2022). Using interpretable machine learning to identify compound meteorological drivers of crop yield failure. *Copernic. Meet.* 322, 743.

Tavakol, A., Rahmani, V., and Harrington, J. (2020). Probability of compound climate extremes in a changing climate: A copula-based study of hot, dry, and windy events in the central United States. *Environ. Res. Lett.* 15, 104058. doi:10.1088/1748-9326/abb1ef

Tencer, B., Bettolli, M. L., and Rusticucci, M. (2016). Compound temperature and precipitation extreme events in southern South America: Associated atmospheric circulation, and simulations by a multi-RCM ensemble. *Clim. Res.* 68, 183–199. doi:10.3354/cr01396

Toreti, A., Cronie, O., and Zampieri, M. (2019). Concurrent climate extremes in the key wheat producing regions of the world. *Sci. Rep.* 9, 5493. doi:10.1038/s41598-019-41932-5

Tschumi, E., Lienert, S., van der Wiel, K., Joos, F., and Zscheischler, J. (2022a). A climate database with varying drought-heat signatures for climate impact modelling. *Geoscience Data J.* 9, 154–166. doi:10.1002/gdj3.129

Tschumi, E., Lienert, S., van der Wiel, K., Joos, F., and Zscheischler, J. (2022b). The effects of varying drought-heat signatures on terrestrial carbon dynamics and vegetation composition. *Biogeosciences* 19, 1979–1993. doi:10.5194/bg-19-1979-2022

Vogel, J., Paton, E., Aich, V., and Bronstert, A. (2021). Increasing compound warm spells and droughts in the Mediterranean Basin. *Weather Clim. Extrem.* 32, 100312. doi:10.1016/j.wace.2021.100312

Vorobevskii, I., Kronenberg, R., and Bernhofer, C. (2022). Linking different drought types in a small catchment from a statistical perspective–Case study of the Wernersbach catchment, Germany. *J. Hydrology X* 15, 100122. doi:10.1016/j. hydroa.2022.100122

Wang, J., Chen, Y., Liao, W., He, G., Tett, S. F., Yan, Z., et al. (2021). Anthropogenic emissions and urbanization increase risk of compound hot extremes in cities. *Nat. Clim. Chang.* 11, 1084–1089. doi:10.1038/s41558-021-01196-2

Wang, L., Liao, S., Huang, S., Ming, B., Meng, Q., and Wang, P. (2018). Increasing concurrent drought and heat during the summer maize season in Huang–Huai–Hai Plain, China. *Int. J. Climatol.* 38, 3177–3190. doi:10.1002/joc.5492

Weber, T., Bowyer, P., Rechid, D., Pfeifer, S., Raffaele, F., Remedio, A. R., et al. (2020). Analysis of compound climate extremes and exposed population in Africa under two different emission scenarios. *Earth's Future* 8, e2019EF001473. doi:10. 1029/2019ef001473

Wu, S., Chan, T. O., Zhang, W., Ning, G., Wang, P., Tong, X., et al. (2021a). Increasing compound heat and precipitation extremes elevated by urbanization in South China. *Front. Earth Sci.* 9. Available at: https://www.frontiersin.org/articles/ 10.3389/feart.2021.636777 (Accessed September 23, 2022).

Wu, S., Wang, P., Tong, X., Tian, H., Zhao, Y., and Luo, M. (2021b). Urbanization-driven increases in summertime compound heat extremes across China. *Sci. Total Environ.* 799, 149166. doi:10.1016/j.scitotenv.2021.149166

Wu, X., Hao, Z., Hao, F., Li, C., and Zhang, X. (2019a). Spatial and temporal variations of compound droughts and hot extremes in China. *Atmosphere* 10, 95. doi:10.3390/atmos10020095

Wu, X., Hao, Z., Hao, F., Singh, V. P., and Zhang, X. (2019b). Dry-hot magnitude index: A joint indicator for compound event analysis. *Environ. Res. Lett.* 14, 064017. doi:10.1088/1748-9326/ab1ec7

Wu, X., Hao, Z., Hao, F., Zhang, X., Singh, V. P., and Sun, C. (2021c). Influence of large-scale circulation patterns on compound dry and hot events in China. *JGR. Atmos.* 126, e2020JD033918. doi:10.1029/2020JD033918

Wu, X., Hao, Z., Hao, F., and Zhang, X. (2019c). Variations of compound precipitation and temperature extremes in China during 1961–2014. *Sci. Total Environ.* 663, 731–737. doi:10.1016/j.scitotenv.2019.01.366

Wu, X., Hao, Z., Tang, Q., Singh, V. P., Zhang, X., and Hao, F. (2021d). Projected increase in compound dry and hot events over global land areas. *Int. J. Climatol.* 41, 393–403. doi:10.1002/joc.6626

Wu, X., Hao, Z., Zhang, X., Li, C., and Hao, F. (2020). Evaluation of severity changes of compound dry and hot events in China based on a multivariate multi-index approach. *J. Hydrology* 583, 124580. doi:10.1016/j.jhydrol.2020. 124580

Wu, X., and Jiang, D. (2022). Probabilistic impacts of compound dry and hot events on global gross primary production. *Environ. Res. Lett.* 17, 034049. doi:10. 1088/1748-9326/ac4c5b

Xu, F., and Luo, M. (2019). Changes of concurrent drought and heat extremes in the arid and semi-arid regions of China during 1961–2014. *Atmos. Sci. Lett.* 20, e947. doi:10.1002/asl.947

Yang, Y., Zhao, N., Wang, Y., and Chen, M. (2022). Variations in summertime compound heat extremes and their connections to urbanization in China during 1980–2020. *Environ. Res. Lett.* 17, 064024. doi:10.1088/1748-9326/ac61c5

Ye, L., Shi, K., Xin, Z., Wang, C., and Zhang, C. (2019a). Compound droughts and heat waves in China. *Sustainability* 11, 3270. doi:10.3390/su11123270

Ye, L., Shi, K., Xin, Z., Wang, C., and Zhang, C. (2019b). Rapid increase in the compound droughts and heat waves in China. *AGU Fall Meet. Abstr. 41.* Available at: http://adsabs.harvard.edu/abs/2019AGUFM (Accessed February 12, 2021).

Yu, R., and Zhai, P. (2020a). Changes in compound drought and hot extreme events in summer over populated eastern China. *Weather Clim. Extrem.* 30, 100295. doi:10.1016/j.wace.2020.100295

Yu, R., and Zhai, P. (2020b). More frequent and widespread persistent compound drought and heat event observed in China. *Sci. Rep.* 10, 14576. doi:10.1038/s41598-020-71312-3

Zhan, W., He, X., Sheffield, J., and Wood, E. F. (2020). Projected seasonal changes in large-scale global precipitation and temperature extremes based on the CMIP5 ensemble. *J. Clim.* 33, 5651–5671. doi:10.1175/JCLI-D-19-0311.1

Zhang, J., Gao, Y., Luo, K., Leung, L. R., Zhang, Y., Wang, K., et al. (2018). Impacts of compound extreme weather events on ozone in the present and future. *Atmos. Chem. Phys.* 18, 9861–9877. doi:10.5194/acp-18-9861-2018

Zhang, W., Luo, M., Gao, S., Chen, W., Hari, V., and Khouakhi, A. (2021a). Compound hydrometeorological extremes: Drivers, mechanisms and methods. *Front. Earth Sci.* 9, 673495. doi:10.3389/feart.2021.673495

Zhang, Y., Yang, P., Gao, Y., Leung, R. L., and Bell, M. L. (2020). Health and economic impacts of air pollution induced by weather extremes over the continental US. *Environ. Int.* 143, 105921. doi:10.1016/j.envint.2020.105921

Zhang, Y., Yang, X., and Chen, C. (2021b). Substantial decrease in concurrent meteorological droughts and consecutive cold events in Huai River Basin, China. *Int. J. Climatol.* 41, 6065–6083. doi:10.1002/joc.7168

Zhou, P., and Liu, Z. (2018). Likelihood of concurrent climate extremes and variations over China. *Environ. Res. Lett.* 13, 094023. doi:10.1088/1748-9326/aade9e

Zhou, S., Williams, A. P., Berg, A. M., Cook, B. I., Zhang, Y., Hagemann, S., et al. (2019a). Land–atmosphere feedbacks exacerbate concurrent soil drought and atmospheric aridity. *Proc. Natl. Acad. Sci. U. S. A.* 116, 18848–18853. doi:10.1073/pnas.1904955116

Zhou, S., Zhang, Y., Park Williams, A., and Gentine, P. (2019b). Projected increases in intensity, frequency, and terrestrial carbon costs of compound drought and aridity events. *Sci. Adv.* 5, eaau5740. doi:10.1126/sciadv. aau5740

Zong, L., Yang, Y., Xia, H., Gao, M., Sun, Z., Zheng, Z., et al. (2022). Joint occurrence of heatwaves and ozone pollution and increased health risks in beijing, China: Role of synoptic weather pattern and urbanization. *Atmos. Chem. Phys.* 22, 6523–6538. doi:10.5194/acp-22-6523-2022

Zscheischler, J., Martius, O., Westra, S., Bevacqua, E., Raymond, C., Horton, R. M., et al. (2020). A typology of compound weather and climate events. *Nat. Rev. Earth Environ.* 1, 333–347. doi:10.1038/s43017-020-0060-z

Zscheischler, J., and Seneviratne, S. I. (2017). Dependence of drivers affects risks associated with compound events. *Sci. Adv.* 3, e1700263. doi:10.1126/sciadv. 1700263

Frontiers in
Earth Science

Investigates the processes operating within the major spheres of our planet

Advances our understanding across the earth sciences, providing a theoretical background for better use of our planet's resources and equipping us to face major environmental challenges.

Discover the latest Research Topics

See more →

frontiers

Frontiers in
Earth Science

frontiers | Research Topics